UNIVERSITAT DE BARCELONA

Polynuclear manganese compounds with carboxylate bridging ligands models of redox enzymes. Insertion inside mesoporous supports. Study of their magnetic and catalytic properties

Luis Escriche Tur

Polynuclear manganese compounds with carboxylate bridging ligands models of redox enzymes. Insertion inside mesoporous supports. Study of their magnetic and catalytic properties.

Luis Escriche Tur

UNIVERSITAT DE BARCELONA

ENS DE LYON

Lyon 1

Polynuclear manganese compounds with carboxylate bridging ligands models of redox enzymes. Insertion inside mesoporous supports. Study of their magnetic and catalytic properties.

Luis Escriche Tur

UNIVERSITAT DE BARCELONA

ENS DE LYON

Lyon 1

Programa de doctorat: Química Inorgànica Molecular

Títol de la tesi: Polynuclear manganese compounds with carboxylate bridging ligands models of redox enzymes. Insertion inside mesoporous supports. Study of their magnetic and catalytic properties.

Doctorand: Luis Escriche Tur

Directors/es:

Montserrat Corbella Cordomí
Departament de Química Inorgànica
i Orgànica (Secció Inorgànica)
Facultat de Química
Unviversitat de Barcelona

Belén Albela
Laboratoire de Chimie

École Normale Supérieure de Lyon
Université de Lyon-1

Catalan version:

Montserrat Corbella Cordomí, Professora Titular del Departament de Química Inorgànica i Orgànica (Secció Inorgànica) de la Facultat de Química de la Universitat de Barcelona, i Belén Albela, "maître de conférences" al Laboratoire de Chimie de l'École Normale Supérieure de Lyon,

CERTIFIQUEN: que el treball titulat "Polynuclear manganese compounds with carboxylate bridging ligands models of redox enzymes. Insertion inside mesoporous supports. Study of their magnetic and catalytic properties." que presenta el Sr. Luis Escriche Tur per optar al grau de Doctor per la Universitat de Barcelona i l'Université de Lyon-1 ha estat realitzat sota la seva direcció en règim de cotutela en el marc d'un conveni entre la Universitat de Barcelona i l'École Normale Supérieure de Lyon, el treball de la qual ha estat realitzat al Departament de Química Inorgànica i Orgànica (Secció Inorgànica) i al Laboratoire de Chimie de l'École Normale Supérieure de Lyon.

Barcelona, 12 de setembre de 2016.

French version:

Montserrat CORBELLA CORDOMI, « Professora Titular » du département de Chimie Inorganique et Organique (Section Inorganique) de la Faculté de Chimie de l'Université de Barcelona, et Belén ALBELA, maître de conférences du Laboratoire de Chimie de l'École Normale Supérieure de Lyon,

CERTIFIENT : que le travail avec le titre « Polynuclear manganese compounds with carboxylate bridging ligands models of redox enzymes. Insertion inside mesoporous supports. Study of their magnetic and catalytic properties. » qu'est présenté par Mr. Luis ESCRICHE TUR en vue de l'obtention du grade de Docteur de l'Université de Lyon-1 et l'Université de Barcelona a été réalisé sous sa direction en régime de cotutelle dans le cadre d'une convention entre l'Université de Barcelona et l'École Normale Supérieure de Lyon, le travail de laquelle a été réalisé au Département de Chimie Inorganique et Organique (Section Inorganique) de la Faculté de Chimie de l'Université de Barcelona et au Laboratoire de Chimie de l'École Normale Supérieure de Lyon.

Barcelona, 12 septembre 2016.

Montserrat Corbella Cordomí Belén Albela

Catalan version:

Montserrat Corbella Cordomí, Professora Titular del Departament de Química Inorgànica i Orgànica (Secció Inorgànica) de la Facultat de Química de la Universitat de Barcelona,

CERTIFICA: que ha sigut la tutora responsable dels estudis de Doctorat realitzats dins del programa de Doctorat de Química Inorgànica Molecular pel Sr. Luis Escriche Tur.

Barcelona, 12 de setembre de 2016.

French version:

Montserrat CORBELLA CORDOMI, professeure du département de Chimie Inorganique et Organique (Section Inorganique) de la Faculté de Chimie de l'Université de Barcelona,

CERTIFIE : qu'elle a été la tutrice des études de Doctorat réalisés dans le programme de Doctorat de Chimie Inorganique Moléculaire pour Mr. Luis ESCRICHE TUR.

Barcelona, 12 septembre 2016.

Montserrat Corbella Cordomí

SUMMARY

1. Summary in English

Manganese compounds are of relevance because of their interesting magnetic and catalytic properties. For instance, since the discovery of the first single-molecule magnet, manganese compounds have been a huge matter of interest for the development of information storage devices and for the study of fundamental properties, such as single-ion anisotropy and magnetic interactions. Moreover, the active site of several metalloproteins comprises mono- or polynuclear manganese complexes. Owing to the existence of amino acids containing carboxylate groups and the nature of the physiological media, carboxylate and oxo bridges play an important role for the structure and reactivity of metalloproteins. Last but not the least, these bio-systems do not only consist of a catalytic site, since metal ions are surrounded by a very precise environment. This morphology gives place to enzymatic cavities with the required hydrophobicity and size that guarantee their effectiveness. For this work, the most important metalloproteins are manganese catalases (Mn-CAT) and the water oxidizing center (WOC) in photosystem II (PSII).

Mn-CATs are enzymes found in some acid lactic bacteria that are in charge of the catalytic H_2O_2 decomposition. Their active site comprises a Mn_2O_2 unit where the Mn oxidation state alternates between II and III. Owing to the harmful properties of H_2O_2 and the decontrolled and undesired presence of this oxidant in some pathologies, antioxidant therapies with synthetic catalases are considered in order to prevent or soften the possible injurious reactions of H_2O_2.

The WOC in PSII, which consists of a heterometallic $[Mn_4CaO_5]$ cubane-like cluster, performs the light-induced oxidation of H_2O to O_2. Even though there are a huge number of related studies, the role of Ca^{2+} in the catalytic cycle of water oxidation is still incompletely understood. Moreover, Sr^{2+} can eventually replace Ca^{2+} and display similar (but not equal) chemical properties. Therefore, synthetic Mn-Ca^{2+}/Sr^{2+} WOC-biomimetic compounds may indirectly provide useful information to understand the role of Ca^{2+} in the WOC.

Biomimetic compounds provide a unique way for investigating the chemical properties of active sites. Indeed, the structural determination of the active site can be performed using biomimetic compounds as models. However, their success is limited when reactivity is at stake, since confinement is absent. The insertion of biomimetic compounds in porous solids

offers the possibility of mimicking different properties found in the native catalytic site, such as hydrophobicity and confinement. This could solve the limitations observed in molecular analogues and open up new challenges in molecular recognition.

The results presented in this manuscript are classified in sections, which concern molecular chemistry (Section I), materials science (Section II), and catalytic properties (Section III). Then, each section was divided in several chapters: a brief introduction explaining the techniques and some generalities regarding the subsequent results, named Introductory Remarks; the Experimental Section; and between two and five chapters exposing the results and discussion, separated in order to guarantee a continuous reading.

SECTION I

In this Section the syntheses, characterizations, and magnetic properties of manganese compounds with oxidation states II, III, or IV are presented. All compounds were synthesized using benzoic acid derivatives *n*-RC_6H_4COOH, where *n*-R = 2-MeO, 3-MeO, 4-MeO, or 4-^{t}Bu, 2,2'-bipyridine (bpy) or 1,10-phenantroline (phen), and two different counter-anions (X), NO_3^- and ClO_4^-. From these experiments, twenty-six new compounds were obtained, from which twenty-one crystal structures have been determined. More precisely, the structural determination was performed for seven dinuclear Mn^{III} compounds, $[\{Mn^{III}_2O(bpy)(L)\}_2(\mu\text{-}O)(\mu\text{-}n\text{-}RC_6H_4COO)_2]X_2$ (L = solvent or counter-anion); two heterometallic clusters, $[Mn^{IV}_6M_2O_9(4\text{-}^tBuC_6H_4COO)_{10}(4\text{-}^tBuC_6H_4COOH)_5]$ (M = Ca^{2+} or Sr^{2+}); two tetranuclear systems, $[Mn^{III}_4O_2(4\text{-}RC_6H_4COO)_{7-m}(L)_{2m}(phen)_2](ClO_4)_{1+m}$ (R = MeO or ^{t}Bu); one dodecanuclear compound $[Mn_{12}O_{12}(3\text{-}MeOC_6H_4COO)_{16}(H_2O)_4]$; and eleven mono- or polynuclear Mn^{II} compounds.

Regarding the magnetic properties, the magnetic susceptibility as a function of the temperature was studied for all compounds, and a rationalization of the nature and magnitude of the magnetic interactions is reported and related to their structural and electronic factors. For the dinuclear Mn^{III} compounds the magnetization versus temperature plots at different magnetic fields were recorded, and their analyses allowed us to determine the single-ion zero-field splitting parameters (D_{Mn} and E_{Mn}). Moreover, we studied the effect of the relative orientation of the Jahn-Teller axes on the magnetic properties. Extensive magneto-structural correlations were performed with twenty-six analogous Mn^{III}_2 compounds, including the ones presented here.

For the Mn^{II} compounds electron paramagnetic resonance (EPR) spectra have also been recorded and analyzed. With the simulation and fits of the EPR spectra of these compounds the zero-field splitting parameters (D_{Mn} and E_{Mn}) have been determined.

Particularly, for the two heterometallic Mn^{IV}-Ca^{2+}/Sr^{2+} compounds the magnetic properties have also been analyzed with the support of density functional theory (DFT) calculations (carried out by G. Aullón and J. Jover from the University of Barcelona). In spite of the diamagnetic character of the alkaline earth ions, their influence on the magnetic behavior has been evidenced and correlated with their polarizing effect. Moreover, these results are consistent with other Mn-Ca^{2+}/Sr^{2+} compounds that are models of the active site of photosystem II. These studies pave the way to understand the role of Ca^{2+} ion in the catalyzed water oxidation by photosystem II.

The tetranuclear compounds, which have $[Mn^{III}_4O_2]^{8+}$ cores, exhibit an unusual ground state ($S = 0$) for this kind of tetranuclear compound. This result was explained with the analysis of the spin states distribution. In addition, the effect of the axial zero-field splitting, D_{Mn}, and the relative orientation of the Jahn-Teller axes on the magnetic properties for these compounds was also investigated.

Finally, the dodecanuclear compound, with $[Mn^{IV}_4Mn^{III}_8O_{12}]^{16+}$ core, exhibits the behavior of a single-molecule magnet, showing slow relaxation processes of the magnetization at low temperature.

SECTION II

As mentioned before, the insertion of biomimetic compounds in porous materials could lead to the improvement of the catalytic properties. The aforementioned dinuclear Mn^{III} compounds are models of the active site of Mn-catalases. Therefore, two of these dinuclear compounds were inserted in two mesoporous silica supports (MCM-41 type, with 2D hexagonal array), one without organic function and the other functionalized with pyridyl moieties. Materials loading different amounts of Mn complex were prepared to lately see the effect of the Mn concentration on the catalysis. The morphology of the resulting materials was characterized with X-ray diffraction (XRD), N_2 sorption isotherms, and transmission electron microscopy (TEM). The molecular properties of these hybrid materials were determined with several techniques, such as solid nuclear magnetic resonance (NMR), X-ray photoelectron spectroscopy (XPS), elemental analyses, inductively coupled plasma optical emission spectrometry (ICP-OES), infrared (IR) spectroscopy, thermogravimetric analyses

(TGA), and magnetic measurements, using the molecular compounds as models when needed. The results show that the hexagonal array of the silica remains intact after the functionalization and insertion of the compounds. Moreover, the dinuclear Mn^{III}_2 unit seems to be preserved inside the mesopores.

Secondly, mesoporous silica (MCM-41) was prepared and functionalized with four different groups: *n*-propyl (C_3), *n*-octyl (C_8), phenyl (Ph), and *para*-(ethoxycarbonyl)phenyl (EtO_2CPh) silanes. These supports were prepared to subsequently incorporate hydrophobic and neutral compounds, for instance, the heterometallic or dodecanuclear compounds mentioned above. The dodecanuclear compound was successfully inserted in the Ph-modified silica, without showing severe modifications of its magnetic properties (preserving the SMM behavior). The Mn-Ca^{2+} compound was inserted in both the C_3- and Ph-modified supports. However, the structure of this cluster is altered when inserted in the mesopores.

The ester function of the EtO_2CPh-modified silica was converted to carboxylic group by high-temperature acid hydrolysis. This support will be tested for the grafting of molecular manganese compounds with benzoate ligands.

SECTION III

In this section the catalase activities of both molecular Mn^{III}_2 compounds, $[\{Mn^{III}_2O(bpy)(L)\}_2(\mu\text{-}O)(\mu\text{-}n\text{-}RC_6H_4COO)_2]X_2$, and Mn-$SiO_2$ materials that are models of the native Mn-catalase are reported. Note that while the molecular compounds are just models of the active site of the native enzyme, the hybrid materials aim to mimic both the active site and the protein fold, providing the active site with confinement.

The molecular compounds display catalytic activity toward the H_2O_2 decomposition in acetonitrile, evidencing that they are not only structural but also functional models of the catalase active site. Their efficiency was compared and related to the electronic effects promoted by the R group and to the interactions with the X counter-anions (NO_3^- and ClO_4^-). However, these molecular compounds display no activity in water solution, due to the low stability of the Mn_2 unit in water solution and to the lack of confinement.

The non-functionalized hybrid material shows catalase activity in acetonitrile and it is more efficient than the corresponding molecular compounds. This fact is likely due to the presence of silanolate groups in the solid that buffers a basic pH and favors the catalyzed H_2O_2

decomposition. According to EPR spectroscopy and XPS analyses, the reaction seems to take place inside the support, and the Mn oxidation state likely swings between II and III.

Contrary to the molecular compounds, this material is active in pure water. However, the mesostructure of this material is disrupted during the reaction. Hence, functionalization of the pores was tested in order to increase the stability of both the silica walls and the Mn complex.

The catalase activities of the pyridyl-modified Mn-SiO_2 materials containing different amounts of molecular compound were tested. The results revealed that the catalase activity of these materials is dependent not only on the concentration of active center (Mn complex) but also on its local distribution in the pores. The pyridyl-modified materials showed a better stability than those non-functionalized, since the mesostructured is preserved after the reaction in water.

2. Resum (Summary in Catalan)

Els compostos de manganès pertanyen a un camp d'investigació rellevant degut a l'interès que desperten les seves propietats magnètiques i catalítiques. Per exemple, des del descobriment del primer imant unimolecular, els compostos de manganès han adquirit rellevància sent objecte d'estudi per al desenvolupament de dispositius d'emmagatzematge d'informació i per a l'estudi de propietats fonamentals, com l'anisotropia dels ions i les interaccions magnètiques. A més, el centre actiu de moltes metal·loproteïnes està format per complexos mono- o polinuclears de manganès. Degut a l'existència d'aminoàcids que contenen grups carboxilat i de la naturalesa del medi fisiològic, els ponts carboxilat i oxo juguen un important paper en l'estructura i reactivitat de les metal·loproteïnes. Per últim però no el menys important, l'activitat d'aquests sistemes biològics no depèn només del centre actiu, ja que els ions metàl·lics estan envoltats d'un "plec proteic" molt precís. Aquesta morfologia dóna lloc a cavitats enzimàtiques amb la hidrofobicitat requerida i grandàries que garanteixen la seva efectivitat. Per aquest treball, les metal·loproteïnes més rellevants són les catalases de manganès (Mn-CAT) i el centre d'oxidació de l'aigua (WOC) en el fotosistema II (PSII).

Les Mn-CATs són enzims que es troben en alguns bacteris d'àcid làctic i que duen a terme la descomposició catalítica del H_2O_2. El centre actiu d'aquests enzims consisteix en una unitat Mn_2O_2 en la que l'estat d'oxidació del Mn alterna entre II i III. Degut a les propietats nocives

del H_2O_2 i a la presència descontrolada i no desitjada d'aquest oxidant en algunes patologies, s'estan desenvolupant teràpies antioxidants mitjançant catalases sintètiques amb la finalitat de prevenir o suavitzar els possibles danys causats pel H_2O_2.

El WOC en el PSII, que consisteix en un clúster heterometàl·lic [Mn_4CaO_5], duu a terme l'oxidació del H_2O a O_2 induïda per la llum solar. Tot i que hi ha un gran nombre d'estudis sobre el tema, el paper del Ca^{2+} en el cicle catalític de l'oxidació del H_2O no està completament clar. A més, el Sr^{2+} pot substituir eventualment al Ca^{2+}, mostrant propietats químiques similars (però no idèntiques). Per aquesta raó, compostos heterometàl·lics de Mn-Ca^{2+}/Sr^{2+} poden aportar indirectament informació útil per comprendre millor el paper del Ca^{2+} en el WOC.

Els compostos biomimètics són una bona eina per investigar les propietats químiques dels centres actius. De fet, es pot dur a terme la determinació estructural del centre actiu utilitzant compostos biomimètics com a models. Tot i així, el seu èxit es veu limitat quan la reactivitat entra en escena, ja que s'obvia el confinament. La inserció de compostos biomimètics en sílice mesoporosa ofereix la possibilitat de mimetitzar diferents propietats que presenta el centre actiu de la proteïna, com la hidrofobicitat o el confinament. Això podria donar una solució a les limitacions que s'observen en anàlegs moleculars i pot obrir la porta a nous reptes en reconeixement molecular.

Els resultats que es presenten en aquest manuscrit es classifiquen en seccions, les quals corresponen a la química molecular (Secció I), la ciència de materials (Secció II) i les propietats catalítiques (Secció III). Aleshores, cada secció es divideix en diversos capítols que consten de: una breu introducció explicant les tècniques i algunes generalitats dels resultats d'aquella secció, anomenada Comentaris Introductoris; la Secció Experimental; i entre dos i cinc capítols exposant els resultats i discussió, que s'han separat amb la finalitat de garantir una lectura contínua.

SECCIÓ I

En aquesta secció es presenta la síntesi, caracterització i propietats magnètiques de compostos de manganès amb estats d'oxidació II, III o IV. Tots aquests compostos s'han sintetitzat utilitzant derivats de l'àcid benzoic *n*-RC_6H_4COOH, on *n*-R = 2-MeO, 3-MeO, 4-MeO o 4-^{t}Bu, 2,2'-bipiridina (bpy) o 1,10-fenantrolina (phen), i dos contraions (X) diferents, NO_3^- i ClO_4^-. A partir d'aquests experiments, s'han obtingut vint-i-sis compostos, i s'ha resolt l'estructura cristal·lina de vint-i-un d'ells. Més concretament, s'ha dut a terme la

caracterització estructural de set compostos dinuclears de Mn^{III}, $[\{Mn^{III}_2O(bpy)(L)\}_2(\mu\text{-}O)(\mu\text{-}n\text{-}RC_6H_4COO)_2]X_2$ (L = dissolvent o contraió), de dos clústers heterometàl·lics, $[Mn^{IV}_6M_2O_9(4\text{-}^tBuC_6H_4COO)_{10}(4\text{-}^tBuC_6H_4COOH)_5]$ (M = Ca^{2+} o Sr^{2+}), de dos sistemes tetranuclears, $[Mn^{III}_4O_2(4\text{-}RC_6H_4COO)_{7-m}(L)_{2m}(phen)_2](ClO_4)_{1+m}$ (R = MeO o ^{t}Bu), un compost dodecanuclear $[Mn_{12}O_{12}(3\text{-}MeOC_6H_4COO)_{16}(H_2O)_4]$ i onze compostos mono- o polinuclears de Mn^{II}.

En quant a les propietats magnètiques, s'ha estudiat la susceptibilitat magnètica en funció de la temperatura per a tots els compostos i se n'ha racionalitzat la naturalesa i la magnitud de la interacció magnètica en relació a paràmetres estructurals i electrònics. Pels compostos dinuclears de Mn^{III}, s'han enregistrat les magnetitzacions enfront de la temperatura a diferents camps magnètics, i el seu anàlisi ha permès determinar els paràmetres de desdoblament a camp nul dels ions Mn (D_{Mn} i E_{Mn}). A més, s'ha estudiat l'efecte de l'orientació relativa dels eixos Jahn-Teller en les propietats magnètiques. S'han dut a terme unes extenses correlacions magneto-estructurals amb vint-i-sis compostos anàlegs de Mn^{III}, incloent els que es presenten en aquest treball.

Pels compostos de Mn^{II} s'han enregistrat i analitzat els espectres de ressonància paramagnètica electrònica (EPR). A partir de la simulació i ajustos dels espectres d'aquests compostos, s'han pogut determinar els paràmetres de desdoblament a camp nul dels ions Mn (D_{Mn} i E_{Mn}).

Concretament pels dos compostos heterometàl·lics Mn^{IV}-Ca^{2+}/Sr^{2+}, les propietats magnètiques s'han analitzat amb el suport de càlculs basats en la teoria del funcional de la densitat (DFT) (realitzats per G. Aullón i J. Jover de la Universitat de Barcelona). Malgrat el caràcter diamagnètic dels ions alcalinoterris, s'ha posat de manifest la seva influència en el comportament magnètic i s'ha correlacionat amb el seu caràcter polaritzant. A més, aquests resultats són consistents amb els obtinguts per altres compostos Mn^{IV}-Ca^{2+}/Sr^{2+} models del centre actiu del fotosistema II. Aquests estudis són una base per entendre el paper del Ca^{2+} en la catàlisi d'oxidació de l'aigua duta a terme pel fotosistema II.

Els compostos tetranuclears, amb *core* $[Mn^{III}_4O_2]^{8+}$, exhibeixen un estat fonamental $S = 0$, que és inusual per aquests tipus de compostos. L'explicació a aquest resultat s'ha trobat analitzant la distribució d'estats d'espín. A més, també s'ha estudiat l'efecte de l'anisotropia axial, D_{Mn}, i l'orientació relativa dels eixos Jahn-Teller en les propietats magnètiques.

Finalment, el compost dodecanuclear, amb *core* $[Mn^{IV}_4Mn^{III}_8O_{12}]^{16+}$, exhibeix el comportament esperat per un imant unimolecular, mostrant un procés de relaxació lenta de la magnetització a baixa temperatura.

SECCIÓ II

Com s'ha comentat anteriorment, la inserció de compostos biomimètics en materials porosos pot proporcionar millores importants en les propietats catalítiques. Els compostos dinuclears de Mn^{III} que s'han mencionat anteriorment són models del centre actiu de les Mn-CATs. Per aquesta raó, s'han inserit dos d'aquests compostos en dos suports de sílice mesoporosa (del tipus MCM-41, amb distribució hexagonal), una sense funció orgànica i l'altre funcionalitzada amb grups piridil. S'han preparat materials carregant diferents quantitats de complex de manganès per veure posteriorment quin és l'efecte de la concentració de Mn en la catàlisi. La morfologia dels materials resultants s'ha caracteritzat per difracció de raig X (XRD), isotermes de sorció de N_2 i microscòpia electrònica de transmissió (TEM). Les propietats moleculars d'aquests materials híbrids s'han determinat amb l'ajuda de diverses tècniques, com per exemple, ressonància magnètica nuclear (NMR), espectroscòpia de fotoelectrons emesos per raig X (XPS), anàlisis elementals, espectroscòpia d'emissió òptica de plasma d'acoblament inductiu (ICP-OES), espectroscòpia d'infraroig (IR), anàlisi termogravimètric (TGA) i mesures magnètiques, fent servir els compostos moleculars com a referència quan és necessari. Els resultats mostren que la distribució hexagonal de la sílice mesoporosa roman intacta després de la funcionalització i la inserció dels compostos. A més, sembla que l'entitat dinuclear Mn^{III}_2 es conserva a dins dels mesoporus.

Per una altra banda, s'ha preparat la sílice mesoporosa (MCM-41) i s'ha funcionalitzat amb quatre grups diferents: els silans amb grups *n*-propil, (C_3), *n*-octil (C_8), fenil (Ph) i *para*-(etoxicarbonil)fenil (EtO_2CPh). Aquests suports s'han preparat per a la incorporació de compostos hidrofòbics i neutres, com per exemple, els compostos heterometàl·lics i el dodecanuclear mencionats abans. La inserció del compost dodecanuclear en sílice mesoporosa modificada amb grups fenil ha donat bons resultats i el nou material no mostra grans canvis en les seves propietats magnètiques (preservant el comportament d'imant unimolecular). El compost de Mn-Ca^{2+} s'ha inserit en suports funcionalitzats tant amb grups *n*-propil com fenil. No obstant, l'estructura dels clústers canvia quan s'insereix en els mesoporus.

La funció èster del material funcionalitzat amb *para*-(etoxicarbonil)fenil s'ha convertit en grup carboxílic, mitjançant un procés d'hidròlisi àcida a alta temperatura. Aquest suport es farà servir en un futur per a l'ancoratge de compostos de manganès amb lligands benzoat.

SECCIÓ III

En aquesta secció es presenta l'activitat catalasa dels compostos moleculars Mn^{III}_2, $[\{Mn^{III}_2O(bpy)(L)\}_2(\mu\text{-}O)(\mu\text{-}n\text{-}RC_6H_4COO)_2]X_2$, i dels materials Mn-$SiO_2$ que són models del centre actiu de les Mn-CAT. S'ha de tenir en compte que, mentre que els compostos de coordinació només són models del centre actiu de l'enzim natiu, els materials híbrids aspiren a mimetitzar el centre actiu en el plec proteic.

Els compostos moleculars exhibeixen activitat catalítica enfront la descomposició del H_2O_2, evidenciant que no només són models estructurals del centre actiu de les catalases sinó també que són models funcionals. La seva eficàcia s'ha comparat i correlacionat amb els efectes electrònics promoguts pels grups R i amb les interaccions a través dels contraions X (NO_3^- i ClO_4^-). Tot i així, aquests compostos moleculars mostren una activitat negligible en solució aquosa, segurament degut a la baixa estabilitat de la unitat Mn_2 en aigua i a la falta de confinament.

Els materials híbrids no funcionalitzats mostren activitat catalasa en acetonitril i són més eficients que els compostos moleculars corresponents. Aquest fet pot ser degut a la presència de grups silanolat en el sòlid que tamponen un pH bàsic, afavorint la catàlisi de descomposició del H_2O_2. Els resultats obtinguts de l'espectroscòpia EPR i dels anàlisis de XPS suggereixen que la reacció té lloc dins el suport i que l'estat d'oxidació del manganès alterna entre II i III.

A diferència dels compostos moleculars, aquest material és actiu en solució aquosa. No obstant, la mesoestructura del material es veu pertorbada durant la reacció. Per aquesta raó, s'han funcionalitzat els porus amb la finalitat d'incrementar l'estabilitat tant de les parets de la sílice com del complex de Mn.

S'ha estudiat l'activitat catalasa de materials Mn-SiO_2 modificats amb grups piridil i que contenen quantitats diferents de compost molecular. Els resultats revelen que l'activitat catalasa d'aquests materials depèn no només de la concentració del centre actiu (complex de Mn) sinó també de la seva distribució dins els porus. Els materials modificats amb grups piridil mostren estabilitat més alta que els no funcionalitzats, ja que la mesoestructura es preserva després de dur a terme la reacció en solució aquosa.

3. Résumé (Summary in French)

Les composés de manganèse sont d'une grande importance du fait de leurs propriétés magnétiques et catalytiques. Depuis la découverte du premier aimant moléculaire (Mn_{12}), les composés de manganèse ont été d'un grand intérêt pour le développement de dispositifs de stockage d'information et pour l'étude de propriétés fondamentales telles que l'anisotropie d'ions métalliques et les interactions magnétiques à plusieurs centres. De plus, le site actif de certaines métalloprotéines est constitué de complexes mono- ou polynucléaires du manganèse. En particulier, les groupements carboxylate sont souvent présents autour des ions métalliques au site actif de ces protéines. En effet, on trouve souvent des ponts carboxylato et oxo dans les sites actifs à plusieurs centres métalliques, jouant un rôle important pour la structure et la réactivité des métalloprotéines. Finalement, ces biosystèmes ne sont qu'un site catalytique, car les ions métalliques sont entourés par un environnement très précis. La structure secondaire de la protéine donne lieu à des cavités enzymatiques avec l'hydrophobicité nécessaire et la taille garantissant leur effectivité. Les métalloprotéines ciblées lors de cette étude sont les catalases au manganèse (Mn-CAT) et le centre d'oxydation de l'eau (WOC) du photosystème II (PSII).

Les catalases au manganèse sont des enzymes qui se trouvent dans quelques bactéries lactiques et qui sont responsables de la décomposition catalytique du H_2O_2. Leur centre actif est constitué d'une unité Mn_2O_2 et l'état d'oxydation du manganèse alterne entre II et III. A cause des propriétés nocives du H_2O_2 et de la présence dérégulée et non souhaitée de cet oxydant qui pourrait être à l'origine de certaines maladies, des thérapies antioxydantes par des catalases synthétiques sont proposées pour prévenir ou adoucir les effets nocifs du H_2O_2.

Le WOC du PSII, qui comporte un cluster héterométallique [Mn_4CaO_5], catalyse l'oxydation de l'eau en oxygène moléculaire avec l'utilisation de l'énergie solaire. Malgré le grand nombre d'études rapportées, le rôle du Ca^{2+} dans le cycle catalytique de l'oxydation de l'eau n'est pas encore totalement compris. De plus, l'ion Sr^{2+}peut éventuellement remplacer l'ion Ca^{2+}en présentant des propriétés chimiques similaires (mais pas identiques). Par conséquence, l'étude de composés Mn-Ca^{2+}/Sr^{2+}pourrait fournir des informations utiles qui, de façon indirecte, aideraient à mieux comprendre le rôle de l'ion Ca^{2+} dans le WOC.

Les complexes biomimétiques sont un outil de choix pour l'étude de propriétés physico-chimiques des sites actifs des métalloprotéines. En effet, la détermination structurale d'un site actif peut être réalisée en utilisant des composés biomimétiques comme modèles. Cependant, leur succès est limité quand la réactivité rentre sur scène, puisque l'effet du

confinement est absent. L'insertion de composés biomimétiques dans des matériaux poreux offre la possibilité d'imiter plusieurs propriétés présentes dans le site actif, telles que l'hydrophobicité et le confinement. Cette approche permet de palier aux limitations observées avec l'utilisation d'analogues moléculaires et ouvre de nouvelles perspectives en reconnaissance moléculaire.

Les résultats présentés ici sont classés en sections qui abordent la chimie moléculaire (Section I), la science des matériaux (Section II) et les propriétés catalytiques (Section III). Chaque section est divisée en plusieurs chapitres : une brève introduction qui explique les techniques et quelques généralités sur les résultats de chaque section, la partie expérimentale et entre les chapitres avec les résultats et la discussion, séparés afin de faciliter la lecture.

SECTION I

Dans cette section les synthèses, les caractérisations et les propriétés des composés de manganèse dans les états d'oxydation II, III ou IV sont présentées. Tous les composés ont été préparés en utilisant des ligands dérivés de l'acide benzoïque *n*-RC_6H_4COOH, avec *n*-R = 2-MeO, 3-MeO, 4-MeO out 4-^{t}Bu, 2,2'-bipyridine (bpy) ou 1,10-phenantroline (phen), et deux contre-anions (X) différents, NO_3^- and ClO_4^-. Vingt-six nouveaux composés ont été obtenus, et pour vingt-et-un d'entre eux la structure cristalline a pu être déterminée : sept composés dinucléaires de Mn^{III}, $[\{Mn^{III}_2O(L)(bpy)\}_2(\mu\text{-}O)(\mu\text{-}n\text{-}RC_6H_4COO)_2]X_2$ (L = solvant ou contre-anion), deux clusters hétérométalliques, $[Mn^{IV}_6M_2O_9(4\text{-}^tBuC_6H_4COO)_{10}(4\text{-}^tBuC_6H_4COOH)_5]$ (M = Ca^{2+} o Sr^{2+}), deux systèmes tetranucléaires, $[Mn^{III}_4O_2(4\text{-}RC_6H_4CO_2)_{7-m}(L)_{2m}(phen)_2](ClO_4)_{1+m}$, un composé dodécanucléaire $[Mn_{12}O_{12}(3\text{-}MeOC_6H_4CO_2)_{16}(H_2O)_4]$ et onze composés mono- ou polynucléaires de Mn^{II}.

En ce qui concerne les propriétés magnétiques, l'étude de susceptibilité magnétique en fonction de la température a été effectuée pour tous les composés. L'interaction d'échange magnétique a pu être reliée à des facteurs électroniques et structuraux. Pour les composés dinucléaires de Mn^{III} l'aimantation en fonction de la température pour différents champs magnétiques a été enregistrée, ce qui a permis la détermination de l'anisotropie des ions Mn (D_{Mn} et E_{Mn}). De plus, l'effet de l'orientation relative des axes Jahn-Teller des ions Mn^{III} sur les propriétés magnétiques a été étudié. Enfin, des corrélations magnéto-structurales ont pu être établies pour une série de vingt-six composés analogues comportant l'unité Mn^{III}_2, incluant les composés présentés dans cette étude.

Pour les composés de Mn^{II} les spectres RPE ont été enregistrés et analysés. Des simulations de ces spectres ont permis de déterminer l'anisotropie de l'ion Mn (D_{Mn} et E_{Mn}).

Dans le cas des composés hétérométalliques Mn^{IV}-Ca^{2+}/Sr^{2+} les propriétés magnétiques ont été analysées avec l'aide des calculs DFT (réalisés par G. Aullón et J. Jover à l'Université de Barcelone). Même si ces ions alcalino-terreux sont diamagnétiques, ils ont une influence sur le comportement magnétique qui a été reliée à l'effet polarisant de ces ions. De plus, ces résultats sont en accord avec ceux montrés par d'autres composés Mn^{IV}-Ca^{2+}/Sr^{2+} modèles du site actif du photosystème II. Ces études pavent un chemin pour arriver à comprendre le rôle de l'ion Ca^{2+} dans la catalyse d'oxydation de l'eau par le photosystème II.

Les composés tétranucléaires avec un motif central $[Mn^{III}_4O_2]^{8+}$ présentent un état fondamental $S = 0$, qui est inhabituel pour ce type de composés tétranucléaires. Ces résultats peuvent être expliqués en analysant la distribution d'états de spin. De plus, l'effet de l'anisotropie axiale, D_{Mn}, et de l'orientation relative des axes Jahn-Teller des ions métalliques sur les propriétés magnétiques a été également étudié pour ces composés.

Enfin, le composé dodécanucléaire, avec le centre $[Mn^{IV}_4Mn^{III}_8O_{12}]^{16+}$, présente le comportement typique d'un aimant moléculaire, montrant une relaxation de l'aimantation lente à basse température.

SECTION II

L'incorporation de composés biomimétiques dans des matériaux poreux peut améliorer leurs propriétés catalytiques. Les composés dinucléaires du Mn^{III} sont modèles du site actif des Mn-CAT. Selon cette approche, deux de ces composés dinucléaires ont été insérés dans deux supports de silice mésoporeuse (type MCM-41, avec une distribution des pores hexagonale 2D), une sans fonctions organiques et l'autre fonctionnalisée avec des groupements pyridyle. Des matériaux comportant différentes quantités de complexe de Mn ont été préparés pour étudier postérieurement l'effet de la concentration de Mn sur la catalyse. La morphologie des matériaux résultants a été caractérisée par diffraction aux rayons X sur poudre, microscopie électronique à transmission (TEM) et par l'étude des isothermes d'adsorption d'azote. L'analyse des propriétés moléculaires de ces matériaux hybrides a été effectuée à l'aide de plusieurs techniques, telles que la spectroscopie RMN du solide, IR et XPS, des analyses élémentaires et thermogravimétriques ainsi que des mesures magnétiques, avec l'utilisation des composés moléculaires comme modèles quand cela était nécessaire. Les résultats montrent que la distribution hexagonale de la silice reste intacte après la fonctionnalisation

et l'incorporation des composés de manganèse. De plus, l'unité dinucléaire Mn^{III}_2 se préserve dans les mésopores.

D'autre part, les supports de silice mésoporeuse (MCM-41) ont été fonctionnalisés avec quatre groupements différents : les silanes *n*-propyle (C_3), *n*-octyle (C_8), phényle (Ph), and 4-éthylbenzoate (EtO_2CPh). Ces solides ont été préparés pour permettre l'incorporation de composés hydrophobes et neutres, comme par exemple, les composés hétérométalliques Mn-Ca et le complexe dodécanucléaire Mn_{12} cités ci-dessus. Le composé dodécanucléaire a été inséré avec succès dans le support de silice comportant des groupements phényle, sans montrer modifications importantes de ses propriétés magnétiques (puisque le comportement aimant moléculaire est préservé). Le composé de Mn-Ca^{2+} a été incorporé dans deux supports différents, l'un comportant des fonctions *n*-propyle et l'autre des fonctions phényle. Cependant, la structure de ce cluster s'altère quand il est inséré dans les mésopores.

Enfin, le groupement ester de la fonction 4-éthylbenzoate greffée sur la matrice de silice a été transformé en acide carboxylique par hydrolyse acide à haute température. Ce support sera testé pour le greffage de composés moléculaires de manganèse comportant des ligands benzoate.

SECTION III

Dans cette section, l'activité catalytique des deux composés modèles des catalases à manganèse, $[\{Mn^{III}_2O(L)(bpy)\}_2(\mu\text{-}O)(\mu\text{-}n\text{-}RC_6H_4COO)_2]X_2$, et des matériaux Mn-$SiO_2$ correspondants est détaillée. Il faut remarquer que pendant que les composés moléculaires sont seulement modèles du site actif de l'enzyme natif, les matériaux hybrides ont été conçus pour mimer à la fois le site actif et la cavité protéique qui fournit le confinement au site actif.

Les composés moléculaires présentent une activité catalytique importante vis-à-vis de la décomposition du H_2O_2 dans l'acétonitrile, indiquant qu'ils ne sont pas seulement des modèles structuraux du site actif des Mn-CATs mais également des modèles fonctionnels de cette métalloprotéine. Leur activité catalase est due principalement aux effets électroniques promus par le groupement R et aux interactions du substrat avec les contre-anions X (NO_3^- et ClO_4^-). Cependant, ces composés moléculaires montrent une activité catalase presque nulle en solution aqueuse, à cause de la faible stabilité de l'unité Mn_2 en solution aqueuse et en absence de confinement.

Les matériaux hybrides non fonctionnalisés montrent une activité catalase importante en acétonitrile et sont plus actifs que les analogues moléculaires. Cela est probablement dû à la

présence de groupements silanolate dans le solide, qui assurent un pH basique et favorisent la décomposition catalytique du H_2O_2. Les études par spectroscopie EPR et les analyses des spectres XPS suggèrent que la réaction catalytique a lieu à l'intérieur du support et que l'état d'oxydation du Mn oscille entre II et III.

Contrairement aux composés moléculaires, les matériaux hybrides sont actifs dans l'eau. Cependant, la mesostructure du matériau est perturbée pendant la réaction. Afin d'augment la stabilité du matériau la surface intérieure a été fonctionnalisée. L'activité catalase des matériaux hybrides Mn-SiO_2 avec des fonctions pyridyle et différentes quantités du composé moléculaire ont été testés. Les résultats révèlent que l'activité de ces matériaux ne dépend pas seulement de la concentration du centre actif (complexe de Mn) mais aussi de la distribution des sites actifs dans les pores. Les matériaux modifiés avec des fonctions pyridyle ont montré une meilleure stabilité que les solides non fonctionnalisés, puisque la mésostructure est préservée après la réaction en solution aqueuse.

INDEX

CONTENTS IN BRIEF

TABLE OF CONTENTS

LIST OF ABBREVIATIONS

AC	alternating current
AF	antiferromagnetic
BET	Brunauer-Emmett-Teller (method for extracting information from the N_2 sorption isotherms)
BdB	Broekhoff and De Boer (method for calculating pore diameter)
BJH	Barret-Joyner-Halenda (method for calculating the pore diameter)
bpy	2,2'-bypiridine
CAT	catalase
CPMAS	cross-polarization magic angle spinning
CTA^+	cethyltrimethylammonium
C_3	*n*-propyl function
C_8	*n*-octyl function
DC	direct current
DFT	density functional theory
EPR	electron paramagnetic resonance
EtOH	ethanol
EtO_2CPh	*para*-(ethoxycarbonyl)phenyl function
F	ferromagnetic
FC	field-cooled
FWHM	full width at half maximum of a peak
HK	Horváth Kawazoe (method for calculating the pore diameter)
HO_2CPh	*para*-(carboxyl)phenyl function
HPDEC	High Power Decoupled
ICP-OES	inductively coupled plasma optical emission spectrometry
IR	infrared
IUCr	International Union of Crystallography
L	monodentate ligand
LP	*Lactobacillus plantarum*
LUS	Laval University silica
MCM	Mobil Composition Matter
MeOH	methanol
MO	molecular orbitals

MRI	magnetic resonance imaging
NMR	nuclear magnetic resonance
NN	bidentate nitrogen-based ligand
Ph	phenyl function
phen	1,10-phenantroline
PSII	photosystem II
Py	4-pyridylethyl function
R	substituent of the aromatic ring of the benzoate derivatives
RNA	ribonucleic acid
ROS	reactive oxygen species
SBA	Santa Barbara Amorphous
SEM	scanning electron microcopy
SIESTA	Spanish Initiative for Electronic Simulations with Thousands of Atoms
SOD	superoxide dismutase
SMM	single-molecule magnet
TEM	transmission electron microcopy
TEM-EDX	energy-dispersive X-ray spectroscopy coupled to TEM
TEOS	tetraethyl orthosilicate
TGA	thermogravimetric analysis
TMA^+	tetramethylammonium
TMS	trimethylsilyl
Tos^-	tosylate
TT	*Thermus thermophilus*
WOC	water oxidizing center
X	counter-anion
XANES	X-ray absorption near edge structure
XPS	X-ray photoelectron spectroscopy
XRD	X-ray diffraction
ZFC	zero-field-cooled
ZFS	zero-field splitting

LIST OF COMPOUNDS AND MATERIALS

Dinuclear Mn^{III} compounds

1 $[\{Mn(bpy)(H_2O)\}(\mu\text{-}2\text{-}MeOC_6H_4COO)_2(\mu\text{-}O)\{Mn(bpy)(NO_3)\}]NO_3$

2 $[\{Mn(bpy)(H_2O)\}(\mu\text{-}2\text{-}MeOC_6H_4COO)_2(\mu\text{-}O)\{Mn(bpy)(ClO_4)\}]ClO_4$

3 $[\{Mn(bpy)(NO_3)\}_2(\mu\text{-}3\text{-}MeOC_6H_4COO)_2(\mu\text{-}O)]$

4 $[\{Mn(bpy)(H_2O)\}(\mu\text{-}3\text{-}MeOC_6H_4COO)_2(\mu\text{-}O)\{Mn(bpy)(NO_3)\}]\,NO_3$

5 $[\{Mn(bpy)(H_2O)\}(\mu\text{-}3\text{-}MeOC_6H_4COO)_2(\mu\text{-}O)\{Mn(bpy)(ClO_4)\}]\,ClO_4$

6 $[\{Mn(bpy)(EtOH)\}(\mu\text{-}4\text{-}MeOC_6H_4COO)_2(\mu\text{-}O)\{Mn(bpy)(ClO_4)\}]$

7 $[\{Mn(bpy)(EtOH)\}(\mu\text{-}4\text{-}^tBuC_6H_4COO)_2(\mu\text{-}O)\{Mn(bpy)(ClO_4)\}]\,ClO_4$

Mono- and polynuclear Mn^{II} compounds

8 $[\{Mn(bpy)_2\}_2(\mu\text{-}2\text{-}MeOC_6H_4COO)_2](ClO_4)_2$

9 $[\{Mn(bpy)_2\}_2(\mu\text{-}3\text{-}MeOC_6H_4COO)_2](ClO_4)_2$

10 $[\{Mn(bpy)_2\}_2(\mu\text{-}4\text{-}MeOC_6H_4COO)_2](ClO_4)_2$

11 $[\{Mn(phen)_2\}_2(\mu\text{-}2\text{-}MeOC_6H_4COO)_2](ClO_4)_2$

12 $[\{Mn(phen)_2\}_2(\mu\text{-}3\text{-}MeOC_6H_4COO)_2](ClO_4)_2$

13 $[Mn(H_2O)(3\text{-}MeOC_6H_4COO)(phen)_2](ClO_4)$

14 $[\{Mn(phen)_2\}_2(\mu\text{-}4\text{-}MeOC_6H_4COO)_2](ClO_4)_2$

15 $[\{Mn(phen)_2\}_2(\mu\text{-}4\text{-}^tBuC_6H_4COO)_2](ClO_4)_2$

16 $[Mn_3(bpy)_2(\mu\text{-}3\text{-}MeOC_6H_4COO)_6]$

17 $[Mn_3(bpy)_2(\mu\text{-}4\text{-}MeOC_6H_4COO)_6]$

18 $[Mn(bpy)(4\text{-}^tBuC_6H_4COO)_2]$

19 $[Mn(H_2O)_2(2\text{-}MeOC_6H_4COO)_2(phen)]$

20 $[Mn_3(\mu\text{-}3\text{-}MeOC_6H_4COO)_6(phen)_2]$

21 $[Mn_3(\mu\text{-}4\text{-}MeOC_6H_4COO)_6(phen)_2]$

Heterometallic $Mn^{IV}_6M_2$ compounds ($M = Ca^{2+}$ or Sr^{2+})

22 $[Mn_6Ca_2O_9(4\text{-}^tBuC_6H_4COO)_{10}(4\text{-}^tBuC_6H_4COOH)_5]$

23 $[Mn_6Sr_2O_9(4\text{-}^tBuC_6H_4COO)_{10}(4\text{-}^tBuC_6H_4COOH)_5]$

Tetranuclear Mn^{III} compounds

24 $[Mn_4(\mu\text{-}O)_2(\mu\text{-}4\text{-}MeOC_6H_4COO)_7(phen)_2]ClO_4$

25 $[Mn_4(\mu\text{-}O)_2(\mu\text{-}4\text{-}^tBuC_6H_4COO)_6(H_2O)_2(phen)_2][Mn_4(\mu\text{-}O)_2(\mu\text{-}4\text{-}^tBuC_6H_4COO)_6(CH_3CN)_2(phen)_2](ClO_4)_4$

Dodecanuclear $Mn^{III/IV}$ compound

26 $[Mn_{12}O_{12}(3\text{-}MeOC_6H_4COO)_{16}(H_2O)_4]$

As-made materials and supports

SiO_2-CTA	as-made mesoporous silica, CTA^+ = cetyltrimethylammonium
SiO_2-Ex	surfactant-extracted mesoporous silica
SiO_2-TMA	tetramethylammonium (TMA^+) functionalized mesoporous silica
Py@SiO_2-TMA	SiO_2-TMA functionalized with 4-pyridylehyl groups
C_3@SiO_2	SiO_2-Ex functionalized with *n*-propyl groups
C_8@SiO_2	SiO_2-Ex functionalized with *n*-octyl groups
Ph@SiO_2	SiO_2-Ex functionalized with phenyl groups
EtO_2CPh@SiO_2	SiO_2-Ex functionalized with *para*-(ethoxycarbonyl)phenyl groups
HO_2CPh@SiO_2	hydrolyzed EtO_2CPh@SiO_2 material

Catalase-biomimetic Mn-SiO_2 materials

$[Mn_2O]_{0.5}$@SiO_2	compound **1** or **2** inserted into SiO_2-TMA, $[Mn^{III}_2]/TMA^+ = 0.5$
$[Mn_2O]_{0.1}$@SiO_2	compound **1** inserted into SiO_2-TMA, $[Mn^{III}_2]/TMA^+ = 0.1$
$[Mn_2O]_{0.21}$-Py@SiO_2	compound **1** inserted into Py@SiO_2-TMA, $[Mn^{III}_2]/TMA^+ = 0.21$
$[Mn_2O]_{0.12}$-Py@SiO_2	compound **1** inserted into Py@SiO_2-TMA, $[Mn^{III}_2]/TMA^+ = 0.12$
$[Mn_2O]_{0.04}$-Py@SiO_2	compound **1** inserted into Py@SiO_2-TMA, $[Mn^{III}_2]/TMA^+ = 0.04$

Big clusters-SiO_2 materials with hydrophobic functions

C_3@SiO_2-$[Mn_6Ca_2]$	compound **22** inserted into C_3@SiO_2
Ph@SiO_2-$[Mn_6Ca_2]$	compound **22** inserted into Ph@SiO_2
Ph@SiO_2-$[Mn_{12}]$	compound **26** inserted into Ph@SiO_2

INTRODUCTION

INTRODUCTION

1. Molecular Magnetism of Manganese Compounds

Manganese compounds are of interest because they may be used as catalysts in several industrial processes,[1–7] for instance, due to their ability to oxidize both inorganic and organic substrates.[6,7] They have also a huge impact in fundamental research because of their magnetic properties.[8,9] Indeed, Mn ions in the most common oxidation states, II, III, and IV, with respective configurations d^5, d^4, and d^3, have several unpaired electrons and are paramagnetic.

The existence of more than one metal ion in a compound (categorized as polynuclear) may give rise to different metal-metal interactions. These interactions may be mediated by bridging ligands or take place directly between the *d* orbitals of the metal ions. In the case of manganese compounds, the first way of interaction is far more common and it is a subject of interest in many fields.[8–10] The interaction between the two metal ions through the bridging ligands may be then (*a*) favorable, where the unpaired electrons tend to be coupled, or (*b*) unfavorable, where the unpaired electrons remain unpaired. These two situations refer to antiferromagnetic (*a*) or ferromagnetic (*b*) interactions, respectively.[11]

Manganese compounds with carboxylate and oxo bridges

Ligands play a crucial role for the structure of a given compound, as well as for its magnetic properties. In particular, Mn ions show a high tendency to be coordinated by N and O atoms.[12] Depending on the connectivity offered by the donor atoms, a specific ligand can give rise to structures of different nuclearity and geometry. In the literature systems ranging from mono- to polynuclear Mn_{84} compounds[13] may be found, spanning from atomic to nanoscale dimensions (Figure 1). Indeed, the size of the Mn_{84} cluster, ~4.2 nm, is comparable to that shown by small metal nanoparticles.

Carboxylate ligands are of importance for coordination chemists because they show a huge versatility of coordination modes (Figure 2)[14,15] and may be decisive for the magnetic properties of polynuclear compounds.[16] In addition, the presence of carboxylate ligands, bridging and terminal, in some metalloproteins[10] grants these ligands significance for the study of biomolecules. For instance, many synthetic and simpler analogues have been developed mainly for the structural determination of an active site.[17]

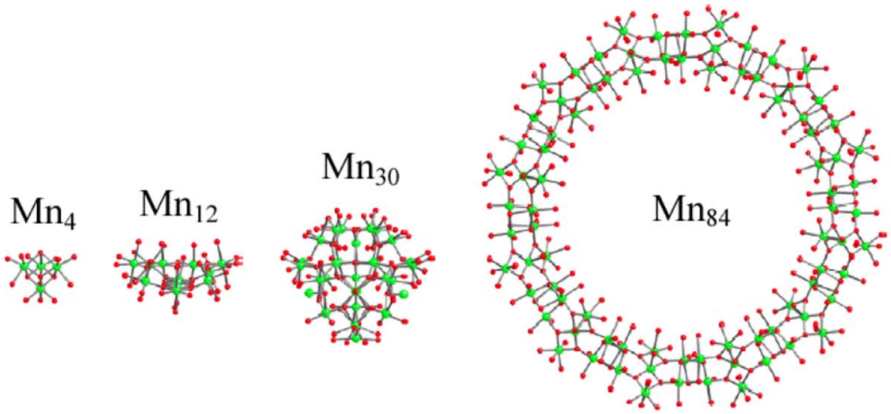

Figure 1. Crystal structures of the cores of Mn_4, Mn_{12}, Mn_{30}, and Mn_{84} clusters, drawn in the same scale. The figure was adapted from *Angewandte Chemie International Edition* 2004 by Tasiopoulos *et al.*[13]

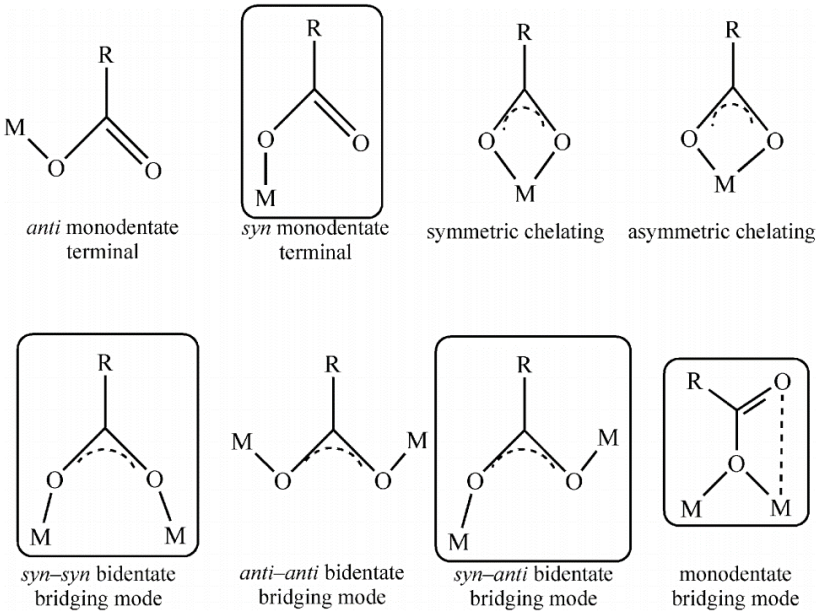

Figure 2. Carboxylate binding modes in metal complexes. The bridges more relevant for this work are framed. This figure was taken from *European Journal of Inorganic Chemistry* 2009 by Gómez and Corbella.[15]

Similarly, oxo bridges are widely found in polynuclear Mn compounds. However, its presence is less controlled by synthetic chemists because they are formed intrinsically, mainly dependent on the oxidation state of Mn. For instance, polynuclear Mn^{III} and Mn^{IV} compounds are very likely to present oxo bridges. On the contrary, oxo bridges in Mn^{II} compounds are rare. Nonetheless, Mn^{II} ions can be linked by aquo or hydroxo ligands. Oxo, hydroxo, and aquo bridging ligands may have a greater influence in the magnetic interactions than carboxylate ones, since they bring the Mn ions to a closer distance.

Single-molecule magnets (SMM)

For many years, molecular magnetism focused on the factors that determine or modulate the magnetic interaction between two ions, by correlating the structural parameters, obtained from the crystal structures, with those from the magnetic measurements. In 1993, a renaissance in cluster chemistry has awaken since the discovery of the first single-molecule magnet (SMM) (Figure 3).[18]

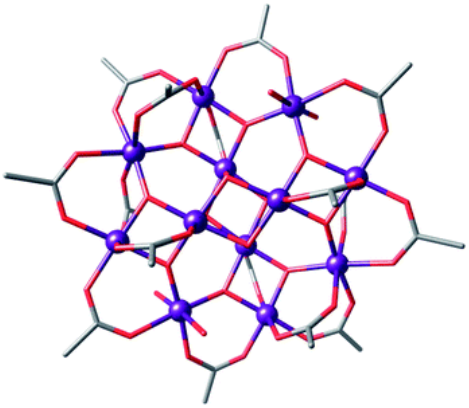

Figure 3. Crystal structure of the first single-molecule magnet, with formula $[Mn_{12}O_{12}(CH_3COO)_{16}(H_2O)_4]$.[18] Color code: Mn, purple; C, gray; O, red.

Magnets are widely used in a large number of applications, the most remarkable being information storage. Each piece of information (a bit) corresponds to a magnetic domain of about several nanometers that keeps a permanent magnetic moment without the constant presence of a magnetic field. SMMs are molecules capable of acting as nanoscale magnets below a critical temperature (blocking temperature), but promoted by individual molecules and not by a domain. In principle, these bistable magnetic units could act as a data storage device.[19] Hence, in order to reduce the size of the magnetic domains in information storage devices, the use of SMM was proposed. However, there is a lower limit to the size of the memory elements below which information cannot be permanently stored because the magnetization fluctuates freely. Even so, small domains (or molecules) can be theoretically used either by working at low temperature or by taking advantage of the onset quantum size effects.[20]

It is difficult to see how molecular systems would overtake the useful properties of the robust, inert, and cheap non-molecular materials. In principle, molecular systems can be designed with specific arrangements of magnetic ions, but the structure of these systems can only be restrictively controlled for some atomic positions and some magnetic interactions.[9] Nevertheless, molecular systems offer some key advantages over conventional magnetic

materials. For instance, they can form more complex and diverse structures than those obtained from conventional materials, allowing the incorporation of functionalities.

Single-ion anisotropy

The magnetic anisotropy or zero-field splitting (ZFS) is one of the most important properties that characterizes a metal ion with more than one unpaired electron.[21] In fact, the slow relaxation process of the magnetization in SMMs is essentially controlled by an energy barrier that can fix the spin direction. This global magnetic anisotropy of a polynuclear compound is directly related to the ZFS of the metal ions.[8,11] However, the conditions that determine the value and sign of ZFS are, so far, unclear.

Motivated by these considerations, scientists moved back to study simple mononuclear compounds, where the magnetic anisotropy is easy to investigate.[21–23] Particularly, Mn ions have attracted much attention because they display significant ZFS[8,11,21] and due to the possibility of Mn compounds to behave as SMMs.[9,20] Therefore, a wide number of works have been reported in order to understand and rationalize the origin of magnetic anisotropy of Mn ions using both theoretical and experimental methods.[21,22,24–36] Beyond fundamental interest, these works aim to guide upcoming syntheses that provide better SMMs.[23,37]

Magnetic measurements and electron paramagnetic resonance (EPR) are probably the most common techniques that stumble upon ZFS. Hence, the parameters related to the magnetic anisotropy could be determined using these techniques. Since tailoring and tuning of the ZFS parameters is still an unachievable dream, there is a great interest in correlating these parameters with geometrical and electronic factors.[23] Moreover, understanding how the single-ion ZFS is transmitted to the global molecular anisotropy in polynuclear compounds and its effect on the overall magnetic properties may be crucial to prepare systems with more promising magnetic properties.

2. Bioinorganic Chemistry of Manganese

Apart from the explained above, manganese is an essential element for living organisms. It is indeed found in several metalloproteins, such as photosystem II, superoxide dismutase (SOD), Mn-catalase, and several oxidoreductases.[10,38] In physiological conditions the most relevant oxidation states for Mn ions are II, III, and IV. These ions are habitually coordinated by oxygen and nitrogen atoms belonging to amino acid residues of the protein, such as the imidazole substituent in histidine and carboxylate groups provided by aspartate or glutamate.

Owing to its variability of oxidation states, manganese plays a crucial role in the active site of redox enzymes. While Mn^{II} ions may play a structural role or act as Lewis acid, higher oxidation states (III and IV) become useful when electron transfer is required.[39] Table 1 lists some examples of enzymes whose active site contains Mn ions. The active site of a metalloprotein can consist of one or more Mn ions and, in the latter case, carboxylate, oxo, hydroxo, and aquo ligands can act as bridges between Mn ions.

Table 1. List of some metalloproteins whose active site contains Mn ions and the reactions that they catalyze.[10,39,40]

Enzyme (distribution)	Core	Enzyme reaction	
Arginase (yeast, bacteria mammals)	Mn^{II}_2	arginine → urea + ornithine	Hydration
Xylose isomerase (bacteria)	Mn^{II}_2	glucose → fructose	Isomerization
Ribonuclease (retrovirus, bacteria)	Mn^{II}_2	RNA + H_2O → cleaved RNA	Hydrolysis
Mn-catalase (thermophilic and heme-deficient bacteria)	$Mn^{II}_2 \leftrightarrow Mn^{III}_2$	2 H_2O_2 → 2 H_2O + O_2	Dismutaion (redox)
Photosystem II (plants, algae)	$Mn^{III}_3Mn^{IV} \leftrightarrow Mn^{IV}_4$ *	2 H_2O → O_2+ 4 H^+ + 4 e^-	Oxidation (redox)
Superoxide dismutase (mammals, many bacteria)	$Mn^{II} \leftrightarrow Mn^{III}$	2 $O_2^{-\bullet}$ + 2 H^+ → H_2O_2 + O_2	Dismutation (redox)
Catechol dioxygenase (some bacteria)	$Mn^{II} \leftrightarrow Mn^{III}$	catechol + O_2 → *cis,cis*-muconic acids	Oxidation (redox)

* The mechanism is still incompletely understood (see below).[41]

Biomimetic compounds provide a unique way for investigating the chemical properties of active sites. The high control and versatility that chemists may accomplish with discrete molecular compounds give the opportunity to mimic the environment around Mn ions and study several variations. Such compounds indirectly provide valuable information regarding the reactivity of the active site and may be used as references in different spectroscopic techniques.

Concept of oxidative stress

Reactive oxygen species (ROS), represented by superoxide ($O_2^{-\bullet}$), hydrogen peroxide (H_2O_2) and hydroxyl radical ($HO^\bullet$), are endogenously produced in cells under aerobic conditions during the auto-oxidation of redox enzymes. ROS play an indispensable physiological role; however, their effects oppose one to another as they can both promote and prevent cell death, inflammation, or aging.[10,42,43]

$O_2^{-\bullet}$ and H_2O_2 are produced from the one- and two-electron reductions of molecular oxygen (O_2), respectively. These two oxidants react rapidly with vulnerable targets; therefore, cells are loaded with high amounts of very efficient ROS scavengers, as for example catalase, peroxidases (H_2O_2 scavengers) or superoxide dismutases ($O_2^{-\bullet}$ scavengers). Consequently, a balance between the intracellular $O_2^{-\bullet}$ and H_2O_2 production and their scavenger-mediated decomposition keeps these two oxidants concentration in steady-state. Whereas $O_2^{-\bullet}$ (small but charged) is not able to cross membranes, H_2O_2 (small and uncharged) crosses membranes at a moderate efficiency, making cells sensitive to the extracellular H_2O_2 concentration.[42,44] Moreover, H_2O_2 reacts with intracellular ferrous iron, leading to the formation of the hydroxyl radical ($HO^\bullet$) (Fenton reaction).[45] $HO^\bullet$ is an extremely powerful oxidant that, for instance, is responsible for direct DNA damage (since neither H_2O_2 nor $O_2^{-\bullet}$ are able to damage DNA directly).[42]

As with any signaling mechanism, ROS can become cytotoxic if found in high concentrations or in the wrong place. The phenomenon of ROS overproduction, which contributes to oxidative stress, has been found in a great number of pathologies[46–49] such as cancer, multiple sclerosis, Alzheimer's or Parkinson diseases. Nevertheless, the role of ROS in such diseases is sometimes controversial since they may present various effects at the same time. For example, the production of ROS on tumors can range from tumor-production effects to tumor-destroying effects. In fact, some anticancer agents induce apoptosis by promoting the production of ROS, which contributes both to their efficacy and to their toxicity[43,50] (damaging tumor cells and non-cancerous cells, which may cause side-effects).

Owing to the harmful properties of ROS, antioxidant therapies have been considered for a wide variety of disorders associated with oxidative stress, which have shown promising *in vivo* results.[51–54] Unfortunately, clinical trials to test the effect of antioxidant therapies are limited and have presented disappointing results in lots of cases. Nevertheless, the use of improved antioxidant therapies is still considered nowadays in particular cases where the oxidative stress is shown in earlier stages before the development of severe clinical

manifestations, such as in children with α-1 antitrypsin deficiency (characterized by H_2O_2 accumulation due to the lack of catalase activity).[55] Antioxidant therapy in combination with conventional therapies is also considered for diseases in which ROS play an important role in neuron-degeneration, such as multiple sclerosis,[56,57] Alzheimer's,[58] or Parkinson's[59] syndromes. In these cases, the chosen antioxidants should be able to penetrate the blood-brain barrier, which is the major obstacle that reduces the efficacy of many agents.[56] Targeting antioxidants to the desired position opens up a new challenge in molecular recognition, as oxidative stress is produced locally or is notably harmful for the most vulnerable targets. For instance, mitochondrially targeted antioxidants could result effective reducing oxidative stress in asthma.[60] Similarly, neonatal brain injury could be diminished or prevented by using antioxidants able to cross both the placenta and the blood-brain barrier.[61]

Manganese catalases and catalase-biomimetic compounds

Within all antioxidants, catalases (CATs) are the enzymes that perform the decomposition of H_2O_2 into H_2O and O_2. This reaction is spontaneous and favorable under physiological conditions (pH = 7, 37 °C),[62] but the kinetics is slow and needs to be catalyzed. The redox potentials (versus a normal hydrogen electrode) of the two half-reactions O_2/H_2O_2 and H_2O_2/H_2O at pH = 7 are +0.28 and +1.35 V, respectively. In mammals the active site of CATs consists of a heme group. On the contrary, some lactic acid bacteria that are heme-deficient have Mn-dependent catalases (Mn-CATs).

So far, the crystal structures of Mn-CATs from the *Lactobacillus plantarum* (LP)[63] and *Thermus thermophilus* (TT)[64] have been reported. The active site of this type of CAT comprises a dinuclear Mn unit with oxo and carboxylate bridges (Figure 4), in which the oxidation states in the Mn_2 pair alternate between (II,II) and (III,III).[65]

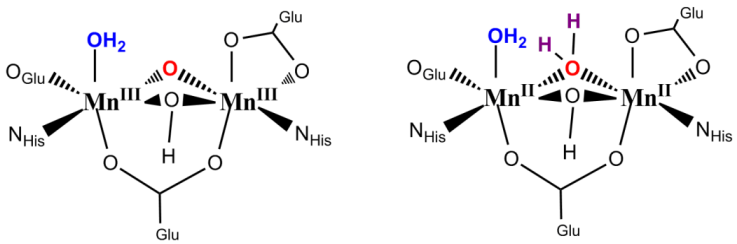

Figure 4. Drawings based on the crystal structure of the active site of Mn-CAT from LP[63] in the oxidized (left) and reduced forms (right). Abbreviations: His = histidine, Glu = glutamate.

The structural complexity of these enzymes guarantees their catalytic efficiency. The active site is isolated from the solvent and surrounded by a very precise environment, these facts

stabilizing the Mn_2O_2 cluster in water solution. The access to the active site is highly controlled by enzymatic cavities and/or channels that specifically allow H_2O_2 to travel from the solvent to the active site, as shown in Figure 5 and Figure 6.

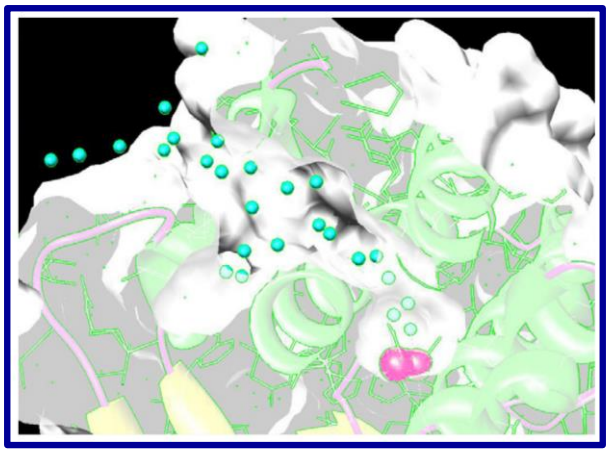

Figure 5. The 22 Å long access channel in TT. The pink and cyan spheres correspond to the Mn ions and to water molecules, respectively. The figure was taken from *Archives of Biochemistry and Biophysics* 2012 by Whittaker.[65]

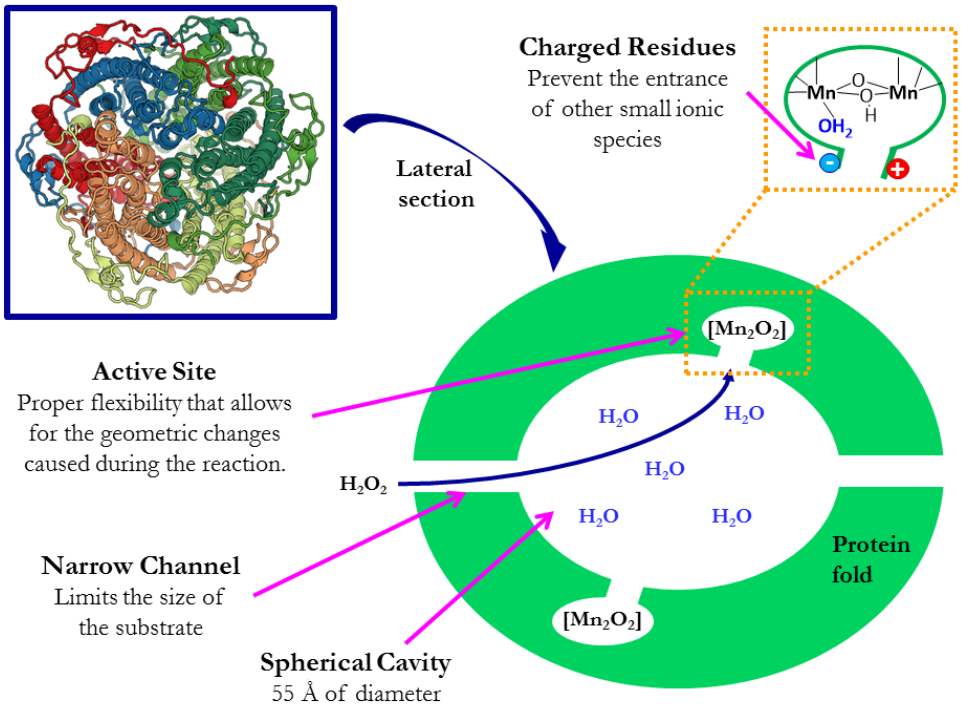

Figure 6. Qualitative representation of Mn-CAT from LP based on its crystal structure.[63]

From these structural and other spectroscopic data, a mechanism for the catalytic cycle of H_2O_2 decomposition carried out by LP was proposed (shown in Figure 7).[65,66] The neutral hydrogen peroxide substrate reaches one of the Mn ions, displacing the terminally bound

water molecule. A glutamate group assists the movement of protons from the bound substrate to the bridging solvents as electrons are transferred from the H_2O_2 to the Mn ions. Then, a dioxygen molecule is exchanged by a water molecule. Secondly, a new H_2O_2 molecule would enter the active site to form a $\mu_{1,1}$-bridging peroxide complex. In this step the glutamate group also have an important relevance to the proton transfer. Finally, a reductive cleavage of the O–O bond is produced. As may be observed, the oxidation states of the Mn ions alternate between (II,II) and (III,III).

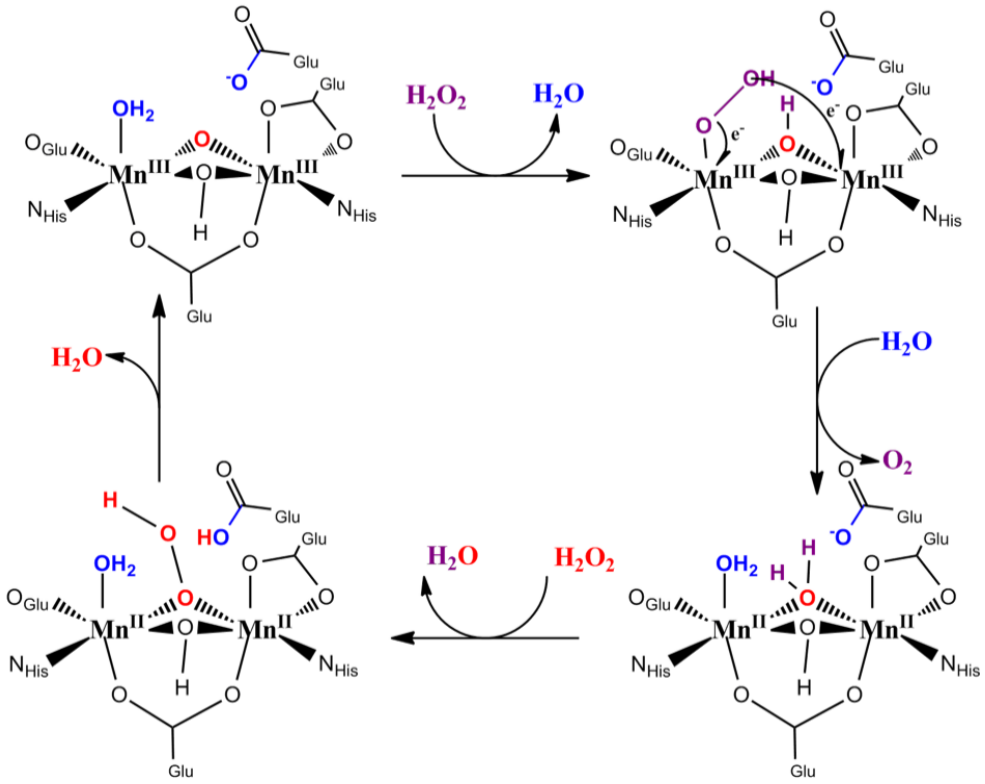

Figure 7. Proposed catalytic cycle for H_2O_2 decomposition catalyzed by Mn-CAT from LP.[63,65] Abbreviations: Glu = glutamate, His = histidine.

Carboxylate ligands in coordination mode $\mu_{1,3}$ are commonly found in metalloproteins performing multi-electronic transfers. The presence of this $\mu_{1,3}$-bridge endorses that the electron transfer takes place between the pairs Mn^{II}_2 and Mn^{III}_2, without involving mixed-valence species.[40,67] Moreover, the fact that the two Mn ions have the same NO_5 coordination sphere provides a symmetrical environment that promotes that both Mn ions have the same oxidation state.[67]

The protein fold surrounding the active site does not only give structural stability to the Mn_2O_2 cluster, but also it is responsible for softening the $Mn^{III}_{(aq)}/Mn^{II}_{(aq)}$ redox potential

(1.54 V) to lower values, in order to guarantee that all steps of the catalytic cycle are spontaneous.

Regarding the kinetics of the reaction, both Mn-CATs follow a Michaelis-Menten mechanism, reaching saturation at high concentrations of H_2O_2. The initial reaction rate (r_i) is defined by the expression:

$$r_i = \frac{k_{cat}[\mathrm{CAT}][\mathrm{H_2O_2}]_0}{K_M + [\mathrm{H_2O_2}]_0} \qquad \text{Eq. 1}$$

where $k_{cat} = 2.0 \cdot 10^5$ and $2.6 \cdot 10^5$ s^{-1} and $K_M = 350$ and 83 mM for the Mn-CATs from LP and TT, respectively.[67]

Hydrogen networks are of huge importance to guarantee the efficiency of these enzymes. Therefore, Mn-CATs show the highest activity when pH = 7–10 and drops to zero at extreme pH values (pH < 5 or > 12). The loss of activity at pH < 5 is attributed to the protonation of the oxo bridges and the consequent formation of an "open" form of the dinuclear cluster.[68]

Efforts to mimic the active site and such a good catalytic performance of this enzyme have been carried out. A large number of functional models of the Mn-CATs were summarized in 2012 by Signorella and Hureau.[67] More recently, mononuclear Mn^{III} porphyrin and Schiff-base complexes have received much devotion,[69–73] since some of them are active in water.[69,72,73] This have deflected the attention from Mn^{III}_2 mimics, reducing the emergence of this latter type.[74] Moreover, dinuclear models with the required stability and activity in physiological conditions have not been reported so far.

Very recently, the Mn-CAT from *Anabaena* was isolated and its crystal structure was determined,[75] being the first structural characterization of a Mn-CAT from any photosynthetic organism. Even though the structure of the protein fold of this new catalase superposes well on those of LP and TT, the active site configuration is significantly different from the other Mn-CATs. In *Anabaena*, the active site of this enzyme also comprises two Mn ions, both with NO_5 coordination environments, coordinated to histidine and glutamate residues. However, these two ions are linked through two carboxylate ligands in a $\mu_{1,3}$-bridging mode, without oxo bridge (at least in the reduced formed). The sixth coordination position in each Mn ion is completed by a terminal water molecule. These changes in the nature and location of the active site water molecules suggest that the binding mode of H_2O_2 is likely to be different from that of LP or TT catalases.[75] The symmetrical environment in the Mn-CAT from *Anabaena* possibly favors a $\mu_{1,2}$-brigding mode for H_2O_2, replacing both

solvent molecules. The access channel in this enzyme also seems to differ from LP CAT, since the central channel is blocked by Ca^{2+} ions. Instead, H_2O_2 may enter through inter subunit space. However, these extra Ca^{2+} ions may be a crystallization artifact.[75] This new determination not only shows that Mn-CATs can be divided in two evolutionary independent groups but also provides an alternative template for the design of new catalase mimetics.[75]

Water oxidizing center: role of Ca^{2+} ion and Sr^{2+}-substitution

Photosynthesis has been the center of attention for many researchers from several fields, including bioinorganic chemistry. Beyond fundamental interest, these studies are very important for the development of artificial photosynthetic systems that may convert sun light energy into high value chemicals, such as hydrogen.[41]

As commented above, there are many metalloproteins involving one or more Mn ions in enzymatic functions. Particularly, a heterometallic [Mn_4CaO_5] cubane-like cluster (Figure 8) constitutes the water-oxidizing center (WOC) within photosystem II (PSII), a membrane-bound protein that performs the light-induced oxidation of H_2O to O_2, being responsible for the production of a great part of the atmospheric oxygen on Earth and the fixation of carbon dioxide.[10,76]

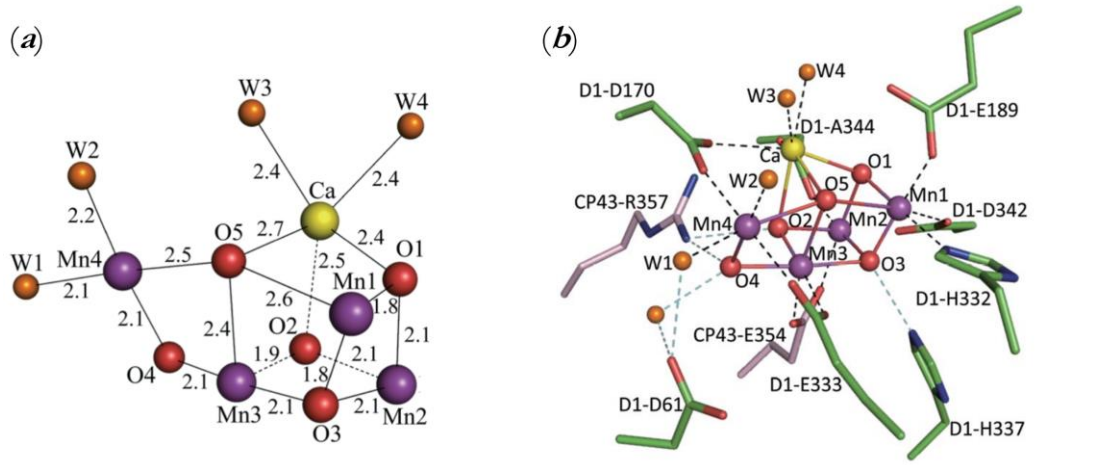

Figure 8. Crystal structure of the [Mn_4CaO_5] cluster that constitutes the water-oxidizing of *Thermosynechococcus vulcanus*: (***a***) simplified view with selected interatomic distances (Å), and (***b***) stereo view of the cluster and its ligand environment. This figure was taken from *Nature* 2011 by Umena *et al.*[76]

In the proposed catalytic cycle (known as the Kok cycle) a four-electron oxidation of two H_2O molecules takes place in five intermediate S_i states (i = 0–4), in which the Mn oxidation

state mainly swings between III and IV, and some structural changes may be observed in the coordination environment of the Mn ions.[77–80] Searching for synthetic analogues, a huge number of manganese clusters may be found in the literature, including homo-[81] and heterometallic Mn-Ca[82–91] compounds. However, only three compounds with a $[Mn^{IV}_3CaO_4]^{6+}$ cubane-like core have been reported.[89,90,92]

In spite of researchers' efforts, electronic changes in the WOC still remain incompletely understood and are still subject to debate.[41] Furthermore, Ca^{2+} ion plays a crucial role in oxygen evolution because alkali- or lanthanide-substitution or Ca^{2+}-depletion resulted in the inhibition or worsening of the catalytic process.[93] It also has influence on the geometrical and electronic structure of the WOC (related to the electron and proton transfer)[94] and maintains the correct configuration of the surrounding network of water molecules, contrary to other metal ions.[95] These facts suggest that Ca^{2+} ion is neither replaceable nor dispensable. Moreover, data comparison between the S_i states and a series of Mn^{IV} compounds revealed that the Ca^{2+} ion is apparently modifying the electronic structure of the Mn ions, also suggesting that the assignment of formal oxidation states is insufficient for accurately understanding the electronic structural changes of Mn.[96]

Sr^{2+} has been considered a good candidate for replacing Ca^{2+} in the majority of the systems, even though Ca^{2+} is significantly smaller (ionic radii of 1.14 Å for Ca^{2+} and 1.32 Å for Sr^{2+}). Several Mn compounds containing Ca^{2+} or Sr^{2+} ions and their relevance for the WOC were summarized very recently in a review by Gerey *et al.*[41] For instance, Mn-Sr^{2+} and Mn-Ca^{2+} compounds show comparable activities in O_2 chemistry due to their similarities generating H-bonding networks.[97] They also display very similar redox potentials, fact that seems to be related to the resemblance between their acidities – in comparison to other Mn-$M^{x'}$ compounds (where $M^{x'}$ = Na^+, Zn^{2+}, Y^{3+}, Sc^{3+}, or Mn^{3+}, besides Ca^{2+} or Sr^{2+}).[91,98] Consistently, the Sr^{2+}-substituted PSII is active toward H_2O oxidation while the substitution of the Ca^{2+} ion (in the native site) for other cations or Ca^{2+}-depletion results in the inhibition of the activity. Some of these cations, such as Cd^{2+}, Cu^{2+}, and Dy^{3+}, may fulfill the structural role of Ca^{2+}, but they are not able to provide the required electronic modifications. This fact seems to be related to the functional role of Ca^{2+} to activate H_2O, which can be partially fulfilled with a cation with similar Lewis acidity, such as Sr^{2+}.[93,99,100] However, the Sr^{2+}-substitution is not innocent, because it causes some obvious structural changes in the WOC[101,102] and it negatively affects the kinetics of H_2O oxidation.[103]

3. Encapsulation of Manganese Compounds in Mesoporous Silica

Mesoporous materials

Porous materials have been studied since the middle of the 18th century. Axel F. Cronstedt (1722–1765), famous Swedish mineralogist, was the first scientist that described, 250 years ago, the distinctive property of zeolites: the unique frothing characteristics when heated in a blow-pipe flame.[104] However, zeolites had to wait 200 years before chemists started to grow interest in these porous materials.[105]

Along with a uniform pore distribution (between 0.4 and 1.3 nm), these aluminosilicates possess acidic sites that can behave as potential catalysts for various reactions. It is worth remarking the industrial potential of zeolites in petrochemical and refinery processes.[105] In addition, they are rather adaptable through the combination of ingenious syntheses and structural analyses. However, the small pore size of these materials brings about diffusion limitations, especially at high concentrations of substrates. Hence, the development of zeolite materials with greater porosity has been under study (see below).[106,107] Nevertheless, the development of zeolite materials took place simultaneously with the advance of other porous materials, such as mesoporous silica, microporous metal organic frameworks, and covalent organic frameworks. The chemical and structural properties of these latter porous materials overtook the zeolite field.[105] For instance, mesoporous silica may be prepared with narrow distribution of pore size from 0.4 to 100 nm. Based on IUPAC, porous materials can be classified into three categories according to the pore diameter: microporous (less than 2 nm), mesoporous (between 2 and 50 nm), and macroporous materials (more than 50 nm).[108] Because of a good balance between accessibility and diffusion, mesoporous materials are of huge relevance for this work.

Some of the most well-known and common mesoporous materials include the MCM (Mobil Composition of Matter) materials, such as MCM-41 (2D hexagonal), MCM-48 (cubic), and MCM-50 (lamellar) solids. The formation of these materials, whose syntheses are performed at pH = 10–13, consists in polymerizing silica precursors around a template (promoted by electrostatic interactions) formed by a supramolecular arrangement of surfactant molecules in aqueous solution.[109] The surfactants commonly used are long alkyl chains ended by a hydrophilic quaternary ammonium head, with a counter-anion that preserves the neutrality. The length of the organic chain of the surfactant will dictate the size of the pore, affording pore diameters of a few nanometers for surfactant tails containing between eight (C_8) and twenty-two (C_{22}) carbon atoms.[108,110] Cetyltrimethylammonium tosylate, chloride, and

bromide are some examples of surfactants, which give porosities with diameters close to 4 nm (BdB[111] method). Surfactant molecules tend to auto-assemble in aqueous solution when a certain concentration is reached, called critical micelle concentration. Moreover, depending on the concentration of surfactant, liquid crystals with different organizations can be formed: 2D hexagonal, cubic, or lamellar.[112] The subsequent polymerization of silica precursor around the surfactant template will give birth to mesoporous structures.

The 2D hexagonal MCM-41 is the most frequently used mesoporous support.[113–115] Its synthesis has been profoundly studied and optimized using specific counter-anions of the surfactant or microwave radiation.[116–118] Figure 9 shows the formation mechanism of MCM-41. The mesostructure is formed by the cooperative molecular assembly of the surfactant molecules with the inorganic precursors. The advantage of using MCM-41 silica is that its thermal stability is better than lamellar MCM-50, and that channels are more accessible than cubic MCM-48, which favors both the homogeneity in functionalization and diffusion of the substrate for catalysis.

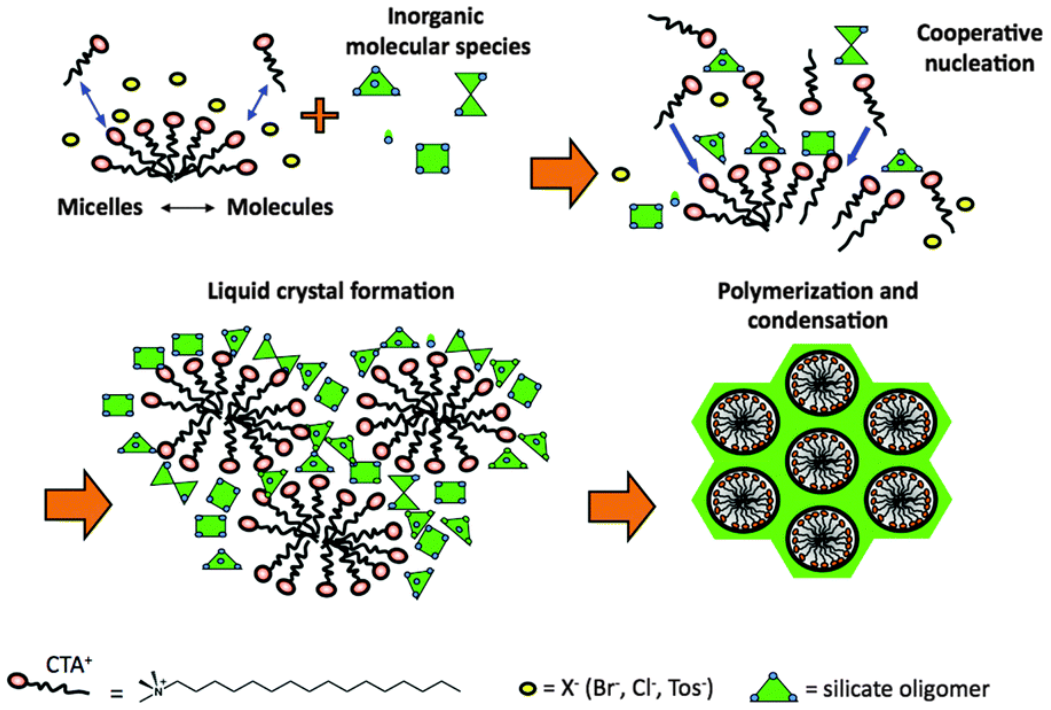

Figure 9. Formation mechanism of MCM-41 under basic conditions. The figure was taken from *New Journal of Chemistry* 2016 by Albela and Bonneviot.[115] Abbreviations: CTA^+ = cetyltrimethylammonium, Tos^- = tosylate.

Other important mesoporous silica materials are those belonging to the SBA (Santa Barbara Amorphous) family, which are synthesized using silica precursors under acidic conditions and cationic surfactants or neutral triblock co-polymers,[109,110,119] such as Pluronic P-123. The

SBA-15, which presents a similar 2D hexagonal structure to MCM-41, is the most popular within this family. The advantages of SBA-15 rely on its superior thermal stability[108] in comparison to MCM-41 and on its greater pore diameters,[120] which can reach values of ~15 nm (BJH[121] method).

Owing to the beneficial properties of zeolites, intensive efforts have been performed to synthesize mesoporous zeolite materials, aiming to extend their applications.[106,107] Four main synthesis strategies to introduce mesoporosity to zeolite materials can be distinguished:[106] (*a*) the use of a dual templating route, including the common zeolite structure directing agents and a secondary template for the mesostructure; (*b*) the use of a single but multifunctional template; (*c*) the use of reaction conditions that make secondary templates unnecessary; and (*d*) leaching reactions performed on pre-made zeolites. All these methods provide zeolites with interconnected micro- and mesoporosity aiming to overcome diffusion limitations and to catalyze reactions with large substrates. However, in spite of the broad spectrum of applications of mesoporous zeolites,[106] the functionalization is so far more versatile for mesoporous silica than for mesoporous zeolites.

Functionalization of mesoporous silica

Organic functions may be introduced in mesoporous silica either during the synthesis or as a modification of the porous support. These procedures are often called co-condensation (or direct synthesis) or post-functionalization, respectively. Hence, the function can be located in the solid framework or in the pore fixed by electrostatic or covalent interactions.[115] Between them, the post-grafting approach offers more molecular flexibility and does not alter the structure of the as-made material, contrary to co-condensation techniques. Moreover, the functionalization of the material should lead to a well-defined environment and to an almost homogeneous distribution of functions. In order to guarantee these two conditions, it is necessary to control both the environment at the short and long distances.

The most relevant post-grafting processes are summarized in a review by Albela and Bonneviot.[115] The easiest strategy to obtain a single site may be performed by diluting the function on the surface (either incorporating less function or reducing the number of host sites), but low amounts of the targeted function are normally incorporated.[122] An alternative strategy is the use of a dismountable platform containing two or three functions at designed distances, commonly called molecular imprinting method (Figure 10a).[123–125] Although this method allows one to control the specific distance between the nearest functions (equal to

the length of the spacer), the amount of incorporated functions is not higher than in the previous strategy. Moreover, the synthesis of the precursors is not always straightforward. In order to increase the amount of function incorporated and to control the distance at short and at long distances, the "protection-deprotection" method was developed (Figure 10b).[126] With this method, the incorporation of high amounts of function and a good control at short and long distances is achieved by using a bulky patterning group that protects the desired group and can be removed after grafting. However, limited types of functions can be incorporated.

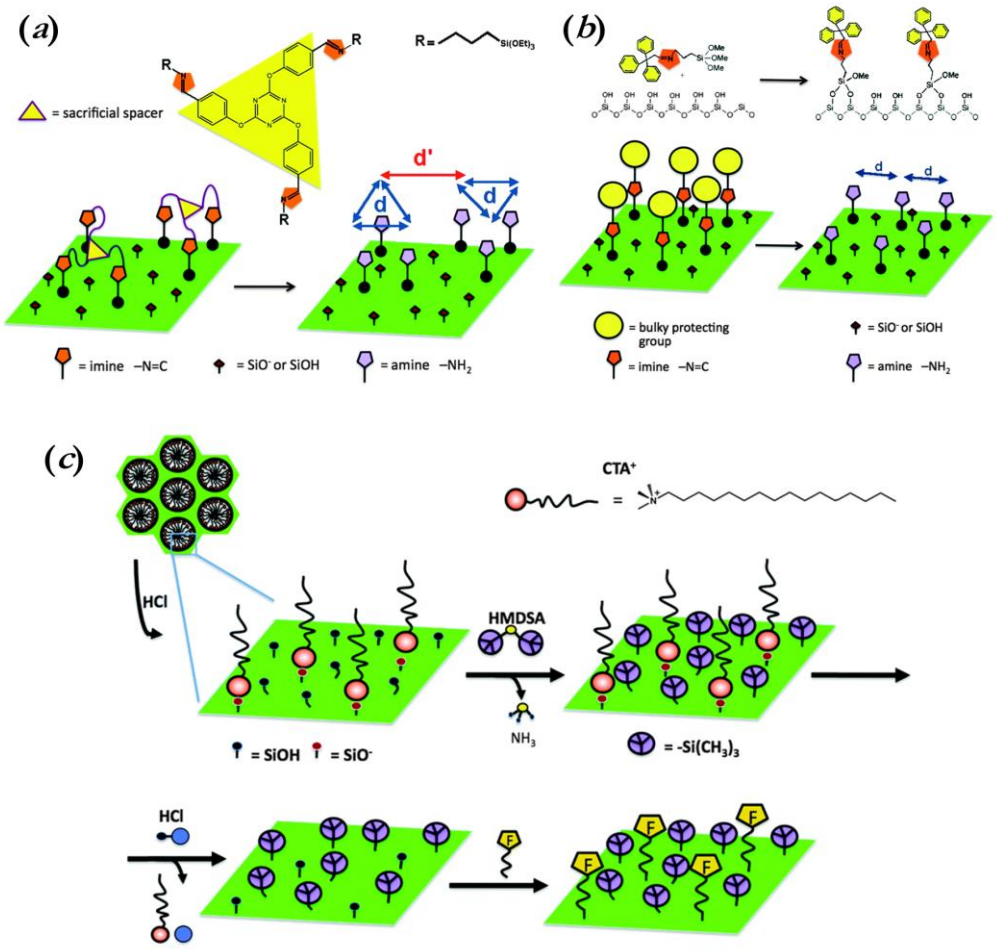

Figure 10. Principal post-grafting methods for the design of multifunctional materials: (***a***) molecular imprinting; (***b***) protection-deprotection method; and (***c***) molecular stencil patterning. The figure was taken from *New Journal of Chemistry* 2016 by Albela and Bonneviot.[115]

An alternative to the latter is that called molecular stencil patterning (Figure 10c),[127–129] described by Bonneviot and coworkers. The advantage of this method over the rest is the possibility to incorporate several different functions with a homogeneous distribution. It basically consists in using as a molecular pattern a charged molecule that is homogeneously distributed on the surface of the solid. Indeed, the electrostatic self-repulsion between the

cationic heads of a molecule as the CTA^+ surfactant (cetyltrimethylammonium) generates a regularly patterned surface. Then, the desired function may be grafted in the remaining space. The second function may be lately grafted in the solid after removal of the surfactant by acid treatment. The homogeneous distribution of functions afforded with this technique was proved for a material possessing trimethylsilyl and europium(III) coordinated to post-grafted 1,10-phenanthroline using energy-dispersive X-ray spectroscopy coupled to transmission electron microscopy (TEM-EDX).[128] Finally, the method was improved by replacing the CTA^+ ions with a much smaller masking agent, tetramethylammonium (TMA^+).[130] This replacement is performed by ionic exchange under very soft conditions. Then, TMA^+ ions may be used as masking agent, as they will be homogeneously distributed on the surface like the CTA^+ ions. The advantage of TMA^+ over CTA^+ is that it provides the channels with more free space, so large molecules can be incorporated finding no steric hindrance.

Encapsulation of catalase-biomimetic compounds

Biological systems are able to perform reactions where diffusion control, regioselectivity and enantioselectivity are finely controlled. These systems, such as receptors or enzymes, have been optimized by natural selection to operate at physiological conditions (low temperatures, quasi-neutral pH, and aqueous solution). Metalloproteins are supramolecular systems used by living organisms that consist of a catalytic site, made of one or more metal ions, and a very precise environment. This morphology gives place to enzymatic cavities with the required hydrophobicity and size that guarantees their effectiveness.[10]

In order to have a good analogy with bio-systems, it is important to have access to a large variety of active sites and organic environments. Micropores impose restrictions on accessibility and diffusion. For instance, an organic function is about 0.5 to 1.0 nm long, and accessibility requires a clearance of at least 1 nm. However, the use of materials with too large pore diameters will make the confinement far less effective. Therefore, the optimal pore diameters should be between 3 and 5 nm.[115]

The insertion of Mn-CAT model compounds in porous solids offers the possibility of mimicking different properties found in the native catalytic site, such as hydrophobicity and confinement.[113,117,131,132] Indeed, the encapsulation of antioxidants into nanocarriers can provide not only an improvement of stability but also a higher therapy efficiency.[133] However, in addition to high antioxidant activity, a successful nano-antioxidants should comply the following requirements:[133] (*a*) having a targeting group that drives specifically the antioxidant

to the desired organ or tissue; (*b*) avoiding the premature release of antioxidant species; (*c*) no cytotoxicity; (*d*) having an appropriate administration and excretion routes in the human body. Such requirements could only be achieved with the syntheses of advanced hybrid materials with molecular multi-functionalities, as shown in Figure 11.

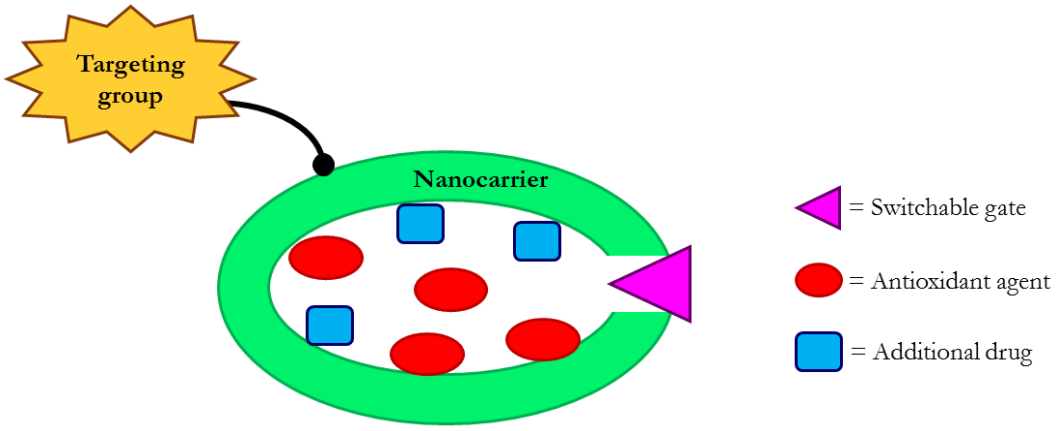

Figure 11. Illustration of the ideal and futuristic nano-antioxidant. This figure was inspired from *Free Radical Research* 2014 by Du *et al.*[133]

Among inorganic-based materials, mesoporous silica has attracted much attention because of its biocompatibility at practical concentrations and its ability to protect pharmaceutical principles from premature release or undesired degradation in living systems, acting as an effective drug delivery system.[134,135] Moreover, the versatile control over the internal and external surface functionalization is advantageous for the adaptability to any guest environment.[134,136]

Some examples of the design of hybrid materials based on Mn complexes, models of SOD,[137–139] CAT,[140,141] or WOC,[142] grafted on different types of silica have been reported, either on hollow mesoporous microspheres,[137] silica gel,[138,141] amorphous silica nanoparticles,[139] core-shell nanoparticles,[140] or SBA-15.[142] Between them, it is worth commenting that by Rumberger *et al.*,[142] where the immobilization of a Mn^{IV}_2 compounds inside SBA-15 prevented the active site from dimerization/oligomerization processes and guarantees the effectiveness of the hybrid material toward the H_2O oxidation.

Providing mesoporous silica materials with the desired molecular recognition, high biocompatibility, and specificity is rather challenging and it is nowadays an extensive subject of study. Fortunately, this is becoming achievable because of the great advances on mesoporous silica functionalization attained upon the course of time.[115,136] For instance, parameters such as the particle size and morphology, which have a great importance for the

biocompatibility[135] and for the diffusion rates or homogeneous dispersion of guests,[136] can be relatively well controlled by choosing the appropriate synthetic conditions.[136]

A distinctive characteristic of the mesoporous silica nanoparticles is that they have two defined surfaces: the internal and the external one. The functionalization of the internal surfaces, as well as the pore size, can be exploited to attain selectivity[136] or to tailor the drug delivery.[135] On the other side, the external functionalization may be a key process because all the functionalities concerning interactions between the particles and the environment will be of relevance when the material is exposed to blood. Hence, on the external surface of the nanoparticles one may graft either functions that increase the biocompatibility or targeting groups.[143] Last but not the least, there are several methods for the incorporation of "gatekeepers" in the entrance of the pores.[144] The so-called gatekeepers are functions that grant access to the pores under any internal or external stimulus, for example, induced by light, temperature, pH, magnetic field, or any reaction or interaction with biomolecules. These are elegant approaches where the driving force to switch gating mechanisms between an open state and a closed state take advantage of electrostatic interactions, the rupture/formation of covalent bonds, or changes in the physical properties of molecules or macromolecules.[144]

Another approach that is worth mentioning is the synthesis of artificial metalloenzymes, which come from the combination of an active metal center and an apoenzyme, this last one providing the secondary coordination sphere. The goal of these artificial metalloenzymes is to merge the advantageous properties of native enzymes, such as selectivity and biocompatibility, and the catalytic properties of transition metal catalysts.[145–148] Indeed, these bioinspired systems have shown promising results for the asymmetric synthesis of organic products in water solution. However, in spite of the relative success of these systems, there are still many remaining challenges that should be overcome. For instance, the artificial metalloenzymes does not always show an advantage over the small-molecule catalysts or show poor selectivities.[146] Moreover, identifying and optimizing the peptide scaffolds for the desired catalytic function is very difficult,[146] making crucial the use of rational computational modelling or directed evolution (iterative rounds of apoenzyme mutagenesis).[146,147] These studies or modifications are time-consuming and could be problematic since some residues may be key for the stability and structure of the enzymes.[147] Artificial metalloenzymes, owing to their complexity, should address some of the challenges in enantioselectivity for which there are no solutions in conventional asymmetric catalysis.[148]

Encapsulation of big clusters

The interest of Mn compounds of high nuclearity lies in their high magnetic moment, which enables them to act as contrast agents in magnetic resonance imaging (MRI). The controlled insertion of these systems in porous materials could guarantee their integrity and stability. Mesoporous silica is a promising carrier for these guests, since it additionally offers the possibility to modulate the environment around the guest molecules, affecting the selectivity and recognition of these systems.[115]

In particular, nanoclusters presenting the behavior of a Single-Molecule Magnet (SMM) have become an area of interesting research. SMMs represent nanoscale magnetic objects of a sharply defined size, which may be used as high-density information storage at the molecular level. However, the plausible applications require the control and organization of oriented molecules or molecular aggregates in a material where each individual species can be used as a bit of information. The insertion of SMM in mesoporous silica may offer a new synthetic route toward the applicability of these systems. By choosing the appropriate support, the design of a specific host-guest site becomes possible, reducing the guest-guest interactions. For the host-guest interaction, two possibilities arise: (*a*) the use of a non-binding function, or (*b*) the use of a binding function. While the first strategy would provide a weak guest-host interactions and a hypothetical low modification of the guest, the second one promotes a stronger host-guest interaction and an obvious modification of the guest. Some examples of SMM-SiO_2 hybrid materials are found in the literature, where different dodecanuclear compounds with $[Mn^{IV}_4Mn^{III}_8O_{12}]^{16+}$ core and carboxylate ligands were inserted into the channels of either MCM-41[149,150] or SBA-15[151–153] silica, showing only slight modifications of the magnetic properties (small effect of the support). However, in most of the cases the supports lack of confinement because the silica surface was not modified.[149–152]

4. Objectives

The main objective of this work is the synthesis of manganese compounds and hybrid materials that may have a relevance from a bioinorganic and magnetic point of view. Previous works in our group centered their attention on dinuclear Mn^{III} compounds with formula $[\{Mn^{III}_2O(L)(NN)\}_2(\mu\text{-}O)(\mu\text{-}n\text{-}RC_6H_4COO)_2]X_2$ (L = solvent or counter-anion, NN = 2,2'-bipyridine (bpy) or 1,10-phenantroline (phen), and X = NO_3^- and ClO_4^-), which may be structural or functional models of the active site from Mn-CAT enzymes. Moreover, the Mn^{II} compounds with the same kinds of ligands are of interest from the magnetic point of view.

Considering the explained above, the following objectives should be kept in mind:

- Explore the synthesis of analogous dinuclear Mn^{III} compounds with the benzoic acid derivatives *n*-RC_6H_4COOH, where *n*-R = 2-MeO, 3-MeO, 4-MeO, or 4-^{t}Bu, and bpy or phen. The goal of these experiments is to provide a wide range of compounds from which one may get a better understanding of their magnetic properties, such as the Mn···Mn magnetic interactions and the zero-field splitting.
- Synthesize Mn^{II} compounds with the same ligands as those used for the Mn^{III} ones in order to study the magnetic properties (magnetic susceptibility and EPR spectroscopy).
- The synthesis of Mn^{IV}-Ca^{2+} compounds with carboxylate bridges aiming to obtain structural models of the water oxidizing center (WOC) and analyze the effect of Ca^{2+} ion on the fundamental properties of the obtained compounds.
- The insertion of the molecular compounds into mesoporous supports to obtain hybrid materials. MCM-41 mesoporous silica was chosen over SBA-15 because it is synthesized under basic conditions, enabling one to use a cationic masking agent (tetramethylammonium), which allows the subsequent incorporation of cationic Mn complexes by ionic exchange, such as those of the dinuclear Mn^{III} compounds mentioned above.
- Study the effect of the functionalization of the inner walls of the silica on the stability of the hybrid materials. To incorporate the functions, the molecular stencil pattering method, which provides a good control on the amount and distribution of the functions, have been selected.
- Characterization of the Mn complex inside mesoporous silica and the study of the effect of the confinement on the magnetic properties.
- Study of the catalase activities of both molecular Mn^{III}_2 compounds and the hybrid materials in acetonitrile and water.

5. Manuscript Structure

The results presented in this manuscript are classified in three main topics: molecular chemistry (Section I), materials science (Section II), and catalytic properties (Section III). Each section is separated in several chapters, including not only those with the exposition of results but also those called "Introductory Remarks" and "Experimental Section". The

"Introductory Remarks" chapters (Chapter 1.1, Chapter 2.1, and Chapter 3.1) attempt to give a qualitative and understandable explanation of the characterization techniques used in this work and to provide the reader with general information concerning the materials under study. The so-called "Experimental Section" (Chapter 1.2, Chapter 2.2, and Chapter 3.2) contains a description of the procedures and devices used for the syntheses and characterizations of these materials and for the catalytic tests.

In Section I, the results have been organized according to the type of molecular compounds obtained. As commonly occurred in experimental chemistry, the desired type of compound was not obtained for all the experiments performed in this work; instead, other compounds with different nuclearties were isolated from some of these tests.

SECTION I: Molecular Compounds

1.1. Introductory Remarks

In the following chapters the synthesis and characterization of new Mn compounds with carboxylate bridging ligands in which Mn ions display oxidation states II, III or IV will be described. These compounds are of interest for the inorganic chemistry community because of their magnetic properties and due to the presence of mono- and polynuclear Mn clusters in the active site of several metalloproteins.

Excepting the Mn^{II} compounds in Chapter 1.4, the compounds presented in this section can be easily synthesized from the direct comproportionation reaction between a Mn^{II} salt (generally, NO_3^- or ClO_4^-) and NBu_4MnO_4 in the presence of the corresponding carboxylic acid and chelating ligands. Mn^{II} compounds were synthesized from Mn^{II} carboxylate. In this work we used benzoic acid derivatives with formula *n*-RC_6H_4COOH, where *n*-R = 2-MeO, 3-MeO, 4-MeO or 4-^{t}Bu, and 2,2'-bipyridine (bpy) or 1,10-phenantroline (phen). The subsequent isolation of crystalline samples of these compounds allowed for their characterization and the study of their magnetic properties.

Single-crystal X-ray diffraction

Single-crystal X-ray diffraction is one of the most important characterization techniques used in molecular chemistry. It is a non-destructive analytical method that provides structural information of crystalline substances, such as cell dimensions, bond lengths, bond angles, and the absolute configuration. XRD is based on a constructive interference of monochromatic X-rays and a crystalline sample, which occurs when conditions satisfy the Bragg's Law ($n\lambda = 2d \sin\theta$). This law relates the wavelength of the radiation (λ) to the diffraction angle (θ) and the lattice spacing in the crystalline sample (d). These diffracted X-rays are collected and processed. A typical structure contains several thousand unique reflections, which may be assigned to different indices (hkl). The diffracted intensity due to (hkl) planes of a crystal depends on the intensity that each atom diffracts and on its position in the crystal structure. Indeed, the more electronic density of an atom and the closer it is to a diffraction plane, the greater contribution on the corresponding reflection. This pattern of reflections has a reciprocal Fourier transform relationship to the crystalline lattice and unit cell in real space. This step is referred to the solution of the crystal structure. After the structure is solved, it is further refined using least-squares techniques. Two of the most

common software packages used to carry out the resolution of crystal structures are the WINGX[154] and, more recently, the ShelXle,[155] which are user interfaces for SHELX programs.[156] Then, the structures should be validated with the PLATON program[157] or through the website of *CheckCif*, a service of the International Union of Crystallography (IUCr).[158]

There are three groups of parameters for each atom: the site occupancy factor, the coordinates and the thermal displacements. Particularly, the **thermal displacement** parameters describe how much atoms are "vibrating" due to thermal agitation, in accord to their electron density. In fact, they are key parameters that should be checked during the refinement, since they may indicate if the assignment has been properly performed and the presence or absence of disorder.

Non-hydrogen atoms are refined with a determined site occupancy factor considering three atomic coordinates and six anisotropic displacements. On the contrary, hydrogens atoms are calculated or placed in logical positions with isotropic thermal parameters riding on their respective carbon or oxygen atoms. Thus, the thermal displacement of a non-hydrogen atom is embodied as an ellipsoid and that of a hydrogen atom as a sphere. The number of parameters to be refined depends on the number of crystallographically independent non-hydrogen atoms. A reliable refinement requires a minimum number of observations per refined parameter, and the IUCr recommends a data-to-parameter ratio of eight for non-centrosymmetric structures and 10 for centrosymmetric structures. However, it is sometimes tough to achieve such data-to-parameter ratio and constraints and restraints may be essential to indirectly improve it. **Constraints** are equations that relate two or more parameters or assign fixed numerical values to certain parameters, reducing the number of parameters to refine. On the other hand, **restraints** include additional information that one may have about a group or a molecule, for instance, that the aromatic systems tend to be flat or that the oxygen atoms of a perchlorate anion are equivalent. Figure 12 shows the effect of three restraints on anisotropic displacement parameters. Restraints may not be needed at all, but they can become crucial when correlations among certain parameters occur, such as for the refinement of disorders, pseudo-symmetry or twinned structures.[159]

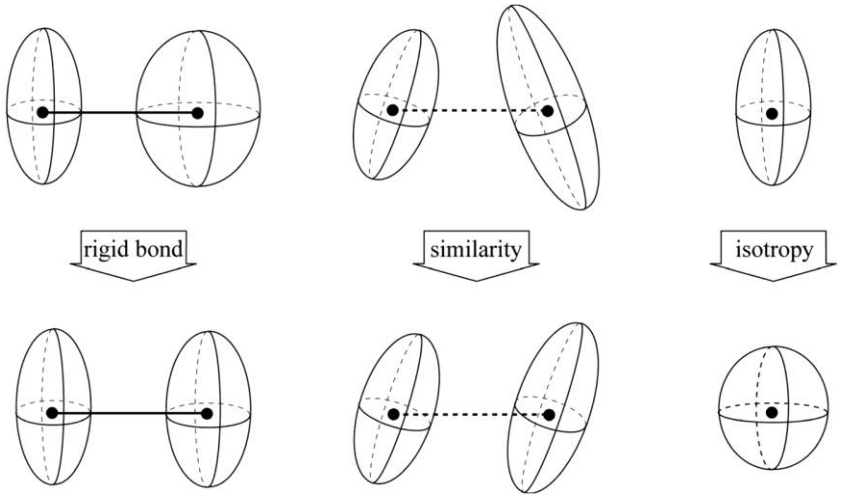

Figure 12. Illustrative representation of three restraints on anisotropic displacement parameters. The figure was taken from *Crystallography Reviews* 2009 by Müller.[159]

Obtaining good single-crystals that will consistently provide good diffraction patterns is crucial to stay out of trouble and it is less time consuming. Indeed, it is much easier to refine a structure based on good than on bad data. Therefore, crystal growth and crystal handling are of such importance.[159] **Crystallization** starts when the concentration of a compound is higher than the solubility of the product. However, crystallization is kinetically hindered and crystal growth only comes from supersaturated solutions. In order to obtain nice single-crystal with the required size, it is necessary to achieve a metastable state of supersaturation. Figure 13 shows three of the most popular methods of crystal growth, consisting in (*a*) increasing the concentration by evaporation of the solvent, (*b*) slow cooling of the solution, and (*c*) gas-phase diffusion of a precipitant into a solution.

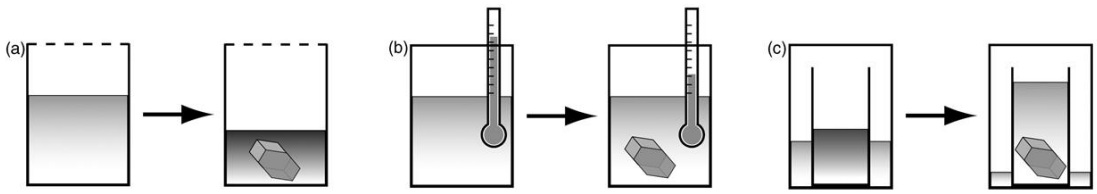

Figure 13. Thee popular crystallization methods: (***a***) slow evaporation of the solvent, (***b***) slow cooling of the solution, and (***c***) gas-phase diffusion of a precipitant into a solution. The figure was taken from *Crystallography Reviews* 2009 by Müller.[159]

Once one has obtained the crystals, it is important to keep them as undisturbed as possible before mounting them on the diffractometer, meaning that the environmental conditions should not be unnecessarily changed. The crystals should be kept in the mother liquor or submerged in special oils, since solvent molecules may have been co-crystallized with the

target compound. On the contrary, drying the crystals will lead to the evaporation of solvent molecules and to the succeeding collapse of the crystal structure.

Nevertheless, it is worth remarking that an X-ray crystal structure is not sufficient for the characterization of a new material, since the crystal used in this analysis does not necessarily represent the entire sample. Thus, additional data referred to the entire sample should be always given, such as elemental analyses.

Infrared spectroscopy

Infrared (IR) spectroscopy is commonly used in molecular chemistry because it allows to identify structures because of their functional groups. IR absorption takes place when the absorbed radiation matches the transition energy at which a certain bond or group vibrate. The energy required depends on the types of atoms associated to the vibrating bond and on its bond order.

Carboxylate groups display two very intense bands assigned to the asymmetric (ν_a) and symmetric (ν_s) vibrations, which arise at 1620–1550 and 1410–1380 cm^{-1}, respectively. The separation between these two bands ($\Delta\nu = \nu_a - \nu_s$) is indicative of the coordination mode. Figure 14 shows the three coordination modes with their $\Delta\nu$ values. To sum up, for $\mu_{1,3}$-carboxylate bridges, $\Delta\nu \approx 200$ cm^{-1}; whereas for $\mu_{1,1}$-carboxylate bridges, $\Delta\nu > 200$ cm^{-1}. The presence of protonated carboxylate ligands can be confirmed with the position of the asymmetric vibration (ν_a), which will be shift to ~1700 cm^{-1}.[14]

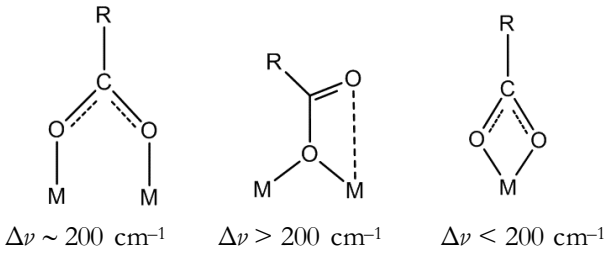

$\Delta\nu \sim 200$ cm^{-1} $\Delta\nu > 200$ cm^{-1} $\Delta\nu < 200$ cm^{-1}

Figure 14. Coordination modes for carboxylate ligands and the separation between the asymmetric (ν_a) and symmetric (ν_s) vibrations, defined as $\Delta\nu = \nu_a - \nu_s$.[14]

Moreover, the benzoate derivatives used in this work (n-$RC_6H_4COO^-$) display some other characteristic bands assigned to the stretching vibrations of C_{sp^3}–H of the R group. For example, when n-R = 4-^{t}Bu three peculiar bands arise at 2970 (medium), 2909 (weak), and 2871 (weak) cm^{-1}.

The rest of the ligands and counter-anions have also some characteristic bands that are close to the carboxylate ones. The capping ligands 2,2'-bipyridine (bpy) and 1,10-phenantroline (phen) display vibrations assigned to the aromatic rings at ~1600, 1498, 1480 and 1450 cm^{-1} (bpy) or at ~1600, 1520 and 1427 cm^{-1} (phen). Bands assigned to the Mn–O_{bridge}–Mn bonds arise at much lower wavenumbers, between 740 and 560 cm^{-1}, and they are usually weak. The two counter-anions used in this work, NO_3^- and ClO_4^- ions, display very intense and relatively broad bands at ~1380 and ~1100 cm^{-1}, respectively. Moreover, ClO_4^- ions display another one at 625 cm^{-1} of lower intensity.[16,160]

Molecular magnetism

After having fully characterized a compound, one may proceed to study its magnetic properties. Note that, in order to guarantee the reproducibility, it is important to ensure that the crystal used for the structure determination is representative of the entire sample. Hence, one need to carefully choose the experimental conditions in which compounds are obtained.

One of the aims in **molecular magnetism** is to understand the interaction of molecular substances containing unpaired electrons with an applied magnetic field (H). When a magnetic field is applied, magnetic samples will be affected and a magnetization (M) will be produced. In this work, we focus our attention on the molecular properties of polynuclear Mn compounds, where the paramagnetic ions are linked through bridging ligands, particularly by oxo and/or carboxylate ligands.

The *d* orbitals of the Mn ions, which contain the unpaired electrons, may interact with those of the neighbors through the bridging ligands, leading to new molecular orbitals (MO). Each linear combination of *d* orbitals and of the bridging ligand will lead at least to three MO: one of them strictly bonding, another "non-bonding", and a third one being antibonding (Figure 15). If the overlap between these orbitals is efficient, the two unpaired electrons will be coupled in the same MO. On the contrary, if the overlap between these orbitals is poor, the energy gap between the "non-bonding" and antibonding MO will be small and these electrons will be placed in different MO. The energy gap between these orbitals in complexes with d^n ions is around 0–500 cm^{-1}. As a consequence, the temperature will be very important in thermal population of these orbitals and it will be possible to study this with Boltzmann statistics (see below).

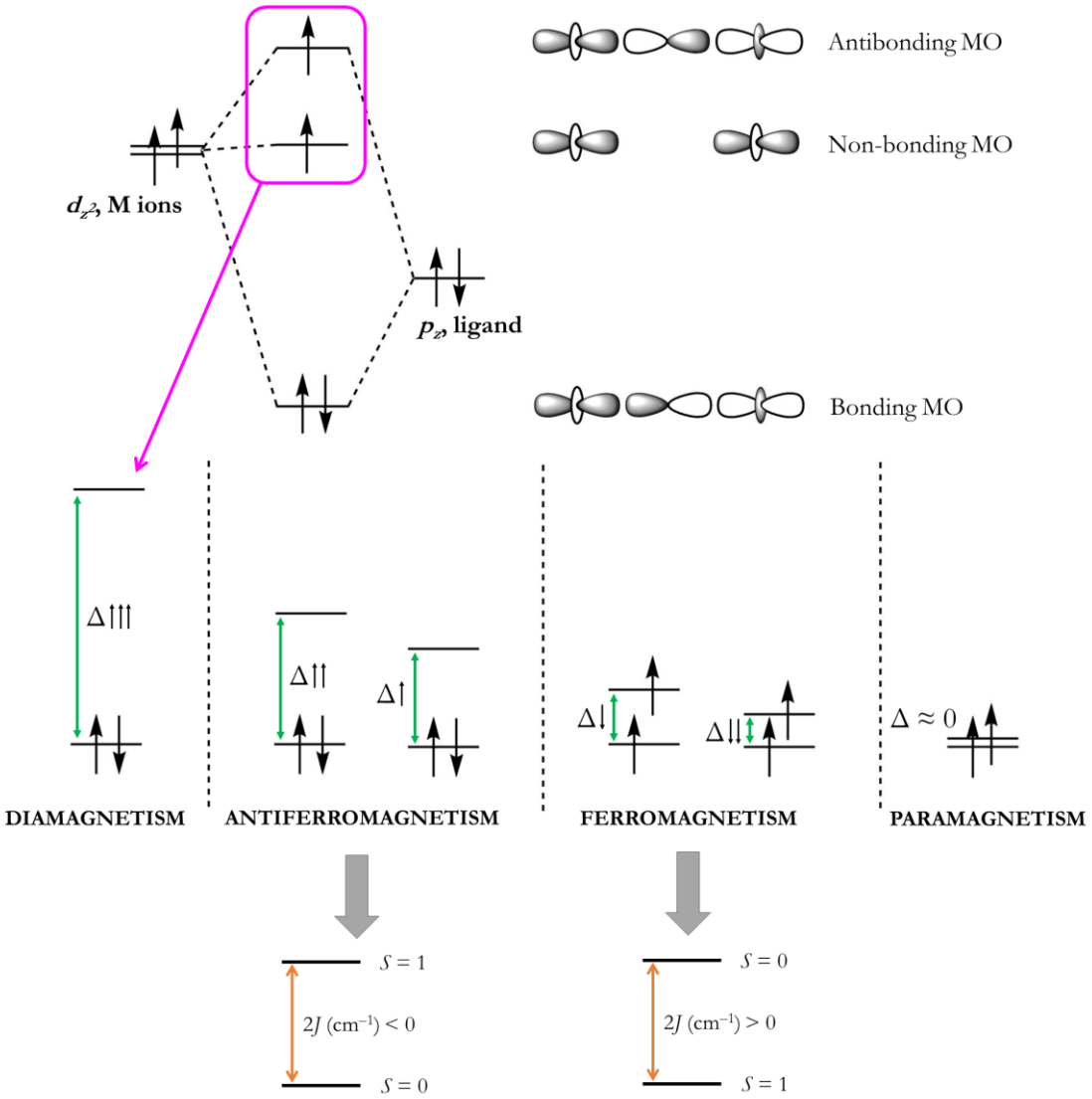

Figure 15. Relationship between the MOs of an M–X–M system and the concepts of dia-, antiferro-, ferro-, and paramagnetism. The figure was adapted from *Coordination Chemistry* 2008 by Ribas Gispert.[161]

If the two electrons are placed in the same MO, the final ground state is a spin singlet (S = 0) and the interaction will be called **antiferromagnetism**. On the other hand, if the two electrons are placed in different MO the ground state is a spin triplet (S = 1) and the interactions will be called **ferromagnetism**.

In the upper limit, the energy gap would be so large that the electrons would remain coupled even at room temperature; hence, in this case one could speak of **diamagnetism**. In the lower limit, if the overlap between the atomic orbitals is non-existing, the electrons will be unpaired but not interacting at all, behaving purely independent; thus, one could speak of **paramagnetism**.

The energy gap between these $S = 0$ and $S = 1$ states depends on the magnetic interaction and is defined with the **magnetic coupling constant *J***. According to Kahn[8] and Hoffmann[162] models, this parameter can be decomposed into two components, one ferromagnetic and one antiferromagnetic: $J = J_F + J_{AF}$. While the antiferromagnetic component (J_{AF}) favors the singlet spin state ($S = 0$) and is proportional to the squared energy gap between MO ($J_{AF} \propto \Delta^2$), the ferromagnetic one (J_F) favors the triplet state ($S = 1$) and depends on the coulomb repulsion between electrons placed in near centers.

Hence, the sign and value of J will be determined by the balance of these anti- and ferromagnetic components; thus, by the competition with the energy gap between the non-bonding and antibonding MO and the coulomb repulsion caused by the proximity of electrons taking part in the interaction.

In the case of Mn ions, there are several *d* orbitals containing unpaired electrons, depending on their oxidation state. In this work, Mn compounds with oxidation state II, III and IV will be found, having d^5, d^4 and d^3 configurations, respectively. The resulting magnetic interaction between two Mn ions (J) will arise from the addition of all plausible combinations of atomic orbitals ($J = \sum J_{ij}$).

As mentioned before, **molar magnetization** (M) expresses the density of permanent or induced magnetic dipole moments in a magnetic material. According to **Boltzmann statistics**, the number of particles, N_i, in a sample of N particles of a system that will be found in a non-degenerate state with energy E_i, when it is part of a system in thermal equilibrium at a particular temperature (T) is expressed by the Boltzmann distribution:

$$N_i = \frac{Ne^{-E_i/kT}}{\sum_i e^{-E_i/kT}} \qquad \text{Eq. 2}$$

where k is the Boltzmann constant (0.695 cm^{-1} K^{-1}). From this, it is also derived the Boltzmann probability factor as $P_i = N_i/N$. Then, for the calculation of the overall magnetic moment (magnetization) of a macroscopic sample, it is necessary to sum all the individual moments of each eigenstate, weighted according to their Boltzmann distribution (population):

$$M = N_A \sum_i \mu_i P_i = N_A \frac{\sum_i \mu_i e^{-E_i/kT}}{\sum_i e^{-E_i/kT}} \qquad \text{Eq. 3}$$

where N_A is the Avogadro number and μ_i is the magnetic moment of one molecule.

Based on Brillouin Function, the magnetization may increase linearly with the magnetic field, at small H and/or high T, or may be independent of H, at strong H and/or low T. In this

latter case, the magnetization is proportional to the number of unpaired electrons following the expression:

$$M = N_A g \mu_B S \qquad \text{Eq. 4}$$

where g is a dimensionless parameter that is 2.00 for a free electron, μ_B is the Bohr magneton, which express the magnetic moment of an electron, and S is the spin quantum number, defined as $S = n/2$, where n is the number of unpaired electrons.

The **magnetic susceptibility** (χ) indicates the degree of magnetization (M) of a material in response to an applied magnetic field (H), defined as $\chi = M/H$. For molecular compounds, the molar magnetic susceptibility (χ_M) is used. As χ_M is proportional to the population of each eigenstate, the study of this property as a function of T may provide very useful information concerning the magnetic interaction in molecular compounds. Generally, authors use the $\chi_M T$ versus T plot, which is the one giving the most intuitive representation. Figure 16 shows the $\chi_M T$ versus T plots for dinuclear Mn^{III} systems with different magnetic behavior. For paramagnetic compounds ($J = 0$) $\chi_M T$ is independent of T and its value is proportional to the spin following the Curie Law:

$$\chi_M T = \frac{N_A g^2 \mu_B}{3k} S(S+1) = 0.125 g^2 S(S+1) \qquad \text{Eq. 5}$$

On the other hand, $\chi_M T$ values increase as the temperature falls when the interaction is ferromagnetic and decreases when it is antiferromagnetic. This fact may be explained with Boltzmann statistics. To do so, we chose the example of a Mn^{III}_2 system. The energy levels of such dinuclear systems consist in five different eigenstates with S = 0, 1, 2, 3 and 4. If the interaction between these two ions is ferromagnetic (F), the ground state will be $S = 4$, whereas it will be $S = 0$ if the interaction is antiferromagnetic (AF). At low T, only (or mainly) the ground state will be populated; hence, $\chi_M T$ = 10 (F) or 0 (AF) $cm^3\ mol^{-1}\ K$, according to Eq. 5. As the temperature increases, the population in the excited states increases with a consequent decrease in the population of the ground state. At room temperature, all states are populated following Boltzmann statistics and the electrons behave in a non-coupled manner, giving $\chi_M T$ values close to 6.0 $cm^3\ mol^{-1}\ K$ (corresponding to the addition of two non-interacting Mn^{III} ions). Moreover, the shape of the curve is sensitive not only to the sign but also the magnitude of the Mn···Mn interaction (J), as shown in Figure 16.

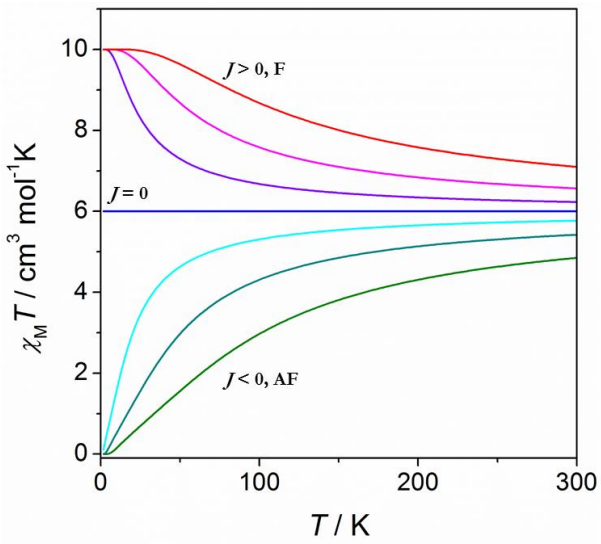

Figure 16. $\chi_M T$ versus T plots for a Mn^{III}_2 systems displaying anti- (AF) and ferromagnetic (F) behavior.

The exchange energy resulting from electrostatic interactions between the electrons share by two atoms, *i* and *j*, with spins S_i and S_j has been successfully represented by the Heisenberg-Dirac-van Vleck Hamiltonian. This Hamiltonian describes phenomenologically the interaction between several spins and allows the calculation of the interaction energy between two (or more) paramagnetic ions:

$$\hat{H} = -2J_{ij}\hat{S}_i\hat{S}_j \qquad \text{Eq. 6}$$

where J_{ij} is the exchange constant between spins S_i and S_j. The use of this Hamiltonian may be extended to any system, where the interactions with all the spins will be represented as:

$$\hat{H} = -2\sum_i^j J_{ij}\hat{S}_i\hat{S}_j \qquad \text{Eq. 7}$$

However, three different Hamiltonians are commonly used in the literature, these being $\hat{H} = -2\boldsymbol{J_{ij}}\hat{S}_i\hat{S}_j$, $\hat{H} = -\boldsymbol{J_{ij}}\hat{S}_i\hat{S}_j$ or $\hat{H} = \boldsymbol{J_{ij}}\hat{S}_i\hat{S}_j$. Therefore, it is always very important to indicate which is the Hamiltonian used. In our case, we normally use the one in Eq. 6 – excepting in Chapter 1.5, where, for the sake of clarity, we used the Hamiltonian $\hat{H} = -\boldsymbol{J_{ij}}\hat{S}_i\hat{S}_j$.

Apart from the aforesaid magnetic interaction, additional effects that modify the energy levels may occur. One of them (and the most remarkable for this work) is the **zero-field splitting (ZFS)**. The essence of ZFS lies in a weak interaction of the spins mediated by the spin-orbit coupling.[21] In transition metal ion systems, the ZFS term is used to describe any effect that removes the spin degeneracy in anisotropic polyelectronic systems ($S > 1/2$).[161] The most significant ZFS parameters refers to the axial (D) and rhombic (E) anisotropies,

where $E \leq D/3$. The axial anisotropy parameter (D) splits the $S = n/2$ levels into states $M_S = \pm 0, 1, \ldots, n/2$ for non-fractional S and into $M_S = \pm 1/2, 3/2, \ldots, n/2$ for fractional S values. On the other hand, the rhombic anisotropy parameters (E) split the positive and negative M_S states.[8,161] Figure 17 exemplifies the axial ZFS.

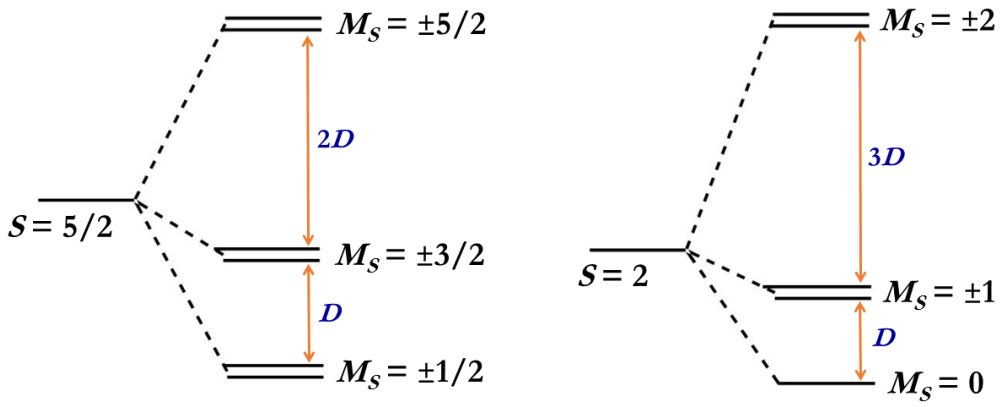

Figure 17. Qualitative representation of the axial zero-field splitting of the energy terms with $S = 2$ and $S = 5/2$.

These anisotropy parameters are of great importance for Mn ions. In fact, it is well known that Mn^{II} ions display small ZFS parameters ($|D| < 0.3$ cm^{-1}),[21,24–31,36,32–34] whereas those for Mn^{III} ions are much greater ($|D| = 2$–5 cm^{-1}).[21,22,163,164] In magnetism, the ZFS becomes visible when the thermal population of energy levels is unequal; thus, it can only be detected at low temperatures. Hence, magnetization, which is measured at low T and reaches strong magnetic fields ($H = 5$ T), becomes a good technique for quantifying the ZFS parameters of Mn^{III} ions. Figure 18 shows how the axial ZFS affects the magnetization curves. The non-superposition of the iso-field curves will be indicative of a substantial magnetic anisotropy. However, small ZFS parameters, such as those displayed for Mn^{II} ions, will not be detected using this technique.

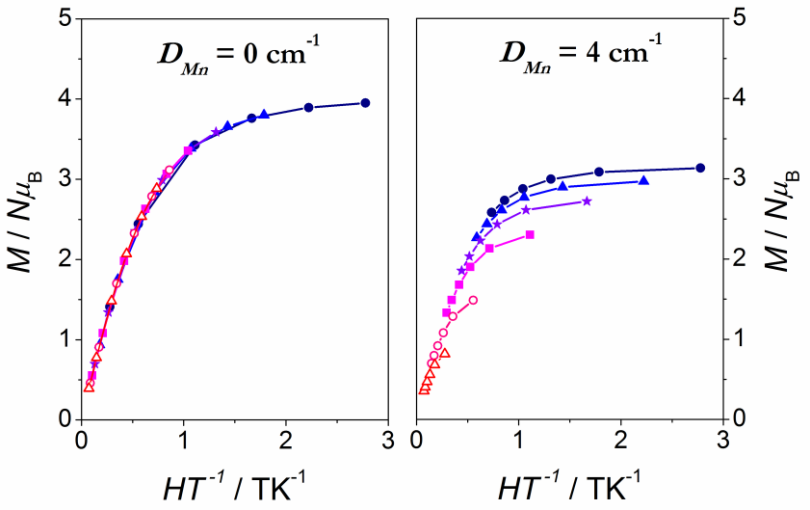

Figure 18. $M/N\mu_B$ (N = Avogadro number) versus HT^{-1} plots for a Mn^{III} compound with D_{Mn} = 0 and D_{Mn} = 4 cm^{-1}; T = 1.8–6.8 K and H = 0.5 (open triangles), 1.0 (open circles), 2.0 (squares), 3.0 (stars), 4.0 (full triangles) and 5.0 T (full circles).

Electron paramagnetic resonance

Electron paramagnetic resonance (EPR) studies the electron spin excitation at a particular frequency as a function of an external magnetic field. To understand how EPR works, it is important to firstly talk about the electronic Zeeman effect.

The **Zeeman effect** explains how the different M_S states split according to the Zeeman Hamiltonian $\hat{H} = g\mu_B\hat{S}$. The g value for a free electron is $g_e \approx 2.00$. Figure 19 shows the splitting of these states for an $S = 2$ state. As these states split, the population will not be exactly the same owing to Boltzmann distribution. These slight but existing differences in occupancy will gives rise to a net absorption of radiation, which will take place when the energy difference of a permitted transition is equal to $h\upsilon$ (h = Planck constant, υ = frequency of the applied radiation), taking into consideration the **spectroscopic selection rules**, $\Delta M_S = \pm 1$ and $\Delta S = 0$.[161] Two frequencies, those of the X (υ = 9.5 GHz) and Q (υ = 35 GHz) bands, are commonly used in EPR spectroscopy, and the magnetic field usually ranges from 0 to ~6 T.

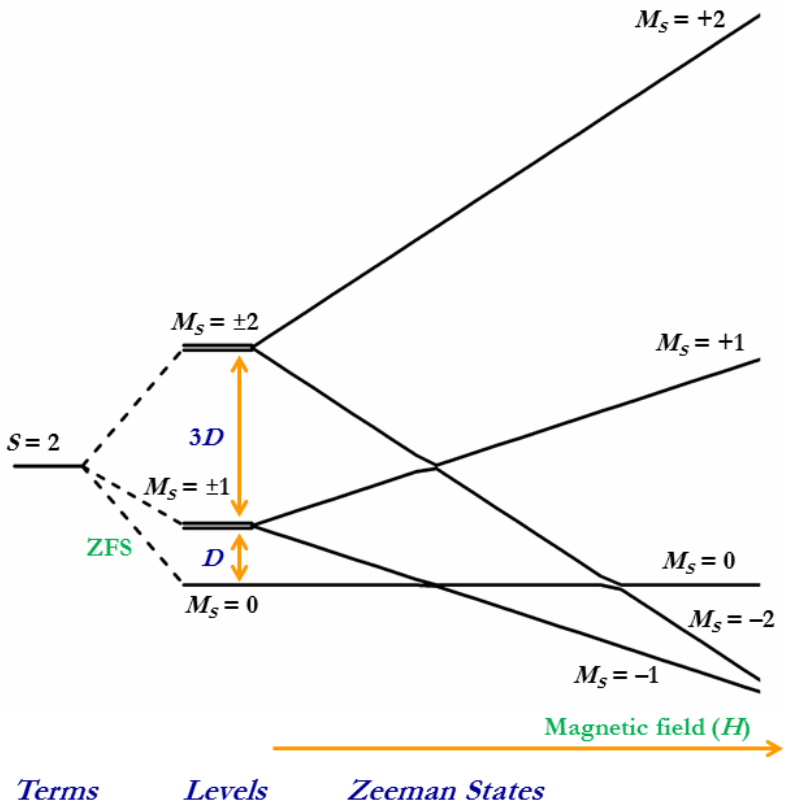

Figure 19. Qualitative representation of the zero-field splitting (ZFS) and Zeeman effect for an S = 2 with significant D.

As electrons are not isolated because they are on a molecule, they always have an orbital component. Depending on the type of orbital in which an electron is placed, it will resonate with a g value different from that of a free electron. The experimental g value can be calculated with the formula:

$$g = \frac{h\upsilon}{\mu_B H} \qquad \text{Eq. 8}$$

EPR spectroscopy becomes very useful to study molecular materials with small ZFS (D and $E \approx h\upsilon$). Figure 20 shows the first derivative of the EPR spectra and Zeeman plots (simulated with the PHI program)[165] for an S = 1 states as a function of the axial anisotropy (D), where D = 0, 0.05, and 0.08 cm^{-1}. As may be observed, for an isotropic system (D = 0) a single signal appears at $g \approx 2.00$ and the Zeeman plots are the same for the three directions of the magnetic field ($x = y = z$). On the contrary, when axial anisotropy (D) becomes relevant, the Zeeman plot in the z direction is rather different from those in the y and x direction ($x = y \neq z$). Because of this, the EPR signal of the isotropic state splits, showing four ΔM_S = 1 (green arrows) and one ΔM_S = 2 (pink arrows) transitions. This latter transitions should be forbidden, according to the selection rules; however, when anisotropy

is present, the M_S states mix and that allows for this transition.[8] It is worth noting that there are substantial differences between the EPR spectra for D = 0.05 and 0.08 cm^{-1}. In fact, the splitting of the signals is proportional to the value of D. Nevertheless, if $D >> h\upsilon$, the plausible $\Delta M_S = 1$ transitions shift to high magnetic field ($H > 6$ T), so conventional EPR spectroscopy becomes useless. In this situation, one would need to use high-frequency high-field EPR.

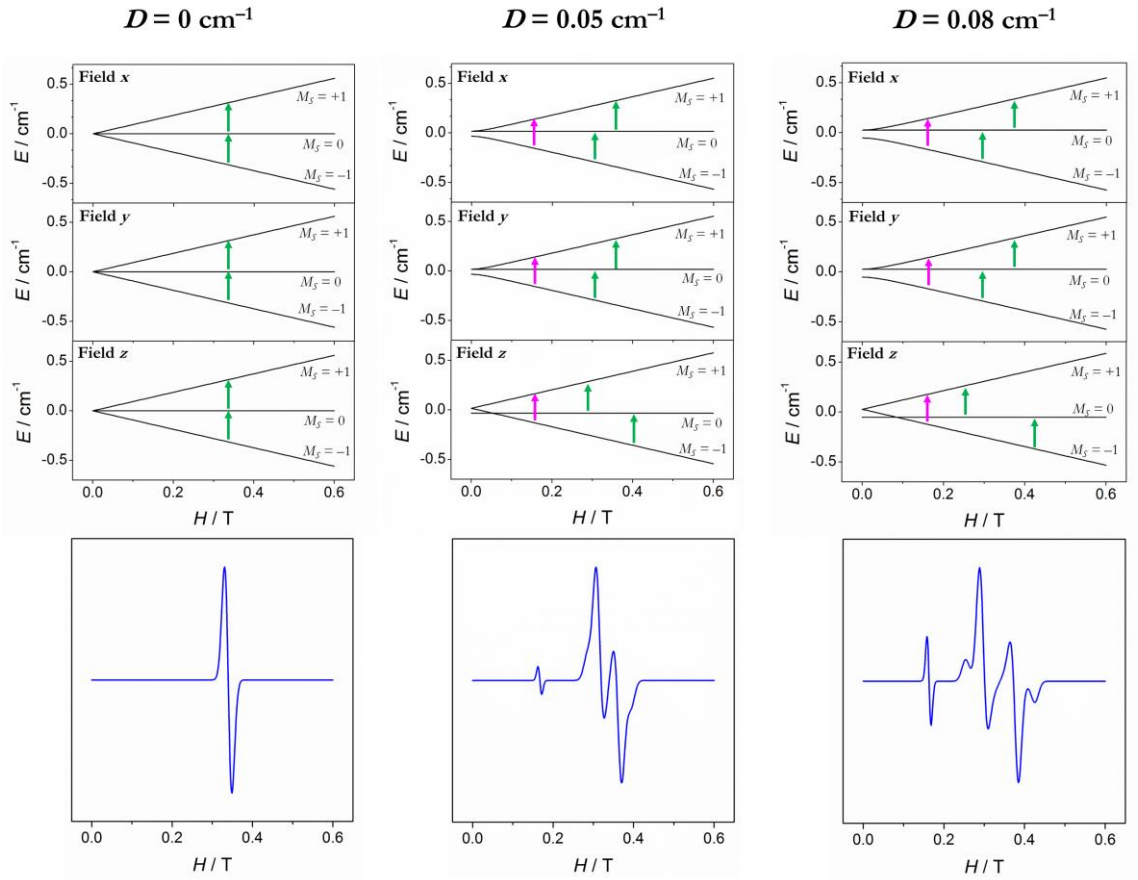

Figure 20. Effect of the axial zero-field splitting on Zeeman plots and EPR spectra for an $S = 1$ state. The green arrows correspond to the permitted transitions ($\Delta M_S = 1$) and the pink arrows to the forbidden transition ($\Delta M_S = 2$) (see text).

1.2. Experimental Section

Synthesis

All manipulations were performed under aerobic conditions. Reagents and solvents were obtained from commercial sources and used without further purification. NBu_4MnO_4 was prepared as described in the literature.[166]

Caution! Perchlorate salts of compounds containing organic ligands are potentially explosive. Only small quantities of these compounds should be prepared.

Synthesis of Mn^{III} compounds

$[\{Mn(bpy)(H_2O)\}(\mu\text{-}2\text{-}MeOC_6H_4COO)_2(\mu\text{-}O)\{Mn(bpy)(NO_3)\}]NO_3$ (1). 2-$MeOC_6H_4COOH$ (0.24 g, 1.6 mmol), previously dissolved in acetonitrile, was added to a solution of $Mn(NO_3)\cdot 4H_2O$ (0.32 g, 1.28 mmol). An acetonitrile solution of NBu_4MnO_4 (0.12 g, 0.32 mmol) was added to the previous mixture in small portions during 1–2 min while, almost simultaneously, 10 mL acetonitrile solution of 2,2'-bipyridine (bpy) (0.25 g, 1.6 mmol) was added, also in small portions. The resulting black solution (total volume ~60 mL) was stirred for 15 min and shortly afterward filtered to separate a dark precipitate. Dark crystals were isolated by filtration after 6 days of slow evaporation at room temperature, washed with ether and dried under vacuum. Yield: 40%. X-ray quality single-crystals were obtained by very slow evaporation of the mother solution after 15 days. Anal. Calcd. for $C_{36}H_{32}Mn_2N_6O_{14}\cdot 2H_2O$ (M.W. = 918.58 g mol^{-1}) (%): C, 47.07; H, 3.95; N, 9.15. Found (%): C, 46.04; H, 3.88; N, 9.13. Selected IR data (cm^{-1}): 3409 (br), 3093 (w), 3058 (w), 3031 (w), 2970 (w), 1601 (s), 1565 (m), 1498 (w), 1488 (m), 1449 (m), 1359 (s), 1294 (w), 1276 (w), 1245 (m) 1177 (w), 1162 (w), 1147 (w), 1102 (w), 1033 (m), 1021(w), 844 (w), 765 (s), 729 (m), 661 (m), 536 (w), 463 (w).

$[\{Mn(bpy)(H_2O)\}(\mu\text{-}2\text{-}MeOC_6H_4COO)_2(\mu\text{-}O)\{Mn(bpy)(ClO_4)\}]ClO_4$ (2). An analogous procedure was followed as for **1**, but using $Mn(ClO_4)_2\cdot 6H_2O$ (0.46 g, 1.28 mmol) and only 30 mL of acetonitrile. Dark crystals were isolated after 10 days of slow evaporation at room temperature. Yield: 60%. Very thin single-crystals were obtained by leaving the solution undisturbed in the refrigerator after 1 month. Anal. Calcd. for $C_{36}H_{32}Cl_2Mn_2N_4O_{16}\cdot 0.25CH_3CN$ (M.W. = 967.70 g mol^{-1}) (%): C, 45.30; H, 3.35; N, 6.15; Cl, 7.33. Found (%): C, 45.10; H, 3.35; N, 6.13; Cl, 7.33. Selected IR data (cm^{-1}): IR (cm^{-1}):

3419 (br), 3093 (w), 3084 (w), 3013 (w), 2973 (w), 2839 (w), 1602 (s), 1561 (s), 1497 (w), 1471 (m), 1448 (m), 1377 (s), 1322 (w), 1280 (w), 1247 (m) 1107 (s,br), 1032 (m), 848 (w), 762 (s), 730 (m), 663 (m), 625 (m), 573 (w), 475 (w), 415 (w).

[{Mn(bpy)(NO_3)}$_2$(μ-3-$MeOC_6H_4COO$)$_2$(μ-O)]·H_2O (3·H_2O). 3-$MeOC_6H_4COOH$ (1.6 mmol, 0.24 g) and $Mn(NO_3)_2·4H_2O$ (1.28 mmol, 0.32 g) were dissolved in acetonitrile. Then, a pre-filtered acetonitrile solution (10 mL) of NBu_4MnO_4 (0.32 mmol, 0.12 g) was added to the previous solution in small portions for 1–2 minutes while, almost simultaneously, an acetonitrile solution (10 mL) of 2,2'-bipyridine (bpy) (1.6 mmol, 0.25 g) was added, also in small portions. The resulting black solution (total volume ~25 mL) was stirred for 10–15 minutes and shortly afterward filtered to separate any possible precipitate. After keeping the solution in the refrigerator for one day, dark crystals were collected by filtration. Yield: 67%. Anal. Calcd for $C_{36}H_{30}Mn_2N_6O_{13}·H_2O$ (M.W. = 882.55 g mol^{-1}) (%): C, 48.99; H, 3.65; N, 9.52. Found (%): C, 47.71; H, 3.67; N, 9.16. Selected IR data (cm^{-1}): 3388 (br), 3088 (w), 2999 (w), 2929 (w), 2837 (w), 1610 (m), 1560 (s), 1497 (w), 1471 (w), 1448 (m), 1383 (vs), 1300 (s), 1282 (s), 1245 (s), 1155 (w), 1107 (m), 1082 (w), 1043 (s), 1032 (s), 919 (w), 902 (m), 876 (w), 762 (s), 728 (s), 681 (w), 662 (w), 653 (w), 634 (w), 445 (m), 415 (w).

[{Mn(bpy)(H_2O)}(μ-3-$MeOC_6H_4COO$)$_2$(μ-O){Mn(bpy)(NO_3)}]NO_3·1/2 H_2O·1/2 CH_3CN (4·1/2 H_2O·1/2 CH_3CN). An analogous procedure was followed as for **3**, but using 50 mL of acetonitrile and adding 1 mL of H_2O 5 min after the addition of all reagents. After three days in the refrigerator, dark crystals were collected by filtration. Yield: 55%. Anal. Calcd for $C_{36}H_{32}Mn_2N_6O_{14}·1/2\,CH_3CN·1/2\,H_2O$ (M.W. = 912.08 g mol^{-1}) (%): C, 48.72; H, 3.81; N, 9.98. Found (%): C, 49.07; H, 3.79; N, 9.87. Selected IR data (cm^{-1}): 3397 (br), 3107 (w), 3078 (w), 3059 (w), 3031 (w), 3003 (w), 2973 (w), 2938 (w), 2836 (w), 1601 (m), 1561 (s), 1496 (w), 1466 (w), 1446 (m), 1384 (vs), 1320 (s), 1279 (m), 1248 (s), 1166 (m), 1117 (w), 1103 (w), 1047 (w), 1054 (w), 1032 (s), 993 (w), 916 (w), 884 (w), 833 (w), 728 (m), 762 (s), 727 (s), 664 (w), 645 (w), 456 (w, br), 412 (w).

[{Mn(bpy)(H_2O)}(μ-3-$MeOC_6H_4COO$)$_2$(μ-O){Mn(bpy)(ClO_4)}]ClO_4·3 H_2O (5·3 H_2O). 3-$MeOC_6H_4COOH$ (1.6 mmol, 0.24 g) and $Mn(ClO_4)_2·6H_2O$ (1.32 mmol, 0.46 g) were dissolved in acetonitrile. Then, solid NBu_4MnO_4 (0.32 mmol, 0.12 g) was added to the previous solution in small portions for 1–2 minutes while, almost simultaneously, an acetonitrile solution (10 mL) of 2,2'-bipyridine (bpy) (1.6 mmol, 0.25 g) was added, also in small portions. The resulting black solution (total volume ~20 mL) was stirred for 15 minutes. Afterwards, the volume was reduced to 5 mL using a rotary evaporator (35 °C, 0.2

Bar) and filtered to separate any possible residue. The solution was layered with *n*-hexane (10 mL) and CH_2Cl_2 (5 mL). After four days, dark crystals were isolated by filtration and dried under vacuum. Yield: 65%. Anal. Calcd for $C_{36}H_{32}Cl_2Mn_2N_4O_{16}\cdot 3\ H_2O$ (M.W. = 1011.48 g mol^{-1}) (%): C, 42.75; H, 3.79; N, 5.54. Found (%): C, 43.04; H, 3.77; N, 5.34. Selected IR data (cm^{-1}): 3420 (br), 3106 (w), 3091 (w), 3065 (w), 2972 (w), 2940 (w), 2840 (w), 1608 (m), 1560 (s), 1496 (w), 1471 (m), 1448 (s), 1381 (s), 1313 (m), 1280 (m), 1248 (m), 1106 (vs), 1032 (vs), 917 (w), 886 (w), 786 (m), 754 (s), 728 (s), 663 (w), 623 (m), 545 (w, br), 459 (m), 415 (w).

[{Mn(bpy)(EtOH)}(μ-4-$MeOC_6H_4COO$)$_2$(μ-O){Mn(bpy)(ClO_4)}]$ClO_4\cdot$1/3 CH_3CN ·1/3 H_2O (6·1/3 CH_3CN ·1/3 H_2O). 4-$MeOC_6H_4COOH$ (1.6 mmol, 0.24 g) and $Mn(ClO_4)_2\cdot 6H_2O$ (1.32 mmol, 0.46 g) were dissolved in acetonitrile. Then, a pre-filtered acetonitrile solution (10 mL) of NBu_4MnO_4 (0.32 mmol, 0.12 g) was added to the previous solution in small portions for 1–2 minutes while, almost simultaneously, an acetonitrile solution (10 mL) of 2,2'-bipyridine (bpy) (1.6 mmol, 0.25 g) was added, also in small portions. The resulting black solution (total volume ~30 mL) was stirred and reduced to ~6 mL. This solution was mixed with absolute ethanol (20 mL) and filtered to separate any possible residue. Tiny black crystals were obtained after two days in the refrigerator. Yield: 45%. Anal. Calcd for $C_{38}H_{36}Cl_2Mn_2N_4O_{16}\cdot 1/3\,CH_3CN\cdot 1/3\ H_2O$ (M.W. = 1005.18 g mol^{-1}) (%): C, 46.20; H, 3.78; N, 6.04; Cl, 7.05. Found (%): C, 46.67; H, 3.80; N, 6.16; Cl, 7.08. Selected IR data (cm^{-1}): IR (cm^{-1}): 3364 (br), 3113 (w), 3086 (w), 2957 (w), 2930 (w), 2901 (w), 2836 (w), 1604 (s), 1552 (s), 1497 (w), 1470 (m), 1446 (m), 1417 (m), 1391 (s), 1313 (m), 1255 (s), 1171 (s) 1103 (s, br), 1049 (s), 926 (w), 853 (w), 784 (m), 765 (m), 729 (m), 662 (w), 623 (s), 512 (w), 415 (m).

[{Mn(bpy)(EtOH)}(μ-4-^{t}BuC_6H_4COO)$_2$(μ-O){Mn(bpy)(ClO_4)}]ClO_4 (7). 4-^{t}BuC_6H_4COOH (1.6 mmol, 0.28 g) and $Mn(ClO_4)_2\cdot 6H_2O$ (1.28 mmol, 0.46 g) were dissolved in absolute ethanol (10 mL). Next, solid NBu_4MnO_4 (0.32 mmol, 0.12 g) was added to the previous solution in small portions for 1–2 minutes while, almost simultaneously, 10 mL of an absolute ethanol solution of 2,2'-bipyridine (bpy) (1.6 mmol, 0.25 g) was added, also in small portions. The resulting black solution (total volume ~20 mL) was stirred for 15 minutes and shortly afterward filtered in order to separate any possible precipitate. The solution was left undisturbed in the refrigerator for a week. Dark crystals were isolated by filtration, washed with ethanol and dried under vacuum. Yield: 32%. Anal. Calcd for $C_{44}H_{48}Cl_2Mn_2N_4O_{14}$ (M.W. = 1037.65 g mol^{-1}) (%): C, 50.93; H, 4.66; N, 5.40. Found (%): C, 50.32; H, 4.49; N, 5.52. Selected IR data (cm^{-1}): 3366 (br), 3116 (w), 3087 (w), 3054 (w), 2962 (m), 2910 (w), 2867

(w), 1611 (m), 1588 (m), 1548 (m), 1499 (w), 1472 (m), 1448 (m), 1382 (s), 1313 (w), 1270 (w), 1250 (w), 1195 (w) 1107 (s), 1032 (s), 922 (w), 862 (w), 789 (m), 777 (m), 748(w), 730 (m), 711 (m), 664 (w), 620 (m), 544 (w), 476 (w), 418 (w).

Synthesis of Mn^{II} compounds

$Mn(n\text{-}MeOC_6H_4COO)_2 \cdot m H_2O$ (n = 2 or 4). 2-$MeOC_6H_4COOH$ or 4-$MeOC_6H_4COOH$ (26 mmol, 3.9 g) was dissolved in H_2O (200 mL) and then mixed with a suspension of $MnCO_3$ (13 mmol, 1.5 g) in H_2O (200 mL). The mixture was constantly stirred at 95 ºC for 6 h. Then, the hot solution was filtered to separate impurities of MnO_2 and the surplus $MnCO_3$. The volume of the solution was reduced to 200 mL by heating. A white solid was obtained after letting cool down the solution. The solid was filtered under vacuum and washed with Et_2O. For n = 2, yield: 57%. $C_{16}H_{14}MnO_6$ (M.W. = 357.16 g mol^{-1}). Anal. Calcd (%): C, 53.80; H, 3.95. Found (%): C, 52.20; H, 3.90. For n = 4, yield: 51%. $C_{16}H_{14}MnO_6 \cdot 2 H_2O$ (MW = 393.25 g mol^{-1}). Anal. Calcd (%): C, 48.87; H, 4.61. Found (%): C, 49.2; H, 4.70.

$[Mn_3(3\text{-}MeOC_6H_4COO)_6(EtOH)_2]_n$. 3-$MeOC_6H_4COOH$ (26 mmol, 3.9 g) was dissolved in H_2O (100 mL) and then mixed with a suspension of $MnCO_3$ (13 mmol, 1.5 g) in H_2O (100 mL). The mixture was constantly stirred at 95 ºC for 6 h. Then, the hot solution was filtered to separate impurities of MnO_2 and the surplus $MnCO_3$. The volume of the solution was reduced to 20 mL by heating to give a pale pink solution. The solution was allowed to cool down and then technical EtOH (5 mL) was added, immediately becoming pale yellow. The resulting pale yellow solution was left undisturbed in the refrigerator. After one month, big pale pink crystals were obtained. Yield: 43%. X-ray suitable crystals were obtained from the mother liquor. $C_{52}H_{54}Mn_3O_{20}$ (M.W. = 1163.78 g mol^{-1}). Anal. Calcd (%): C, 53.67; H, 4.67. Found (%): C, 53.37; H, 4.80.

$Mn(4\text{-}^tBuC_6H_4COO)_2 \cdot 3 H_2O$. $Mn(AcO)_2$ (5.61 mmol, 1.37 g) was dissolved in hot water (10 mL) and added to a solution of 4-^{t}BuC_6H_4COOH (5.61 mmol, 1 g) in water (40 mL). The resulting mixture was stirred at 95 ºC for 48 h in order to evaporate the acetic acid. Afterwards, a white solid was filtered and dried under vacuum. *Note:* the product is soluble in Et_2O, so this solvent should not be used for washing. Yield: 62% (based on total 4-^{t}BuC_6H_4COOH). $C_{22}H_{26}MnO_4$ (M.W. = 463.42 g mol^{-1}). Anal. Calcd (%): C, 57.02; H, 6.96. Found (%): C, 57.70; H, 6.80.

$[\{Mn(bpy)_2\}_2(\mu\text{-}2\text{-}MeOC_6H_4COO)_2](ClO_4)_2$ (8). $Mn(2\text{-}MeOC_6H_4COO)_2$ (0.30 mmol, 0.11 g) was dissolved in a EtOH:H_2O 1:1 (v/v) mixture (30 mL) by stirring for around 24 h.

Then, a solution of $NaClO_4$ (0.33 mmol, 0.041 g) in EtOH:H_2O 1:1 (v/v) (10 mL) was added to the previous one. Meanwhile, 2,2'-bipyridine (bpy) (0.72 mmol, 0.11 g) was dissolved in EtOH (10 mL) and added to the previous solution. The resulting yellow solution (solvent: 50 mL of EtOH:H_2O 3:2) was stirred for 15 m and filtered to separate any possible impurity. Then, the solution was left undisturbed at room temperature. The crystallization of the product begins after a month of slow evaporation and may last around 6 months. Yield: 65%. X-ray suitable single-crystals were obtained from the mother liquor. $C_{56}H_{46}Cl_2Mn_2N_8O_{14}$ (M.W. = 1235.79 g mol^{-1}). Anal. Calcd (%): C, 54.43; H, 3.75; N, 9.07. Found (%): C, 54.49; H, 3.90; N, 9.19. IR (cm^{-1}): 3435 (br), 3114 (w), 3078 (w), 3007 (w), 2981 (w), 2950 (w), 2841 (w), 1592 (s), 1567 (s), 1489 (m), 1472 (m), 1438 (s), 1403 (s), 1313 (m), 1280 (m), 1245 (m), 1193 (w) 1171 (m), 1092 (br,s), 1015 (s), 847 (m), 774 (m), 750 (m), 737(m), 647 (w), 622 (m), 572 (w), 520 (w), 410 (m).

[{Mn(bpy)$_2$}$_2$(μ-3-MeOC$_6$H$_4$COO)$_2$](ClO$_4$)$_2$ (9). $[Mn_3(3\text{-}MeOC_6H_4COO)_6(EtOH)_2]_n$ (0.25 mmol, 0.09 g) and $Mn(ClO_4)_2$ (0.25 mmol, 0.09 g) were dissolved in a mixture composed of CH_3CN (15 mL) and H_2O (5 mL). Then, bpy (1.0 mmol, 0.16 g) was dissolved in CH_3CN (10 mL) and added to the previous solution, giving a yellow solution (total volume ~40 mL). After 7 months of slow evaporation, yellow crystals were filtered and washed with cold CH_3CN. Yield: 76%. X-ray suitable single-crystals were isolated from the mother liquor. $C_{56}H_{46}Cl_2Mn_2N_8O_{14}$ (M.W. = 1235.79 g mol^{-1}). Anal. Calcd (%): C, 54.43; H, 3.75; N, 9.07. Found (%): C, 54.19; H, 3.83; N, 9.18. IR (cm^{-1}): 3446 (br), 3112 (w), 3087 (w), 2935 (w), 2834 (w), 1602 (s), 1575 (s), 1492 (w), 1474 (m), 1452(m), 1438 (s), 1397 (s), 1312 (m), 1279 (m), 1244 (m), 1161 (w) 1086 (br,s), 1046 (m), 1015 (w), 814 (w), 768 (s), 738 (m), 683 (w), 666 (w), 648 (w), 622 (m), 558 (w), 422 (m).

[{Mn(bpy)$_2$}$_2$(μ-4-MeOC$_6$H$_4$COO)$_2$](ClO$_4$)$_2$ (10). $Mn(4\text{-}MeOC_6H_4COO)_2 \cdot 2\ H_2O$ (0.50 mmol, 0.20 g) was dissolved in CH_3CN:H_2O 1:1 (v/v) (20 mL), to which a solution of $NaClO_4$ (0.50 mmol, 0.073 g) in CH_3CN:H_2O 1:1 (10 mL) was added. Then, another solution of bpy (1.20 mmol, 0.19 g) in CH_3CN:H_2O 1:1 (10 mL) was also added. The resulting yellow solution was left undisturbed at room temperature to obtain yellow needles after 3 weeks of slow evaporation. Yield: 82%. Single-crystals suitable for X-ray characterization were obtained after two months of keeping the solution in the fridge. $C_{56}H_{46}Cl_2Mn_2N_8O_{14}$ (M.W. = 1235.79 g mol^{-1}). Anal. Calcd (%): C, 54.43; H, 3.75; N, 9.07. Found (%): C, 54.31; H, 3.81; N, 9.18.

[{Mn(phen)$_2$}$_2$(μ-2-MeOC$_6$H$_4$COO)$_2$](ClO$_4$)$_2$ (11). $Mn(2\text{-}MeOC_6H_4COO)_2$ (0.12 mmol, 0.042 g) was dissolved in a EtOH:H_2O 3:2 (v/v) mixture (25 mL) by stirring for around 24

h. Then, a solution of $NaClO_4$ (0.12 mmol, 0.014 g) in EtOH:H_2O (v/v) (10 mL) was added to the previous one. Meanwhile, 2,2'-bipyridine (bpy) (0.23 mmol, 0.046 g) was dissolved in EtOH (10 mL) and added to the other solution. The resulting yellow solution (solvent: 45 mL of EtOH:H_2O 4:5) was stirred for 15 minutes and filtered to separate any possible impurity. After 2 weeks of slow evaporation at room temperature, big yellow crystals were collected by filtration and washed with EtOH. Yield: 80%. $C_{64}H_{46}Cl_2Mn_2N_8O_{14}$ (M.W. = 1331.88 g mol^{-1}). Anal. Calcd (%): C, 57.71; H, 3.48; N, 8.41. Found (%): C, 56.47; H, 3.37; N, 8.20. IR (cm^{-1}): 3442 (br), 3065 (w), 2964 (w), 2832 (w), 1610 (s), 1588 (s), 1564 (s), 1513 (m), 1492 (w), 1458 (w), 1223 (m), 1390 (m), 1340 (w), 1300 (w), 1274 (w), 1241 (w), 1153 (m) 1100 (vs), 1015 (m), 847 (s), 778 (w), 759 (w), 730 (m), 660 (w), 642 (w), 615 (m), 567 (w), 419 (w).

[{Mn(phen)$_2$}$_2$(μ-3-MeOC$_6$H$_4$COO)$_2$](ClO$_4$)$_2$ (12). $[Mn_3(3\text{-}MeOC_6H_4COO)_6(EtOH)_2]_n$ (0.10 mmol, 0.12 g) and $NaClO_4$ (0.30 mmol, 0.040 g) were dissolved in MeOH. Then, 1,10-phenantroline (phen) (0.60 mmol, 0.12 g) was dissolved in MeOH and added to the previous mixture, giving a yellow solution (total volume ~50 mL). After stirring for 15 minutes, the solution was filtered to separate any possible impurities. After two weeks of slow evaporation at room temperature, yellow crystals were filtered and washed with MeOH. Yield: 80%. $C_{64}H_{46}Cl_2Mn_2N_8O_{14}$ (M.W. = 1331.88 g mol^{-1}). Anal. Calcd (%): C, 57.71; H, 3.48; N, 8.41. Found (%): C, 55.89; H, 3.55; N, 8.40. IR (cm^{-1}): 3435 (br), 3062 (w), 2999 (w), 2940 (w), 2840 (w), 1618 (s), 1577 (m), 1520 (m), 1456 (w), 1428 (s), 1306 (s), 1283 (m), 1231 (w), 1150 (m) 1186 (vs), 1043 (m), 852 (s), 775 (m), 731 (s), 622 (s) 423 (w).

[Mn(H$_2$O)(3-MeOC$_6$H$_4$COO)(phen)$_2$](ClO$_4$) (13). $[Mn_3(3\text{-}MeOC_6H_4COO)_6(EtOH)_2]_n$ (0.04 mmol, 0.045 g) and $NaClO_4$ (0.12 mmol, 0.014 g) were dissolved in CH_3CN (10 mL). H_2O (2 mL) was added to assist the complete dissolution of all reagents. Then, phen (0.12 mmol, 0.046 g) dissolved in CH_3CN (10 mL) was added to the previous solution. After 20 days of slow evaporation yellow crystals were filtered and washed with CH_3CN. Yield: 80%. X-ray suitable crystals were obtained from the mother liquor. $C_{32}H_{25}ClMnN_4O_8$ (M.W. = 683.95 g mol^{-1}). Anal. Calcd (%): C, 56.19; H, 3.68; N, 8.19. Found (%): C, 55.85; H, 3.77 N, 8.23. IR (cm^{-1}): 3442 (m), 3063 (w), 3008 (w), 2935 (w), 2837 (w), 1558 (m), 1517 (s), 1425 (s), 1379 (s), 1341 (w), 1315 (w), 1280 (w), 1249 (m), 1098 (s), 1035 (m), 854 (s), 772 (s), 724 (s), 623 (m), 421 (m).

[{Mn(phen)$_2$}$_2$(μ-4-MeOC$_6$H$_4$COO)$_2$](ClO$_4$)$_2$ (14). $Mn(4\text{-}MeOC_6H_4COO)_2 \cdot 2\ H_2O$ (0.30 mmol, 0.14 g) and $NaClO_4$ (0.12 mmol, 0.014 g) were dissolved in a CH_3CN:H_2O 2:1 mixture (15 mL). Then, a solution of phen (0.60 mmol, 0.12 g) in CH_3CN (5 mL) was added to the

previous solution and the mixture was stirred for 15 minutes. Afterwards, 30 mL of MeOH were added. After a month of slow evaporation yellow single-crystals were filtered and washed with MeOH. Yield: 95%. $C_{64}H_{46}Cl_2Mn_2N_8O_{14}$ (M.W. = 1331.88 g mol^{-1}). Anal. Calcd (%): C, 57.71; H, 3.48; N, 8.41. Found (%): C, 57.34; H, 3.59; N, 8.48. IR (cm^{-1}): 3435 (br), 3062 (w), 2999 (w), 2941 (w), 2840 (w), 1618 (s), 1578 (s), 1521 (s), 1456 (w), 1482 (s), 1306 (s), 1231 (m), 1150 (m), 1086 (vs), 1042 (m), 852 (s), 776 (m), 731 (s), 722 (s), 423 (w).

[{Mn(phen)$_2$}$_2$(μ-4-^{t}BuC$_6$H$_4$COO)$_2$](ClO$_4$)$_2$ (15). Mn(4-^{t}BuC$_6$H$_4$COO)$_2$·3 H$_2$O (0.12 mmol, 0.054 g) and NaClO$_4$ (0.12 mmol, 0.014 g) were dissolved in absolute EtOH (10 mL). Phen (0.23 mmol, 0.046 g) dissolved in absolute EtOH was added to the previous solution and the mixture was stirred for 10 minutes. Then, 4 mL of H$_2$O were added and the solution was left undisturbed at room temperature. After two weeks of slow evaporation, yellow crystals were filtered and washed with EtOH. Yield: 18%. X-ray suitable crystals were obtained from the mother liquor. IR (cm^{-1}): 3430 (br), 3071 (w), 2950 (w), 1609 (s), 1558 (m), 1515 (m), 1394 (s), 1339 (w), 1298 (w), 1267 (w), 1194 (w), 1152 (m), 1099 (vs), 1012 (w), 850 (s), 792 (m), 775 (m), 731 (s), 623 (s), 543 (w), 420 (w).

[Mn$_3$(bpy)$_2$(μ-3-MeOC$_6$H$_4$COO)$_6$] (16). [Mn$_3$(3-MeOC$_6$H$_4$COO)$_6$(EtOH)$_2$]$_n$ (0.04 mmol, 0.045 g) was dissolved in CH$_3$CN (10 mL) and H$_2$O (5 mL). Then, bpy (0.078 mmol, 0.012 g) dissolved in CH$_3$CN (10 mL) was added to the previous solution. After 1 month of slow evaporation, yellow crystals were filtered and washed with CH$_3$CN. Yield: 43%. $C_{68}H_{58}Mn_3N_4O_{18}$ (M.W. = 1384.02 g mol^{-1}). Anal. Calcd (%): C, 59.01; H, 4.22; N, 4.05. Found (%): C, 58.72; H, 4.22; N, 4.15. IR (cm^{-1}): 3444 (br), 3108 (w), 3001 (w), 2963 (w), 2938 (w), 2831 (w), 1598 (m), 1565 (s), 1473 (w), 1452 (m), 1400 (s), 1315 (m), 1282 (m), 1239 (s), 1177 (w), 1157 (m), 1108 (w), 1047 (s), 1018 (m), 902 (m), 785 (m), 764 (s), 684 (w), 670 (w), 647 (w), 625 (w), 543 (w), 450 (w).

[Mn$_3$(bpy)$_2$(μ-4-MeOC$_6$H$_4$COO)$_6$] (17). Bpy (0.50 mmol, 0.08 g) dissolved in EtOH was added to a suspension of Mn(4-MeOC$_6$H$_4$COO)$_2$·2 H$_2$O (0.75 mmol, 0.29 g) in EtOH. The resulting pale yellow mixture was stirred for 10 minutes. Then, the solid was separated by filtration and washed with Et$_2$O. Yield: 76%. X-ray suitable single-crystals were obtained by slow diffusion of a solution of bpy (0.008 g) in CH$_3$CN (8 mL) to another one containing Mn(4-MeOC$_6$H$_4$COO)$_2$·2H$_2$O (0.03 g) in CH$_3$CN (8 mL) after 6 months. $C_{68}H_{58}Mn_3N_4O_{18}$ (M.W. = 1384.02 g mol^{-1}). Anal. Calcd (%): C, 59.01; H, 4.22; N, 4.05. Found (%): C, 56.65; H, 4.05; N, 4.05. IR (cm^{-1}): 3433 (br), 3081 (w), 2953 (w), 2835 (w), 1606 (s), 1557 (s), 1488 (w), 1471 (m), 1440 (m), 1390 (s), 1310 (m), 1256 (s), 1168 (s), 1140 (m), 1103 (w), 1029 (w), 851 (m), 785 (s), 763 (m), 737 (w), 699 (m), 615 (m), 569 (w), 509 (w), 414 (m).

[Mn(bpy)(4-^{t}BuC$_6$H$_4$COO)$_2$]·H$_2$O (18). A solution of bpy (2 mmol, 0.33 g) in CH_3CN was added to an acetonitrile solution containing Mn(4-^{t}BuC$_6$H$_4$COO)$_2$·3 H$_2$O. Almost immediately a pale yellow suspension was formed. After 5 minutes of stirring, the solid was filtered and washed with CH_3CN. Yield: 70%. Single-crystals were obtained from the mother liquor after several months since the separation of the previous solid. $C_{32}H_{36}MnN_2O_5$ (M.W. = 583.57 g mol^{-1}). Anal. Calcd (%): C, 65.86; H, 6.22; N, 4.08. Found (%): C, 63.63; H, 6.39; N, 4.03. IR (cm^{-1}): 3425 (br), 3067 (w), 2963 (m), 2903 (w), 2868 (w), 1602 (s), 1553 (s), 1491 (w), 1475 (m), 1441 (m), 1401 (s), 1316 (w), 1267 (w), 1190 (w), 1148 (w), 1106 (w), 1058 (w), 1017 (m), 861 (m), 788 (m), 769 (m), 714 (m), 649 (w), 585 (w), 543 (w), 559 (w), 414 (w).

[Mn(H$_2$O)$_2$(2-MeOC$_6$H$_4$COO)$_2$(phen)] (19). Phen (0.12 mmol, 0.023 g) dissolved in EtOH (10 mL) was added to a solution of Mn(2-MeOC$_6$H$_4$COO)$_2$ (0.12 mmol, 0.042 g) in EtOH:H$_2$O 4:3 (35 mL). The resulting pale yellow solution was stirred for 15 minutes. After 1 month of slow evaporation, yellow crystals were filtered and washed with EtOH. Yield: 65%. X-ray suitable single-crystals were obtained from the mother liquor. $C_{28}H_{26}MnN_2O_8$ (M.W. = 573.45 g mol^{-1}). Anal. Calcd (%): C, 58.64; H, 4.57; N, 4.89. Found (%): C, 58.56; H, 4.69; N, 5.03. IR (cm^{-1}): 3448 (s), 2967 (w), 2939 (w), 2837 (w), 1603 (s), 1544 (s), 1513 (m), 1423 (m), 1376 (s), 1292 (w), 1270 (m), 1236 (m), 1186 (w), 1163 (w), 1099 (m), 1057 (w), 1019 (m), 859 (m), 832 (m), 767 (s), 733 (m), 660 (w), 637 (w), 554 (w), 443 (w).

[Mn$_3$(μ-3-MeOC$_6$H$_4$COO)$_6$(phen)$_2$] (20). [Mn$_3$(3-MeOC$_6$H$_4$COO)$_6$(EtOH)$_2$]$_n$ (0.04 mmol, 0.045 g) was dissolved in EtOH (15 mL) and H$_2$O (5 mL). Then, phen (0.078 mmol, 0.015 g) dissolved in EtOH (10 mL) was added to the previous solution. After 1 or 2 months of slow evaporation, yellow crystals were filtered and washed with CH_3CN. Yield: 46%. $C_{72}H_{58}Mn_3N_4O_{18}$ (M.W. = 1432.06 g mol^{-1}). Anal. Calcd (%): C, 60.67; H, 4.08; N, 3.91. Found (%): C, 58.98; H, 4.18; N, 4.05. IR (cm^{-1}): 3433 (br), 3068 (w), 2999 (w), 2929 (w), 2828 (w), 1600 (m), 1568 (s), 1540 (s), 1516 (m), 1451 (m), 1395 (s), 1314 (w), 1282 (w), 1242 (m), 1106 (w), 1042 (m), 904 (w), 849 (m), 764 (m), 727 (m), 669 (w), 637 (w), 533 (w).

[Mn$_3$(μ-4-MeOC$_6$H$_4$COO)$_6$(phen)$_2$]·EtOH (21). Mn(4-MeOC$_6$H$_4$COO)$_2$·2 H$_2$O (0.12 mmol, 0.42 g) was dissolved in a mixture of EtOH (15 mL) and H$_2$O (5 mL). Then, phen (0.078 mmol, 0.015 g) dissolved in EtOH (10 mL) was added. The resulting pale yellow solution was stirred for 10 minutes and filtered to separate any possible impurity. After two months of slow evaporation, yellow crystals were filtered and washed with EtOH. Yield: 44%. $C_{72}H_{58}Mn_3N_4O_{18}$·EtOH (M.W. = 1478.13 g mol^{-1}). Anal. Calcd (%): C, 60.13; H, 4.36; N, 3.79. Found (%): C, 60.12; H, 4.46; N, 3.87. IR (cm^{-1}): 3420 (br), 3064 (w), 2995 (w), 2957

(w), 2929 (w), 2833 (m), 1607 (s), 1559 (s), 1510 (s), 1398 (s), 1312 (w), 1255 (s), 1169 (m), 1144 (w), 1101 (w), 1034 (m), 852 (m), 783 (s), 731 (m), 700 (w), 616 (s), 568 (w), 510 (w).

Synthesis of heterometallic compounds

$[Mn_6Ca_2O_9(4\text{-}^tBuC_6H_4COO)_{10}(4\text{-}^tBuC_6H_4COOH)_5]$ (22). A mixture of $Mn(CH_3COO)_2{\cdot}4H_2O$ (0.25 mmol, 0.060 g), $4\text{-}^tBuC_6H_4COOH$ (8.2 mmol, 1.46 g) and $Ca(NO_3)_2{\cdot}xH_2O$ (0.25 mmol, 0.060 g) were dissolved in CH_3CN (60 mL) and then heated up to 80°C. The resulting orange solution was softly stirred for 15 minutes while solid NBu_4MnO_4 (0.5 mmol, 0.18 g) was added in small portions. The dark red solution was allowed to cool at room temperature and filtered with the aim to separate any possible solid residue. After two or three days of slow evaporation, dark red crystals were collected by filtration, washed with EtOH and dried under vacuum. Yield (based on total Mn): 60%. Anal. Calcd for $C_{165}H_{200}Ca_2Mn_6O_{39}{\cdot}0.25\,CH_3CN$ (M.W. = 3227 g mol^{-1}) (%): C, 61.59; H, 6.27; N, 0.11; Mn, 10.21; Ca, 2.48. Found (%): C, 58.94; H, 6.39; N, 0.11; Mn, 10.49; Ca, 2.24. Selected IR data (cm^{-1}): 3427 (br), 2964 (m), 2905 (w), 2869 (w), 1691 (m), 1610 (m), 1587 (m), 1541 (m), 1501 (w), 1462 (w), 1400 (s), 1315 (w), 1268 (m), 1194 (m), 1107 (w), 855 (w), 780 (m), 750 (w), 726 (m), 710 (m), 630 (m), 526 (w).

This compound may also be synthesized using $Ca(CH_3COO)_2{\cdot}xH_2O$ (0.25 mmol, 0.040 g) as calcium source instead of $Ca(NO_3)_2{\cdot}xH_2O$. Unlike the procedure previously described, a white suspension appeared before the addition of the NBu_4MnO_4, identified by IR spectroscopy as $Mn(4\text{-}^tBuC_6H_4COO)_2$. After cooling, the solution was filtered to separate the surplus $Ca(CH_3COO)_2$. After a week of slow evaporation, dark red crystals were collected by filtration, washed with EtOH and dried under vacuum. Yield (based on total Mn): 10%.

Both synthetic routes lead to the crystallization of **22**, providing single-crystals from the mother liquor. The crystals obtained using $Ca(NO_3)_2$ were very small and, even though we could determine the cell parameters and isotropically refine all atoms, we were unable to finish the refinement of the crystal structure. In contrast, crystals obtained using $Ca(CH_3COO)_2$ were highly diffracting and we could successfully refine the crystal structure.

The molar conductivity (Λ_M) of compound **22** is 1.6 S cm^2 mol^{-1} in CH_2Cl_2 solution and 23 S cm^2 mol^{-1} in CH_3CN solution (the expected values for a 1:1 electrolyte are 10–24 S cm^2 mol^{-1} in CH_2Cl_2 and 120–160 S cm^2 mol^{-1} in CH_3CN).[167] These values are in agreement with a neutral compound.

$[Mn_6Sr_2O_9(4\text{-}^tBuC_6H_4COO)_{10}(4\text{-}^tBuC_6H_4COOH)_5]$ (23). An analogous procedure was followed as for **22**, but using $Sr(NO_3)_2$ (0.25 mmol, 0.053 g) and only 40 mL of CH_3CN. After one or two days, dark red crystals were collected by filtration, washed with EtOH and dried under vacuum. Yield (based on total Mn): 7%. Single-crystals suitable for X-ray analysis were obtained from the mother liquor. Anal. Calcd for $C_{165}H_{200}Mn_6O_{39}Sr_2 \cdot 0.20\ CH_3CN$ (M.W. = 3320 g mol^{-1}) (%): C, 59.83; H, 6.09; N, 0.08. Found (%): C, 58.02; H, 6.31; N, 0.08. Selected IR data (cm^{-1}): 3443 (br), 2964 (m), 2898 (w), 2869 (w), 1691 (m), 1611 (m), 1586 (m), 1540 (m), 1501 (w), 1462 (w), 1398 (s), 1315 (w), 1268 (m), 1193 (m), 1107 (w), 855 (w), 782 (m), 750 (w), 726 (m), 710 (m), 625 (m), 526 (w).

Synthesis of tetranuclear compounds with $[Mn^{III}_4O_2]^{8+}$ core

$[Mn_4(\mu\text{-}O)_2(\mu\text{-}4\text{-}MeOC_6H_4COO)_7(phen)_2]ClO_4$ (24). $4\text{-}MeOC_6H_4COOH$ (2.89 mmol, 0.44 g) and $Mn(ClO_4)_2 \cdot 6H_2O$ (1.32 mmol, 0.48 g) were dissolved in acetonitrile. Then, solid NBu_4MnO_4 (0.33 mmol, 0.12 g) was added to the previous solution in small portions during 1–2 min while, almost simultaneously, 10 mL acetonitrile solution of 1,10-phenanthroline (phen) (0.83 mmol, 0.16 g) was added, also in small portions. The resulting dark solution (total volume ~20 mL) was stirred for 10 minutes and dried with a rotary evaporator. The resulting black oil was dissolved in an CH_3CN:EtOH (10:10 mL) mixture and filtered to separate any possible residue. Dark red crystals were obtained after a week of slow evaporation at room temperature. Yield: 25%. Anal. Calcd for $C_{80}H_{65}ClMn_4N_4O_{27}$ (M.W. = 1769.59 g mol^{-1}) (%): C, 54.30; H, 3.70; N, 3.17. Found (%): C, 53.67; H, 3.73; N, 3.17. Selected IR data (cm^{-1}): IR (cm^{-1}): 3446 (br), 3070 (w), 2931 (w), 2836 (w), 1602 (s), 1559 (s), 1507 (m), 1457 (w), 1420 (m), 1380 (s), 1359 (s), 1314 (m), 1256 (s), 1170 (s) 1086 (m), 1025 (m), 852 (w), 790 (m), 749 (w), 667 (w), 621 (m), 504 (w), 437 (w).

$[Mn_4(\mu\text{-}O)_2(\mu\text{-}4\text{-}^tBuC_6H_4COO)_6(H_2O)_2(phen)_2][Mn_4(\mu\text{-}O)_2(\mu\text{-}4\text{-}^tBuC_6H_4COO)_6(CH_3CN)_2(phen)_2](ClO_4)_4$ (25). $4\text{-}^tBuC_6H_4COOH$ (1.75 mmol, 0.31 g) and $Mn(ClO_4)_2 \cdot 6H_2O$ (0.8 mmol, 0.29 g) were dissolved in acetonitrile (10 mL). Then, solid NBu_4MnO_4 (0.20 mmol, 0.082 g) was added to the previous solution in small portions during 1–2 minutes while, almost simultaneously, an acetonitrile solution (10 mL) of 1,10-phenanthroline (phen) (0.50 mmol, 0.10 g) was added, also in small portions. Finally, solid $NaClO_4 \cdot H_2O$ (10.6 mmol, 1.3 g) was added. The resulting dark red solution (total volume ~25 mL) was stirred for 15 min and shortly afterward filtered to separate any possible residue. After leaving the solution undisturbed for three weeks, dark red crystals were isolated by

filtration, washed with ether and dried under vacuum. X-ray suitable single-crystal were obtained under the same conditions but using less $NaClO_4 \cdot H_2O$ (9.8 mmol, 1.2 g). Yield: 16%. Anal. Calcd for $C_{92}H_{103}Cl_2Mn_4N_5O_{23}$ (average formula, referred to one Mn_4 unit) (M.W. = 1937.48 g mol^{-1}) (%): C, 57.03; H, 5.38; N, 3.61. Found (%): C, 58.10; H, 5.32; N, 3.50. Selected IR data (cm^{-1}): 3434 (br), 3075 (w), 2960 (m), 2906 (w), 2869 (w), 1597 (s), 1555 (s), 1521 (s), 1462 (w), 1383 (s), 1310 (w), 1269 (w), 1193 (w) 1101 (s), 1015 (w), 854 (m), 786 (m), 722 (m), 652(m), 623 (m), 601 (m), 548 (w), 479 (m).

Synthesis of the dodecanuclear compound 26

$[Mn_{12}O_{12}(3\text{-}MeOC_6H_4COO)_{16}(H_2O)_4]$ (26). 3-$MeOC_6H_4COOH$ (8.2 mmol, 1.25 g) and $Mn(CH_3COO)$ (0.5 mmol, 0.12 g) were dissolved in acetonitrile (40 mL) and heated up to 80 ºC. The resulting solution was stirred for 20 minutes while solid NBu_4MnO_4 (0.25 mmol, 0.093 g) was added in small portions. The dark solution was allowed to cool at room temperature and filtered with the aim to separate any possible solid residue. After a week of slow evaporation, dark crystals were collected by filtration, washed with acetonitrile and dried under vacuum. Yield (based on total Mn): between 5 and 20%. Anal. Calcd for $C_{128}H_{120}Mn_{12}O_{64}$ (M.W. = 3341.54 g mol^{-1}) (%): C, 46.01; H, 3.62. Found (%): C, 45.44; H, 3.70. Selected IR data (cm^{-1}): 3432 (br), 2937 (w), 2833 (w), 1559 (m), 1521 (w), 1455 (m), 1405 (s), 1345 (m), 1284 (m), 1247 (m), 1118 (w), 1044 (m), 995 (w), 918 (w), 878 (w), 790 (w), 762 (m), 705 (w), 668 (w), 652 (w), 602 (w), 550 (w), 510 (w).

Structural analysis for Mn_6 wheels

Experimental structural data were retrieved from the Cambridge Structural Database (WebCSD v1.1.1 updated in July 22nd, 2015). A search for structures with six almost coplanar Mn ions linked through oxygen atoms and with minimum one ion in the center (bound at least to three of the oxygen atoms) was performed, finding a total of 20 different structures.

Physical characterization

C, H and N analyses were carried out by the "Centres Científics i Tecnològics" of the Universitat de Barcelona. Mn and Ca semi-quantitative analysis for **22** was performed with **inductively coupled plasma optical emission spectrometry (ICP-OES)** by the "Centres

Científics i Tecnològics" of the Universitat de Barcelona from a solution of **22** (~5 mg) pre-treated in hot HNO_3. **Infrared spectra** were recorded on KBr pellets in the 4000–400 cm^{-1} range with a Thermo Nicolet Avatar 330 FTIR spectrometer. **Magnetic measurements** were performed on microcrystalline samples in a Quantum Design MPMS XL5 SQUID Magnometer at the "Unitat de Mesures Magnètiques" (Universitat de Barcelona). **Direct current (DC) magnetic susceptibility** was measured between 2 and 300 K and with a magnetic field of 0.02 T. **Alternating current (AC) magnetic susceptibility** was measured for **26** between 12 and 1.8 K and with AC field of $4 \cdot 10^{-4}$ T, oscillating at frequencies of 10, 35, 122, 426, 1488 Hz, and a DC field of 0 T. **Magnetization measurements** for compounds **1**–**6** were made in the range 1.8–6.8 K and at six different magnetic fields (0.5, 1.0, 2.0, 3.0, 4.0 and 5.0 T). For the rest of the compounds, the magnetization was only measured at 2 K between 0 and 5 T. **Field-Cooled (FC) and Zero-Field-Cooled (ZFC) magnetization experiments** were performed for compound **26** in the following way: firstly, the sample is cooled to 2 K and, then, the magnetic susceptibility is measured under a magnetic field of 0.002 T as the temperature increases from 2.0 to 50 K (ZFC); afterwards, the magnetic susceptibility is measured upon cooling (from 50 to 2 K) under the same magnetic field (0.002 T) (FC). **Magnetization isotherm measurements** were only performed for compound **26** at 2 K and between 5 and –5 T. Pascal's constant were used to estimate the diamagnetic corrections for the compound. The fit of the experimental magnetic data was performed by minimizing the functions $R_{SUS} = \Sigma[(\chi_M T)_{exp} - (\chi_M T)_{calcd.}]^2 / \Sigma[(\chi_M T)_{exp}]^2$ and/or $R_{MAG} = \Sigma[(M/N\mu_\beta)_{exp} - (M/N\mu_\beta)_{calcd.}]^2 / \Sigma[(M/N\mu_\beta)_{exp}]^2$. **Solid-state EPR** spectra were recorded at X-band (9.4 GHz) frequency using a Bruker ESP-300E spectrometer, from room temperature to 4 K at the "Unitat de Mesures Magnètiques" (Universitat de Barcelona). **Ionic conductivity (Λ_M)** measurements were made on 1 mM solutions of **22** in CH_2Cl_2 and in CH_3CN using a CDC401 electrode.

Single-crystal X-ray crystallography

The data collection for compounds **1**, **2**, **3**, **4**, **5**, **7**, **9**, **12**, **13**, **14**, **22**, **23**, **24**, **25**, and **26** (at 90–100 K) and for **15** and **19** (at 302 K) was performed on a Bruker Apex-II diffractometer; whereas for **6**, **8**, **10**, **17**, and for Mn^{II} 3-methoxybenzoate ($[Mn_3(3\text{-}MeOC_6H_4COO)_6(EtOH)_2]_n$) it was made at room temperature on a MAR345 diffractometer; both equipped with a graphite monochromatic Mo Kα radiation (λ = 0.71073 Å). Cell parameters were refined by least-squares method. Between 4226 and 252992 reflections were

collected using the *Φ*- and *ω*-scan (Bruker Apex-II) or *Φ*-scan (MAR345) method. Data were corrected for absorption effects using multi-scan (**1**, **3**, **5**, **7**, **9**, **12**, **13**, **14**, **15**, **19**, **22**, **23**, **24**, and **26**) or empirical (**2**, **4**, **6**, **8**, **10**, **17**, **24**, and Mn^{II} 3-methoxybenzoate) method (SADABS).[168] The data collection for manganese(II) 3-methoxybenzoate was performed on the MAR345 diffractometer. The data was also corrected for absorption effects using a multi-scan method (SADABS).[168] Tables containing crystallographic data collection and structure refinement details are summarized in Appendix I (Tables S1–S9).

The structures were solved by direct methods and refined by full-matrix least-squares using SHELXL-97.[156] Non-hydrogen atoms were refined anisotropically, whereas hydrogen atoms were computed and refined with isotropic thermal parameters riding on their respective carbon or oxygen atoms. Particularly for compounds **24** and **25**, solvent hydrogen atoms interacting with neighbors were placed in ideal positions.

Compound **1**·H_2O·0.5 CH_3CN crystallizes in monoclinic space group *C*2/*c*. In the asymmetric unit, only half of the cationic complex $[\{Mn(bpy)(H_2O)_{0.5}(NO_3)_{0.5}\}_2(\mu\text{-}2\text{-}MeOC_6H_4COO)_2(\mu\text{-}O)]^+$ may be found. The other half is generated by a 2-fold axis. The voids between complexes are filled by one disordered nitrate ion per molecule of complex and disordered solvent (water and acetonitrile). A total of 306 parameters were refined in the final refinement on F^2 using 106 restraints.

Compound **2**·CH_3CN crystallizes in monoclinic space group *P*21/*c*. The asymmetric unit consists of a cationic complex $[\{Mn(bpy)(H_2O)\}(\mu\text{-}2\text{-}MeOC_6H_4COO)_2(\mu\text{-}O)\{Mn(bpy)(ClO_4)\}]^+$, a perchlorate ion and an acetonitrile molecule. A total of 562 parameters were refined in the final refinement on F^2 using only one restraint. The isolated crystals of compound **2** were very thin (0.02 mm thickness), being poorly diffracting at high angles. Other attempts of crystallization were done, but no single crystals of better quality were obtained. Nevertheless, the absence of disorder and the simplicity of the crystal structure made us able to refine the crystal structure without any trouble.

Compound **3**·2 CH_3CN crystallizes in monoclinic space group *C*2/*c*. The asymmetric unit consists of half of the neutral complex $[\{Mn(bpy)(NO_3)\}_2(\mu\text{-}3\text{-}MeOC_6H_4COO)_2(\mu\text{-}O)]$ located on a 2-fold rotation axis and a molecule of acetonitrile. A total of 286 parameters were refined in the final refinement on F^2 using no restraints.

Compound **4**·1/2 H_2O·1/2 CH_3CN crystallizes in triclinic space group $P\bar{1}$. The asymmetric unit consists of a cationic complex $[\{Mn(bpy)(H_2O)\}(\mu\text{-}3\text{-}MeOC_6H_4COO)_2(\mu\text{-}$

O){Mn(bpy)(NO_3)}]$^+$, a nitrate anion, an acetonitrile molecule with 50% occupancy and a water molecule with 50% occupancy. A total of 556 parameters were refined in the final refinement on F^2 using 63 restraints.

Compound **5** crystallizes in triclinic space group $P\bar{1}$. The asymmetric unit consists of a cationic complex [{Mn(bpy)(H_2O)}(μ-3-$MeOC_6H_4COO$)$_2$(μ-O){Mn(bpy)(ClO_4)}]$^+$, a perchlorate anion and disordered molecules of solvent. The program SQUEEZE (part of the PLATON package of crystallographic software)[157] was used to calculate the solvent disorder and remove its contribution to the overall intensity data.[169] Fifty-one electrons were found in a 161 Å^3 void, corresponding to the diffuse contribution of a dichloromethane and a water molecule. A total of 592 parameters were refined in the final refinement on F^2 using 286 restraints.

Compound **6**·1/3 CH_3CN·1/3 H_2O crystallizes in trigonal space group $R\bar{3}$. The asymmetric unit consists of a [{Mn(bpy)(H_2O)}(μ-3-$MeOC_6H_4COO$)$_2$(μ-O){Mn(bpy)(ClO_4)}]$^+$ complex, a perchlorate anion and disordered acetonitrile (on the 3-fold axis) and water molecules (around and on the 3-fold axis). A total of 591 parameters were refined in the final refinement on F^2 using 38 restraints.

Compound **7** crystallizes in orthorhombic space group *Pca*2(1). The asymmetric unit consists of two conformational isomers of the cationic complex [{Mn(bpy)(EtOH)}(μ-4-^{t}BuC_6H_4COO)$_2$(μ-O){Mn(bpy)(ClO_4)}]$^+$ and two perchlorate anions. A total of 1244 parameters were refined in the final refinement on F^2 using 480 restraints.

Manganese(II) 3-methoxybenzoate, [Mn_3(3-$MeOC_6H_4COO$)$_6$(EtOH)$_2$]$_n$, crystallizes in monoclinic space group *P*21/*c*. The asymmetric unit consists of half a [Mn_3(3-$MeOC_6H_4COO$)$_6$(EtOH)$_2$] entity, displaying two different Mn^{II} ions. A total of 364 parameters were refined in the final cycle of refinement on F^2 using 2 restraints.

Compound **8** crystallizes in triclinic space group $P\bar{1}$. The asymmetric unit consists of half a [{Mn(bpy)$_2$}$_2$(μ-2-$MeOC_6H_4COO$)$_2$]$^{2+}$ complex and one ClO_4^- anion. The other half of the complex is generated by an inversion center. A total of 407 parameters were refined in the final cycle of refinement on F^2 using 15 restraints.

Compound **9** crystallizes in monoclinic space group *P*21/*c*. The asymmetric unit consists of half a [{Mn(bpy)$_2$}$_2$(μ-3-$MeOC_6H_4COO$)$_2$]$^{2+}$ complex and a ClO_4^- anion. The other half of the complex is generated by an inversion center. A total of 370 parameters were refined in the final cycle of refinement on F^2 without using any restraint.

Compound **10** crystallizes in triclinic space group $P\bar{1}$. The asymmetric unit consists of half a $[\{Mn(bpy)_2\}_2(\mu\text{-}4\text{-}MeOC_6H_4COO)_2]^{2+}$ complex and a ClO_4^- anion. The other half of the complex is generated by an inversion center. A total of 364 parameters were refined in the final cycle of refinement on F^2 using 3 restraints.

Compound **12** crystallizes in triclinic space group $P\bar{1}$. The asymmetric unit consists of half a $[\{Mn(phen)_2\}_2(\mu\text{-}3\text{-}MeOC_6H_4COO)_2]^{2+}$ complex and a ClO_4^- anion. The other half of the complex is generated by an inversion center. A total of 424 parameters were refined in the final cycle of refinement on F^2 without using any restraint.

Compound **13** crystallizes in triclinic space group $P\bar{1}$. The asymmetric unit consists of a $[Mn(H_2O)(3\text{-}MeOC_6H_4COO)(phen)_2]^+$ complex and a ClO_4^- anion. A total of 424 parameters were refined in the final cycle of refinement on F^2 without using any restraint.

Compound **14** crystallizes in monoclinic space group $C2/m$. The asymmetric unit consists of a fourth part of a $[\{Mn(phen)_2\}_2(\mu\text{-}4\text{-}MeOC_6H_4COO)_2]^{2+}$ complex and half a ClO_4^- anion. The rest of complex is generated by an inversion center and a mirror plane. A total of 239 parameters were refined in the final cycle of refinement on F^2 using 36 restraints.

Compound **15** crystallizes in triclinic space group $P\bar{1}$. The asymmetric unit consists of half a $[\{Mn(phen)_2\}_2(\mu\text{-}4\text{-}^tBuC_6H_4COO)_2]^{2+}$ complex and a ClO_4^- anion. The rest of complex is generated by an inversion center. A total of 427 parameters were refined in the final cycle of refinement on F^2 using 4 restraints.

Compound **17** crystallizes in triclinic space group $P\bar{1}$. The asymmetric unit consists of half a $[Mn_3(bpy)_2(\mu\text{-}4\text{-}MeOC_6H_4COO)_6]$ complex. The rest of complex is generated by an inversion center. A total of 448 parameters were refined in the final cycle of refinement on F^2 without using any restraint.

Single-crystals of the mononuclear compound **18** were isolated and mounted on a diffractometer. However, the crystals were very thin, so they did not provide good diffraction frames and the structure could not be determined.

Compound **19** crystallizes in monoclinic space group Cc. The asymmetric unit consists of four slightly different complexes with formula $[Mn(H_2O)_2(2\text{-}MeOC_6H_4COO)_2(phen)]$. The H atoms of the water ligands were fixed in logical positions considering the plausible H bonds, with isotropic thermal parameters riding on their respective O atoms. A total of 448 parameters were refined in the final cycle of refinement on F^2 without using any restraint.

Both compounds **22** and **23** crystallize in hexagonal space group *P*63/*m*. Their asymmetric unit consists of a sixth part of the $[Mn_6M_2O_9]^{10+}$ cluster (M = Ca^{2+} for **22** and Sr^{2+} for **23**) with two non-equivalent Mn ions placed on a mirror plane and one M^{2+} ion placed on a threefold axis. The entire cluster is generated by these two last symmetry operators. The space between clusters are filled by acetonitrile molecules. No counter anion was found. One of the hydrogen atoms was computed with 5/6 (83.33%) overall occupancy to balance the charge of the $[Mn_6M_2O_9]^{10+}$ core, consistent with five hydrogen atoms delocalized in six identical positions (explanation in the Results and Discussion part). A total of 376 parameters were refined in the final cycle of refinement on F^2 using five restraints.

As commented before, **22** may be obtained using calcium nitrate or acetate. Single-crystals obtained from both calcium sources were isolated and mounted on the diffractometer, the cell parameters of both crystals being practically identical. However, the crystal structure obtained via calcium nitrate could not be fully refined because the solvent molecules made the refinement unstable (due to the lack of reflections). On the other hand, the synthesis with calcium acetate provided bigger single-crystals, whose crystal structure could be fully refined. Hence, the results presented before correspond to crystals obtained from the calcium acetate.

Compound **24**·1/2 EtOH·5/4 CH_3CN·1/4 H_2O crystallizes in triclinic space group *P*1. The asymmetric unit consists of two conformational isomers of the $[Mn_4(\mu\text{-}O)_2(\mu\text{-}4\text{-}MeOC_6H_4COO)_7(phen)_2]^+$ complex, two perchlorate anions and some solvent molecules (H_2O, CH_3CN and EtOH). A total of 2240 parameters were refined in the final refinement on F^2 using 75 restraints.

Compound **25**·4 CH_3CN crystallizes in triclinic space group *P*21/*c*. The asymmetric unit consists of a half part of the $[Mn_4(\mu\text{-}O)_2(\mu\text{-}4\text{-}^tBuC_6H_4COO)_6(H_2O)_2(phen)_2]^{2+}$ and of the $[Mn_4(\mu\text{-}O)_2(\mu\text{-}4\text{-}^tBuC_6H_4COO)_6(CH_3CN)_2(phen)_2]^{2+}$ complexes, two perchlorate anions, and two acetonitrile molecules. The whole complexes are generated by an inversion center situated in the middle of them. A total of 1243 parameters were refined in the final refinement on F^2 using 542 restraints.

Compound **26**·5 CH_3CN crystallizes in monoclinic space group *P*2/*n*. The asymmetric unit consists of a half part of the $[Mn_{12}(\mu\text{-}O)_{12}(\mu\text{-}3\text{-}MeOC_6H_4COO)_{16}(H_2O)_4]$ complex and acetonitrile molecules. The entire complex is generated by a twofold axis. A total of 986 parameters were refined in the final refinement on F^2 using 31 restraints.

Computational details

The theoretical studies found in Chapter 1.5 were performed by Dr. Gabriel Aullón and Dr. Jesus Jover of the University of Barcelona. Calculations were performed using the SIESTA code (*Spanish Initiative for Electronic Simulations with Thousands of Atoms*).[170] The generalized-gradient functional proposed by Perdew, Burke, and Ernzerhof (PBE) was used.[171] Only valence electrons were included in the calculations, with the core electrons being replaced by norm-conserving scalar relativistic pseudopotentials factorized in the Kleinman–Bylander form,[172] generated according to the procedure of Trouiller and Martins.[173] In the calculations, values of 50 meV for the energy shift and 250 Ry for the mesh cutoff were employed because they provide a good compromise between accuracy and computer time to estimate exchange coupling constants.

The crystal structures of compounds **22** and **23** were used for the calculations, keeping the experimental symmetry in which all six manganese ions are equivalents. The *t*Bu substituents (on the aromatic ring) were simplified to methyl groups in order to optimize the computational resources. The broken-symmetry approximation without spin projection was employed, considering the spin Hamiltonian mentioned in the text.[174–176] The same calculations were also performed for three hypothetical compounds with Sr^{2+}, Mg^{2+} or without central ions. Aiming to preserve the structural parameters, the frozen symmetry of **22** was used for these hypothetical compounds, following the methodology reported by Ruiz *et al.*[177–179] To calculate the exchange coupling constants (J), the energies for a high-spin state (where the six manganese spins are aligned in parallel, hence $S = 9$) and different low-spin solutions were computed (see Appendix IV). Four exchange pathways were considered from these energies to obtain their J values.

1.3. Dinuclear Compounds with $[Mn^{III}_2O]^{4+}$ Core

First insights

The interest in the magnetic properties of dinuclear Mn^{III} compounds with $[Mn_2(\mu\text{-}O)(\mu\text{-}R'COO)_2]^{2+}$ core lies in the versatility of its magnetic behavior, which ranges from moderate ferro- to antiferromagnetic, with a ground state $S = 4$ and $S = 0$, respectively. The Mn ions in these compounds show an octahedral geometry with pronounced axial and rhombic distortions. The axial distortion is distinctive of Mn^{III} ions, the octahedra can be elongated in the direction of the terminal ligands or compressed in the direction of the oxo bridging ligand. In general, those compounds that have compressed octahedra display ferromagnetic coupling, while those with elongated octahedra show antiferromagnetic coupling. When the predominant distortion is rhombic, the interaction may be either ferro- or antiferromagnetic.[180–184]

Compounds with tridentate amines as blocking ligands usually display compressed octahedra and, accordingly, a significant ferromagnetic interaction is observed.[180,185–188] Nevertheless, some compounds displaying rhombic distortion may be also found, which show a weak antiferromagnetic interaction.[66,189]

When the capping ligand is bidentate, such as 2,2'-bipyridine (bpy) or 1,10-phenantroline (phen), the sixth position of the coordination octahedra is occupied by a monodentate ligand, which provides greater flexibility on the coordination environment and gives distortions of different type and degree.[181] However, there is only one compound displaying compressed octahedra around the Mn^{III} ions, $[\{Mn(bpy)(N_3)\}_2(\mu\text{-}C_6H_5COO)_2(\mu\text{-}O)]$, and it shows an important ferromagnetic coupling.[190,191] The rest of them display elongated coordination octahedra toward the monodentate ligands. However, the magnitude of this distortion is sensitive to the specific monodentate ligand and its donor or acceptor character.[181,183]

In the last years, we have focused our attention on the study of the magnetic properties of this kind of dinuclear compound with benzoate-derivative bridges[181–183,192,193] and the factors that determine the magnetic interaction. The interest is centered in the structural changes promoted by the monodentate ligand and the steric hindrance due to the substituent of the benzoate derivative. The analysis of the magnetic properties of compounds with 2-$RC_6H_4COO^-$ bridging ligands showed that the magnetic interaction for this kind of

compound also depends on the relative orientation of the Jahn-Teller axes of the Mn^{III} ions and the planarity between the aromatic ring and the carboxylate group.[181]

Furthermore, the magnetic anisotropy or zero-field splitting (ZFS) is one of the most important properties that characterizes a metal ion with $S > ½$.[21] Particularly, Mn^{III} ion is known to display significant axial (D) and rhombic (E) anisotropy parameters.[22] The ZFS effect has been studied on several occasions for mononuclear compounds, providing an idea about the nature and magnitude of these parameters.[21,22,163,164] Nevertheless, the determination of the single-ion anisotropy for polynuclear compounds is very challenging, since the overall magnetic properties are dependent on both the isotropic (Mn···Mn interactions) and the asymmetric interactions (referred to ZFS).[21,35]

This chapter contains the synthesis, characterization, and a profound analysis of the magnetic properties of a family of seven compounds with general formula $[\{Mn(bpy)L\}_2(\mu\text{-}O)(\mu\text{-}n\text{-}RC_6H_4COO)_2]X_2$, where n-R = 2-MeO (**1** and **2**), 3-MeO (**3**, **4**, and **5**), 4-MeO (**6**), or 4-tBu (**7**), X = NO_3 (**1**, **3**, and **4**) or ClO_4 (**2**, **5**, **6**, and **7**), and L = H_2O, EtOH, or X. The magnetic coupling constant and the ZFS parameters of the Mn^{III} ions have been determined and the limits of detection for the sign and magnitude of these parameters have been evaluated. Moreover, the analysis of the structural parameters and the magnetic data of twenty-six analogous compounds has been carried out with the aim to find the ligands that could contribute to obtain systems with an $S = 4$ ground state.

Synthesis

The dinuclear Mn^{III} compounds **1–7** were obtained from the comproportionation reaction between Mn^{II} and MnO_4^- in the presence of a benzoic acid derivative and 2-2'-bipyridine (bpy), which leads to compounds with the general formula $[\{Mn(bpy)(L)\}(\mu\text{-}n\text{-}RC_6H_4COO)_2(\mu\text{-}O)\{Mn(bpy)(L')\}]X_{2-m}$, where n-R = 2-MeO (**1** and **2**), 3-MeO (**3–5**), 4-MeO (**6**) or 4-^{t}Bu (**7**) and X = NO_3 (**1**, **3**, and **4**) or ClO_4 (**2** and **5–7**). L and L' are monodentate ligands that can be H_2O, EtOH or X. The stoichiometry of this reaction is:

$$1.6\ MnX_2 + 2\ n\text{-}RC_6H_4COOH + 0.4\ NBu_4MnO_4 + 2\ bpy \rightarrow [\{Mn(bpy)(L)\}(\mu\text{-}n\text{-}RC_6H_4COO)_2(\mu\text{-}O)\{Mn(bpy)(L')\}]X_{2-m} + 0.4\ NBu4X + 0.8\ HX + x\ H_2O$$

If both positions (L and L') are occupied by X, like in compound **3**, a neutral complex is formed. In the rest of compounds (**1**, **2**, and **4**–**7**), only one of the monodentate positions is occupied by the anion X, so the complex is a monovalent cation. The synthesis of compounds with X = NO_3 and *n*-R = 4-MeO and 4-^{t}Bu was also previously reported, but no X-ray suitable crystals were obtained.[192]

The perchlorate compounds (**2** and **5**–**7**) are much more soluble than nitrate compounds (**1**, **3**, and **4**) in acetonitrile solution, as reported before for analogous compounds with *n*-R = 2-Me and *n*-R = 2-F.[183] Thus, while the nitrate compounds **3** and **4** could be crystallized from the acetonitrile solution, the perchlorate compounds **5**–**7** did not crystallize from the mother liquor. Compound **5** was obtained by slow diffusion of *n*-hexane (precipitant) to an acetonitrile solution of **5** layered with CH_2Cl_2. Compounds **6** and **7** are insoluble in ethanol solution, so they were crystallized by mixing a very concentrated solution of acetonitrile mother liquor with ethanol (**6**) or using ethanol instead of acetonitrile in the synthesis (**7**). Both compounds with *n*-R = 2-MeO, **1** and **2**, could be crystallized from the acetonitrile mother liquor, but compound **2** (with perchlorate) took more time to crystallize.

IR spectra of these compounds show two characteristic bands at ~1560 and 1365 cm^{-1}, corresponding to the asymmetric (ν_a) and symmetric (ν_s) vibrations of the carboxylate groups, respectively. The value $\Delta\nu = \nu_a(COO) - \nu_s(COO) \approx 200$ cm^{-1} is indicative of carboxylate ligands coordinated in bidentate bridging mode ($\mu_{1,3}$).[14] The bands centered at ~1600, 1498, 1480 and 1450 cm^{-1} are assigned to the bipyridine. The Mn-O-Mn group displays a moderate band at ~730 cm^{-1}. The spectra of compound **1**, **3**, and **4** exhibit an intense band at 1352 cm^{-1} corresponding to the nitrate anion, which overlaps the ν_s(COO). In the spectra of compound **2** and **5**–**7**, an intense band at 1120 cm^{-1} and a moderate band at 623 cm^{-1} are observed, being assigned to the perchlorate anion.

Compounds **3** and **4** are structural isomers that only differ from one of the monodentate ligands (**3**, L = L' = NO_3; **4**, L = H_2O and L'= NO_3) and are obtained under very similar conditions. However, the presence of water in the mother liquor favors the formation of **4**, whereas **3** is obtained in dry acetonitrile. Fortunately, these two compounds can be easily differentiated by the shape of their crystals (Figure S1) and their IR spectra in the 960–800 cm^{-1} window (Figure S2). While **3** crystallizes as big blocks and displays a band centered at 902 cm^{-1} of moderate intensity and two weak ones at 919 and 876 cm^{-1}, **4** crystallizes as small star-shaped agglomerations of needles and shows a pair of bands at 916 and 884 cm^{-1}. To determine the proper conditions to obtain the two compounds separately, several syntheses

were performed controlling the addition of water. A pure sample of **3** was only isolated when dry acetonitrile was used. On the other hand, **4** was crystallized with a H_2O/CH_3CN volume ratio of 0.02. Note that higher ratios than this are unnecessary and lead to the decomposition of the Mn compound. If H_2O vapor diffusion is used as crystallization method, a mixture of the two compounds was obtained, indicating that humidity should be controlled. Hence, it is convenient to observe the sample under a magnifying glass to ensure the purity of the sample.

Description of structures

The crystal structures of compounds **1**–**7** are shown in Figure 21. Note that in the crystal structure of **7** two co-crystallized conformational isomers were found, named Subunits 1 and 2. In all these compounds (**1**–**7**), the two Mn^{III} ions show a distorted octahedral environment and are linked by one oxo and two $\mu_{1,3}$-*n*-$RC_6H_4COO^-$ bridges. Each manganese ion is bound to a 2,2'-bipyridine (bpy) ligand, and the hexacoordination of each Mn ion is completed by a monodentate ligand. In compound **3**, the monodentate ligands are nitrate anions, so the resulting complex is neutral. In compounds **1**, **2** and **4**–**7**, one of the monodentate ligands is a NO_3^- (**1**, **4**) or a ClO_4^- anion (**2** and **5**–**7**) and the other one is a molecule of water (**1**, **2**, **4**, and **5**) or EtOH (**6** and **7**), resulting in a cationic complex.

The Mn···Mn distance is ~3.15 Å and the Mn–O_b–Mn angle is ~123º. The Mn–O_b bond distances of the oxo bridges are ~1.78 Å and the Mn–N distances are ~2.06 Å. The carboxylate ligands are coordinated in a *syn-syn* conformation mode. One of the oxygen atoms is placed *trans* to the monodentate ligand, with a Mn–O_t distance of ~2.16 Å, whereas the other oxygen atom is placed in a *cis* position, with a shorter Mn–O_c distance (~1.96 Å). The Mn–L bond lengths of the monodentate ligands are the largest in the first coordination sphere and are in the range 2.17–2.48 Å. Selected interatomic distances for these compounds are listed in Table S10 (for **1**), Table S11 (for **2**), Table S12 (for **3**), Table S13 (for **4**–**6**), and Table S14 (for **7**). More particular details concerning the structures and intermolecular interactions may be found in Appendix II.

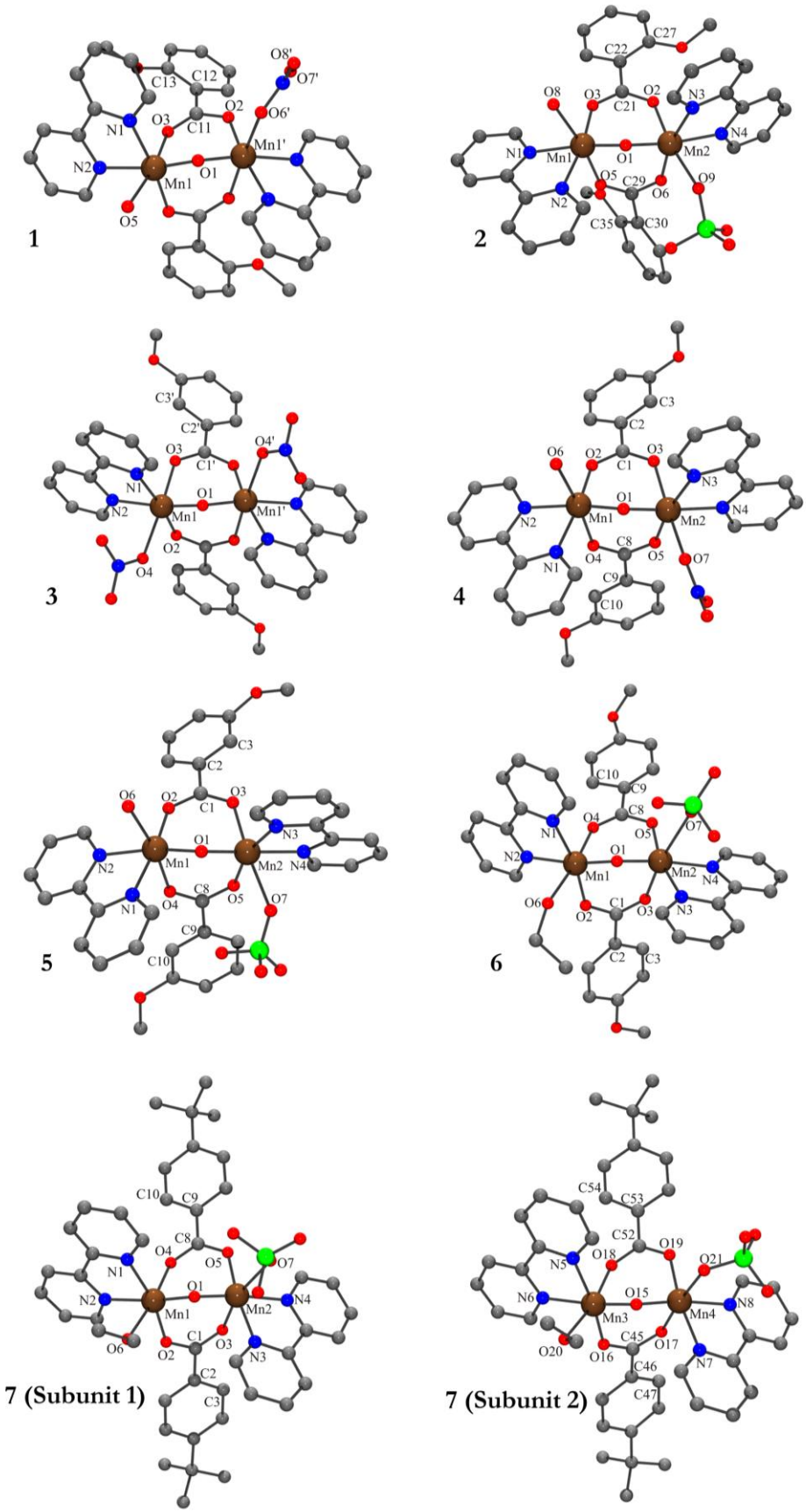

Figure 21. Crystal structures of cationic complexes of compounds **1**–**7**. Hydrogen atoms were omitted for clarity. Color code: Mn, brown; C, gray; O, red; N, blue; Cl, green.

The structural parameters of these compounds are in agreement with those reported for compounds with the same $[Mn_2(\mu\text{-}O)(\mu\text{-}n\text{-}RC_6H_4COO)_2]^{2+}$ core.[181,183,184,192–195] However, it is worth remarking that **6**, with a Mn2–O7 of 2.48 Å ($Mn–O_{ClO4}$), has the longest Mn–L bond distance found for this kind of compound.

The relative orientation of the two coordination octahedra is near perpendicularity, with torsion angle τ(L–Mn···Mn–L) between 68 and 117º, in agreement with those reported in the literature.[181,183,184,192–194] One of the subunits of compound **7** has the smallest angle of this family of compounds, being 68º.

In compounds with the R group in *meta* and *para* position (n = 3 and 4), the carboxylate group and the aromatic ring of the benzoate derivative are almost coplanar, having a twist angle ω($O–C_{carb}–C_{ar}–C'_{ar}$) in the range of 0–17º. The values of these angles are also in agreement with those reported for compounds with *meta*- and *para*-benzoate derivatives (n = 3 and 4).[184,192,194] In contrast, compounds with *ortho*-benzoate derivatives (n = 2), show higher ω values.[181,183,193] Accordingly, in compound **1** the aromatic ring and the carboxylate group of the 2-methoxybenzoate ligand are not coplanar, having a twist angle ω($O–C_{carb}–C_{ar}–C'_{ar}$) of 36.2º. In compound **2**, the 2-methoxybenzoato ligand that is *trans* to the ClO_4^- ion is closer to planarity than that being *trans* to the H_2O molecule, with respective twist angles ω($O–C_{carb}–C_{ar}–C'_{ar}$) of 50.3 and 8º.

As mentioned before, all Mn^{III} ions in these compounds display elongated octahedra along the monodentate ligand direction; thus, the Jahn-Teller elongation axes should be approximately situated on the O_t–Mn–L direction. Besides, they also show a rhombic distortion (the $Mn–O_b$ bond distances is significantly smaller than $Mn–O_c$). Considering the z axis in the O_t–Mn–L direction and the x axis in the oxo-bridge direction (Figure 22), approximate values of the octahedron axes lengths can be found by addition of Mn-ligand distances: $x = d(Mn–O_b) + d(Mn–N_t)$, $y = d(Mn–O_c) + d(Mn–N_c)$ and $z = d(Mn–L) + d(Mn–O_t)$.

Formerly, G. Fernandez *et al.* described the distortion parameter (λ)[183] as $\lambda = (z - y)/(y - x)$ and it was used for several series of compounds.[181,184,192] This parameter, which normally ranges from 0.2 to 3.5, offers the possibility to identify the predominant distortion (elongated octahedron if $\lambda > 2$, rhombic distortion if $2 > \lambda > 1$, compressed octahedron if $\lambda < 1$). However, it does not allow us to quantify both distortions separately, which could be essential to better rationalize the axial and rhombic anisotropies of the Mn^{III} ions (see below). In addition, λ shows an overstatement of the elongation when the rhombic distortion is very

small. For instance, the Mn2 ion in **6** shows a very small rhombic distortion ($x \approx y$); so, the λ parameter becomes enormous (value of 10) compared to the other Mn^{III} ions in compounds **1**–**5**, **7** (values between 1.3 and 3.8) (see Table 2).

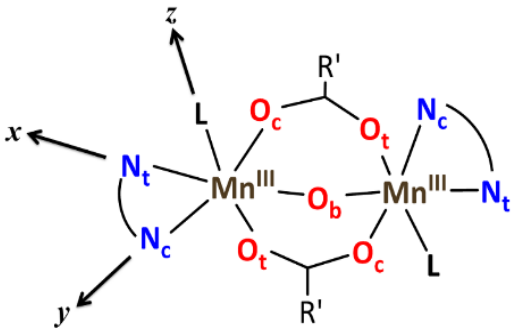

Figure 22. Schematic representation of the structure of the dinuclear Mn^{III} complexes with the axes of the octahedron.

Hence, in order to quantify both distortions, we defined two parameters for the elongation (Δ) and rhombicity (ρ) with the following formulas:

$$\Delta = \frac{z-\overline{xy}}{\overline{xy}} \quad \text{Eq. 9;} \qquad \rho = \frac{y-x}{x} \quad \text{Eq. 10}$$

where $\overline{xy} = (x+y)/2$. While Δ represents how different the Jahn-Teller axis is from the average length between x and y axes, ρ represents the distortion within the xy plane. Both parameters are dimensionless and can be expressed in the form of percentage for better clarity. For all these compounds (**1**–**7**), Δ should be greater than ρ ($\Delta > \rho$) and both of them should be positive, characteristic of elongated octahedra with small or moderate rhombic distortion. This model can be also applied to compressed octahedra, in this case $\Delta < 0$. In both kinds of octahedra, $|\Delta| > |\rho|$ (the absolute value of the elongation parameter should be greater than the absolute value of the rhombic one). If $|\Delta| < |\rho|$, the axes are improperly assigned. And if $|\Delta| \approx |\rho|$, the octahedron has a pronounced rhombic distortion or the axes are improperly assigned.

The axes length and the Δ and ρ parameters for compounds **1**–**7** are listed in Table 2. Note that the average values of the axes follow the trend $z > y > x$ with their respective standards deviations (s) following the trend $s_z > s_y > s_x$, which indicates that the length for z axes is the most variable. The resulting Δ and ρ distortions are in the ranges 10.0–17.9% and 1.7–5.8%, respectively; and, in accord to the explained above, these values are consistent with elongated octahedra with different degrees of rhombic distortion.

Table 2. x, y and z axes lengths and the elongation (Δ), rhombicity (ρ), and distortion (λ) parameters of each Mn ion for compounds **1–7**.

		x / Å	y / Å	z / Å	Δ / %	ρ / %	λ
1	Mn1	3.846	4.037	4.367	10.80	4.97	1.73
2	Mn1	3.844	4.021	4.396	11.79	4.60	2.12
	Mn2	3.845	4.006	4.42	12.60	4.19	2.57
3	Mn1	3.8558	4.0194	4.4255	12.39	4.24	2.48
4	Mn1	3.841	4.063	4.353	10.15	5.78	1.31
	Mn2	3.833	4.009	4.451	13.52	4.59	2.51
5	Mn1	3.8546	4.0331	4.3373	9.98	4.63	1.70
	Mn2	3.8406	4.0039	4.5362	15.65	4.25	3.26
6	Mn1	3.8209	4.0201	4.4436	13.34	5.21	2.13
	Mn2	3.8733	3.9398	4.6048	17.87	1.72	10.0
7	Mn1	3.849	4.003	4.375	11.44	4.00	2.42
	Mn2	3.827	3.97	4.507	15.61	3.74	3.76
	Mn3	3.84	3.999	4.373	11.57	4.14	2.35
	Mn4	3.838	4.006	4.472	14.02	4.38	2.77
Average		**3.84**	**4.01**	**4.43**			
s		**0.01**	**0.03**	**0.08**			

x = d(Mn–O_b) + d(Mn–N_t); y = d(Mn–O_c) + d(Mn–N_c); z = d(Mn–O_L) + d(Mn–O_t); $\Delta = (z - \overline{xy})/\overline{xy}$ (Eq. 9), $\overline{xy} = (x + y)/2$; $\rho = (y - x)/x$ (Eq. 10); s = standard deviation.

Magnetic properties

Magnetic susceptibility (χ_M) data were recorded for compound **1–7** from 300 to 2 K. $\chi_M T$ versus T plots for **1–7** are shown in Figure 23. Note that the curves are remarkably different. The $\chi_M T$ values at room temperature are between 5.3 and 6.3 $cm^3\ mol^{-1}\ K$, which are close to the expected value for two uncoupled Mn^{III} ions. For compounds **3–5**, the $\chi_M T$ values remain almost constant until 100 K; but they increase below this temperature, reaching maximum values of 7.1 (**3**), 7.0 (**4**) and 6.7 (**5**) $cm^3\ mol^{-1}\ K$ at ~13 K. This behavior is indicative of a ferromagnetic coupling (spin ground state S = 4). Below 13 K, $\chi_M T$ values slightly decrease due the zero-field splitting, as expected for Mn^{III} ions. On the other hand, for compounds **1**, **2**, **6**, and **7**, the $\chi_M T$ values decrease as the temperature falls (more pronouncedly in the case of **7**), indicative of an antiferromagnetic coupling (spin ground state S = 0). However, these compounds show different behavior at very low temperature: for **7** the $\chi_M T$ reaches zero, characteristic of an isolated singlet ground state; while for **1**, **2**, and **6** the $\chi_M T$ values at 2 K are 2.2 (**1**), 3.3, (**2**), and 0.9 (**6**) $cm^3\ mol^{-1}\ K$, indicating a non-negligible population in the first excited states.

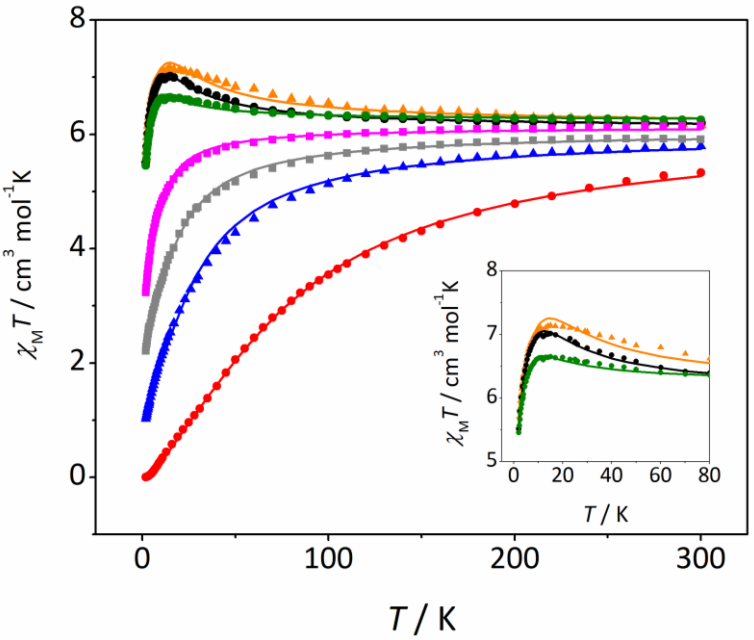

Figure 23. $\chi_M T$ versus T plots for compounds **1** (pink squares), **2** (gray squares), **3** (orange triangles), **4** (black circles), **5** (green circles), **6** (blue triangles) and **7** (red circles). The solid lines are the best fits of the experimental data.

$\chi_M T$ versus T data of compound **7** were fitted with the PHI program,[165] considering the Heisenberg spin Hamiltonian $H = -2JS_1S_2$, whose results are presented in Table 3. On the other hand, the magnetic data of compounds **1–6** could not be fitted considering an isotropic system; it was necessary to include the ZFS parameters to fit their experimental $\chi_M T$ versus T data.

The zero-field splitting (ZFS) effect removes the degeneration of the M_S states of each S level, and the energy gap between the M_S states (D_S and E_S) depend on the magnitudes and signs of the anisotropy parameters of the Mn^{III} ions, D_{Mn} and E_{Mn}.[8] In the case of Mn^{III} ions with elongated octahedral geometry like in compounds **1–7**, negative and moderate values of D_{Mn} are expected.[21,22,163,164] The low symmetry of the octahedra in these compounds also causes a pronounced rhombic distortion; so, significant E_{Mn} values are also expected.[163,164] In addition, D_{Mn} and E_{Mn} are directional and, consequently, their relative orientation may affect the ZFS of each state (D_S and E_S). Particularly for the compounds presented here, D_{Mn} vectors should be approximately located along the z axes according to Figure 22. Hence, their relative orientation (β angle) may have a pronounced effect on the M_S splitting, since they would be around orthogonality ($\beta \approx 90^o$). This can affect the low temperature range of the $\chi_M T$ versus T plot if there is any populated state with $S \neq 0$. So, this could have some influence for compounds with weak or moderate antiferromagnetic magnetic interactions.

With the aim to see the effect of the relative disposition of the distortion axes, several simulations of the $\chi_M T$ versus T plot were carried out with fixed values of $2J$ and D_{Mn}, but modifying the β angles between 0 and 90º. As could be expected, for systems with strong antiferromagnetic interaction the effect of the β angle on the $\chi_M T$ versus T plot is negligible. However, for systems with weak and moderate antiferromagnetic interaction, a significant effect on the shape of the graph was observed. Figure 24 shows the $\chi_M T$ versus T plot for systems with $2J = \pm 1$ cm^{-1} and $D_{Mn} = -4$ cm^{-1}. For the antiferromagnetic system with parallel Jahn-Teller axes ($\beta = 0$), $\chi_M T$ values fall to zero at low temperature, as expected for a ground state $S = 0$; however, when the axes are orthogonal ($\beta = 90$º), a significant deviation of the graph is observed.

It is well known that for systems with ferromagnetic interaction, the ZFS of the ground state $S = 4$ justifies the decay of the $\chi_M T$ values at low temperatures. This effect is influenced by the relative orientation of the Jahn-Teller axes (as in antiferromagnetic compounds): the $\chi_M T$ maximum shifts to a higher temperature and the $\chi_M T$ value of the maximum decreases for $\beta = 90$º.

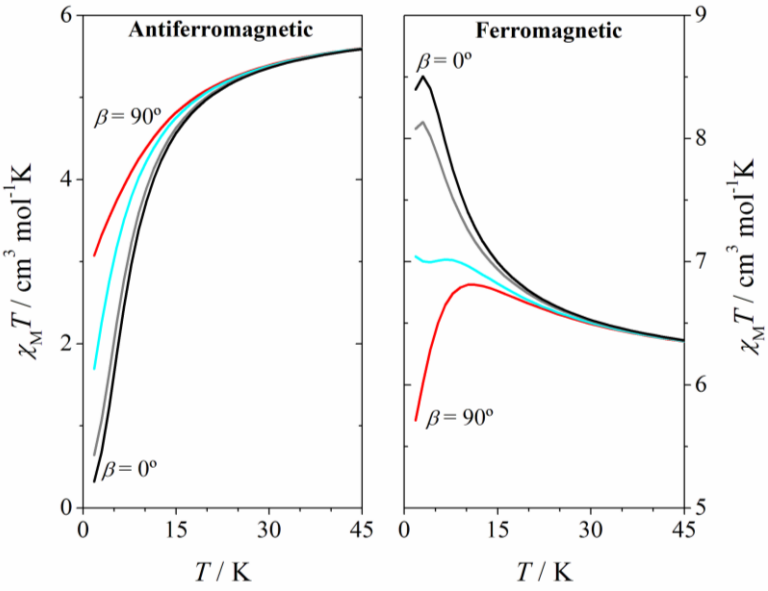

Figure 24. Effect of the relative orientation of axial anisotropy axes (β) on the $\chi_M T$ versus T plots of a hypothetical Mn^{III}_2 compound with $g = 2.0$, $2J = \pm 1.0$ cm^{-1}, $D_{Mn} = -4.0$ cm^{-1} and $\beta = 0$º (black), 30º (gray), 60º (cyan) and 90º (red); considering the Hamiltonian $H = -2JS_1S_2$.

To acquire more information, magnetization (M) data were collected for compounds **3**–**6** in the range 1.8–6.8 K, applying magnetic fields between 0.5 and 5.0 T. $M/N\mu_B$ versus HT^{-1} plots for compounds **4**–**6** are shown in Figure 25 and Figure S10. The non-superposition of

the various isofield lines is indicative of a significant ZFS. All plots present similar features, without showing saturation at the highest field and lowest temperature, with maximum $M/N\mu_\beta$ values around 6 $N\mu_\beta$ for the ferromagnetic compounds **3**–**5** and 2.8 $N\mu_\beta$ for the antiferromagnetic compound **6**. For compound **7**, which shows $\chi_M T$ values close to zero at low temperature, no significant magnetization signal can be expected.

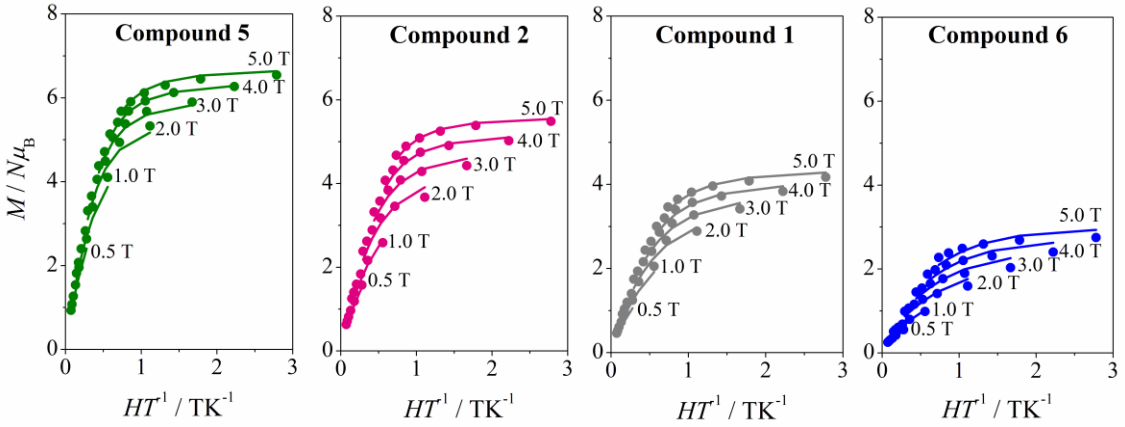

Figure 25. $M/N\mu_\beta$ versus HT^{-1} plots for **5** (green), **2** (pink), **1** (gray), and **6** (blue). The solid lines are the best fits of the experimental data.

The question arises whether one can determine the sign of ZFS parameters by fitting $\chi_M T$ versus T and $M/N\mu_\beta$ versus HT^{-1} plots and upon the precision of the results obtained from these fits. To answer these matters, several simulations of the $\chi_M T$ versus T and $M/N\mu_\beta$ versus HT^{-1} plots were performed screening different $2J$ and D_{Mn} values, all of them considering a relative orientation of the Jahn-Teller axes $\beta = 90^o$.

For compounds with antiferromagnetic coupling ($S = 0$ ground state), the effect of the D_{Mn} parameter can only be observed if the first excited state ($S = 1$) is populated; for moderate or strong antiferromagnetic interaction ($|2J| > 6$ cm^{-1}), the population of this excited state at low temperature is almost negligible and the effect of the D_{Mn} parameter is unnoticed. The ZFS of the $S = 1$ state strongly depends on the D_{Mn} parameter, since $|D_{S=1}| = 4.2|D_{Mn}|$.

For compounds with ferromagnetic coupling ($S = 4$ ground state), the effect of the D_{Mn} parameter is always observable because it affects the ground state. However, for the same D_{Mn} value, the ZFS of the $S = 4$ ($D_{S=4}$) is much smaller than the ZFS of the $S = 1$ ($|D_{S=1}| = 10|D_{S=4}|$ for parallel Jahn-Teller axes).

When the anisotropy parameter (D_{Mn}) is small, ($|D_{Mn}| \leq 2$ cm^{-1}), the effects of their magnitude and sign on the $\chi_M T$ versus T and $M/N\mu_\beta$ versus HT^{-1} plots are unimportant:

although its effect could be noticed in the $M/N\mu_\beta$ versus HT^{-1} plot, the assignment of the sign of D_{Mn} would be ambiguous. On the other hand, for greater $|D_{Mn}|$ values the differences between the plots simulated with positive and negative D_{Mn} values become more relevant as $|D_{Mn}|$ increases.

The information obtained from each one of these plots complement the other one. Magnetization plots are very sensitive to the magnitude and sign of D_{Mn}, except for compounds with moderate-strong antiferromagnetic coupling. However, the quantification of the magnetic coupling constant ($2J$) should not be performed using this plot. The $\chi_M T$ versus T plot is, contrary to the previous one, highly affected by the $2J$ value, but the D_{Mn} parameter only affects in the low temperature range. For compounds with weak antiferromagnetic interaction, different behavior could be observed as a function of the sign of D_{Mn}. When $D_{Mn} > 0$, $\chi_M T$ values tend to zero upon cooling and, consequently, the D_{Mn} value cannot be determined from these data; whereas, when $D_{Mn} < 0$, the $\chi_M T$ versus T plot shows a deviation at low temperature ($\chi_M T$ values do not reach zero) and the magnitude of D_{Mn} should have some influence in the fit of the experimental data. For ferromagnetic compounds, the $\chi_M T$ versus T plots show differences depending on the magnitude of D_{Mn}, but the effect of the sign is sometimes insignificant.

To sum up, the determination of the magnitude and sign of the ZFS parameters of the single ion (D_{Mn}) can only be performed for compounds displaying ferromagnetic or weak antiferromagnetic coupling. For a good accuracy it is necessary to fit the $\chi_M T$ versus T and $M/N\mu_\beta$ versus HT^{-1} data simultaneously, the first one allow to determine the magnetic coupling constant ($2J$) and the magnetization data the ZFS parameters of the single ions (D_{Mn}).

Therefore, $\chi_M T$ versus T and $M/N\mu_\beta$ versus HT^{-1} plots of compound **1–6** were fitted simultaneously using the PHI program ($H = -2JS_1S_2$),[165] considering the zero-field splitting (ZFS) parameters of manganese ions (D_{Mn} and E_{Mn}) and a relative orientation of the Jahn-Teller axes of 90º. Table 3 shows the results for the best fits of the experimental data for compounds **1–7**. Compounds **1–6** show negative values of the D_{Mn}. Particularly for compounds **1, 2,** and **6**, with a weak antiferromagnetic behavior, the sign and magnitude of the D_{Mn} is relevant for both the $\chi_M T$ versus T and $M/N\mu_\beta$ versus HT^{-1} plots. Moreover, the values obtained for D_{Mn} are consistent with elongated Mn^{III} ions with distorted octahedral geometry, which typically give

moderate and negative D_{Mn}.[21,22,163,164] The $E_{Mn}/|D_{Mn}|$ ratios, which are in the range 0.19–0.27, are in agreement with elongated octahedra with rhombic distortion ($x \neq y$). Furthermore, a good correlation between the $E_{Mn}/|D_{Mn}|$ ratio and the rhombic distortion (ρ) is found, as could be seen in Figure 26. This highlights the importance of quantifying the axial and rhombic distortions of the Mn^{III} ions separately.

Table 3. List of magnetic parameters obtained from the fit of $\chi_M T$ versus T and $M/N\mu_\beta$ versus H plots.

Ref.	g	$2J$ [a] / cm^{-1}	D_{Mn} [b] / cm^{-1}	E_{Mn} [c] / cm^{-1}	$E_{Mn}/\lvert D_{Mn}\rvert$	R_{sus} (R_{MAG}) [d]
1	2.01	–2.3	–4.6	+1.0 [e]	0.22	$3.1\cdot10^{-5}$ ($3.0\cdot10^{-3}$)
2	2.01	–0.7	–3.0	-	-	$9.0\cdot10^{-5}$ ($1.1\cdot10^{-3}$)
3	2.04	+1.8	–5.1	+1.1	0.22	$1.3\cdot10^{-4}$ ($2.5\cdot10^{-4}$)
4	2.02	+1.3	–4.1	+1.1	0.27	$2.3\cdot10^{-5}$ ($3.4\cdot10^{-4}$)
5	2.04	+0.52	–3.1	+0.66	0.21	$2.4\cdot10^{-5}$ ($9.5\cdot10^{-4}$)
6	2.00	–4.8	–5.3	+1.0 [e]	0.19	$3.1\cdot10^{-4}$ ($4.3\cdot10^{-3}$)
7	2.04	–16.0	-	-	-	$1.5\cdot10^{-4}$ (-)

[a] Referred to the spin Hamiltonian $H = -2JS_1S_2$; [b] ZFS parameter related to the axial anisotropy; [c] ZFS parameter related to the rhombic anisotropy; [d] $R_{SUS} = \Sigma[(\chi_M T)_{exp} - (\chi_M T)_{calcd.}]^2 / \Sigma[(\chi_M T)_{exp}]^2$; $R_{MAG} = \Sigma[(M/N\mu_\beta)_{exp} - (M/N\mu_\beta)_{calcd.}]^2 / \Sigma[(M/N\mu_\beta)_{exp}]^2$; [e] Kept constant.

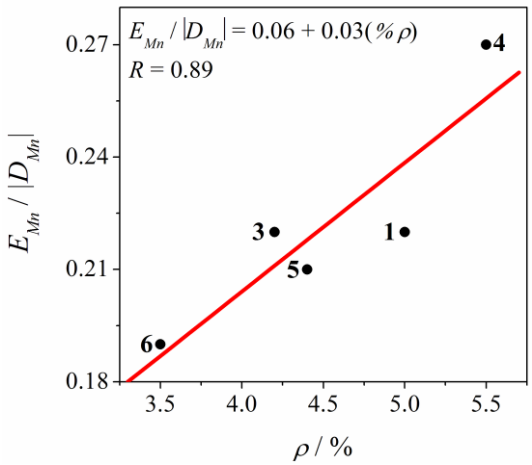

Figure 26. $E_{Mn}/|D_{Mn}|$ ratio versus rhombicity parameter (ρ) for compounds **1** and **3–6**. Compound **2** has not been included in this graph because its experimental data could have been fitted without considering the E parameter. The red line corresponds to the linear fit.

Magneto-structural correlations

Table 4 summarizes the magnetic coupling constants and selected structural parameters for compounds **1**–**7** and nineteen other analogous compounds with benzoate derivative bridges ([{Mn(L)(NN)}$_2$(μ-O)(μ-*n*-RC$_6$H$_4$COO)$_2$]X$_2$). As may be observed, the magnetic coupling constants for these compounds (2*J*) range from –16.0 to +17.6 cm^{-1}, compound **7** showing the most antiferromagnetic coupling. These compounds are classified according to the positions of the R group. As mentioned before, magneto-structural correlations for compounds with the R group in *ortho* position (*n* = 2) had been reported previously.[181] The structural parameters analyzed were: the distortion of the octahedra, the relative orientation of both polyhedra and the twist angles between the benzoate ring and the COO group (Figure 27). Now, the same structural parameters are analyzed for compounds with the R group in *meta* and *para* position (*n* = 3 and 4, respectively).

In previous work by Corbella and coworkers, the influence of different structural parameters in the magnetic interaction was individually evidenced.[181] Now, we would like to correlate these parameters aiming to find the one being more predominant for the magnetic interactions.

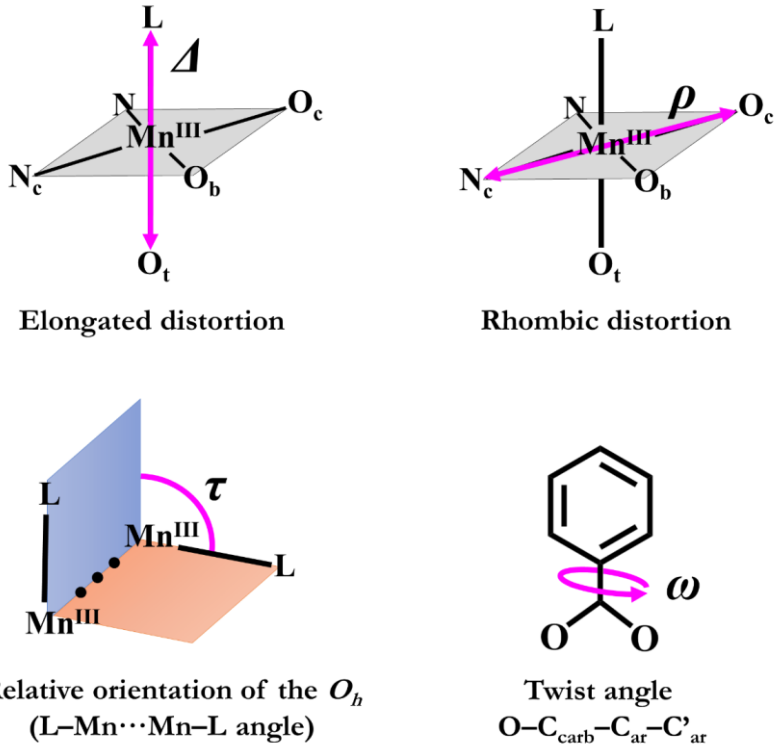

Figure 27. Structural parameters considered in the magneto-structural correlations for compounds with formula [{Mn(L)(NN)}$_2$(μ-O)(μ-*n*-RC$_6$H$_4$COO)$_2$]X$_2$.

Table 4. Magnetic coupling constants $2J$ and selected structural parameters for $[\{Mn(L)(NN)\}_2(\mu\text{-}O)(\mu\text{-}n\text{-}RC_6H_4COO)_2]X_2$ compounds.

Ref	*n*-R	NN	X	L	$2J^a$ / cm^{-1}	Δ^b / %	ρ^c / %	ω^d / º	τ^e / º	γ^f / º
A[193]	2-Cl	Phen	ClO_4	H_2O/H_2O	–12.6	11.2	4.5	77.9	88.3	-
B[181]	2-Cl	Bpy	ClO_4	H_2O/ClO_4 (3/1)	–10.9	13.3	3.5	56.5	92.6	-
C[183]	2-Me	Bpy	ClO_4	H_2O/ClO_4	–5.6	13.8	3.7	46.9	101.1	-
D[183]	2-F	Bpy	ClO_4	H_2O/ClO_4	–3.5	12.7	4.8	19.5	93.6	-
1[195]	2-MeO	Bpy	NO_3	H_2O/NO_3	–2.3	10.8	5.0	36.2	78.1	0
2[195]	2-MeO	Bpy	ClO_4	H_2O/ClO_4	–0.7	12.2	4.4	29.2	95.2	-
E[183]	2-Me	Bpy	NO_3	H_2O/NO_3	–0.5	10.7	4.2	28.8	97.2	79
F[181]	2-Cl	Phen	-	NO_3/NO_3	–0.3	9.7	4.7	38.1	101.7	22
G[183]	2-F	Bpy	NO_3	H_2O/NO_3	+1.4	11.2	5.0	18.6	89.2	18
H[193]	2-Cl	Phen	ClO_4	H_2O/H_2O	+2.7	9.7	4.9	46	102	-
I[181]	2-Cl	Bpy	NO_3	H_2O/NO_3	+3.0	9.4	5.4	25.4	108.5	22
J[196]	2-COOH	Bpy	NO_3	H_2O/NO_3 (3/1)	+4.7	11.2	4.6	19.9	96.4	68
5	3-MeO	Bpy	ClO_4	H_2O/ClO_4	+0.5	12.8	4.4	10.7	102.3	-
4	3-MeO	Bpy	NO_3	H_2O/NO_3	+1.3	11.8	5.2	11.8	92.8	8
3	3-MeO	Bpy	NO_3	NO_3/NO_3	+1.8	12.4	4.2	16.9	117.2	3
K[194]	3-Cl	Phen	ClO_4	H_2O/H_2O	+5.7	11.6	4.7	3.9	120.6	-
L[194]	3-Cl	Bpy	NO_3	H_2O/H_2O	+11.8	9.0	5.4	5.8	112.7	-
7	4-tBu	Bpy	ClO_4	$EtOH/ClO_4$	–16.0	13.2	4.1	3.8	73.7	-
M[184]	4-Br	Bpy	ClO_4	$EtOH/ClO_4$	–6.8	14.6	4.0	10.7	94.1	-
6	4-MeO	Bpy	ClO_4	$EtOH/ClO_4$	–5.2	15.6	3.5	11.7	95.5	-
N[184]	4-Cl	Phen	ClO_4	EtOH/EtOH	0	11.1	4.1	6.7	88.9	-
O[192]	4-F	Bpy	NO_3	H_2O/H_2O	+1.4	10.0	5.1	9.3	99	-
P[192]	4-Me	Bpy	NO_3	H_2O/H_2O	+1.5	10.9	4.4	7.3	112	-
Q[182]	H	Bpy	-	OH/NO_3	+2.0	10.8	5.3	10.2	94.9	8
R[192]	4-CF_3	Bpy	NO_3	H_2O/H_2O	+5.7	10.6	4.2	7.5	116	-
S[191]	H	Bpy	-	N_3/N_3	+17.6	5.3	7.4	5.0	108.1	-

[a] $H = -2J(S_1S_2)$; [b] average Elongation (Eq. 9): $\Delta = (z - \overline{xy})/\overline{xy}$, $\overline{xy} = (x + y)/2$; [b] average rombicity (Eq. 10): $\rho = (y - x)/x$; [d] average O–C_{carb}–C_{ar}–C_{ar}' angle; [e] relative orientation of the O_h: L–Mn···Mn–L angle; [f] Mn–O–N–O torsion angle; abbreviations: bpy = 2,2'-bipyridine, phen = 1,10-phenantroline.

Distortion of octahedra (Δ and ρ). The compounds analyzed here show elongated coordination octahedra with a significant rhombic distortion. Thus, their shape is governed by the parameters defined above, Δ and ρ. With the aim to improve the correlation between the distortion of the octahedra and the magnetic interaction, these parameters have been calculated for all the compounds reported in Table 4 from their crystal data. For all compounds except **S**, the Mn^{III} ions display an elongated octahedral environment (Δ = 9.0–15.6%) with notable rhombic distortion (ρ = 3.5–5.4%). Compound **S** (with L = N_3/N_3)[191] displays compressed octahedra towards the Mn–O_{oxo} bond, therefore $\rho > \Delta$. In regard to the explanation above, the axial distortion of the manganese ions in this compound should

be calculated considering the z axis in the direction of the Mn–O_{oxo} bond, which would give $\Delta < 0$. Anyhow, we kept the definition of axes as presented in Figure 22 in order to compare this compound with the rest.

In previous works[181–183] it was reported that the elongation of the octahedra is related to the antiferromagnetic behavior. With the aim to see the effect of both distortion parameters on the magnetic coupling, Figure 28 shows the contour plot of the rhombicity parameter (ρ) versus the elongation parameter (Δ) and the magnetic interaction ($2J$) for compounds collected in Table 4. Two facts can be deduced from this graph: firstly, the Δ and ρ parameters are inversely proportional; and, secondly, compounds with ferromagnetic interaction show $\Delta \approx \rho$, while compounds with an antiferromagnetic interaction show $\Delta >> \rho$. These results are consistent with those reported previously;[181] however, the new distortion parameters, which consider the elongation and the distortion of the xy plane separately, give a more accurate correlation.

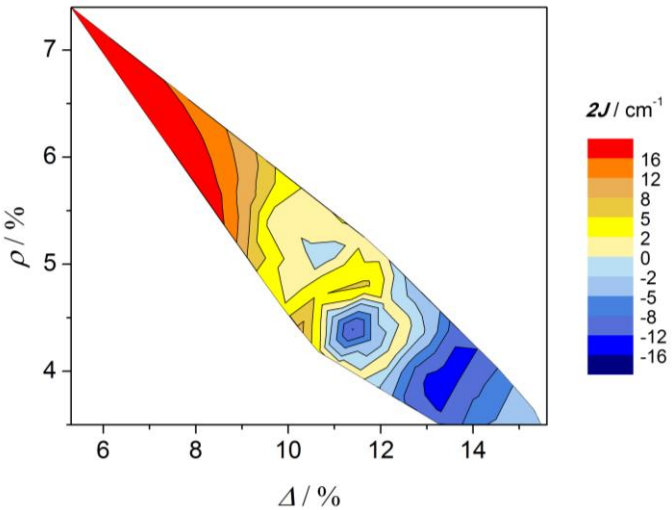

Figure 28. Magnetic coupling constant $2J$ versus elongation parameter (Δ) and rhombicity parameter (ρ) for compounds with formula $[\{Mn(L)(NN)\}_2(\mu\text{-}O)(\mu\text{-}n\text{-}RC_6H_4COO)_2]X_2$.

Effect of the monodentate ligands. The effect of the monodentate ligands was concisely studied in some previous works.[181,184] As therein mentioned, compounds with L = ClO_4 or EtOH show more elongated coordination octahedra than those with L = NO_3, and this fact favors the antiferromagnetic behavior. A more accurate analysis of the effect of the L ligand on the magnetic interaction is reported here for the compounds collected in Table 4. To see the range of the elongation parameter (Δ) in relation to the monodentate ligand, these compounds may be classified depending on the couple of monodentate ligands present in the dinuclear entity: L = EtOH/ClO_4, H_2O/EtOH, H_2O/H_2O, H_2O/NO_3, and NO_3/NO_3.

Compounds with L = H_2O/H_2O have been separated depending on their counter-anion (X). Figure 29 shows the range of values for the elongation parameter (⊿) and for the magnetic coupling constant ($2J$) for the six groups of compounds.

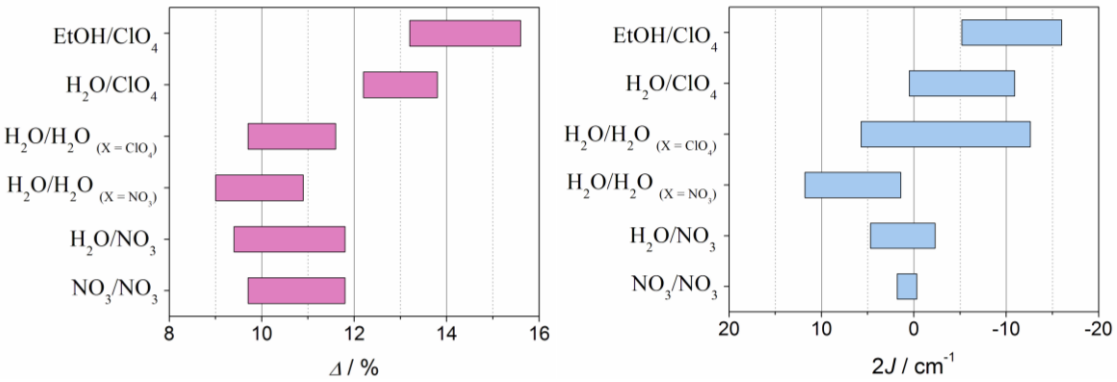

Figure 29. Ranges for elongation parameter ⊿ (left) and magnetic coupling constant J (right) for $[\{Mn(L)(NN)\}_2(\mu\text{-}O)(\mu\text{-}n\text{-}RC_6H_4COO)_2]X_2$ compounds depending on their L ligand.

Concerning the distortion parameter, compounds with perchlorate as monodentate ligand display the largest elongations of the octahedra, ⊿ values being between 12 and 16%. This effect is magnified if they also contain ethanol. On the other hand, compounds containing water or nitrate show similar ⊿ values, but in a lower range (9–12%) than the ones with perchlorate.

Accordingly, compounds with perchlorate ligands show a more antiferromagnetic interaction than those with nitrate ligands. Surprisingly, compounds with L = H_2O/H_2O and perchlorate as counter-anions (non-coordinated) show more antiferromagnetic couplings than those with nitrate counter-anions, and this difference is more acute than that found for the elongation parameter (⊿). So, most compounds with perchlorate ligand or counter-anion show antiferromagnetic behavior, while compounds with nitrate ligand or counter-anion show ferromagnetic behavior. The cause of this fact may lie either in the resulting packing that each counter-anion provides or in the electronic effects promoted by hydrogen bonds Mn–$OH_2\cdots$X (through the monodentate ligand).

Moreover, it was reported[183] that the magnetic interaction is also sensitive to the orientation of the nitrate ligand. When the NO_3^- ligand is positioned perpendicular to the z axis, with γ (MnONO torsion angle) close to 90º, it may act as a π-acid ligand and decreases the antiferromagnetic contributions. The three new compounds herein reported with nitrate ligand (**1**, **3** and **4**) show a parallel disposition of these ligands, so a negligible π-acid effect of this ligand can be expected.

Relative orientation of octahedra, τ(L–Mn–Mn–L). Another parameter affecting the magnetic interaction is the relative orientation of the octahedra, defined as the torsion angle between monodentate ligands (τ). Aiming to see the relationship between this angle and the elongation parameter (Δ) and their influence on the magnetic interaction, a contour plot of these structural parameters (Δ and τ) and the magnetic interaction is shown in Figure 30. In general, compounds with elongated octahedra show minor values of the τ angles and show antiferromagnetic behavior.

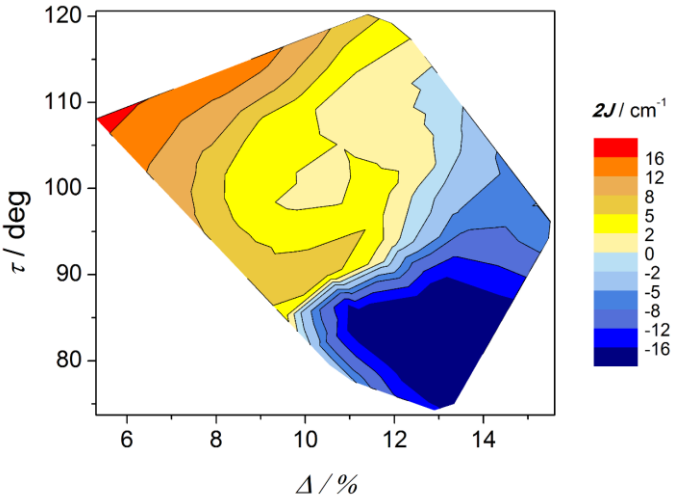

Figure 30. Magnetic coupling constant $2J$ versus the relative orientation of octahedra (τ) and elongation parameter (Δ) for compounds with formula $[\{Mn(L)(NN)\}_2(\mu\text{-}O)(\mu\text{-}n\text{-}RC_6H_4COO)_2]X_2$.

Twist angle O–C_{carb}–C_{ar}–C'_{ar} (ω). This angle indicates the relative disposition of the COO group and the aromatic ring of the carboxylate bridging ligand: ω = 0º, coplanar; 90º, orthogonal. This angle is very sensitive to the position of the R group of the carboxylate ligand. Figure 31 shows the magnetic coupling constant versus this angle.

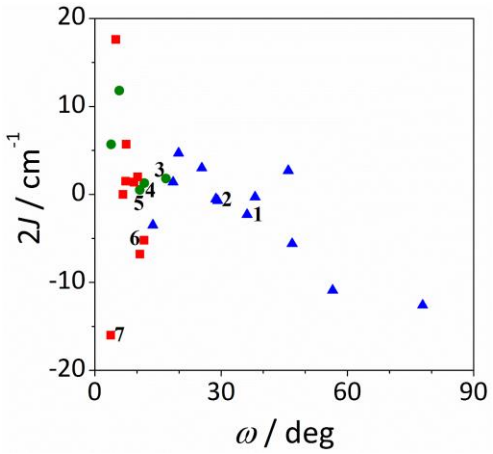

Figure 31. Magnetic coupling constant $2J$ versus twist angle O–C_{carb}–C_{ar}–C'_{ar} (ω) for compounds with formula $[\{Mn(L)(NN)\}_2(\mu\text{-}O)(\mu\text{-}n\text{-}RC_6H_4COO)_2]X_2$ for n = 2 (blue triangles), 3 (green circles) and 4 (red squares).

For compounds with the R group in *meta* and *para* position (n = 3 and 4), this angle is in all cases small ($\omega < 20^{o}$) and, thus, its effect on the magnetic interaction would be irrelevant. For compounds with the R group in *ortho* position (n = 2) the values of this angle range from ~20 to ~80º, so, as it was reported previously,[181] this parameter have some influence in the magnetic properties. The ω value generally depends on the steric hindrance of the R group.

The correlation between this angle, the elongation parameter, and the magnetic interaction is shown in Figure 32. As indicated, compounds with substantial elongation of the octahedra show antiferromagnetic behavior. However, for $\Delta > 10\%$ two regions where compounds display strong antiferromagnetic behavior may be seen in the two extremes of the ω values.

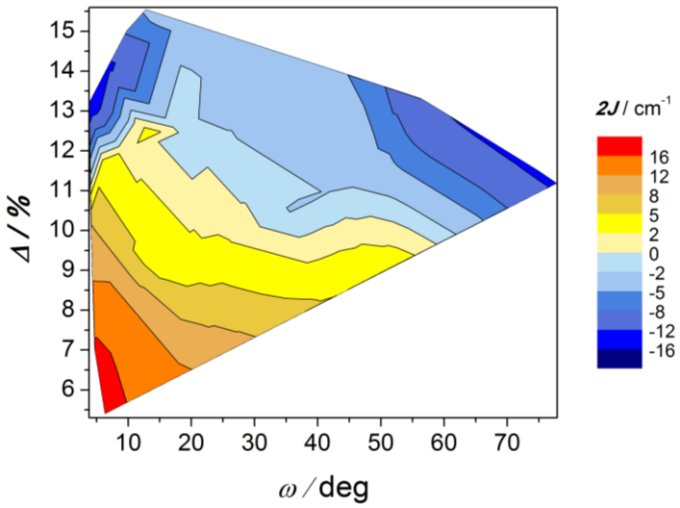

Figure 32. Magnetic coupling constant $2J$ versus twist angle O–C_{carb}–C_{ar}–C'_{ar} (ω) and the elongation parameter (Δ) for compounds with formula $[\{Mn(L)(NN)\}_2(\mu\text{-}O)(\mu\text{-}n\text{-}RC_6H_4COO)_2]X_2$.

The effect of the ω angle on the magnetic coupling had been reported for compounds **A** and **H**, two conformational isomers that has different ground state (*spinomers*). According to these theoretical studies, for $\omega \approx 0$ and 90º, the disposition of the orbitals of the carboxylate ligands is appropriate for overlapping with the *d* orbitals of the Mn ions; while for $\omega \approx 45^{o}$, the topology of the orbitals changes and the antiferromagnetic contribution is reduced.[193] The results shown in Figure 32 are in agreement with this study; for similar elongation values, the weaker antiferromagnetic behavior is observed for a stacked configuration of the benzoate ring ($\omega \approx 40^{o}$). On the other hand, the most ferromagnetic compounds show small ω and Δ values; the slight elongation of the octahedra should be the major contribution to the ferromagnetic character.

The effect of the twist of the phenyl ring (ω) and the relative orientation of the octahedra (τ) on the magnetic coupling constant ($2J$) can be seen in Figure 33. As in the precedent graph,

two well defined regions with important negative $2J$ values are observed for τ angles below 100º at the two extremes of the ω values. For $\omega < 10$º, the magnetic interaction seems to be dictated by τ angle, since the bigger this angle is, the more ferromagnetic. Nevertheless, as the phenyl ring losses the coplanarity with the COO group ($\omega > 10$º), ω becomes more relevant than τ for the magnetic coupling.

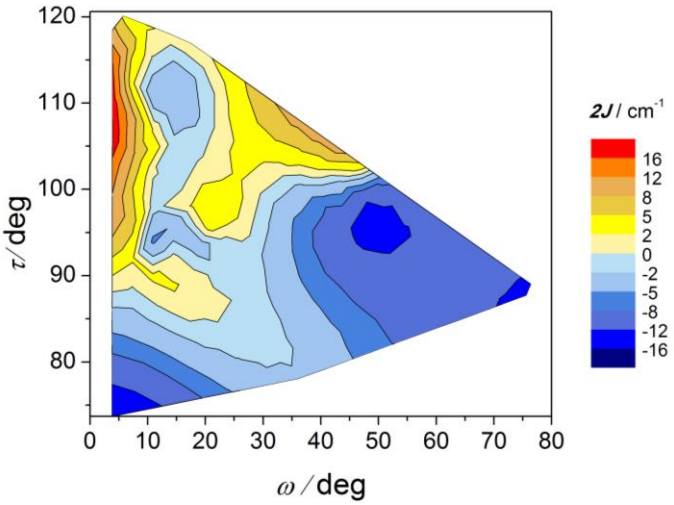

Figure 33. Magnetic coupling constant $2J$ versus twist angle O–C_{carb}–C_{ar}–C'_{ar} (ω) and relative orientation of the octahedra (τ) for compounds with formula $[\{Mn(L)(NN)\}_2(\mu\text{-}O)(\mu\text{-}n\text{-}RC_6H_4COO)_2]X_2$.

Electronic effect of the R group. The electro-donating character of the R group, as well as its position in the aromatic ring, could modify the electronic density on the Mn ions and, consequently, the magnetic coupling. It is interesting to highlight that the five compounds with the R group in *meta* position (3-R) exhibit a ferromagnetic coupling, while compounds with the R group in *para* or *ortho* position (4-R or 2-R) could show both magnetic behaviors. Moreover, with 2-R group there are more compounds showing antiferromagnetic interaction than ferromagnetic. The most relevant difference between the compounds with 3-R groups and compounds with 2-R or 4-R groups is in the relative disposition of the coordination octahedra (τ) that, in most cases, is greater than 100º for compounds with 3-R substituents.

Moreover, it was previously reported that, with similar structural parameters, compounds with an electron-withdrawing groups show a more ferromagnetic behavior than those with electron-donating groups.[192] The Hammett constant (σ) is related to the electronic effect of the R group, and have two contributions, due to the inductive and resonance effects.[197,198] Resonance contribution can only occur for substituents in *ortho* and *para* position. So, when the R group is in meta position, the σ_{meta} only depends on the inductive effect. Moreover, inductive effects diminish with the distance between R and COO groups. Thus, for the same

R group, σ_{meta} is generally greater than σ_{para} and, consequently, the 3-R group has a major electron-withdrawing character than a 4-R group.

Summary

Seven new dinuclear Mn^{III} compounds with benzoate derivative bridges $[\{Mn(bpy)L\}_2(\mu\text{-}O)(\mu\text{-}n\text{-}RC_6H_4COO)_2]X$ were synthesized (X = NO_3 or ClO_4; n-R = 2-MeO, 3-MeO, 4-MeO, or 4-^{t}Bu; and L = monodentate ligand). According to XRD, the X anions tend to be coordinated to the Mn ions and may occupy the place of the monodentate ligands L. Two structural isomers that only differ in their monodentate ligands have been obtained with the 3-$MeOC_6H_4COO^-$ ligand. For all compounds, the Mn^{III} ions show elongated octahedra with a pronounced rhombic distortion, the distortion axis being in the direction of the monodentate ligand. To quantify these distortions separately, elongation and rhombicity parameters ($\perp$ and ρ, respectively) were defined.

The magnetic measurements revealed that compounds with *n*-R = 3-MeO display a ferromagnetic behavior with ground state $S = 4$, whereas compounds with *n*-R = 2-MeO, 4-MeO, and 4-^{t}Bu show an antiferromagnetic behavior with ground state $S = 0$. The Jahn-Teller axes of the Mn ions in these compounds are close to orthogonality and this fact has an important effect on the magnetic behavior in the low temperature range for compounds with ferromagnetic or weak antiferromagnetic behavior. Fitting all the magnetic data simultaneously, χ_M and M, makes possible to determine the sign and magnitude of the ZFS parameters. For all compounds, D_{Mn} values are moderate and negative (between –3.0 and –5.3 cm^{-1}) and the $E_{Mn}/|D_{Mn}|$ ratio is correlated with the rhombicity parameter (ρ).

Structural and magnetic data of twenty-six analogous compounds have been analyzed and some new conclusions may be drawn:

a) The elongation ($\perp$) and rhombicity (ρ) parameters are inversely proportional.

b) The most elongated octahedra correspond to compounds with L = ClO_4 or EtOH. Consequently, compounds with L = EtOH/ClO_4 show the most antiferromagnetic behavior.

c) The torsion angle between the phenyl and the COO groups of the benzoate derivative ligand (ω) is only important for compounds with the R group in *ortho* position.

d) The structural parameters leading to a ferromagnetic behavior are: rhombic distortion of the octahedra, coplanarity between the phenyl ring and COO group, and large angle between the Jahn-Teller axes.

e) All compounds with the R group in *meta* position (n = 3) exhibit ferromagnetic interaction; this position promote a major electron-withdrawing character to the R group.

1.4. Mono- and Polynuclear Mn^{II} Compounds

First insights

Mn^{II} complexes are of interest because they are widely present in numerous enzymes, as an essential ingredient of their active site.[10] Mn^{II} ion can be implicated in both redox or non-redox processes, or acting as a catalysis or having a structural role.[199–202] Owing to its single-ion high spin (S = 5/2) and comparable size, Mn^{II} is commonly used as a probe to replace diamagnetic ions, such as Mg^{2+},[203,204] in other biological systems. Additionally, some Mn^{II} compounds can be used as catalysts in several industrial processes, commonly for the epoxidation of olefins,[1–5] making them good candidates to replace 2nd and 3rd row transition metal ions in oxidation catalysis.

From the analysis of EPR spectra for Mn^{II} compounds, important information can be extracted, since the splitting of the magnetic sublevels will depend on the zero-field splitting (ZFS) parameters, D and E. Indeed, even slight distortions from a regular octahedral environment can result in significant ZFS in Mn^{II} and highly complicated EPR spectra.[28] Furthermore, it is well known that, for several transition metal ions, the ZFS can probe their structural and electrostatic environment.[21] For example, the ZFS for Mn^{II} ions is much greater when it is bonded to halide ligands.[24–31,36] It also depends on the coordination number, since pentacoordinated ions display greater axial ZFS parameters ($|D|$ = 0.25–0.30 cm^{-1}) than hexacoordinated ones ($|D|$ = 0.0008–0.1750 cm^{-1}).[32,33] Moreover, the ZFS parameters could also be affected by the ratio between the N- and O-based ligands. However, the amount of experimental data available concerning mixed N/O environments is very limited to propose a good correlation.[34]

The reaction between Mn^{II} carboxylate and bidentate ligands (NN), such as 2,2'-bipyridine (bpy) and 1,10-phenanthroline (phen), leads to the formation of Mn^{II} compounds with different nuclearity: mononuclear, dinuclear, trinuclear or 1D systems.[15,16] The carboxylate groups display a wide variety of coordination modes, such as monodentate terminal, chelating, bidentate bridging and monodentate bridging modes. Particularly in these compounds, the carboxylate ligands could bridge the Mn^{II} ions in $\mu_{1,1}$ or $\mu_{1,3}$ coordination modes, and in the latter case in either a *syn-syn* or *syn-anti* conformation.

The magnetic interaction between neighboring Mn^{II} ions depends on the coordination mode of the carboxylate ligand. For instance, dinuclear compounds with $\mu_{1,1}$-carboxylate bridges

present a ferromagnetic interaction, while those with $\mu_{1,3}$-carboxylate bridges show an antiferromagnetic interaction.[16]

We herein present dinuclear $[\{Mn(NN)_2\}_2(\mu\text{-}n\text{-}RC_6H_4COO)_2](ClO_4)_2$, trinuclear $[Mn_3(NN)_2(\mu\text{-}n\text{-}RC_6H_4COO)_6]$, and mononuclear $[Mn(NN)_{3-m}(n\text{-}RC_6H_4COO)_m(H_2O)_m](ClO_4)_{2-m}$ (with m = 1 or 2) compounds with n-$MeOC_6H_4COO^-$ (n = 2, 3, 4) or 4-^{t}Bu$C_6H_4COO^-$ ligands, and NN = bpy or phen. These systems show some diversity on the spin ground state. For the dinuclear systems the ground state could be either S = 0 or S = 5 and for the trinuclear systems the ground state is S = 5/2. EPR spectroscopy is a useful tool to differentiate the ground state and nuclearity of these compounds. Ferromagnetic dinuclear compounds shows a unique band at g ≈ 2, while the antiferromagnetic ones show far more complex spectra, which depends on the intensity of the magnetic interaction. Moreover, the trinuclear and mononuclear compounds show very different spectra in spite of having the same ground spin state (S = 5/2). From the fit of the EPR spectra, the zero filed splitting parameters (D and E) will be determined.

Synthesis

The synthesis of analogous Mn^{II} compounds, similar to these reported here, had been reported in previous works by Corbella and coworkers.[15,16,205,206] Firstly, Mn^{II} carboxylates are prepared by heating a mixture of $MnCO_3$ or $Mn(CH_3COO)_2$ and the corresponding benzoic acid derivative in water. The reaction between these pre-synthesized Mn^{II} carboxylates and bidentate nitrogen-based ligands (NN) leads to the formation of different types of compounds, depending on the carboxylate/NN ratio, the presence or absence of ClO_4^-, the solvent used, or the stability of the compounds. In this work, the reactions were carried out between $Mn(n\text{-}RC_6H_4COO)_2$, where n-R = 2-MeO, 3-MeO, 4-MeO or 4-^{t}Bu, and two different NN ligands, 2,2'-bipyridine (bpy) or 1,10-phenantroline (phen). All reactions were performed in MeOH, EtOH, or CH_3CN, though the presence of water in the reaction media was required in nearly all cases, since it assists the dissolution of the Mn^{II} carboxylates. Table 5 and Figure 34 list the compounds reported here.

Table 5. List of Mn^{II} compounds obtained with different *n*-$RC_6H_4COO^-$ and NN ligands.

Label	Core	*n*-R	NN	Formula
8*	$[Mn^{II}_2]^{4+}$	2-MeO	bpy	$[\{Mn(bpy)_2\}_2(\mu\text{-}2\text{-}MeOC_6H_4COO)_2](ClO_4)_2$
9*	$[Mn^{II}_2]^{4+}$	3-MeO	bpy	$[\{Mn(bpy)_2\}_2(\mu\text{-}3\text{-}MeOC_6H_4COO)_2](ClO_4)_2$
10*	$[Mn^{II}_2]^{4+}$	4-MeO	bpy	$[\{Mn(bpy)_2\}_2(\mu\text{-}4\text{-}MeOC_6H_4COO)_2](ClO_4)_2$
11	$[Mn^{II}_2]^{4+}$	2-MeO	phen	$[\{Mn(phen)_2\}_2(\mu\text{-}2\text{-}MeOC_6H_4COO)_2](ClO_4)_2$
12*	$[Mn^{II}_2]^{4+}$	3-MeO	phen	$[\{Mn(phen)_2\}_2(\mu\text{-}3\text{-}MeOC_6H_4COO)_2](ClO_4)_2$
13*	$[Mn^{II}]^{2+}$	3-MeO	phen	$[Mn(H_2O)(3\text{-}MeOC_6H_4COO)(phen)_2](ClO_4)$
14*	$[Mn^{II}_2]^{4+}$	4-MeO	phen	$[\{Mn(phen)_2\}_2(\mu\text{-}4\text{-}MeOC_6H_4COO)_2](ClO_4)_2$
15*	$[Mn^{II}_2]^{4+}$	4-^{t}Bu	phen	$[\{Mn(phen)_2\}_2(\mu\text{-}4\text{-}^tBuC_6H_4COO)_2](ClO_4)_2$
16	$[Mn^{II}_3]^{6+}$	3-MeO	bpy	$[Mn_3(bpy)_2(\mu\text{-}3\text{-}MeOC_6H_4COO)_6]$
17*	$[Mn^{II}_3]^{6+}$	4-MeO	bpy	$[Mn_3(bpy)_2(\mu\text{-}4\text{-}MeOC_6H_4COO)_6]$
18	$[Mn^{II}]^{2+}$	4-^{t}Bu	bpy	$[Mn(bpy)(4\text{-}^tBuC_6H_4COO)_2]$
19*	$[Mn^{II}]^{2+}$	2-MeO	phen	$[Mn(H_2O)_2(2\text{-}MeOC_6H_4COO)_2(phen)]$
20	$[Mn^{II}_3]^{6+}$	3-MeO	phen	$[Mn_3(\mu\text{-}3\text{-}MeOC_6H_4COO)_6(phen)_2]$
21	$[Mn^{II}_3]^{6+}$	4-MeO	phen	$[Mn_3(\mu\text{-}4\text{-}MeOC_6H_4COO)_6(phen)_2]$

* The crystal structure of which was determined. Abbreviations: bpy = 2,2'-bipyridine, phen = 1,10-phenantroline.

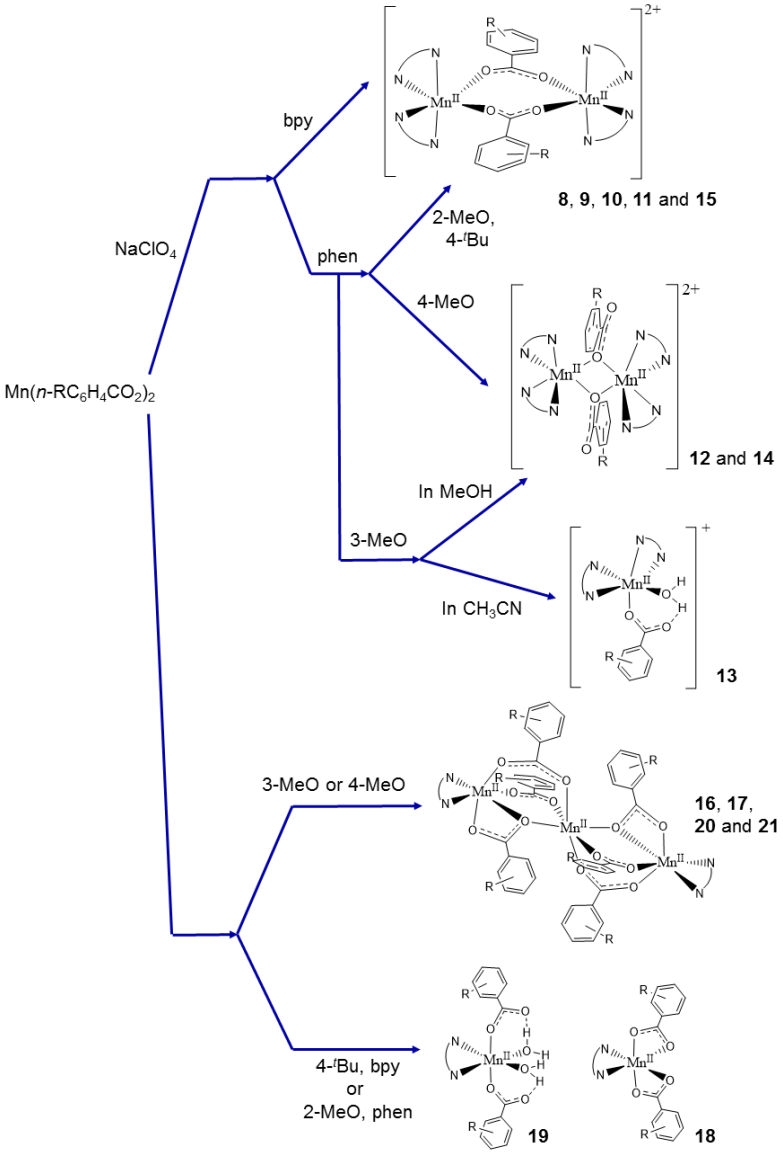

Figure 34. Diagram showing compounds that were obtained depending on the reagents, stoichiometry, and solvent.

When $NaClO_4$ was added besides the latter reagents in 1:2:1 ratio, ionic dinuclear compounds with formula $[\{Mn(NN)_2\}_2(\mu\text{-}n\text{-}RC_6H_4COO)_2](ClO_4)_2$ (**8**, **9**, and **10**, with NN = bpy; **11**, **12**, **14**, and **15**, with NN = phen) were obtained in almost all cases. These compounds were normally synthesized in CH_3CN or EtOH. However, for *n*-R = 3-MeO and NN = phen, a mononuclear compound with formula $[Mn(H_2O)(3\text{-}MeOC_6H_4COO)(phen)_2](ClO_4)$ (**13**) was obtained in both solvents. The formation of the dinuclear compound **12** was only attained in MeOH. It was not possible to isolate any dinuclear compound for *n*-R = 4-^{t}Bu and NN = bpy.

Regarding the dinuclear compounds, two different coordination modes of the carboxylate ligand can be found, even though the synthetic method is the same. Fortunately, the coordination modes of this ligand can be easily differentiated with the 1620–1300 cm^{-1} window of the IR spectra of these compounds. The carboxylate ligands display two bands assigned to the asymmetric and symmetric vibrations. Values of $\Delta\nu = \nu_a(COO) - \nu_s(COO) <$ 200 cm^{-1} indicate that the carboxylate ligands show a $\mu_{1,3}$-coordination mode, whereas values of $\Delta\nu >$ 200 cm^{-1} are indicative of a $\mu_{1,1}$-coordination mode.[14,16] All dinuclear compounds containing bpy (**8**, **9** and **10**) show bands assigned to this ligand centered at ~1600, 1498, 1480 and 1450 cm^{-1}. Nearby, the two bands corresponding to the carboxylate ligands arise at ~1550 and ~1390 cm^{-1}, with a $\Delta\nu <$ 200 cm^{-1}, consistent for a $\mu_{1,3}$-coordination mode. In contrast, two different peculiarities in the IR spectra of compounds containing phen (**11**, **12**, **14** and **15**) were found. Apart from the bands assigned to the phen ligand (at ~1600, 1520 and 1427 cm^{-1}), compounds **11** and **15** display two bands at ~1550 and ~1390 cm^{-1} ($\Delta\nu \approx$ 160 cm^{-1}) assigned to the carboxylate ligands, indicating that the coordination mode is likely the same as compounds with bpy. However, **12** and **14** show two bands at 1570 and 1310 cm^{-1}, with $\Delta\nu \approx$ 260 cm^{-1}, consistent for a $\mu_{1,1}$-coordination mode.

The reason why one type of bridge is preferentially formed is very difficult to rationalize. As explained by Gómez *et al.*, two factors could contribute to this different behavior: the steric and the electronic effects. In the referenced work, only compounds containing phen and the R group in *meta* or *para* position show a $\mu_{1,1}$-coordination mode.[16] Compounds with R = MeO follow the same tendency: while compounds **12** and **14**, with respective *n*-R = 3-MeO and 4-MeO, have a $\mu_{1,1}$-brigde; compound **11**, with *n*-R = 2-MeO, exhibits a $\mu_{1,3}$-coordination mode. However, compounds **15** (with *n*-R = 4-^{t}Bu), whose carboxylate show a $\mu_{1,3}$-coordination mode, does not follow the expected trend. The cause of this variation may lay on the presence of the highly voluminous ^{t}Bu group that, in spite of being in *para* position, can be the source of a steric inherence. Indeed, the formation of the $\mu_{1,1}$-brigde shortens the Mn···Mn distance

from ~4.65 (for a $\mu_{1,3}$-brigde) to ~3.46 Å, also setting the facing phen ligands closer (see below).

When no perchlorate salt is added, neutral compounds of different nuclearities are obtained.[15,205] In this case, five trinuclear (**16**, **17**, **20**, and **21**) and two mononuclear compounds (**18** and **19**) were acquired. The synthesis of the trinuclear compounds was perform with a Mn^{II} carboxylate and bpy or phen in a 3:2 ratio, leading to compounds with formula $[Mn_3(\mu\text{-}n\text{-}RC_6H_4COO)_6(NN)_2]$. The two mononuclear compounds, with formula $[Mn(H_2O)_x(NN)(n\text{-}RC_6H_4COO)_2]$ (x = 1 or 2), were obtained from the reaction between Mn^{II} carboxylate and bpy or phen in a 1:1 ratio. Using CH_3CN or EtOH did not make any difference for the type of product that was formed, but it did for the way of crystallization (time, crystallinity, etc.) and/or the purity of the sample. For instance, nice yellow crystals of **19** were obtained in EtOH, while sample contaminated by some brown solid precipitated in CH_3CN. No compound was obtained for *n*-R = 2-MeO and NN = bpy. For *n*-R = 4-^{t}Bu and NN = phen, we did not succeed to stablish a reproducible synthetic procedure.

As commented before, the presence of water in the reaction media was required in nearly all cases, since it assists the dissolution of the Mn^{II} carboxylates. Nevertheless, H_2O also guaranteed the formation of the dinuclear compounds **10** and **15** because it prevented the fast precipitation of the corresponding neutral compounds, observed after several minutes of stirring when additional H_2O was not added.

Description of structures

In this part we present the crystal structures of the Mn^{II} compounds of which we obtained X-ray suitable single-crystals. We also isolated good single-crystals of the Mn^{II} carboxylate precursor with *n*-R = 3-MeO, so its crystal structure is described below.

$[Mn_3(3\text{-}MeOC_6H_4COO)_6(EtOH)_2]_n$. Figure S11 shows the crystal structure of manganese(II) 3-methoxybenzoate. Selected interatomic distances and angles are listed in Table S15. This compound displays a 1D chain structure with two asymmetric Mn ions with different geometries, labeled as Mn1 (distorted trigonal bipyramidal geometry) and Mn2 (octahedral geometry). The repeated entity comprises the Mn2-Mn1-Mn1 unit, with Mn2···Mn1 and Mn1···Mn1 distances of 3.38 and 3.59 Å, respectively. The Mn2 and Mn1 ions are linked through two $\mu_{1,3}$-carboxylate ligands in a *syn-syn* mode and one $\mu_{1,1}$-carboxylate ligand. The adjacent Mn1 ions are linked though two $\mu_{1,3}$-carboxylate ligands in a *syn-anti* mode. The penta-coordination of the Mn1 ions is completed by an EtOH molecule.

Dinuclear compounds with $\mu_{1,3}$-*n*-$RC_6H_4COO^-$ bridges (8, 9, 10, and 15). The cationic complexes of these dinuclear compounds are represented in Figure 35. Selected interatomic distances and angles are listed in Table 6.

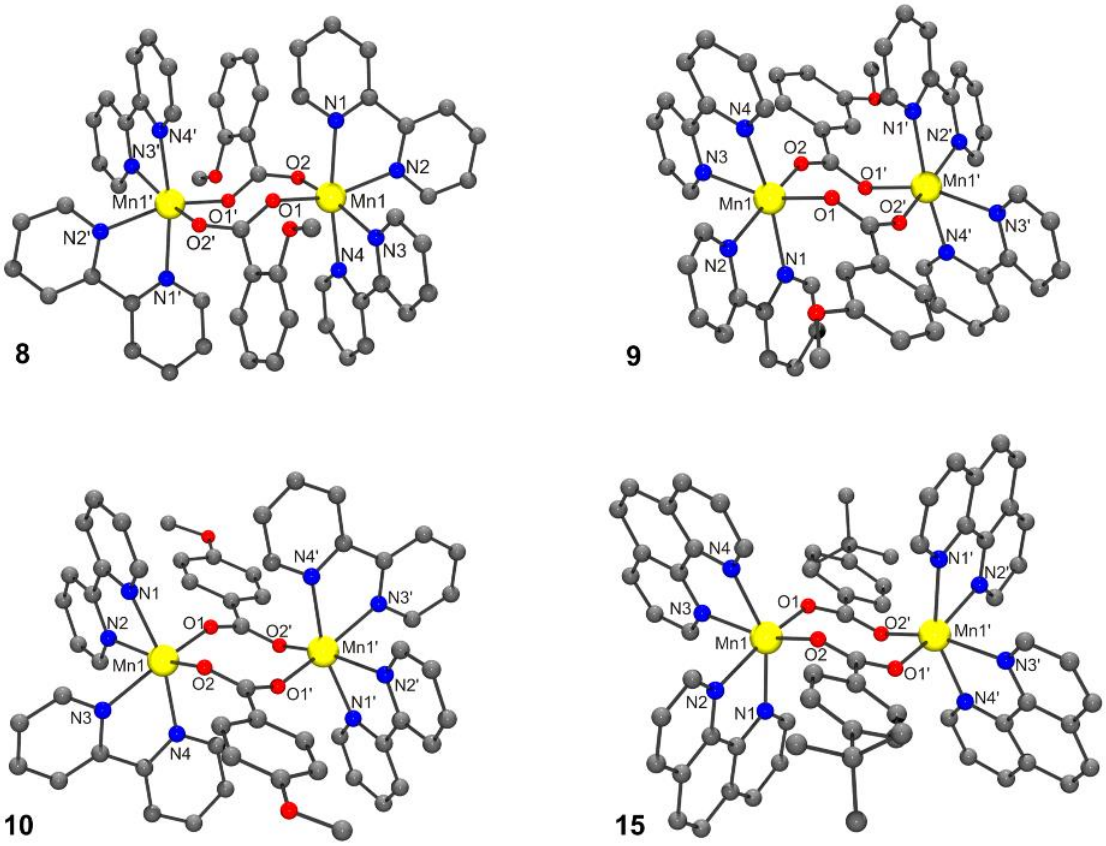

Figure 35. Crystal structures of the cationic complexes of compounds **8**, **9**, **10**, and **15**. Hydrogen atoms are omitted for clarity.

All compounds show an analogous structure, consisting of a cationic complex with formula $[\{Mn(NN)_2\}_2(\mu\text{-}n\text{-}RC_6H_4COO)_2]^{2+}$ and two perchlorate anions. The two Mn^{II} ions are bridged by two $\mu_{1,3}$-*n*-$RC_6H_4COO^-$ ligands in *syn-anti* mode, with Mn···Mn distances ranging from 4.54 to 4.75 Å. The hexacoordination of each Mn ions is completed by two bpy (**8**, **9** and **10**) or phen (**15**) ligands. The Mn–O and Mn–N distances are in the range 2.09–2.14 Å and 2.26–2.36 Å, respectively, leading to distorted octahedral environment around the Mn^{II} ions. All distances are in agreement with those reported for analogous compounds.[16,205–211] Compound **9** shows π-stacking between bpy ligands of neighboring molecules that is extended along a longitudinal axis (Figure S12).

Table 6. Selected interatomic distances (Å) and angles (º) with standard deviations in parentheses for compounds **8**, **9**, **10**, and **15**.

	8 (2-MeO, bpy)		**9 (3-MeO, bpy)**
Mn1···Mn1'	4.751(2)	Mn1···Mn1'	4.6398(2)
Mn1–O1	2.1071(15)	Mn1–O1	2.1342(5)
Mn1–O2	2.1243(16)	Mn1–O2	2.1093(6)
Mn1–N1	2.2780(16)	Mn1–N1	2.2507(6)
Mn1–N2	2.2771(16)	Mn1–N2	2.2855(6)
Mn1–N3	2.2732(17)	Mn1–N3	2.3068(6)
Mn1–N4	2.2748(16)	Mn1–N4	2.2375(6)
O2–Mn1–N3	162.55(5)	O1–Mn1–N3	159.77(2)
O1–Mn1–N2	157.13(5)	O2–Mn1–N2	169.74(3)
N4–Mn1–N1	168.75(5)	N4–Mn1–N1	165.99(2)
	10 (4-MeO, bpy)		**15 (4-^{t}Bu, phen)**
Mn1···Mn1'	4.542(2)	Mn1···Mn1'	4.604(2)
Mn1–O1	2.129(3)	Mn1–O1	2.091(3)
Mn1–O2	2.125(3)	Mn1–O2a	2.140(4)
Mn1–N1	2.258(3)	Mn1–N1	2.292(4)
Mn1–N2	2.296(3)	Mn1–N2	2.294(3)
Mn1–N3	2.299(3)	Mn1–N3	2.359(4)
Mn1–N4	2.261(3)	Mn1–N4	2.286(3)
O1–Mn1–N3	161.47(10)	O1–Mn1–N2	164.63(14)
O2–Mn1–N2	162.57(10)	O2'–Mn1–N3	159.87(13)
N1–Mn1–N4	165.74(10)	N1–Mn1–N4	155.09(13)

Symmetry codes: for **8**, ('): 1-x,-y,-z; for **9**, (') 1-x,2-y,-z; for **10**, (') 1-x,-y,1-z, for **15**; (') 1-x;1-y,2-z.

Dinuclear compounds with $\mu_{1,1}$-*n*-RC$_6$H$_4$COO$^-$ bridges (12 and 14). The cationic complexes of compounds **12** and **14** are represented in Figure 36. Selected interatomic distances and angles are listed in Table 7.

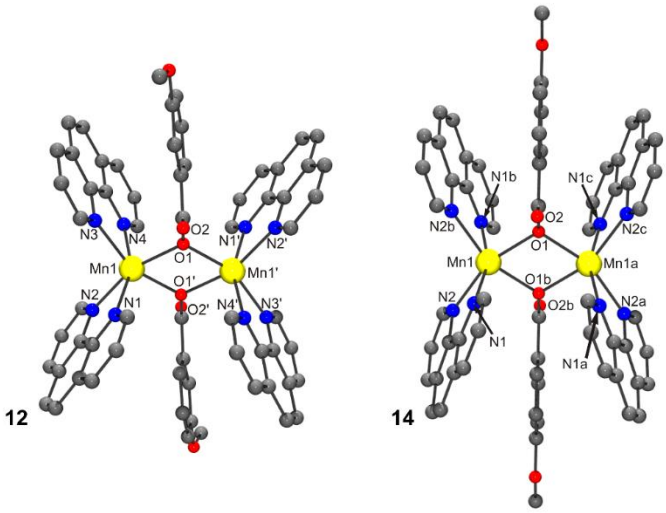

Figure 36. Crystal structures of the cationic complexes of compounds **12** and **14**. Hydrogen atoms are omitted for clarity.

Table 7. Selected interatomic distances (Å) and angles (º) with standard deviations in parentheses for compounds **12** and **14**.

	12 (3-MeO, phen)		**14 (4-MeO, phen)**
Mn1···Mn1'	3.4596(7)	Mn1···Mn1a	3.444
Mn1–O1	2.1617(12)	Mn1–O1	2.182(2)
Mn1–O1'	2.1931(13)	Mn1–O1b	2.182(2)
Mn1–N1	2.2605(15)	Mn1–N1	2.261(3)
Mn1–N2	2.2545(14)	Mn1–N2	2.267(3)
Mn1–N3	2.2592(15)	Mn1–N1b	2.261(3)
Mn1–N4	2.2579(15)	Mn1–N2b	2.267(3)
O1–Mn1–N2	157.74(5)	N1b–Mn1–N1	161.09(15)
O1'–Mn1–N3	161.61(5)	O1–Mn1–N2	159.23(11)
N4–Mn1–N1	158.61(5)	O1b–Mn1–N2b	159.23(11)
Mn1–O1–Mn1'	105.21(5)	Mn1–O1b–Mn1a	104.2

Symmetry codes: for **12**, ('): -x+1,-y,-z+1; for **14**, (a) x,-y,z, (b) -x,y,-z

Both compounds display a very similar structure. The two Mn^{II} ions are linked through two $\mu_{1,1}$-*n*-$RC_6H_4COO^-$ bridges, with Mn···Mn distances of ~3.45 Å. Two phen ligands are linked to each Mn^{II} ion, leading to distorted octahedral geometry. The Mn–O distances are in the range 2.16–2.18 Å while the Mn–N are 2.26 Å. The Mn_2O_2 ring is planar, with Mn–O–Mn close to 105º. The phenyl ring and the carboxylate groups are almost coplanar, indicating that the benzoate groups are perpendicular to the Mn_2O_2 ring. As may be seen comparing the structures of compounds containing $\mu_{1,3}$- and $\mu_{1,1}$-brigdes (Figure 35 and Figure 36, respectively), the NN ligands are closer in the latter, as a consequence of the shorter Mn···Mn distance. This forces the phenyl ring, which is in the middle of the NN ligands, to remain perpendicular to the Mn_2O_2 ring. The 3-MeO and the 4-MeO groups in compounds **12** and **14** remain in the same plane as the phenyl ring, so their presence in the $\mu_{1,1}$-brigdes does not disturb. On the other hand, the *t*Bu group has two methyl groups that stand out from plane of the phenyl group, being able to cause steric hindrance. Hence, the formation of a dinuclear compound comprising $\mu_{1,1}$-4-*t*$BuC_6H_4COO^-$ bridges could be tentatively considered improvable. The structural parameters for compounds **12** and **14** are in agreement with those reported for analogous compounds with $[Mn_2(\mu_{1,1}\text{-R'CCO})_2]^{2+}$ core.[16,212–214]

Compound **12** shows π-stacking between phen ligands of neighboring molecules that is extended along the *b*-axes, leading to a chain (Figure S13). Compound **14** also shows π-stacking between phen ligands of neighboring molecules, but this time extended along the *a*- and *b*-axes, leading to a layer (Figure S14).

Trinuclear $[Mn_3(bpy)_2(\mu\text{-}4\text{-}MeOC_6H_4COO)_6]$ compound (17). The structure of compound **17** is shown in Figure 37. Selected interatomic distances and angles are listed in Table 8.

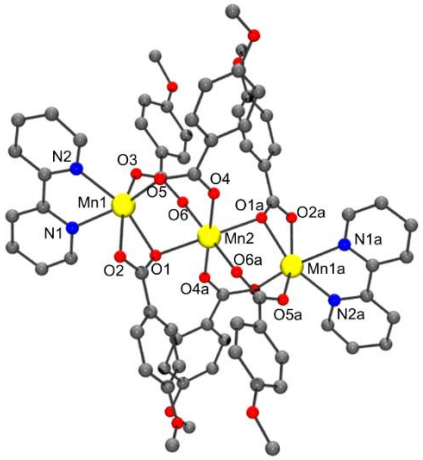

Figure 37. Crystal structure of compound **17**. Hydrogen atoms are omitted for clarity.

Table 8. Selected interatomic distances (Å) and angles (º) with standard deviations in parentheses for compound **17**.

Mn1···Mn2	3.595	O1–Mn1–N2	160.67(12)
Mn1···Mn1a	7.190(5)	O3–Mn1–N1	162.49(12)
Mn1–O1	2.252(3)	O5–Mn1–O2	160.29(12)
Mn1–O2	2.326(4)	O6a–Mn2–O6	180.00(14)
Mn1–O3	2.101(3)	O4–Mn2–O4a	180.00(11)
Mn1–O5	2.095(4)	O1–Mn2–O1a	180.000(1)
Mn1–N1	2.294(4)		
Mn1–N2	2.257(4)	Mn2–O1–Mn1	105.93(13)
Mn2–O1	2.252(3)		
Mn2–O4	2.199(3)		
Mn2–O6	2.145(3)		

Symmetry codes: (a) -x+1,-y+1,-z

The structure of this compound consists of three Mn^{II} ions in a linear array, where the central Mn ion is locate on a crystallographic inversion center. This central ion (Mn2) is coordinated by six oxygen atoms of six 4-methoxybenzoate ligands and is linked to each terminal Mn ions (Mn1) through three 4-methoxybenzoate ligands, with Mn···Mn distances of ~3.60 Å. While two of these ligands link the Mn ions with both oxygen atoms ($\mu_{1,3}$) in a *syn-syn* mode, the third one links them through just one oxygen atom ($\mu_{1,1}$). The Mn–O distances ranges from 2.15 to 2.25 Å. The other oxygen atom (O2) of this latter ligand is weakly bonded to the terminal Mn ion, with Mn–O distances of 2.33 Å. The hexacoordination of the terminal

ions is completed by a phen ligand, with Mn – N distances of ~2.27 Å. These structural parameters are in agreement with those reported for analogous compounds.[15,205,215–220]

The central Mn ion shows a quite regular environment, since the Mn–O distances are quite similar and the angles of the facing bonds are 180º. However, the terminal ions show a substantial elongation in the direction of the $\mu_{1,1}$ bridge.

Mononuclear $[Mn(H_2O)_m(NN)_{3-m}(n\text{-}RC_6H_4COO)_m](ClO_4)_{2-m}$ (m= 1 or 2) compounds (13 and 19). Figure 38 shows the crystal structure of the two mononuclear compounds **13** and **19**. Selected structural parameters are listed in Table 9. As may be observed, the Mn^{II} ion in the two compounds show a distorted octahedral geometry.

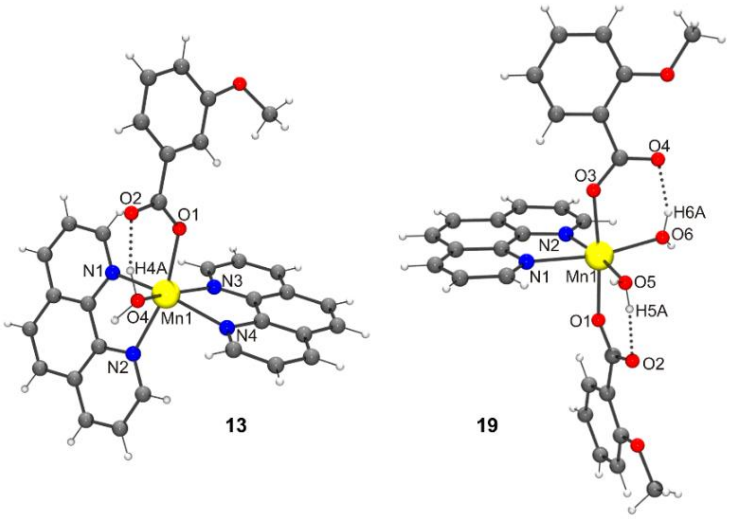

Figure 38. Crystal structures for the cationic complex of **13** and for one of the subunits of compound **19**.

Table 9. Selected interatomic distances (Å) and angles (º) with standard deviations in parentheses for the mononuclear compound **13** and for one of the subunits of compound **19**.

	13 (3-MeO, phen)		**19 (2-MeO, phen)**
Mn1–O1	2.134(2)	Mn1–O1	2.154(3)
Mn1–O4	2.173(2)	Mn1–O3	2.156(3)
Mn1–N1	2.257(3)	Mn1–O5	2.164(2)
Mn1–N2	2.269(3)	Mn1–O6	2.179(2)
Mn1–N3	2.271(3)	Mn1–N2	2.266(3)
Mn1–N4	2.263(3)	Mn1–N1	2.285(3)
N1–Mn1–N4	161.71(10)	Mn1–O1	2.154(3)
O1–Mn1–N2	163.31(9)	Mn1–O3	2.156(3)
O4–Mn1–N3	160.00(9)	Mn1–O5	2.164(2)

The structure of compound **13** consists of a cationic complex with formula $[Mn(H_2O)(3\text{-}MeOC_6H_4COO)(phen)_2]^+$ and a perchlorate anion. The carboxylate ligand is coordinated in monodentate mode. The Mn–O distances are ~2.15 Å. There are hydrogen bonds between the H_2O molecule and the hanging oxygen atom of the carboxylate ligand (O2). The hexacoordination of the Mn^{II} ion is completed by two terminal phen ligands, with Mn–N distances of ~2.26 Å.

The structure of compound **19** comprises four neutral complexes with formula $[Mn(H_2O)_2(2\text{-}MeOC_6H_4COO)_2(phen)]$ with very similar structural parameters (Figure S15 and Table S16). Figure 38 and Table 9 only concern the structure of one of these complexes. In this compound, the two carboxylate ligands are coordinated in monodentate mode. Each hanging oxygen atoms of these lingads is interacting with one of the H_2O molecules through hydrogen bonds. The hexacoordination of the Mn^{II} ion is completed by one terminal phen ligands, with Mn–N distances of ~2.28 Å. Each H_2O molecule also forms H bonds with the nearest neighbor complex, and this is extended along the *a*-axis, forming chains (Figure S16).

Mononuclear compound 18. Crystals of compound **18** were poorly diffracting and its crystal structure could not be refined. However, some atoms could be assigned to several Q peaks. As seems, the structure this compound consists of a neutral complex with formula $[Mn(bpy)(4\text{-}^tBuC_6H_4COO)_2]$, where the carboxylate ligands are coordinated in bidentate mode.

Magnetic properties

Magnetic susceptibility data were recorded for all polynuclear compounds (**8–12, 14–17 and 19–22**) from room temperature to 2 K. Magnetization measurements were performed at 2 K from 0 to 5.0 T.

Dinuclear $[\{Mn(NN)_2\}_2(\mu\text{-}n\text{-}RC_6H_4COO)_2](ClO_4)_2$ compounds (8–12, 14 and 15). $\chi_M T$ versus T plots for the dinuclear compounds are represented in Figure 39 (a, b and d). At 300 K, $\chi_M T$ values are between 8.5 and 9.3 $cm^3\ mol^{-1}\ K$, close the expected value for two uncoupled Mn^{II} ions (8.75 $cm^3\ mol^{-1}\ K$). At lower temperatures, two different behaviors are found. For compounds with a $\mu_{1,3}$-bridges (**8**, **9**, **10**, **11** and **15**), $\chi_M T$ values remain constants until ~75 K. Below this temperature, $\chi_M T$ values decrease as the temperature fall, being indicative of an antiferromagnetic behavior. χ_M values increase as the temperature falls reaching maximum values in the range 0.27–0.49 $cm^3\ mol^{-1}$ between 5.5 and 9.9 K (Figure

39, insets of graph a and b). $M/N\mu_\beta$ values increase with the field (H) without reaching saturation (Figure 39 graph c), which is in accord with antiferromagnetic interaction.

On the other hand, for compounds with a $\mu_{1,1}$-bridges (**12** and **14**) $\chi_M T$ values increase as the temperature fall, reaching maximum values of ~14.6 cm^3 mol^{-1} K at ~2.5 K, close to the expected for a ground state with $S = 5$ (15 cm^3 mol^{-1} K). Below this temperature, a very slight decrease is observed as a consequence of the ZFS and/or intermolecular interactions. $M/N\mu_\beta$ values increase linearly at low fields and almost reaches saturation at high fields (~5 T), being also indicative of 10 unpaired electrons.

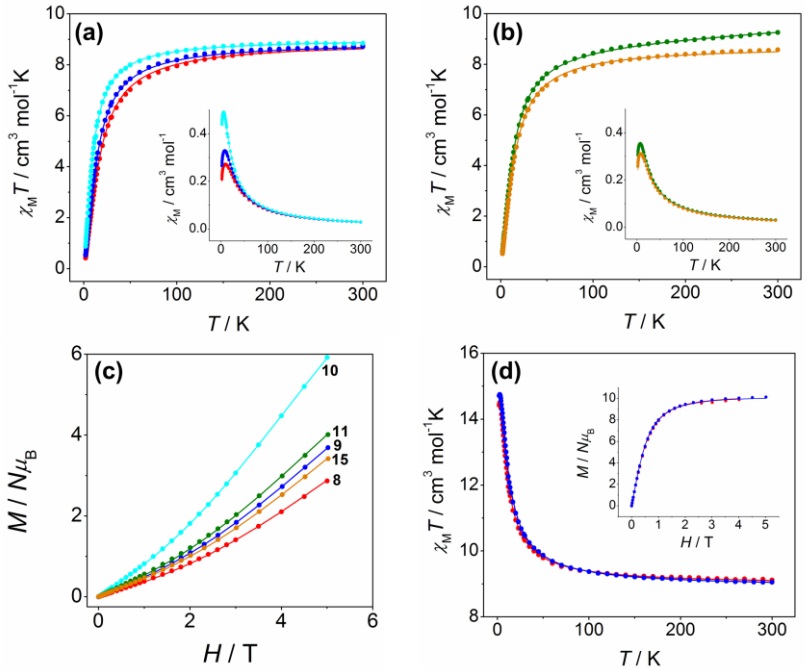

Figure 39. (***a***) $\chi_M T$ versus T and χ_M versus T (inset) plots for compounds **8** (red), **9** (blue), and **10** (cyan); (***b***) $\chi_M T$ versus T plots and χ_M versus T (inset) for compounds **11** (green) and **15** (orange); (***c***) $M/N\mu_\beta$ versus H plots for compounds **8**, **9**, **10**, **11**, and **15**; (***d***) $\chi_M T$ versus T and $M/N\mu_\beta$ versus H plots (inset) for compounds **12** (red) and **14** (blue). The solid lines correspond to the best fit of the experimental data.

$\chi_M T$ versus T and $M/N\mu_\beta$ plots were fitted simultaneously with the PHI program, which uses the Hamiltonian $H = -2JS_1S_2$.[165] The results of the fit are collected in Table 10. The two ferromagnetic compounds (**12** and **14**) were fitted taking into account intermolecular interactions (zJ'), which improved the fit and reproduce the slight decrease of the $\chi_M T$ values below 2.5 K.

Table 10. Magnetic parameters obtained from the fit of $\chi_M T$ versus T and $M/N\mu\beta$ versus H data for the dinuclear compounds with formula $[\{Mn(NN)_2\}_2(\mu\text{-}n\text{-}RC_6H_4COO)_2](ClO_4)_2$.

	g	$2J$ [a] / cm^{-1}	zJ' [b] / cm^{-1}	R_{SUS} (R_{MAG})
8	2.02	–2.4	-	$1.0\cdot10^{-4}$ ($7.0\cdot10^{-5}$)
9	2.02	–2.0	-	$2.5\cdot10^{-5}$ ($1.6\cdot10^{-5}$)
10	2.03	–1.4	-	$1.9\cdot10^{-5}$ ($5.8\cdot10^{-5}$)
11[c]	2.02	–1.8	-	$2.0\cdot10^{-5}$ ($1.0\cdot10^{-4}$)
12	2.02	+1.1	–0.002	$3.3\cdot10^{-6}$ ($4.2\cdot10^{-4}$)
14	2.01	+1.3	–0.001	$9.2\cdot10^{-5}$ ($9.5\cdot10^{-5}$)
15	2.00	–2.0	-	$3.8\cdot10^{-5}$ ($9.3\cdot10^{-5}$)

[a] Referred to $H = -2JS_1S_2$; [b] Intermolecular interactions; [c] Fitted considering a $TIP = 2\cdot10^{-3}$ cm^3 mol^{-1}; $R_{SUS} = \Sigma[(\chi_M T)_{exp} - (\chi_M T)_{calcd.}]^2 / \Sigma[(\chi_M T)_{exp}]^2$; $R_{MAG} = \Sigma[(M/N\mu\beta)_{exp} - (M/N\mu\beta)_{calcd.}]^2 / \Sigma[(M/N\mu\beta)_{exp}]^2$;

These results are in accord with the work reported by Gómez *et al.*, where analogous compounds containing $\mu_{1,3}$-*n*-$RC_6H_4COO^-$ bridges show antiferromagnetic interactions while the ones with $\mu_{1,1}$-*n*-$RC_6H_4COO^-$ bridges display ferromagnetic interactions.[16] The ferromagnetic behavior of the $\mu_{1,1}$-bridge is principally observed in Mn^{II} compounds having Mn–($\mu_{1,1}$-O)–Mn angles ~104º. However, several compounds with Mn–O–Mn angles ranging from 104º to 108º displaying antiferromagnetic behavior have been reported.[212–214]

Trinuclear $[Mn_3(NN)_2(\mu\text{-}n\text{-}RC_6H_4COO)_6]$ compounds (16, 17, 20, and 21). $\chi_M T$ versus T plots for the trinuclear compounds are represented in Figure 40. At 300 K, $\chi_M T$ values are ~13.5 cm^3 mol^{-1} K, close to the expected value for three uncoupled Mn^{II} ions (13.13 cm^3 mol^{-1} K). When the temperature decreases, $\chi_M T$ values fall until reaching ~4.5 cm^3 mol^{-1} K at 2 K, which are very close to the expected value for a ground state $S = 5/2$ (4.36 cm^3 mol^{-1} K). This behavior is indicative of an antiferromagnetic behavior. The ground state $S = 5/2$ is confirmed by the field dependence of the magnetization at 2 K (inset of Figure 40), which shows $M/N\mu\beta$ values consistent with 5 unpaired electrons.

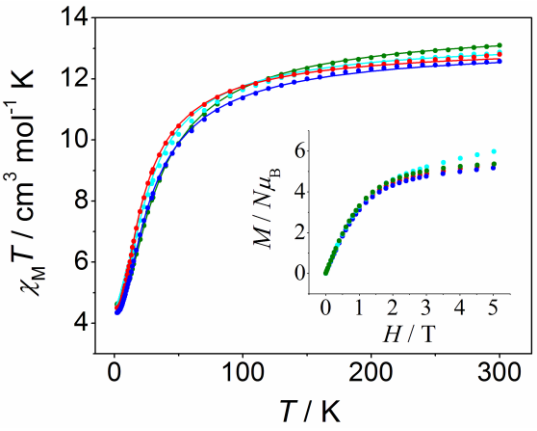

Figure 40. $\chi_M T$ versus T and $M/N\mu\beta$ versus H plots (inset) for compounds **16** (red), **17** (blue), **20** (cyan), and **21** (green). The solid lines correspond to the best fit of the experimental data.

$\chi_M T$ versus T plots were fitted with the PHI program[165] considering the Hamiltonian $H = -2J(S_1S_2 + S_2S_3) - 2J_{13}(S_1S_3)$ (see Figure 41), where it is assumed that $J_{13} = 0$ due to the large Mn···Mn distance between the terminal ions (~7.2 Å). The results of these fits are collected in Table 11. The fit of the $M/N\mu_\beta$ versus H data was also attempted, but those of compounds **20** and **21** showed a deviation at high field and could not be fitted considering an isotropic system. Trying to find an explanation, several simulations were performed with D_{Mn} values of the terminal ions between –0.1 and +0.1 cm^{-1} and the J values obtained from the fits. The D_{Mn} of the central ion was considered negligible, since it displays a very regular octahedron. However, no modification of the $M/N\mu_\beta$ versus H or $\chi_M T$ versus T plots was observed upon D_{Mn} variation.

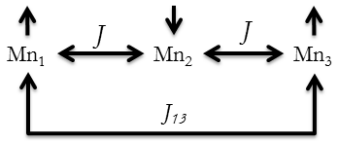

Figure 41. Possible magnetic interactions in the linear trinuclear compounds.

Table 11. List of magnetic parameters obtained from the best fit of $\chi_M T$ versus T plots.

Compound		g	$2J^a$ /cm^{-1}	R_{SUS}
16	3-MeO/bpy	2.04	–2.1	$5.9\cdot10^{-5}$
17	4-MeO/bpy	2.00	–2.5	$3.4\cdot10^{-5}$
20	3-MeO/phen	2.02	–2.2	$3.2\cdot10^{-4}$
21	4-MeO/phen	2.05	–2.9	$3.9\cdot10^{-5}$

[a] Referred to $H = -2J(S_1S_2 + S_2S_3) - 2J_{13}(S_1S_3)$, with $J_3 = 0$; $R_{SUS} = \Sigma[(\chi_M T)_{exp} - (\chi_M T)_{calcd.}]^2/\Sigma[(\chi_M T)_{exp}]^2$

As commented above, the Mn ions in this compound are linked though three carboxylate ligands: two in $\mu_{1,3}$ mode and *syn-syn* conformation and one in $\mu_{1,1}$ mode, as shown in Figure 42. In these compounds the most efficient way for the magnetic interaction between the Mn_t···Mn_c ions is through the carboxylate ligand coordinated in a $\mu_{1,1}$ mode; moreover, the dangling oxygen atom (O_d) of this carboxylate is coordinated to the Mn_t ion and this fact could provide a new way for the magnetic interaction. Unfortunately, the structural data of the compounds reported here is too scarce to provide new insights in the magneto-structural correlations, since only the crystal structure of compound **17** could have been determined. Selected structural parameters and J values for compound **17**, as well as those of some other analogous Mn^{II} compounds reported in the literature, are listed in Table 12. In most of the cases, while the Mn–O_b distances are in the 2.17–2.23 Å range, the Mn_t–O_d distances are between 2.25 and 2.82 Å.

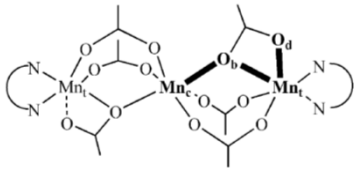

Figure 42. Schematic representation of the structure of trinuclear compounds with formula $[Mn_3(NN)_2(\mu_{1,3}\text{-R'COO})_4(\mu_{1,1}\text{-R'COO})_2]$.[15]

Table 12. Selected structural parameters and $2J$ values for compounds with general formula $[Mn_3(NN)_2(\mu_{1,3}\text{-R'COO})_4(\mu_{1,1}\text{-R'COO})_2]$.

Label	Formula	$2J$ [a] / cm^{-1}	d_{bridge} [b] / Å	d_{ter} [c] / Å	Δd [d] / Å	γ [e] / º
17	$[Mn_3(bpy)_2(4\text{-}MeOC_6H_4COO)_6]$	–2.5	2.252	2.326	0.074	105.9
A2[215]	$[Mn_3(dpa)_2(^iPrCOO)_6]$	–3.7	2.194	2.376	0.182	110.8
B2[216]	$[Mn_3(bpy)_2(CH_3COO)_6]$	–4.4	2.179	2.608	0.429	112.1
C2[205]	$[Mn_3(bpy)_2(ClCH_2COO)_6]$	–3.8	2.184	2.611	0.427	112.1
D2[217]	$[Mn_3(ClCH_2COO)_6(pybim)_2]$	–3.6	2.184	2.823	0.639	109.1
E2[218]	$[Mn_3(^iPrCOO)_6(phen)_2]$	–3.2	2.185	2.439	0.254	107.9
F2[219]	$[Mn_3\ (CH_3COO)_6(dapdoH_2)_2]$	–3.2	2.177	2.402	0.225	111.7
G2[218]	$[Mn_3(bpy)_2(^iPrCOO)_6]$	–3.7	2.175	2.471	0.296	106.67
H2[15]	$[Mn_3(bpy)_2(4\text{-}ClC_6H_4COO)_6]$	–2.8	2.223	2.344	0.121	105.8
I2[220]	$[Mn_3(C_6H_5COO)_6\{(ph)(2\text{-}py)CO\}_2]$	–2.7	2.251	2.249	–0.002	106.3
J2[15]	$[Mn_3(2\text{-}ClC_6H_4COO)_6(phen)_2]$	–2.9	2.265	2.279	0.014	106.6

[a] Referred to the Hamiltonian $H = -2J(S_1S_2 + S_2S_3) - 2J_{13}(S_1S_3)$, where $J_3 = 0$; [b] Average value between the Mn_t–O_b and Mn_c–O_b distances; [c] Mn_t-O_d distance; [d] $\Delta d = d_{ter} - d_{bridge}$; [e] Mn_t-O_b-Mn_c angle; Abbreviations: dpa = 2,2'-dipyrilamine; pybim = 2-(2-piridyl)benxidaxole; phen = 1,10-phenantroline; $dapdoH_2$ =2,6-diacetylpyridine dioxime; (2-py)CO = di-2-piridyl ketone.

For some compounds, the d_{bridge} and the d_{ter} distances are quite similar; so, the interaction between the Mn ions through this carboxylate could be considered as a combination of a $\mu_{1,1}$- and a $\mu_{1,3}$-carboxylate bridges, this latter in *syn-anti* conformation. In order to quantify the degree of these contribution, the Δd parameter, defined as the difference between the d_{bridge} and the d_{ter} distances, was used previously.[15] Values of $\Delta d \approx 0$ indicate that the carboxylate ligand has both contribution ($\mu_{1,1} + \mu_{1,3}$), whereas great values indicate that the carboxylate ligand shows a marked $\mu_{1,1}$-mode. The influence of the coordination mode of this carboxylate to the magnetic interaction could be seen in Figure 43, which shows $2J$ versus Δd plot for the compounds summarized in Table 12. A quite good linear correlation could be observed; only compound D2 is out of this tendency. As may be seen, the magnetic interaction becomes more antiferromagnetic as the $\mu_{1,3}$-character decreases.

Moreover, the Mn–O_b–Mn angles (γ) in these compounds vary between 106 and 112º. As reported for Cu^{II} compounds,[8] the magnetic interaction is very sensitive to M–O_b–M angles.

So, the relationship between this angle (γ) and the magnetic interaction was evaluated. The fit of these data shows a certain linear relation. As shown in Figure 43, the magnetic interaction becomes more antiferromagnetic as this angle opens. Hence, both factors may affect the resulting magnetic interaction.

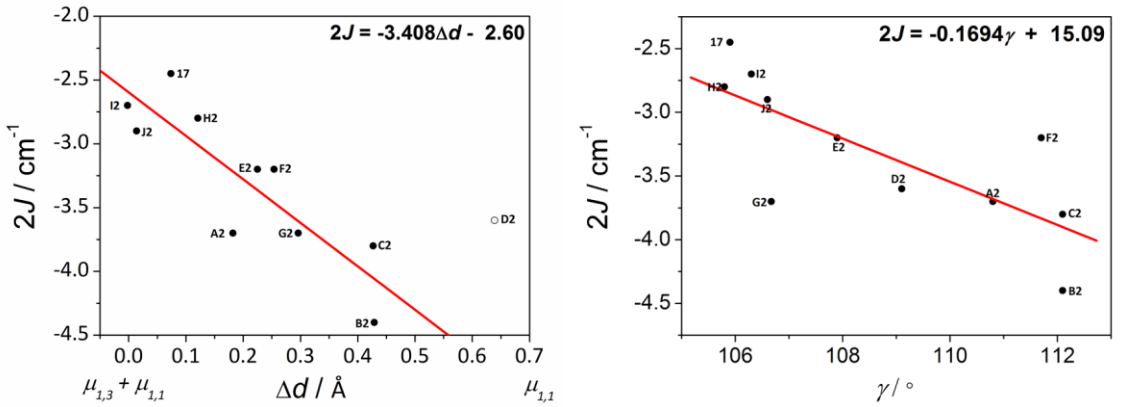

Figure 43. 2*J* versus Δ*d* (right) and 2*J* versus γ plots for trinuclear compounds with formula $[Mn_3(NN)_2(\mu_{1,3}\text{-R'COO})_4(\mu_{1,1}\text{-R'COO})_2]$. The red line is the linear correlation for these plots. Compound **D2** has not been considered for the fit of the 2*J* versus Δ*d* plot.

EPR spectroscopy

The X-band EPR spectra of all Mn^{II} compounds herein reported (**8**–**21**) were recorded on powdered samples at different temperatures. At room temperature, all of them show a band centered at $g \approx 2$; however, the spectra become more complicated as the temperature falls. To exemplify, Figure 44 shows the spectra at different temperatures for a dinuclear compound (**15**) and a trinuclear one (**17**). At 4 K, the spectra of each compound shows peculiar features that allows its identification.

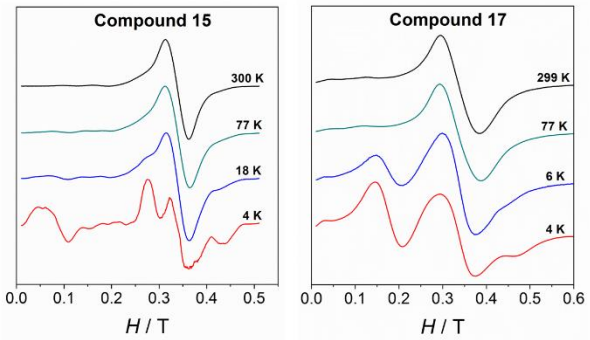

Figure 44. Variable-temperature X-band EPR spectra for the dinuclear compound **15** and the trinuclear compound **17**.

The fit of the EPR spectra was performed with the PHI program.[165] It is worth noting that, even though this program is able to fit EPR spectra, the initial values from which the fit will

begin are of importance for the final result. Hence, several simulations screening different D and E values were performed in order to choose the best initial values. All spectra were fitted considering a linewidth between 1.0 and 1.8 cm^{-1}.

Mononuclear compounds (13, 18, and 19). The EPR spectra at 4 K of the mononuclear compounds (**13**, **18**, and **19**) are shown in Figure 45. As may be observed, they show some differences.

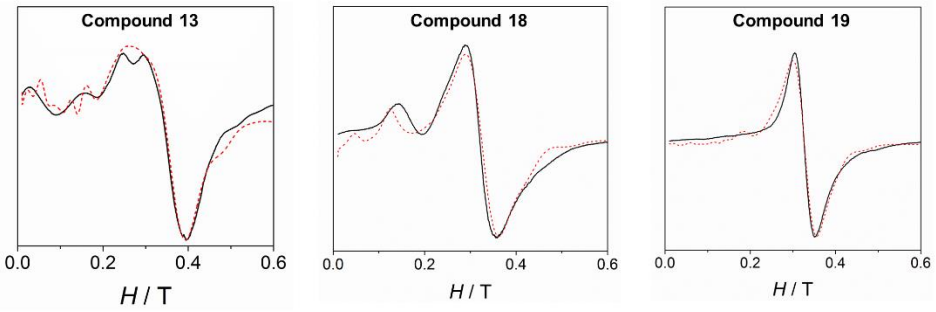

Figure 45. X-band EPR spectra for the mononuclear compound **13**, **18**, and **19** at 4 K. The dashed lines correspond to the best fit of the experimental data.

The three compounds display a broad and intense band at $g \approx 2$ and some more features more or less pronounced at $g \neq 2$, around the intense band. These three spectra were fitted with the PHI program[165] by considering a high-spin Mn^{II} ion with ZFS of single ion (D_{Mn} and E_{Mn}). The result from these fits are listed in Table 13.

Table 13. Results from the fit of the EPR spectra of the three mononuclear compounds.

Ref.	g	$\lvert D_{Mn}\rvert$ / cm^{-1}	$\lvert E_{Mn}\rvert$ / cm^{-1}	$\lvert E_{Mn}\rvert / \lvert D_{Mn}\rvert$
13	2.0	0.064	0.010	0.16
18	2.10	0.045	0.015	0.33
19	2.08	0.033	0.010	0.30

13, [Mn(H$_2$O)(3-MeOC$_6$H$_4$COO)(phen)$_2$](ClO$_4$); **18**, [Mn(bpy)(4-^{t}BuC$_6$H$_4$COO)$_2$(H$_2$O)]; **19**, [Mn(H$_2$O)$_2$(2-MeOC$_6$H$_4$COO)$_2$(phen)].

The D_{Mn} values obtained from these fits are consistent with Mn^{II} ions with distorted octahedral geometry.[33] Several simulations were performed changing the sign of D_{Mn} and E_{Mn}. While the shape of the spectra only depends on the $|E_{Mn}|$, they vary with the sign and magnitude of D_{Mn}. However, such differences were too slight to unambiguously establish the sign of this parameter.

Dinuclear [{Mn(NN)$_2$}$_2$(μ-*n*-RC$_6$H$_4$COO)$_2$](ClO$_4$)$_2$ compounds (8–12, 14 and 15). For the dinuclear compounds the shape of the EPR spectra at low temperature depends on their

magnetic behavior: while ferromagnetic compounds display a broad and intense signal at $g \approx 2$ (Figure 46), similar to those recorded at room temperature, the antiferromagnetic compounds show much more complex spectra (Figure 47). The antiferromagnetic compounds show an $S = 0$ ground state, so they are expected to be EPR silent. However, the small J values allow the lowest excited states $S = 1$ and $S = 2$ to be populated at 4 K.

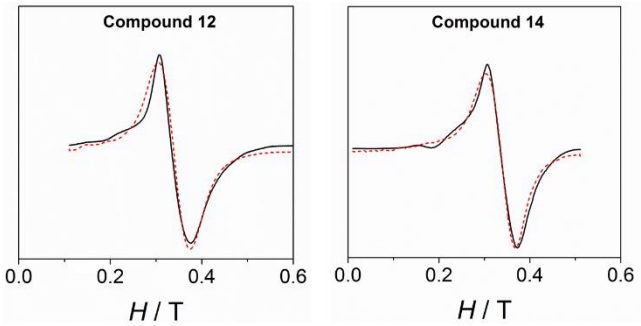

Figure 46. X-band EPR spectra for the ferromagnetic dinuclear compound **12** and **14** at 4 K. The dashed lines correspond to the best fit of the experimental data.

The cause of the difference between the EPR spectra of anti- or ferromagnetic compounds relies on the values of the zero-field splitting parameters, $|D_S|$ and $|E_S|$, of the states populated at low temperature. In fact, $|D_S|$ and $|E_S|$ become smaller as the spin increases.[8] Accordingly, the zero-field splitting parameters of the $S = 5$ ground state of the ferromagnetic compounds are much smaller than those of the first excited states, $S = 1$ and $S = 2$, of the antiferromagnetic compounds.

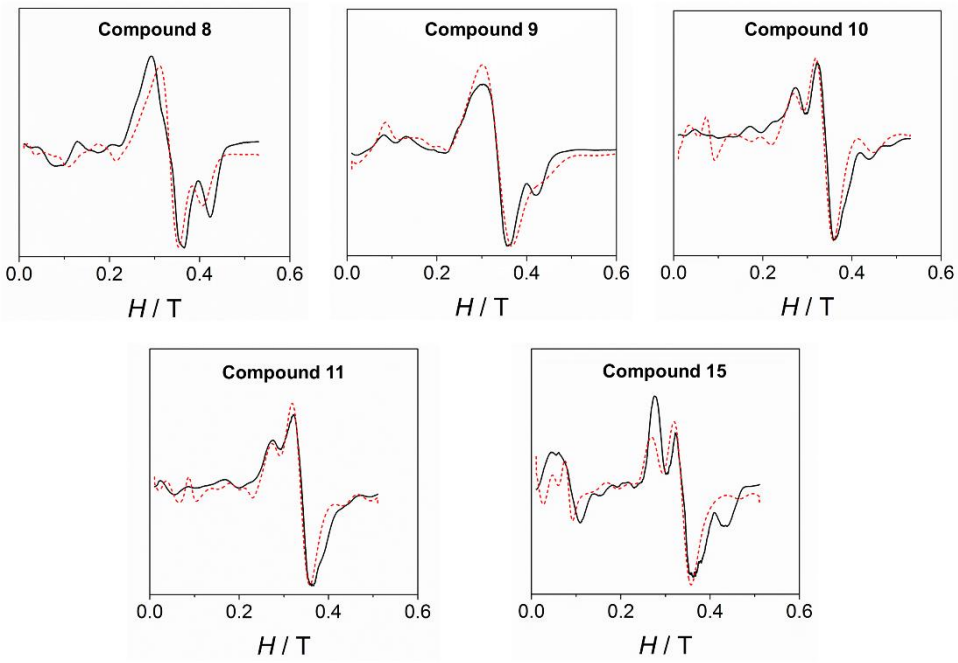

Figure 47. X-band EPR spectra for the antiferromagnetic dinuclear compounds **8**, **9**, **10**, **11**, and **15** at 4 K. The dashed lines correspond to the best fit of the experimental data.

The EPR spectra at 4 K of the dinuclear compounds were fitted with the PHI program[165] with the aim of evaluating the single-ion ZFS parameters (D_{Mn} and E_{Mn}), considering two high-spin Mn^{II} ions with the magnetic coupling constant ($2J$) and the g factor obtained from the fit of the magnetic data. Contrary to the Mn^{III}_2 compounds (see Chapter 1.3), the octahedra of coordination in these compounds are parallel; so, there is no need to consider their relative orientation in the fit. The results of these fits are collected in Table 14.

Table 14. Single-ion ZFS parameters obtained from the fit of the EPR spectra of the dinuclear compounds with formula $[\{Mn(NN)_2\}_2(\mu\text{-}n\text{-}RC_6H_4COO)_2](ClO_4)_2$.

Ref.	*n*-R/NN	mode	$2J$ / cm^{-1}	D_{Mn} / cm^{-1}	$\lvert E_{Mn}\rvert$ / cm^{-1}	$\lvert E_{Mn}\rvert / \lvert D_{Mn}\rvert$
8	2-MeO/bpy	$\mu_{1,3}$	–2.4	±0.070	0.020	0.29
9	3-MeO/bpy	$\mu_{1,3}$	–2.0	±0.083	0.017	0.20
10	4-MeO/bpy	$\mu_{1,3}$	–1.4	+0.125	0.006	0.05
11	2-MeO/phen	$\mu_{1,3}$	–1.8	+0.104	0.013	0.13
12	3-MeO/phen	$\mu_{1,1}$	+1.1	±0.030–0.048	0.009–0.012	0.19–0.33
14	4-MeO/phen	$\mu_{1,1}$	+1.3	±0.032–0.050	0.009	0.18–0.28
15	4-*t*Bu/phen	$\mu_{1,3}$	–2.0	+0.121	0.017	0.14

Finding a good simulation for the EPR spectra of the dinuclear compounds was far more complicated than for the mononuclear ones. For the ferromagnetic compounds **12** and **14**, which display a single broad band, the anisotropy parameters could not be determined with accuracy and, consequently, the results are expressed as a range. As mentioned above, the $D_{S=5}$ and $E_{S=5}$ parameters are smaller than the respective $D_{S<5}$ and $E_{S<5}$ for the same D_{Mn} and E_{Mn}.[8] Hence, the EPR spectra at low temperature of a ferromagnetic Mn^{II}_2 compound with ground state $S = 5$ will be much less sensitive to the ZFS parameters of the Mn^{II} ions than the antiferromagnetic ones, where the first excited states are $S = 1$ and $S = 2$ are responsible for the splitting in the EPR spectra. Indeed, while $D_{S=5} \approx 0.44\ D_{Mn}$, $D_{S=1} \approx -6.4\ D_{Mn}$ and $D_{S=2} \approx -0.95\ D_{Mn}$.[8]

Moreover, a surprising peculiarity was found: the sign of D_{Mn} was certainly relevant for the shape of the EPR spectra of compounds **10**, **11** and **15**. The EPR spectra of these compounds display very different features whether D_{Mn} is positive or negative. Even so, the spectra remain unchangeable when the sign of E_{Mn} changes.

These latter facts suggest that one may likely establish the sign of D_{Mn} in some precise situations. However, the sign of D_{Mn} can be only determined with HF-EPR spectra measurements, at least for mononuclear compounds.[221] Therefore, in order to understand the effect of the sign of D_{Mn} on the resulting EPR spectra, several simulations were

performed. Figure 48 show the spectra for a hypothetical dinuclear compound with $g = 2.00$ and $2J = -2.4$ cm^{-1} for two different D_{Mn} values and four different E_{Mn} values.

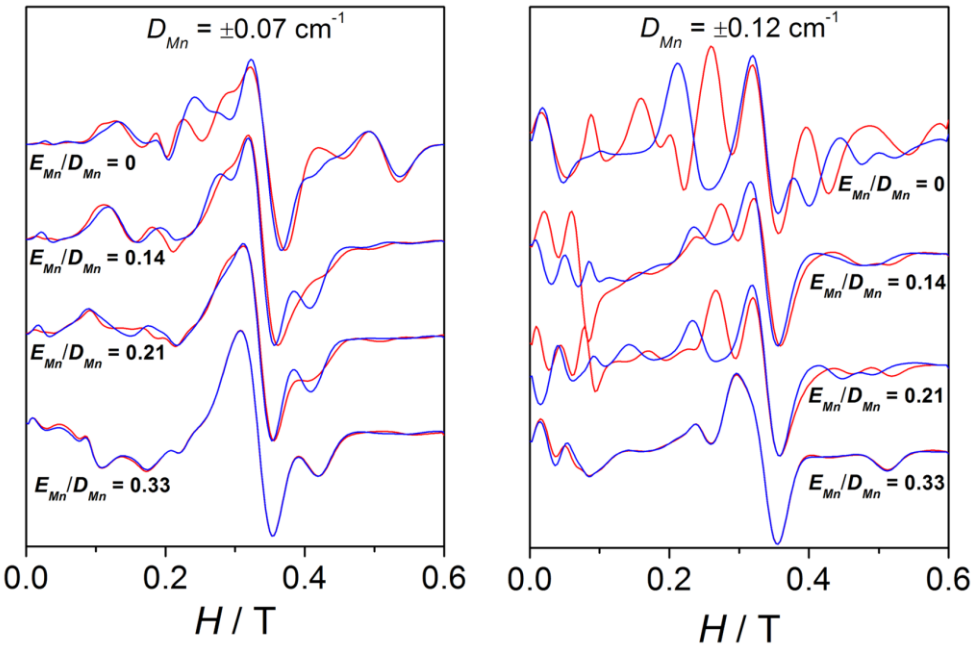

Figure 48. X-band EPR spectra for a hypothetical dinuclear compound with $g = 2.00$ and $2J = -2.4$ cm^{-1} for two different values of D_{Mn} and four different $|E_{Mn}|/|D_{Mn}|$ ratios. Red lines and blue lines correspond to the simulations performed with positive and negative D_{Mn}, respectively.

As observed, for a "small" D_{Mn} value of 0.07 cm^{-1}, the distinction between the spectra simulated with positive (red) or negative (blue) D_{Mn} values appears very difficult to accomplish, since the bands are more or less situated in the same position and only the intensity differs. On the other hand, for a higher D_{Mn} value (0.12 cm^{-1}), the differences between the spectra with positive or negative D_{Mn} values become greater, as the bands do not only have different intensity but also appear at different fields. However, such variances become thinner as E_{Mn} increases, showing almost identical spectra when $|E_{Mn}|/|D_{Mn}| = 0.33$. The sign of D_{Mn} is indeed very difficult to determine upon approaching the rhombic limit ($E/D = 0.33$).[222–224] Hence, the degree of divergence between the spectra with positive and negative D_{Mn} depends on the magnitude of this parameter and the $|E_{Mn}|/|D_{Mn}|$ ratio: (*a*) the higher D_{Mn} becomes, the more different the spectra are; and (*b*) the higher the $|E_{Mn}|/|D_{Mn}|$ ratio is, the less distinctive the spectra become.

To understand the cause of these latter points, a deeper analysis of the EPR spectra and the Zeeman plots was performed. Firstly, it is worth recalling two important points: (*a*) in terms of populations the most relevant states are those with $S = 0$ (ground state, which display no EPR transitions), $S = 1$ (first excited state), and $S = 2$ (second excited state), whose

populations at 4 K are 66.3, 28.0, and 5.3%, respectively; and (*b*) when axial anisotropy (*D*) becomes relevant the Zeeman plot in the z magnetic field direction is rather different from those in the *y* and *x* ones ($x = y \neq z$), so the resulting EPR spectra comes from the addition of the permitted transitions of the three Zeeman plots.

Therefore, the Zeeman plots in the x/y and z magnetic field directions for a hypothetical Mn^{II}_2 system with $2J = -2.4$ cm^{-1} and $D_{Mn} = \pm 0.12$ cm^{-1} were simulated, and the expected transitions were marked according to the selection rules (see Chapter 1.1). It is worth noting that no mixture of M_S states coming from different S levels was observed for $H < 1.0$ T, so the EPR signals that are observed should come from the transitions between the different M_S states within the same S level. Figure 49 shows the Zeeman plots in the x/y and z magnetic field directions of the first excited state, $S = 1$, for a Mn^{II}_2 system with positive and negative D_{Mn}. As may be observed, the expected transitions should arise at the same field and should have the same intensity. Hence, the cause of the difference between the spectra with D_{Mn} of different sign should lie in the second excited state ($S = 2$).

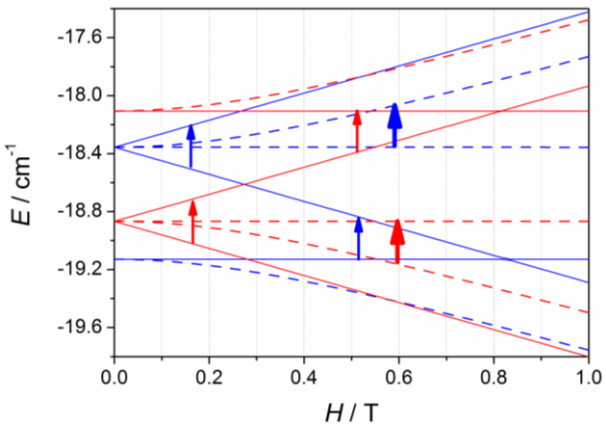

Figure 49. Zeeman plots in the x/y (dashed lines) and z (straight lines) magnetic field directions for the first excited state ($S = 1$) of a Mn^{II}_2 system with $2J = -2.4$ cm^{-1} and positive (red) and negative (blue) ZFS ($D_{Mn} = \pm 0.12$ cm^{-1}). The arrows point out the expected transitions in the X-band EPR spectra. The transitions coming from the *x* and *y* magnetic field direction are represented as thicker arrows than those from the z magnetic field direction because their contributions are double.

Figure 50 shows the Zeeman plots in the x/y and z magnetic field directions of the second excited state, $S = 2$, for a Mn^{II}_2 system with positive and negative D_{Mn}. Contrary to the $S = 1$, the expected transitions coming from the $S = 2$ are rather different in both position and intensity as a function of the sign of D_{Mn}. These latter facts indicate that the differences between the spectra with positive and negative D_{Mn} rely on the transitions coming from the second excited state, $S = 2$.

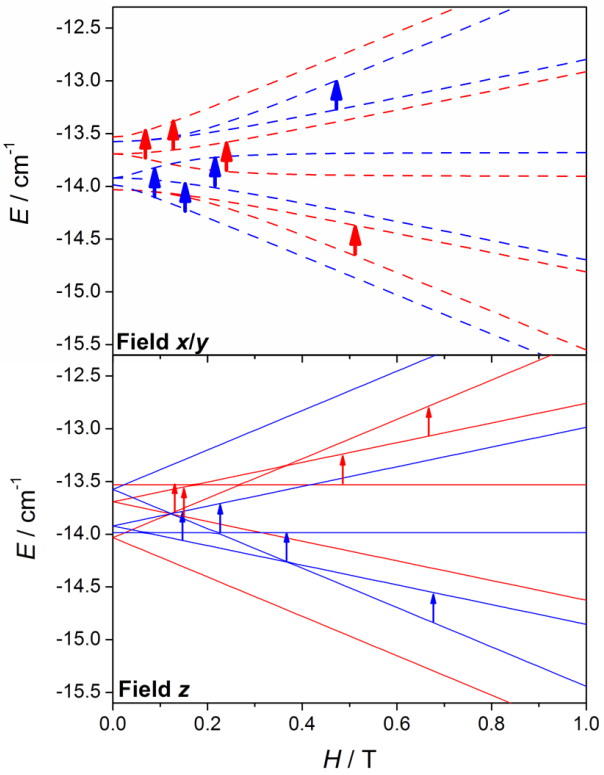

Figure 50. Zeeman plots in the x/y (dashed lines) and z (straight lines) magnetic field directions for the second excited state ($S = 2$) of a Mn^{II}_2 system with $2J = -2.4$ cm^{-1} and positive (red) and negative (blue) ZFS ($D_{Mn} = \pm 0.12$ cm^{-1}). The arrows point out the expected transitions in the X-band EPR spectra. The transitions coming from the x and y magnetic field directions are represented as thicker arrows than those from the z direction because their contributions are double.

Another arising question is what dictates the sign of D_{Mn} in Mn^{II} ions. As far as we know, there are several studies in the literature concerning the ZFS of Mn^{II} ions;[33,221,223–225] however, the factors determining the sign of D_{Mn} still remains unknown.

Trinuclear $[Mn_3(NN)_2(\mu\text{-}n\text{-}RC_6H_4COO)_6]$ compounds (16, 17, 20, and 21). The EPR spectra of the trinuclear compounds (**16**, **17**, **20** and **21**) are very sensitive to the temperature. The spectrum recorded at room temperature show a very broad band centered at $g \approx 2$. This band generally remains the most intense signal until very low temperature. At 4 K, the spectra of compounds **16**, **17** and **21** becomes quite complicated: there are an intense signal at low field ($g \approx 4$), a weaker one at $g \approx 2$, and some others at high field (Figure 51). The EPR spectra at 4 K for compound **20** is quite different from the rest, showing the most intense band at $g \approx 2$ and a smaller one at low field.

The EPR spectra of the trinuclear compounds may not be fitted by considering the whole system, since each iteration takes around half an hour. So, in this case the ZFS of the Mn^{II} ions could not be determined. As seen from the magnetic measurements, these compounds show a ground state $S = 5/2$. The first and second excited states $S = 3/2$ and $S = 7/2$ are

found in the 5.5–7.3 and 7.6–10 cm^{-1} ranges, respectively, depending on the 2*J* values. At 4 K, the population of these states is quite low, being 6.5–11.2% and 2.3–5.1% for the respective $S = 3/2$ and $S = 7/2$ states. Hence, at this temperature, the greatest contribution to the EPR spectra will be the ground state, whose population ranges from ~80 to ~90%.

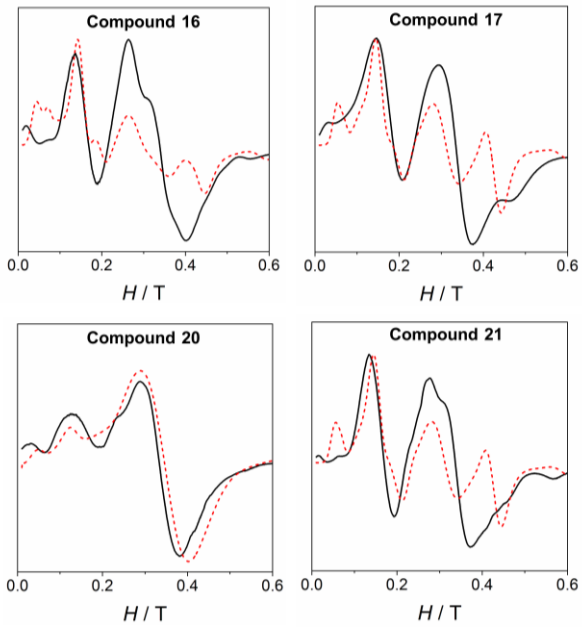

Figure 51. X-band EPR spectra for the trinuclear compounds **16**, **17**, **20** and **21** at 4 K. The dashed lines correspond to the best fit of the experimental data.

Therefore, the spectra at 4 K were fitted with the PHI program[165] considering an isolated spin state $S = 5/2$ with axial (D) and rhombic (E) ZFS. The results of these fits are listed in Table 15. The results for **16**, **17** and **21** are in agreement with those reported for analogous compounds, whose $D_{5/2}$ and $E_{5/2}$ are ~0.16 and ~0.05 cm^{-1}.[15] Compound **20** displays much smaller ZFS; however, the lack of structural data for this compound does not allow us to reach any conclusion.

Table 15. Results from the fit of the EPR spectra of the trinuclear compounds with formula $[Mn_3(NN)_2(\mu\text{-}n\text{-}RC_6H_4COO)_6]$.

Ref.	*n*-R	NN	$2J^a$ /cm^{-1}	$\lvert D_{5/2}\rvert$ /cm^{-1}	$\lvert E_{5/2}\rvert$ /cm^{-1}	$\lvert E_{5/2}\rvert / \lvert D_{5/2}\rvert$
16	3-MeO	bpy	–2.1	0.14	0.040	0.28
17	4-MeO	bpy	–2.5	0.14	0.046	0.33
20	3-MeO	phen	–2.2	0.045	0.015	0.33
21	4-MeO	Phen	–2.9	0.14	0.046	0.33

[a] Referred to the Hamiltonian $H = -2J(S_1S_2 + S_2S_3) - 2J_{13}(S_1S_3)$, considering $J_{13} = 0$;

Figure 51 shows the experimental and fitted curves for these compounds. As observed, the intensity of the band at $g \approx 2$ for compounds **16**, **17** and **21** seems to be underestimated, since

it is much weaker in the fitted spectra (red dashed lines) than in the experimental ones (black line). Nevertheless, one should remember that the fits have been performed by considering just the ground state and the greater intensity of these band may be due to the excited states.

To explain this the Zeeman plot for this kind of trinuclear compound was simulated considering a $D_{Mn} = 0.1$ cm^{-1}. It is worth noting that the axial ZFS (D) of the three Mn ions was considered. The central ion, even though it is quite regular (O6a–Mn2–O6, O4–Mn2–O4a, and O1–Mn2–O1a angles of 180º), shows a substantial elongation in the direction of the $\mu_{1,1}$-carboxylate ligand. This simulation revealed that there is a relation between the magnitudes of the ZFS of each states, where $D_{5/2} \approx 0.95\ D_{3/2} \approx 6.2\ D_{7/2}$. So, while the two first states will have very similar D, the second excited state $S = 7/2$ has a much smaller D parameter. The spectrum for a spin state $S = 7/2$ with $D = 0.025$ cm^{-1} and $E = 0.0075$ cm^{-1} (equivalent to the fitted $D_{5/2}$ and $E_{5/2}$ parameters divided by 6) was simulated, displaying just a broad and intense signal at $g \approx 2$. Hence, the higher intensity of this band in the experimental spectra may be due to a small contribution (population in the range 2.3–5.1%) of the second excited state $S = 7/2$.

Summary

Several new Mn^{II} compounds, comprising seven dinuclear, four trinuclear and three mononuclear ones, have been synthesized. The crystal structure of all dinuclear and two of the mononuclear compounds was determined; however, X-ray quality single-crystals were only obtained for one of the trinuclear compounds. In the polynuclear compounds, the Mn ions are linked through carboxylate ligands in different coordination modes. For instance, the dinuclear compounds **8**, **9**, **10** and **15** display $\mu_{1,3}$-carboxylate bridges in *syn-anti* mode, whereas the dinuclear compounds **12** and **14** show $\mu_{1,1}$-carboxylate bridges. This difference in the coordination mode affects the magnetic behavior of these compounds: **8**, **9**, **10** and **15** display antiferromagnetic behavior and **12** and **14** ferromagnetic interactions, being consistent with previous works in our group.[16]

The Mn^{II} ions in the trinuclear compound (**17**) are bridged through three carboxylate ligands, two $\mu_{1,3}$-carboxylate bridges in *syn-syn* mode and one $\mu_{1,1}$-carboxylate bridge. The magnetic measurements for the trinuclear compounds (**16**, **17**, **20** and **21**) revealed that they present antiferromagnetic behavior of slightly different magnitude. Compound **17** was incorporated in the magneto-structural that were previously reported by Gómez et *al.*[15]

EPR spectra at different temperatures were recorded for all the Mn^{II} compounds herein presented. Each type of compound gives some peculiar features that allow its identification. For the mono- and dinuclear compounds, the spectra at 4 K were fitted considering the entire system, determining the ZFS of single ion (D_{Mn} and E_{Mn}). For the dinuclear compounds the spectra of those showing ferro- or antiferromagnetic interaction are very different. Moreover, for the antiferromagnetic dinuclear compounds **10**, **11**, and **15** the shape of the EPR spectra is very sensitive to the sign of D_{Mn}. In fact, the shape of the spectra for an antiferromagnetic dinuclear system is very sensitive to the sign of D_{Mn} when $D_{Mn} > 0.10$ cm^{-1} and the $|E_{Mn}|/|D_{Mn}|$ ratio is low.

For the trinuclear compounds, the single-ion ZFS parameters could not be determined, so the EPR spectra at 4 K were fitted by considering that only the ground state, with $S = 5/2$, is populated. The intensity of one of the main bands for these latter compounds, which arises at $g = 2$, is normally underestimated in the fits. The higher intensity of this band in the experimental spectra is likely due to the omission of the contribution of the excited states. Indeed, the second excited state $S = 7/2$ has much smaller ZFS parameters than the ground and first excited state and only display an intense and broad band at $g \approx 2$. A low contribution of this state may likely contribute to the intensification of this signal.

1.5. Heterometallic Compounds having $[Mn^{IV}_6M_2O_9]^{10+}$ Core with M = Ca^{2+} and Sr^{2+}

First insights

As commented in the introduction, the syntheses of Mn^{IV}-Ca^{2+} compounds are of relevance from a biochemical point of view because of the presence of a heterometallic cluster containing both Mn^{IV} and Ca^{2+} ions in the water oxidizing center (WOC) of photosystem II.[10,76] As a result, in the last two decades researchers have performed intense investigations of both the enzyme and manganese compounds that mimic the structure and function of the WOC.[41] However, several aspects regarding the mechanism, as well as the exact role of Ca^{2+} ion in the WOC, remain incompletely understood.

It is well known that, besides its structural role, the presence of Ca^{2+} ion in Mn compounds is not innocent, since it may cause electronic modifications on the Mn ions.[96,226,227] The magnetic properties of Mn compounds are directly related to the electronic configuration of the Mn ions. Hence, the study of the magnetic properties of these compounds, compared with those containing other cations, may provide useful information concerning the effect of Ca^{2+}.

Moreover, Ca^{2+} and Sr^{2+} ions display similar (but not equal) chemical properties and are occasionally interchangeable. Some synthetic Mn-Ca and Mn-Sr models have indeed contributed to a better understanding of the structural and chemical functions of Ca^{2+} ion in the WOC.[41]

We herein present the syntheses and the crystal structures of two wheels with formula $[Mn_6M_2O_9(4\text{-}^tBuC_6H_4COO)_{10}(4\text{-}^tBuC_6H_4COOH)_5]$, where M = Ca^{2+} (**1**) or Sr^{2+} (**2**). Several compounds with a Mn_6 wheel-like core have been reported in the literature, showing a wide range of combinations of Mn oxidation states and central ions.[228–242] These wheels can be classified in two types: (a) those where the Mn ions are linked through two oxo- or oxo-derivatives, and (b) those where the Mn ions are alternately bridged through one and two oxo- or oxo-derivatives. Type (a) wheels prove the versatility of these compounds, which include several $Mn^{z}_6M^{z'}_x$ moieties, where z is the Mn oxidation state, $M^{z'}$ is the central ion with the z' oxidation state, and x is 1 or 2. Then, these wheels include the compounds with $Mn^{II}_6Mn^{II}$,[228] Mn^{III}_6Na,[237,238] Mn^{III}_6Li moieties,[236] and several mixed valence compounds with $Mn^{II/III}_6Mn^{II}$ moieties.[229–235] In contrast, most of type (b) wheels are compounds with

$Mn^{IV}_6Ce^{IV}_x$,[240,241] and $Mn^{IV}_6Bi^{III}_2$ moieties;[242] only one $Mn^{III}_6Mn^{II}$ wheel has been described.[239] All these compounds are of great interest for inorganic chemists due to their magnetic properties. For instance, a lot of them present a net ferromagnetic behavior and some are single-molecule magnets (SMM) at low temperature.[232,235,239]

Among the three $Mn^{IV}_6M^{x}_x$ wheels, the magnetic analysis is only reported for the Ce^{IV} compounds. Here, we also report the study of the magnetic properties of the new Mn^{IV}_6 wheels (with Ca^{2+} and Sr^{2+}). With the aim to elucidate the effect of the alkaline earth ions on the magnetic properties, DFT calculations have been performed for compounds **22** (Ca^{2+}) and **23** (Sr^{2+}) and for three hypothetical compounds with the structural parameters of **22** (where Ca^{2+} has been replaced with Sr^{2+}, Mg^{2+} or M^{2+}-depletion).

Synthesis of $[Mn^{IV}_6M_2O_9(4\text{-}^tBuC_6H_4COO)_{10}(4\text{-}^tBuC_6H_4COOH)_5]$ (M = Ca^{2+} for 22, and M = Sr^{2+} for 23).

Two heterometallic compounds were synthesized from the comproportionation reaction between $Mn(AcO)_2$ and NBu_4MnO_4 in presence of a M^{2+} salt and 4-*tert*-butylbenzoic acid (4-$^tBuC_6H_4COOH$) in hot acetonitrile, procedure inspired in that described by Mukherjee *et al.* for the synthesis of an asymmetric $[Mn^{IV}_3CaO_4]^{6+}$ cubane.[90] Figure 52 shows a concise synopsis of the reactions performed and some experimental observations. In our case, the use of Ca^{2+} acetate or nitrate leads to the formation of **22**, in which the latter provides much higher yield. The same procedure was also tested using magnesium and strontium nitrate. While all attempts to obtain the analogous compound with Mg^{2+} ion were unsuccessful, the use of the Sr^{2+} source leads to the formation of **23**. However, the synthesis of **23** hardly yielded a 10% of the theoretical amount based on total Mn in spite of our endeavors. In all reactions, an excess of 4-$^tBuC_6H_4COOH$ was used, which may be required to favor the protonation of the acetate ions. The resulting acetic acid is very likely removed because of the high temperature.

The Mn^{II}/Mn^{VII} molar ratio (1:2) gives an oxidation state of +5.33 for each manganese ion. If all the Mn^{IV} came from the comproportionation between Mn^{II} and Mn^{VII}, more than a half of the Mn^{VII} would be wasted. But, as the amount of **22** obtained exceeds the theoretical value based on this reaction, what occurs is that the comproportionation reaction is combined with the reduction of Mn^{VII} during the synthesis (at least for **22**).

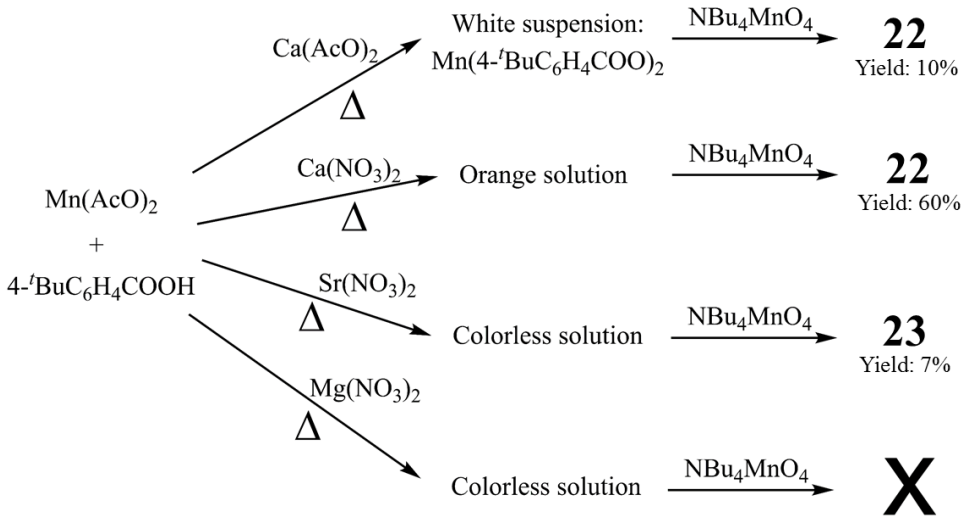

Figure 52. Reactions carried out to obtain heterometallic Mn^{IV}-M^{2+} compounds.

As commented before, **22** may be obtained using two different calcium sources: calcium nitrate and calcium acetate. The use of the last one leads to good X-ray quality crystals, but the yield of the reaction is low. On the contrary, the use of calcium nitrate leads to the crystallization of **22** in a 60% yield; however, the obtained single-crystals were too small and the structure could not be fully refined. Although both synthetic routes lead to the formation of **22**, a significant difference is observed in the first stage, which consists in the dissolution of Mn^{II} and Ca^{2+} sources and 4-^{t}BuC$_6$H$_4$COOH in hot acetonitrile. If calcium nitrate is used, the solution turns orange at 70 °C, indicating that part of the Mn^{II} is being oxidized to Mn^{III}. In contrast, a white suspension, identified as Mn(4-^{t}BuC$_6$H$_4$COO)$_2$, appears at the same temperature when using calcium acetate. Contrary to this fact, the solution does not turn orange during the first stage when using $Sr(NO_3)_2$ (synthesis of **23**), indicating that there is no oxidation to Mn^{III}. In all cases, the solution turns dark red after the addition of MnO_4^-, which corresponds to the Mn^{IV} compound.

Particularly for **22**, the crystal size is very sensitive to the stirring intensity, especially if calcium nitrate is chosen as the calcium source. If the solution is vigorously stirred during the addition of NBu_4MnO_4, a dark red powder is obtained just after the reaction; whereas if it is softly stirred, the isolated solid is crystalline. This confirms that **22** is instantly formed and, because of its insolubility in acetonitrile, the stirring induces a fast precipitation instead of a slow crystallization.

Description of structures

Compound **22** and **23**, with formula $[Mn^{IV}_6M_2O_9(4\text{-}^tBuC_6H_4COO)_{10}(4\text{-}^tBuC_6H_4COOH)_5]$ (M = Ca^{2+} for **22**, and Sr^{2+} for **23**), display very similar structures that mainly differ in the M^{2+} ions. Figure 53 shows the crystal structure of **22**; the analogous picture of **23** is shown in Appendix IV (Figure S17).

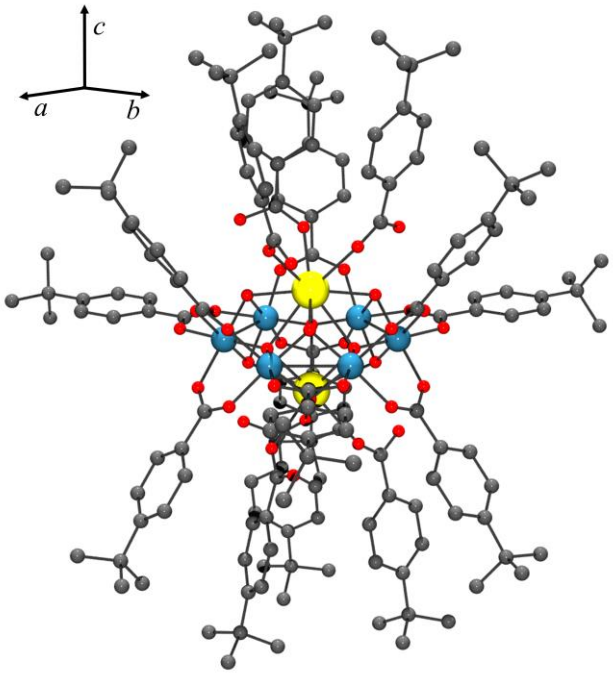

Figure 53. Crystal structure of **22**, with H atoms omitted for clarity. Color code: Mn^{IV}, blue; Ca, yellow; O, red; C, gray. The analogous crystal structure of **23** is shown in Appendix IV (Figure S17).

These compounds contain a $[Mn^{IV}_6M_2O_9]^{10+}$ core which comprises a planar Mn^{IV}_6 ring where the Mn ions are alternately bridged by $(\mu_3\text{-}O)_2(\mu\text{-}RCOO)$ and $(\mu_4\text{-}O)(\mu\text{-}RCOO)_2$ ligands. The two M^{2+} ions are located in the center and at both sides of the wheel (Figure 54 and Figure S18). The μ_3-O ligand (O1) binds two Mn ions and the M^{2+} ion placed in the same side of the wheel, while the μ_4-O ligand (O2) is linked to two Mn ions and the two M^{2+} ions, as shown in Figure 55.

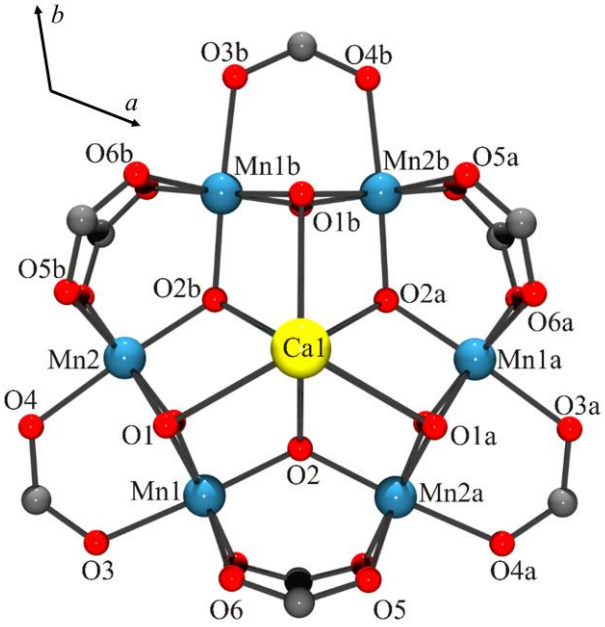

Figure 54. *c*-Axis view of the crystal structure of **22**. The substituent 4-^{t}BuC$_6$H$_4$- has been omitted for better clarity. An analogous figure for **23** is shown in Appendix IV (Figure S18).

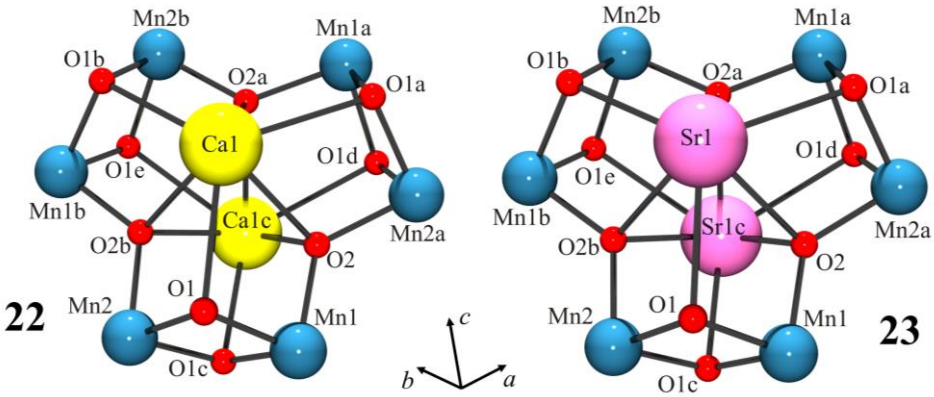

Figure 55. $[Mn^{IV}_6M_2O_9]^{10+}$ core of **22** (Ca^{2+}) and **23** (Sr^{2+}).

In both compounds, the M^{2+} ions are located above and below the Mn^{IV}_6 plane (at 1.83–1.90 Å from it) and linked to the oxo ligands, generating three fused $[Mn_2M_2O_4]^{4+}$ cuboids (Figure 55). The coordination number of these ions is nine, six of the positions are occupied by three μ_3-O^{2-} bridges (O1) and three μ_4-O^{2-} bridges (O2). Each M^{2+} ion completes its coordination with three monodentate carboxylate ligands (Figure 56). The presence of hydrogen bonds between μ_3-O^{2-} ions (O1) and the nearest hydrogen atoms of the monodentate carboxylate ligands stabilizes the resulting rigid structure. The IR spectra of these compounds display a band at 1691 cm^{-1}, assigned to the C=O vibration, which confirms the existence of these monodentate ligands.[160]

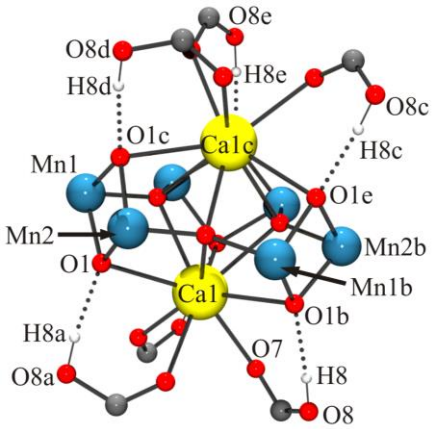

Figure 56. Intramolecular hydrogen bonds (dotted lines) present in **22**. Analogous intramolecular interactions are found in **23**.

The fifteen carboxylate ligands (nine bridging Mn ions and six coordinated to the M^{2+} ions) are surrounding the $[Mn^{IV}_6M_2O_9]^{10+}$ core and the substituent groups of the benzoate ligands point to the exterior, coming of a hydrophobic cage where the metal ions stay isolated from the environment (Figure 53 and Figure S17).

To balance the ten positive charges of the core, ten negative charges are needed. Nine of them are compensated with the 4-^{t}BuC$_6$H$_4$COO$^-$ bridges. If the six monodentate carboxylate ligands were protonated, a mono-charged complex would result and the presence of a counter ion in the structure would be required (1:1 electrolyte). However, no counter ion was found in these structures. With the aim to confirm the neutrality of these compounds, the molar conductivity of **22** was measured in two different solvents, but these values are much lower than the expected for a 1:1 electrolyte, confirming that the compound is neutral. Hence, only five of these monodentate ligands should be protonated. Nevertheless, these ligands are symmetrically equivalent; so, each one contains a hydrogen atom with 5/6 occupancy, consistent with five hydrogen atoms disordered in six identical positions.

Table 16 contains selected structural parameters for **22** and **23**. Note that both compounds show almost identical structural parameters, where the most significant differences can be found around the M^{2+} ions. These differences are commented subsequently. The Mn–O distances are consistent for Mn^{IV} ions, without Jahn-Teller axis. Moreover, the oxidation state IV for the Mn ions is confirmed by the magnetic measurements.

Table 16. Selected interatomic distances (Å) and angles (º) for **22** and **23** with standard deviations in parentheses.

	22 (M = Ca)	**23** (M = Sr)
Mn1–O1	1.840(2)	1.842(3)
Mn1–O2	1.829(3)	1.812(4)
Mn1–O3	1.985(3)	1.982(4)
Mn1–O6	1.961(2)	1.966(3)
Mn2–O1	1.841(2)	1.836(3)
Mn2–O4	1.999(3)	1.998(4)
Mn2–O2b	1.811(3)	1.801(4)
Mn2–O5b	1.947(2)	1.948(3)
Mn1···Mn2	2.7189(9)	2.7234(13)
Mn1···Mn2a	3.269(1)	3.282(1)
Mn1···Mn1a	5.203(2)	5.211(1)
Mn2···Mn2a	5.182(2)	5.206(2)
Mn1···Mn2b	5.988(1)	6.006(1)
M1–O1	2.632(2)	2.681(3)
M1–O2	2.506(2)	2.594(3)
M1–O7	2.465(3)	2.577(3)
M1···M1c	3.656(2)	3.803(1)
Mn1···M1	3.5166(8)	3.5591(9)
Mn2···M1	3.5063(8)	3.5566(9)
Mn1–O1–Mn2	95.22(9)	95.54(14)
Mn1–O2–Mn2a	127.87(17)	130.6(2)
Mn1–O1–O1c–Mn2	171.0(1)	172.9(2)

Symmetry codes for **22**: (a) 1-y,1+x-y,z; (b) -x+y,1-x,z; (c) x,y,1/2-z. Symmetry codes for **23**: (a) 1-x+y,1-x,z; (b) 1-y,x-y,z; (c) x,y,1/2-z.

The shortest Mn···Mn distances are 2.72 Å (Mn1···Mn2) and correspond to Mn ions linked by two oxo bridges (O1). In contrast, the Mn···Mn distances corresponding to Mn ions linked by one oxo bridge (O2) are 3.27–3.28 Å (Mn1···Mn2a). The Mn1–O1–Mn2 angles are ~95º, being similar to the values reported in the literature for compounds with $[Mn^{IV}_2(\mu_3\text{-}O)_2(\mu\text{-}RCOO)]^{3+}$ subunits.[243] The Mn_2O_2 ring in **22** and **23** are closer to planarity (with Mn1–O1–O1c–Mn2 angles of ~172º) than in the discrete dinuclear compounds reported in the literature (159–165º).[243]

The $[Mn^{IV}_2(\mu_4\text{-}O)(\mu\text{-}RCOO)_2]^{4+}$ subunit is uncommon and to the best of our knowledge, no dinuclear compounds with this core have been reported in the literature. However, two theoretical studies that contain optimized structural parameters for a hypothetical dinuclear $[Mn^{IV}_2(\mu\text{-}O)(\mu\text{-}RCOO)_2(NH_3)_6]^{4+}$ complex were found in the literature. In these studies, the Mn–O–Mn angle is expected to range from 126 to 133º.[226,244] The Mn1–O2–Mn2a angles in **22** and **23** are within this range, being 127.8 and 130.6º, respectively.

c-Axis views of the packing of **22** and **23** are shown in Figure S19 and Figure S20. Every six molecules form a six-member ring and such rings share sides, spread out along the *a*- and *b*-axes. The layers are stacked up and extended along the *c*-axis, forming a channel of solvent located in the middle of each six-member ring.

As explained before, there are not many differences between the structural parameters of **22** and **23**; for instance, the Mn···Mn and Mn–O distances vary at the most 0.01 Å between the two compounds. However, Sr^{2+} ion has an ionic radii larger than the Ca^{2+} one (1.32 and 1.14 Å, respectively), and this causes slight but key variations in the structural parameters of the wheel. These differences are reflected in the M–O distances and in the respective Ca1···Ca1c and Sr1···Sr1c distances, which are meaningfully larger in the case of **23** (Sr^{2+}). The wheel diameter (defined by the Mn1···Mn2b distance) may be considered identical because they differ less than 0.02 Å. So as to provide the bigger Sr^{2+} ion with more space, the Mn_2O_2 ring of the double oxo bridge becomes more planar (greater Mn1–O1–O1c–Mn2 angle by ~2º) and the Mn1–O2–Mn2a bridge is slightly unfolded in **23**. Lastly, the effect of the greater size of the Sr^{2+} ion is also reflected with the widening of the unit cell, in light of the larger *a*, *b* and *c* axes presented by **23**.

The structural parameters in **22** and **23** are similar to those found in analogous $Mn^{IV}_6M^{II}_x$ wheels reported in the literature, which contain Ce^{IV} or Bi^{III} ions[240–242] instead of Ca^{2+} or Sr^{2+} ions. However, some slight (but significant) structural differences may be found in both the Mn_2O_2 and the Mn_2O subunits, which may be of importance for their magnetic behavior (see below).

Structural analysis

As mentioned in the introduction, the Mn_6 wheels can be classified in two types: (a) those where the Mn ions are linked through two oxo or oxo-derivatives, and (b) those where the Mn ions are alternately bridged by one and two oxo or oxo-derivatives. Table 17 summarizes the Mn_6 wheels that can be found in the literature so far. Type (a) compounds are formed by Mn^{II} or Mn^{III} ions with one small monovalent or divalent ion in the center, such as Mn^{II}, Li^+ or Na^+, that is usually coplanar or very close to the Mn_6 plane (no more than 0.7 Å from it).[228–238] It is worth emphasizing that the Mn^{II} or mixed-valence $Mn^{II/III}$ wheels always show a Mn^{II} ion in the center,[228–235] while the Mn^{III}_6 wheels show alkaline ions (Na^+ or Li^+).[236–238] Type (b) mainly comprises Mn^{IV}_6 wheels with one or two large ions in the center,[240–242] although a Mn^{III}_6 with a Mn^{II} ion in the center has been reported.[239] It is interesting to note

that, within the four Mn^{III}_6 wheels reported in the literature,[236–239] only one belongs to type (b) and, in this case, the central ion is Mn^{II} instead of the alkaline ions that type (a) exhibit.

Table 17. List of $Mn^{z}_6M^{z'}_x$ wheels containing one or two central ions and selected structural parameters.

	Refcode [a]	Mn^{z}_6 [b]	$M^{z'}$ [c]	x [d]	r [e] / Å	Wheel diameter [f] / Å	$M^{z'}\cdots Mn_6$ [g] / Å	$M^{z'}$–(μ-O^{2-}) / Å
Type (a)	VAHCAK[228]	Mn^{II}_6	Mn^{2+}	1	0.97	6.63	0.69	2.22
	VAHCEO[228]	Mn^{II}_6	Mn^{2+}	1	0.97	6.60	0.00	2.22
	IPULUA[229]	$Mn^{II}_3Mn^{III}_3$	Mn^{2+}	1	0.97	6.52	0.41	2.15–2.24
	NOHGUN[230]	$Mn^{II}_3Mn^{III}_3$	Mn^{2+}	1	0.97	6.62	0.08	2.19–2.24
	NOHHAU[230]	$Mn^{II}_3Mn^{III}_3$	Mn^{2+}	1	0.97	6.62	0.10	2.18–2.22
	PAKPAT[231]	$Mn^{II}_3Mn^{III}_3$	Mn^{2+}	1	0.97	6.61	0.00	2.18–2.26
	PAKPEX[231]	$Mn^{II}_3Mn^{III}_3$	Mn^{2+}	1	0.97	6.60	0.00	2.19–2.21
	PAKPIB[231]	$Mn^{II}_3Mn^{III}_3$	Mn^{2+}	1	0.97	6.63	0.00	2.21
	YIMCIH[232]	$Mn^{II}_2Mn^{III}_4$	Mn^{2+}	1	0.97	6.49	0.00	2.17–2.21
	RAQGOG[233]	$Mn^{II}_2Mn^{III}_4$	Mn^{2+}	1	0.97	6.51	0.00	2.19–2.21
	CIYKAX[234]	$Mn^{II}_2Mn^{III}_4$	Mn^{2+}	1	0.97	6.58	0.00	2.17–2.22
	WEZWAA[235]	$Mn^{II}_2Mn^{III}_4$	Mn^{2+}	1	0.97	6.59	0.00	2.16–2.25
	AQAKUZ[236]	Mn^{III}_6	Li^{+}	1	0.90	6.32	0.00	2.13–2.23
	NOCJEU[237]	Mn^{III}_6	Na^{+}	1	1.16	6.41	0.00	2.30
	VUNFOA[238]	Mn^{III}_6	Na^{+}	1	1.16	6.44	0.00	2.30–2.33
Type (b)	SOPSAS[239]	Mn^{III}_6	Mn^{2+}	1	0.97	6.52	0.45	2.06
	HITTAG[240]	Mn^{IV}_6	Ce^{IV}	1	1.01	5.99	1.54	2.28–2.47
	TUZJUU[241]	Mn^{IV}_6	Ce^{IV}	2	1.01	6.10	1.94	2.55–2.64
	22	Mn^{IV}_6	Ca^{2+}	2	1.14	5.99	1.83	2.46–2.63
	DACDIW[242]	Mn^{IV}_6	Bi^{III}	2	1.17	6.01	1.84*	2.38–2.65
	DACDOC[242]	Mn^{IV}_6	Bi^{III}	2	1.17	5.99	1.89*	2.38–2.75
	23	Mn^{IV}_6	Sr^{2+}	2	1.32	6.00	1.90	2.59–2.68

[a] CSD refcode; [b] z = Mn oxidation state; [c] M$^{z'}$ = central ion; [d] x = number of central ions; [e] ionic radii of the M$^{z'}$ ion for the specified oxidation state and coordination number 6; [f] defined as the average Mn···Mn distances of the facing-neighbor; [g] distance between the M$^{z'}$ ion and the Mn_6 plane. * Average values.

There is a noteworthy dependence of the wheel diameter on the oxidation state of the Mn ions that form the ring; remarkably, the Mn^{IV}_6 wheels have the smallest diameter (Figure 57). This dependence can easily be rationalized by the Mn-oxo distance decreases, which are shorter for a higher oxidation state and, consequently, lead to a decrease in the wheel diameter.

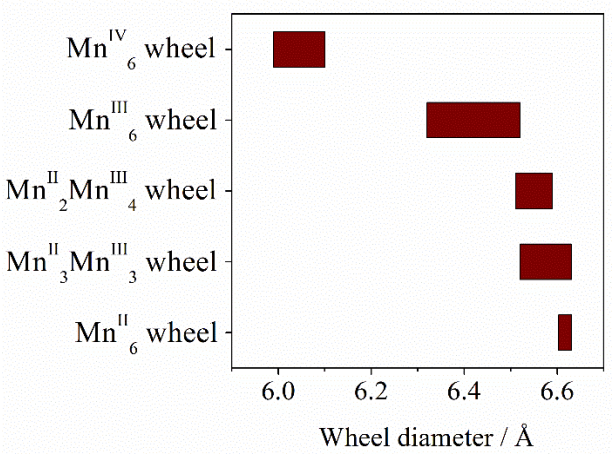

Figure 57. Ranges of wheel diameter, defined as the average Mn···Mn distances of the facing-neighbor, for wheels with different oxidation state of Mn.

Regarding type (b) wheels, it is worth noting that the wheel diameter does not depend on the ionic radii of the central $M^{x'}$, but seems to be dictated by the Mn oxidation state, being ~6.0 Å for Mn^{IV} and ~6.5 Å for Mn^{III}. Moreover, the Mn^{IV}_6 wheels always have large ions in the center, whose ionic radii ranges from 1.01 to 1.32 Å. These large $M^{x'}$ ions do not fit in the Mn_6 plane, thus they are at 1.5–2.0 Å above it. If a smaller $M^{x'}$ ion could be incorporated in a Mn^{IV}_6 wheel, the M–oxo distances would be shorter and the central ion would tend to be closer to the Mn_6 plane. The question arises whether as to this central ion would possibly fit in the Mn_6 plane or would this require a larger ring. We tried to synthesize an analogous Mn^{IV}_6 compound with Mg^{2+} as central ions, but the isolated solid did not contain any Mg^{2+}. Hence, the incorporation of a much smaller $M^{x'}$ ion such as Mg^{2+} (whose ionic radii is 0.86 Å) in a Mn^{IV}_6 wheel could be tentatively considered improbable.

Magnetic properties

Magnetic susceptibility data were recorded for **22** and **23** from 300 to 2 K. $\chi_M T$ versus T plots are shown in Figure 58. The $\chi_M T$ values at room temperature are 11.3 (for **22**) and 10.6 $cm^3\ mol^{-1}\ K$ (for **23**), close to the expected value for six uncoupled Mn^{IV} ions (11.2 $cm^3\ mol^{-1}\ K$). For both compounds $\chi_M T$ values decrease as the temperature falls, indicating a net antiferromagnetic behavior, although the more pronounced decline observed for **23** reveals that it presents a stronger antiferromagnetic behavior. χ_M versus T plots of both compounds (inset in Figure 58) show a maximum at 13 and 30 K for **22** and **23**,

respectively; below this temperature χ_M values tend to 0, indicating that the ground state of these compounds is $S = 0$.

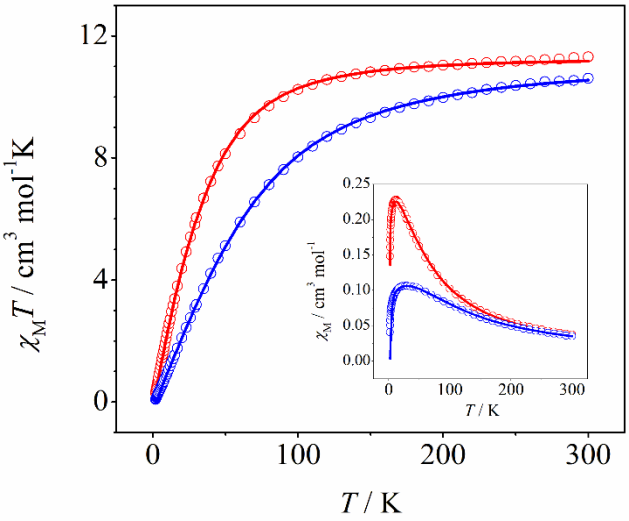

Figure 58. $\chi_M T$ versus T plots and χ_M versus T (inset) for **22** (red) and **23** (blue); the solid line corresponds to the best fit of the experimental data.

Figure 59 shows the four different Mn···Mn exchange pathways that may be considered to explain the magnetic behavior. The most important magnetic interactions are with the neighbor Mn^{IV} ions, J_1 and J_2 for the $[Mn^{IV}_2(\mu_3\text{-O})_2(\mu\text{-RCOO})]^{3+}$ and $[Mn^{IV}_2(\mu_4\text{-O})(\mu\text{-RCOO})_2]^{4+}$ subunits, respectively. Moreover, there are the magnetic interaction between alternated Mn^{IV} ions (J_3) and the magnetic interaction between the facing-neighbor (J_4). The Heisenberg spin Hamiltonian (H) considered is

$$H = -J_1(S_1S_2 + S_3S_4 + S_5S_6) - J_2(S_2S_3 + S_4S_5 + S_1S_6) - J_3(S_1S_3 + S_2S_4 + S_3S_5 + S_4S_6 + S_1S_5 + S_2S_6) - J_4(S_1S_4 + S_2S_5 + S_3S_6) \quad \text{Eq. 11}$$

where $S_1 = S_2 = S_3 = S_4 = S_5 = S_6 = 3/2$.

Note: The Heisenberg spin Hamiltonian in PHI program is $H = -2JS_1S_2$. However, all J values presented in this chapter are referred to the spin Hamiltonian $H = -JS_1S_2$, as in Eq. 11.

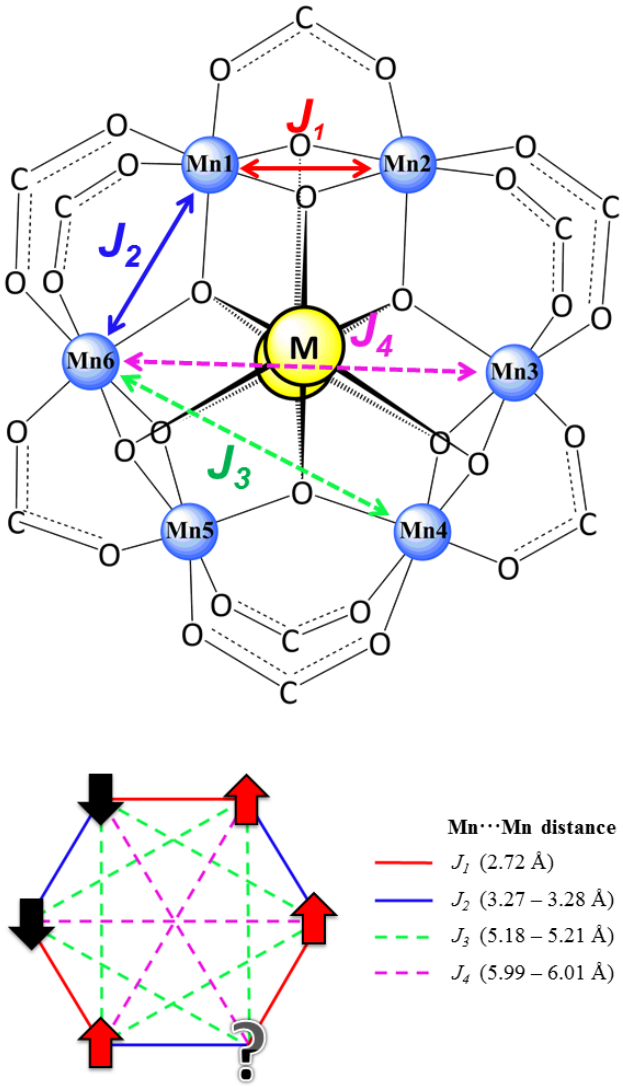

Figure 59. Schematic representation of the possible Mn···Mn exchange pathways in **22** (Ca^{2+}) and **23** (Sr^{2+}). The ranges of Mn···Mn distances for each bridging block are shown in parentheses.

Several fittings of the experimental data were performed, screening different values of the magnetic coupling constants and constraining or omitting some parameters, but no appropriate fitting was obtained without having good initial values. Therefore, the results of the DFT calculations (presented below) were used to guide the fitting, concretely to anticipate the nature and the magnitude of each magnetic coupling. The experimental data were fitted (300–2 K) using the *PHI* program[165] and, with the aim to avoid overparametrization, the *g*-factor was fixed to 2.00.

In a first approach, the experimental data were fitted considering J_3 and J_4 negligible. In spite of obtaining reasonable values of J_1 and J_2, the theoretical curve did not reproduce properly the shape of the maxima of the χ_M versus T plots (shown in Figure S21 and in Table 18). Therefore, the inclusion of these parameters seems to be necessary to fit the whole data.

Nevertheless, J_3 and J_4 could not be determined fitting the experimental data because they ended up in abnormal values. The fit was also performed considering $J_3 = J_4$, to get an average value, but the obtained values were too high.

Therefore, the experimental curves were fitted with J_3 and J_4 set to the values of the DFT calculations to better determine J_1 and J_2 and to avoid overparametrization. The results of the fit are collected in Table 18 (Fit 2). As observed, the most important magnetic coupling constants J_1 and J_2 are of opposite sign, indicating an antiferromagnetic and a ferromagnetic coupling, respectively. This fact was unpredictable and made the fitting very challenging. A survey of the residual between the experimental and calculated data for different J_1 and J_2 couples (Figure 60) shows that, for both compounds, the accuracy for J_2 values are minor than for J_1 values; hence, small changes of J_1 profoundly affects the quality of the fitting.

Table 18. List of magnetic coupling constant from the fits of $\chi_M T$ versus T plots for **22** and **23** and those from DFT calculations (see Figure 59 for the J assignment). Fit 1 considers only two coupling constants with the neighbor ions, and Fit 2 includes four magnetic exchanges incorporating long distance interactions.

	22 (M = Ca^{2+})			**23 (M = Sr^{2+})**		
J / cm^{-1}	**Fit 1**	**Fit 2**	**Calc**	**Fit 1**	**Fit 2**	**Calc**
J_1	**–10.4 ± 0.1**	**–8.8 ± 0.1**	**–12.5**	**–20.3 ± 0.2**	**–17.5 ± 0.1**	**–29.7**
J_2	**+10.5 ± 0.5**	**+14.4 ± 0.6**	**+27.8**	**+13.7 ± 0.7**	**+19.7 ± 0.5**	**+17.3**
J_3	-	–1.6*	–1.6	-	–3.3*	–3.3
J_4	-	–1.5*	–1.5	-	–1.3*	–1.3
R [a]	$5.4 \cdot 10^{-4}$	$3.5 \cdot 10^{-5}$		$3.8 \cdot 10^{-3}$	$3.6 \cdot 10^{-4}$	

[a] $R = \Sigma[(\chi_M T)_{exp} - (\chi_M T)_{calcd.}]^2 / \Sigma[(\chi_M T)_{exp}]^2$; * Taken from the DFT results.

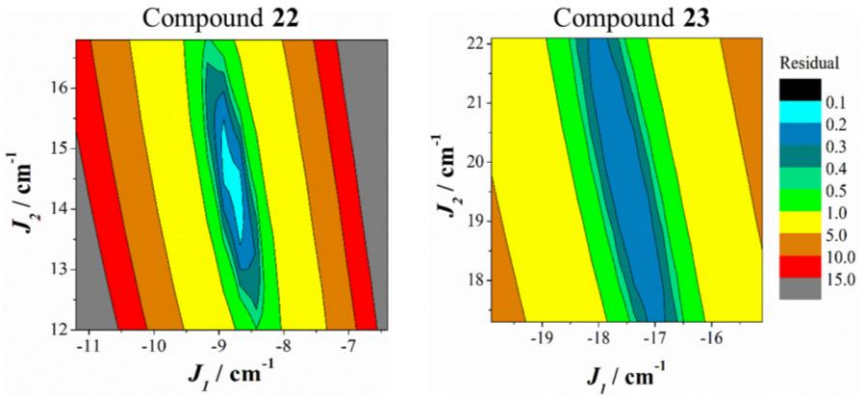

Figure 60. Contour plot of the residual for different J_1 and J_2 values. The J_3 and J_4 values, obtained from the DFT calculations, were fixed. Residual means the error of the fit and smallest values corresponds to the best fits.

The diagram of energy levels (shown in Figure S22) calculated with the *J* values of this latter fit, confirms that the ground state is $S = 0$. This diagram also reveals that the separation between states is greater for **23** than for **22**, thus the ground state is more isolated in **23.**

For **22**, the magnitude of the ferromagnetic interaction ($J_2 \approx +14$ cm^{-1}) is greater than that of the antiferromagnetic one ($J_1 \approx -9$ cm^{-1}); whereas for **23**, with strontium, the magnitude of both interactions is similar ($J_1 \approx -18$ cm^{-1} and $J_2 \approx +20$ cm^{-1}). Comparison between both compounds shows that the most relevant difference is in the value of the antiferromagnetic interaction J_1, stronger for **23** than for **22**. This fact could explain the variation in the net magnetic behavior between both compounds. From DFT calculations (see below), J_1 and J_2 are assigned to the $[Mn^{IV}_2(\mu_3\text{-}O)_2(\mu\text{-}RCOO)]^{3+}$ and $[Mn^{IV}_2(\mu_4\text{-}O)(\mu\text{-}RCOO)_2]^{4+}$ subunits, respectively. These results suggest that the magnetic behavior for **22** and **23** is mainly governed by the competition between the magnetic interactions with the adjacent Mn ions (J_1 and J_2). Consequently, there is spin frustration, as shown in Figure 59.

The *J* value for the $[Mn^{IV}_2(\mu_3\text{-}O)_2(\mu\text{-}RCOO)]^{3+}$ subunit ($J_1 \approx -9$ cm^{-1} for **22** and -18 cm^{-1} for **23**) is significantly weaker than expected for this kind of core (from –248 to –73 cm^{-1}),[243] probably due to the addition of both structural and electronic perturbations presumably caused by the M^{2+} ions. On the one hand, the attachment of the M^{2+} ions (located in *trans* to carboxylate ligand) to the $[Mn^{IV}_2(\mu_3\text{-}O)_2(\mu\text{-}RCOO)]^{3+}$ subunits makes the Mn_2O_2 ring closer to planarity than in discrete dinuclear compounds,[243] enlarging the Mn···Mn distance (from ~2.65 to 2.72 Å) for an identical Mn–O–Mn angle of 95°. On the other hand, there is also a plausible electronic effect of the M^{2+} ions that may affect the Mn···Mn interaction (see below).

As mentioned before, the $[Mn^{IV}_2(\mu_4\text{-}O)(\mu\text{-}RCOO)_2]^{4+}$ subunit is practically unknown and therefore, there is a shortage of knowledge of its exchange interaction (J_2). Nevertheless, there are two theoretical studies reported in the literature for hypothetical $[Mn^{IV}_2(\mu\text{-}O)(\mu\text{-}RCOO)_2(NH_3)_6]^{4+}$ complexes.[226,244] In basis to these studies, the Mn···Mn interaction for this subunit would be antiferromagnetic. Contrary, this interaction in **22** and **23** is ferromagnetic ($J_2 \approx +14$ cm^{-1} for **22** and +20 cm^{-1} for **23**). The structural differences between this subunit in hypothetical complexes and in these wheels are insufficient to interpret the switch from antiferromagnetic to ferromagnetic interaction.

Several studies have focused their attention on the electronic changes caused by Ca^{2+} over Mn ions in Mn-Ca cubane-like structures (Mn-Ca^{2+} WOC and model compounds). The presence of Ca^{2+} (Lewis acid) modifies the electronic structure of Mn and this effect is similar

to the observed with the protonation of the oxo bridges.[96] The same explanation seems to justify the quenching of antiferromagnetic exchange (from –230 to –8 cm^{-1}). Either protonation or the attachment of a Lewis acid such as Ca^{2+} weakens the Mn–O bonds and decreases dramatically their participation in the antiferromagnetic π pathways,[226,227] and in some cases a reversal to ferromagnetic coupling is observed.[226] With this frame, the attachment of either Ca^{2+} or Sr^{2+} (with similar acidities) to the Mn^{IV}_6 wheel may have important influence on the Mn···Mn interactions of both the Mn_2O_2 and Mn_2O subunits, altering the antiferromagnetic π pathways that dominate these interactions. This influence could be greater for the Mn_2O subunit, in which a single oxygen atom with tetrahedral environment interacts with two M^{2+} ions.

Up to now, four Mn^{IV} wheels with Bi^{III} and Ce^{IV} in the center are reported in the literature,[240–242] but the fit of the magnetic data was reported only for the cerium compounds.[240,241] The most relevant structural parameters and the magnetic coupling constant are collected in Table 19.

Table 19. Structural parameters and magnetic coupling constants for $Mn^{IV}_6M^{z'}_x$ wheels.

Double-oxo bridge: $[Mn^{IV}_2(\mu_3\text{-}O)_2(\mu\text{-}RCOO)]^{3+}$ subunit									
	$M^{z'}$	***x***	***r*** [a] **(Å)**	***z'/r*** [b] **($Å^{-1}$)**	**Mn···Mn (Å)**	**Mn–O (Å)**	**Mn–O–Mn (º)**	**Mn–O–O–Mn (º)**	***J*$_1$ (cm^{-1})**
A3[240]	Ce^{IV}	1	1.01	3.96	2.71	1.86; 1.81*	93.3; 96.5*	169.2	–11.6
B3[241]	Ce^{IV}	2	1.01	3.96	2.70	1.85	93.6	163.7	12.4
22	Ca^{2+}	2	1.14	1.75	2.72	1.84	95.22	171.0	–8.8
23	Sr^{2+}	2	1.32	1.52	2.72	1.84	95.54	172.9	–17.5
Single-oxo bridge: $[Mn^{IV}_2(\mu_4\text{-}O)(\mu\text{-}RCOO)_2]^{4+}$ subunit									
	$M^{z'}$	***x***	***r*** [a] **(Å)**	***z'/r*** [b] **($Å^{-1}$)**	**Mn···Mn (Å)**	**Mn–O (Å)**	**Mn–O–Mn (º)**	***J*$_2$ (cm^{-1})**	
A3[240]	Ce^{IV}	1	1.01	3.96	3.29	1.83	127.7	–1.2	
B3[241]	Ce^{IV}	2	1.01	3.96	3.40	1.91	125.2	+8.3	
22	Ca^{2+}	2	1.14	1.75	3.27	1.82	127.9	+14.4	
23	Sr^{2+}	2	1.32	1.52	3.28	1.81	130.6	+19.7	

[a] Ionic radii of the $M^{z'}$ ion; [b] charge/ionic radii (in Å) ratio of the $M^{z'}$ ion; * The first one is measured with the oxo ligand linked to the Ce^{IV} ion and the second one with the other oxo ligand. **A3**: $[CeMn_6O_9(CH_3COO)_9(MeOH)(H_2O)_2]ClO_4$; **B3**: $[Ce_2Mn_6O_6(OH)_5(^tBuPO_3)_6(CH_3COO)_3]$.

For the Mn_2O_2 subunit, the most significant differences are found in the Mn–O–Mn angles, and in the planarity of the core (Mn–O–O–Mn angle). In both cases, these angles increase with the ionic radii of the $M^{z'}$ ions. For the compounds with two central ions (x = 2), J_1 switches from a positive value for the cerium compound – with the greatest z'/r ratio – to the highest negative value for the strontium one (**23**) – with the smallest z'/r ratio. A similar dependence of the structural and magnetic parameters is observed for the Mn_2O subunit.

The Mn–O–Mn angle increases with the ionic radii of the $M^{x'}$ ion and, with the exception of the compound with only one cerium (x = 1), J_2 increases. Thus, the greater the angle is and/or the more voluminous $M^{x'}$ ions are, the more ferromagnetic J_2 becomes.

Unfortunately, the number of analogous wheels is too scarce to propose a good correlation. However, some points could be remarked: (*a*) the presence of one or two $M^{x'}$ ions could change the magnetic interactions; (*b*) there is a relation between the $M^{x'}$ radii and the wheel structural parameters; (*c*) the magnetic properties seems to be correlated with both the structural parameters and the electronic properties of the $M^{x'}$, without knowing which is the actual contribution of each one to the Mn···Mn interaction.

Theoretical calculations

In order to understand the magnetic behavior of **22** and **23**, theoretical studies based on DFT calculations were performed. First, the magnetic coupling constants for **22** and **23** from their crystallographic data were calculated. All paramagnetic centers are Mn^{IV}, a d^3 metal ion in a pseudooctahedral environment, containing three unpaired electrons. The energy for nine different spin distributions were computed, corresponding to one high-spin and eight low-spin states. Four different coupling constants for these highly symmetric compounds were considered: two alternate J_1 and J_2 exchange constants for neighboring manganese ions, and two others between non-adjacent ones across the alkaline earth ion, J_3 and J_4. The J values, derived from their computed relative energies, are shown in Table 18. The relative energies for the calculated spin distributions are shown in Table S17.

The calculations for **22** and **23** show an important ferromagnetic interaction for the $[Mn_2(\mu_4\text{-}O)(\mu\text{-}RCOO)_2]^{4+}$ subunit where the $Mn^{IV}\cdots Mn^{IV}$ distance is around 3.3 Å, being $J_2 \approx +28$ cm^{-1} (**22**) and +17 cm^{-1} (**23**). For the $[Mn_2(\mu_4\text{-}O)_2(\mu\text{-}RCOO)]^{3+}$ subunit (with Mn···Mn distances ~2.7 Å), an antiferromagnetic interaction is found, being $J_1 \approx -12$ cm^{-1} (**22**) and –30 cm^{-1} (**23**). These results are in accordance with the fitting parameters, as they present the same signs and relative magnitudes for J_1 and J_2.

Up to this point, we have seen that there are substantial differences between the magnetic behavior of **22** (Ca^{2+}) and **23** (Sr^{2+}); the latter presents a stronger net antiferromagnetic behavior. Hence, it seems that there is some effect of the alkaline earth ions, fact that could be due to the structural dissimilarities between **22** and **23** presented before, to electronic contributions of the M^{2+} ions, or to the addition of the two previous factors. With the aim

to provide further insights into the influence of alkaline earth ion over the magnetic behavior, the calculations performed for **22** and **23** were extended to three hypothetical compounds. To do so, the Ca^{2+} ions were replaced with Mg^{2+} or Sr^{2+} and the Ca^{2+} ions were also depleted in the frozen geometry of **22**, following the methodology reported by Ruiz *et al.*[177–179] At first glance, it would be desirable to calculate *J* values with the energies obtained for the optimized geometries. However, small deviations that may occur during the optimization can lead to large changes in the magnetic behavior.[26] For this reason, the structural parameters of **22** were used for the hypothetical compounds. As a result, three hypothetical compounds, labeled as Mg^{2+} *model*, Sr^{2+} *model*, and M^{2+}-absent *model*, that only differ in the central ions were studied. It should be noted that such calculations just provide qualitative indications, recognizing the limitations of using the structure of **22**.[179]

Comparison of the results obtained for **22** (Ca^{2+} *crystal*) and the three hypothetical compounds may provide a further insight into the electronic effects of the M^{2+} ions; whereas the comparison between Sr^{2+} *model* and **23** (Sr^{2+} *crystal*) could demonstrate the effect of the structural changes around the Mn^{IV} ions.

Table 20 shows the calculated coupling constants for **22**, **23** and the three hypothetical compounds. The magnetic coupling constant of the double-oxo bridge (J_1) follows the trend: M^{2+}-absent *model* < Sr^{2+} *model* < Ca^{2+} *crystal* (**22**) < Mg^{2+} *model*. This trend seems to be correlated with the polarizing character of these ions, which goes from M^{2+}-absent *model* (no-polarizing effect) to Mg^{2+} (the most polarizing). Similarly, the magnetic interaction of the single-oxo bridge (J_2) seems to follow the same trend, with the exception of the M^{2+}-absent model. The cause of this divergence could be the electronic environment of the oxo-bridge in this subunit, which changes drastically because of the interaction with the two M^{2+} ions. Structural parameters also appear to be relevant for the magnetic interactions because J_1 and J_2 values undergo a change when a structural modification is done (from Sr^{2+} *model* to Sr^{2+} *crystal* (**23**)).

Table 20. Calculated magnetic coupling constants (in cm^{-1}) for **22**, **23** and the three hypothetical compounds.

J / cm^{-1}	Sr^{2+} *crystal* (23)	Sr^{2+} *model**	Ca^{2+} *crystal* (22)	Mg^{2+} *model**	M^{2+}-absent *model**
J_1	**–29.7**	**–16.7**	**–12.5**	**+1.6**	**–42.1**
J_2	**+17.3**	**+15.3**	**+27.8**	**+56.5**	**+42.6**
J_3	–3.3	–2.0	–1.6	–5.8	–11.0
J_4	–1.3	–1.4	–1.5	–2.9	–4.8
	← Structural change →		← Change of M^{2+} ion →		

* Hypothetical isoelectronic compounds using the geometry of **22**, but replacing Ca^{2+} ions with Mg^{2+} or Sr^{2+} ones or just removing the Ca^{2+} ions.

To illustrate the previous statements, the energy diagrams of four spin configurations are represented in Figure 61. As an example, we chose the full ferromagnetic (*hs*) and the full antiferromagnetic (*ls6*) configurations, together with the two lowest in energy that contain ferro and antiferromagnetic contributions (*ls7* and *ls4*). All energies were arbitrary referred to the full ferromagnetic configuration (*hs*). As may be noticed, the spin configurations that contain antiferromagnetic contribution (*ls6*, *ls7*, and *ls4*) become more unstable with the polarizing character of the M^{2+} ions. This theory is consistent with the experimental behavior of the $Mn^{IV}{}_6M^{z'}{}_2$ wheels. For instance, the compound with $M^{z'} = Ce^{IV}$ (**B3** in Table 19) shows a net ferromagnetic behavior, according to the high z'/r ratio (3.96 $Å^{-1}$) of the Ce^{IV} ion. Consistently, **23** (with Sr^{2+}) presents a stronger antiferromagnetic behavior than **22** (with Ca^{2+}), also in agreement with their z'/r ratios (1.52 for Sr^{2+}, 1.75 for Ca^{2+}). Nevertheless, if one relatively compares Ca^{2+} *crystal* (**22**), Sr^{2+} *model* and Sr^{2+} *crystal* (**23**), it may be noticed that a change of ion affects with a similar magnitude than a structural modification does. Hence, the effect of the structural parameters should not be considered negligible.

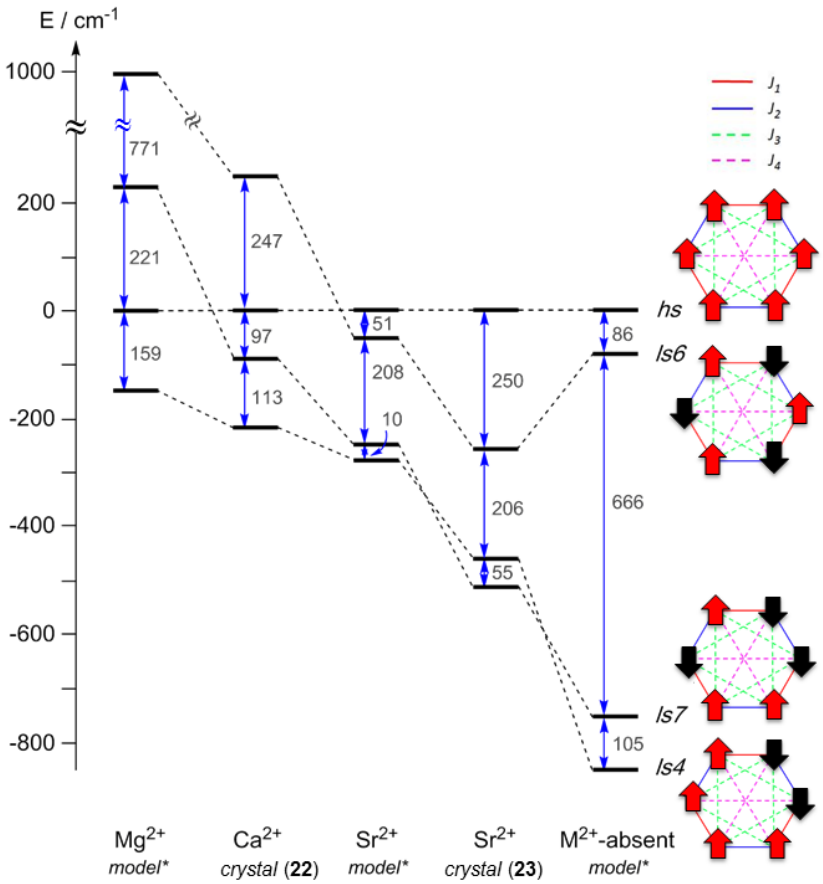

Figure 61. Energy levels of the different spin states for compounds with a $[Mn^{IV}{}_6M_2O_9]^{10+}$ core. High-spin states (*hs*) are arbitrarily taken as zero. * Hypothetical isoelectronic compounds using the geometry of **22**, but replacing Ca^{2+} ions with Mg^{2+} or Sr^{2+} ones or just removing the Ca^{2+} ions.

Summary

Two new heterometallic compounds with formula $[Mn^{IV}_6M_2O_9(4\text{-}^t BuC_6H_4COO)_{10}(4\text{-}^t BuC_6H_4COOH)_5]$ were synthesized with M = Ca^{2+} and Sr^{2+}. The resolution of their crystal structures revealed that the core of these compounds consists of a planar Mn^{IV}_6 ring, where Mn ions are alternately bridged by $(\mu_3\text{-}O)_2(\mu\text{-}RCOO)$ and $(\mu_4\text{-}O)(\mu\text{-}RCOO)_2$ ligands. Two alkaline earth ions (Ca^{2+} or Sr^{2+}) are located in the center and at both sides of the wheel, linked to the oxo bridges, generating three fused $[Mn_2M_2O_4]^{4+}$ cuboids. The structural parameters around the Mn ions are affected by the presence of M^{2+} ions, because they differ from the dinuclear compounds with analogues bridges.

The analysis of the structural data of the Mn_6 wheels shows that these compounds could be classified in two groups in basis to the number of oxo bridges. The diameter of the wheels does not depend on the ionic radii of the $M^{x'}$, contrary to one's expectations; however, it depends on the oxidation state of the Mn ions. Furthermore, the formation of Mn^{IV}_6 wheels seems to be more favorable for large ions than for small ones, such as Mg^{2+}.

The net antiferromagnetic behavior found for these compounds is mostly due to the competition between the ferro- and antiferromagnetic interactions between adjacent Mn^{IV} ions. DFT calculations revealed that the ferromagnetic contribution corresponds to the $[Mn_2(\mu_4\text{-}O)(\mu\text{-}RCOO)_2]^{4+}$ subunit (J_2). In spite of the diamagnetic character of the alkaline earth ions, their influence on the magnetic behavior was evidenced and correlated with their polarizing effect and electron withdrawing character. Moreover, the magnetic interactions between non-adjacent ions was not negligible.

1.6. Tetranuclear Compounds with $[Mn^{III}_4O_2]^{8+}$ Core

First insights

In the past years many tetranuclear Mn compounds have been synthesized and characterized either to mimic the water oxidizing center[81] or to study the ground-state spin frustration that is characteristic in this kind of compound.[245,246] Moreover, such clusters possess large numbers of unpaired electrons, making them attractive as precursors to magnetic materials.[20] Some of the first compounds synthesized contained a $[Mn_4O_2]^{6+/7+/8+}$ core, where the metals could be arranged in either a planar or non-planar ("butterfly") fashion (Figure 62), and the Mn oxidation states are $Mn^{II}_2Mn^{III}_2$, $Mn^{II}Mn^{III}_3$ or Mn^{III}_4.[245–259]

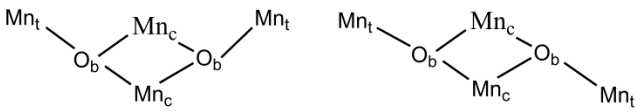

Figure 62. Schematic representation of two arrangements for $[Mn_4(\mu_3\text{-}O)_2]$ core. Label code: Mn_c = central Mn ion, Mn_t = terminal Mn ion, and O_b = bridging oxygen atom.

The variability of the ground-state spin and the presence of spin frustration in these tetranuclear compounds have been profoundly studied for both Mn^{III}_4 and mixed-valence compounds. The resulting ground state depends on the relative magnitude of the magnetic interactions between the central Mn ions (J_{cc} or J_1) and those between central and terminal ions (J_{ct}), both being antiferromagnetic. In particular, for the Mn^{III}_4 compounds the most common ground states have $(S_T, S_{cc}, S_{tt}) = (2, 2, 4)$ if $|J_1|/|J_{ct}| < 2.5$ or $(3, 1, 4)$ if $|J_1|/|J_{ct}| = 2.5$–4.9. When $|J_1|/|J_{ct}| > 4.9$, five energetically degenerate states, $(n, 0, n)$ with $n = 0$–4, become the ground state, corresponding to two non-interacting Mn_t ions.[246]

The analysis of the magnetic data for these compounds is rather challenging, since there are five Mn···Mn interactions and the presence of Mn^{III} ions may lead to substantial zero-field splitting (ZFS) effects that make such properties more difficult to understand. In fact, among several examples found in the literature, the analyses were performed applying severe approximations[246,259] or without analyzing the data completely, especially in the low temperature range.[245,247,250]

In this work we present the synthesis and crystal structures of two new $[Mn^{III}_4O_2]^{8+}$ compounds with general formula $[Mn_4(\mu\text{-}O)_2(\mu\text{-}4\text{-}RC_6H_4COO)_{7-m}(L)_{2m}(phen)_2](ClO_4)_{1+m}$, where R = 4-MeO (**24**) or 4-^{t}Bu (**25**) and m = 0 or 1. We also report a deeper study of the magnetic properties and the influence of the relative magnitude of the different $Mn_c\cdots Mn_t$ interactions in the resulting diagram of energy for the S_T spin states. The inclusion of the axial anisotropy parameter (D_{Mn}) and the consideration of the relative disposition of the Jahn-Teller axes of the Mn^{III} ions enabled us to completely fit the magnetic data and to estimate approximate values of the ZFS of the Mn^{III} ions.

Synthesis

Both tetranuclear compounds **24** and **25** were obtained from the reaction of comproportionation between Mn^{II} and MnO_4^- in the presence of a substituted derivative of benzoic acid and 1,10-phenanthroline (phen), leading to a dark red solution. The stoichiometry of this reaction is

$$3.2\ Mn(ClO_4)_2 + 7-m\ 4\text{-}RC_6H_4COOH + 0.8\ NBu_4MnO_4 + 2\ phen \rightarrow [Mn_4(\mu\text{-}O)_2(\mu\text{-}4\text{-}RC_6H_4COO)_{7-m}(L)_{2m}(phen)_2](ClO_4)_{1+m} + 0.8\ NBu_4ClO_4 + 5.4-m\ HClO_4 + n\ H_2O$$

where R = MeO or ^{t}Bu and L is a monodentate ligand. If R = MeO, compound **24** is formed, which contains seven carboxylate ligands (m = 0). On the other hand, compound **25** is formed when R = ^{t}Bu, which contains six carboxylate ligands and two monodentate ligands (L) (m = 1).

The mother liquors of **24** and **25** were left to slowly evaporate, but no solid was obtained from none of them, indicating that both compounds are highly soluble in acetonitrile. Thus, they needed to be crystallized by mixing the mother solution with absolute ethanol (**24**) or by adding a huge excess of ClO_4^- anion (**2**). For compound **24**, the crystallization from different CH_3CN:EtOH mixtures was tried, but no differences were observed changing the CH_3CN/EtOH volume ratio (from 0.3 to 0.7). In all cases, the reaction yield was about 25% considering the stoichiometry of the reaction above. In contrast, we had some difficulties finding the optimum conditions to obtain compound **25** in appreciable yield. Its crystallization needed to be assisted by the addition of about 22 equivalents of ClO_4^- anion, leading to **25** in 16% yield. If the amount of ClO_4^- anion used is decreased, the crystallization becomes very slow and ineffective. For instance, it took nearly three months to obtain only a couple of crystals of **25** using 11.5 equivalents of ClO_4^-.

IR spectra of these compounds show several characteristic bands assigned to the asymmetric and symmetric vibrations of the carboxylate groups (~1560 and 1365 cm^{-1}, respectively), the phen (~1600, 1520, 1456, 854, 720 cm^{-1}) and the ClO_4^- anion (~1110 and ~620 cm^{-1}). The value $\Delta\nu = \nu_a(COO) - \nu_s(COO) \approx 200$ cm^{-1} is indicative of carboxylate ligands coordinated in bidentate bridging mode ($\mu_{1,3}$).[14]

Description of structures

The crystal structure of compound **24** consists of two entire $[Mn_4(\mu\text{-}O)_2(\mu\text{-}4\text{-}MeOC_6H_4COO)_7(phen)_2]^+$ complexes with no imposed symmetry, two perchlorate anions and molecules of solvent. Selected interatomic distances and angles are listed in Table 21.

The two complexes are conformational isomers that slightly differ in some structural parameters (see Figure S23). Both of them contain a $[Mn^{III}_4(\mu_3\text{-}O)_2]$ core with seven carboxylate bridges and two chelating 1,10-phenanthroline (phen) on the periphery. The four Mn atoms are arranged in a butterfly-like structure (Figure 62), where there is a $Mn_{c2}O_2$ rhombus to which two terminal (Mn_t) ions are attached – one to each μ_3-O ligand (see Figure 63). The $Mn_{c2}O_{b2}$ rhombus is far from being planar, with Mn2–O1–O2–Mn3 and Mn5–O25–O24–Mn6 angles of 166 and 169º. These Mn_c ions are also linked through a carboxylate bridge that likely binds the $Mn_{c2}O_{b2}$ rhombus, as observed for other systems in the $[Mn_2(\mu\text{-}O)_2(\mu\text{-}RCOO)]$.[243,244] The two terminal Mn ions are placed above the plane of the Mn_2O_2 rhombus, having Mn_t–Mn_c–Mn_c–O_b angles of ~15º (defined as Mn1–Mn3–Mn2–O1, Mn4–Mn2–Mn3–O2, Mn8–Mn6–Mn5–O25 and Mn7–Mn5–Mn6–O24 angles in Table 21). Each Mn_t ion is also linked to the central ions (Mn_c) by either one or two carboxylate groups. Within the seven carboxylate ligands, four of them are approximately in the plane of the central $Mn_{c2}O_2$ rhombus, whereas the other three ones are perpendicular to this plane.

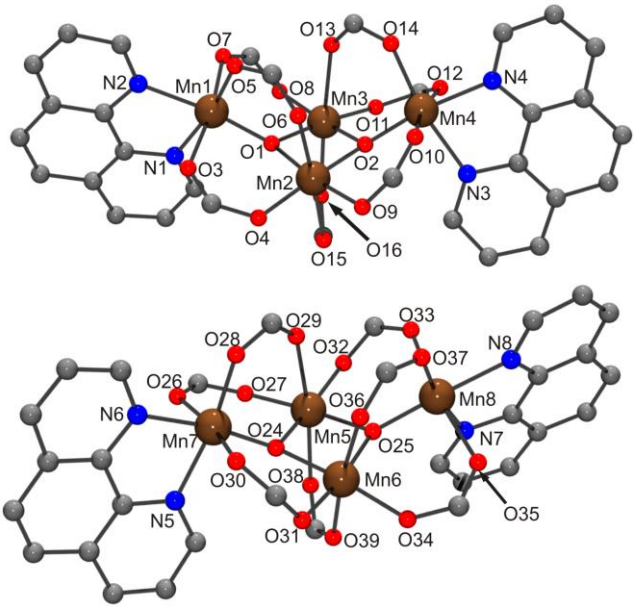

Figure 63. Cationic complexes of **24**. 4-$MeOC_6H_4$– groups and H atoms of phen have been omitted for better clarity. Color code: Mn^{III}, brown; C, gray; N, blue; O, red.

Table 21. Selected interatomic distances (Å) and angles (º) for compound **24** with standard deviations in parentheses.

Mn1–O1	1.834(2)	Mn5–O24	1.900(2)
Mn1–O5	1.940(2)	Mn5–O25	1.903(2)
Mn1–N2	2.061(3)	Mn5–O32	1.927(2)
Mn1–N1	2.079(3)	Mn5–O27	1.943(2)
Mn1–O7	2.124(2)	Mn5–O38	2.109(2)
Mn1–O3	2.143(2)	Mn5–O29	2.174(2)
Mn2–O2	1.908(2)	Mn6–O24	1.898(2)
Mn2–O1	1.909(2)	Mn6–O25	1.900(2)
Mn2–O4	1.961(2)	Mn6–O34	1.932(2)
Mn2–O9	1.962(2)	Mn6–O31	1.968(2)
Mn2–O15	2.148(2)	Mn6–O36	2.204(2)
Mn2–O6	2.171(2)	Mn6–O39	2.245(2)
Mn3–O2	1.896(2)	Mn7–O24	1.834(2)
Mn3–O1	1.898(2)	Mn7–O28	1.938(2)
Mn3–O11	1.945(2)	Mn7–N6	2.064(3)
Mn3–O8	1.966(2)	Mn7–N5	2.083(3)
Mn3–O16	2.201(2)	Mn7–O30	2.141(2)
Mn3–O13	2.213(2)	Mn7–O26	2.193(2)
Mn4–O2	1.834(2)	Mn8–O25	1.847(2)
Mn4–O14	1.943(2)	Mn8–O37	1.911(2)
Mn4–N4	2.049(3)	Mn8–N7	2.069(3)
Mn4–N3	2.092(3)	Mn8–N8	2.076(3)
Mn4–O10	2.144(2)	Mn8–O35	2.179(2)
Mn4–O12	2.153(2)	Mn8–O33	2.181(2)
Mn2···Mn3	2.8595(7)	Mn5···Mn6	2.8393(7)

Mn1···Mn2	3.3085(9)	Mn5···Mn7	3.2837(9)
Mn1···Mn3	3.3617(9)	Mn6···Mn7	3.409(1)
Mn2···Mn4	3.3553(8)	Mn5···Mn8	3.3813(9)
Mn3···Mn4	3.3033(9)	Mn6···Mn8	3.3323(8)
Mn1···Mn4	5.525(1)	Mn7···Mn8	5.693(1)
O1–Mn1–N2	170.49(11)	O24–Mn5–O32	171.57(10)
O5–Mn1–N1	169.48(10)	O25–Mn5–O27	172.99(10)
O7–Mn1–O3	172.00(9)	O38–Mn5–O29	173.53(10)
O2–Mn2–O4	176.16(10)	O24–Mn6–O34	175.18(10)
O1–Mn2–O9	172.61(9)	O25–Mn6–O31	170.49(9)
O15–Mn2–O6	176.63(9)	O36–Mn6–O39	172.68(9)
O1–Mn3–O11	174.01(9)	O24–Mn7–N6	168.58(10)
O2–Mn3–O8	171.57(9)	O28–Mn7–N5	170.86(11)
O16–Mn3–O13	176.50(9)	O30–Mn7–O26	170.93(10)
O2–Mn4–N4	170.18(10)	O37–Mn8–N7	169.16(11)
O14–Mn4–N3	168.83(10)	O25–Mn8–N8	171.81(10)
O10–Mn4–O12	170.46(9)	O35–Mn8–O33	170.26(9)
Mn1–O1–Mn3	128.50(11)	Mn7–O24–Mn6	131.98(12)
Mn1–O1–Mn2	124.21(11)	Mn7–O24–Mn5	123.12(12)
Mn3–O1–Mn2	97.37(9)	Mn6–O24–Mn5	96.77(10)
Mn3–O2–Mn2	97.49(10)	Mn6–O25–Mn5	96.58(10)
Mn4–O2–Mn3	124.66(11)	Mn8–O25–Mn6	125.56(11)
Mn4–O2–Mn2	127.49(11)	Mn8–O25–Mn5	128.77(12)
Mn2–O1–O2–Mn3	166.6(1)	Mn5–O25–O24–Mn6	169.2(1)
Mn1–Mn3···Mn2–O1	15.5(1)	Mn8···Mn6···Mn5–O25	14.7(1)
Mn4–Mn2···Mn3–O2	15.9(1)	Mn7···Mn5···Mn6–O24	13.9(1)
O15–Mn2···Mn1–O7	85.5(1)	O33–Mn8···Mn6–O39	89.8(1)
O16–Mn3···Mn4–O10	82.6(1)	O38–Mn5···Mn7–O30	91.7(1)

Compound **25** displays a similar crystal structure to **24**. The asymmetric unit consists of a half of $[Mn_4(\mu\text{-}O)_2(\mu\text{-}4\text{-}^tBuC_6H_4COO)_6(H_2O)_2(phen)_2]^{2+}$ and $[Mn_4(\mu\text{-}O)_2(\mu\text{-}4\text{-}^tBuC_6H_4COO)_6(CH_3CN)_2(phen)_2]^{2+}$ complexes, two perchlorate anions and molecules of solvent. The most relevant interatomic distances and angles are listed in Table 22. The cationic complexes also possess a $[Mn^{III}_4(\mu_3\text{-}O)_2]$ core but the Mn atoms do not have a butterfly arrangement (Figure 64). Instead, the terminal Mn ions (Mn_t) are situated in opposite sides of the $Mn_{c2}O_2$ plane (Mn_4 planar structure in Figure 62), with Mn_t–Mn_c–Mn_c–O_b angles of ~19º (defined as Mn1–Mn2–Mn2a–O1 and Mn3–Mn4–Mn4b–O8 angles in Table 22). As in **24**, either one or two carboxylate groups bridge the terminal Mn ions with the rhombus, but there is not the seventh carboxylate ligand that binds the two Mn_c ions. The positions of this seventh carboxylate are instead occupied by monodentate ligands that

also lay in opposites sides of the $Mn_{c2}O_{b2}$ rhombus. The two cationic complexes of **25** differ in their monodentate ligand, one of them containing two H_2O molecules and the other two CH_3CN molecules. The $Mn_{c2}O_{b2}$ rhombus is completely planar, having Mn2–O1–O1a–Mn2a and Mn4–O4–O4b–Mn4b angles of nearly 180º. Whether this is the cause or the effect of the difference between the structures of **24** and **25** is uncertain.

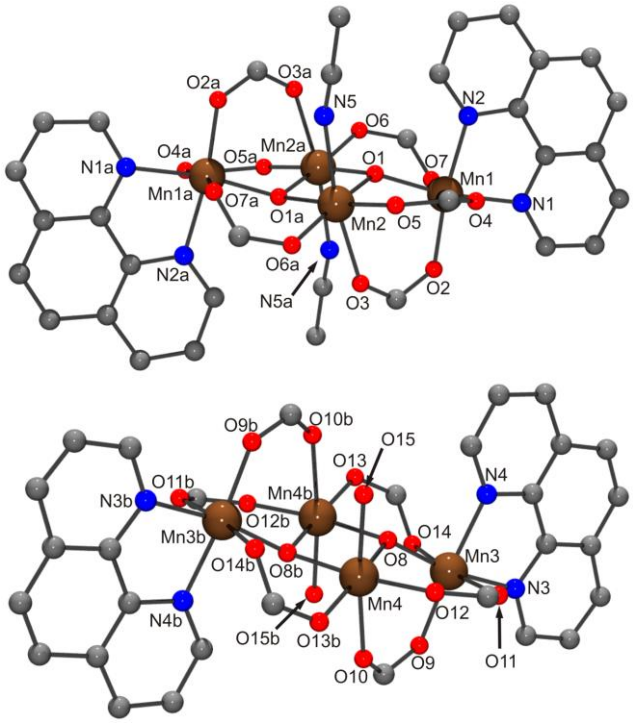

Figure 64. Cationic complexes of **25**. 4-^{t}BuC$_6$H$_4$– groups and H atoms of phen have been omitted for better clarity. Color code: Mn^{III}, brown; C, gray; N, blue; O, red.

Table 22. Selected interatomic distances (Å) and angles (º) for compound **25** with standard deviations in parentheses.

Mn1–O1	1.866(3)	Mn3–O8	1.861(3)
Mn1–O2	1.908(3)	Mn3–O9	1.926(3)
Mn1–N2	2.039(3)	Mn3–N4	2.033(3)
Mn1–N1	2.043(3)	Mn3–N3	2.037(3)
Mn1–O4	2.137(3)	Mn3–O11	2.087(3)
Mn1–O7	2.205(3)	Mn3–O14	2.218(3)
Mn2–O1	1.862(3)	Mn4–O8	1.891(3)
Mn2–O6a	1.914(3)	Mn4–O8b	1.908(3)
Mn2–O1a	1.918(3)	Mn4–O13b	1.937(3)
Mn2–O5	1.936(3)	Mn4–O12	1.940(3)
Mn2–O3	2.161(3)	Mn4–O10	2.141(3)
Mn2–N5	2.343(4)	Mn4–O15	2.219(3)
O1–Mn2a	1.918(3)	O8–Mn4b	1.908(3)
O6–Mn2a	1.914(3)	O13–Mn4b	1.937(3)
Mn2···Mn2a	2.8713(12)	Mn4···Mn4b	2.8909(12)

Mn1···Mn2	3.2623(8)	Mn3···Mn4	3.2488(8)
Mn1···Mn2a	3.3711(8)	Mn3···Mn4b	3.3607(8)
Mn1···Mn1a	5.9807(9)	Mn3···Mn3b	5.9448(9)
O2–Mn1–N2	171.23(13)	O9–Mn3–N4	170.02(12)
O1–Mn1–N1	169.46(13)	O8–Mn3–N3	168.50(12)
O4–Mn1–O7	167.96(10)	O11–Mn3–O14	170.55(10)
O1–Mn2–O6a	171.49(12)	O8–Mn4–O13b	171.32(12)
O1a–Mn2–O5	175.54(12)	O8b–Mn4–O12	173.29(11)
O3–Mn2–N5	169.34(12)	O10–Mn4–O15	171.24(10)
Mn2–O1–Mn1	122.13(14)	Mn3–O8–Mn4	119.96(14)
Mn1–O1–Mn2a	126.00(14)	Mn3–O8–Mn4b	126.15(14)
Mn2–O1–Mn2a	98.87(12)	Mn4–O8–Mn4b	99.09(12)
Mn2–O1–O1a–Mn2a	180.0(2)	Mn4–O4–O4b–Mn4b	180.0(1)
Mn1···Mn2···Mn2a–O1	18.5(1)	Mn3···Mn4···Mn4b–O8	19.8(1)
O7–Mn1···Mn2–N5	98.0(1)	O14–Mn3···Mn4–O15	97.5(1)

Symmetry codes: (a) 1–x,1–y,–z; (b) –x,1–y,1–z.

In spite of the differences between **24** and **25**, lots of structural parameters around the Mn ions are alike in both structures. The $Mn_c\cdots Mn_c$ distances are the shortest within the Mn···Mn ones, having values of ~2.85 (**24**) or ~2.88 (**25**) Å and with $Mn_c–O_b–Mn_c$ angles in the range 96 – 99º. The $Mn_c\cdots Mn_t$ distances where Mn ions are linked by a triple (μ-O)(μ-RCOO)$_2$ bridge (~3.25–3.31 Å) are shorter than the ones where the Mn ions are linked by a double (μ-O)(μ-RCOO) bridge (~3.35–3.41 Å). Similarly, the $Mn_c–O_b–Mn_t$ angles corresponding to the triple bridges (~120–126º) are smaller than the ones corresponding to the double bridges (~126–132º). As a result of the butterfly-like arrangement in compound **24**, the Mn_t ions are more distant (~5.60 Å) than the ones in **25** (~5.96 Å). All these structural parameters are in accord with those for compounds with $[Mn_4O_2]^{6+/7+/8+}$ core and carboxylate bridges.[245–260]

All Mn atoms in compounds **24** and **25** have an elongated pseudo-octahedral geometry, displaying Jahn-Teller distortion, as expected for Mn^{III} ions. Moreover, Jahn-Teller axes in Mn_c ions are almost parallel, while they are nearly perpendicular to those of Mn_t ions (Figure 65). Considering the z axes in the direction of the Jahn-Teller axes and unfairly assigning the x and y axes, approximate values of the octahedron axes lengths can be found by the addition of the Mn-ligands distances (see Table S18). To quantify the distortions of the coordination octahedra, the procedure described in Chapter 1.3 (Eq. 9 and Eq. 10) was followed. Note that all Mn ions display an elongated distortion (z axes are longer than x and y axes) and an almost inappreciable rhombic distortion (x and y axes are very similar in length) (see Table

S18). The central ions, Mn2, Mn3, Mn5, and Mn6 in **24**, and Mn2 and Mn4 in **25** (with ⊿ = 11.6–18.1%), are much more elongated than the terminal ones, (⊿ =7.8–10.5%).

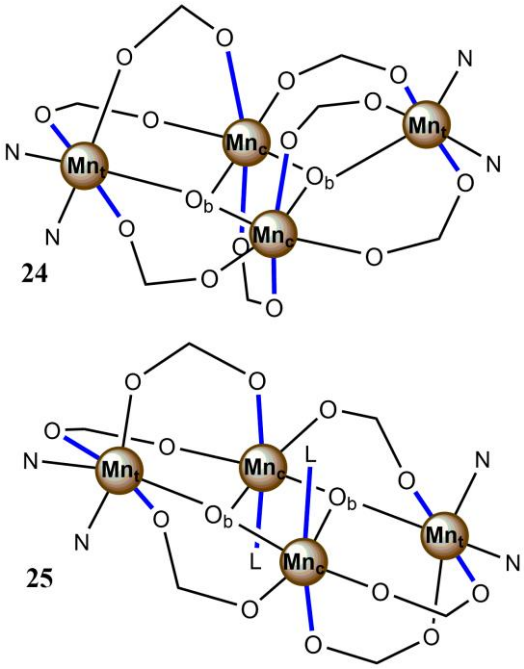

Figure 65. Schematic representation of the cationic complexes of **24** and **25**. Blue lines correspond to the Jahn-Teller axes. L could be H_2O or CH_3CN.

Magnetic properties

Magnetic susceptibility (χ_M) data were recorded for compound **24** and **25** from 300 to 2 K. $\chi_M T$ versus T and χ_M versus T plots for **24** and **25** are shown in Figure 66. Note that the molecular weight of **25** was referred to one Mn_4 unit, considering an average formula between the two entities. The $\chi_M T$ values at room temperature are 8.3 $cm^3 \cdot mol \cdot K$, which is quite below the expected value for four Mn^{III} ions (12.0 $cm^3 \cdot mol \cdot K$). $\chi_M T$ decreases with the temperature almost linearly until ~90 K and below this temperature it decreases drastically to ~0.4 $cm^3 \cdot mol \cdot K$ at 2 K, indicating a strong antiferromagnetic behavior. χ_M versus T plots for both compounds show nearly superimposable graphs between 300 and 80 K, but they differ below this temperature. While χ_M versus T plot of compound **24** displays a maximum at 9 K (χ_M ~ 0.14 $cm^3 \cdot mol$), the one of **25** is situated at 6 K (χ_M ~ 0.27 $cm^3 \cdot mol$). This difference can be also seen in the $\chi_M T$ versus T plots. The presence of these maxima suggest that both compounds have a ground state with $S = 0$. Magnetization (M) data were collected at 2.0 K and $M/N\mu\beta$ versus H plots for compounds **24** and **25** are shown in Figure 67. For

24, $M/N\mu_\beta$ increases progressively with the magnetic field (H) reaching $M/N\mu_\beta$ = 1.5 at ~5 T without saturating. On the other hand, $M/N\mu_\beta$ for **25** increases linearly until ~1.6 T and then grows more pronouncedly, reaching $M/N\mu_\beta$ = 2.9 at ~5 T (twice the value for **24**).

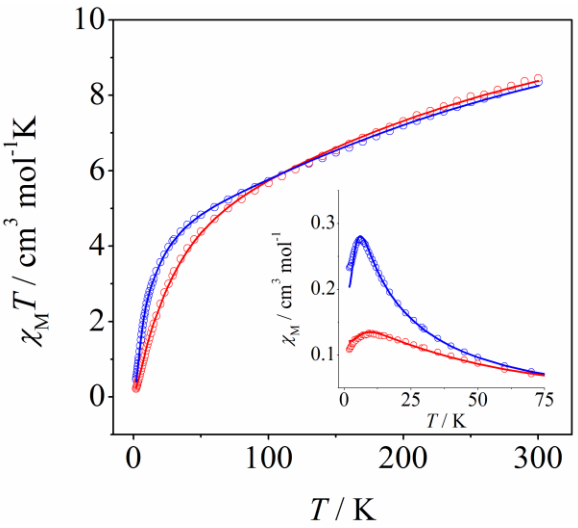

Figure 66. $\chi_M T$ versus T and χ_M versus T (inset) plots for compounds **24** (red) and **25** (blue). The solid lines correspond to the best fit to the experimental data. The molecular weight of **25** was referred to one Mn_4 unit, considering an average formula between the two entities.

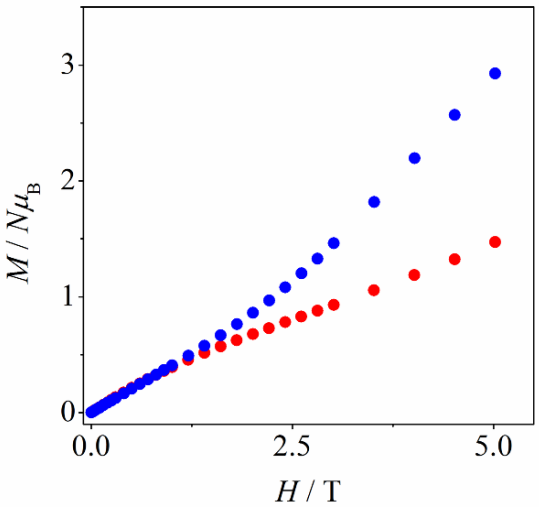

Figure 67. $M/N\mu_\beta$ versus H plots at 2 K for compound **24** (red) and **25** (blue). The molecular weight of **25** was referred to one Mn_4 unit, considering an average formula between the two entities.

Four different Mn···Mn exchange pathways may be considered (shown in Figure 68): the magnetic interaction with the Mn ions bound with a double oxo bridge J_1 ($Mn_c \cdots Mn_c$); two central-terminal Mn ion interactions ($Mn_c \cdots Mn_t$) J_2 and J_3; and the magnetic interactions between terminal Mn ions ($Mn_t \cdots Mn_t$) J_4. The Heisenberg spin Hamiltonian (H) considered is

$$H = -2J_1(S_1S_2) - 2J_2(S_1S_3 + S_2S_4) - 2J_3(S_2S_3 + S_1S_4) - 2J_4(S_3S_4) \qquad \text{Eq. 12}$$

where $S_1 = S_2 = S_3 = S_4 = 2$.

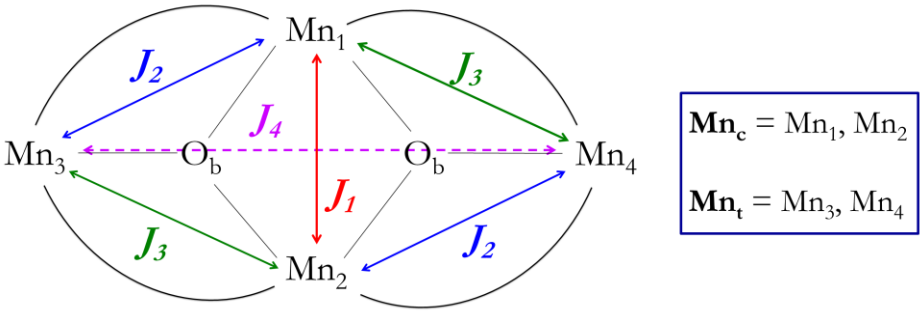

Figure 68. Schematic representation of the possible Mn···Mn exchange pathways in compounds **24** and **25**.

Several fits of the experimental data were performed, screening different values of the magnetic coupling constants (results shown in Figure S24). In all of them, the interaction between terminal Mn ions was considered negligible ($J_4 = 0$). In fact, this interaction, with a Mn···Mn distance of ~5.6 Å, is expected to be of comparable magnitude to intermolecular interactions. Firstly, the experimental data were fitted considering $J_2 = J_3$ to get an average value of the central-terminal interactions, as usually performed for this kind of compound with a $[Mn_4O_2]^{m+}$ core (m = 6–8);[246,247,250,259–261] but the shape of the curve could not be reproduced with any of these fits. The inclusion of D_{Mn} parameter, but still keeping $J_2 = J_3$, neither provide better fits. Therefore, the fits were performed considering $J_2 \neq J_3$, which gave more appropriate reproductions of the experimental curves. However, the shape of the maxima in the χ_M versus T plots was not completely reproduced in these latter fits, indicating that the inclusion of ZFS parameters could provide better results. Hence, the experimental data were fitted (300–2 K) using the *PHI* program[165] and taking into account the axial zero-field splitting (D_{Mn}) and the relative orientation between Mn ions, which happens to be almost parallel between the central Mn ions and around perpendicularity between the central and terminal ions, as represented in Figure 65. The best fits correspond to $g = 2.01$, $2J_1 = -45.5$ cm^{-1}, $2J_2 = -15.1$ cm^{-1}, $2J_3 = -4.4$ cm^{-1}, and $D_{Mn} = -3.5$ cm^{-1} with $R_{SUS} = 7.9 \times 10^{-5}$ for **24**; and to $g = 2.01$, $2J_1 = -43.0$ cm^{-1}, $2J_2 = -14.7$ cm^{-1}, $2J_3 = -8.2$ cm^{-1}, and $D_{Mn} = -3.6$ cm^{-1} with $R_{SUS} = 6.1 \times 10^{-5}$ for **25.** With this set of J values, the calculated energy levels reveal that the ground state is $S = 0$ in both cases.

The inclusion of D_{Mn} and the relative orientation of the octahedra substantially improved the fits of the experimental data, since the entire curves were much better reproduced. The D_{Mn} values obtained from the fits are consistent with elongated Mn^{III} ions with distorted octahedral geometry, which is expected to be moderate and negative.[21,22,163,164] The rhombic

zero-field splitting parameter was not considered ($E_{Mn} = 0$) in accord with the low rhombic distortion of the Mn^{III} ions of these compounds ($\rho < 2\%$, see Table S18). Even though the ground states for these compounds have $S = 0$, the zero-field splitting of the first excited states may be of importance for the χ_M versus T plot when such states are populated at low temperature, as explained in Chapter 1.3. Accordingly, the calculated energy levels for these compounds (omitting D_{Mn}) revealed that there are several low-lying excited states with $S \neq 0$, being $S = 1$ at 3.5 (**24**) or 0.65 cm^{-1} (**25**), $S = 2$ at 11 (**24**) or 2.8 cm^{-1} (**25**), and $S = 3$ at 27 (**24**) or 10 cm^{-1} (**25**).

The strongest magnetic coupling constant (J_1) is unambiguously assigned to the double-oxo bridge, since a strong antiferromagnetic interaction is expected for this subunit and it is consistent with that observed in analogous compounds (Table S19). The assignment of J_2 and J_3 to the double-carboxylate or single-carboxylate bridges appears much more challenging; for analogous systems they are indeed considered too similar to be differentiated, obtaining just an average value between them. However, its distinction was necessary in order to achieve a good fit of the experimental data for **24** and **25** (Figure 69). Aiming to their assignment, comparison between the structural parameters of these subunits and dinuclear Mn^{III} compounds with (μ-O)(μ-R'COO) or (μ-O)(μ-R'COO)$_2$ bridges. Only two examples of dinuclear Mn^{III} compounds with a single-carboxylate bridge were found, in which the magnetic coupling constant are quite different ($2J$ = –19.5 and +1.33 cm^{-1} for $H = -2JS_1S_2$).[262,263] However, both compounds display compressed Mn^{III} octahedra ($\angle \approx -10\%$, $\rho \approx 1.5$–6%), contrary to **24** and **25**, making them non-comparable. The magnetic properties of dinuclear Mn^{III} compounds with double-carboxylate bridge have been extensively studied in Chapter 1.3, and the value of the magnetic interaction of the double-carboxylate subunit may be approximately predicted using the magneto-structural correlation therein presented. However, the double-carboxylate subunits in compounds **24** and **25**, with $\angle \approx 7.8$–18% and $\rho < 4\%$, are very different from those in the dinuclear Mn^{III} compounds. As may be observed in Figure 28 (found in Chapter 1.3), there are not any compound with ρ below 4%. Hence, the assignment of these bridging blocks to certain values is very risky. We also tried to assign J_2 and J_3 by comparing the structural parameters of other compounds with $[Mn^{III}_4O_2]^{8+}$ core and carboxylate bridges (Table S20 and Table S21), but no clear assignment could be done.

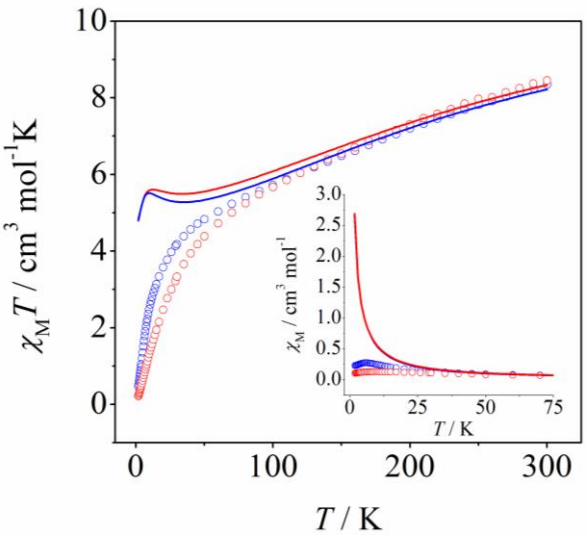

Figure 69. Experimental (open circles) and simulated (straight lines) $\chi_M T$ versus T and χ_M versus T (inset) plots for compounds **24** (red) and **25** (blue). The simulation was performed with $2J_1$ and D_{Mn} values obtained from the fit and with the average value between $2J_2$ and $2J_3$ (9.7 cm^{-1} for **24** and 11.5 cm^{-1} for **25**). The molecular weight of **25** was referred to one Mn_4 unit, considering an average formula between the two entities.

The magnetic properties of other compounds with $[Mn^{III}_4O_2]^{8+}$ core that display similar structure to that for **24** and **25** were reported in the literature.[246–248,259,260] As commented above, J_2 and J_3 were not distinguished and an average value of the $Mn_t \cdots Mn_c$ interaction (J_{ct}) was provided. These compounds usually show different spin ground states depending on the J_1/J_{ct} ratio. The most common ground state is (S_T, S_{cc}, S_{tt}) = (3, 1, 4) for J_1/J_{ct} = 2.5–4.9.[246,248,250,259] When $J_1/J_{ct} > 4.9$, then five energetically degenerate states, (n, 0, n) with n = 0–4, become the ground state,[247,251,260] corresponding to two non-interacting Mn_t ions.[246] In the lower limit, when $J_1/J_{ct} < 2.5$ the ground state would be (2, 2, 4). On the contrary, the compounds herein presented (**24** and **25**) display a (0, 0, 0) ground state. The explanation of this fact lies in the differentiation of the two types of interactions between the terminal and central ions, J_2 and J_3 (following the diagram shown in Figure 68). It is important to remember that there are two different $Mn_c \cdots Mn_t$ cores: those consisting of (μ-O)(μ-R'COO) ligands and those having (μ-O)(μ-R'$COO)_2$ ligands. Figure 70 shows energy versus J_3/J_2 plots of the first spin states for hypothetical $[Mn^{III}_4O_2]^{8+}$ compounds, all energies referred to the lower S_T = 0 state. When J_3 and J_2 are equal (J_3/J_2 = 1), the spin ground state is a S_T = 3 and there are several states with S_T = 0–4 that are energetically degenerated. However, this degeneration breaks and all states increase in energy as the J_3/J_2 ratio decreases. For J_3/J_2 values between ~0.6–0.7, the lowest spin states will be mixed and spin frustration is then plausible. When J_3/J_2 is below 0.6, the spin ground state is S_T = 0.

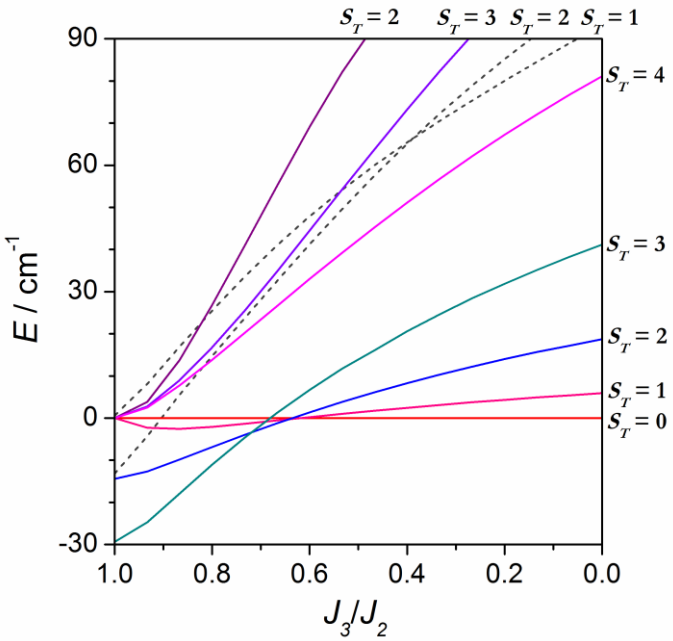

Figure 70. Energy at zero field for the first spin states as a function of J_3/J_2 ratio for a hypothetical $[Mn^{III}_4O_2]^{8+}$ compound with $2J_1 = -45.6$ cm^{-1}, $J_2 = -15$ cm^{-1}, $D_{Mn} = 0$, and variable J_3 values.

A deeper analysis of the energy levels as a function of the J_3/J_2 ratio may provide useful information concerning the composition of each eigenstate. Indeed, the eigenstates are the result of the combination of several basic elements that represents different configurations of single-ion states. It worth remembering that, for the situation in Figure 70, the most relevant ground state is $S_T = 3$ (for $J_3/J_2 > 0.7$) and $S_T = 0$ (for $J_3/J_2 < 0.6$). As an example, Figure 71 shows the percentage composition of the three most relevant (S_T, S_{cc}, S_{tt}) basic element in which the Hamiltonian is constructed for the eigenstates with $S_T = 0$ and $S_T = 3$ that are lowest in energy, calculated with the PHI program.[165] The spin configurations that represent these basic elements are represented in Figure 72. As may be observed, at $J_3/J_2 = 1$ the $S_T = 0$ and the $S_T = 3$ states mainly correspond to spin configurations with (S_T, S_{cc}, S_{tt}) = (0, 0, 0) and (3, 1, 4), respectively, with contributions of at least an ~80%. However, the composition of these states changes upon decreasing the J_3/J_2 ratio and the assignment to a single spin configuration becomes unachievable. This fact is also observed for the rest of the eigenstates included in Figure 70 excepting for the $S_T = 4$ state, whose highest contribution is never lower than 70% and corresponds to the (4, 0, 4) configuration.

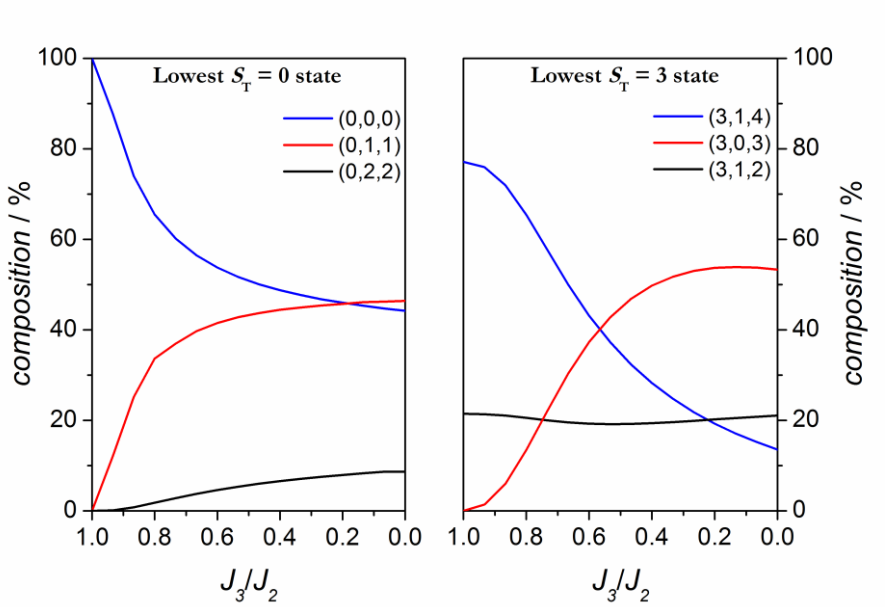

Figure 71. Percentage composition of the three most relevant (S_T, S_{cc}, S_{tt}) basic element in which the Hamiltonian is contracted for the eigenstates with $S_T = 0$ and $S_T = 3$ that are lowest in energy.

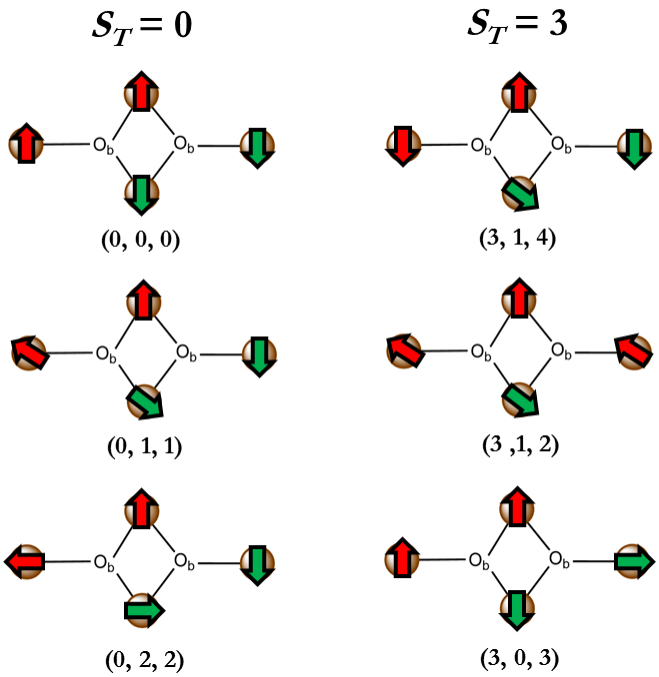

Figure 72. Possible spin configuration representing the most relevant (S_T, S_{cc}, S_{tt}) spin states that configure the two lowest eigenstates with $S_T = 0$ and $S_T = 3$.

Summary

Two new tetranuclear compounds having $[Mn^{III}_4O_2]^{8+}$ core with 4-$MeOC_6H_4COO^-$ (**24**) or 4-$^t BuC_6H_4COO^-$ (**25**) have been obtained. Compound **24** crystallizes from a mixture containing the acetonitrile mother liquor and ethanol. On the other hand, compound **25** had to be crystallized with the addition of large amounts of extra ClO_4^- ion in the mother liquor.

The crystal structures for these compounds were solved, revealing that the Mn ions are arranged in a "butterfly" (**24**) or planar (**25**) fashion, (Figure 62). The structural parameters for these two compounds are rather similar; however, there are some substantial differences: (*a*) whereas compound **25** has six carboxylate ligands linking the central (Mn_c) and terminal (Mn_t) ions, compound **24** has in addition a seventh carboxylate ligand that links the two Mn_c ions; (*b*) the $Mn_{c2}O_{b2}$ rhombus is completely planar for **25**, while it is far from being planar for **24**, with Mn_c–O_b–O_b–Mn_c angles of ~168º. All Mn^{III} ions display a pronounced elongation, with elongation parameters ($\angle$) ranging from ~8 to 18%, and small rhombic distortion, consistent with the Jahn-Teller distortion expected for Mn^{III} ions. Moreover, the Jahn-Teller axes in Mn_c ions are almost parallel, while they are nearly perpendicular to those of Mn_t ions.

The magnetic measurements revealed that these compounds show a ground state with S_T = 0. Good fits of the experimental data were achieved by considering three different magnetic interactions: that between Mn_c ions (J_1) and those between Mn_c and Mn_t ions (J_2 and J_3). Then, the inclusion of the axial anisotropy parameter (D_{Mn}) and the consideration of the relative orientation of the Jahn-Teller axes led to much better fits. It is worth noting that there are two different $Mn_c \cdots Mn_t$ bridges: those consisting of (μ-O)(μ-R'COO) ligands and those having (μ-O)(μ-R'$COO)_2$ ligands. Although the distinction of these two interactions appears rather coherent, the assignment of J_2 and J_3 to a particular bridging block was not achieved.

A deep analysis of the energy levels as a function of the J_3/J_2 ratio (from 1.0 to 0.0) provided very useful information. The distribution of energy levels completely changes with the J_3/J_2 ratio, having a S_T = 0 ground state when $J_3/J_2 < 0.6$. On the other hand, the assignment of the states to a particular configuration was unachievable because the composition of these states changes upon decreasing the J_3/J_2 ratio.

1.7. Dodecanuclear Compound with $[Mn^{IV}_4Mn^{III}_8O_{12}]^{16+}$ Core

First insights

As commented in Chapter 1.5, we were interested in obtaining Mn^{IV}-Ca^{2+} compounds. We tested the synthetic procedure presented in the aforesaid chapter with all the carboxylic acids chosen for this work (*n*-RC_6H_4COOH, *n*-R = 2-MeO, 3-MeO, 4-MeO and 4-*t*Bu); however, the desired heterometallic compound could be obtained only with the 4-*tert*buthylbenzoic acid. Using the 2-methoxybenzoic acid (*n*-R = 2-MeO) in the synthesis leads to a compound with a Mn/Ca molar ratio of ~1; unfortunately, we could not isolate X-ray suitable single-crystals of this compound. The 4-methoxybenzoic acid is not very soluble in acetonitrile and tends to crystallize one or two days after letting the solution undisturbed; so, we did not succeed to obtain any pure sample with this synthetic procedure. Finally, with the 3-methoxybenzoic acid we neither achieved to obtain any Mn-Ca compound. Instead, a dodecanuclear compound **26** with formula $[Mn_{12}O_{12}(3\text{-}MeOC_6H_4COO)_{16}(H_2O)_4]$ could be isolated and characterized. The synthetic procedure was lately adapted and slightly optimized.

These compounds, with formula $[Mn_{12}O_{12}(R'COO)_{16}(L)_4]$ (R' = variable, L = molecule of solvent), have been extensively studied since have first syntheses in the 1980s[264,265] because of their interesting magnetic properties.[264–271] The magnetization of the Mn_{12} cluster is highly anisotropic, and the magnetization relaxation time becomes long enough to give rise to pronounced hysteresis below 4 K.[18] This behavior is not analogous to that of a bulky ferromagnet, in which magnetization hysteresis results from the motion of domain walls. On the contrary, these processes are promoted by a single-molecule, which acts as a magnet (SMM). In principle, these bistable magnetic units could act as a data storage device.

The anisotropy of a Mn_{12} compound is caused by the axial zero-field splitting (D) of the ground state. From D, the potential-energy barrier (U_{calc}) may be calculated with the formula $U_{calc} = DS_z^2$, where S_z is the spin for the ground state. However, the energy barrier experimentally determined (U_{eff}) for the spin moment to flip is usually smaller than U_{calc} because some of the molecules may tunnel from $M_S = n$ to $M_S = -n$ ($n = 1, 2, \ldots, S_z$). Hence, the required energy for the spin moment to flip from "up" to "down" is dependent on the balance of both the axial anisotropy and quantum tunneling, and is known as the effective anisotropy barrier (U_{eff}), being $U_{eff} \leq U_{calc}$.

Synthesis

Compound **26** was synthesized directly from the comproportionation reaction between a Mn^{II} salt and MnO_4^- in presence of 3-methoxybenzoic acid in hot acetonitrile, leading to a compound with formula $[Mn_{12}O_{12}(3\text{-}MeOC_6H_4COO)_{16}(H_2O)_4]$.

There are basically two different synthetic procedures to prepare $[Mn_{12}O_{12}(R'COO)_{16}(H_2O)_x]$ (x = 3 or 4) compounds. On the one side, the acetate groups on the compound with R' = CH_3 can be substituted in a toluene solution by other carboxylates, reaction driven by the greater acidity of the incoming carboxylic acid and/or the removal by distillation of the azeotrope of acetic acid and toluene.[266] On the other hand, these compounds can be synthesized from the direct reaction of Mn^{II} with NBu_4MnO_4 in the presence of the desired carboxylic acid. Yields are generally much greater for those obtained with the ligand substitution method.[266] The compound presented here (**26**) was prepared with the second approach and consequently, the yield of this procedure remains between 5 and 20%, in accord with the ones reported in the literature synthesized with this method.[266]

With this method, compound **26** was obtained upon crystallization from the mother liquor in approximately one week. Two different types of crystals were observed with a magnifying glass: the solution contained dark thin needles and black cubes, which may correspond to different isomers. Several attempts were performed in order to isolate their crystallization, for instance, increasing the time of crystallization to likely obtain two different fractions. Other solvents were also tested, but all attempts led to a mixture of both crystals. Choosing and picking one by one the desired crystals was also considered, but the small size of the crystals and the existence of agglomerations consisting of both kinds made us impossible to obtain pure samples with good yields.

Description of structure

Two types of crystals were found in the crystallization of compound **26**: thin needles and cubes, both rather tiny. Note that the crystal structure was determined with a needle. The structure of the cubic crystals remains unknown.

The structure of compound **26**, determined from these needle-like crystals, is shown in Figure 73. For the sake of clarity, atoms have been only partially labeled. Selected interatomic distances are listed in Table S22, and a fully labeled structure of the asymmetric unit is shown in Figure S25. The structure of **26** is characteristic of a member of this Mn_{12} family.[18,264,266–268]

There is a central $[Mn^{IV}_4O_4]^{8+}$ cubane unit in the middle of a nonplanar ring of eight Mn^{III} atoms. The peripheral ligation is provided by sixteen 3-$MeOC_6H_4COO^-$ bridges and four H_2O molecules. The Mn^{IV} ions are linked through a double-oxo bridge, with $Mn^{IV}\cdots Mn^{IV}$ distances between 2.81 and 2.92 Å. These Mn^{IV} ions are linked to the Mn^{III} ions of the ring either through one oxo ligand (single bridge) or through two oxo and one carboxylate ligands (triple bridge), showing $Mn^{III}\cdots Mn^{IV}$ distances of ~3.45 and ~2.76 Å, respectively. Finally, the Mn^{III} ions are bridged between them by (μ-O)(μ-3-$MeOC_6H_4COO)_2$ or (μ-O)(μ-3-$MeOC_6H_4COO)_2$ ligands, displaying an average $Mn^{III}\cdots Mn^{III}$ distance of ~3.38 Å. Hence, the Mn···Mn distances follow the trend $d(Mn^{III}\cdots Mn^{IV})_{double\text{-}oxo}$ (~2.76 Å) < $d(Mn^{IV}\cdots Mn^{IV})$ (2.81–2.92 Å) < $d(Mn^{III}\cdots Mn^{III})$ (~3.38 Å) ≈ $d(Mn^{III}\cdots Mn^{IV})_{single\text{-}oxo}$ (~3.45 Å). The difference in the Mn···Mn distances depends not only on the Mn oxidation states but also on bridging ligands. In general, those subunits corresponding to double-oxo bridges are much shorter than those corresponding to single-oxo bridges. The Mn–O distances ranges from ~1.85 to ~2.22 Å. All these structural parameters are in accord with other Mn_{12} compounds reported in the literature.[18,264,266–268]

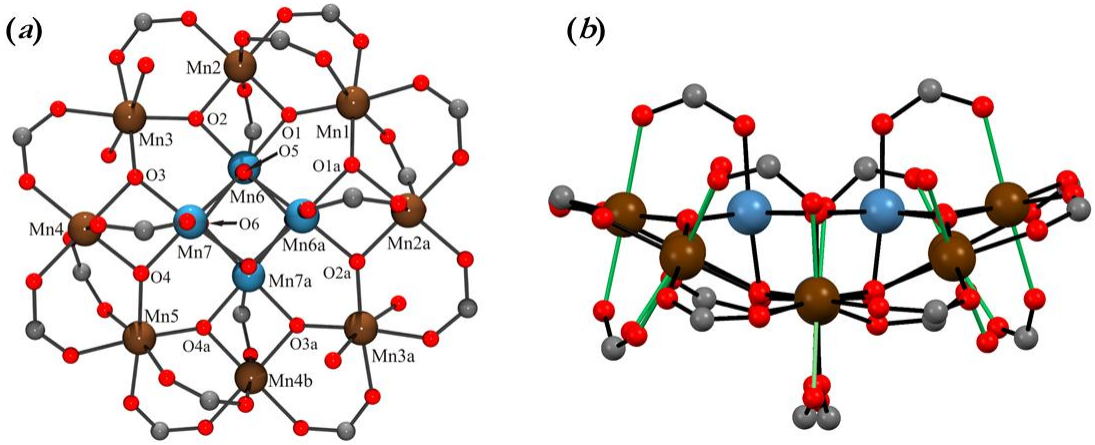

Figure 73. (***a***) Partially labeled crystal structure and (***b***) side-view showing the disposition of the Jahn-Teller axes (green bonds) for compound **26**. The 3-methoxyphenyl groups have been omitted for clarity. Color code: Mn^{III}, brown; Mn^{IV}, blue; O, red; C, gray.

The Mn^{III} ions in this compound display elongated octahedra, the Jahn-Teller axes being in the directions of the water ligands (Mn3) or towards the axes having two carboxylate ligands in trans position (Mn1, Mn2, Mn4, and Mn5). The length axes and the elongation (⊿) and rhombicity (ρ) parameters were calculated as explained in Chapter 1.3, considering that the z axes are those of the Jahn-Teller distortion. All Mn^{III} ions (Mn1, Mn2, Mn3, Mn4 and Mn5) show a notable axial distortion and almost inexistent rhombic distortion, with ⊿ ≈ 6.0–15% and ρ < 1.0% (Table S23). It is worth noting that Mn5 ion, with ⊿ = 6.0%, is much less

elongated than the rest of the Mn^{III} ions, whose elongation parameters (Δ) range from 10.8 to ~15%. On the contrary, the Mn^{IV} ions are, as expected, more regular, with both Δ and ρ < 1.0%. The Jahn-Teller axes in this compound are nearby parallel (Figure 73b); thus, a high overall magnetic anisotropy is expected at low temperature.

Magnetic properties

Direct current (DC) magnetic susceptibility data were recorded for compound **26** from 300 to 2 K. $\chi_M T$ versus T plot is shown in Figure 74. The $\chi_M T$ value at room temperature is 19.6 $cm^3\ mol^{-1}\ K$, much smaller than expected for an uncoupled group of eight Mn^{III} and four Mn^{IV} ions (31.5 $cm^3\ mol^{-1}\ K$). Between 300 and 150 K, $\chi_M T$ values slightly decrease as temperature falls. These two facts may be indicative of the presence of intramolecular exchange interaction. Below this temperature, $\chi_M T$ values abruptly increase, reaching a maximum value of 48.1 $cm^3\ mol^{-1}\ K$ at 7.5 K, followed by a decrease at very low temperature. This behavior is indicative of predominant ferromagnetic interactions. The decrease at very low temperature may be attributed to intermolecular interactions. The maximum $\chi_M T$ value (48.1 $cm^3\ mol^{-1}\ K$) is indicative of a high spin ground state (S) and is between the expected value for ground states with $S = 9$ ($\chi_M T = 45\ cm^3\ mol^{-1}\ K$) and $S = 10$ ($\chi_M T = 55\ cm^3\ mol^{-1}\ K$).

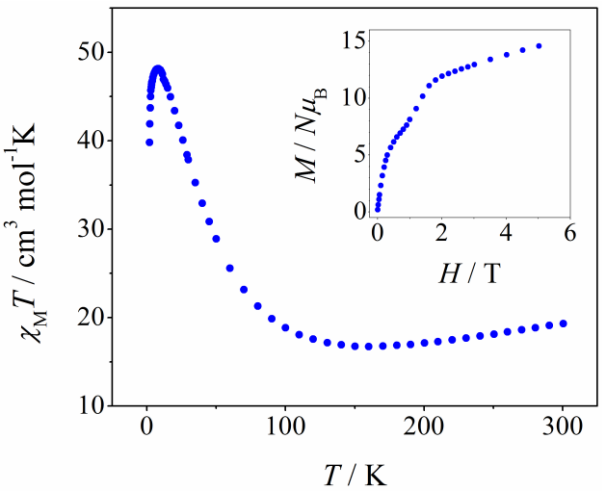

Figure 74. $\chi_M T$ versus T and $M/N\mu_\beta$ versus H (inset) plots for compound **26**.

Magnetization (M) data were collected for **26** at 2 K using a magnetic field from 0 to ~5 T, and $M/N\mu_\beta$ versus H plot for compound **26** is shown in the inset of Figure 74. $M/N\mu_\beta$ progressively increases with the magnetic field (H) reaching $M/N\mu_\beta = 14.5$ at ~5 T without

showing saturation. At 2 K, the magnetization shows a relatively narrow hysteresis loop, showing a jump at $H \approx 0$ T (Figure 75). As usually observed for Mn_{12} SMM, the loops exhibit well-defined steps due to quantum tunneling magnetization.[268,272] Field-Cooled (FC) and Zero-Field-Cooled (ZFC) magnetic susceptibilities were measured, but no clear blocking temperature (T_B) was observed. Only a slight deviation between the FC and ZFC may be seen below ~2.5 K (Figure S26).

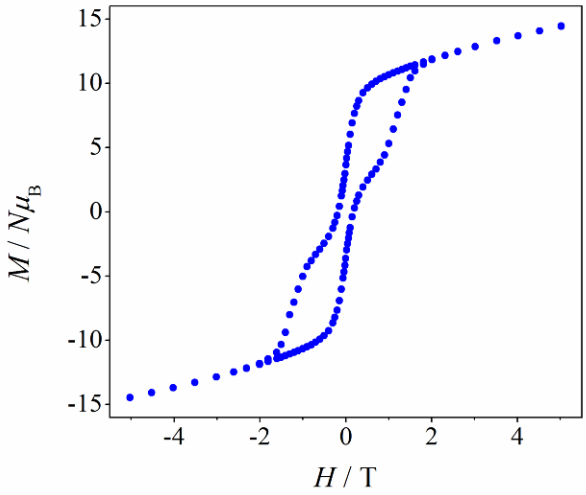

Figure 75. Hysteresis loop for powdered sample of compound **26**, measured at 2 K.

Alternating current (AC) magnetic susceptibility data were collected for this compound between 12 and 1.8 K with an AC field of $4 \cdot 10^{-4}$ T, oscillating at frequencies in the range 10–1488 Hz. Figure 76 shows the plots of the in-phase (χ_M') and out-of-phase (χ_M") magnetic susceptibilities versus temperature for compound **26**. Both plots are consistent with the existent of a slow relaxation process and are the fingerprints that SMMs usually show. The plateau observed in the $\chi_M'T$ versus T plot is consistent with the maximum value in the $\chi_M T$ versus T plot, which is close to 48 cm^3 mol^{-1} K. It is worth noting that two maxima are observed in both the χ_M' versus T and χ_M" versus T plots, indicating that two relaxation processes occur (see below).

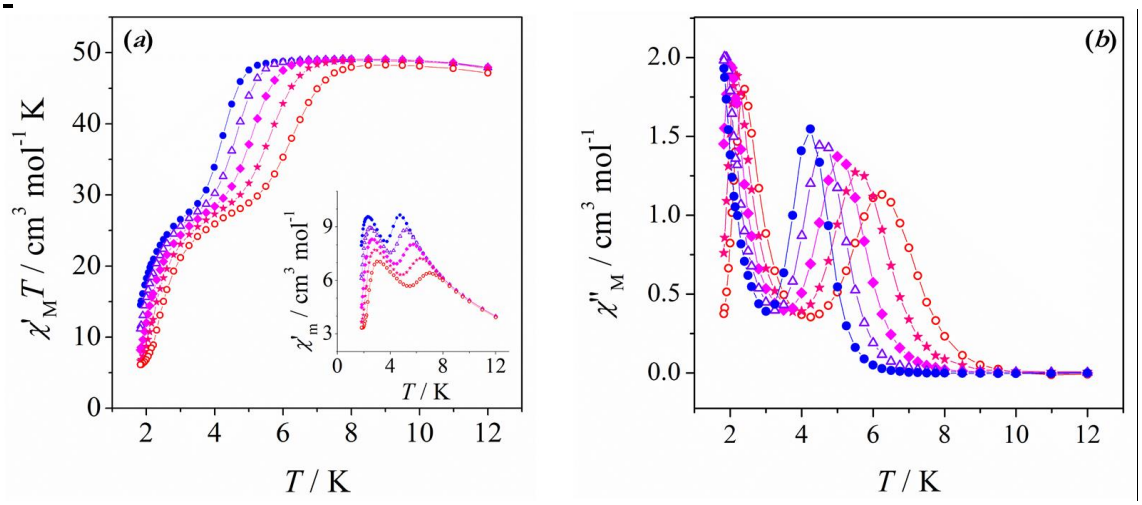

Figure 76. Plots of (***a***) in-phase (χ_M') and (***b***) out-of-phase (χ_M") magnetic susceptibilities versus temperature for microcrystalline samples of compound **26**. Five different frequencies were used: 10 Hz (full circles), 35 Hz (triangles), 122 Hz (squares), 426 Hz (stars), and 1488 Hz (open circles).

The magnetic moment of a paramagnetic molecule (or a group of them) flips from "up" to "down" when an external magnetic field is applied. In order to do so, it must either climb over the potential-energy barrier (DS_z^2) or pass through the barrier by quantum tunneling. An out-of-phase AC magnetic susceptibility signal is observed when the rate at which this magnetic moment flips is close to the operating frequency of the AC magnetic field. A maximum in the out-of-phase AC signal occurs when the rate at which the magnetic moment flips is equal to the frequency of the oscillating field. The magnetic moment of a typical paramagnetic specie flips at a rate of ~10^9 Hz and, thus, it does not show out-of-phase signal at frequencies between 10–1500 Hz. However, when the anisotropic barrier is larger than the thermal excitation, the rate at which the magnetic moment flips becomes lazy, appearing an out-of-phase AC magnetic susceptibility (χ_M") peak. Indeed, the maximum in the χ_M" versus T occurs when the relaxation time (τ) is equivalent to the applied frequency.[266,18] This is the case of SMM such as the Mn_{12} compounds.

The origin of two relaxation processes has been reported before, also for Mn_{12} compounds.[266,267] In the cited references, the two maxima are caused by the coexistence of two isomers displaying different disposition of the Jahn-Teller axes, phenomenon called Jahn-Teller isomerism. The structures of the two isomers are indeed not superimposable, emphasizing the non-superimposability of the axial water molecules:[266] the Jahn-Teller axes for one of the isomers are almost parallel, whereas the other one has an abnormal disposition of the Jahn-Teller axes.[266,267] This structural difference is important for the electronic environments of the Mn^{III} ions, changing the resulting magnetic properties. In those cases, the effective anisotropy barrier (U_{eff}) is much bigger for the isomer with the Jahn-Teller

distortion axes with a nearly parallel orientation ($U_{eff} \approx 62$ K) than those having an abnormal (non-parallel) disposition of Jahn-Teller axes ($U_{eff} \approx 35$ K). They have also different ground states, being $S = 10$ for that having parallel Jahn-Teller axes and $S = 9$ for the other one. Hence, a plausible explanation for the two peaks in the AC magnetic susceptibility plots for compound **26** could be the coexistence of two "Jahn-Teller isomers". Note that the maximum in the DC magnetic susceptibility plot ($\chi_M T = 48.1$ cm^3 mol^{-1} K) is in the middle of the value expected for ground states with $S = 9$ and $S = 10$. A schematic representation of the spin configuration for Mn_{12} compounds with these two ground states is shown in Figure 77. For $S = 10$, the interaction network consists of a ferromagnetic-coupled Mn^{IV}_4 cubane that is antiferromagnetic coupled to a ferromagnetic nonplanar Mn^{III}_8 ring. On the other hand, the distribution of spin moments becomes more difficult to rationalize for an $S = 9$ ground state, since the change is expected to take place in the Mn^{III} ion containing the axial water ligands.

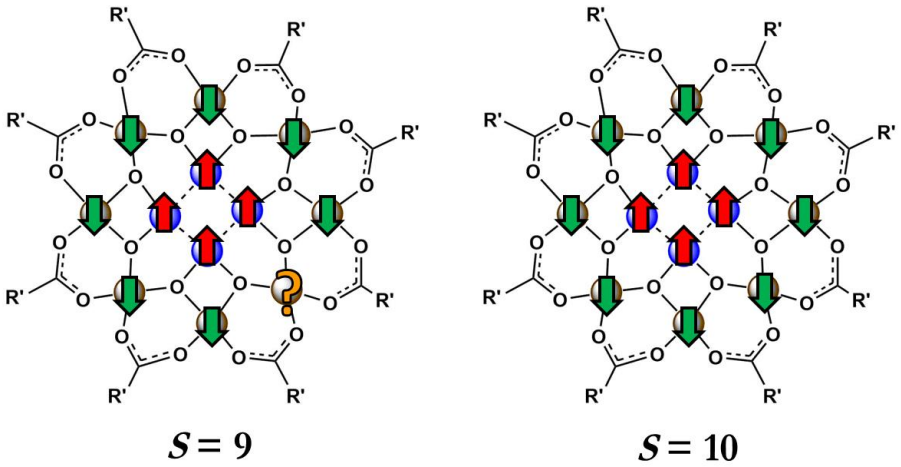

Figure 77. Schematic representation of the spin configuration for Mn_{12} compounds with $S = 9$ and $S = 10$ ground states. Color codes: Mn^{III}, brown; Mn^{IV}, blue.

The effective anisotropy barrier (U_{eff}) may be quantified by analyzing the frequency dependencies of the χ_M" signals as a function of the temperature. From the peaks of the χ_M" versus T, the magnetization relaxation time (τ) can be determined at each temperature. Then, U_{eff} and τ_0 can be calculated from the fit of the following expression, based on Arrhenius Law:

$$\tau = \tau_0 \exp(U_{eff}/kT_{max}) \qquad \text{Eq. 13}$$

from which one may extract:

$$\ln(1/\tau) = \ln(1/\tau_0) - U_{eff}/kT_{max} \qquad \text{Eq. 14}$$

where τ is the magnetization relaxation time (so $1/\tau$ is the frequency in Hz), T_{max} is the temperature at which the maximum in the χ_M" versus T plot occurs, U_{eff} is the effective anisotropy barrier, and k is the Boltzmann constant. Figure 78 shows the two Arrhenius plots for each peak in the χ_M" versus T plot. A table with the results is also included in the figure. Note that the two values obtained for U_{eff} (32 and 66 K) will be consistent with the coexistence of two "Jahn-Teller isomers". In accord with the explained above, the peak around 5 K (U_{eff} = 66 K) may correspond to the isomer having almost parallel Jahn-Teller axes (and thus, the one that the crystal structure was determined) while the peak around 2 K (U_{eff} = 32 K) could be due to the isomer with an atypical disposition of Jahn-Teller axes.

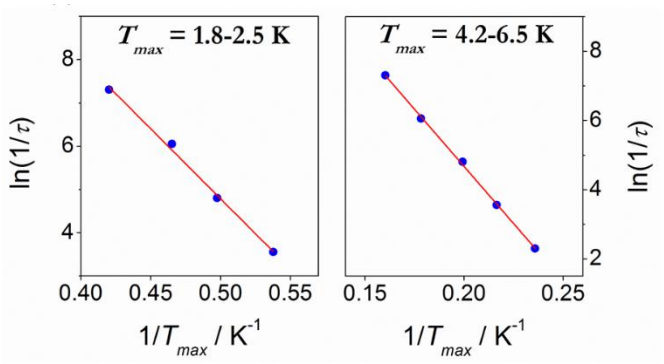

Relaxation time (τ_0) and effective anisotropy energy barrier (U_{eff}) for compound **26**:

T_{max}	τ_0 / s	U_{eff} / cm^{-1}	U_{eff} / K
1.8–2.5 K	7.81^{-10}	22	32
4.2–6.5 K	$1.74 \cdot 10^{-8}$	46	66

$$\tau = \tau_0 e^{(U_{eff}/kT_{max})}$$

Figure 78. Arrhenius plot of the logarithm of the inverse relaxation time ($1/\tau$) versus the inverse T_{max} for **26**. T_{max} is temperature of the maximum in the χ_M" versus T plot at each oscillation frequency. The solid lines correspond to the fit to Eq. 14, the results are presented in the text and in the table on the right of the Arrhenius plots.

Summary

A new Mn_{12} compound with formula $[Mn_{12}O_{12}(3\text{-}MeOC_6H_4COO)_{16}(H_2O)_4]$ was synthesized and structurally characterized. The AC magnetic susceptibility versus temperature plots show maxima at specific temperatures depending on the frequency of the oscillating field, which indicates the presence of magnetization relaxation processes. The presence of two maxima in these plots and the values of the effective energy barrier for each maximum suggests the coexistence of two "Jahn-Teller isomers", in accord with the study reported by Aubin *et al.*[266]

SECTION II: Mn-SiO_2 Hybrid Materials

2.1. Introductory Remarks

The support chosen for the insertion of Mn compounds is MCM-41 type mesoporous silica, which presents a 2D hexagonal array.[113,117] This material was prepared following the ultrafast microwave-assisted synthesis from an aqueous colloidal silica solution in the presence of a cetyltrimethylammonium (CTA^+) template, reported by Chaignon *et al.*[118]

A classic hydrothermal synthesis of mesoporous silica consists in four main steps: the surfactant dissolution, the addition of the silica precursor, the autoclave heating, and the filtration and washing of the as-made material. The resulting characteristics of the material are highly dependent on the synthesis conditions and on the chosen reagents. Microwave radiation allows for heating the polar entities "locally", such as the charged heads of the surfactant and silicate anions, as well as for a fast temperature ramp. The addition of these two facts provokes both an inhomogeneous heating effect and the absence of effective thermal expansion, which leads to a highly chemically and thermally stable material in a very short period of time. Indeed, the heating step just was extremely shortened, taking only 10 min instead of the 20 h required for classical heating.[118]

The surfactant may be chemically extracted from the as-made silica (SiO_2-CTA) in an ethanol solution of HCl, leading to extracted silica (SiO_2-Ex), a material that only consists of the silica mold and the pores are completely empty. The chemical extraction presents some advantages against the extraction by calcination, since it is faster, prevents from thermal dilatation of the walls and the pore contraction due to the formation of new Si–O–Si bonds, and allows the recycling of the surfactant.[118]

X-ray diffraction (XRD)

The hexagonal array of the as-made material can be confirmed via powder X-ray diffraction (XRD). Although the silica polymerizes in an amorphous fashion around the surfactant, the template itself presents a long-range order. Indeed, the diffraction pattern observed (Figure 79) comes from the hexagonal arrangement of the pores, whose space group is *P*6mm. Thanks to the Bragg's law, the interplanar distance (d) can be calculated from the scattering angle (θ) with the formula $2d \sin(\theta) = n\lambda$, where n is a positive integer and λ is the wavelength of the incident radiation. For our material, four main peaks are displayed at 2θ = 2.1°, 3.7°, 4.3° and 5.6°, corresponding to the diffraction of planes (100), (110), (200) and (210),

respectively. By definition, the cell parameters for a hexagonal symmetry follow the restrictions: $a = b \neq c$, $\alpha = \beta = 90^{\circ}$ and $\gamma = 120^{\circ}$. Hence, the lattice parameter a_0, defined as the distance between the centers of the pores, can be calculated with the formula $a_0 = 2d_{100}/3^{1/2}$, which gives 4.7 nm for this material.

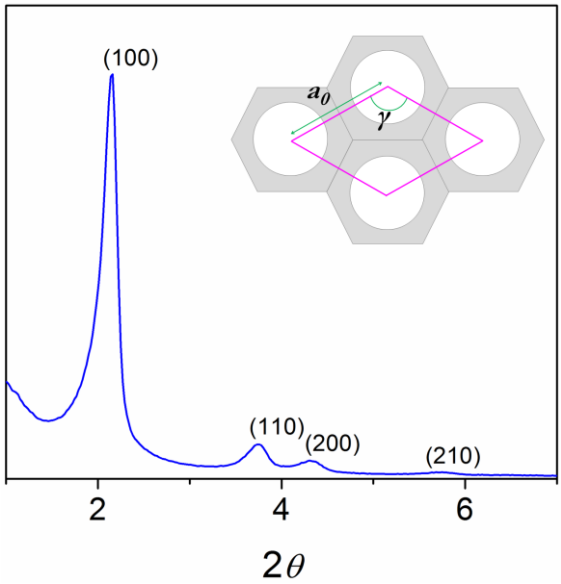

Figure 79. Powder X-ray diffraction pattern for the as-made material and a figure that illustrates the hexagonal arrangement of mesoporous silica, where a_0 represents the distance between the centers of the pores.

^{29}Si nuclear magnetic resonance (NMR)

From ^{29}Si nuclear magnetic resonance (NMR), crucial information can be deduced concerning the environments of Si atoms in our materials. Based on the number of oxygen atoms linked to the silicon and on the second neighbors linked to those oxygen atoms, a nomenclature has been stablished to name different silicon atoms (Figure 80). Silicon atoms bonded to four, three, two or one oxygen are named Q, T, D, and M, respectively. Then, the number of oxygen atoms that are linked to another silicon atom is indicated with an exponent. For instance, a Q^3 is a Si atom linked to four oxygen atom and three of these are linked to silicon atoms. In practical situation, no Q^1 silicon is detected owing to the low probability for silicates to have three unreacted silanol groups. ^{29}Si NMR is a convenient technique to indirectly evaluate the stability of the material based on the ratio of the Q^2 and Q^3 signals attributed to silanol groups over the Q^4 signal of silicon atoms inside the walls.

Figure 81 shows the ^{29}Si HPDEC (High Power Decoupled) spectra for material SiO_2-Ex (surfactant-extracted mesoporous silica). The signal displayed by this material was deconvoluted to retrieve quantitative signals from each silicon species. The results for this

fit are listed in Table 23. The deconvolution leads to an average $Q^2/Q^3/Q^4$ distribution around 4.5/36/59.5%, which is consistent with a higher Si content in the inside of the walls than on the surface.

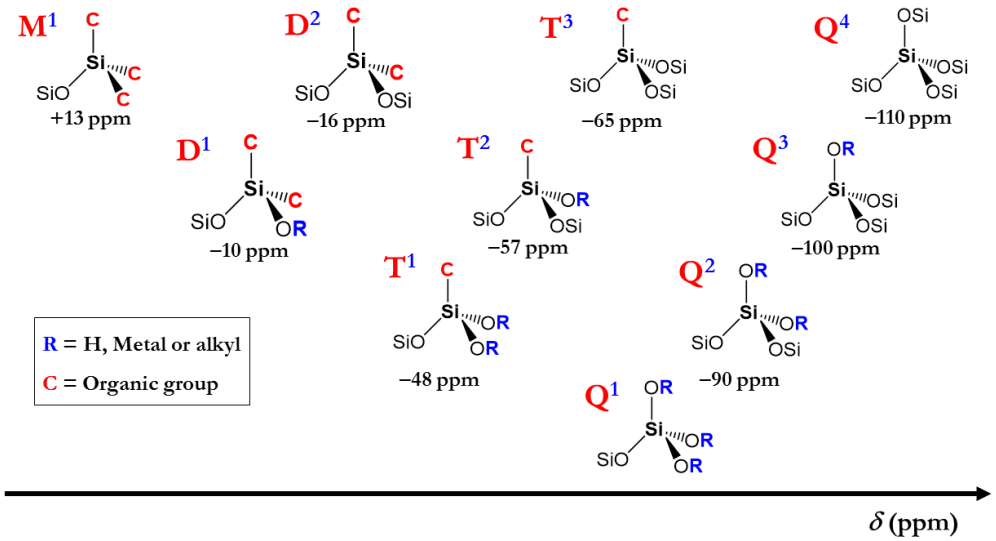

Figure 80. Silicon classification for NMR studies and approximate chemical shifts. The figure was adapted from the PhD thesis of L. Fang.[273]

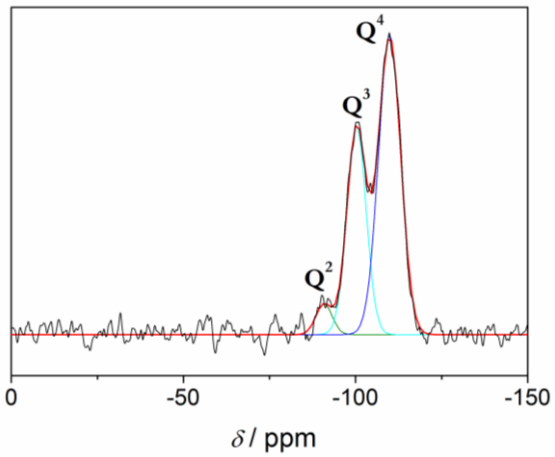

Figure 81. ^{29}Si HPDEC spectra for material SiO_2-Ex (black line). The colored lines correspond to the cumulative peak (red) and to the spectrum deconvolution, assigned to Q^4 (blue), Q^3 (cyan) and Q^4 (green).

Table 23. Summary of results obtained from the fit of the ^{29}Si HPDEC NMR spectrum for material SiO_2-Ex.

Si type	δ [a] / ppm	FWHM [b]	Area / %
Q^4	-110	7.6	59.5
Q^3	-100	6.6	36
Q^2	-91	5.6	4.5

[a] Chemical shift; [b] Full Width at Half Maximum.

Nitrogen sorption isotherms

The N_2 sorption isotherms are crucial to obtain information concerning the mesoporosity and the nature of the surface. To do so, the materials need to be pre-treated under vacuum at high temperature in order to remove the solvent (basically water). In fact, a ~5% in weight of mesoporous silica corresponds to solvent. The pre-treatment temperature is 130 or 80 °C, this latter for samples containing temperature-sensitive organic groups. Then, the tube with the pre-treated sample is placed on the corresponding device to perform the measurement. Small amounts of nitrogen are added to the sample at 77 K, and the resulting pressure is measured to provide the isotherm, which represents the adsorbed volume (V_a) versus the relative pressure (p/p_0). To exemplify, the isotherm for material SiO_2-Ex is shown in Figure 82. This material exhibits a type IV isotherm according to the IUPAC nomenclature,[274] without hysteresis as usually observed for MCM-41 2D hexagonal mesoporous silica.[117,275,276] Note that five different regions can be differentiated: (*a*) a first steep increase of volume at very low pressure corresponding to the microporosity; (*b*) a second moderate increase between $p/p_0 \approx 0.02–0.3$ assigned to the BET multilayer adsorption; (*c*) a very steep increase correlated with the capillary condensation of N_2 inside the pores at $p/p_0 \approx 0.35$; (*d*) a low sloping plateau indicative of the covering of the external surface with N_2 between $p/p_0 \approx 0.4–0.92$; and (*e*) a small increase assigned to the filling of spaces between adjacent particles, which occurs at p/p_0 close to 1.0 (large meso- or macroporosity).

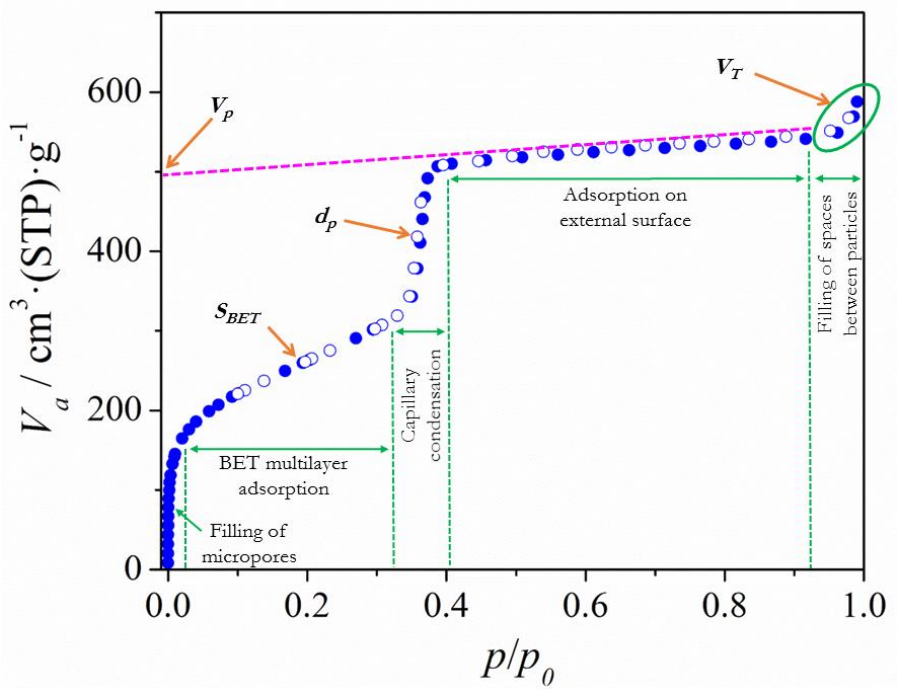

Figure 82. N_2 adsorption (full circles) and desorption (open circles) isotherm at 77 K for material SiO_2-Ex with indicative signs of the physical processes that occur and the most remarkable information that can be extracted. STP = Standard Temperature and Pressure.

To determine every piece of information from the isotherm, some data treatment is necessary. Figure 83 and Figure 84 shows the plots that are normally extracted from an isotherm. The results of these plots will be presented afterwards (Table 24).

The **BET** (for Brunauer-Emmett-Teller) **method** is based on the Langmuir mechanism of multilayer adsorption, which consists in covering a surface with N_2 molecules, from a monolayer to a multilayer with a random distribution of sites.[277] By linearly fitting the $p/[V_a(p–p_0)]$ versus p/p_0 plot in the range p/p_0 = 0.05–0.25, the specific surface area (S_{BET}) and the BET constant C can be extracted. This plot does not make the distinction between internal and external surface, which will have to be done with the *t*-plot (see below). The C constant represents the affinity of the sorbent gas with the silica surface; the higher C is, the more affine. Indeed, the polar silanol groups of the surface induce a dipolar moment in the apolar N_2 molecule to interact. Hence, the more polar the surface is, the easier this induction will be. For typical MCM-41 silica like ours, $S_{BET} \approx 1000$ m^2 g^{-1} and $C \approx 100$.

The ***t*-plot** is a representation of V_a versus the adsorption layer thickness (t).[278,279] t parameter may be calculated with the expression $t = 0.354 \cdot V_a/V_m$, where V_m is the monolayer volume and 0.354 corresponds to the N_2 monolayer thickness (in nm). This method permits to differentiate between external and internal surface and between micro- and mesoporosity. Indeed, the linear fit for $t < 0.5$ will provide the internal surface (a_{int}) and the micropore volume (V_{micro}), whereas that for $t > 1$ nm will give the external surface (a_{ext}) and the mesopore volume (V_{meso}, commonly labeled as V_p).

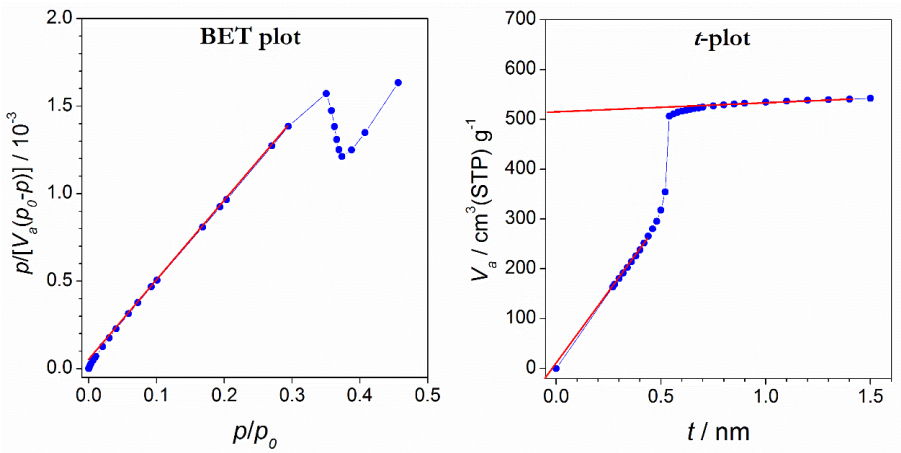

Figure 83. BET plot (blue) and its linear fit (red) and *t*-plot (blue) and its fits for material SiO_2-Ex.

Microporosity does not properly define the smallest cavities in our case. Certainly, such "microporosity" is produced in the first step of the synthesis. The molecules of surfactant remain in solution as micelles. The electrostatic repulsion between their positively charged

heads makes them be at a certain distance. Then, the silicate polyhedra condensate over these micelles, around and between the charged heads. Hence, the micropores should be more accurately called roughness in our materials. Indeed, this roughness has remained on the inner surface as a reminiscence of the formation mechanism of the porous solid.

The **capillary condensation** is the most characteristic part of the isotherm for a mesoporous material. Its shape, as well as the range of pressures where it occurs and the presence or absence of hysteresis loop, provides the most remarkable information concerning the pore nature and size.[274,275] In the case of our material, the capillary condensation is quite narrow, indicative of a high pore size uniformity.[117,274,275] On the contrary, a capillary condensation occurring in a wide range of pressures would be consistent with a broad pore size distribution.

The differences between the capillary condensation (in adsorption) and evaporation (in desorption) are highly related to the quality of the mesostructure.[275,276] Indeed, the hysteresis loop may be promoted either by the lack of uniformity of pore diameter along the cylindrical channels, by the presence of defects such as the existence of large cavities, or by the interconnectivity between channels.[276] However, when the capillary condensation occurs at relative pressures below ~0.42, like in our case, the hysteresis loop does not appear in the N_2 sorption isotherms.[280–283] Such a behavior is attributed to the instability of the liquid nitrogen meniscus,[284] which occurs when the capillary condensation is taking place within a narrow range of tubular pores of effective width 3.3–4.3 nm.[280–283] Hence, both the uniformity of the pores and the small pore diameter could be the explanation of the reversible nitrogen condensation steps observed for MCM-41 materials.

Furthermore, the relative pressure where the capillary condensation occurs is directly correlated with the **pore diameter (d_p)**. Concerning its determination, there are several methods to calculate it depending on the expected pore size. A usual method for microporous materials is the Horváth Kawazoe (HK) method.[285] For mesoporous samples, the Barret-Joyner-Halenda method (BJH)[121] is more commonly applied. Figure 84 shows these two plots for SiO_2-Ex. While the peak maximum represents the average pore diameter/radius, the amplitude of the peak is related to the pore distribution. As may be seen, the extracted mesoporous silica used in this study has a very narrow pore size distribution, in accord with the shape of the capillary condensation.

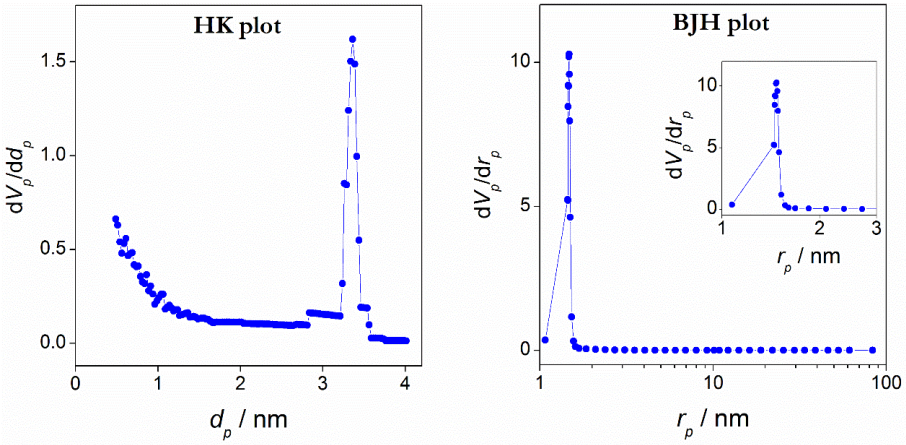

Figure 84. Horváth Kawazoe (HK) and Barret-Joyner-Halenda method (BJH) plots for material SiO_2-Ex. d_p and r_p are the pore diameter and the radius, respectively.

The two methods give rather different results (d_{HK} = 3.4 nm and d_{BJH} = 3.0 nm). In fact, none of the two methods is adapted for small mesopores. As may be observed in Figure 84, the peak corresponding to the pore diameter is close to one of the extremes of the curve. On account of this, a more precise value should be provided by the Broekhoff and De Boer (BdB) method, which is valid for cylindrical pores with diameters above 1.5 nm.[111] The pore diameter is related to the relative pressure at the inflexion point (p_i/p_0) with the following expression:[286]

$$d_p = 155.8457 \cdot (p_i/p_0)^3 - 81.96198 \cdot (p_i/p_0)^2 + 14.60994 \qquad \text{Eq. 15}$$

giving a pore diameter equal to 3.8 nm for SiO_2-Ex, which is consistent with independent measurements and calculations on powder X-ray diffraction profiles.

The most remarkable results obtained from the former plots are listed in Table 24. From these results, some conclusions may be drawn: firstly, the external area is much smaller than the internal one ($a_{ext} << a_{int}$); secondly, the microporous volume is insignificant compared to the mesoporous volume ($V_{int} << V_{meso}$); and thirdly, the highest contribution to the pore volume comes from the mesoporosity, since $V_{meso}/V_T = 0.88$.

Table 24. Summary of results obtained from the N_2 sorption isotherms for material SiO_2-Ex.

BET plot		*t*-plot		Pore diameter (d_p) / nm	
S_{BET} / m² g⁻¹	948	a_{int} / m² g⁻¹	904	**HK**	3.4
C	102	a_{ext} / m² g⁻¹	27	**BJH**	3.0
V_T / cm³ g⁻¹	0.91	V_{micro} / cm³ g⁻¹	0.0082	**BdB**	3.8
		V_{meso} / cm³ g⁻¹	0.80		

It is worth noting that these parameters will be sensitive to any change in the nature of the surface or to the filling of the pores. Hence, a close inspection of these parameters for all the intermediates obtained up to the synthesis of the Mn-SiO_2 material is recommended.

In the following pages, only some of these parameters will be listed, where d_p will be referred to the pore diameter according to the BdB method and the pore volume (V_p) will be equivalent to the mesopore one (V_{meso}). The specific surface area (S_{BET}) will not always be provided because, as the pores are filled, the surface becomes more irregular and the BET method should not be applied. Indeed, the required linear correlation between p/p_0 = 0.05 and 0.25 could not be established for many samples.

Thermogravimetric analysis (TGA)

The thermogravimetric analysis (TGA) is a simple but useful characterization technique. The profile of weight loss upon heating the sample from room temperature to ~1000 ºC may provide some information about its composition. Figure 85 shows the TGA and TG derivative for an as-made (SiO_2-CTA) and extracted (SiO_2-Ex) mesoporous silica materials.

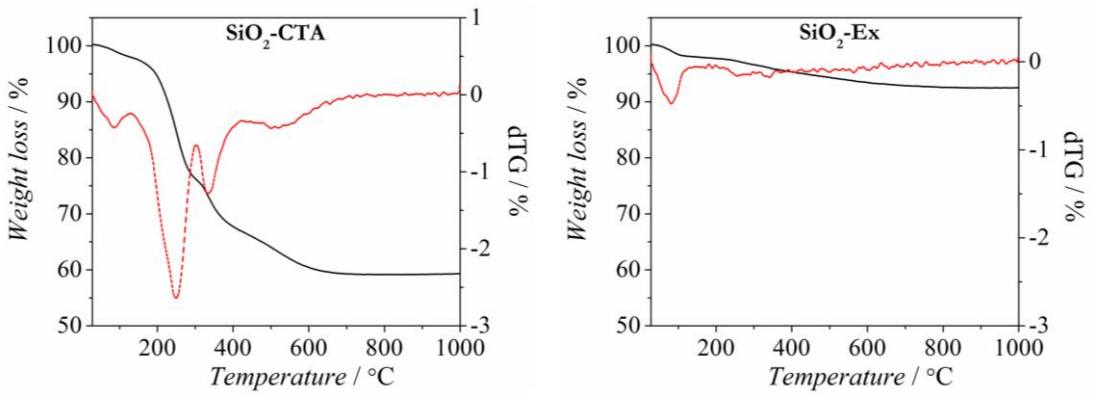

Figure 85. Thermogravimetric analyses for the as-made (SiO_2-CTA) and extracted silica (SiO_2-Ex).

The as-made material shows two main weight losses centered at ~250 and 330 ºC, and a third one that occurs in a wider range (500–600 ºC). The residual mass, which mainly corresponds to silicon oxide, is about 60%. The extracted silica material (SiO_2-Ex), although the channels are empty, displays a significant and constant weight loss. Firstly, a weight loss (~2%) assigned to the evaporation of the solvent (H_2O) is observed between 25 and ~150 ºC. The rest of the weight loss corresponds to the condensation of silanol groups. This latter process is extended from 200 to 1100 ºC, showing no defined peaks in the TG derivative. Note that this condensation of silanol groups will take place in all our materials. The residual

mass in this material, which is about 90%, is accordingly much higher than for the as-made material. It is very important to remember that humidity will tend to condense inside the pores. Hence, after several months of storage, it is important to dry the sample upon heating before using it or perform any characterization technique.

Scanning electron microscopy (SEM)

As explained above, the synthetic route herein used provides a chemically and thermally stable mesoporous silica. Concerning the particles size, this synthesis is not meant to provide nanoparticles. Indeed, the scanning electron microscopy (SEM) images show a complete size polydispersity for one of the materials that will be studied (Figure 86). The sample consists of particles and agglomerations whose sizes range from ~0.5 to ~20 μm.

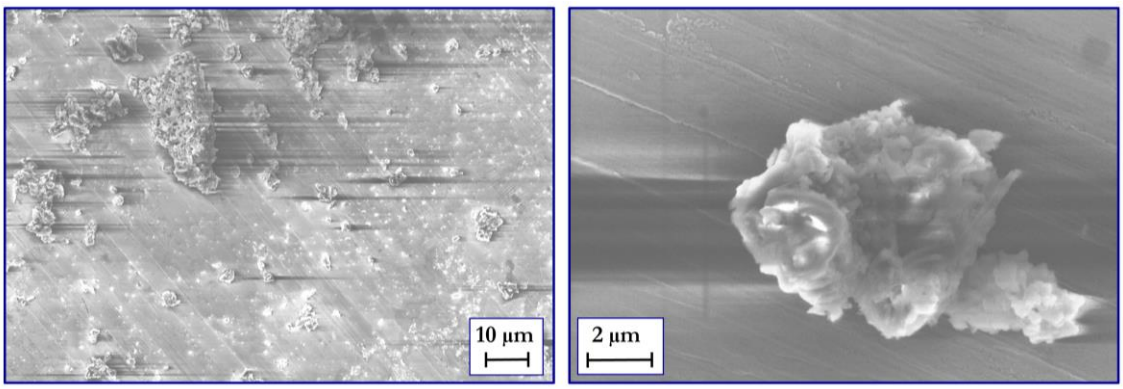

Figure 86. Scanning electron microscopy (SEM) images for one of the materials, labeled as $[Mn^{III}_2O]@SiO_2$, that will be presented in the following pages.

From bulky to nanometric materials

The synthesis of mesoporous silica nanoparticles is nowadays highly investigated. However, there are still several limitations that may be overcome for further applications.[134,287–289] If mesoporous silica nanoparticles were used, both the synthesis and characterization of the new materials would be highly difficult to accomplish. Hence, we herein present the synthesis of Mn-SiO_2 hybrid materials in the most optimized way in order to study how molecular compounds behave when supported on mesoporous silica. Another advantage of using relatively large particles is that the inner surface has statistically more importance than the external one, making the materials easier to study. Nevertheless, if one would like to use the materials either as antioxidant or contrast agents in a future, the synthetic procedures may be adapted for nanoparticles of the desired size (50–150 nm) and the bulky materials may be also used as references.

2.2. Experimental Section

Synthesis of supports

The manganese complexes were inserted into LUS mesoporous silica[116,117] by ionic exchange using a masking agent as described elsewhere.[130] The mesoporous silica was prepared as explained below, following the ultra-fast microwave assisted synthesis reported by J. Chaignon *et al.*[118]

Sodium silicate solution. Ludox HS-40 (187 mL, 1.6 mol SiO_2) was added to a sodium hydroxide (32 g, 0.80 mol) in 800 mL of distilled water, and then stirred at 40 °C overnight until obtaining a colorless solution.

SiO_2-CTA. Cetyltrimethylammonium tosylate (CTATos) (7.84 g, 17 mmol) was stirred in water (284 mL) at 60 °C until its complete dissolution. Meanwhile, the sodium silicate solution previously prepared (196 mL) was also stirred at 60 °C for 1 h, and then added to the surfactant one by pouring it slowly on the edge of the recipient. After a vigorous shaking by hand, the resulting white mixture was placed in several autoclaves and heated in a Berghof speed-wave oven. It provides a microwave irradiation at 2450 MHz with a power of 1450 W. The experimental conditions used were: T = 180 °C, ramp = 1 min, plateau = 9 min (total heating time = 10 min). The autoclaves were allowed to cool at room temperature. Then, a white solid was filtered, washed with distilled water (around 500 mL) and dried at 80 °C to obtain 13.00 g of SiO_2-CTA. Anal. Calcd. for $SiO_2 \cdot 0.13\ CTA \cdot 0.40\ H_2O$ (%): C, 28.45; H, 6.05; N, 1.75. Found: C, 28.75; H, 5.95; N, 1.72; S, 0.00. Residual mass at 1100 °C (%): 55.43.

SiO_2-Ex. The surfactant was extracted by stirring SiO_2-CTA (300 mg) and HCl 1M (0.75 mL) in technical ethanol (60 mL) during 1 h. Then, the solid was filtered, washed twice with technical ethanol (20 mL) and dried overnight at 80 °C. To synthesize larger amounts of SiO_2-Ex, the following procedure was followed: the surfactant was extracted by stirring SiO_2-CTA (~12 g) and HCl 1 M (24 mL) in technical ethanol (800 mL) during 1 h. Then, the solid was filtered, washed twice with technical ethanol (800 mL) and dried overnight at 80 °C, to obtain ~7 g of SiO_2-Ex. Residual mass at 1100 °C (%): 92.54.

Functionalization of supports

SiO_2-TMA. Tetramethylammonium bromide (7.08 g, 45 mmol) was stirred with ethanol 70% (600 mL) at 40 °C for 1 h. Then, SiO_2-CTA (12.5 g) was added to the previous solution and the resulting suspension was stirred at 40 °C for 1 h. A white solid was separated by filtration and washed twice with ethanol 70% (200 mL) and acetone (200 mL). This procedure was repeated three times to ensure an entire exchange of the surfactant. Finally, the solid was dried at 80 °C to obtain 8.42 g of product. Anal. Calcd. for $SiO_2 \cdot 0.105$ TMA$\cdot 0.35$ H_2O (%): C, 6.80; H, 2.66; N, 1.98. Found: C, 7.03; H, 2.61; N, 1.93. Residual mass at 1100 °C (%): 81.23.

Py@SiO_2-TMA. SiO_2-TMA (7.0 g) was stirred and heated up to 130 ºC under Ar. Then, it was kept at this temperature under vacuum for 2 h and was allowed to cool down to room temperature under Ar. Afterwards, 2-(4-pyridylethyl)triethoxysilane (2.9 mL, 10.7 mmol) mixed in cyclohexane (100 mL) was added to the pre-treated solid and the mixture was stirred for 1 h. Cyclohexane (200 mL) was subsequently added and the resulting suspension was stirred at 80 ºC overnight (18 h). The following morning, a white solid was filtered, washed twice with cyclohexane (100 mL), technical ethanol (100 mL) and acetone (100 mL), and dried overnight at 80 ºC to obtain 7.6 g of Py@SiO_2-TMA. Anal. Calcd. for $SiO_2 \cdot 0.08$ TMA$\cdot 0.11$ PySi$\cdot 0.30$ H_2O (Py = 4-pyridylethyl) (%): C, 15.19; H, 2.89; N, 3.09. Found: C, 15.53; H, 2.97; N, 2.94. Residual mass at 1100 °C (%): 74.80.

C_3@SiO_2. SiO_2-Ex (6.33 g) was stirred and heated up to 130 ºC under Ar. Then, it was kept at this temperature under vacuum for 2 h and was allowed to cool down to room temperature under Ar. Afterwards, trimethoxy(propyl)silane (17 mL, 94 mmol) mixed in cyclohexane (80 mL) was added to the pre-treated solid and the mixture was stirred for 1 h. Cyclohexane (240 mL) was subsequently added and the resulting suspension was stirred at 80 ºC overnight (18 h). Then, a white solid was filtered, washed twice with cyclohexane (90 mL), technical ethanol (90 mL) and acetone (90 mL), and dried overnight at 80 ºC to obtain 6.26 g of C_3@SiO_2. Anal. Calcd. for $SiO_2 \cdot 0.096$ $C_3Si \cdot 0.23$ H_2O (%): C, 4.87; H, 1.61; N, 0.00. Found: C, 4.88; H, 1.60; N, 0.00. Residual mass at 1100 °C (%): 91.52.

C_8@SiO_2. The same procedure as for C_3@SiO_2 was followed but using 24 mL of trimethoxy(octyl)silane (88 mmol) mixed in cyclohexane (90 mL) for 6.5 g of SiO_2-Ex. After 1 h of stirring under Ar, cyclohexane (270 mL) was added to perform the reaction overnight. The entire procedure was repeated twice over the resulting solid to obtain 5.84 g of C_8@SiO_2. Residual mass at 1100 °C (%): 84.54.

Ph@SiO_2. The same procedure as for C_3@SiO_2 was followed but using 17 mL of trimethoxy(phenyl)silane (89 mmol) for 6.0 g of SiO_2-Ex to obtain 6.4 g of Ph@SiO_2. Anal. Calcd. for SiO_2·0.075 C_3Si·0.33 H_2O (%): C, 7.313; H, 1.41; N, 0.00. Found: C, 7.33; H, 1.42; N, 0.00. Residual mass at 1100 °C (%): 84.03.

EtO_2CPh@SiO_2. SiO_2-Ex (1.0 g) was stirred and heated up to 130 ºC under Ar. Then, it was kept at this temperature under vacuum for 2 h and was allowed to cool down to room temperature under Ar. Afterwards, ethyl 4-(triethoxysilyl)benzoate (0.75 mL, 2.17 mmol) mixed in cyclohexane (14 mL) was added to the pre-treated solid and the mixture was stirred for 1 h. Cyclohexane (42 mL) was subsequently added and the resulting suspension was stirred at 80 ºC overnight (18 h). Then, a white solid was filtered, washed twice with cyclohexane (14 mL), technical ethanol (14 mL) and acetone (14 mL), and dried overnight at 80 ºC to obtain 1.04 g of Ph@SiO_2. Anal. Calcd. for SiO_2·0.050 EtO_2CPhSi·0.35 H_2O (%): C, 7.18; H, 1.54; N, 0.00. Found: C, 7.07; H, 1.53; N, 0.00. Residual mass at 1100 °C (%): 82.14.

HO_2CPh@SiO_2. Material EtO_2CPh@SiO_2 (190 mg) was treated at 100 ºC overnight with a 1 M HCl aqueous solution (30 mL). Then, a white powder was filtered and washed twice with water (10 mL). Residual mass at 1100 °C (%): 84.15.

Synthesis of Mn-SiO_2 hybrid materials

$[Mn_2O]_{0.5}$@SiO_2. SiO_2-TMA (0.5 g) was pre-treated at 130 °C under vacuum for 1 h and then allowed to cool down to room temperature. Meanwhile, compound **1** (250 mg, 0.272 mmol) was stirred for 1 h in acetonitrile (75 mL). Then, the dark brown manganese solution was slowly added over SiO_2-TMA and stirred for 24 h. The resulting brown suspension was filtered, obtaining a dark brown powder and a clear brown solution. The powder was washed twice with acetonitrile (20 mL) and dried at 80 °C overnight to obtain 0.51 g of solid. Anal. Calcd. for SiO_2·0.033 $[Mn_2O(2\text{–}MeOC_6H_4COO)_2(bpy)_2]$·0.005 TMA·0.35 H_2O (%): C, 15.91; H, 1.93; N, 2.10; Si, 30.80; Mn, 3.98. Found: C, 15.85; H, 1.95; N, 2.08; Si, 30.80; Mn, 3.98; Cl, 0.00. Residual mass at 1100 °C (%): 72.04. The same procedure was carried out but using compound **2** (251 mg, 0.272 mmol) and a solid with the same characteristics was obtained. Elemental analyses: C, 15.79; H, 1.87; N, 2.01; Cl, 0.00. Residual mass at 1100 °C (%): 70.84. These two solids were considered equivalent and labeled $[Mn_2O]_{0.5}$@SiO_2.

$[Mn_2O]_{0.1}$@SiO_2. The same procedure as for material $[Mn_2O]_{0.5}$@SiO_2 was followed but using 70 mg (0.076 mmol) of **1** for 0.70 g of SiO_2-TMA. The resulting brown suspension was

filtered, obtaining a dark brown powder and a colorless solution. The powder was washed twice with acetonitrile (20 mL) and dried at 80 °C overnight to obtain 0.71 g of solid. Anal. Calcd. for SiO_2·0.0084 $[Mn_2O(2–MeOC_6H_4COO)_2(bpy)_2]$·0.088 TMA·0.35 H_2O (%): C, 10.05; H, 2.46; N, 2.18; Si, 35.90; Mn, 1.18. Found: C, 9.52; H, 2.48; N, 2.30; Si, 34.96; Mn, 1.19. Residual mass at 1100 °C (%): 79.49.

$[Mn_2O]_{0.21}$-Py@SiO_2. Py@SiO_2-TMA (6.9 g) was stirred and heated up to 80 °C under Ar. Then, it was kept at this temperature under vacuum for 2 h and was allowed to cool down to room temperature under Ar. Meanwhile, compound **1** (1.26 g, 1.37 mmol) was stirred in acetonitrile (400 mL) for a while. Afterwards, the dark brown manganese suspension was slowly added over the pre-treated Py@SiO_2-TMA (and kept under Ar) and the resulting mixture was stirred for 24 h. The resulting brown suspension was filtered, obtaining a dark brown powder and a colorless solution. The powder was washed twice with acetonitrile (50 mL each) and dried at 80 °C overnight to obtain 7.0 g of solid. Anal. Calcd. for SiO_2·0.010–0.020 PySi·0019 $[Mn_2O(2–MeOC_6H_4COO)_2(bpy)_2]$·0.010–0.020 TMA·0.25 H_2O (Py = 4-pyridylethyl) (%): C, 18.12–18.36; H, 2.37–2.41; N, 2.80–2.85; Si, 33.13–33.21; Mn, 2.24–2.25. Found: C, 17.96; H, 2.47; N, 2.72; Si, 31.66; Mn, 2.16. Residual mass at 1100 °C (%): 72.42.

$[Mn_2O]_{0.12}$-Py@SiO_2. The same procedure as for $[Mn_2O]_{0.21}$-Py@SiO_2 was followed but using 105 mg of **1** (0.11 mmol) for 1.0 g of Py@SiO_2-TMA and 45 mL of acetonitrile. The resulting brown suspension was filtered, obtaining a dark brown powder and a colorless solution. The powder was washed twice with acetonitrile (15 mL) and dried at 80 °C overnight to obtain 1.0 g of solid. Anal. Calcd. for SiO_2·0.11 Py·0.011 $[Mn_2O(2–MeOC_6H_4COO)_2(bpy)_2]$·0.030 TMA·0.35 H_2O (%): C, 16.88; H, 2.50; N, 2.82; Si, 34.06; Mn, 1.32. Found: C, 16.12; H, 2.54; N, 2.74; Si, 33.49; Mn, 1.29. Residual mass at 1100 °C (%): 73.86.

$[Mn_2O]_{0.04}$-Py@SiO_2. The same procedure as for $[Mn_2O]_{0.21}$-Py@SiO_2 was followed but using 140 mg of **1** (0.15 mmol) for 4.0 g of Py@SiO_2-TMA and 120 mL of acetonitrile. The resulting brown suspension was filtered, obtaining a dark brown powder and a colorless solution. The powder was washed twice with acetonitrile (30 mL) and dried at 80 °C overnight to obtain 4.1 g of solid. Anal. Calcd. for SiO_2·0.11 Py·0.0034 $[Mn_2O(2–MeOC_6H_4COO)_2(bpy)_2]$·0.055 TMA·0.35 H_2O (%): C, 14.92; H, 2.86; N, 2.79; Si, 34.81; Mn, 0.42. Found: C, 14.57; H, 2.82; N, 2.89; Si, 34.49; Mn, 0.41. Residual mass at 1100 °C (%): 75.99.

C_3@SiO_2-[Mn_6Ca_2]. C_3@SiO_2 (0.54 g) was stirred and heated up to 80 ºC under Ar. Then, it was kept at this temperature under vacuum for 2 h and was allowed to cool down to room temperature under Ar. Meanwhile, compound **22** (109 mg, 0.034 mmol) was stirred in acetonitrile (30 mL) for a while. Afterwards, the dark manganese suspension was slowly added over the pre-treated C_3@SiO_2 and the resulting mixture was stirred under Ar for 24 h. The resulting brown suspension was filtered, obtaining a dark brown powder and a light brown solution. The powder was washed twice with acetonitrile (10 mL) and dried at 80 °C overnight to obtain 0.55 g of solid. Anal. Found (%): C, 8.33; H, 1.67; N, 0.00; Si, 28.92; Mn, 1.20. Residual mass at 1100 °C (%): 79.68.

Ph@SiO_2-[Mn_6Ca_2]. Ph@SiO_2 (0.51 g) was stirred and heated up to 80 ºC under Ar. Then, it was kept at this temperature under vacuum for 2 h and was allowed to cool down to room temperature under Ar. Meanwhile, compound **22** (160 mg, 0.050 mmol) was stirred in acetonitrile (30 mL) for a while. Afterwards, the dark manganese suspension was slowly added over the pre-treated Ph@SiO_2 and the resulting mixture was stirred under Ar for 24 h. The resulting brown suspension was filtered, obtaining a dark brown powder and a light brown solution. The powder was washed twice with acetonitrile (10 mL) and dried at 80 °C overnight to obtain 0.52 g of solid. Anal. Found (%): C, 11.78; H, 1.75; N, 0.00; Si, 28.92; Mn, 1.20. Residual mass at 1100 °C (%): 72.42.

Ph@SiO_2-[Mn_{12}]. Ph@SiO_2 (0.50 g) was stirred and heated up to 80 ºC under Ar. Then, it was kept at this temperature under vacuum for 2 h and was allowed to cool down to room temperature under Ar. Meanwhile, compound **26** (80 mg, 0.024 mmol) was stirred in acetonitrile (22 mL) for a while. Afterwards, the dark manganese suspension was slowly added over the pre-treated Ph@SiO_2 (and kept under Ar) and the resulting mixture was stirred for 24 h. The resulting brown suspension was filtered, obtaining a dark brown powder and a light brown solution. The powder was washed twice with acetonitrile (24 mL) and dried at 80 °C overnight to obtain 0.51 g of solid. Anal. Calcd. for SiO_2· 0.055 PhSi· 0.0030 $[Mn_{12}O_{12}(3\text{-}MeOC_6H_4COO)_{16}(H_2O)_4]$·0.25 H_2O (%): C, 10.67; H, 1.42; N, 0.00; Si, 36.85; Mn, 2.46. Found: C, 10.20; H, 1.44; N, 0.00; Si, 35.34; Mn, 2.33. Residual mass at 1100 °C (%): 79.21.

Physical characterization

Chemical analyses (C, H, N and Cl) were carried out by the "Centres Científics i Tecnològics" of the Universitat de Barcelona and by the "Servei de Microanàlisi" of the

"Consell Superior d'Investigacions Científiques" (CSIC). **Inductively coupled plasma optical emission spectrometry (ICP-OES)** was performed to determine Mn and Si percentages by the "Centres Científics i Tecnològics" of the Universitat de Barcelona from a solution of the Mn-SiO_2 material (~20 mg) pre-treated at 90 ºC with a mixture of HF 49% (200 μL) and HNO_3 70% (1 mL) into an autoclave. **Infrared spectra** were recorded on KBr pellets in the 4000-400 cm^{-1} range with a Thermo Nicolet Avatar 330 FTIR spectrometer. **Thermogravimetric analysis (TGA)** was carried out with a NETZSCH STA 409 PC Luxx device under aerobic conditions with a 10 °C/min temperature increase. **Nitrogen sorption isotherms** at 77 K were determined with a volume device Belsorp Marx on solids that were dried under vacuum overnight at 130 °C (samples SiO_2-Ex and SiO_2-TMA) or at 80 °C (samples of Mn-SiO_2 materials and functionalized supports). The accuracy of the parameters obtained from this technique comprises around a 3% of relative error. **Low angle X-Ray powder diffraction (XRD)** was carried out using a Brucker D8 Advance diffractometer equipped with a VÅNTEC 1 detector and using Cu K_α monochromatic radiation at the "Centre de Diffractométrie Henri Longchambon" in Lyon. **Solid NMR spectra** were measured on an Advance III Bruker 500 MHz Wide Bore spectrometer, with a CP/MAS DVT (double resonance, variable temperature) probe 4 mm. The delay time between pulses (pulse width 5 μs) in HPDEC experiments was set to 500 s. Spinning speed was set to about 10 kHz and the number of scans was between 300 and 600. The frequencies used were 125 MHz for ^{13}C and 99.36 MHz for ^{29}Si. **Transmission electron microscopy (TEM) analysis** was performed at the "Centre Lyonais de Microscopie" of the "Institut National des Sciences Appliquées" (INSA) from Lyon with a TOPCON Em-002b and operated at 120 kV, dispersing material $[Mn_2O]_{0.5}$@SiO_2 in ethanol and depositing it on a Holey carbon 300 mesh copper grid. **Scanning electron microscopy (SEM)** was performed in a Zeiss SUPRA 55 VP device using secondary electron mode and a voltage of 5 KV. **Magnetic susceptibility (χ_M)** measurements (2-300 K) were carried out in a Quantum Design MPMS XL5 SQUID Magnometer at the Unitat de Mesures Magnètiques of the University of Barcelona. Two different magnetic fields were used for the magnetic susceptibility measurements, 0.02 T (2–29 K) and 0.3 T (2–300 K), with imposable graphs. Pascal's constants were used to estimate the diamagnetic corrections. The fit was performed by minimizing functions $R_{SUS} = \Sigma[(\chi_M T)_{exp} - (\chi_M T)_{calcd.}]^2 / \Sigma[(\chi_M T)_{exp}]^2$. **X-ray Absorption Near Edge Structure (XANES)** of well-pounded microcrystalline powders of homogeneous thickness and calculated weight samples of compound **1** and material $[Mn_2O]_{0.5}$@SiO_2 were collected at room temperature at the synchrotron ALBA in Barcelona (Spain) on the BL22 (CLÆSS) beam line. The

measurements were carried out at the Mn K-edge in the transmission mode. The experiments were calibrated by verifying that the first inflection point in all manganese foil spectra recorded together with XANES spectra of the compounds was at 6539 eV. **X-ray photoelectron spectroscopy (XPS)** experiments were performed at the "Centres Científics i Tecnològics" of the Universitat de Barcelona in a PHI 5500 Multitechnique System (from Physical Electronics) with a monochromatic X-ray source (Al $K\alpha$ line of 1486.6 eV energy and 350 W), placed perpendicular to the analyzer axis and calibrated using the $3d_{5/2}$ line of Ag with a full width at half maximum (FWHM) of 0.8 eV. The analyzed area was a circle of 0.8 mm diameter, and the selected resolution for the spectra was 187.85 eV of pass energy and 0.8 eV/step for the general spectra and 23.5 eV of pass energy and 0.1 eV/step for the spectra of the different elements. A low energy electron gun (less than 10 eV) was used in order to discharge the surface when necessary. All measurements were made in an ultra-high vacuum (UHV) chamber pressure between $5x10^{-9}$ and $2x10^{-8}$ torr. Binding energies were further referenced to the C_{sp2} peak at 284.6 eV. **UV-visible** spectra were recorded with a Varian Cary 100 Scan spectrophotometer.

2.3. Catalase-Biomimetic Mn-SiO_2 Based Materials

First insights

As commented in the introduction, the insertion of Mn-CAT model compounds in porous solids offers the possibility to emulate some characteristics of the enzymatic cavity, and is likely to increase the stability of such models in the reaction media. Aiming to mimic the cavity of the Mn-CAT enzyme, two of the Mn^{III}_2 compounds, **1** and **2**, were inserted in the nanochannels of mesoporous silica (MCM-41 type). These compounds, with formula $[\{Mn^{III}(bpy)(H_2O)\}(\mu\text{-}2\text{-}MeOC_6H_4COO)_2(\mu\text{-}O)\{Mn^{III}(bpy)(X)\}]X$, where X = NO_3 (**1**) and ClO_4 (**2**), were chosen due to their higher activity in comparison with the other Mn^{III}_2 compounds reported in this work. Their synthesis and characterization is presented in Chapter 1.3 and the study of their catalytic properties will be subsequently explained in Chapter 3.3.

Firstly, both compounds were inserted into mesoporous silica containing the TMA^+ ions. It is worth noting that TMA^+ ions are only held on the surface by electrostatic forces; hence, the driving force of the insertion is the ionic exchange, since both compounds, **1** and **2**, are ionic. Then, a further functionalization of the inner surface of the support was considered in order to increase the stability of the support itself and to induce some changes in the catalytic properties of the material. Hence, supports containing organic functions and TMA^+ ions were synthesized to incorporate the compounds also by ionic exchange. Two functions, trimethylsilyl (TMS) (nonbinding and highly hydrophobic) and 4-pyridylethyl (Py) functions (binding and moderately hydrophobic) were tested. The use of TMS functions led to a highly hydrophobic material that was very difficult to disperse in water. On the other hand, when the silica was functionalized with Py, the material was easily dispersed both in acetonitrile and water. Besides, the Py function may act as an acid-base auxiliary and/or may help to retain the Mn complex inside the silica to minimize the leaching during the application (catalase activity).

Materials loaded with different amounts of Mn complex were synthesized and the physicochemical properties of the materials and the supported Mn complex were studied. In the following pages, five new materials are described: $[Mn_2O]_x@SiO_2$ (x = 0.5 and 0.1) and $[Mn_2O]_x$-Py@SiO_2 (x = 0.21, 0.12, and 0.04), where x is the Mn_2/TMA molar ratio used in

the synthetic procedure. Owing to its relative simplicity and high Mn/Si molar ratio, a complete physicochemical characterization was possible for material $[Mn_2O]_{0.5}@SiO_2$. Therefore, a deep discussion about the physical and chemical characteristics of this material will be firstly presented in the following pages.

Synthesis and characterization of material $[Mn_2O]_{0.5}@SiO_2$

Synthesis strategy. Cationic complexes of compounds **1** and **2** were inserted into the nanopores of mesoporous silica by ionic exchange.[130] A step-by-step procedure to obtain material $[Mn_2O]_{0.5}@SiO_2$ is shown in Figure 87. 2D hexagonal LUS silica (MCM–41 type), prepared at high temperature using cetyltrimethylammonium tosylate (CTATos) as a surfactant, was chosen as a support.[117,113,131,132] It possesses a large pore volume of 0.80 ± 0.01 $cm^3\ g^{-1}$ and a narrow pore size distribution (pore diameter = 3.8 ± 0.1 nm) that may be suitable for the insertion of compounds **1** and **2**, which are approximately 1.3 nm wide. The cationic surfactant of the as–made silica (SiO_2-CTA) was exchanged for tetramethylammonium cations (TMA^+) using the procedure described by K. Zhang *et al.*,[130] leading to the formation of SiO_2-TMA with molar composition $SiO_2 \cdot 0.105\ TMA \cdot 0.35\ H_2O$.

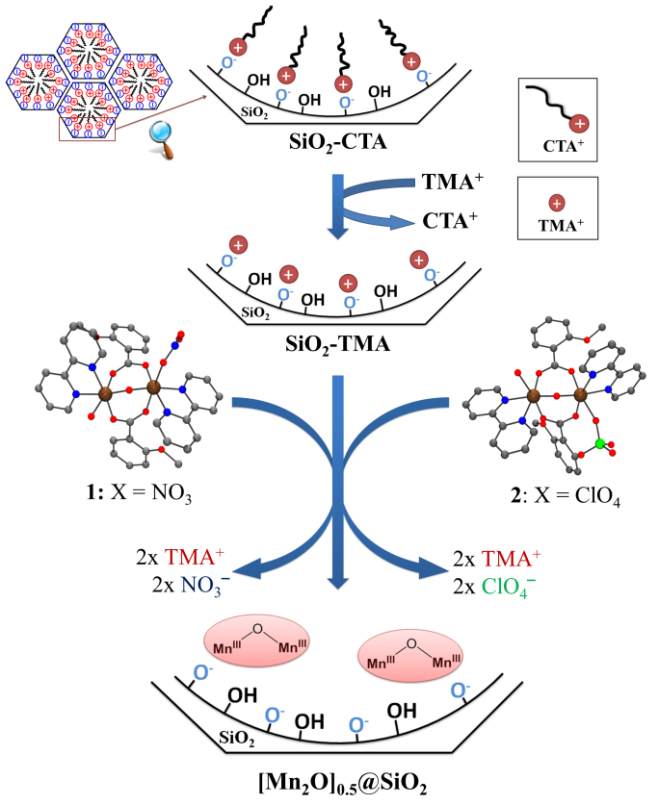

Figure 87. Synthetic procedure to obtain the Mn-SiO_2 based material $[Mn_2O]_{0.5}@SiO_2$ from "as-made" silica (SiO_2-CTA). The insertion performed from compound **1** or **2** leads to the same material. Abbreviations: CTA^+, cetyltrimethylammonium; TMA^+, tetramethylammonium.

$[Mn_2O]_{0.5}$@SiO_2 was prepared from the mixture of an acetonitrile solution of compound **1** or **2** and SiO_2-TMA at room temperature. TMA^+, which is only held into the silica by electrostatic forces, is easily displaced when other positively charged species with more affinity for silica are present. The $[Mn_2]^{2+}/TMA^+$ molar ratio used was 0.5, which corresponds to 1.0 for charge ratio.

The elemental analyses (see results in the Experimental Section, Chapter 2.2) revealed that material $[Mn_2O]_{0.5}$@SiO_2, obtained from **1** or **2**, have the same molar composition and their IR spectra were superimposable (Figure S27). The results obtained from thermogravimetric analysis as well as from N_2 sorption isotherms for both materials may be considered identical (Table 25 and Figure 88), as the differences between the solids are within the experimental error. These facts prove that the counter-anions have an unperceived effect and, obviously, that they remain in solution without being retained by the silica.

Table 25. Textural properties of materials SiO_2-CTA, SiO_2-Ex, SiO_2-TMA and $[Mn_2O]_{0.5}$@SiO_2.

				$[Mn_2O]_{0.5}$@SiO_2	
	SiO_2-CTA	**SiO_2-Ex**	**SiO_2-TMA**	**From 1**	**From 2**
d_{100} / nm	4.1	-	4.1	4.1	4.1
a_0[a] / nm	4.7	-	4.8	4.7	4.8
Intensity[b] / 10^3 counts	100	-	230	139	119
HWHH[c] 2θ / °	0.24	-	0.23	0.27	0.28
S_{BET}[d] / m^2 g^{-1}	-	945	-	-	-
C	-	102	73	53	50
Porous volume[e] /mL g^{-1}	-	0.80	0.69	0.36	0.36
Pore diameter[f] /nm	-	3.8	3.7	2.8–3.4	2.8–3.3

[a] Parameter calculated from d_{100} with the formula $a_0 = 2*d_{100}/3^{1/2}$; [b] height at the maximum of (100) peak; [c] half-width at half-height; [d] calculated using BET method;[277] [e] calculated using the *t*-plot;[278,279] [f] Using BdB method.[111]

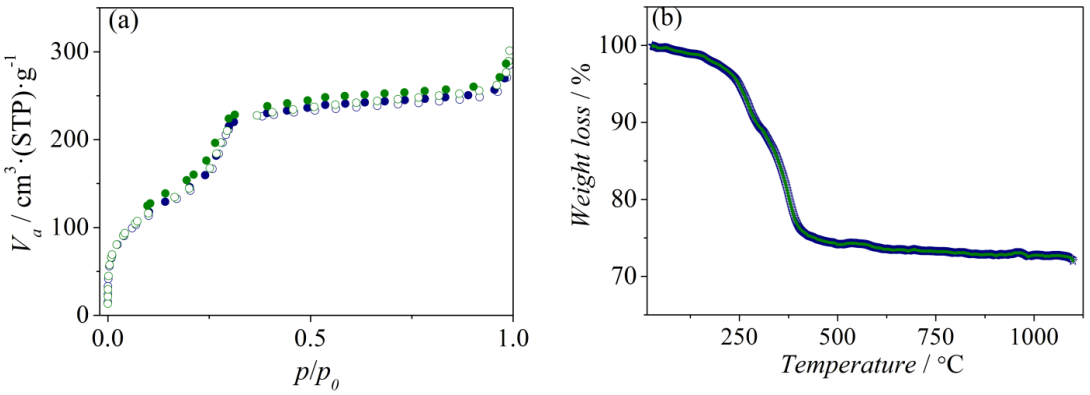

Figure 88. N_2 sorption isotherms at 77 K (a) and weight loss versus temperature (b) for material $[Mn_2O]_{0.5}$@SiO_2 obtained from the insertion of compounds **1** (blue) and **2** (green) into SiO_2-TMA.

Morphology of the hybrid material. The hexagonal array of the internal pores of the material was unaltered during the insertion of the Mn complex, as shown from the X–ray diffraction (XRD) patterns (Figure 89), being 4.8 ± 0.1 nm the distance between the centers of the pores (a_0) (Table 25). The transmission electron microscopy (TEM) images of the hybrid material $[Mn_2O]_{0.5}$@SiO_2 (Figure 90) confirm the persistence of the cylinder array along the (110) plane. The low temperature nitrogen sorption isotherms of the surfactant-extracted support, SiO_2-Ex, and the hybrid solids, SiO_2-TMA and $[Mn_2O]_{0.5}$@SiO_2, exhibit a type IV isotherm according to the IUPAC nomenclature, without hysteresis as usually observed for MCM-41 2D hexagonal mesoporous silica.[113,274] The decrease of pore volume from 0.80 to 0.36 $cm^3\ g^{-1}$ after the insertion confirms the presence of the Mn complex inside the pores (Table 25). This is also consistent with the decrease of intensity of the peak (100) observed in XRD of material $[Mn_2O]_{0.5}$@SiO_2 (Table 25), since a lower intensity is expected for those solids whose contrast between silica wall and the channel atom occupancy is lower.[128,129] The BET constant C of the hybrid material ($C \approx 50$) is much lower than that of the SiO_2-Ex ($C \approx 105$) (Table 25), indicating that the surface has become more hydrophobic. Moreover, the capillary condensation shifts to a lower range of pressures in the solid $[Mn_2O]_{0.5}$@SiO_2 (Figure 89), corresponding to a pore size reduction of about 0.7 nm. It also occurs progressively in a wider range of pressures and not in a series of steps, indicating that the Mn complex was properly spread along the whole channel. In this case, the pore size distribution is broad due to the inequality and roughness of the surface caused by the Mn complex shape, covering values between 2.8–3.3 nm according to Broekhoff and de Boer (BdB) analysis (Table 25).[111]

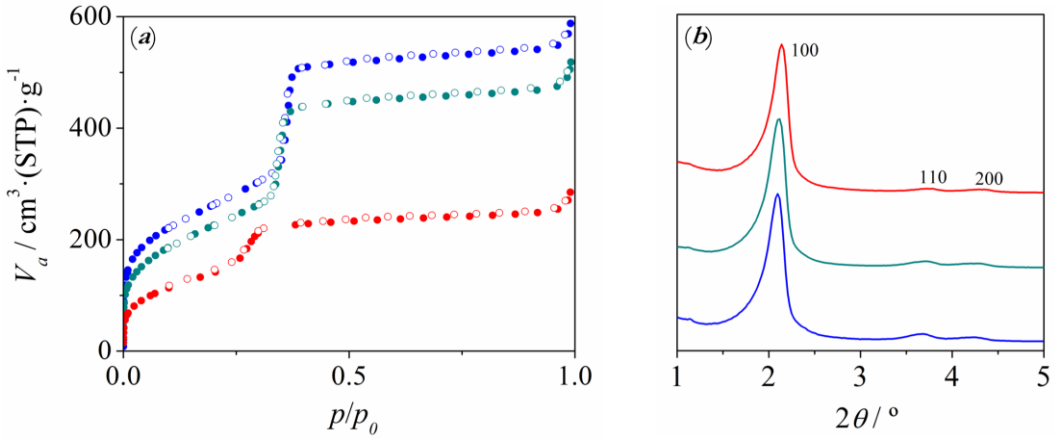

Figure 89. (***a***) N_2 adsorption (full circles) and desorption (empty circles) isotherms at 77 K of materials SiO_2-Ex (blue), SiO_2-TMA (dark cyan) and $[Mn_2O]_{0.5}$@SiO_2 (red); and (***b***) small-angle powder XRD patterns of materials SiO_2-CTA (blue), SiO_2-TMA (dark cyan) and $[Mn_2O]_{0.5}$@SiO_2 (red). The intensity was normalized with the (100) peak.

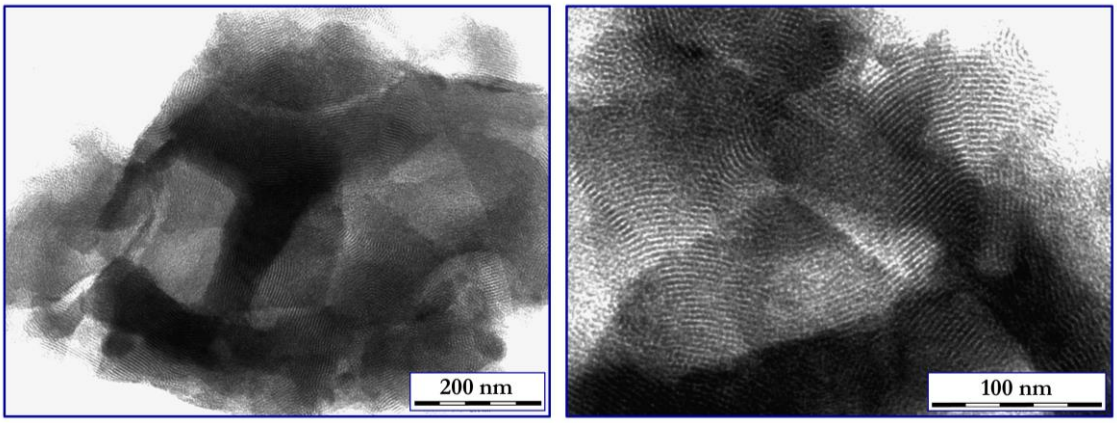

Figure 90. TEM images of the material $[Mn_2O]_{0.5}@SiO_2$. Both images show agglomerations of particles of the hybrid material.

Characterization of the Mn(III) complex inside the silica support. The calculated formula from the elemental analyses and inductively coupled plasma optical emission spectrometry (ICP-OES) for the $[Mn_2O]_{0.5}@SiO_2$ hybrid material is $SiO_2 \cdot 0.033\ [Mn_2O(2\text{–}MeOC_6H_4COO)_2(bpy)_2] \cdot 0.005\ TMA \cdot 0.35\ H_2O$, which corresponds to a ~4% Mn in weight. This metal loading corresponds to *ca.* 66% of the cationic exchange capacity assuming two positive charges for both **1** and **2** complexes and that both X^- ions are removed. Strikingly, the remaining quantity of TMA^+ ions in the solid is much less than the 34% expected for a mere cation exchange of 2 TMA^+ per complex as it is only 5% of the initial content of SiO_2-TMA. The missing TMA^+ ions are removed according to another reaction that is likely neutralization. Indeed, the acetonitrile solutions of the Mn(III) compounds contain traces of water and are acidic, allowing a partial protonation of the silanolate groups and the release of additional TMA^+ ions. The thermogravimetric analysis (TGA) shows two main weight losses in the range 200–400 °C that are mainly assigned to the decomposition of the Mn complex ligands and suit perfectly with the calculated formula (see more details in Appendix VII).

The IR spectrum of $[Mn_2O]_{0.5}@SiO_2$ contains the vibrational fingerprints of the Mn complex ligands and TMA^+ ions, particularly in the window 1700–1200 cm^{-1} (Figure 91). Despite a low concentration, the narrow peak at 1488 cm^{-1} typical of CH_3 scissoring vibrational mode of the TMA^+ shows up in the middle of bands belonging to the ligand and attests for its presence in $[Mn_2O]_{0.5}@SiO_2$.[130] Nearby, the bands centered at 1604, 1473 and 1442 cm^{-1} are assigned to the bipyridine (bpy) ligand. A fourth and weak band is expected at 1496 cm^{-1} for the bpy ligand, but it is masked by the band assigned to TMA^+ (see above). At 1558 and 1396 cm^{-1} arise the asymmetric and symmetric vibrations of the carboxylate groups, respectively.

It is worth noting that the symmetric vibration shifts from ~1370 (as observed in the IR spectra of compound **1** and **2**) to 1396 cm^{-1} when the complexes are incorporated in the silica pores, suggesting a slight change of structural parameters upon which carboxylate bridges are participating. Nevertheless, in spite of decreasing, the $\Delta\nu$ value ($\Delta\nu = \nu_a(COO) - \nu_s(COO)$) is in the range found for bidentate carboxylate ligands coordinated to two metal ions in $\mu_{1,3}$ bridging mode.[14] Moreover, the absence of bands at ~1700 cm^{-1} excludes the presence of protonated carboxylate groups, and consequently excludes the decoordination of these ligands. The broadening of the signals may be either due to distribution of slightly different species on the surface, caused by the heterogeneity of the environment,[290] or due to dynamic effects.[291] Precise information concerning the IR spectra of compounds **1** and **2** is found in Chapter 1.3.

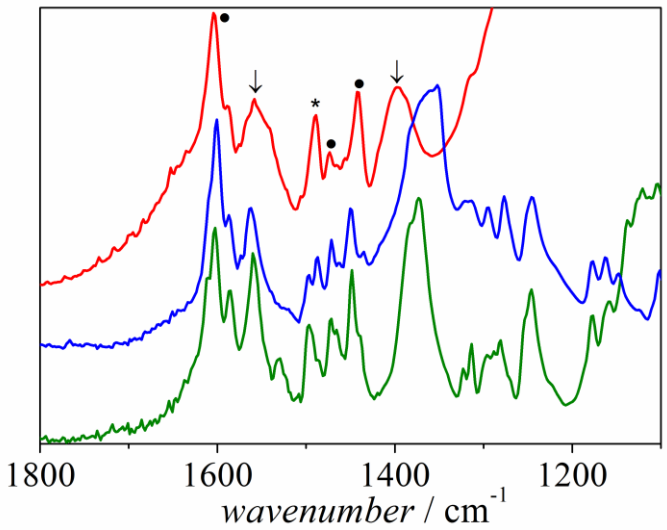

Figure 91. Infrared spectra (range 1800–1100 cm^{-1}) of compound **1** (blue line), compound **2** (green line) and material $[Mn_2O]_{0.5}@SiO_2$ (red line). The star (*), the arrows (↓) and circles (●) point out IR vibrations of TMA^+, carboxylate and bipyridine, respectively.

In order to characterize the nature of the Mn(III) complex within the silica support, XAS measurements of compound **1** (as model) and material $[Mn_2O]_{0.5}@SiO_2$ were performed. Mn K-edge XANES and the pre-edge before the main K-edge are sensitive to the oxidation state and bonding environment of manganese.[261,292] Between them, the pre-edge region is much less influenced by the medium as compared to the edge jump region.[293] Compound **1** shows a pre-edge peak at 6541 eV, while for the material $[Mn_2O]_{0.5}@SiO_2$ two features, at 6540 eV and 6543 eV, could be observed (Figure S28). Moreover, for the hybrid material, the first inflexion point of the Mn K-edge is shifted by 1.8 eV, in comparison to compound **1**. Both factors suggest some changes in the hybrid material. According to the XPS analysis and the

magnetic measurements (see below), the difference between the Mn K-edge XANES spectra of **1** and $[Mn_2O]_{0.5}$@SiO_2 could have been promoted by the radiation. So, this technique did not allow us to obtain valuable information about the manganese complex inside the silica.

XPS measurements of compound **1** (as model) and material $[Mn_2O]_{0.5}$@SiO_2 were performed with the aim of clarifying the oxidation state of the Mn ions inside de support. The results obtained from the fit of the C 1s, the N 1s and the Mn 3s peaks are summarized in Table 26. The C 1s signals of compound **1** and material $[Mn_2O]_{0.5}$@SiO_2 are very similar and are distributed in three main XPS features, assigned to C_{sp2} (284.6 eV), C–N and C–O_{ether} (~286 eV) and $C_{carboxylate}$ (~288 eV) (Figure 92).[294,295] Moreover, the C/Mn_2 and N/Mn_2 ratios (being 35 and 4, respectively) are consistent with the existence of the $[Mn^{III}_2O(2\text{-}MeOC_6H_4COO)_2(bpy)_2]^{2+}$ unit in material $[Mn_2O]_{0.5}$@SiO_2.

Table 26. Summary of the C 1s, N 1s and Mn3s photoelectron results for compound **1** and material $[Mn_2O]_{0.5}$@SiO_2.

	Compound 1			**Material $[Mn_2O]_{0.5}$@SiO_2**		
	Position / eV	**Δ[a] / eV**	**Area ratio[b]**	**Position /eV**	**Δ[a] / eV**	**Area ratio[b]**
C 1s	284.6	0.0	1.0	284.6	0.0	1.0
	285.8	1.2	0.4	286.2	1.6	0.4
	288.1	3.5	0.1	287.5	2.9	0.1
N 1s	399.6	0.0	1.0	399.3	0.0	1.0
	406.2	6.6	0.6	402.4	3.1	0.6
Mn 3s	83.6	0.0	1.0	83.0	0.0	1.0
	89.2	5.6	0.8	88.6	5.6	0.6

[a] Peak separation; [b] All areas are normalized with the highest one in each transition.

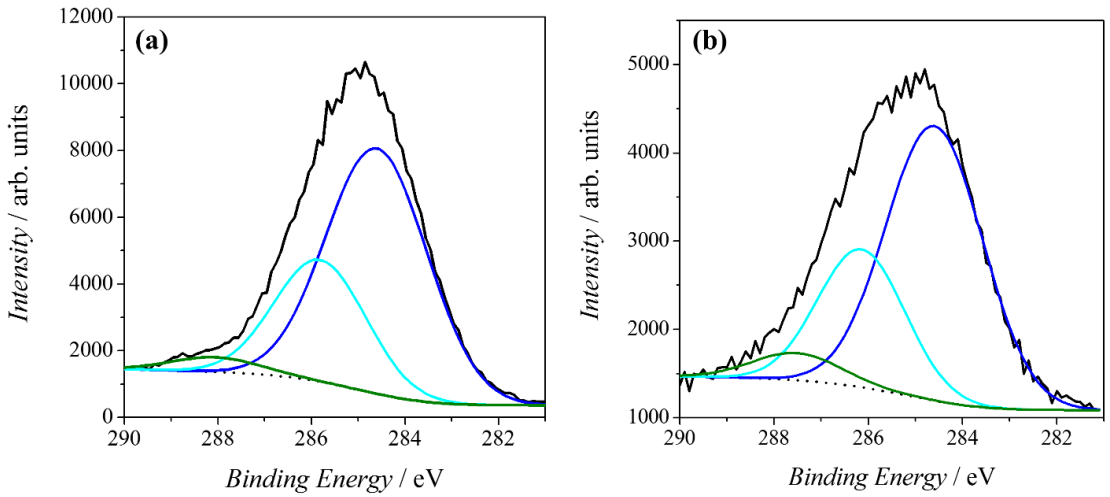

Figure 92. C 1s peak of the XPS spectra for compound **1** (a) and material $[Mn_2O]_{0.5}$@SiO_2 (b). The solid black lines correspond to the experimental plots and the dotted lines to the background. The colored lines correspond to the spectra deconvolutions, with three contributions assigned to C_{sp2} (blue), C–N and C–O_{ether} (cyan) and $C_{carboxylate}$ (green).

Figure 93 shows the Mn 3s spectra for **1** and material $[Mn_2O]_{0.5}@SiO_2$. The Mn 3s doublet splitting (ΔMn 3s) provides a reliable way of determining the oxidation state of manganese, being smaller for higher oxidation state.[296] Both solids display ΔMn 3s equal to 5.6 eV (Table 26), being in agreement with those reported by J. Nelson *et al* for a series of Mn(III) complexes with carboxylate and oxo bridges,[297] and also with the values collected in Table S24 for Mn compounds with different oxidation states (II, III, and IV). This fact confirms that for material $[Mn_2O]_{0.5}@SiO_2$ the oxidation state of the Mn ions is III.

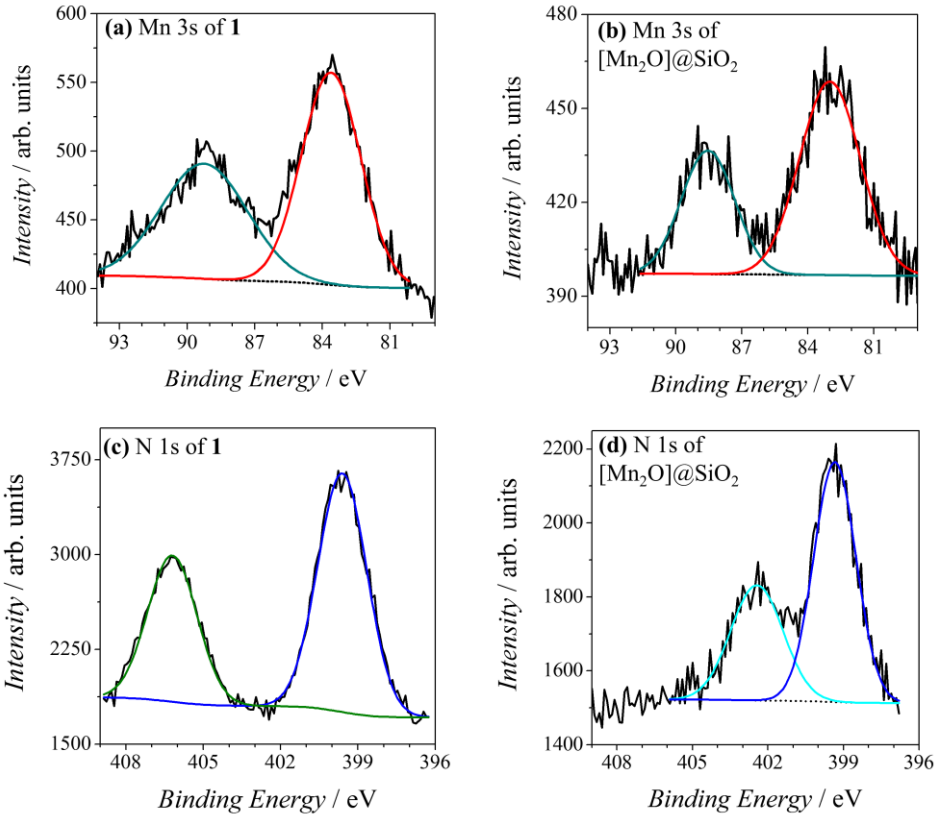

Figure 93. Mn 3s (a and b) and N 1s (c and d) peaks of the XPS spectra for compound **1** (a and c) and material $[Mn_2O]_{0.5}@SiO_2$ (b and d). The solid black lines correspond to the experimental plots, the dotted lines to the background and the colored lines to the spectra deconvolutions.

The N 1s spectrum of compound **1** (shown in Figure 93) displays two main peaks, assigned to the N atoms of the bpy (blue peak centered at 399.6 eV) and to the NO_3^- anions (green peak centered at 406.2 eV).[294] As expected, the NO_3^- peak is not present in the N 1s spectrum of material $[Mn_2O]_{0.5}@SiO_2$, consistent with the absence of the counter-anion in the hybrid material as explained above. Indeed, the overall N/Mn_2 ratio is lower for $[Mn_2O]_{0.5}@SiO_2$ than for **1** and agrees with two bpy ligands for each Mn_2 entity, in agreement with the loss of NO_3^- ions during the synthesis of the Mn-Si hybrid. Note that the amount of TMA^+ ions in material $[Mn_2O]_{0.5}@SiO_2$ is almost negligible according to the elemental analyses and ICP-

OES, with a bpy/TMA^+ molar ratio of ~13. Moreover, the peak around 401 eV is now split in two components, centered at 399.3 (blue) and 402.4 eV (cyan). The first and more intense peak could be assigned to N_{sp2} neutral atoms,[298] while the second and weaker could be attributed to some change in the coordination of one of the bpy ligands likely due to the interaction with the silica support.[290,294]

Magnetic measurements were also carried out for material $[Mn_2O]_{0.5}$@SiO_2. $\chi_M T$ versus T plot of this material (shown in Figure 94) indicates that there is a non-negligible interaction between the Mn ions, which strongly supports the assumption about the Mn^{III}_2 unit being maintained in the silica pores. The $\chi_M T$ value at room temperature (5.8 cm^3 mol^{-1} K) is close to the expected value for two uncoupled Mn(III) ions. The data was fitted from 300 to 17 K using the PHI program ($H = -2JS_1S_2$),[165] omitting the data at low temperature (17 – 2 K) to avoid zero-field splitting effects. The best fit corresponds to $g = 1.98$, $2J = -1.2$ cm^{-1}, $R_{sus} = 3.4 \times 10^{-5}$. This $2J$ value is between those found for **1** and **2**, thus it is also in the expected range for a $[Mn^{III}_2O(2\text{-}RC_6H_4COO)_2]^{2+}$ subunit (between –12 and +5 cm^{-1}).[181] Unfortunately, we could not fit the whole curve due to a deviation in the low temperature range. As it was mentioned, magnetic properties of this kind of complex are very sensitive to structural and electronic parameters.[181,183,193] So, this deviation may be ought to the existence of more than one species that could slightly differ in some structural parameters. We achieved to fit the whole curve by keeping constant the parameters referred to the Mn anisotropy, with very similar values to those of the molecular analogues (compounds **1** and **2**). However, reporting this last fit would be meaningless because it involves the assumption of unknown parameters, such as D_{Mn}, E_{Mn} and the relative orientation of the Jahn-Teller axes of the Mn^{III} ions.

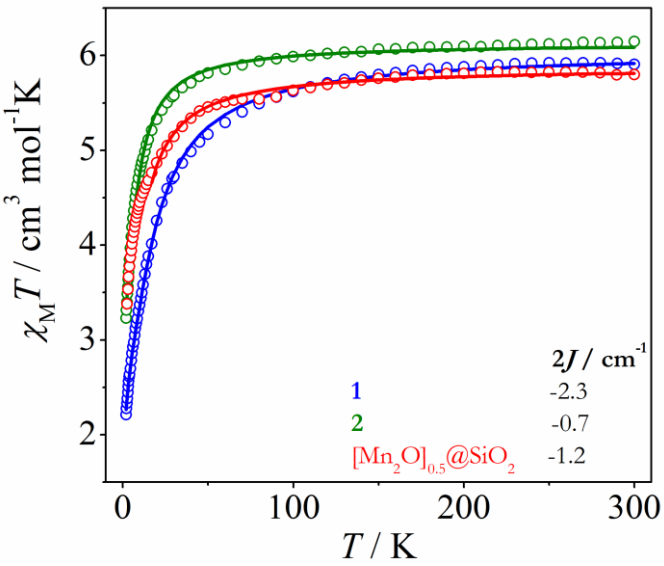

Figure 94. $\chi_M T$ versus T plots for compounds **1** (blue) and **2** (green), and material $[Mn_2O]_{0.5}$@SiO_2 (red). The solid lines are the best fits of the experimental data.

Synthesis of a less loaded material: $[Mn_2O]_{0.1}@SiO_2$

Material $[Mn_2O]_{0.1}@SiO_2$ was synthesized from the support SiO_2-TMA and compound **1** following the same procedure as material $[Mn_2O]_{0.5}@SiO_2$, but using just 0.1 equivalents of **1** per equivalent of TMA^+. The same techniques were used for the characterization of this new material; however, its low Mn content (~1.15% in weight) did not allow to better determine some properties of the Mn complex. For instance, we could not obtain a good magnetic susceptibility curve or a nice XPS spectrum of this material.

As may be observed from the N_2 sorption isotherms (Figure 95 and Table 27), the mesoporosity remains intact after the insertion of **1**. Nonetheless, material $[Mn_2O]_{0.1}@SiO_2$ exhibits a higher pore volume (0.58 mL g^{-1}) than the previous material $[Mn_2O]_{0.5}@SiO_2$ (0.36 mL g^{-1}) (Table 25), in accord with the lower content of Mn compound for $[Mn_2O]_{0.1}@SiO_2$.

It is worth noting that this series of materials, consisting of $[Mn_2O]_{0.1}@SiO_2$ and its two precursors (SiO_2-Ex and SiO_2-TMA), shows a secondary capillary evaporation (only seen in desorption) at $p/p_0 \approx 0.5$ and thus the width of these secondary pores is larger than that of the primary pores. This fact was also reported in the literature for several MCM-41 type materials.[275] This process may be likely attributed to some small defects of the mesoporous structures. However, as these secondary pores represent a relatively small amount of pore volume, their effect on the insertion and on the final application can be considered negligible.

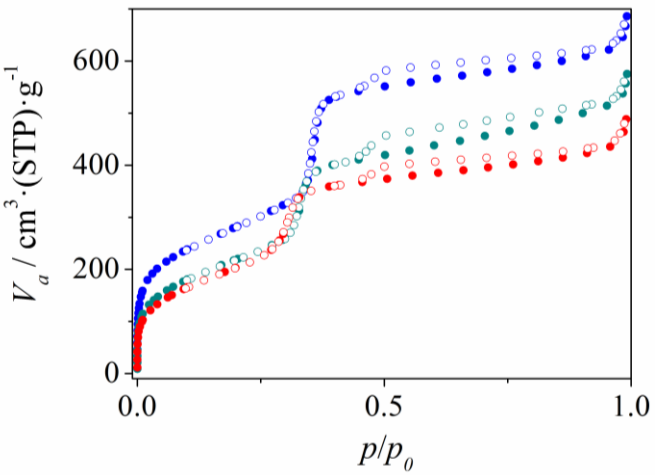

Figure 95. N_2 adsorption (full circles) and desorption (empty circles) isotherms at 77 K of materials SiO_2-Ex (blue), SiO_2-TMA (dark cyan) and $[Mn_2O]_{0.1}@SiO_2$ (red).

Table 27. Textural properties of materials SiO_2-CTA, SiO_2-Ex, SiO_2-TMA and $[Mn_2O]_{0.1}$@SiO_2.

	SiO_2-Ex	SiO_2-TMA	$[Mn_2O]_{0.1}$@SiO_2
S_{BET}[a] / m^2 g^{-1}	1014	-	-
C [a]	110	65	59
Porous volume[b] /mL g^{-1}	0.86	0.66	0.58
Pore diameter[c] /nm	3.8	3.6	3.4

[a] Calculated using BET method;[277] [b] calculated using the *t*-plot;[278,279] [c] Using BdB method.[111]

The calculated formula from the elemental analyses and ICP-OES for the $[Mn_2O]_{0.1}$@SiO_2 hybrid material is $SiO_2 \cdot 0.0084$ $[Mn_2O(2\text{–}MeOC_6H_4COO)_2(bpy)_2] \cdot 0.088$ $TMA \cdot 0.30$ H_2O. This metal loading corresponds to *ca.* 80% of the cationic exchange capacity assuming two positive charges for **1** and that both NO_3^- ions are removed. The remaining quantity of TMA^+ ions in the solid is very close to that expected for a mere cation exchange of two TMA^+ per complex. The thermogravimetric analysis (TGA) shows three main weight losses in the range 200–400 °C that are mainly assigned to the decomposition of the Mn complex ligands and of TMA^+ ions that suit with the weight loss calculated from the empirical formula (see Appendix VII).

Synthesis and characterization of materials with Py function: $[Mn_2O]_x$-Py@SiO_2 (x = 0.21, 0.12 and 0.04)

Synthesis strategy. The cationic complex of compounds **1** was inserted into pyridil-modified MCM-41 mesoporous silica by ionic exchange. A step-by-step procedure to obtain materials $[Mn_2O]_x$-Py@SiO_2 (x = 0.21, 0.12 and 0.04) with pyridyl functions is shown in Figure 96. The synthetic procedure for these material is analogous to that performed for the insertion of Mn compounds inside non-functionalized mesoporous silica, but a new step was added. The inner and external surface of material SiO_2-TMA was modified with pyridyl function using a post-grafted strategy.[128–130,132,290,291] This modification is based on the reaction of condensation between 2-(4-pyridylethyl)triethoxysilane and the silanol groups of material SiO_2-TMA, which will lead to covalently bounding the pyridyl function on the surface. This support was labeled as Py@SiO_2-TMA.

For these $[Mn_2O]_x$-Py@SiO_2 materials, smaller $[Mn_2]^{2+}/TMA^+$ molar ratios than for $[Mn_2O]_{0.5}$@SiO_2 were used, since a complete insertion of the compound was not achieved in this latter material. Hence, three new materials, $[Mn_2O]_x$-Py@SiO_2 (x = 0.21, 0.12 and 0.04), were synthesized, where x is the $[Mn_2]^{2+}/TMA^+$ molar ratio used in the synthesis.

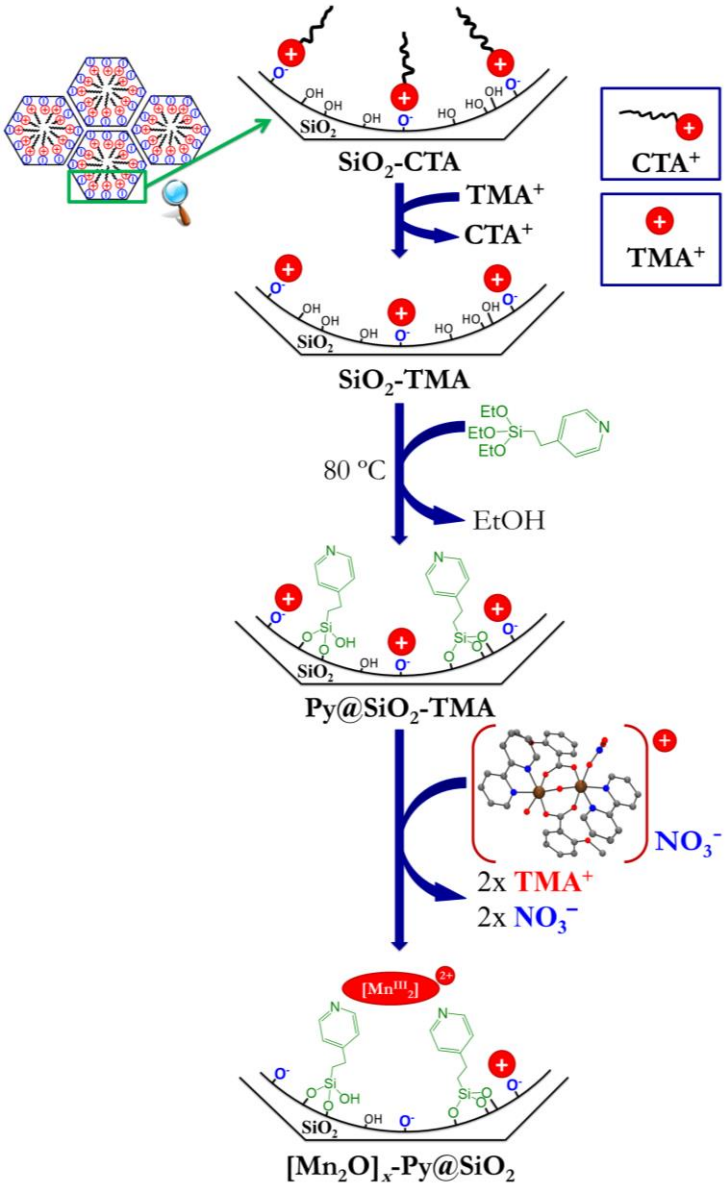

Figure 96. Synthetic procedure to obtain materials $[Mn_2O]_x$-Py@SiO_2 from "as-made" silica (SiO_2-CTA). Abbreviations: CTA^+, cetyltrimethylammonium; TMA^+, tetramethylammonium.

Characterization of material Py@SiO_2-TMA. According to the elemental analyses, the composition of this new support, labeled as Py@SiO_2-TMA, is consistent with the formula $SiO_2 \cdot 0.08$ TMA$\cdot 0.11$ PySi$\cdot 0.30$ H_2O, where PySi = 4-pyridylethyl silyl. This formula is in accord with the TG analysis, where two weight losses are observed: that in the range 180–300 °C, assigned to the TMA^+ ions; and that extended from 300 to 600 °C, assigned to the 4-pyridylethyl function (see more details in Appendix VII).

Figure 97 shows some techniques used for the characterization of the support. The presence of TMA^+ ions may be confirmed with the band at 1496 cm^{-1} in the IR spectrum. Bands at 1608 (s), 1560 (w) and 1420 (m) cm^{-1} are assigned to the pyridyl function. Solid ^{13}C and ^{29}Si

HPDEC (High Power Decoupled) NMR spectra were recorded for Py@SiO$_2$-TMA (Figure 97, (*b*) and (*c*)). The results from the analyses of these spectra are summarized in Table 28. The ^{29}Si NMR spectrum was fitted in order to quantify the relative quantities of each Si type (see explanation of Si types in Chapter 2.1). Note that Q type corresponds to pure inorganic silicon atoms (SiO$_2$) and T type to those of the pyridyl function. The T/Q ratio obtained from this fit is 0.11, consistent with the PySi/SiO$_2$ ratio calculated from the elemental analyses. ^{13}C HPDEC NMR spectroscopy is supposed to provide quantitative information, but we did not achieve to obtain a good signal to perform a rigorous quantification. In fact, the integration results indicate that the relative error may be around 20%. Anyhow, this NMR spectrum is consistent for a solid containing similar amounts of TMA$^+$ ions and pyridyl functions.

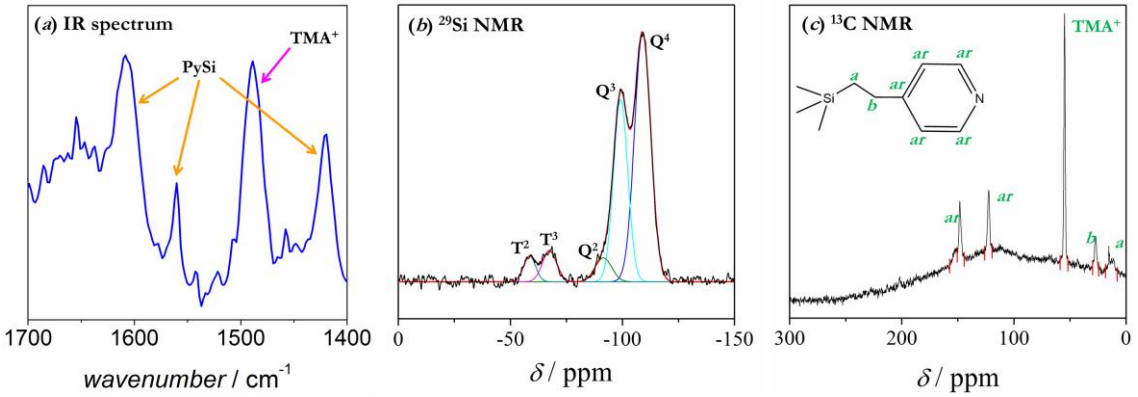

Figure 97. (*a*) Infrared spectrum (from 1700 to 1400 cm^{-1}) (*b*) ^{29}Si and (*c*) ^{13}C HPDEC NMR spectra for material Py@SiO$_2$-TMA. In the ^{29}Si spectrum, the colored lines correspond to the cumulative peak (red) and to the spectrum deconvolution.

Table 28. Summary of results obtained from the fit of the ^{29}Si and ^{13}C HPDEC NMR spectra for material Py@SiO$_2$-TMA.

^{29}Si NMR				^{13}C NMR		
Si type	**δ [a] / ppm**	**FWHM [b]**	**Area / %**	**C type**	**δ [a] / ppm**	**Integration / %**
Q^4	–109	8.5	52.0	C_a	15	5.8
Q^3	–99	7.5	33.3	C_b	27	5.2
Q^2	–92	8.6	5.1	C_{TMA}	55	25.8
T^3	–67	7.5	5.7	C_{ar}	122	10.2
T^2	–59	6.3	3.9	C_{ar}	148	10.1
				C_{ar}	151	4.1

[a] Chemical shift; [b] Full Width at Half Maximum.

The N$_2$ sorption isotherms (shown below) of material Py@SiO$_2$-TMA indicate that the mesostructure is preserved after the functionalization. The decrease of pore volume is consistent with an efficient modification of the inner surface, as well as the decrease of pore

diameter. The capillary condensation occurs in a wider range of pressures than that of the SiO_2-Ex, corresponding to a pore size ranging from 2.8 to 3.3 nm (from BdB analysis).[111]

Characterization of material $[Mn_2O]_x$-Py@SiO_2. Three hybrid materials were synthesized using pyridyl-modified mesoporous silica (Py@SiO_2-TMA) with three different **1**/TMA^+ molar ratios (x). These new materials are labeled as $[Mn_2O]_x$-Py@SiO_2, where x can be 0.21, 0.12, or 0.04. The solid with x = 0.21 was characterized more extensively due to its higher Mn content.

The low temperature nitrogen sorption isotherms of the surfactant-extracted support, SiO_2-Ex, and the hybrid solids, SiO_2-TMA and $[Mn_2O]_x$-Py@SiO_2, (Figure 98 and Figure S29) exhibit a type IV isotherm according to the IUPAC nomenclature, without hysteresis as usually observed for MCM-41 2D hexagonal mesoporous silica.[113,274] The average reduction of ~0.42 mL g^{-1} in pore volume after the functionalization (from SiO_2-Ex to Py@SiO_2-TMA) is much higher than that shown after the insertion of the Mn compound (from material Py@SiO_2-TMA to $[Mn_2O]_x$-Py@SiO_2), which is less than 0.07 mL g^{-1} (Table 29 and Table 30). This fact is consistent with the $[Mn^{III}_2]$/Py molar ratios (<0.21) calculated form the elemental analyses and ICP-OES (see below).

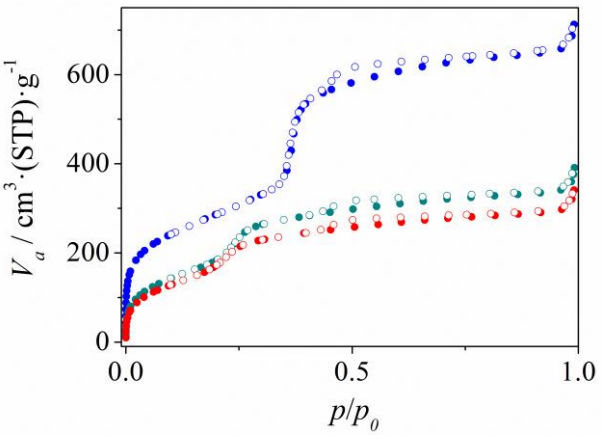

Figure 98. N_2 adsorption (full circles) and desorption (empty circles) isotherms at 77 K of materials SiO_2-Ex (blue), SiO_2-TMA (dark cyan) and $[Mn_2O]_{0.21}$-Py@SiO_2 (red).

Table 29. Textural properties of materials SiO_2-Ex, Py@SiO_2-TMA and $[Mn_2O]_{0.21}$-Py@SiO_2.

	SiO_2-Ex	Py@SiO_2-TMA	$[Mn_2O]_{0.21}$-Py@SiO_2
d_{100} / nm	4.0	4.1	4.1
a_0[a] / nm	4.7	4.8	4.7
HWHH[b] 2θ / °	0.22	0.21	0.22
S_{BET}[c] / m^2 g^{-1}	1032	-	-
C[c]	105	57	44
V_{pore}[d] /mL g^{-1}	0.94	0.48	0.41
d_{pore}[e] /nm	3.9	2.8–3.3	2.6–3.2

[a] Parameter calculated from d_{100} with the formula $a_0 = 2*d_{100}/3^{1/2}$; [b] half-width at half-height; [c] calculated using BET method;[277] [d] calculated using the t-plot;[278,279] [e] Using BdB method.[111]

Table 30. Textural properties of materials SiO_2-Ex, Py@SiO_2-TMA and $[Mn_2O]_x$-Py@SiO_2 with x = 0.12 and x = 0.04

	SiO_2-Ex	Py@SiO_2-TMA	$[Mn_2O]_{0.12}$-Py@SiO_2	SiO_2-Ex	Py@SiO_2-TMA	$[Mn_2O]_{0.4}$-Py@SiO_2
S_{BET}[a] / m^2 g^{-1}	974	-	-	1014	-	-
C[a]	115	62	57	110	65	58
V_{pore}[b] /mL g^{-1}	0.82	0.36	0.33	0.86	0.46	0.42
d_{pore}[c] /nm	3.9	2.8–3.3	2.8–3.3	3.8	2.9–3.4	2.9–3.4

[a] Parameter calculated from d_{100} with the formula $a_0 = 2*d_{100}/3^{1/2}$; [b] half-width at half-height; [c] calculated using BET method;[277] [b] calculated using the t-plot;[278,279] [c] Using BdB method.[111]

The BET constant C for the hybrid materials, Py@SiO_2-TMA and $[Mn_2O]_x$-Py@SiO_2 (~60 and 44–58, respectively), is much lower than that for the SiO_2-Ex (~110) (Table 29 and Table 30), which indicates that the surface has become more hydrophobic after the functionalization. On the other hand, the BET constant C suffers just a slight decrease after the insertion of the Mn compound (from ~60 to 44–58). The capillary condensation shifts to a lower range of pressures for material $[Mn_2O]_{0.21}$-Py@SiO_2 (Figure 98), corresponding to a pore size reduction of ~0.2 nm (Table 29). For the materials loading a smaller amount of compound, $[Mn_2O]_{0.12}$-Py@SiO_2 and $[Mn_2O]_{0.04}$-Py@SiO_2, this reduction is inappreciable (Figure S29), since it is smaller than the experimental error.

Powder XRD analysis was performed for materials SiO_2-Ex, Py@SiO_2-TMA, and $[Mn_2O]_{0.21}$-Py@SiO_2, showing that the 2D hexagonal array was unaltered during both the functionalization of the surface and the insertion of the Mn complex (Figure 99). The distance between the centers of the pores (a_0) is around 4.7 ± 0.1 nm (Table 29), which is equal to those shown by the previous examples (see Table 25).[195]

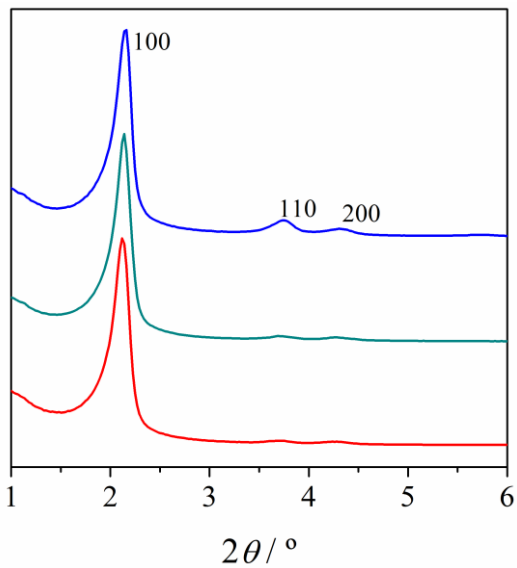

Figure 99. Small-angle powder XRD of materials SiO_2-Ex (blue), Py@SiO_2-TMA (dark cyan) and $[Mn_2O]_{0.21}$-Py@SiO_2 (red). The intensity was normalized with the (100) peak.

The calculated formulas from the elemental analyses and inductively coupled plasma optical emission spectrometry (ICP-OES) for the $[Mn_2O]_x$-Py@SiO_2 hybrid materials are listed in Table 31. Note that the insertion of the Mn complex was performed by ionic exchange, where the TMA^+ ions are replaced with the cationic complex (Figure 96). For the three materials, the TMA^+/Si_{inorg} ratios are lower than the expected by a mere ionic exchange of the TMA^+ ions for the cationic Mn complex. The missing TMA^+ is removed according to another reaction that is likely neutralization, as observed in the synthesis of material $[Mn_2O]_{0.5}$@SiO_2.[195] We could not determine the exact composition of material $[Mn_2O]_{0.21}$-Py@SiO_2, since several formulas agreed with the experimental data. We tried to determine it with other techniques, but it was unsuccessful (see below).

Table 31. Empirical formulas for materials Py@SiO_2-TMA and $[Mn_2O]_x$-Py@SiO_2, calculated from elemental analyses and ICP-OES.

		$[Mn_2O]_x$-Py@SiO_2		
	Py@SiO_2-TMA	***x* = 0.04**	***x* = 0.12**	***x* = 0.21**
PySi/Si_{inorg}	0.11	0.11	0.11	0.09–0.10
$[Mn_2O]/Si_{inorg}$	-	0.0034	0.011	0.019
TMA^+/Si_{inorg}	0.080	0.055	0.030	0.019–0.020
H_2O/Si_{inorg}	0.30	0.35	0.35	0.25
Mn content / %	-	0.41	1.29	2.16

Abbreviations: PySi = 4-pyridylethyl silyl, $[Mn_2O]$ = $[Mn_2O(2–MeOC_6H_4COO)_2(bpy)_2]^{2+}$, TMA^+ = tetramethylammonium, Si_{inorg} = silicon atoms coming from the SiO_2 matrix, without counting those coming from the organo-silane functions.

It is worth remembering that, for the synthesis of materials $[Mn_2O]_x$-Py@SiO_2, solutions containing different amounts of compound **1** were mixed with material Py@SiO_2-TMA, previously pretreated at 80 ºC under vacuum. After the reaction, the brown suspension was filtered, washed, and dried, leading to materials $[Mn_2O]_x$-Py@SiO_2. In the three cases, the solutions obtained after filtration were colorless, indicative of an almost complete insertion of the complex; hence, the yields for the insertions should be close to 100%. However, the $[Mn_2O]/Si_{inorg}$ ratios in Table 31 would unreasonably correspond to a ~110% yield of the ionic exchange, pointing to some systematic error during the syntheses. A possible explanation for these results could lie in the pretreatment of material Py@SiO_2-TMA. This pretreatment basically consists in heating the solid up to 80 ºC under Ar and, then, keeping the solid at 80 ºC under vacuum for two hours. Part of the thin powder could be lost during the implementation of both the current of Ar and the vacuum. The water content in the support Py@SiO_2-TMA could also be the cause of this, since humidity tends to condense

inside the pores within time. Nevertheless, knowing which is the cause of this fact is now implausible, but it should be studied if further experiments are performed.

The TG analyses show two main weight losses between 150 and 650 ºC, assigned to the decomposition of the Mn complex ligands, the 4-pyridylethyl groups, and the TMA^+ ions (see more details in Appendix VII). It is worth remarking that the decomposition of the 4-pyridylethyl groups is affected by the presence of the Mn compound, since the peak centered at 537 ºC in the TG derivative of material Py@SiO_2-TMA disappears after the insertion of the Mn compound. This fact could suggest the existence of a $[Mn^{III}_2O]\cdots$PySi interaction, but it is not a sufficient proof. In fact, the presence of metallic ions, such as Mn, in the solid may catalyze the decomposition of the organic groups, such as the pyridyl function, and modify the position of their TG derivative peaks.

The IR spectra of materials $[Mn_2O]_x$-Py@SiO_2 (Figure 100) contains the vibrational fingerprints of the Mn complex ligands, the 4-pyridylethyl silyl (PySi) function, and the TMA^+ ions.

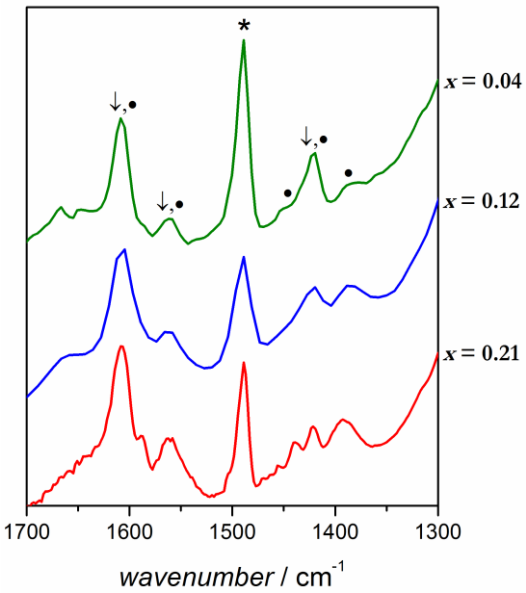

Figure 100. Infrared spectra (1700–1300 cm^{-1} window) for materials $[Mn_2O]_x$-Py@SiO_2 with x = 0.21 (red), 0.12 (blue), and 0.04 (green). The star (*), the arrows (↓) and circles (●) point out IR vibrations of TMA^+ ions, 4-pyridylethyl function, and Mn complex, respectively.

The band typically assigned to the CH_3 scissoring vibrational mode of the TMA^+ shows up at 1488 cm^{-1} and attests for its presence.[130] The bands at 1608 (s), 1560 (w) and 1420 (m) cm^{-1} are assigned to the PySi function. Most of the bands corresponding to the Mn complex, such as the asymmetric vibration of the COO group at 1558 $cm^{-1}$and that of the bipyridine ligand at 1604 cm^{-1}, show up at a very similar position to those assigned to the PySi function. A

group of bands of the bipyridine ligand are expected between 1496 and 1440 cm^{-1}, but they are only observed in the solid with the highest Mn complex loading (with $x = 0.21$). The symmetric vibration of the COO group arises at 1396 cm^{-1}, a higher wavenumber than that of the molecular compound (**1**) (1370 cm^{-1}), as observed for material $[Mn_2O]_{0.5}$@SiO_2.[195]

XPS measurements for material $[Mn_2O]_{0.21}$-Py@SiO_2 were performed, using those for compound **1** and for material Py@SiO_2-TMA as references. The results obtained from the fit of the C 1s, the N 1s and the Mn 3s peaks are summarized in Table 32. The C 1s signals of compound **1** and material $[Mn_2O]_{0.21}$-Py@SiO_2 are distributed in three main XPS features, assigned to C_{sp2} (284.6 eV), C–N and $C–O_{ether}$ (~286 eV) and $C_{carboxylate}$ (~288 eV) (Figure 101); whereas that of material Py@SiO_2-TMA are distributed only in two XPS features, since there is not any carboxylate group.[294,295]

Table 32. Summary of the C 1s, N 1s and Mn3s photoelectron results for compound **1** and material $[Mn_2O]_{0.5}$@SiO_2.

	Compound 1			**Py@SiO_2-TMA**			**$[Mn_2O]_{0.21}$-Py@SiO_2**		
	Position / eV	**Δ[a] / eV**	**Area ratio[b]**	**Position / eV**	**Δ[a] / eV**	**Area ratio[b]**	**Position /eV**	**Δ[a] / eV**	**Area ratio[b]**
C 1s	284.6	0.0	1.0	284.6	0.0	0.6	284.6	0.0	1.0
	285.8	1.2	0.4	285.7	1.1	1.0	286.0	1.4	0.9
	288.1	3.5	0.1	-	-	-	288.0	3.4	0.05
N 1s	399.6	0.0	1.0	399.1	0.0	0.9	399.2	0.0	1.0
	406.2	6.6	0.6	402.7	3.6	1.0	402.7	3.5	0.4
Mn 3s	83.6	0.0	1.0	-	-	-	83.8	0.0	1.0
	89.2	5.6	0.8	-	-	-	89.3	5.5	0.7

[a] Peak separation; [b] All areas are normalized with the highest one in each transition.

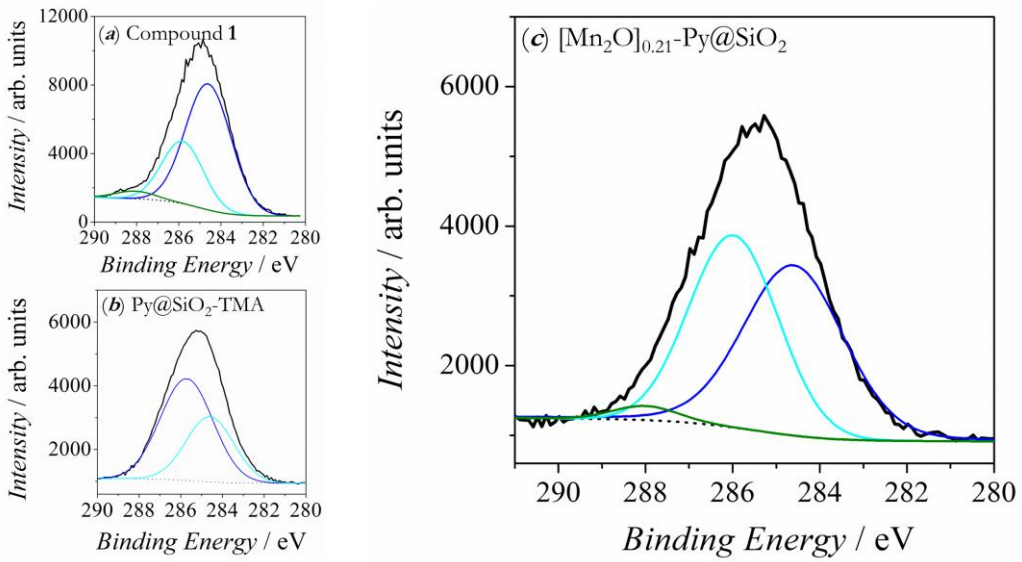

Figure 101. C 1s peak of the XPS spectra for compound **1** (***a***) and materials Py@SiO_2-TMA (***b***) $[Mn_2O]_{0.21}$-Py@SiO_2 (***c***). The solid black lines correspond to the experimental plots and the dot lines to the background. The colored lines correspond to the spectra deconvolutions, assigned to C_{sp2} (blue), C–N and $C–O_{ether}$ (cyan) and $C_{carboxylate}$ (green).

Figure 102 shows the Mn 3s spectra for **1** and material $[Mn_2O]_{0.21}$-Py@SiO_2. The Mn 3s doublet splitting (ΔMn 3s) provides a reliable way of determining the oxidation state of manganese, being smaller for higher oxidation state.[296] Both solids display a rather similar ΔMn 3s of 5.5–5.6 eV (Table 32), being in agreement with those reported by J. Nelson *et al* for a series of Mn(III) complexes with carboxylate and oxo bridges,[297] and also with the values collected in Table S24 for compounds with different oxidation states. This fact confirms that for material $[Mn_2O]_{0.21}$-Py@SiO_2 the oxidation state of the Mn ions is III.

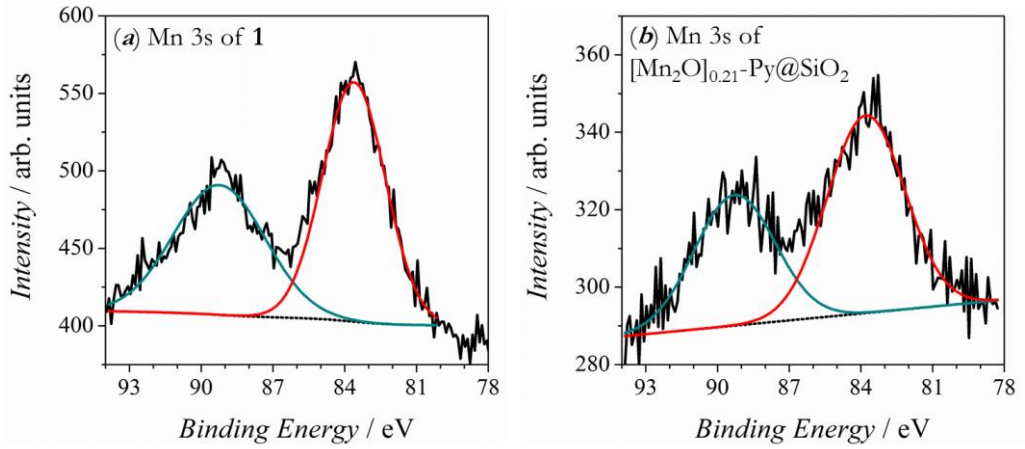

Figure 102. Mn 3s peak of the XPS spectra for compound **1** (***a***) and material $[Mn_2O]_{0.21}$-Py@SiO_2 (***b***). The solid black lines correspond to the experimental plots, the dot lines to the background and the colored lines to the spectra deconvolutions.

The N 1s spectra (shown in Figure 103) of materials Py@SiO_2-TMA and $[Mn_2O]_{0.21}$-Py@SiO_2 can also provide very useful information. It is worth remembering that compound **1** displays two main peaks, corresponding to the N atoms of the bpy ligand (blue peak centered at 399.6 eV) and to the NO_3^-anions (green peak centered at 406.2 eV).[294] The NO_3^- peak is not present in the N 1s spectrum of material $[Mn_2O]_{0.21}$-Py@SiO_2, consistent with the absence of the counter-anion in the hybrid material, as also observed for material $[Mn_2O]_{0.5}$@SiO_2. The peak at ~399 eV (blue) can be unambiguously assigned to N atoms of both the bpy ligand and the PySi function (N_{sp^2}),[298] and they are also observed in the N 1s spectrum of the support, Py@SiO_2-TMA, and that of compound **1**.

The correspondence of the peak at ~403 eV (cyan) is more challenging, since several facts may originate this peak. Firstly, it is worth analyzing the N 1s spectrum for material Py@SiO_2-TMA, which only contains PySi function and TMA^+ ions. Thus, two XPS signals are expected: that corresponding to the pyridine N_{sp^2} atoms of (at ~399 eV) and that of positively charged TMA^+ nitrogen atoms (N^+) (at ~403 eV).[294] However, the N^+/N_{sp^2} ratio

calculated from XPS, 1.11, is not consistent with the amount of TMA^+/PySi ratio from the elemental and TG analyses, 0.73. This fact could mean: (*a*) the amount of TMA^+ is overestimated with XPS; or (*b*) there is a certain quantity of PySi function that is likely protonated or interacting with the SiO_2 surface. This latter possibility (*b*) was already observed in the work by Abry *et al.*,[290] where an important portion of N-based ligands were protonated. The pK_a of 4-pyridylethyl (~5.3) is much lower than that of the silanolate groups interacting with the TMA^+ ions ($pK_a \approx 9$);[299,300] however, it is still possible to have a part of these Py groups protonated. An interaction between the PySi nitrogen atom and the surface could also electronically modify this atom;[290,294] however, the ethylic "chain" is not long enough to allow the head of the 4-pyridylethyl function to reach the surface, in spite of its concavity. On the other hand, an overestimation of TMA^+ with this technique appears reasonable. XPS is a superficial characterization technique and, even though the X-ray can reach several nanometers in depth (~10 nm), the external surface is far more relevant than it should be for a bulky material. In the case of MCM-41 with pores with a distance between center of ~4.7 nm, the external surface could have a large contribution to the final results, taking into consideration that it just represents a ~5% of the total surface. However, the overestimation of the amount of TMA^+ ions could only be explained if the external surface was more rich in TMA^+ ions than the internal surface. Considering these facts, the most rational explanation for the intense XPS peak at ~403 eV seems to be the partial protonation of the Py functions. Nonetheless, additional tests are necessary to confirm it.

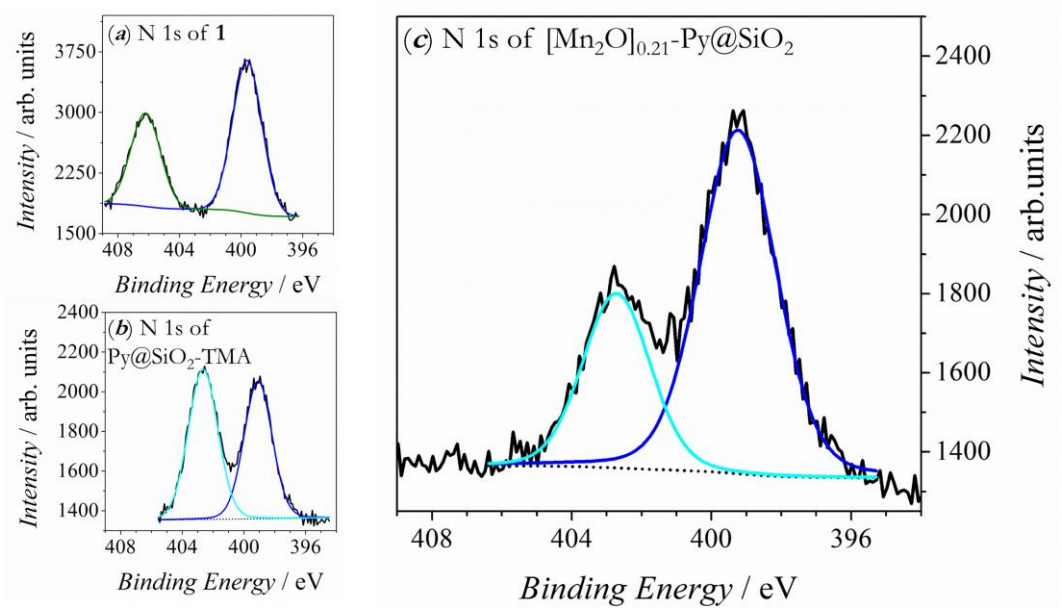

Figure 103. N 1s peak of XPS spectra for compound **1** (***a***), material Py@SiO_2-TMA (***b***), and material $[Mn_2O]_{0.21}$-Py@SiO_2 (***c***). The solid black lines correspond to the experimental plots, the dot lines to the background and the colored lines to the spectra deconvolutions.

Returning to the N 1s spectrum of material $[Mn_2O]_{0.21}$-Py@SiO_2 and taking into consideration the explained above, the assignment of the peak at ~403 eV (cyan) to a certain type of N atom continues being abstruse. In fact, while XPS gives the ratio $N^+/N_{sp2} = 0.40$, where N^+ could be both the N atoms of the TMA^+ ions and of protonated Py function, the elemental analyses indicate that $TMA^+/N_{sp2} \approx 0.11$. For the hybrid material without organic function, $[Mn_2O]_{0.5}$@SiO_2, this peak was attributed to a change in the coordination of one of the bpy ligands, likely due to the interaction with the silica support,[195] since the TMA^+ content was almost negligible. We tried to confirm the empirical formula of the pyridyl functionalized material with other techniques, but we could not find any with the proper exactitude.

Magnetic measurements were also performed for material $[Mn_2O]_{0.21}$-Py@SiO_2. The $\chi_M T$ versus T plot indicates that there is a non-negligible interaction between the Mn ions (Figure 104), which strongly supports the assumption about the Mn^{III}_2 unit being maintained in the silica pores. However, a higher error than usual must be considered due to the low Mn content of this material (Mn in weight = 2.14%). In fact, we needed to adjust the molecular weight to have a $\chi_M T$ value consistent with two uncoupled Mn^{III} ions. In spite of this, the shape of the curve is reliable enough to confirm the existence of a Mn···Mn interaction.

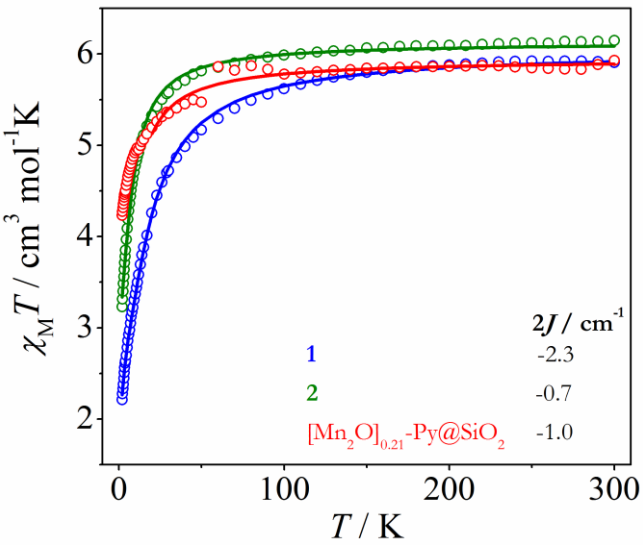

Figure 104. $\chi_M T$ versus T plots for compounds **1** (blue) and **2** (green), and material $[Mn_2O]_{0.21}$-Py@SiO_2 (red). The solid lines are the best fits of the experimental data.

The data was fitted from 300 to 17 K using the PHI program ($H = -2JS_1S_2$),[165] omitting the data at low temperature (17 – 2 K) to avoid zero-field splitting effects. The best fit corresponds to $g = 1.99$, $2J = -1.0$ cm^{-1}, $R_{sus} = 1.1 \times 10^{-4}$. The $2J$ value is between those found for **1** and **2**; thus, it is also in the expected range for a $[Mn^{III}_2O(2\text{-}RC_6H_4COO)_2]^{2+}$ subunit

(between –12 and +5 cm^{-1}).[181] These results are also in accord with those obtained for material $[Mn_2O]@SiO_2$.[195]

We assume that the Mn complex inside materials $[Mn_2O]_x$-Py@SiO_2 with x = 0.12 and 0.04 will likely present the same characteristics as that inside $[Mn_2O]_{0.21}$-Py@SiO_2. However, XPS and magnetic measurements for these materials could not be performed because of the low $[Mn^{III}_2]$ loading in these materials.

Coating of the external surface of the hybrid materials

We attempted to coat material $[Mn_2O]_{0.5}@SiO_2$ with an external layer of SiO_2. The goal of this procedure was to prevent the Mn complex from leaving the pores during the application, likely improving the durability and activity of the catalyst. Such an external layer must be thick enough to plug the entrance of the channels, but thin enough to allow water and substrate (H_2O_2) diffusion.

The procedures tested were based on those reported in the literature for the coating of iron oxide nanoparticles.[301,302] In those works, the silica coating was prepared by treating the iron oxide nanoparticles with tetraethyl orthosilicate (TEOS) (precursor of SiO_2) under basic conditions. We tried to do the same with our bulky material. In a future, this procedure could be adapted to silica nanoparticles. Figure 105 shows the procedure that could be used for silica nanoparticles. However, this figure does not fairly represent reality, since the mesoporous materials prepared in this work consists of agglomerations of several micrometers large (see Chapter 2.1). Each particle of the bulky material has several thousand channels, contrary to Figure 105, where the particle has 18 channels, corresponding to a particle of ~25 nm diameter. Owing to the huge difference in terms of external surface between nanoparticles and bulky materials, our results could be rather different from those obtained with nanoparticles, even though one follows the same experimental procedure.

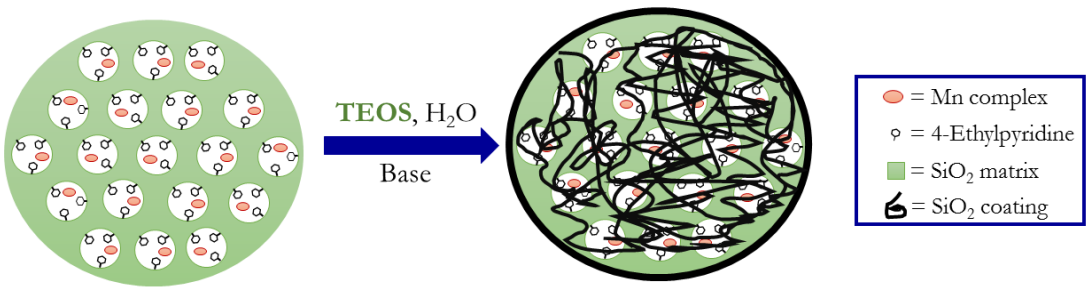

Figure 105. Schematic representation representing the coating of hypothetical Mn-SiO_2 mesoporous nanoparticles.

The deposition of SiO_2 over the particles of our materials is performed by the polymerization of tetraethyl orthosilicate (TEOS) in basic media and in the presence of water, following the reaction:

$$n\ Si(OEt)_4 + 2n\ H_2O \rightarrow (SiO_2)_n + 4n\ EtOH$$

The coexistence of the TEOS (silica precursor) and our material in the same media should preferably lead to the growth of silica over our particles rather than to the nucleation of new SiO_2 particles, as also observed in the literature.[301,302]

This coating was tested in two different solvents (isopropanol and acetonitrile) and with different organic-solvent/water mixtures. It was very tough to find out which the optimal conditions were, since the catalyst (the Mn complex) losses its activity if the amount of water is too high or the media is too basic. Finally, the coating was performed over 100 mg of material $[Mn_2O]_{0.5}$@SiO_2, without pyridyl function, in a 20 mM CH_3CN:H_2O (95:5) solution of Et_3N.

After finding the proper conditions that keep the activity of the catalyst, we proceeded to prepare several materials with different amounts of TEOS in order to get external layers of different thicknesses. Four different concentrations of TEOS were used: 44, 220, 880, and 1320 mM. These amounts of TEOS correspond to respective theoretical SiO_2 layers of around 2, 11, 40, and 70 nm thick, considering an external surface of 50 m^2/g. Control experiments were performed by treating the material $[Mn_2O]_{0.5}$@SiO_2 under the same conditions but omitting the addition of TEOS. Note that, even though some of these SiO_2 layers are thick, the amount of SiO_2 added to these bulky materials after coating would correspond to a negligible amount of the total weight (<< 1%). Hence, both the pore volume and the TG residual mass should not be affected by the coating.

If the coating had been successful, the entrance of the pores would not be as accessible as in material $[Mn_2O]_{0.5}$@SiO_2, so some differences in the capillary condensation/evaporation between these coated and starting materials were expected. However, the results obtained from N_2 sorption isotherms were disappointing. The "coated" materials presented a higher pore volume (Figure S30) and a lower content of organic matter than $[Mn_2O]_{0.50}$@SiO_2, both facts indicating a substantial loss of Mn complex. Moreover, the capillary condensation shifted to a higher pressure, and the pore size distribution was narrower, more consistent with the emptying of the pores than with their blockage.

Summary

Two dinuclear Mn^{III} compounds with formula $[\{Mn^{III}(bpy)(H_2O)\}(\mu\text{-}2\text{-}MeOC_6H_4COO)_2(\mu\text{-}O)\{Mn^{III}(bpy)(X)\}]X$, where X = NO_3 (**1**) and ClO_4 (**2**), were successfully inserted by ionic exchange in mesoporous silica (MCM-41 type). The insertion of compound **1** and **2** into mesoporous silica leads to the same material (with 3.98% Mn in weight), indicating that only the cationic complex is incorporated inside the support. The analysis of the new material shows that the Mn complex occupies half of the available mesoporous volume within the pores and that the hexagonal array was unaltered upon the insertion of the Mn complex. Moreover, a non-negligible antiferromagnetic interaction between Mn(III) ions was observed, indicating that the dinuclear unit is preserved inside the silica.

In this latter attempt, the ionic exchange was incomplete, since a part of the Mn complex stayed in solution. Hence, we synthesized and characterized a solid containing a much lower amount of Mn complex (1.18% Mn in weight).

Furthermore, a second generation of Mn-SiO_2 materials from the reaction between compound **1** and a pyridyl-modified mesoporous silica were synthesized. These materials contain a lower amount of molecular compound (0.41–2.16% Mn in weight) than those supported on the non-functionalized silica. The lower amount of molecular guest present in these materials, combined with their higher complexity, makes the characterization far more challenging than for the first generation of materials (without organic function). The catalytic properties for these materials will be presented in Chapter 3.4.

Finally, we tried to coat the particles of the aforementioned materials with an external SiO_2 layer. However, this coating needs to be optimized, since the first attempts showed an incomplete coverage of the external surface of the particles and an important leaching of the Mn complex.

2.4. Insertion of Big Clusters into SiO_2 containing Hydrophobic Functions

First insights

Compounds with a high spin moment, which possess high Mn content per gram and provoke high perturbation to applied magnetic fields, could either take part in information storage devices or act as contrasts agents in Magnetic Resonance Imaging (MRI). In particular, a contrast agent may obey several requirements, such as biocompatibility and considerable solubility in water. However, these compounds tend to be insoluble and/or unstable in water and are highly oxidant. Hence, mesoporous silica could be used as a transport agent for these compounds. For cationic clusters, SiO_2-TMA with or without further functionalization may be a plausible host; but many of the compounds of interest are neutral. Moreover, the Mn core is normally surrounded by the organic ligands that constitute their structure, leaving the Mn core isolated from the environment, with no accessible positions that may form covalent bonds with the corresponding support. So, these compounds cannot be inserted by ionic exchange nor anchored without causing severe modifications of the cluster structure. Indeed, the only way to covalently anchor such compounds would be to exchange some of the ligands with –SiOH groups, as suggested by Clemente-León *et al*,[149] possibly causing a rather large modification of the magnetic properties of the inorganic compound. Hence, the chosen compounds may be inserted in highly hydrophobic channels where the predominant interactions between the complex and the support were Van der Waals forces, hydrogen bonds, or π-π interactions. The final goal of this project is to stabilize big clusters in water and study how the insertion in porous inorganic supports affects their magnetic properties.

Within this frame, we synthesized four supports containing different functions. Initially, we prepared mesoporous silica with *n*-propyl and *n*-octyl, which have no binding position; so, the expected interactions are Van der Waals forces. Since the main difference between these two functions is the length, we expect to see some differences in the pore size if the full coverage of the inner surface is achieved, as shown in Figure 106. Consistently, the pore diameter of material C_8@SiO_2 is supposed to be smaller than the one for material C_3@SiO_2.

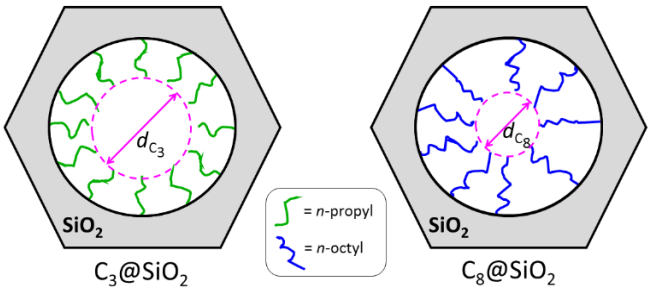

Figure 106. Schematic representation of the channel of the C_3@SiO_2 and C_8@SiO_2 supports, considering full coverage of the inner surface.

Secondly, a support with phenyl function, with non-binding position, was also synthesized. Contrary to the previous aliphatic functions, the phenyl one is less flexible because the aromatic ring is directly linked to the silicon atom and can better retain the guests, since π-π interactions are possible. A pore diameter similar to that expected for material C_3@SiO_2 is highly likely, since the phenyl group is not supposed to occupy much more than such a flexible *n*-propyl group.

Neutral compounds like the heterometallic Mn-Ca (**22**) or the Mn_{12} (**26**) compounds may be suitable guests for these supports, since both are highly hydrophobic and insoluble in polar solvents and present interesting magnetic properties. The insertion of several Mn_{12} compounds and other big clusters in mesoporous silica has already been reported in the literature.[149–153] In these cases, the pore size showed a huge effect on the degree of incorporation,[151,152] at least for SBA-15 materials. Compound **22** is spherical with about 2.4 nm of diameter, whereas **26** has a more ellipsoidal shape of ~1.8 nm wide and ~2.1 nm length. The pores for our extracted silica are ~3.9 nm wide (Bdb method) and, even though a notable decrease of pore diameter is expected after the functionalization, there will be enough space to insert at least one compound in a cross section. Figure 107 shows the synthetic procedure to obtain one of the desired materials. The spread of the complexes along the channel will depend on the diffusion and mobility of molecules inside the channels. For instance, if the host-guest interaction is very strong, the complexes may stay fixed close to the entrance of the channels, blocking the path for other molecules.

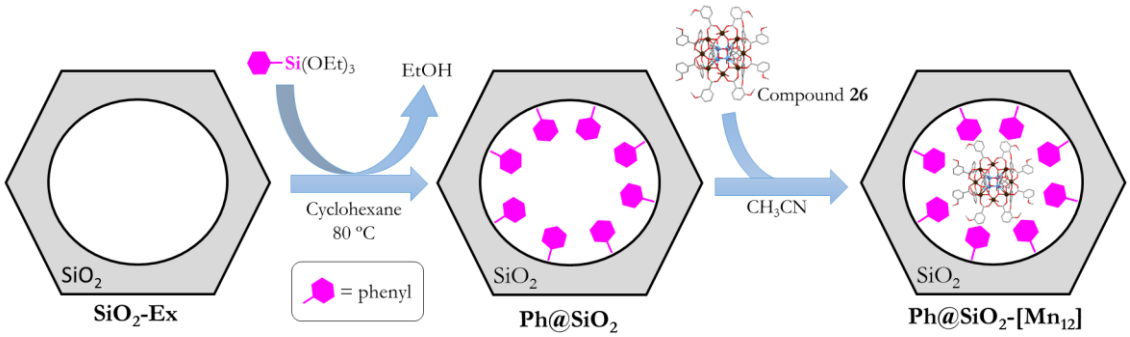

Figure 107. Synthetic procedure to obtain material Ph@SiO_2-[Mn_{12}] from extracted silica (SiO_2-Ex).

Finally, the synthesis of a support containing benzoic acid function was considered with the purpose of anchoring the Mn complexes by carboxylate substitution or by directly synthesizing the Mn complex inside the silica. Therefore, the function of the support would serve as bridging ligand for the Mn ions. The carboxylate substitution has already been reported to synthesize several Mn_{12} compounds starting from the dodecanuclear compound with acetate bridges, which showed much better yield than the corresponding direct synthesis.[266] One may use the same procedure to anchor a Mn complex on the inner walls of mesoporous silica. However, this procedure requires the benzoic acid function to be more acidic than the carboxylic acid of the Mn complex in order to guarantee the protonation of the ligands and their subsequent substitution.

There are several examples in the literature regarding silica functionalization with carboxylate functions.[303–312] In most of them, the carboxylate function is obtained from the acid hydrolysis of cyano groups previously anchored in the support.[303–308] In some others, the –COOH function is obtained from aldehyde-modified silica,[309] grafting a pre-synthesized silane,[310] or directly during the synthesis of the raw material[311] as a result of the thermal degradation of surfactant triblock polymers in the pores of SBA-15.[313] The synthetic procedure proposed by Schoenfeldt and Notestein[312] claimed our attention because it only involves a two-step functionalization and the resulting group is benzoic acid, very similar to the carboxylate ligands that we used to synthesize all our Mn compounds. A schematic representation of the synthesis of a hypothetical material [Mn_{12}]-O_2CPh@SiO_2 is represented in Figure 108. A support containing an ester function was synthesized as reported by the aforementioned authors. The acid hydrolysis of the ester group was attempted in order to obtain a benzoic acid function to further anchor the Mn complexes.

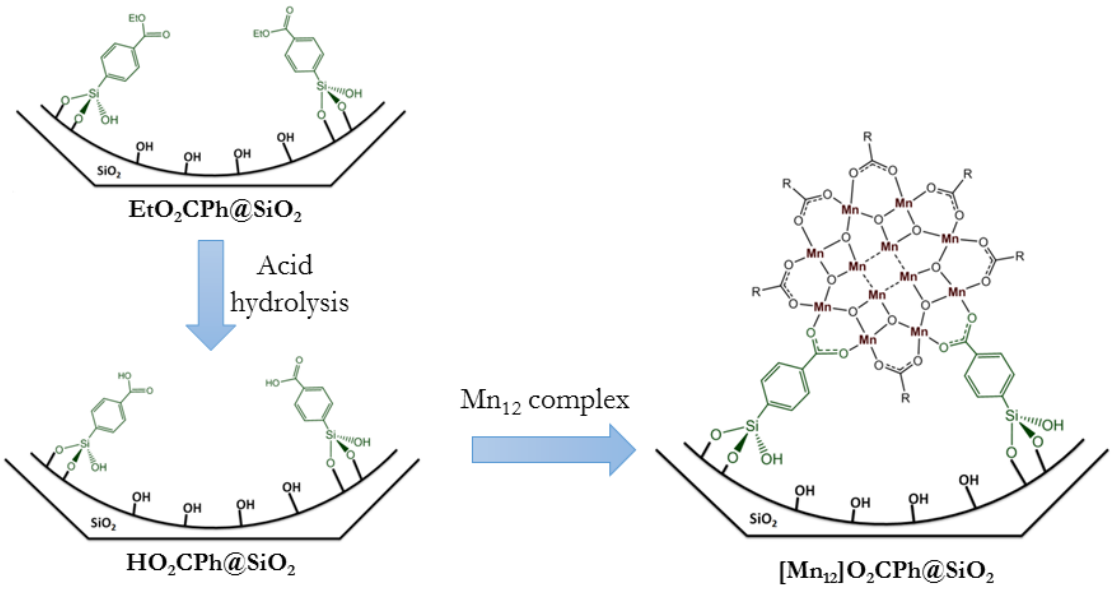

Figure 108. Synthetic route to obtain a hypothetical material [Mn_{12}]-O_2CPh@SiO_2.

Another possibility is the synthesis of the Mn compound directly inside the support HO_2CPh@SiO_2. In this case, the support would provide the ligands of the Mn compound. This procedure could be advantageous because it combines the synthesis of the molecular compound, the isolation, and the insertion in just one step. However, some shortcomings may be predicted, such as the formation of different compounds due to the heterogeneity of the surface or the direct binding of the Mn ions to the silanol groups.

To sum up, in this work we present the synthesis of four different mesoporous silica supports containing *n*-propyl (C_3), *n*-octyl (C_8), phenyl (Ph), and *para*-(ethoxycarbonyl)phenyl (EtO_2CPh) functions. The conversion of the ester to carboxylate of the latter support is also reported. Finally, the insertions of the Mn-Ca compound (**22**) into the supports C_3@SiO_2 and Ph@SiO_2, and the insertion of the Mn_{12} compounds (**26**) into the support Ph@SiO_2 are described. The magnetic properties of these three new Mn-SiO_2 hybrid materials are also presented. Owing to the complexity of these systems and lack of time, no more attempts could be performed to improve the characteristics of these materials. However, these results provide a better understanding about the behavior of big clusters supported on mesoporous silica.

Synthesis and characterization of the supports

Functionalization with C_3, C_8, Ph, and EtO_2CPh. Firstly, 2D hexagonal LUS silica (MCM–41 type) was prepared at high temperature (T = 180 °C) using microwave radiation and cetyltrimethylammonium tosylate (CTATos) as a surfactant.[117,118,113,131,132] The surfactant was extracted with an alcoholic solution of HCl to obtain surfactant-free mesoporous silica (SiO_2-Ex), where the silanol groups of the surface are completely exposed. Material SiO_2-Ex was functionalized with a post-grafting strategy by the temperature-assisted condensation of the corresponding organo-silane (with C_3, C_8, Ph, or EtO_2CPh function) and the silanol groups of material SiO_2-Ex. The resulting amount of function and its disposition will mainly depend on the number and disposition of silanol groups on the surface and plausible steric effects between adjacent functions. Note that the organo-silanes used in this work contain a T type silicon atom, bound to three oxygen and one carbon atoms. Hence, the functions may be grafted to the support either through one, two, or three positions, leading to T^1, T^2, or T^3 Si atoms, respectively. From NMR spectroscopy, we could have deduce which is the predominant type of Si atom. Unfortunately, the quality of the ^{29}Si spectra for these three supports was not enough to determine the T type Si atoms, since their signal was masked with the noise. Nevertheless, it is well known that $RSi(OR')_3$ functions mainly lead to type T^2 or T^3, with average distribution of T^2/T^3 around 40/60%.[314,315] The T^1 Si signal, which is expected at –48 ppm, was not observed; so the amount of this type of Si atom may be considered negligible.[314,315]

From the average distribution of $Q^2/Q^3/Q^4$ for SiO_2-Ex, which is around 4.5/36/59.5%, the approximate number of –SiOH groups lying on the surface may be calculated, giving ~4.1 –SiOH groups/nm^2. Hence, the resulting function/nm^2 cannot be higher than 2, taking into account that just for two molecules of function require at least 5 –SiOH groups/nm^2 placed in the right disposition for the tetrahedral geometry of the Si atom of the function. Therefore, this parameter may be a decisive factor limiting the grafting of functions.

The resulting function/Si_{inorg} molar ratios in relation to their pore size and pore volume variation for materials C_3@SiO_2, Ph@SiO_2, and EtO_2CPh@SiO_2 are listed in Table 33. The more complete data concerning the textural properties of these materials will be presented in Table 34. In the previous chapter, we analyzed the support containing 4-pyridylethyl (Py) function and TMA^+ ions and its data have been also included in Table 33. That support displays a Py/Si_{inorg} molar ratio of 0.11, which indicates that the solid contains ~1 Py/nm^2. It is quite surprising that, even though C_3 and Ph functions are less voluminous than Py and

that the materials herein presented do not contain TMA^+ ions, the C_3/Si_{inorg} and Ph/Si_{inorg} molar ratios are lower than that displayed for Py@SiO_2-TMA.

Table 33. Textural and analytical data related to the function contents for materials Py@SiO_2-TMA, C_3@SiO_2, C_8@SiO_2, Ph@SiO_2, and EtO_2CPh@SiO_2.

Material	Organic Function	ΔV_{pore} [a] / $cm^3\ g^{-1}$	d_{pore} [b] / nm	Weight loss [c] / %	Function/Si_{inorg} molar ratio [d]
Py@SiO_2-TMA	4-pyridylethyl	0.46	2.9	22.6*	0.11
C_3@SiO_2	*n*-propyl	0.16	3.6	7.5	0.096
C_8@SiO_2	*n*-octyl	0.09	3.5	11.9	-
Ph@SiO_2	phenyl	0.14	3.6	11.2	0.075
EtO_2CPh@SiO_2	*para*-(ethoxycarbonyl) phenyl	-	-	12.2	0.050

[a] Difference between the pore volume of SiO_2-Ex and the functionalized material, deduced from N_2 isotherms sorption; [b] Pore diameter Broekhoff and de Boer (BdB) analysis;[111] [c] Data from the TG analysis, corresponding to the weight loss between 200–700 °C; [d] Si_{inorg} = silicon atoms coming from the SiO_2 matrix, without considering those coming from the organo-silane functions; [d] Calculated from the elemental analysis; * The weight loss also includes the TMA^+ ions.

As an example, Figure 109 shows the schematic representation on scale of the Ph@SiO_2. A surface of 1 nm^2 seems to be enough to give shelter to more than one molecule of function, since the functions itself (taking the VdV radii into account) only occupies a fourth part of this area. However, one should also take the curvature of the surface into account. As observed in Figure 109, there is a plausible steric hindrance due to the concavity of the inner surface.

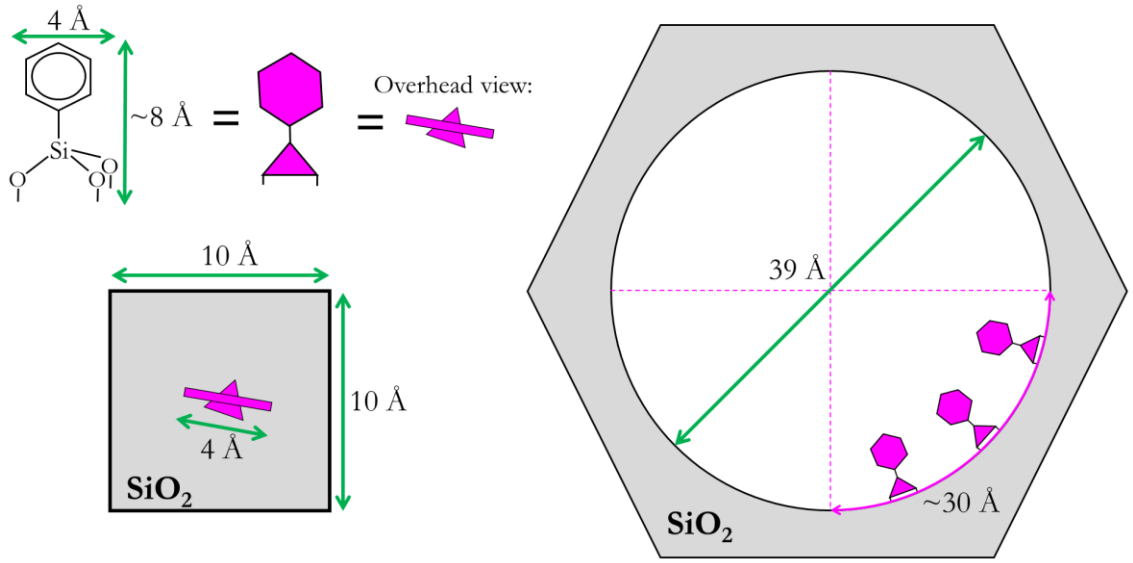

Figure 109. Schematic representation on scale for Ph@SiO_2, with an overhead view of the Ph function in a surface reaching 1 nm^2 and a front view of a cross section of a channel. The pink triangles represent a sideway view of the silicate tetrahedra.

Material C_8@SiO_2, with *n*-octyl (C_8) function, showed some peculiar characteristics. From TG analysis, we could estimate that the C_8/Si_{inorg} molar ratio may range from 0.07 to 0.08. As the *n*-octyl group is bigger than both the phenyl and the *n*-propyl moieties, we expected this function to occupy much more space than the latter ones. However, the difference between the pore volume of SiO_2-Ex and material C_8@SiO_2 is not consistent for this occupancy, since it is much smaller than the one displayed for materials C_3@SiO_2 and Ph@SiO_2 (see Table 33). An explanation to this fact could rise upon the high flexibility of the *n*-octyl group, which allows the chains to interweave with each other and consequently occupy less space than we had firstly considered for an incomplete coverage situation (Figure 110). The pore diameter could provide useful information; however, the value itself corresponds to the average pore diameter along the channel and is dependent on the amount of grafted function and its distribution. So, no conclusion may be drawn from the pore diameter.

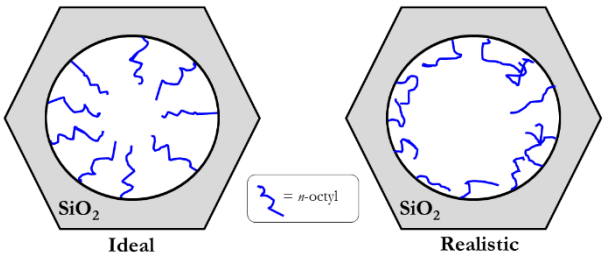

Figure 110. Ideal (left) and more realistic (right) representation, according to N_2 sorption isotherms, of material C_8@SiO_2.

It is surprising that material Py@SiO_2-TMA is the most function-loaded, considering that the 4-pyridylethyl (Py) function is the biggest in this group. However, it is worth noting that the pyridyl functionalization was done over SiO_2-TMA. This latter material was prepared by replacing the surfactant of the raw material SiO_2-CTA with TMA^+ ions, leading to a material containing ~1 TMA^+/nm^2. The resulting distribution of the TMA^+ ions will be determined by the precedent disposition of the CTA^+ ions, which is dictated by the formation of the surfactant micelles during the synthesis of the raw material and the electrostatic repulsions between the heads of the CTA^+ ions. Hence, the distribution of TMA^+ ions is expected to be uniform. In this way, the surface of SiO_2-TMA could be seen like a template, where the Py functions may only be grafted on spaces between TMA^+ ions. Note that within the ~4 surfacing silicon atoms per squared nanometer that the material contains, just one will be occupied by the TMA^+ ion, letting three silanol groups available to graft ~1 Py per nm^2. In addition, the two aliphatic carbon atoms that the 4-pyridylethyl (Py) contains make the

aromatic ring more flexible, which likely decreases the steric hindrance between adjacent pyridyl rings.

The last but not the least parameter that could be affecting the yield of the functionalization is the thermodynamics of the condensation. The amount of function grafted on the silica could be determined by how favorable this condensation is, dictated by the equilibrium between grafted and non-grafted functions. Side reactions, such as silane dimerization, could also take place and consequently decrease the yield of the process.

Hydrolysis of material $EtO_2CPh@SiO_2$. The ester groups of material $EtO_2CPh@SiO_2$ need to be converted to carboxylic acid by acid hydrolysis. Schoenfelt and Notestein reported the preparation of non-porous silica with *para*-(ethoxycarbonyl)phenyl function. Then, the ester group was converted to carboxylic acid by refluxing for 12–24 h in an HCl aqueous solution. The complete hydrolysis was confirmed by ^{13}C NMR spectroscopy, with the disappearance of the peaks assigned to C_{sp3} atoms (~15 and ~60 ppm).[312] In our case, a hydrolysis under the same conditions may be done, but it is important to firstly consider the stability of our structure. Indeed, the mesostructure of our material could be perturbed and a substantial part of the function could be unhooked under such extreme conditions. Hence, more moderate conditions for the hydrolysis were tested, stirring material $EtO_2CPh@SiO_2$ in an acetone-water (95-5) mixture with 2 equivalents of H_2SO_4 at 60 ºC for 2 h. Unfortunately, the solid ^{13}C CPMAS (cross-polarization magic angle spinning) NMR spectra displayed the bands assigned to the C_{sp3} atoms even after repeating three times the same procedure (Figure S34), indicating that the hydrolysis was incomplete. The ^{13}C HPDEC NMR spectra for these materials were also recorded to ideally quantify the yield of the hydrolysis, but the low concentration of function in the solid (0.050 equivalents per SiO_2) led to very noisy spectra upon which quantification with reasonable accuracy was not possible.

In respect to the results above, the hydrolysis under more drastic conditions was tested. About 190 mg of material $EtO_2CPh@SiO_2$ were treated at 100 ºC overnight with a 1 M HCl aqueous solution (30 mL). The thermogravimetric analysis (TGA) of the resulting material $HO_2CPh@SiO_2$ indicates that there are some important changes from the predecessor material (Figure S35). Knowing whether the hydrolysis was successful just with TGA is very difficult, since only 1.9% of the weight corresponds to the ethyl group of the ester. From a first glimpse, one may see that the material $HO_2CPh@SiO_2$ contains a higher amount of water (from room temperature and 200 ºC). The weight loss between 200 and 700 ºC, which is assigned to the organic functions and to the condensation of silanols, is much smaller for

the hydrolyzed material (from 13.9 to 7.4%). In normal circumstances this would indicate a substantial loss of organic function during the hydrolysis. However, the huge amount of water found in material $HO_2CPh@SiO_2$ decreases the percentages of the other temperature ranges, making the comparison more difficult. Several formulas are consistent with the experimental weight loss, the function/Si_{inog} molar ratio ranging from 0.030 to 0.050. The complete conversion to the benzoic acid was confirmed by solid ^{13}C CPMAS NMR (Figure 111). The NMR spectrum for material $EtO_2CPh@SiO_2$ displays resonances at 12 and 15 ppm (–$COOCH_2\mathbf{C}H_3$ and residual –$SiOCH_2\mathbf{C}H_3$), 60 ppm (–$COO\mathbf{C}H_2CH_3$ and residual –$SiO\mathbf{C}H_2CH_3$), 128 and 133 ppm (aromatic) and 165 ppm (–**C**OOR). After the hydrolysis, the resonances at 12, 15 and 60 ppm disappear, confirming that the ethyl groups were removed. The N_2 sorption isotherms for material $HO_2CPh@SiO_2$ shows a clear capillary condensation (Figure 112), confirming the preservation of the mesoporous structure after the hydrolysis. Hence, this material is now ready for the insertion of molecular compounds. Unfortunately, the absence of more sample and the lack of time forced us to postpone these experiments.

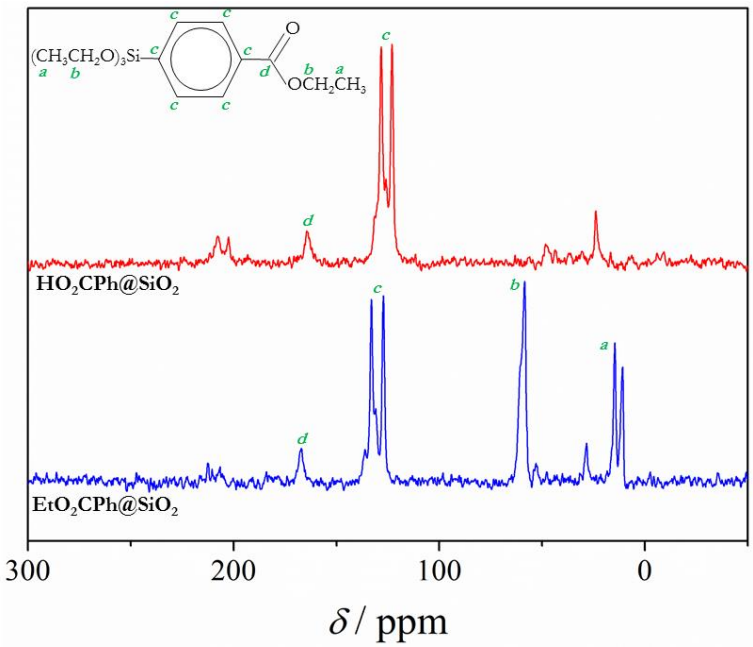

Figure 111. Solid ^{13}C CPMAS spectra for materials $Et_2O_2CPh@SiO_2$ and $HO_2CPh@SiO_2$, the latter one prepared in water at 100 °C.

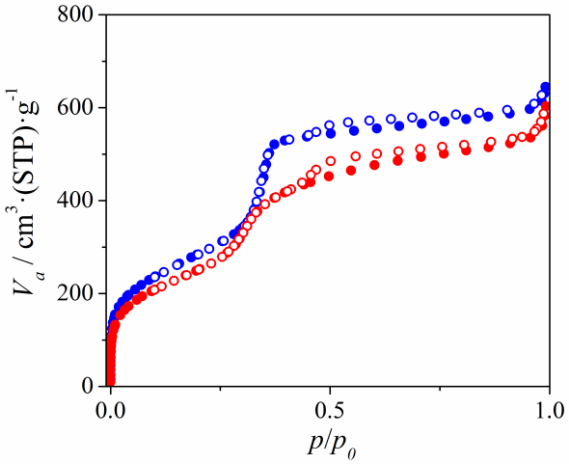

Figure 112. N_2 adsorption (full circles) and desorption (empty circles) isotherms at 77 K for materials SiO_2-Ex (blue) and $HO_2CPh@SiO_2$ (red).

Insertion of the Mn^{IV}-Ca compound (22) in $C_3@SiO_2$ and $Ph@SiO_2$

Synthesis. The heterometallic compound **22**, with formula $[Mn_6Ca_2O_9(4\text{-}^tBuC_6H_4COO)_{10}(4\text{-}^tBuC_6H_4COOH)_5]$, was inserted into materials $C_3@SiO_2$ and $Ph@SiO_2$. These supports possess a pore volume of 0.61 ($C_3@SiO_2$) and 0.78 ($Ph@SiO_2$) cm^3 g^{-1} and an average pore diameter of 3.6 nm that is suitable for the insertion of compound **22**, which may be considered as a sphere of ~2.4 nm diameter. With these pore volumes, these materials could give shelter to ~460 mg of **22** per gram of support; however, some extra space should be taken into account because of Van der Waals interactions and mobility.

Therefore, some first trials were done with the amount of compound to fill ~50% of the pore volume, using 100 mL of CH_3CN for 0.5 g of support. The insertion was monitored with UV-visible spectroscopy by measuring the absorption of the band at 239 nm (characteristic of compound **22**) of the solution before and after the insertion. Unfortunately, ≥95% of the compounds remained in the solution and the isolated materials were pale brown, which is indicative of a rather low yield of the insertion (≤5%). It is hard to rationalize the cause of this low yield, since it could be due to either a low affinity between the supports and the molecular compounds or a lack of diffusion of such a big compound along the channels. So, a longer reaction time could allow compound **22** to go in depth along the channels and a more concentrated solution could force it to get into the pores. Indeed, a better yield (33%) was achieved by decreasing the amount of solvent to 50 mL and increasing the reaction time from one to four days with the phenyl-functionalized support. However, the $[Mn_6Ca_2]/Si_{inorg}$ molar ratio found in the final material was 0.0021, which may be still considered rather low.

A third and last test consisted in stirring an acetonitrile solution (30 mL) of **22** (with an amount of compound corresponding to 50–60% of the pore volume) and pre-treating previously the supports at 80 °C and under Ar, which led to the beige brown powders labeled as C_3@SiO_2-[Mn_6Ca_2] and Ph@SiO_2-[Mn_6Ca_2]. These last tests gave much better yields for the insertion, being 69% and 53% (calculated from the Mn/Si_{inorg} molar ratio), for C_3 and Ph, respectively (see below).

As far as insertion time is concerned, a four-day reaction is not very practical for daily work. Besides, looking at the results presented previously, it does not seem that such a long time is necessary to better insert the Mn compound. Indeed, as reported by Willemin *et al.* for the insertion of Mn_{12} and Mn_4 compounds, reaction times longer than 2 h does not improve the amount of inserted clusters, and may even induce decomposition after 24 h.[151] However, this statement will be also subordinate to the relative size of the pore and the molecular compound and to the nature of the Mn complex-silica interaction. As a future perspective, it is recommended to test the insertion in a much shorter time.

Characterization of the hybrid materials. According to the X-ray diffraction (XRD) patterns, the hexagonal array of the internal pores of the material was unaltered during both the functionalization of the support and the insertion of the compound (Figure 113), all materials displaying distances between the pores centers (a_0) of ~4.7 nm (Table 34). No peaks could be detected at $2\theta > 7°$, suggesting the absence of cluster crystallization at the surface or within the pores of the silica host. The low temperature nitrogen sorption isotherms of the surfactant-extracted support, SiO_2-Ex, and the hybrid solids, C_3@SiO_2, Ph@SiO_2, C_3@SiO_2-[Mn_6Ca_2] and Ph@SiO_2-[Mn_6Ca_2], exhibit a type IV isotherm according to the IUPAC nomenclature, without hysteresis as usually observed for MCM-41 2D hexagonal mesoporous silica.[113,274] The reduction of pore volume (0.06 for C_3 and 0.14 for Ph $cm^3\ g^{-1}$) after the insertion confirms the presence of the compound inside the pores. The BET constant *C* is considerably much lower for materials C_3@SiO_2 or Ph@SiO_2 than for their respective SiO_2-Ex (~110), indicating that the surface has become more hydrophobic after functionalization. However, after the insertion of the Mn complex this parameter is not strongly modified, which indicates that the surface has not suffered further modifications concerning hydrophobicity. The capillary condensation shifts to a lower range of pressures after the functionalization (Figure 114), corresponding to a pore size reduction of about 0.3 nm (from 3.9 to 3.6 nm). It also occurs progressively in a slightly wider range of pressures, indicating that the pore size distribution is a slightly broader for the hybrid material than for SiO_2-Ex.

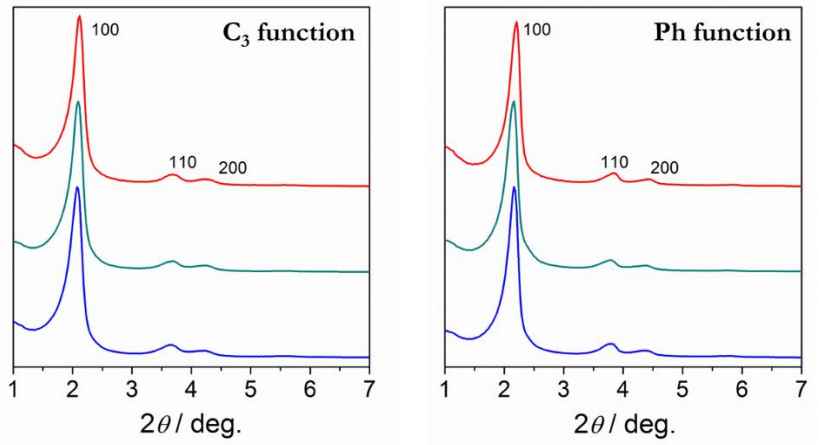

Figure 113. Small-angle powder XRD of materials SiO_2-Ex (blue), C_3@SiO_2 and Ph@SiO_2 (dark cyan), and C_3@SiO_2-[Mn_6Ca_2] and Ph@SiO_2-[Mn_6Ca_2] (red). The intensity was normalized with the (100) peak.

Table 34. Textural properties of materials SiO_2-Ex, C_3@SiO_2, Ph@SiO_2 and C_3@SiO_2-[Mn_6Ca_2] and Ph@SiO_2-[Mn_6Ca_2].

	SiO_2-Ex	C_3@SiO_2	C_3@SiO_2-[Mn_6Ca_2]	SiO_2-Ex	Ph@SiO_2	Ph@SiO_2-[Mn_6Ca_2]
d_{100} / nm	4.1	4.1	4.1	4.1	4.1	4.0
a_0[a] / nm	4.7	4.7	4.7	4.7	4.7	4.6
Intensity[b] / 10^3 counts	193	196	143	196	158	142
HWHH[c] 2θ / °	0.24	0.27	0.26	0.24	0.23	0.23
BET surf. area / $m^2\ g^{-1}$	898	776	725	1092	1002	887
C	109	70	69	106	70	69
Porous volume /mL g^{-1}	0.77	0.61	0.55	0.92	0.78	0.64
Pore diameter[d] /nm	3.9	3.6	3.6	3.9	3.6	3.6

[a] Parameter calculated from d_{100} with the formula $a_0 = 2*d_{100}/3^{1/2}$. [b] Height at the maximum of (100) peak. [c] Half-width at half-height. [d] According to Broekhoff and de Boer (BdB) analysis.[111]

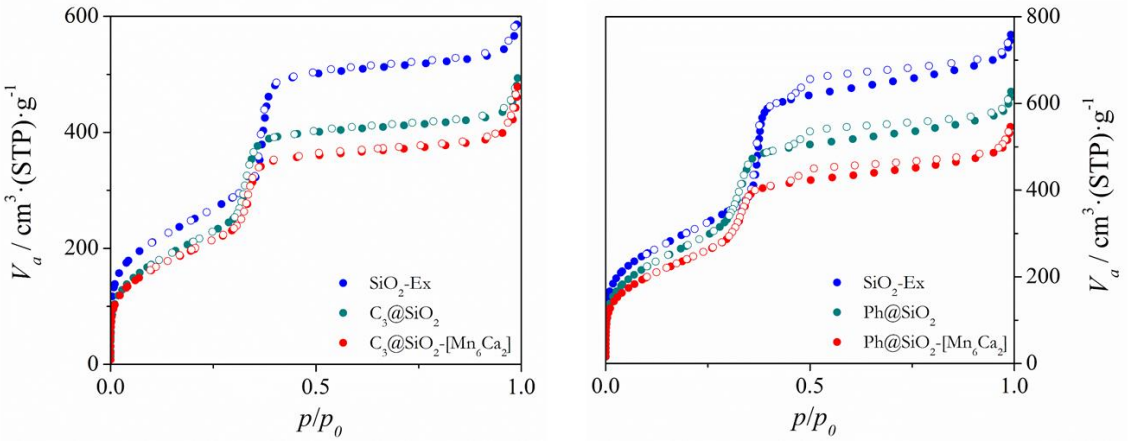

Figure 114. N_2 adsorption (full circles) and desorption (empty circles) isotherms at 77 K for materials SiO_2-Ex (blue), C_3@SiO_2 and Ph@SiO_2 (dark cyan), and C_3@SiO_2-[Mn_6Ca_2] and Ph@SiO_2-[Mn_6Ca_2] (red).

The thermogravimetric analyses (TGA) of materials C_3@SiO_2 and Ph@SiO_2 show substantial weight losses between 200 and 700 ºC assigned to the decompositions of the C_3 and Ph functions (Figure S36). For materials C_3@SiO_2-[Mn_6Ca_2] and Ph@SiO_2-[Mn_6Ca_2], the profile of the TGA changes in this range of temperatures. It displays a new peak in the TG derivative at ~400 ºC corresponding to a ~10% loss in weight (Figure S36), which could be assigned to the decompositions of the ligands of **22**.

For material C_3@SiO_2-[Mn_6Ca_2], the Mn/Ca molar ratio is 2.8, which is the expected value for a cluster containing the Mn_6Ca_2 core. The Mn_6/Si_{inorg} ratio is 0.0031, which corresponds to 69% yield for the insertion. The C/Si_{inorg} ratio should be around 0.82 considering a preservation of the integrity of compound **22** and of the C_3 functions after the treatment. However, the experimental C/Si_{inorg} (~0.54) is much lower than expected, suggesting that either some C_3 groups could have been released during the insertion of the compound or some ligands have been decoordinated from the Mn compound. In fact, the calculated formula that suits the best with the experimental elemental analysis and the weight losses observed in TGA is $SiO_2 \cdot 0.060\ C_3Si \cdot 0.0032\ [Mn_6Ca_2O_9(4\text{-}tBuC_6H_4COO)_{10}] \cdot 0.15\ H_2O$. This formula considers both the unhooking of a 38% of the C_3Si function and the decoordination of five of the monodentate carboxylate ligands. The first one could be rationalized because of the acid pH displayed by the acetonitrile solution of **22** and the presence of traces of water, which could easily lead to the hydrolysis of the Si–O–Si bonds that keep the functions retained on the surface. The decoordination of the monodentate ligands, 4-^{t}BuC$_6$H$_4$COOH, of **22** is possible, since it would not change the charge of the compounds. However, each of the Ca ions would loss between 2 and 3 position of coordination, which could be re-occupied either by water molecules of by the –SiOH groups of the support.

The 1700–1300 cm^{-1} window of IR spectra is normally quite useful because it shows the most important bands assigned to carboxylate ligands. However, in the IR spectra of material C_3@SiO_2-[Mn_6Ca_2], only one band displayed at 1401 cm^{-1} could be assigned to the Mn compound. The rest seems to be masked by the ones corresponding to the support or are too weak to be observed with such a low complex content.

For the material containing the phenyl groups (Ph@SiO_2-[Mn_6Ca_2]), the scene is much more disconcerting. The experimental Mn/Ca molar ratio was 1.9, which is very far from the expected value for a Mn_6Ca_2 cluster. This fact points directly to the non-preservation of the $[Mn_6Ca_2O_9]^{10+}$ core. In fact, this Mn/Ca ratio could be only explained with the rupture of the Mn_6 wheel. In spite of this result, the IR spectrum for this material displays three bands that are clearly assigned to the C–H stretching vibrations of the ^{t}Bu groups (2970, 2909 and 2871

cm^{-1}) and two of those assigned to –COO vibrations (1534 and 1407 cm^{-1}), attesting for the presence of 4-^{t}BuC$_6$H$_4$COO$^-$ ligands, as shown in Figure 115.

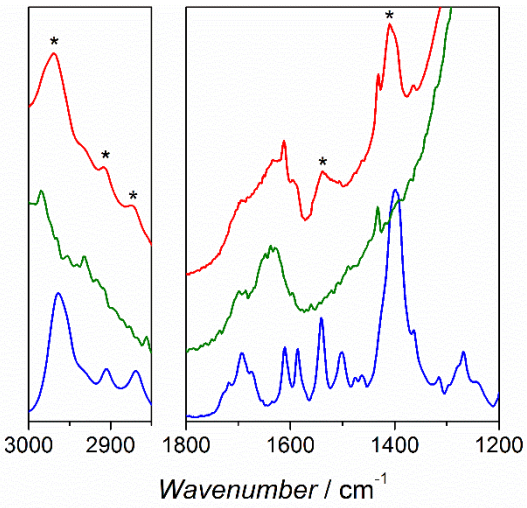

Figure 115. Infrared spectra (3100–2850 and 1800–1200 cm^{-1} ranges) of compound **22** (blue) and materials Ph@SiO$_2$ (green) and Ph@SiO$_2$-[Mn$_6$Ca$_2$] (red). The stars (*) point out IR vibrations of the 4-^{t}BuC$_6$H$_4$COO$^-$ ligands.

In order to obtain more information about the nature of Mn ions inside the silica, XPS measurements for compound **22** (as model) and materials C$_3$@SiO$_2$-[Mn$_6$Ca$_2$] and Ph@SiO$_2$-[Mn$_6$Ca$_2$] were performed. The results obtained from the fit of the C 1s and the Mn 3s peaks are summarized in Table 35. The C 1s signals of compound **22** and materials C$_3$@SiO$_2$-[Mn$_6$Ca$_2$] and Ph@SiO$_2$-[Mn$_6$Ca$_2$] may be deconvoluted in three main XPS features, assigned to C$_{sp2}$ (284.6 eV), C$_{sp3}$ (~285.5 eV) and C$_{carboxylate}$ (~288 eV) (Figure 116).[294,295] The relative area between these peaks changes from the molecular compound to material Ph@SiO$_2$-[Mn$_6$Ca$_2$] as a result of the inclusion of the phenyl function in the feature corresponding to C$_{sp2}$ atoms.

Table 35. Summary of the C 1s and Mn 3s photoelectron results for compound **22** and material C$_3$@SiO$_2$-[Mn$_6$Ca$_2$] and Ph@SiO$_2$-[Mn$_6$Ca$_2$].

	Compound 22			**C$_3$@SiO$_2$-[Mn$_6$Ca$_2$]**			**Ph@SiO$_2$-[Mn$_6$Ca$_2$]**		
	Position / eV	**Δ[a] / eV**	**Area ratio[b]**	**Position /eV**	**Δ[a] / eV**	**Area ratio[b]**	**Position /eV**	**Δ[a] / eV**	**Area ratio[b]**
C 1s	284.6	0.0	1.0	284.6	0.0	1.0	284.6	0.0	1.0
	285.5	0.9	0.7	285.8	1.2	0.6	285.2	0.6	0.2
	289.3	4.7	0.1	288.5	3.9	0.1	287.8	3.2	0.05
Mn 3s	85.0	0.0	1.0	84.4	0.0	1.0	84.1	0.0	1.0
	89.9	4.9	0.8	89.3	4.9	0.4	89.5	5.4	0.8

[a] Peak separation; [b] All areas are normalized with the highest one in each transition.

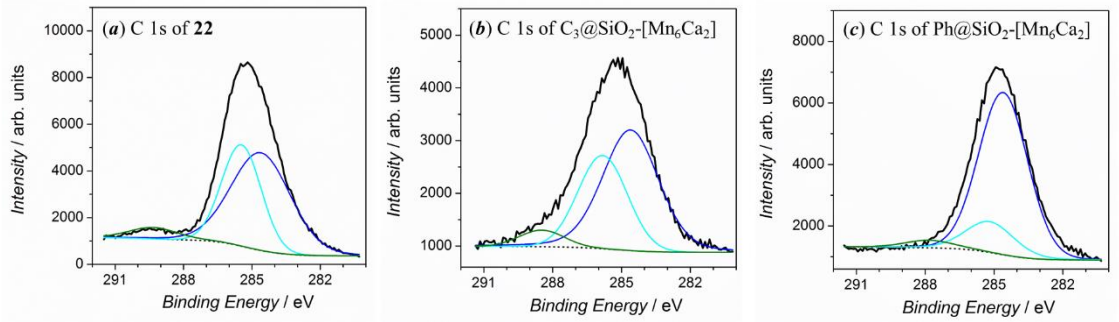

Figure 116. XPS spectra of C 1s peak for compound **22** (***a***) and material C_3@SiO_2-[Mn_6Ca_2] (***b***) and Ph@SiO_2-[Mn_6Ca_2] (***c***). The solid black lines correspond to the experimental plots and the dot lines to the background. The colored lines correspond to the spectra deconvolution, assigned to C_{sp2} (blue), C_{sp3} (cyan) and $C_{carboxylate}$ (green).

Figure 117 shows the Mn 3s spectra for **22** (*a*), material C_3@SiO_2-[Mn_6Ca_2] (*b*), and Ph@SiO_2-[Mn_6Ca_2] (*c*). As explained in Chapter 2.3, the Mn 3s doublet splitting (ΔMn 3s) provides a reliable way of determining the oxidation state of manganese, being smaller for higher oxidation state.[296] In Table S24, the values of this splitting for compounds with different oxidation states are collected. The Mn 3s spectra for these material was rather noisy because of the low Mn content (~1.3% in weight); hence, fitting these spectra with reasonable accuracy was very challenging. Several fits were performed for material C_3@SiO_2-[Mn_6Ca_2], in which ΔMn 3s was always ≤4.9 eV, consistent with oxidation state ≥IV. In such case, it is reasonable to consider ΔMn 3s = 4.9 eV, very similar to that found for **22** (4.9 eV) (Table 35). This fact confirms that the oxidation state of Mn ions for material C_3@SiO_2-[Mn_6Ca_2] is IV. On the other hand, Ph@SiO_2-[Mn_6Ca_2] displays ΔMn 3s = 5.4, quite different from what one may expect for Mn^{IV} ions. According to Table S24, this ΔMn 3s would be indeed in agreement with mixed $Mn^{III/IV}$ ions.

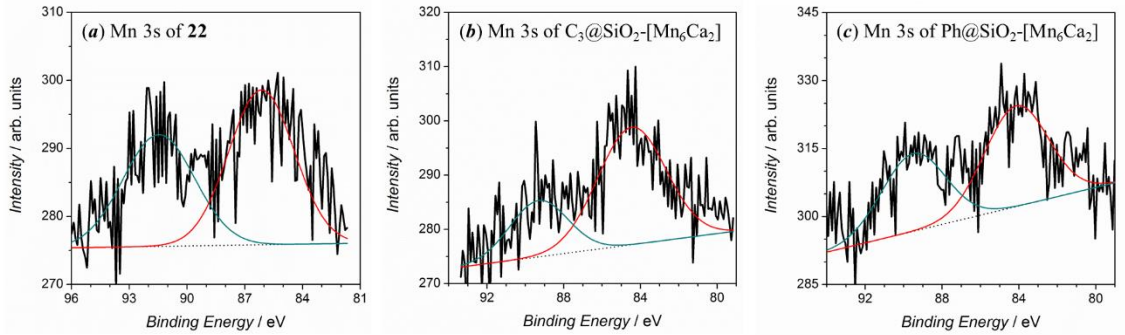

Figure 117. XPS spectra of Mn 3s peaks for compound **22** (***a***) and materials C_3@SiO_2-[Mn_6Ca_2] (***b***) and Ph@SiO_2-[Mn_6Ca_2] (***c***). The solid black lines correspond to the experimental plots, the dot lines to the background and the colored lines to the spectra deconvolution.

Magnetic properties. Magnetic measurements were carried out for materials C_3@SiO_2-[Mn_6Ca_2] and Ph@SiO_2-[Mn_6Ca_2], whose results are shown in Figure 118. Both materials display a very low signal due to their low Mn content and no many conclusions could be drawn from these results. In fact, the lump around 60 K is an artifact that appears in all samples having a low Mn content, being an evidence of the bad quality of the measurements. This lump could be due to condensation of molecular oxygen inside the pores, which becomes non-negligible when the signal of paramagnetic ions is very weak. However, the net magnetic behavior seems to be antiferromagnetic for both materials.

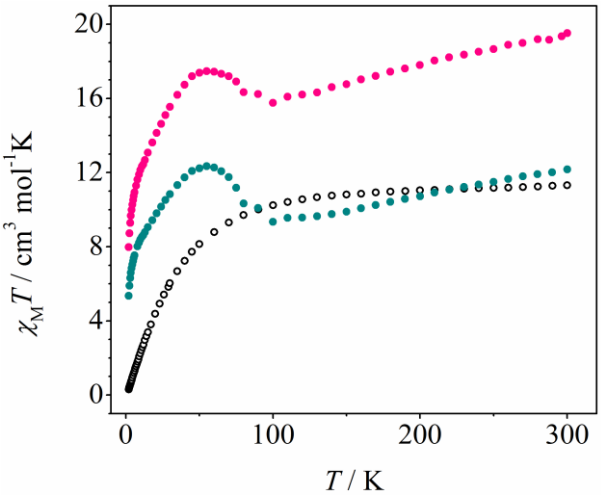

Figure 118. $\chi_M T$ versus T plots for the heterometallic Mn-Ca compound **22** (black) and material C_3@SiO_2-[Mn_6Ca_2] (dark cyan) and Ph@SiO_2-[Mn_6Ca_2] (pink).

Insertion of the Mn_{12} compound (26) in Ph@SiO_2

Synthesis. The dodecanuclear compound **26** was inserted into mesoporous silica (MCM-41 type). However, the small amounts of **26** obtained in its synthesis did not allow us to do a large number of tests and it could only be inserted in the support containing phenyl (Ph) function (Ph@SiO_2). This compound has ellipsoidal shape ranging ~1.8 nm wide and ~2.1 nm length. Material Ph@SiO_2, with a pore volume of 0.78 cm^3 g^{-1} and an average pore diameter of 3.6 nm, should be an appropriate host for this compound. Knowing that it is very difficult to insert a huge amount of compound inside the pores, the reaction was performed with a modest amount of compound and with just the amount of solvent needed to disperse the support. This latter was pre-treated at 80 ºC and under vacuum. The reaction was then performed under argon in order to keep humidity away from the support. The resulting material Ph@SiO_2-[Mn_{12}] shows a Mn_{12}/Si_{inorg} ratio of 0.003, complex loading that corresponds to 86% yield for the insertion (based on total amount of compound).

Characterization of the hybrid materials. The low temperature nitrogen sorption isotherm for material Ph@SiO_2-[Mn_{12}] exhibits a type IV isotherm according to the IUPAC nomenclature, without hysteresis as usually observed for MCM-41 2D hexagonal mesoporous silica,[113,274] indicating that the mesostructure have been unaltered during the insertion. The reduction of pore volume (0.09 $cm^3\ g^{-1}$) after the insertion confirms the presence of the compound inside the pores (Table 36). However, this reduction is much lower than that observed for the functionalization (0.16 $cm^3\ g^{-1}$), indicating that not a huge amount of complex has been inserted. The question arises whether the complex has been homogeneously spread along all the channel or it has preferentially stayed close to the entrance, something very difficult to answer because the capillary condensation for Ph@SiO_2-[Mn_{12}] is very similar to that of Ph@SiO_2 (Figure 119). Another unknown statement is the situation of these complexes: (*a*) between the phenyl functions, interacting with the –SiOH groups; (*b*) or in the middle of the channel, possibly through a π-π interaction between the aromatic ring of the phenyl and the carboxylate ligand.

Table 36. Textural properties of materials SiO_2-Ex, Ph@SiO_2 and Ph@SiO_2-[Mn_{12}].

	SiO_2-Ex	Ph@SiO_2	Ph@SiO_2-[Mn_{12}]
d_{100} / nm	4.1	4.1	-
a_0[a] / nm	4.7	4.7	-
Intensity[b] / 10^3 counts	196	158	-
HWHH[c] 2θ / °	0.24	0.23	-
BET surface area / $m^2\ g^{-1}$	1092	-	-
C	106	67	73
Porous volume /mL g^{-1}	0.92	0.78	0.69
Pore diameter[d] /nm	3.9	3.6	3.6

[a] Parameter calculated from d_{100} with the formula $a_0 = 2*d_{100}/3^{1/2}$. [b] Height at the maximum of (100) peak. [c] Half-width at half-height. [d] According to Broekhoff and de Boer (BdB) analysis.[111]

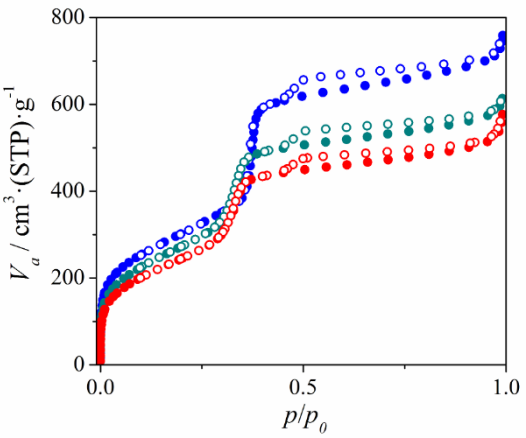

Figure 119. N_2 adsorption (full circles) and desorption (empty circles) isotherms at 77 K for materials SiO_2-Ex (blue), Ph@SiO_2 (dark cyan), and Ph@SiO_2-[Mn_{12}] (red).

The calculated formula from the elemental analysis and the TGA data is $SiO_2 \cdot 0.055\ PhSi \cdot 0.0030\ [Mn_{12}O_{12}(3\text{-}MeOC_6H_4COO)_{16}(H_2O)_4]$, which brings about the loss of 27% of the Ph function during the insertion of the Mn_{12} compound (Ph/Si_{inorg} decreases from 0.075 to 0.050). Note that, as well as with Mn^{III}_2 and $Mn^{IV}_6Ca_2$ compounds, the acetonitrile solution of Mn_{12} compound contains traces of water and is acidic. Hence, the release of protons could promote the protonation of the Si–O–Si bridges of the function and consistently, their hydrolysis. In the TGA the weight loss between 200 and 700 °C increases from 11.2% (for $Ph@SiO_2$) to 15.1% ($Ph@SiO_2$-[Mn_{12}]). The TG derivative shows a new narrow peak at ~340 °C that may be undoubtedly assigned to the decomposition of the ligands of **26** (Figure S37). The residual mass in the TGA of material $Ph@SiO_2$-[Mn_{12}] (80%) is close to the one calculated from the empirical formula (83%, assuming that all Mn has turned MnO_2 at 1100 °C).

The 1800–1100 cm^{-1} window of IR spectrum for material $Ph@SiO_2$-[Mn_{12}] displays several features assigned to the Mn_{12} compound and the phenyl support (Figure 120). The band at 1634 cm^{-1} is assigned to the bending vibration of H_2O.[316] Most of the bands seen in the 1604–1365 cm^{-1} range (at 1597, 1565, 1515, 1488, 1454, 1406 cm^{-1}) correspond to the –COO vibrations of the carboxylate ligands.[14] In between them a weak peak emerges at 1433 cm^{-1}, which very likely corresponds to the phenyl function since it is not observed in the IR spectra of SiO_2-Ex. The Mn_{12} compounds display other bands at lower wavenumbers (from 1360 to 1200 cm^{-1}), but they are covered by the very intense and broad band at 1111 cm^{-1} assigned to the Si–O–Si stretching vibrations.[316] Nevertheless, the appearance and negligible variation of the bands found between 1604 and 1365 cm^{-1} not only proves the presence of **26** in the solid but also confirms that the coordination of carboxylate ligands is barely modified.

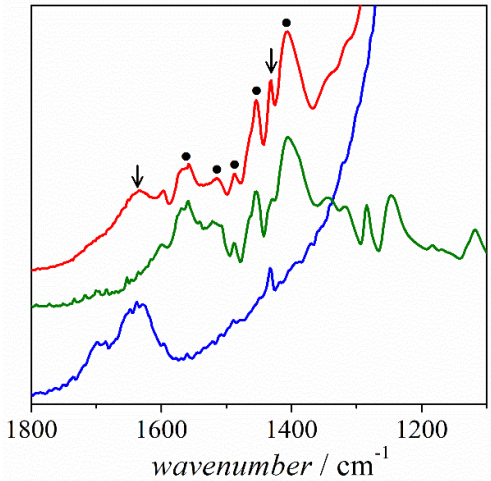

Figure 120. Infrared spectra (range 1800–1100 cm^{-1}) of the Mn_{12} compound **26** (green), the support $Ph@SiO_2$ (blue) and material $Ph@SiO_2$-[Mn_{12}] (red). The arrows (↓) and circles (●) point out IR vibrations of the support and **26**, respectively.

In order to obtain more information about the nature of Mn ions inside the silica, XPS measurements for compound **26** (as model) and material Ph@SiO_2-[Mn_{12}] were performed. The results obtained from the fit of the C 1s and the Mn 3s peaks are summarized in Table 37. The C 1s signals of compound **26** and material Ph@SiO_2-[Mn_{12}] could be distributed in three main XPS features, assigned to C_{sp2} (284.6 eV), C–O_{ether} (~286 eV), and $C_{carboxylate}$ (~288 eV) (Figure 121).[294,295] The relative area between these peaks changes from the molecular compound to material Ph@SiO_2-[Mn_{12}] as a result of the contribution of the phenyl function in the feature corresponding to C_{sp2} atoms.

Table 37. Summary of the C 1s and Mn3s photoelectron results for compound **26** and material Ph@SiO_2-[Mn_{12}].

	Compound 26			Ph@SiO_2-[Mn_{12}]		
	Position / eV	Δ^a / eV	Area ratio^b	Position /eV	Δ^a / eV	Area ratio^b
C 1s	284.6	0.0	1.0	284.6	0.00	1.0
	285.7	1.1	0.4	285.7	1.1	0.3
	288.9	4.3	0.2	288.0	3.4	0.1
Mn 3s	84.6	0.0	1.0	84.4	0.0	1.0
	89.9	5.3	0.7	90.0	5.6	0.5

[a] Peak separation; [b] All areas are normalized with the highest one in each transition.

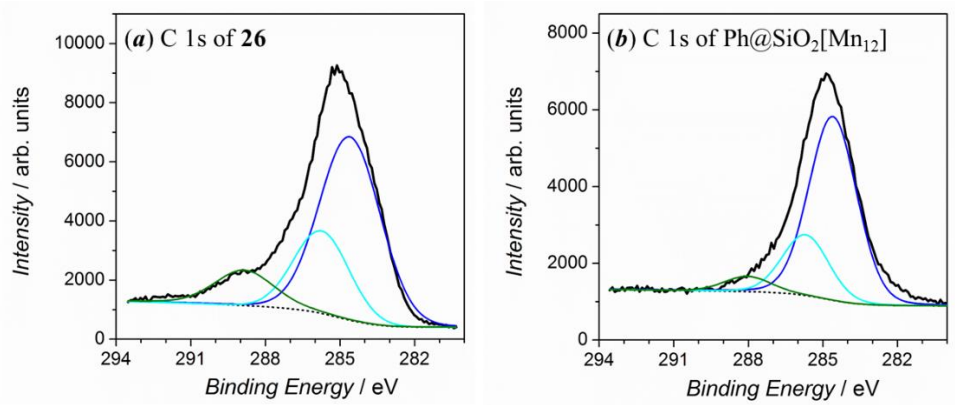

Figure 121. XPS spectra of C 1s peak for compound **26** (***a***) and material Ph@SiO_2-[Mn_{12}] (***b***). The solid black lines correspond to the experimental plots and the dot lines to the background. The colored lines correspond to the spectra deconvolution, assigned to C_{sp2} (blue), C–O_{ether} (cyan) and $C_{carboxylate}$ (green).

Figure 122 shows the Mn 3s spectra for **26** (a) and material Ph@SiO_2-[Mn_{12}] (b). It is worth remembering that the Mn 3s doublet splitting (ΔMn 3s) provides a reliable way of determining the oxidation state of manganese, being smaller for higher oxidation state.[296] The ΔMn 3s for **26**, which is 5.3 eV, is much smaller than expected for a compound containing a $Mn^{IV}_8Mn^{III}_4$ cluster, since a value between those displayed for the compounds containing a Mn^{III}_2 and $Mn^{IV}Mn^{III}$ cluster was awaited. However, the ΔMn 3s are affected by the Mn

cluster size, nuclearity, and ligand type.[297] The Mn 3s spectrum for material Ph@SiO_2-[Mn_{12}] shows a very noisy signal, as a result of the low complex content in the solid. Several fits of this spectrum were performed and, depending on the peak width, ΔMn 3s ranging from 5.1 to 5.8 could be obtained. With such a low precision, it is difficult to reach any conclusion concerning the Mn oxidation state.

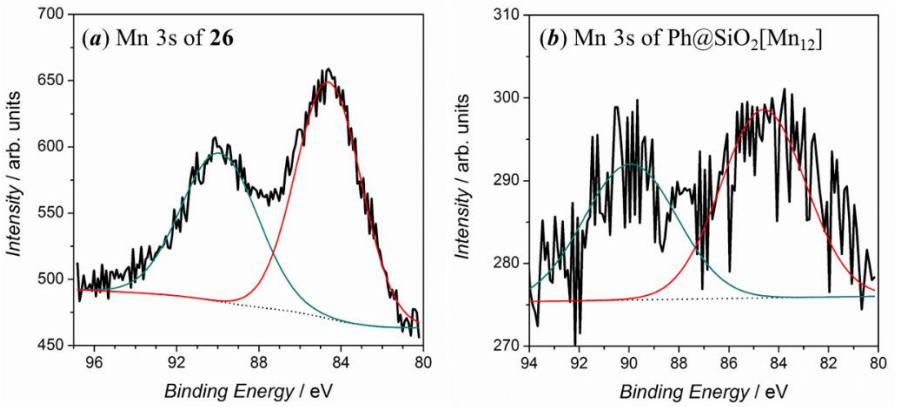

Figure 122. XPS spectra of Mn 3s peaks for compound **26** (***a***) and material Ph@SiO_2-[Mn_{12}] (***b***). The solid black lines correspond to the experimental plots, the dot lines to the background and the colored lines to the spectra deconvolution.

Magnetic properties. It is important to keep in mind that the Mn_{12} compound presents the behavior of a Single-Molecule Magnet (SMM) and that all these results are consistent with the ones reported for other Mn_{12} compounds.[266,267] Magnetic measurements were performed for material Ph@SiO_2-[Mn_{12}] and the results were compared with those obtained for the Mn_{12} compound **26**, which are found in Chapter 1.7. Figure 123 shows the magnetic measurements for **26** and Ph@SiO_2-[Mn_{12}] using both direct current (DC) and alternating current (AC). The two maxima present in the in-phase and out-of-phase AC magnetic susceptibility could be indicative of the coexistence of two Jahn-Teller isomers, as explained by Aubin *et al.*[266] All the information concerning the magnetic measurements of compound **26** is described in Chapter 1.7.

The Mn_{12} complex in material Ph@SiO_2-[Mn_{12}] still preserves the fingerprint of a SMM. Two magnetization relaxation processes (two maxima in the AC magnetic susceptibility) are also observed for this material, indicating that support Ph@SiO_2 was not selective for a particular isomer. The presence of more than one isomer of the Mn_{12} compound in mesoporous silica had already been reported in other occasions,[150,152] even if the secondary isomer is formed during the insertion[150] or it was already present in the molecular analogue.[152]

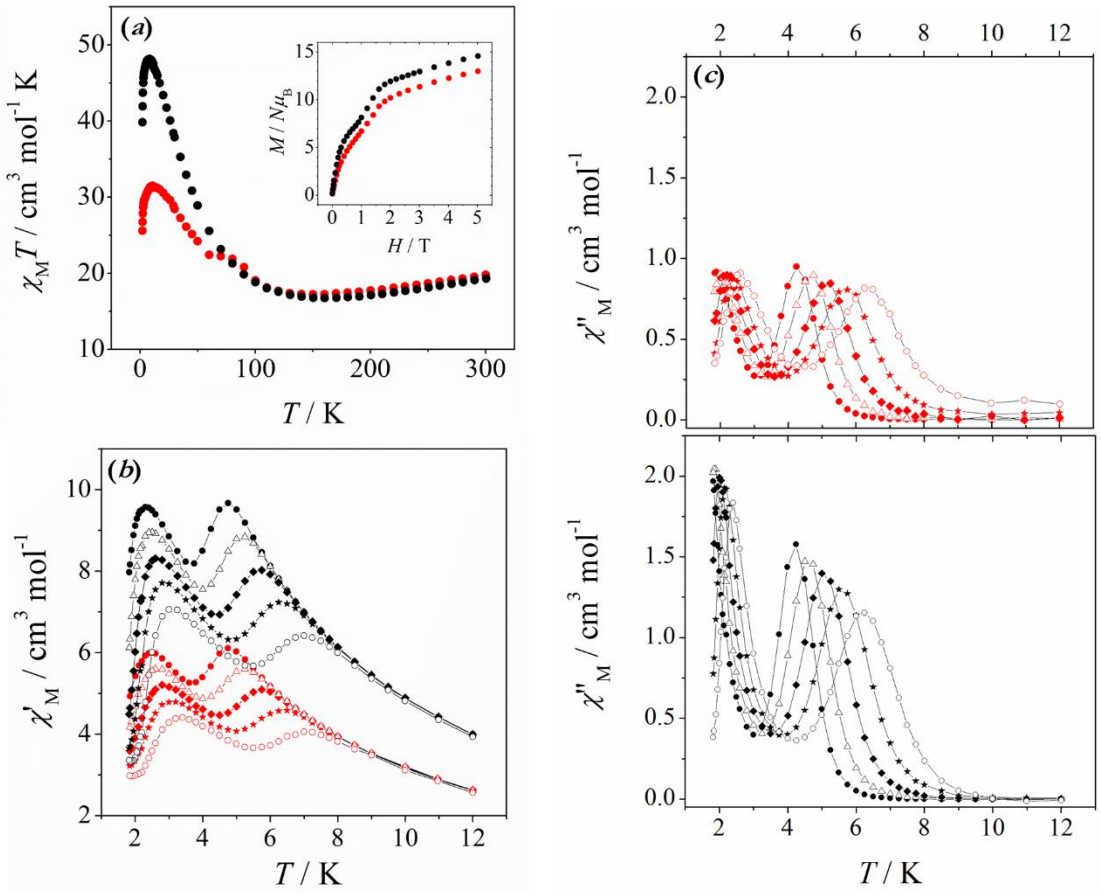

Figure 123. (***a***) DC magnetic susceptibility ($\chi_M T$) versus T plot, in the inset reduced magnetization ($M/N\mu_\beta$) at 2 K versus the applied magnetic field (H); (***b***) in-phase AC magnetic susceptibility ($\chi'_M T$) versus T plot; and (***c***) out-of-phase AC magnetic susceptibility ($\chi''_M T$) versus T plot for the Mn_{12} compound **26** (black) and material Ph@SiO_2-[Mn_{12}] (red). For the AC measurements, five different frequencies were used: 10 Hz (full circles), 35 Hz (triangles), 122 Hz (squares), 426 Hz (stars), and 1488 Hz (open circles).

The effective anisotropy energy barrier (U_{eff}) and the relaxation time (τ_0) were determined as explained in Chapter 1.7, from the plot of $\ln(1/\tau)$ versus $1/T_{max}$ (Figure S38), a kinetic analysis based on Arrhenius Law. Then, for the 2–3 K response, U_{eff} = 34 K and $\tau_0 = 1.0 \cdot 10^{-9}$ s; whereas for the 4–7 K response, U_{eff} = 65 K and $\tau_0 = 2.3 \cdot 10^{-8}$ s. These parameters are close to those observed for **26,** with U_{eff} = 32 K and $\tau_0 = 7.8 \cdot 10^{-10}$ s (2–3 K response) and U_{eff} = 66 K and $\tau_0 = 1.7 \cdot 10^{-8}$ s (4–7 K response). Nevertheless, some obvious differences between the molecular compound and the hybrid material are observed. For instance, the DC magnetic susceptibility ($\chi_M T$) versus T plot indicates that the ferromagnetic coupling is weaker for Ph@SiO_2-[Mn_{12}] than for the molecular compound. Consistently, AC magnetic susceptibilities values are also smaller for material Ph@SiO_2-[Mn_{12}], even though the maximum values are observed in very similar temperatures. These differences may be caused by the variation of some structural parameters when the Mn_{12} complex is inside silica;

however, large modifications in the coordination of the carboxylate bridges are not expected according to IR spectroscopy (see above). Unfortunately, other plausible modifications are very difficult to determine since further structural information is hard to achieve in such a low Mn_{12}-loading. Furthermore, the electrostatic potential that the Mn_{12} complex "feels" is not the same in the material as in the crystal lattice. This potential could likely act on the orbitals of the complex, shifting them in energy and affecting the magnetic properties.

General remarks

Coradin *et al.* reported the insertion of a Mn_{12} and a Cr_{12} compounds in functionalized and non-functionalized mesoporous silica (SBA-15) with pore sizes ranging from 2.5 to 6.0 nm (BJH[121] method). In that work, there was no appreciable difference between the insertion performed on functionalized and non-functionalized mesoporous silica.[152] Those results contrast with the ones reported here for the heterometallic Mn^{IV}-Ca^{2+} compound **22**, since mesoporous silica with different functions (C_3 or Ph) display marked differences at a molecular level. As explained above, the Mn_6Ca_2 cluster of compound **22** suffered severe modifications after the insertion. Besides, these modifications differ depending on the function: while with the C_3 function the cluster seemed to lose some carboxylate ligands, with the Ph function the Mn oxidation state is likely altered. On the other hand, the Mn_{12} cluster preserves its structure after the insertion in support Ph@SiO_2, just showing a slight modification in the magnetic properties.

Summary

Mesoporous silica (MCM-41) was prepared and functionalized with four different functions: *n*-propyl (C_3), *n*-octyl (C_8), phenyl (Ph), and *para*-(ethoxycarbonyl)phenyl (EtO_2CPh) silanes. These functions were grafted by the reaction of condensation between the corresponding silane and silanol groups existing on the surface of the silica. For the supports with C_3, C_8 and Ph functions, a function/Si_{inorg} ratio of 1.1 was used, which lead to solids with 0.096, ~0.075 and 0.075 ratios, respectively. These resulting function/Si_{inorg} ratios confirms that a huge excess of functions was being used (about 10 times more) and that the reactivity of each function is different. Delving into the general characteristics of the silica surface, we reached the conclusion that several effects can dictate the maximum amount of grafted function. On the one side, the concavity of inner surface may possibly cause steric hindrance between tips of adjacent functions and limit the grafting. Hence, the grafting yields follow

the trend $C_3 > C_8 \approx$ Ph, in accord with their size. However, this theory losses reliability when these results are compared with those for the support containing 4-pyridylethyl (Py) and TMA^+ ions that, with a bigger function and with the ions occupying small parts of the surface, the resulting occupancy ($Py/Si_{inorg} = 0.11$) of the surface is higher than for the C_3, C_8, and Ph functions. On the other hand, the grafting yield may be hugely dictated by availability and disposition of the silanol groups. This silica, with ~5 –SiOH/nm^2, should be unable to anchor more than 2 functions per nm^2. Moreover, these silanol groups should be in the right disposition to bind the tetrahedral Si of the function.

The acid hydrolysis of the *para*-(ethoxycarbonyl)phenyl functions was tested after the grafting, in order to convert the ester groups into carboxylic groups. The material with *para*-(ethoxycarbonyl)phenyl functions was treated with a 1M HCl aqueous solution at 100 °C, leading to material HOOCPh@SiO_2. The complete hydrolysis of the ester groups was confirmed with ^{13}C NMR spectroscopy and the preservation of the mesopores was checked with the N_2 sorption isotherms.

The heterometallic Mn^{IV}-Ca compound **22** was inserted in both the supports with C_3 and Ph functions, leading to materials C_3@SiO_2-[Mn_6Ca_2] and Ph@SiO_2-[Mn_6Ca_2], respectively. All results point to the Mn compound suffering modifications during the insertion process. While for C_3@SiO_2-[Mn_6Ca_2] some carboxylate ligands could have been decoordinated from the Mn^{IV}-Ca complex; for Ph@SiO_2-[Mn_6Ca_2] the Mn oxidation state is altered, the Mn^{IV} ions being partially reduced according to XPS.

The Mn_{12} compound **26** was also inserted in the support containing the Ph function, leading to material Ph@SiO_2-[Mn_{12}]. The Mn_{12}/Si_{inorg} ratio of this solid is 0.0030, corresponding to 86% yield for the insertion, assuming the loss of approximately a third part of the Py function. IR spectroscopy revealed that the carboxylate ligands have unlikely suffered notable modifications, since the spectrum for material Ph@SiO_2-[Mn_{12}] may be seen as the mere addition of the support and the compound spectra. The AC magnetic measurements showed that the Mn_{12} complex in material Ph@SiO_2-[Mn_{12}] still preserves the fingerprint of a Single-Molecule Magnet. However, some modifications, in terms of magnitude, have been produced. Indeed, Ph@SiO_2-[Mn_{12}] shows a weaker ferromagnetic behavior than the molecular compound **26**. This difference may be due to either unnoticed structural changes or the dissimilar electrostatic forces in the crystal lattice and in the silica matrix.

SECTION III: Catalase Activity

3.1. Introductory Remarks

In the current section the catalytic activity of Mn^{III}_2 compounds and of hybrid materials based on these latter compounds inserted into mesoporous silica is presented. The compounds and materials were tested for the H_2O_2 decomposition into H_2O and O_2 (catalase activity):

$$2\ H_2O_2 \rightarrow 2\ H_2O + O_2$$

Hence, the efficiency of these catalysts was measured by monitoring the evolution of O_2 from a solution containing both the catalyst and the substrate, H_2O_2.

Gas volumetric analysis

Figure 124 shows the assembly used to monitor the evolution of O_2. This method was also used to determine the catalase activity of analogous compounds.[192,194,317] A closed vessel with a solution or suspension of the corresponding catalyst was connected to a gas-burette. The vessel is closed with a turnover septum stopper, which allows one to inject the solution of H_2O_2 without opening the assembly. The gas-burette was connected to a flask containing hexane (mixture of isomers C_6H_{14}). The evolution of O_2 from the vessel will displace the hexane, and the lecture from the gas-burette will provide the volume of oxygen (V_{O2}) that could be plotted on a graph as a function of time. However, this volume does not correspond to that at standard pressure (V_{O2}^{0}). Therefore, the system was previously calibrated in order to obtain a correction factor.

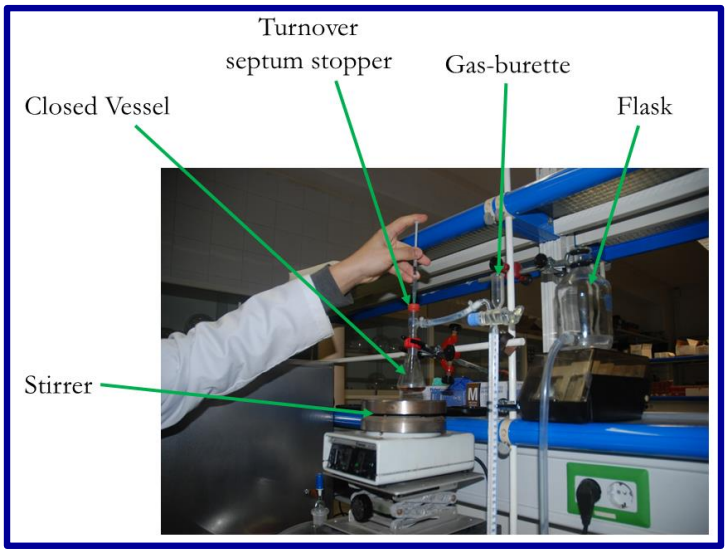

Figure 124. Picture of the assembly used to measure the catalase activity of biomimetic Mn-catalases.

For the calibration, precise amounts of H_2O_2 were oxidized with an excess of manganese(III) acetate (three times the stoichiometric amount). From these experiments, the correction factor applied was $V_{O2}^{0} = 0.63\ V_{O2}$. Then, V_{O2}^{0} can be converted to moles using the ideal gas law.

Ionic conductivity (Λ)

Ionic compounds conduct electricity when dissolved, because the dissociated ions can carry charge through the solution. Hence, the conductivity measurements could be used as a reliable way of measuring the ionic content in a solution and it is expressed in siemens per meter (S m^{-1}). The molar conductivity (Λ_M) is defined as the conductivity divided by the molar concentration of an electrolyte and measures how efficient a given electrolyte conducts electricity in solution. The most common units for Λ_M are S cm^2 mol^{-1}. Moreover, Λ_M is correlated to the type of electrolyte (number of ions) that one may have in solution. A collection of conductivity data for several ionic compounds in different organic solvents was summarized in a review by Geary.[167] Table 38 lists the molar conductivity of electrolytes with different charges in water and in acetonitrile that are more relevant for this work.

Table 38. Molar conductivity (Λ_M) in acetonitrile and in water for different electrolytes.[167,318]

	Λ_M (S cm^2 mol^{-1})	
Electrolyte	**in CH_3CN**	**in H_2O**
1:1	120–160	118–131
2:1	220–300	235–273
3:1	340–420	408–435
4:1	~500	~560

As may be observed, it is possible to identify the type of electrolyte with the molar conductivity of an ionic compounds in both acetonitrile and water solution. Note that the electrolytes in acetonitrile solution generally give lower conductivities than in water, since this latter one dissociates ions more than acetonitrile.[167]

Molar conductivities (Λ_M) of 0.8 mM acetonitrile solutions of compounds **1**, **2**, **6**, and **7** were measured, which are the ones whose catalase activity was studied (see Chapter 3.3). As we performed the catalytic tests in CH_3CN-H_2O media, the molar conductivity of these compounds was also measured in CH_3CN-H_2O 9-1 (v/v). In Table 39 the results of these measurements are listed.

Table 39. Molar conductivity (Λ_M) for 0.8 mM solutions of compounds **1**, **2**, **6**, and **7**, with general formula [{Mn(bpy)(L)}$_2$(μ-O)(μ-*n*-RC$_6$H$_4$COO)$_2$]X$_2$.

				Λ_M (S cm^2 mol^{-1})	
Label	**L**	**n-R**	**X**	**in CH_3CN**	**in CH_3CN-H_2O 9-1 (v/v)**
1	H_2O/NO_3	2-MeO	NO_3	106	189
2	H_2O/ClO_4	2-MeO	ClO_4	271	235
6	$EtOH/ClO_4$	4-MeO	ClO_4	278	284
7	$EtOH/ClO_4$	4-tBu	ClO_4	251	293

As may be observed, all compounds having perchlorate as counter-anions (**2**, **6**, and **7**) yield Λ_M values typical of a 2:1 electrolyte. This indicates that both perchlorate anions dissociate from the divalent Mn complex in acetonitrile, even though one of the counter-anions occupies a monodentate position in solid state. In solution, this monodentate position could be occupied by a molecule of solvent or water, since traces of this latter one may be found in solution. When a higher amount of water is present, the molar conductivities of compounds **6** and **7** are higher, in accord with the higher polarity of water. However, it is worth noting that compound **2**, with *n*-R = 2-MeO, displays a lower value in CH_3CN-H_2O than in CH_3CN, maybe due to the existence of some hydrogen-bonding network with the R group in *ortho* position.

Compound **1**, with X = NO_3, yields a much lower conductivity than those with X = ClO_4, as reported before for analogous compounds.[194,319] The value for **1** corresponds to a 1:1 electrolyte, indicating that one of the nitrate ions remains coordinated to the Mn complex or interacts with it through hydrogen bonds, even in solution (Figure 125). In water, the Λ_M value is higher but still much lower than expected for a 2:1 electrolyte. These facts will be of importance for the catalase activity of these compounds, as will be explained in the following chapter.

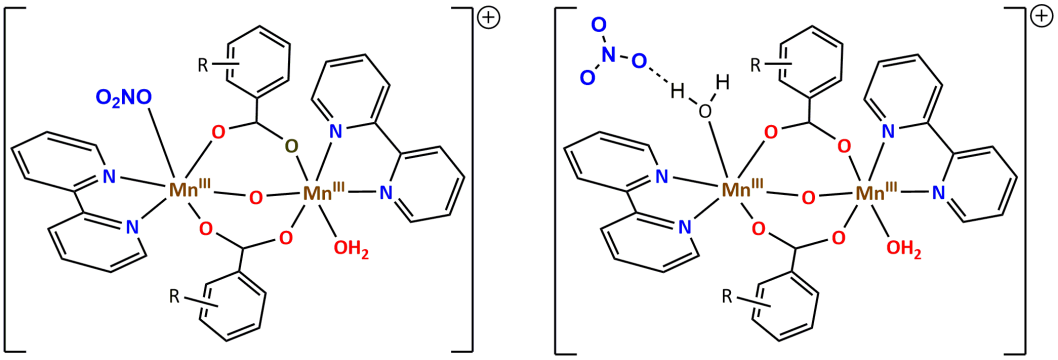

Figure 125. Schematic representation of two plausible (but speculative) interactions between the Mn complex and one of the nitrate ions in acetonitrile solution for compounds with formula [{Mn(bpy)(L)}$_2$(μ-O)(μ-*n*-RC$_6$H$_4$COO)$_2$](NO$_3$)$_2$.

Other techniques

Apart from these two latter experiments, other characterization techniques will be used in this section, such as infrared, X-ray photoelectron, and EPR spectroscopies. All these techniques were already used for the characterization of the starting samples, for either molecular compounds or silica-based materials. The starting samples will be used as references in order to identify or determine the characteristics of the products obtained after the catalytic tests and, consequently, to obtain more information concerning the active species and the changes produced during the catalysis.

3.2. Experimental Section

Physical characterization

Chemical analyses (C, H, N and Cl) were carried out by the "Centres Científics i Tecnològics" of the Universitat de Barcelona and by the "Servei de Microanàlisi" of the "Consell Superior d'Investigacions Científiques" (CSIC). **Inductively coupled plasma optical emission spectrometry (ICP-OES)** was performed to determine Mn and Si percentages by the "Centres Científics i Tecnològics" of the Universitat de Barcelona from a solution of Mn-SiO_2 material (~20 mg) pre-treated at 90 °C with a mixture of HF 49% (200 μL) and HNO_3 70% (1 mL) into an autoclave. **Infrared spectra** were recorded on KBr pellets in the 4000-400 cm^{-1} range with a Thermo Nicolet Avatar 330 FTIR spectrometer. **The ionic conductivity (Λ)** measurements were made on a 0.8 mM acetonitrile solution of the corresponding compound using a CDC401 electrode. **Electron paramagnetic resonance (EPR)** spectra were recorded at X-band (9.4 GHz) frequency using a Bruker ESP-300E spectrometer, from room temperature to 20 K at the "Unitat de Mesures Magnètiques" (Universitat de Barcelona). **X-ray photoelectron spectroscopy (XPS)** experiments were performed by the "Centres Científics i Tecnològics" in a PHI 5500 Multitechnique System (from Physical Electronics) with a monochromatic X-ray source (Al $K\alpha$ line of 1486.6 eV energy and 350 W), placed perpendicular to the analyzer axis and calibrated using the $3d_{5/2}$ line of Ag with a full width at half maximum (FWHM) of 0.8 eV. The analyzed area was a circle of 0.8 mm diameter, and the selected resolution for the spectra was 187.85 eV of pass energy and 0.8 eV/step for the general spectra and 23.5 eV of pass energy and 0.1 eV/step for the spectra of the different elements. A low energy electron gun (less than 10 eV) was used in order to discharge the surface when necessary. All measurements were made in an ultra-high vacuum (UHV) chamber pressure between $5x10^{-9}$ and $2x10^{-8}$ torr. Binding energies were further referenced to the C_{sp2} peak at 284.6 eV.

Catalase activity

The study of the **catalase activity** (H_2O_2 decomposition into H_2O and O_2) was carried out at 25 ºC by volumetric determination of the oxygen evolved with a gas-volumetric burette (precision of 0.1 mL). A 32% H_2O_2 aqueous solution (six different volumes 0.2, 0.3, 0.4, 0.5,

0.6, and 0.7 mL) (Table 40) was added to closed vessels containing acetonitrile solution of the corresponding **molecular compounds** (5 mL, 0.8 mM referred to Mn_2 unit) and the oxygen evolved was volumetrically measured. It is worth emphasizing that the catalase activity was studied in a CH_3CN-H_2O media (5 mL of CH_3CN with the complex or the material and 0.2–0.7 mL of H_2O_2 aqueous solution).

Table 40. Experiments to study the catalytic activity toward H_2O_2 disproportionation of the molecular compounds.

Experiment	$V_{H_2O_2}$ / mL	$[H_2O_2]_0$ / M	$[Mn_2]_0$ / mM	$[H_2O_2]_0/[Mn_2]_0$
a	0.2	0.38	0.77	490
b	0.3	0.55	0.75	735
c	0.4	0.73	0.74	980
d	0.5	0.89	0.73	1220
e	0.6	1.05	0.71	1470
f	0.7	1.20	0.70	1720

$V_{H_2O_2}$ = volume of 32% H_2O_2; $[H_2O_2]_0$ = initial concentration of H_2O_2 in the reaction media; $[Mn_2]_0$ = initial concentration of molecular compound in the reaction media.

The catalytic activity of the **Mn-SiO_2 materials $[Mn_2O]_x$@SiO_2 and $[Mn_2O]_x$-Py@SiO_2** was tested using 0.6 mL of a 32% H_2O_2 aqueous solution (experiment e) that was added to closed vessels containing an acetonitrile suspension of the corresponding material (5 mL, 0.8 mM referred to Mn_2 unit) and the oxygen evolved was volumetrically measured.

The same procedure was repeated for compounds **1** and **2**, and the Mn-SiO_2 materials using **pure water as solvent** instead of CH_3CN.

Blank experiments carried out without the catalyst (in both solvents) showed a negligible disproportionation of H_2O_2. Several **control experiments** were performed as follows: (***a***) the catalytic activity of $Mn(NO_3)_2$ and MnO_2 toward the H_2O_2 disproportion was tested under the same conditions as those used for the molecular compounds with 32% H_2O_2 (0.6 mL) and a 1.6 mM acetonitrile solution (5 mL), equivalent to $[Mn_2]$ = 0.8 mM ($[Mn(NO_3)_2]$ or $[MnO_2]$ = 1.6 mM); (***b***) the catalytic activity of the supports, SiO_2-TMA and Py@SiO_2-TMA, was also tested under the same conditions, by adding 0.6 mL of 32% H_2O_2 to a suspension containing 20–40 mg of support and 5 mL of solvent. The results of these experiments will be commented during the discussion.

pH measurements were made using a PHC10101 electrode in CH_3CN-H_2O 9-1 (v/v) media (5 mL of acetonitrile and 0.6 mL of water). As the electrode was calibrated in water, the pH measured in CH_3CN-H_2O 9-1 (v/v) ($^{s}_{w}pH$) was converted to $^{s}_{s}pH$ (pH measured in CH_3CN-H_2O with electrodes calibrated in the same mixture) using the δ conversion

parameter as described by L. G. Gagliardi *et al.*[320] The following equation was used: ${}^{s}_{s}\mathrm{pH} = {}^{s}_{w}\mathrm{pH} - \delta$, where $\delta = -1.61$ at 20 °C. The pH values given in this work correspond to ${}^{s}_{s}\mathrm{pH}$.

The study of the **pH-dependence** on the catalase activity was performed for compound **2**. The evolution of oxygen was measured at different pH values using the same method and under the same conditions. Et_3N 99% was used to increase the initial pH of the reaction media, yielding ${}^{s}_{s}\mathrm{pH}$ = 7.3, 9.8, 10.7, 11.8 and 12.0, for Et_3N concentrations of 1.3, 2.5, 3.8, 12.6 and 19.0 mM, respectively.

Material $[Mn_2O]_{0.50}@SiO_2$ (22 mg) was dispersed in CH_3CN (10 mL), leading to $[Mn^{III}_2]$ = 0.8 mM. Then, H_2O_2 32% (1.2 mL) was added ($[H_2O_2]_0$ = 1.05 M). Several fractions (of ~ 0.6 mL) of this suspension were filtered at 30, 90, 230, 600 s and 2 h after the addition of H_2O_2. Then, **EPR spectra** of the filtered solutions were recorded at room temperature. The EPR calibration was performed using manganese(II) perchlorate ($[Mn^{II}]$ = 0.044–1.45 mM). The solid separated at 90 s after the addition of H_2O_2 in the previous experiment was washed as soon as possible with CH_3CN (20 mL) and analyzed by **EPR** and **XPS**.

The **effect of the counter-anions** was analyzed for compounds **1**, **2**, and **7**. Several 0.8 mM solutions of these compounds were prepared containing different amounts of sodium perchlorate and sodium nitrate. The experiments were performed at concentrations between 0.36 and 10^3 mM for ClO_4^- and between 1.8 and 94 mM for NO_3^-. Then, a 32% H_2O_2 aqueous solution (0.4 or 0.6 mL) was added to closed vessels containing 5 mL of the corresponding solution together with sodium salt. The oxygen evolved from these vessels was volumetrically measured.

Post-catalysis products

Several post-catalysis products were prepared in order to investigate the stability of the materials under the conditions of the reaction. The superscripts #A and #W correspond to those obtained from the reaction in acetonitrile and in water, respectively. When a number is added, such as #W1 or #W2, this number indicates the number of additions of H_2O_2.

$[Mn_2O]_{0.50}@SiO_2^{\#A}$. $[Mn_2O]_{0.50}@SiO_2$ (100 mg) was stirred in acetonitrile (63 mL) for 1 or 2 min. Then, a 32% H_2O_2 aqueous solution (7.5 mL) was added, causing immediate vigorous evolution of O_2. After 2 hours, the brown solid was separated by filtration, washed with acetonitrile, and dried overnight at 80 °C.

$[Mn_2O]_{0.50}@SiO_2^{\#W}$. An analogous procedure was followed as for $[Mn_2O]_{0.50}@SiO_2^{\#A}$, but using distilled water instead of acetonitrile.

$[Mn_2O]_{0.21}$-Py@$SiO_2^{\#W1}$. $[Mn_2O]_{0.21}$-Py@SiO_2 (100 mg) was stirred in water (26 mL) for 1 or 2 min. Then, a 32% H_2O_2 aqueous solution (3.2 mL) was added, causing immediate vigorous evolution of O_2. After 2 hours, the brown solid was separated by filtration, washed with acetonitrile, and dried overnight at 80 ºC.

$[Mn_2O]_{0.21}$-Py@$SiO_2^{\#W2}$. $[Mn_2O]_{0.21}$-Py@SiO_2 (100 mg) was stirred in water (26 mL) for 1 or 2 min. Then, a 32% H_2O_2 aqueous solution (3.2 mL) was added, causing immediate vigorous evolution of O_2. After 1 hour, a new addition of H_2O_2 was performed. After 1.5 hours, the brown solid was separated by filtration and dried overnight at 80 ºC. Elemental analyses and ICP-OES: C, 11.85; H, 1.71; N, 2.06. Residual mass at 1100 °C (%): 81.0.

Stability in water

These materials were prepared in order to test the stability of the hybrid materials in water suspension.

$[Mn_2O]_{0.50}@SiO_2^{\#M}$. $[Mn_2O]_{0.50}@SiO_2$ (24 mg) was stirred in H_2O (15 mL) for 2 hours. The brown solid was separated by filtration, washed with H_2O (20 mL) and dried overnight at 80 ºC.

$[Mn_2O]_{0.21}$-Py@$SiO_2^{\#M}$. $[Mn_2O]_{0.21}$-Py@SiO_2 (100 mg) was stirred in H_2O (26 mL) for 2 hours. The brown solid was separated by filtration, washed with H_2O (10 mL) and dried overnight at 80 ºC.

3.3. Catalase Activity of Dinuclear Mn^{III} Compounds

First insights

In Section I of this manuscript we presented the synthesis and characterization of several Mn compounds containing carboxylate bridges, many of them being dinuclear. It is worth remembering that the active site of the native Mn-catalase, found in some lactic acid bacteria,[65] comprises two Mn ions that are linked through oxo and carboxylate bridges. Hence, the dinuclear compounds herein presented are structural models of this native active site. Particularly, Mn^{III}_2 compounds in Chapter 1.3 (**1–7**), with the general formula $[\{Mn(bpy)(L)\}_2(\mu\text{-}O)(\mu\text{-}n\text{-}RC_6H_4COO)_2]X_2$, share some structural peculiarities with this active site. Figure 126 shows the crystal structures of the Mn-catalase from *Lactobacillus plantarum*[63] and compound **1**.

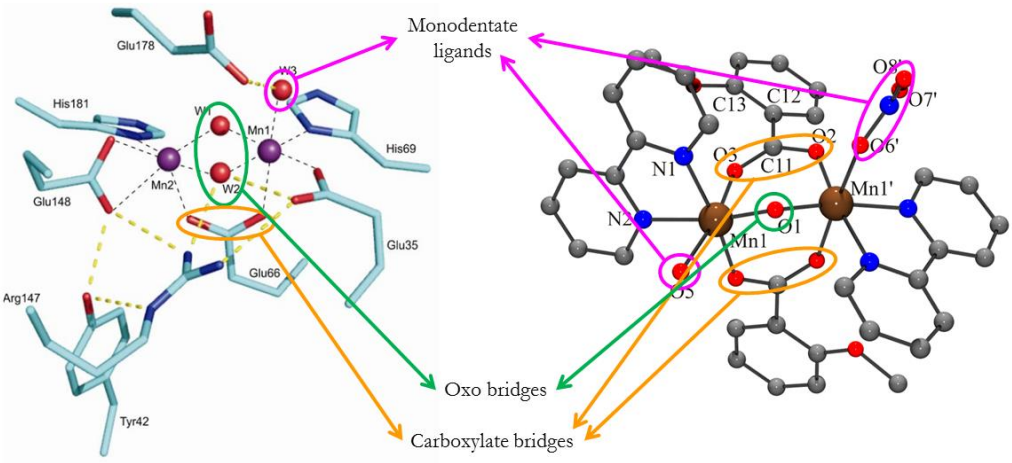

Native Mn-Catalase **Biomimetic Mn-Catalase**

Figure 126. Crystal structures of native Mn-catalase from *Lactobacillus plantarum*[63] and of the biomimetic compound **1**. The figure for the native enzyme has been taken from *Coord. Chem. Rev.* 2012 by Signorella and Hureau.[67]

As may be observed, both the native and biomimetic catalase show two Mn ions that are linked through oxo and carboxylate bridges, have nitrogen-based ligands, and molecules of solvent coordinated. However, there are substantial structural differences that will obviously affect the electronic properties of the Mn_2 unit and the catalytic activity. Hence, it is important to keep them in mind. For instance, while the native catalases have a double-oxo bridge, the biomimetic compounds, **1–7,** contain a single-oxo bridge. These differences could

be also reflected in the Mn··Mn distances, *d*(Mn···Mn); however, the *d*(Mn···Mn) in the Mn^{III}_2 compounds (**1–7**) (~3.15 Å) is very similar to that in the Mn^{III}_2 form of the native catalase from the *Thermus thermophilus* (TT) (~3.14 Å)[64]. On the other hand, in the *Lactobacillus plantarum* (LP) the *d*(Mn···Mn) is remarkably shorter (3.04 Å).[63]

The Mn–L distances for compounds **1–7** range from 1.78 to 2.48 Å and the Mn display an elongated distortion toward the direction of the monodentate ligand. In contrast, the Mn ions in the LP are less distorted, since the *d*(Mn–L) are in the range 1.88–2.44 Å. Moreover, one of the Mn^{III} ions in the catalase from LP displays a compressed distortion toward the direction of one of the oxo bridges, whereas the other one has a much regular environment.

The reduced form of the native catalase, with a Mn^{II}_2 unit, displays a *d*(Mn···Mn) ≈ 3.53 Å,[321,322] significantly longer than those for Mn^{II} compounds with a double-$\mu_{1,1}$-R'COO^- bridge (**12** and **14**) (~3.45 Å). Nevertheless, this distance of ~3.53 Å is typical of those seen in Mn^{II}_2 cores having one single atom bridge together with one or two carboxylate bridges, as reported before in the literature.[322] On the contrary, the reduced form of the catalase from TT, also having a Mn^{II}_2 unit, displays a d(Mn···Mn) ≈ 3.18 Å, consistent with the closed form of the $[Mn^{II}_2(H_2O)(OH)]^{3+}$ core.[323] The magnetic properties for this reduced form has been studied before, concluding that the magnetic coupling constant 2*J* (referred to $H = -2JS_1S_2$) is between –10 and –30 cm^{-1} for TT and around –20 cm^{-1} for LP.[40] The Mn^{II}_2 compounds herein reported, **8–12**, **14**, and **15**, display much lower 2*J* values, ranging from –2.4 to +1.3 cm^{-1}. Unfortunately, the magnetic interactions for the oxidized forms of the native catalase have not been reported to the best of our knowledge.

Very recently, the structure of the Mn-CATs from *Anabaena* was determined.[75] The active site of this enzyme also comprises two Mn ions, but linked only through two carboxylate ligands. So far, only the reduced form, Mn^{II}_2, have been structurally characterized. The Mn^{II}···Mn^{II} distance, with a mean value of 3.8 Å, is much shorter than those displayed by the dinuclear Mn^{II} compounds in Chapter 1.4 with $[Mn^{II}(\mu_{1,3}\text{-R'}COO^-)_2]^{2+}$ core (**8**, **9**, **10**, and **15**, with d(Mn···Mn) = 4.54–4.75 Å).

Biomimetic compounds provide a unique way for testing the mechanism in Mn-catalase enzymes, understanding the limitations of using unequal structural complexes.[67] Moreover, the potential use as catalytic scavengers of H_2O_2 for preventing oxidative stress injuries has encouraged researchers to synthesize catalase biomimetic compounds. Indeed, a better understanding of the factors that guarantee the effectiveness of these H_2O_2 scavenger enzymes could also lead to the syntheses of much better catalysts.

In this chapter we present the catalase activity in acetonitrile-water media for the molecular compounds with *n*-R = 2-MeO (**1** and **2**), 4-MeO (**6**), and 4-*t*Bu (**7**) and in water solution just for **1** and **2**. The effect of the counter-anions, NO_3^- and ClO_4^-, on the catalase activity of these compounds has also been studied. The activities of those compounds having *n*-R = 3-MeO (**3**, **4**, and **7**) have not been profoundly studied and they are not presented in this manuscript.

Catalase activity versus $[H_2O_2]_0$

The catalytic activity toward H_2O_2 decomposition for compounds with R = 2-MeO (**1** and **2**), 4-MeO (**6**), and 4-*t*Bu (**7**) was tested by mixing a 0.8 mM acetonitrile solution of the corresponding compound and different amounts of a 32% aqueous solution of H_2O_2. The initial concentration of H_2O_2 in these experiments ranges from 0.38 to 1.20 M, giving $[H_2O_2]_0/[Mn_2]_0$ molar ratios in the range 490–1720. Note that the resulting reaction media consists of CH_3CN-H_2O mixtures where the H_2O content is lower than 10%. The evolution of oxygen was monitored versus time by a volumetric method and then converted to turnover number (TON), considering a two-steps reaction that comprises the oxidation and reduction of H_2O_2. Following this definition, a TON is equal to the evolution of a molecule of O_2 per mole of Mn^{III}_2, corresponding to the decomposition of two moles of H_2O_2.

In all these experiments, vigorous evolution of O_2 was observed after the addition of hydrogen peroxide. As shown in Table 41, the compounds are able to decompose significant amounts of H_2O_2 (TON ≈ 430–520 in 10 min), which evidences their catalytic activity. During the first minute the TONs follow an almost linear tendency over time; for time > 1 min, the reaction slows until reaching a plateau at ~10 min (Figure 127). The activity of such compounds is of the same magnitude as some other analogues reported in the literature.[192,194]

Table 41. Summary of catalytic results for compound **1**, **2**, **6**, and **7** and for the control experiments performed with $Mn(NO_3)_2$, $Mn(ClO_4)_2$, and MnO_2, with $[H_2O_2]_0$ = 1.05 M and $[Mn^{III}_2]$ = 0.8 mM in CH_3CN-H_2O 9-1 (v/v).

	At 1 min		At 2 min		At 10 min	
Compound	**TON**[a]	**% H_2O_2**[b]	**TON**[a]	**% H_2O_2**[b]	**TON**[a]	**% H_2O_2**[b]
1 (2-MeO/NO_3)	227	31	334	46	515	70
2 (2-MeO/ClO_4)	182	25	257	35	437	60
6 (4-MeO/ClO_4)	125	17	194	26	377	51
7 (4-*t*Bu/ClO_4)	151	20	245	33	436	59
$Mn(NO_3)_2$	1	>1	3	>1	10	1.4
$Mn(ClO_4)_2$	6	>1	6	>1	10	1.4
MnO_2	~10	~1.4	~13	~1.8	~32	~4.4

[a] TON = mmols O_2 / mmols Mn^{III}_2; [b] % H_2O_2 decomposed.

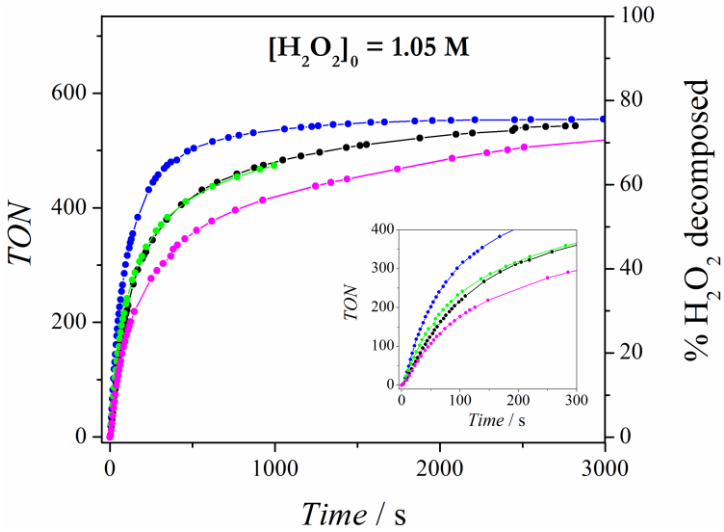

Figure 127. Catalase activity of 0.8 mM solutions of compounds **1** (blue), **2** (green), **6** (pink), and **7** (black) in acetonitrile-water 9-1 (v/v) for $[H_2O_2]_0$ = 1.05 M.

The catalytic activity of $Mn(NO_3)_2$, $Mn(ClO_4)_2$, and MnO_2 towards H_2O_2 disproportionation was also investigated under the same conditions as those used for the dinuclear compounds. In all cases, the activity is at least one order of magnitude smaller than those displayed by the dinuclear compounds (Figure S39 and Table 41).

The catalytic activity of these compounds (**1**, **2**, **6**, and **7**) show a great dependence on the initial concentration of H_2O_2 ($[H_2O_2]_0$). Figure 128 shows, as an example, the turnover number (TON) and the H_2O_2 decomposition versus time for compound **7** and different values of $[H_2O_2]_0$. The higher $[H_2O_2]_0$ is, the faster the plateau is reached, indicating that there is a considerable difference in the initial rate as a function of the concentration of H_2O_2. Moreover, all curves approach the 80% of H_2O_2 decomposition as time passes. This behavior was also observed for compounds **1**, **2**, and **6**.

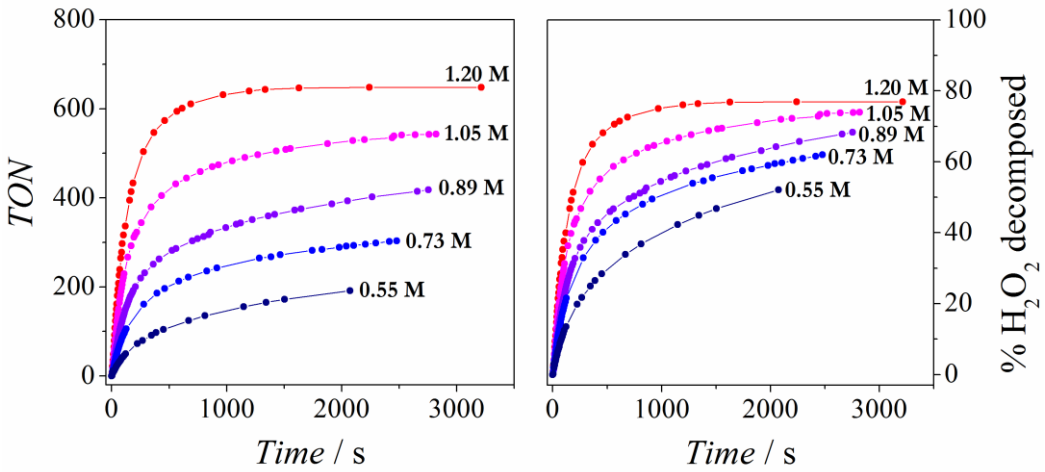

Figure 128. Turnover number (TON) and H_2O_2 decomposition of a 0.8 mM solution of compound **7** in acetonitrile-water for different values of $[H_2O_2]_0$, as specified.

In order to quantify the catalase activity of these compounds, **1**, **2**, **6**, and **7**, the initial rate (r_i) of the reaction was calculated from the slope of the TON versus time plot before reaching a 10% of H_2O_2 decomposition. Note that r_i has to be calculated from the stationary state, where the reaction rate is constant. In some cases, there was an induction period before reaching the stationary state; these points do not have to be considered for the calculation of r_i. In Table 42 are listed the results from this data treatment, according to the following equation:

$$r_i/[\mathrm{Mn_2}] = \frac{n_{\text{decomposed } \mathrm{H_2O_2}}}{\text{time (s)} \cdot n_{\mathrm{Mn_2}}} = k_{cat}[\mathrm{H_2O_2}]_0{}^{n} \qquad \text{Eq. 16}$$

where k_{cat} is the reaction rate constant and n is the order of reaction.

Table 42. List of kinetic parameters for compounds **1**, **2**, **6**, and **7** in acetonitrile-water media.

Compound	$r_i/[Mn_2]$ * / s^{-1}						n	k_{cat}* / M^{-2} s^{-1}
	a	**b**	**c**	**d**	**e**	**f**		
1 (2-MeO/NO_3)	1.82	3.11	5.19	7.07	10.57	-	2	9.49 ± 0.24
2 (2-MeO/ClO_4)	-	2.15	3.58	5.34	7.12	9.11	2	6.46 ± 0.09
6 (4-MeO/ClO_4)	-	1.10	2.19	3.51	4.83	6.37	2	4.37 ± 0.07
7 (4-^{t}Bu/ClO_4)	-	1.43	2.87	4.85	6.46	8.40	2	5.82 ± 0.11

* Definition according to Eq. 16: r_i = reaction initial rate, $[Mn_2]$ = concentration of molecular compound (0.8 mM), k_{cat} = reaction rate constant; r_i calculated for different initial H_2O_2 concentrations: (**a**) 0.38, (**b**) 0.55, (**c**) 0.73, (**d**) 0.89, (**e**) 1.05, and (**f**) 1.20 M.

As may be observed in Figure 129, compounds herein presented follow a second order kinetics (n = 2) in respect to H_2O_2 concentration, since r_i versus $[H_2O_2]^2$ follows a linear tendency. The reaction rate constant (k_{cat}) values follow the tendency **1** (2-MeO/NO_3) > **2** (2-MeO/ClO_4) ≈ **7** (4-^{t}Bu/ClO_4) > **6** (4-MeO/ClO_4). These values are in the range 4.37–9.49 M^{-2} s^{-1} and are generally than those reported for analogous compounds with R = Cl,[194] which range from 2.77 to 4.78 M^{-2} s^{-1}.

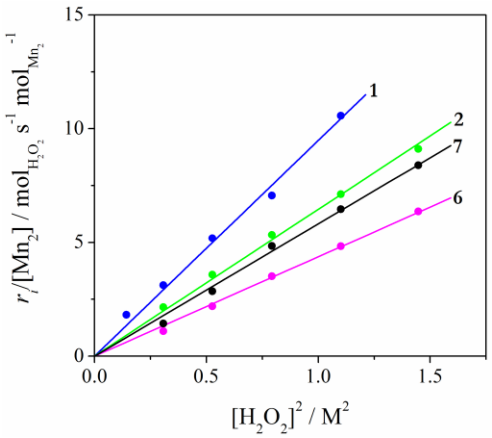

Figure 129. Dependence of the initial rate (r_i) for the H_2O_2 disproportionation as a function of the squared concentration of H_2O_2 ($[H_2O_2]^2$) for compounds **1**, **2**, **6**, and **7** in CH_3CN-H_2O media.

A reason for the lower activity of compounds with R = Cl could lie in the higher electron-withdrawing character of the chloride groups, as was previously reported for a series of analogous compounds.[192] The Hammett constant ($\sigma = pK_H - pK_{n\text{-}R}$) relates the acidity of the benzoic acid derivatives to the electronic character of the R group;[197,198] the bigger σ is, the greater electron-withdrawing character of the R group. In this case, the Hammett constants (σ) follow the trends 2-Cl (+1.26) > 2-MeO (+0.12) and 4-Cl (+0.21) > 4-MeO (–0.27) ≈ 4-^{t}Bu (–0.20), attesting for the higher electron-withdrawing character of the Cl group and explaining the lower activity of those compounds.

The k_{cat} only considers the activity in the first seconds of reaction; however, it would be interesting to compare the activity at short and long term. Hence, a comparison of the TONs performed by different catalysts at 1 and at 10 min was performed. Table 43 summarizes the catalytic results for the compounds presented here and those in the literature having different R groups (R = Me or Cl). At 1 min, the TONs follow the tendency: **1** (2-MeO/NO_3) > **2** (2-MeO/ClO_4) > **X** (4-Cl/NO_3) > **Y** (4-Cl/ClO_4) > **7** (4-^{t}Bu/ClO_4) > **I** (2-Cl/NO_3) > **W** (4-MeO/NO_3) > **6** (4-^{t}Bu/ClO_4) ≈ **B** (2-Cl/ClO_4) > **V** (4-^{t}Bu/NO_3) > **T** (4-Me/NO_3) > **U** (4-Me/ClO_4). At 10 min, this tendency is slightly altered, being: **I** (2-Cl/NO_3) > **B** (2-Cl/ClO_4) > **X** (4-Cl/NO_3) > **Y** (4-Cl/ClO_4) > **1** (2-MeO/NO_3) > **2** (2-MeO/ClO_4) ≈ **W** (4-MeO/NO_3) ≈ **7** (4-^{t}Bu/ClO_4) > **V** (4-^{t}Bu/NO_3) > **6** (4-^{t}Bu/ClO_4) ≈ **T** (4-Me/NO_3) > **U** (4-Me/ClO_4). As observed, while compound **1** is the best catalyst during the first minutes of reaction, compound **I** becomes the best catalyst after 10 min from the addition the substrate (H_2O_2). On the other hand, the Hammett parameters (σ) follow the trend: 4-MeO < 4-^{t}Bu < 4-Me < 2-MeO < 4-Cl < 2-Cl. These differences in the tendencies indicate that the electronic factors of the R group, even though they have an importance for the catalase activity,[192] are insufficient to dictate which would be the best catalyst. Moreover, the position of the R group in the aromatic ring (*ortho* or *para*) may have a great influence in the coordination of hydrogen peroxide. For instance, the presence of an efficient hydrogen-bonding network could result in an increase of the catalase activity.

It is worth noting that most of the compounds having X = NO_3 display higher activities at both 1 and 10 min than the analogues with X = ClO_4, excepting those with *n*-R = 4-^{t}Bu. As observed, for *n*-R = 4-^{t}Bu the NO_3^- compound show lower TONs than the ClO_4^- one. A deeper discussion concerning the effect of the counter-anions on the catalase activity for the compounds with *n*-R = 2-MeO and 4-^{t}Bu will be found below.

Table 43. Turnover number (TON) and reaction rate constant (k_{cat}) for [{Mn(bpy)(L)}$_2$(μ-O)(μ-*n*-$RC_6H_4COO)_2$]X_2 compounds towards the H_2O_2 disproportionation, with [Mn_2] = 0.8 mM and $[H_2O_2]_0$ = 1.05 M.

Label	*n*-R/X	TON		k_{cat}[a] / M^{-2} s^{-1}	σ[b]
		t = 1 min	*t* = 10 min		
T[192]	4-Me/NO_3	81	370	-	–0.16
U[c]	4-Me/ClO_4	30	250	-	–0.16
V[192]	4-*t*Bu/NO_3	113	409	-	–0.20
7	**4-*t*Bu/ClO_4**	**151**	**436**	**5.82**	**–0.20**
W[192]	4-MeO/NO_3	135	437	-	–0.27
6	**4-MeO/ClO_4**	**125**	**377**	**4.37**	**–0.27**
X[194]	4-Cl/NO_3	172	594	4.56	+0.21
Y[194]	4-Cl/ClO_4	160	574	4.78	+0.21
1	**2-MeO/NO_3**	**227**	**515**	**9.49**	**+0.12**
2	**2-MeO/ClO_4**	**182**	**437**	**6.46**	**+0.12**
I[194]	2-Cl/NO_3	141	620	4.01	+1.26
B[194]	2-Cl/ClO_4	123	594	4.15	+1.26

[a] Definition according to Eq. 16, [b] Hammett parameter, [c] private communications.

The catalase activities of other Mn_2 compounds in organic solvents have been reported.[67] Most of them consist of manganese ions bridged by one or two alkoxo/phenoxo groups from Schiff base ligands and follow Michaelis-Menten first order kinetics, with k_{cat} and K_M values being in the range 0.017–250 s^{-1} and 6–310 mM, respectively. Other Mn_2 compounds reported in the literature follow a second order kinetics, $r_i = k_{cat}[H_2O_2][\text{catalyst}]$, with k_{cat} values between 0.065 and 35 M^{-1} s^{-1}.[67] However, it is difficult to fairly compare the activity of the compounds in the literature with those reported here because the mechanism does not follow the same kinetic law. Anyhow, all biomimetic compounds disproportionate H_2O_2 with a much lower efficiency and selectivity than native Mn-catalases, which follow a Michaelis-Menten first order kinetics, with $k_{cat} = 6.2 \cdot 10^3$–$2.6 \cdot 10^5$ s^{-1} and K_M = 1.6–350 mM in water solution.[65,75]

Post-catalysis products

The acetonitrile solutions of compounds **1**, **2**, **6**, and **7** generally keep their brown color during the first seconds after the addition of H_2O_2, typical of Mn^{III} compounds. However, as time passes, the solution becomes colorless and a dark powder precipitates.

IR spectra of the dark powder does not correspond to any of the compounds, but it displays several bands in the 1600–1500 and 700–500 cm^{-1} ranges, indicating that such a powder may correspond to some manganese species with oxo bridges and that the carboxylate and

bipyridine ligands may be present. However, the spectra are of very bad quality and no precise information could be extracted.

The colorless solutions were left undisturbed at room temperature, and solid samples of Mn^{II} compounds were obtained after several days. The IR spectra of these Mn^{II} samples were recorded and compared with those displayed by the Mn^{II} compounds presented in Chapter 1.4. Figure 130 shows a diagram of the Mn^{II} compounds obtained after the reaction. This fact suggests that there is a reorganization around the Mn ions during and/or after the catalytic reaction, but it does not provide information about the structure of the catalytic species.

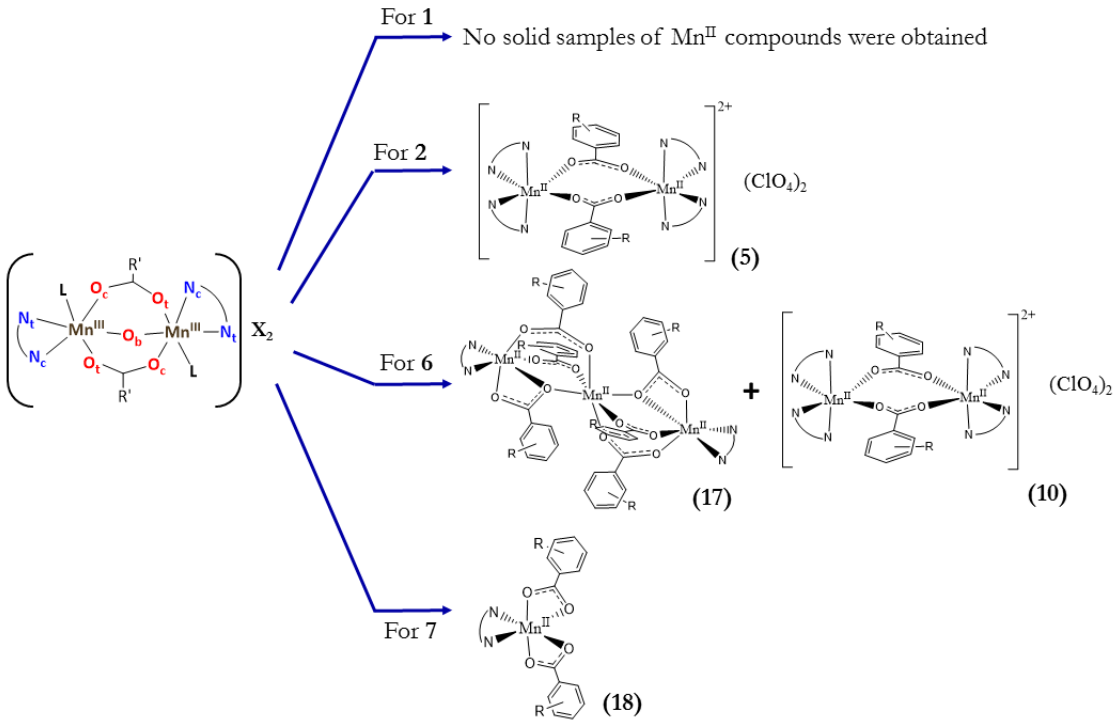

Figure 130. Diagram of the Mn^{II} compounds obtained from the acetonitrile solutions of compounds **1**, **2**, **6**, and **7** after several days from the addition of H_2O_2.

Effect of the counter-anions

As mentioned in the introduction, the active site of the native Mn-catalase is protected from the environment and isolated from the solvent. At the entrance of this cavity, several charged residues prevent halides and oxo-anions from going into the active site, since they may be inhibitors.[63] Our models of the Mn-catalase are ionic and their structure consists of a cationic complex with two counter-anions, perchlorate or nitrate. For this reason, we investigated the effect of the counter-anions on the catalase activity of our compounds.

According to single-crystal XRD (explained above), the crystal structures of compounds **1** and **2** is a 1:1 electrolyte, whose cation is a mono-charged complex with formula $[\{Mn(bpy)(H_2O)\}(\mu\text{-}2\text{-}MeOC_6H_4COO)_2(\mu\text{-}O)\{Mn(bpy)(X)\}]^+$ with the monodentate positions occupied by water and a molecule of counter-anion (X). But these last positions are quite labile, so the substitution of the X ligands is expected in solution. The molar ionic conductivity (Λ_M) of an acetonitrile solution of compound **2** is 271 S cm^2 mol^{-1}, typical for a 2:1 electrolyte solution (220–300 S cm^2 mol^{-1}).[167] This value indicates that the perchlorate anions are completely dissociated from the manganese complex. On the other hand, the Λ_M of an acetonitrile solution of compound **1** (106 S cm^2 mol^{-1}) is much lower than for **2**, being close to the 1:1 electrolyte range (120–160 S cm^2 mol^{-1}).[167] This is consistent with one of the nitrate ions interacting with the manganese coordination sphere. Nevertheless, the addition of a small amount of water to the solution of compound **1** (CH_3CN-H_2O 9-1 (v/v)) makes the Λ_M increase to 189 S cm^2 mol^{-1}, a higher value but still much below the characteristic range for a 2:1 electrolyte solution. These facts prove that the nitrate anion tends to interact more than the perchlorate with the Mn complex and, even though the presence of water may weak this interaction, nitrate anions seem to remain in contact with the complex, either via hydrogen bonds or by a genuine Mn···ONO_2 interaction.

In spite of displaying very similar structures, compound **1** (2-MeO/NO_3) is a better catalyst than **2** (2-MeO/ClO_4), so the cause of this difference may only lie in their X group. This fact was also reported previously by G. Fernández *et al.* for analogous compounds with acetate or chloroacetate bridges, where the ones with X = NO_3 are also better catalysts than the ones with X = ClO_4 even though they have the same cationic complex (L = H_2O/H_2O, L being the labile monodentate ligand in the complex).[317]

To sum up, when **1** is in solution, nitrate ion is likely interacting with the Mn complex in acetonitrile solution and this interaction is weakened with the presence of water. Thus, in spite of the nitrate anion being retained by the Mn complex, this could be effortlessly displaced in presence of another group.

In order to acquire a further knowledge about the effect of these counter-anions, NO_3^- and ClO_4^-, the H_2O_2 decomposition for compounds **1**, **2**, **7** and that reported in the literature with *n*-R = 4-*t*Bu and X = NO_3 (**V**)[192] was tested in the presence of different amounts of sodium perchlorate (0.36 and 10^3 mM) and sodium nitrate (1.8 and 94 mM). Figure 131 and Table S25 summarize the most relevant results obtained from these experiments. Note that

the addition of $NaClO_4$ in the reaction media did not significantly provoke any variation in the catalytic activity and are not included in the table.

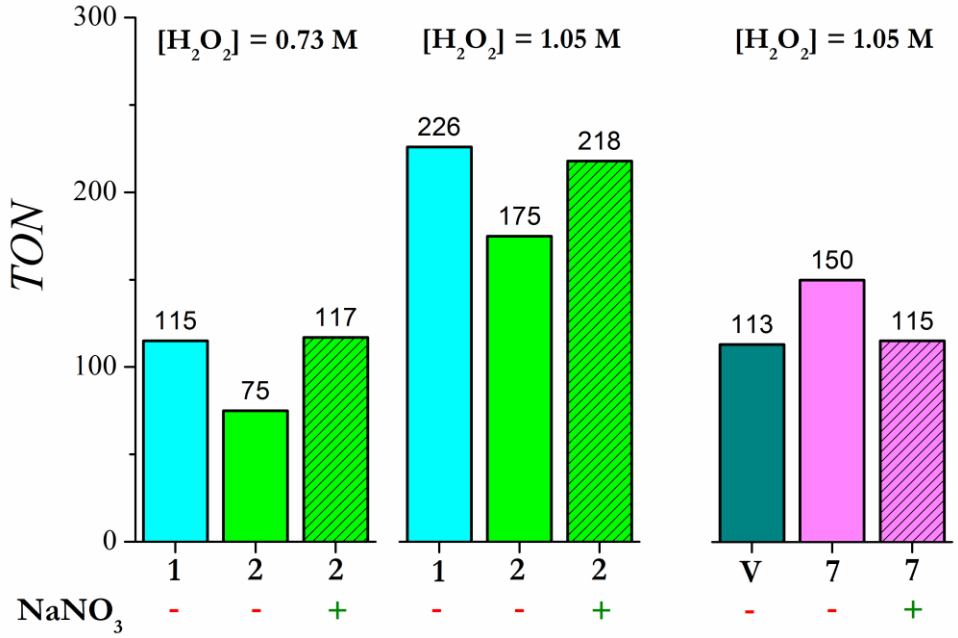

Figure 131. Turnover number (TON) at 1 min after the addition of H_2O_2 over 0.8 mM acetonitrile solutions of compounds **1** (2-MeO/NO_3) (blue) and **2** (2-MeO/ClO_4) (green), **V** (4-^{t}Bu/NO_3)[192] (dark cyan), and **7** (4-^{t}Bu/ClO_4) (purple), and over solutions of compounds **2** or **7** (0.8 mM) with $NaNO_3$ (1.8–8 mM) (patterned).

The addition of $NaNO_3$ showed some peculiarities: (*a*) the catalytic activity of **1** and **V** (X = NO_3) is unaffected by the addition of extra nitrate anion in the media, and (*b*) compounds **2** and **7** (X = ClO_4) in the presence of $NaNO_3$ display the same catalase activity as their nitrate analogue. Hence, while compound **2** becomes a better catalyst, compound **7** losses activity in presence of $NaNO_3$. Nevertheless, this effect is independent of the $NaNO_3$ concentration, as long as this concentration is higher than the stoichiometric amount (two equivalents of NO_3^- per Mn^{III}_2 unit).

These results prove that for the compounds presented here these anions, perchlorate and nitrate, are not inhibitors and do not block the position where H_2O_2 will be coordinated. However, they affect the catalytic properties of the compounds. Between them, the effect of the NO_3^- is predominant due to its higher predisposition to interact with the Mn complex, as illustratively shown in Figure 132. However, this interaction may be favorable (for *n*-R = 2-MeO) or unfavorable (for *n*-R = 4-^{t}Bu) for the catalytic performance. The favorable interaction for the 2-MeO substituent could be due to hydrogen-bonding networks between the nitrate ion, the hydrogen peroxide, and the R group in *ortho* position.

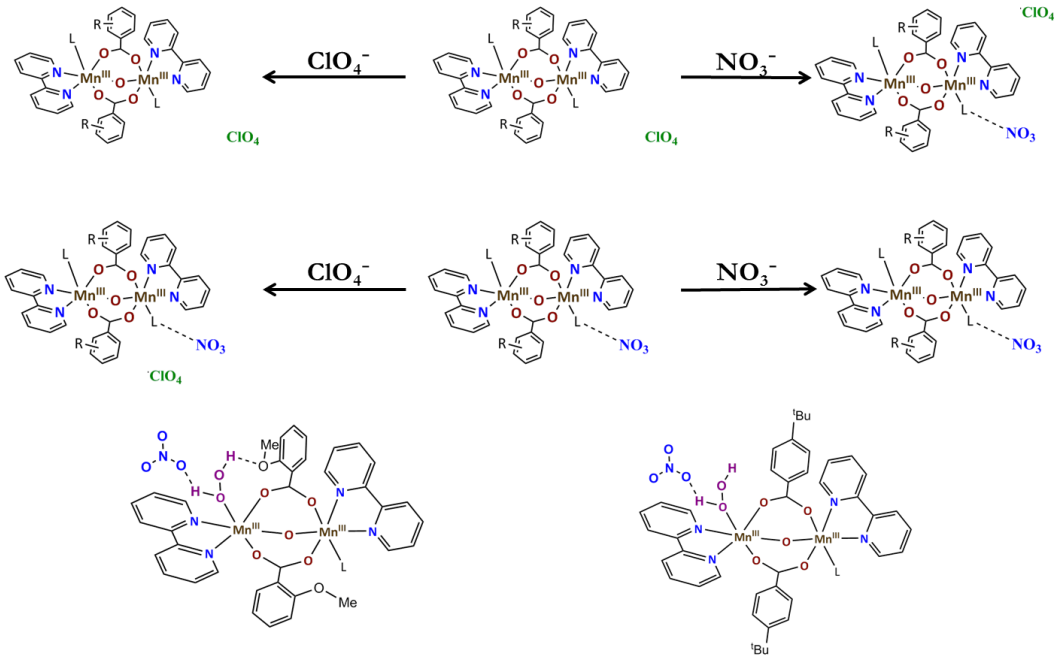

Figure 132. Schematics representing the predominant interaction of NO_3^- ions and a proposition for the more favorable interaction for compounds with *n*-R = 2-MeO.

The catalase activity of the compounds with *n*-R = 4-MeO and X = NO_3 (**W**) was reported in the literature. Its results could be compared with those of compound **6** (4-MeO/ClO_4) and the same experiments reported were performed. However, the catalase activities of these compounds are too similar to draw any conclusion. Indeed, the TONs at 1 min after the addition of H_2O_2 are 125 (**6**) and 135 (**W**).

pH-effect on the catalase activity of compound 2

In the literature there are some antecedents of the pH-dependent catalase activity for different kinds of Mn complexes.[73,324] Hence, the catalase activity of **2** was evaluated at different pH values. The compound with R = 2-MeO and X = ClO_4 (**2**) was chosen because this counter-anion interacts less with the Mn complex in acetonitrile solution than NO_3^- anion (as explained above), so its presence is likely more innocent.

Compound **2** yields a pH = 6.0 in CH_3CN-H_2O 9-1 (v/v). Hence, triethylamine was used to increase the basicity of the reaction media, with $[Et_3N]/[Mn^{III}_2]$ ratios between 0 and ~24. Figure 133 shows the TON versus time at different pH values, and the catalytic results of this experiment are summarized in Table S26. Note that the more basic the reaction media

is, the more efficient the catalyst is. Conversion close to 100% can only be reached at extremely basic pH values (pH > 12).

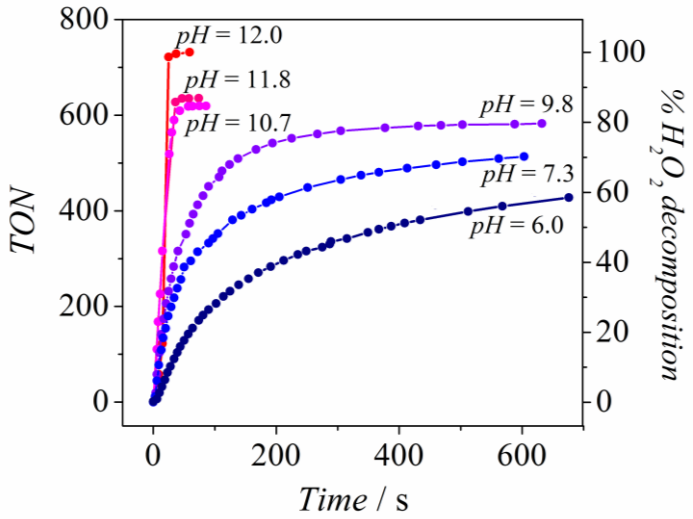

Figure 133. Catalase activity of 0.8 mM solutions of compound **2** in acetonitrile-water 9-1 (v/v) at different pH values, with $[H_2O_2]_0 = 1.05$ M.

Catalase activity in water solution of compounds 1 and 2

In contrast to the activity in acetonitrile (see above), compounds **1** and **2** are not good catalysts in water solution, hardly decomposing around 5% of the $[H_2O_2]_0$ in 10 min (Table 44 and Figure 134). This was predictable since Mn_2 compounds have low stability in aqueous media.[67]

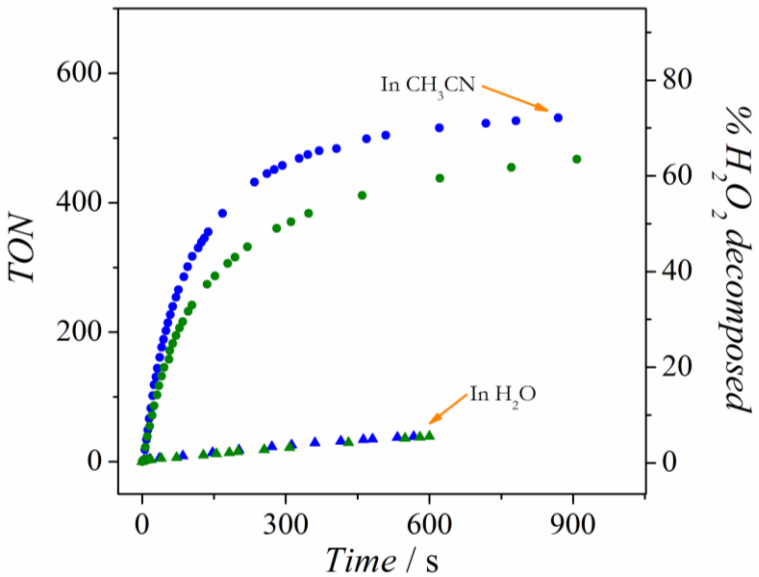

Figure 134. Turnover number (TON) versus time for **1** (blue), **2** (green) (0.8 mM based on $[Mn^{III}_2]$) in acetonitrile (circles) and in water (triangles), with $[H_2O_2]_0 = 1.05$ M.

Table 44. Summary of catalytic results for compound **1** and **2** with $[H_2O_2]_0$ = 1.05 M and $[Mn^{III}_2]$ = 0.8 mM in water.

Sample	At 1 min		At 2 min		At 10 min	
	TON[a]	% H_2O_2[b]	TON[a]	% H_2O_2[b]	TON[a]	% H_2O_2[b]
1	7	1	12	2	39	5
2	6	1	10	1	39	5

[a] TON = mmols O_2 / mmols Mn^{III}_2; [b] % H_2O_2 decomposed.

Summary

The catalytic activity toward H_2O_2 decomposition for compounds **1**, **2**, **6**, and **7** was tested, proving that they are not only structural but also functional models of the Mn-catalase. These compounds are able to catalyze the H_2O_2 decomposition in CH_3CN-H_2O 9-1 (v/v) solution, decomposing up to 1030 times the stoichiometric amount of H_2O_2.

Compounds **1**, **2**, **6**, and **7** show a second order kinetics with respect to H_2O_2 concentration. They are generally much better catalysts than those compounds with R = Cl, reported in the literature.[194] This fact is related to the higher electron-donating character of methoxy and *tert*-butyl groups than that of chloride. Compound **1** (2-MeO/NO_3) is the most efficient in this family of compounds.

After several days from the addition of H_2O_2, Mn^{II} compounds were obtained, suggesting that there is a reorganization around the Mn ions during or after the catalysis, though not providing information about the structure of the catalytic active species.

In acetonitrile solution, nitrate ions tend to interact more with the Mn complex than perchlorate ions. However, the interaction between nitrate ion and Mn complex may be favorable or unfavorable for the catalytic performance. For instance, while this interaction is favorable for the compounds with *n*-R = 2-MeO, **1** and **2**, it disturbs the catalytic activity for those with *n*-*t*Bu, **7** and **V**.

The effect of the pH on the catalase activity was studied for compound **2**, showing that the more basic the pH is, the better catalase activity.

Finally, compounds **1** and **2** display no activity in water solution, probably due to the low stability of Mn_2 complexes in aqueous media.

3.4. Catalase Activity of Mn-SiO_2 Hybrid Materials

First insights

In the previous chapter we presented the catalase activity (decomposition of H_2O_2 into H_2O and O_2) of biomimetic Mn^{III}_2 compounds of the active site of native Mn-catalases. As may be observed, these compounds are not active in water solution in spite of their efficiency in acetonitrile solution, probably due to the low stability of the dinuclear unit in aqueous media.

The synthesis of dinuclear compounds that are functional models of the active site of Mn-catalase has been a huge field of research for inorganic chemists.[67] However, a dinuclear compound is just a naive approximation of the entire native catalases. It is worth remembering that metalloproteins, such as Mn-catalases, are supramolecular structures whose active site consists of one or more metallic ions in a very precise environment. This morphology gives place to enzymatic cavities with the required hydrophobicity and size that guarantees their effectiveness.[10,65]

The insertion of the already mentioned compounds in mesoporous silica (MCM-41 type) offers the possibility of mimicking different properties of the catalytic site, such as hydrophobicity and confinement, which could increase the stability of the catalyst in aqueous media.[290] Within this frame, we present here the catalase activity of Mn-SiO_2 materials based on dinuclear Mn^{III} compounds inserted into mesoporous silica (MCM-41 type). For the syntheses of these hybrid materials, we chose compounds **1** and **2**, with formula $[\{Mn^{III}(bpy)(H_2O)\}(\mu\text{-}2\text{-}MeOC_6H_4COO)_2(\mu\text{-}O)\{Mn^{III}(bpy)(X)\}]X$ (where X = NO_3 or ClO_4, respectively), because they present the highest activity in this family of compounds. Firstly, we studied the catalase activity and the stability of non-functionalized hybrid materials, $[Mn_2O]_x$@SiO_2, in order to acquire a good knowledge of the reactivity of these new materials. Secondly, we studied the activity of pyridyl-modified Mn-SiO_2 materials, $[Mn_2O]_x$-Py@SiO_2, and we analyzed the effect of the concentration of Mn complex inside the solid on the catalytic activity. The syntheses of the materials can be found in Chapter 2.3. The catalase activity of these new hybrid materials is compared with that shown by **1** and **2** to eventually evidence the advantages of the latter over the former. The reactivity is run both in a mixture of acetonitrile-water and in pure water.

Catalase activity of material $[Mn_2O]_{0.5}@SiO_2$

Activity in CH_3CN-H_2O. The catalytic activity towards the H_2O_2 decomposition from an acetonitrile suspension of material $[Mn_2O]_{0.5}@SiO_2$ (0.8 mM based on $[Mn^{III}_2]$) was also tested under the same conditions as compounds **1** and **2** (Chapter 3.3) in order to lately be compared, using a H_2O_2 concentration of 1.05 M. Remember that 1 TON corresponds to the decomposition of two moles of H_2O_2 per mole of Mn^{III}_2. It is necessary to point out that material SiO_2-TMA did not provoke any evolution of oxygen, which excludes any catalytic activity of the support itself for H_2O_2 disproportionation.

Looking briefly at Figure 135, one can say that the TON versus time plot of material $[Mn_2O]_{0.5}@SiO_2$ has the same profile as its molecular analogues, firstly following a linear tendency and lately reaching a plateau. Table 45 summarizes the results obtained from the catalysis. As may be seen, the hybrid material exhibits a better catalase activity than compounds **1** and **2**. The suspension of the hybrid material shows a pH = 8.9 and their activity is in the middle of those displayed for compound **2** at pH = 7.3 and 9.8. This fact suggests that one of the effects for the major activity of the material in comparison to the molecular compounds is the basic media provided by the silanolate groups of the support that are holding the TMA^+ ions – the pK_a of which is about 9.[299,300]

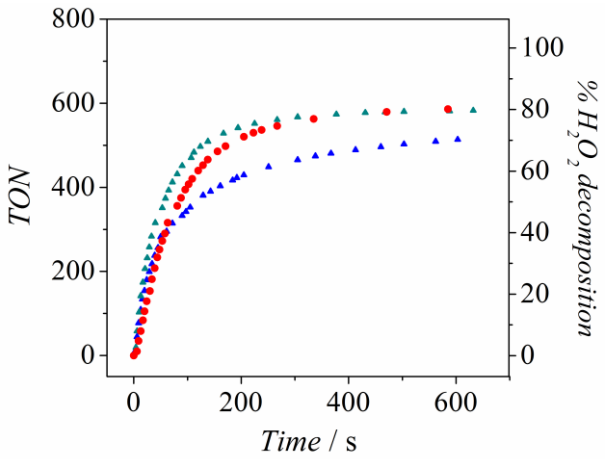

Figure 135. Catalase activity of material $[Mn_2O]_{0.5}@SiO_2$ (0.8 mM based on $[Mn^{III}_2]$) (red) and for compound **2** at pH = 7.3 (blue) and 9.8 (dark cyan) in acetonitrile-water 9-1 (v/v), with $[H_2O_2]_0$ = 1.05 M.

A similar pH-dependence was already reported in the literature for a mutated Mn-catalase[68] and for some Mn^{III}_2 salen complexes,[73,74,324] in which the catalase activity was highly improved at high pH (~11) (that guarantees the integrity of the Mn_2 unit) or because of the presence of an acid-base catalytic auxiliary. In our case, the silanolate moieties in the hybrid material

likely act as an endogenous acid-base auxiliary that could contribute to retain the integrity of the Mn_2 core, improving its activity.

Table 45. Summary of catalytic results for compound **1** and **2** and material $[Mn_2O]_{0.5}$@SiO_2 with $[H_2O_2]_0$ = 1.05 M and $[Mn^{III}_2]$ = 0.8 mM in CH_3CN-H_2O 9-1 (v/v).

		At 1 min		At 2 min		At 10 min	
Sample	**pH**	**TON**[a]	**% H_2O_2**[b]	**TON**[a]	**% H_2O_2**[b]	**TON**[a]	**% H_2O_2**[b]
1	6.0	227	31	334	46	515	70
2	6.0	182	25	257	35	437	60
2	7.3	295	40	366	50	514	70
$[Mn_2O]_{0.5}$@SiO_2	**8.9**	**312**	**42**	**440**	**60**	**587**	**80**
2	9.8	374	51	496	67	582	79

[a] TON = mmols O_2 / mmols Mn^{III}_2; [b] % H_2O_2 decomposed.

Successive additions of H_2O_2 were done in order to test if the catalyst retains its activity. As shown in Figure 136, the catalyst keeps a high activity after several additions, reaching a plateau at almost the same TON after the second and third additions (green lines). In spite of that, the initial rate of H_2O_2 dismutation for the second and third additions is lower than for the first one (red lines), which could be caused by the decrease observed in the pH (from 8.9 to ~7.5).

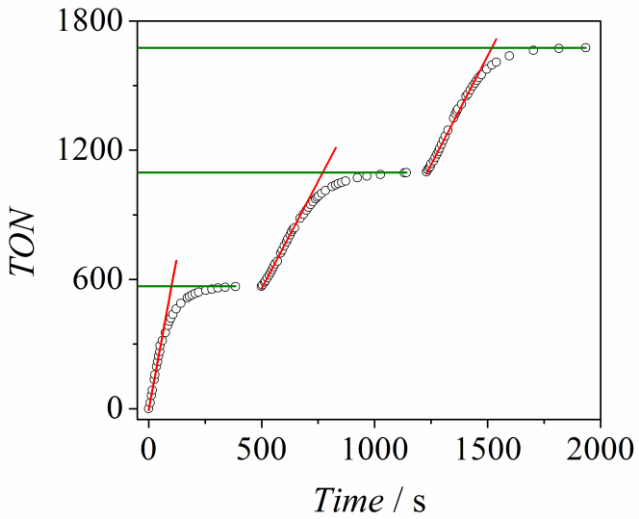

Figure 136. Turnover number versus time for three successive additions (at t = 0, 500 and 1230 s) of H_2O_2 (1312 eq.) to a suspension of material $[Mn_2O]_{0.5}$@SiO_2 (0.8 mM based on $[Mn^{III}_2]$) in CH_3CN-H_2O 9-1 (v/v). Red lines correspond to the initial rate for H_2O_2 dismutation and the green lines to the saturation TON after each addition.

Several EPR spectra were recorded for the solution – separating the solid – at different times, between 30 seconds and 2 hours after the addition of H_2O_2. Non-significant EPR signal was observed in none of them, indicating that the Mn^{2+} content in the solution is < 73 μM (limit

of detection), which corresponds to a 5% of the Mn in material $[Mn_2O]@SiO_2$. As the solution does not present the brown color expected for a Mn^{III} solution, one can conclude that practically all Mn content continues being inside the pores of the silica.

The isolated solid at 90 seconds after the addition of H_2O_2 was analyzed by XPS and EPR spectroscopy. The XPS displays a Mn 3s doublet splitting (ΔMn 3s) of 5.6–5.7 eV, indicating that the Mn oxidation state is mainly III (Table S24). Even though the majority of the Mn oxidation state is III, the EPR spectra (Figure 137) shows six bands in the region of $g \approx 2$ with a hyperfine coupling of ~9 mT. This pattern could be consistent with a dinuclear Mn^{II} complex with a weak magnetic coupling.[317] No evidence of mixed valence systems (Mn^{II}–Mn^{III} or Mn^{III}–Mn^{IV}) was observed. These facts suggest that the catalytic species involves Mn^{II} and Mn^{III} oxidation states and it mainly remains inside the pores. However, the XPS analysis of this sample shows a lower N/Mn_2 ratio than that of the former material $[Mn_2O]_{0.5}@SiO_2$. This could be indicative of a partial unfastening of the bpy ligand from the solid. As indicated, in the hybrid material some N atoms of the bpy ligand could interact with the silanolate groups of the wall, suggesting a weaker Mn–N bond. During the catalytic process, the strength of this bond could decrease, being the bpy ligand more labile. Therefore, the partial release of the bpy from the hybrid material could probably be due to the treatment of the sample (washing and drying) before the measurements. The TMA^+ ions of material $[Mn_2O]_{0.5}@SiO_2$ could be also easily released during the catalysis. However, their contribution is very unlikely to be noticed in XPS, since they just represent a 0.41% of the total weight.

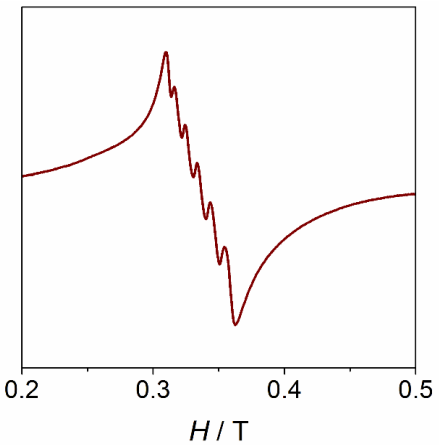

Figure 137. EPR spectra at 20 K of the isolated powder 90 seconds after the addition of H_2O_2 with material $[Mn_2O]_{0.5}@SiO_2$.

Activity in aqueous media. It is worth remembering that compounds **1** and **2** are not good catalysts in water solution, hardly decomposing around 5% of the $[H_2O_2]_0$ in 10 min (Table 46). However, the hybrid material shows catalase activity in aqueous media. As showed in Figure 138 and Table 46, material $[Mn_2O]_{0.5}$@SiO_2 is able to reach TON ≈ 400 in 5 min with linear tendency. Then, it approaches an asymptotic value of 514 at 10 min. Nevertheless, the activity of this material in water is lower than in acetonitrile, especially in the first minute.

Table 46. Summary of catalytic results for compound **1** and **2** and material $[Mn_2O]_{0.5}$@SiO_2 with $[H_2O_2]_0$ = 1.05 M and $[Mn^{III}_2]$ = 0.8 mM in water.

	At 1 min		At 2 min		At 10 min	
Sample	**TON**[a]	**% H_2O_2**[b]	**TON**[a]	**% H_2O_2**[b]	**TON**[a]	**% H_2O_2**[b]
$[Mn_2O]_{0.5}$@SiO_2	98	13	180	25	514	70
1	7	1	12	2	39	5
2	6	1	10	1	39	5

[a] TON = mmols O_2 / mmols Mn^{III}_2; [b] % H_2O_2 decomposed.

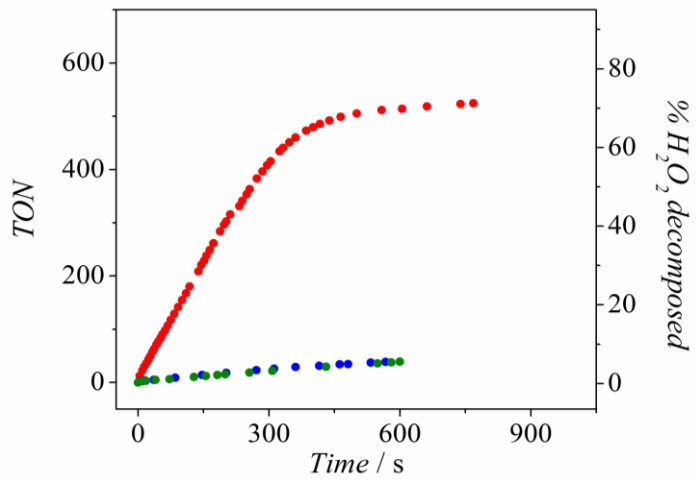

Figure 138. Turnover number (TON) versus time for **1** (blue), **2** (green) and $[Mn_2O]_{0.5}$@SiO_2 (0.8 mM based on $[Mn^{III}_2]$) (red) in water, with $[H_2O_2]_0$ = 1.05 M.

Stability of material $[Mn_2O]_{0.5}$@SiO_2

The morphology and characteristics of material $[Mn_2O]_{0.5}$@SiO_2 after the two-hours reaction with H_2O_2 in CH_3CN-H_2O 9-1 (v/v) ($[Mn_2O]_{0.5}$@$SiO_2^{\#A}$) and in water ($[Mn_2O]_{0.5}$@$SiO_2^{\#W}$) were analyzed. To test the stability in water, material $[Mn_2O]_{0.5}$@SiO_2 was stirred in water for 2 h ($[Mn_2O]_{0.5}$@$SiO_2^{\#M}$) and analyzed. The results of these tests are summarized in Table 47.

Material $[Mn_2O]_{0.5}$@$SiO_2^{\#A}$ preserves the mesostructure and porosity of the former material $[Mn_2O]_{0.5}$@SiO_2, as observed in the XRD pattern and the N_2 sorption isotherms (Figure

139). Nevertheless, the pore volume is higher than the one observed for $[Mn_2O]_{0.5}@SiO_2$ and the weight loss corresponding to the Mn complex ligands decreased, suggesting that the pores are less loaded. This fact is in agreement with the XPS analysis carried out for the isolated solid during the reaction (explained above).

Table 47. Summary of properties for material $[Mn_2O]_{0.50}@SiO_2$ and post-catalysis products.

Sample	Mesostructure	Porous volume / $cm^3 \cdot g^{-1}$	% Weight loss[a]
$[Mn_2O]_{0.5}@SiO_2$	Yes	0.36	21.9
$[Mn_2O]_{0.5}@SiO_2^{\#A}$	Yes	0.58	7.4
$[Mn_2O]_{0.5}@SiO_2^{\#W}$	No	-	-
$[Mn_2O]_{0.5}@SiO_2^{\#M}$	Yes	0.50	9.1

[a] Loss of the Mn complex ligands in the range 200–400 °C, according to TGA.

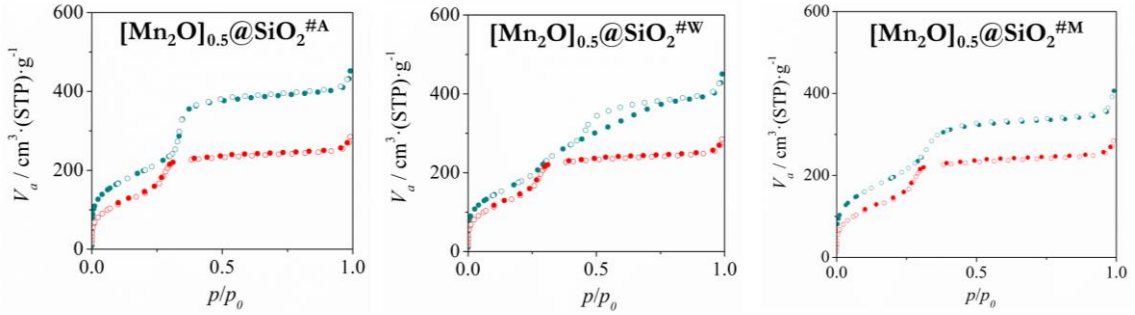

Figure 139. N_2 adsorption (full circles) and desorption (empty circles) isotherms at 77 K of materials $[Mn_2O]_{0.5}@SiO_2^{\#A}$, $[Mn_2O]_{0.5}@SiO_2^{\#W}$, $[Mn_2O]_{0.5}@SiO_2^{\#M}$ (dark cyan), and $[Mn_2O]_{0.5}@SiO_2$ (red).

Contrary to the previous one, material $[Mn_2O]_{0.5}@SiO_2^{\#W}$ displayed a poor XRD pattern and N_2 sorption isotherms without a clear capillary condensation (Figure 139), meaning that the mesostructure was disrupted after the reaction with H_2O_2.

To know whether this fact is due to the water or the H_2O_2, the stability of material $[Mn_2O]_{0.5}@SiO_2$ was also checked in water suspension. After 2 hours of treatment, the resulting solid ($[Mn_2O]_{0.5}@SiO_2^{\#M}$) displays the typical N_2 sorption isotherms of a mesostructured material (Figure 139). So, the support itself is not disrupted by the presence of water; but it has also a higher pore volume than its former material ($[Mn_2O]_{0.5}@SiO_2$).

To sum up, the presence of water is not responsible for the damage of the mesostructure of the support; this is only altered when both water and H_2O_2 are present. In addition, both the presence of water and the reaction with H_2O_2 likely favor the release of part of the bpy ligands. However, the loss of loading could occur during the process of isolation of the solid.

These facts could be attributed to the nudity of the silica inner surface. Even though the ultra-fast microwave assisted synthesis leads to highly ordered and chemically stable

mesoporous silica,[118] the pore surface is formed by Q^3 (mainly) and Q^2 silanol groups, which are sensitive to nucleophilic attacks and to strong oxidants. Therefore, modification of the silica internal surface could help to overcome these limitations. Hydrophobization and covering of the pore surface would hopefully limit the internal water diffusion and increase the stability of both the Mn complex and the structure of the nanochannels.

Catalase activity of material $[Mn_2O]_{0.1}@SiO_2$

The catalase activity of material $[Mn_2O]_{0.1}@SiO_2$ was tested under the same conditions as the latter one. Note that this material was synthesized using a $[Mn_2O]/TMA^+$ molar ratio of 0.1, contrary to 0.5 used for $[Mn_2O]_{0.1}@SiO_2$. Consequently, the Mn content in the current material is much lower, with $[Mn^{III}_2O]/Si$ molar ratio of 0.0084 for $[Mn_2O]_{0.1}@SiO_2$ and 0.033 for $[Mn_2O]_{0.5}@SiO_2$ according to the analyses presented in Chapter 2.3. We synthesized this material, which contains less Mn complex, in order to see the effect of the dispersion of active sites on the catalase activity and to guide forthcoming syntheses that provide better catalysts. In fact, the distance between active sites in the solid is dictated by the amount of incorporated complex, and that may be crucial for the catalytic activity.

Because of its different Mn loading, we were interested in testing its efficiency from two points of view, in terms of turnover number (TON) and of fraction of H_2O_2 decomposition. Hence, we performed the catalytic tests using three different amounts of material $[Mn_2O]_{0.1}@SiO_2$: (e_1) with the same weight of solid but lower concentration of active site than for material $[Mn_2O]_{0.5}@SiO_2$; (e_2) with nearly the same concentration of active site as for $[Mn_2O]_{0.5}@SiO_2$; and (e_3) with a higher concentration of active site. The results from these tests are shown in Table 48 and Figure 140 and are compared with those of material $[Mn_2O]_{0.5}@SiO_2$.

Table 48. List of conditions to perform the catalytic experiments in CH_3CN-H_2O 9-1 (v/v) for materials $[Mn_2O]_x@SiO_2$ with x = 0.1 or 0.5, using 5 mL of CH_3CN and $[H_2O_2]_0$ = 1.05 M.

Sample	$m_{material}$ / mg	$[Mn^{III}_2]$ / mM	At 1 min		At 2 min		At 10 min	
			TON[a]	% H_2O_2[b]	TON[a]	% H_2O_2[b]	TON[a]	% H_2O_2[b]
x = 0.1 (e_1)	11	0.23	110	4	289	11	950	37
x = 0.1 (e_2)	36	0.77	160	21	307	40	617	81
x = 0.1 (e_3)	55	1.18	168	33	290	58	416	82
x = 0.5	11	0.8	312	42	440	60	587	80

[a] TON = mmols O_2 / mmols Mn^{III}_2; [b] % H_2O_2 decomposed.

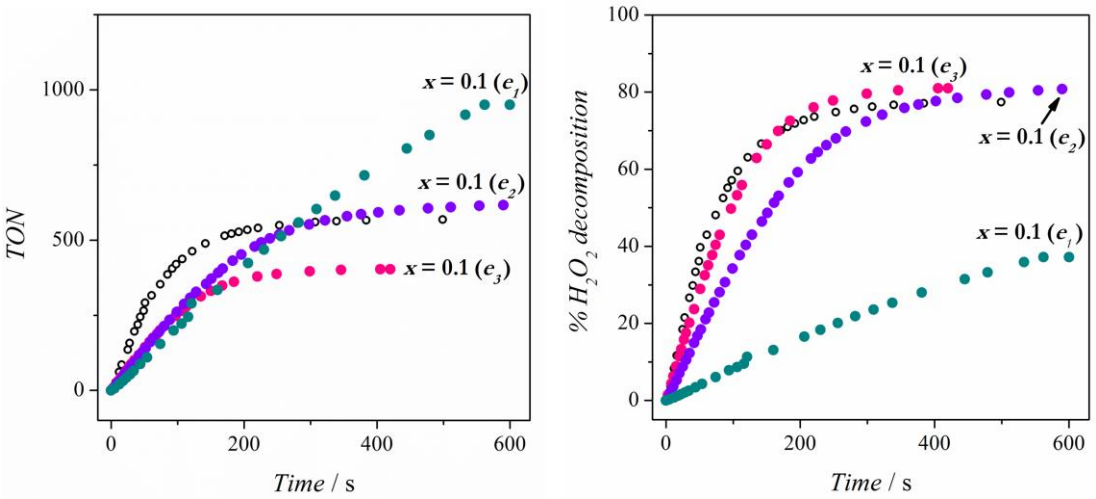

Figure 140. Catalase activity in CH_3CN-H_2O 9-1 (v/v) for materials $[Mn_2O]_x$@SiO_2 where x = 0.5 (open circles) or 0.1 (colored circles), with $[H_2O_2]_0$ = 1.05 M. For material $[Mn_2O]_{0.1}$@SiO_2 three different concentrations were used: 0.23 (e_1, dark cyan), 0.77 (e_2, purple), and 1.18 mM (e_3, pink) based on $[Mn^{III}_2]$. For $[Mn_2O]_{0.5}$@SiO_2, $[Mn^{III}_2]$ = 0.8 mM.

During the first two minutes of reaction, material $[Mn_2O]_{0.1}$@SiO_2 is less active than material $[Mn_2O]_{0.5}$@SiO_2, since both the TONs and the fraction of H_2O_2 decomposition are smaller. It is also important to remark that, even when similar Mn_2 concentrations are used (e_2, 0.77 mM), the material carrying more Mn complex per gram of solid (x = 0.5) displays a higher activity. Nonetheless, at the lowest concentration (e_3, 0.23 mM), material $[Mn_2O]_{0.1}$@SiO_2 reaches a TON of 950 at t = 10 min, proving that the catalyst is able to decompose high amounts of H_2O_2 (up to 1900 equivalents).

Before analyzing these results, it is worth remembering the differences between materials $[Mn_2O]_{0.5}$@SiO_2 and $[Mn_2O]_{0.1}$@SiO_2. For instance, material $[Mn_2O]_{0.1}$@SiO_2 was synthesized with a lower amount of Mn compound. As the compounds replace the TMA^+ ions of the support, the amount of TMA^+-silanolate pairs is higher than in the first material. Consequently, material $[Mn_2O]_{0.1}$@SiO_2 displays a pH of ~11 in CH_3CN-H_2O 9-1 (v/v), much higher than that yielded by $[Mn_2O]_{0.5}$@SiO_2 (pH = 8.9). According to the results shown in Figure 133 (Chapter 3.3), which show the pH-dependence of the catalase activity for compound **2**, we expected that $[Mn_2O]_{0.1}$@SiO_2 displayed a higher activity than $[Mn_2O]_{0.5}$@SiO_2, since the more basic pH is, the higher activity. However, the results were unfortunately surprising, since $[Mn_2O]_{0.1}$@SiO_2 is less active than $[Mn_2O]_{0.5}$@SiO_2. These results prove that the catalase activity of these materials is not only dependent on the concentration of active sites but also on its local distribution in the pores.

Catalase activity of pyridyl-modified hybrid materials

The catalase activity of the three hybrid materials containing 4-pyridylethyl functions and three different Mn complex loading, $[Mn_2O]_x$-Py@SiO_2 (x = 0.04, 0.12, and 0.21), was tested in CH_3CN-H_2O 9-1 (v/v). It is worth remembering that x refers to the Mn_2/TMA^+ molar ratio used in the syntheses and, thus, it is proportional to the Mn complex loading.

Material $[Mn_2O]_{0.21}$-Py@SiO_2. With this material two experiments were performed: (e_1) with the same concentration of active site as for $[Mn_2O]_{0.5}$@SiO_2; and (e_2) with a higher concentration of active site. The results of these tests are shown in Table 49 and Figure 141 and compared with those obtained for $[Mn_2O]_{0.5}$@SiO_2.

Table 49. List of conditions to perform the catalytic experiments in CH_3CN-H_2O 9-1 (v/v) for $[Mn_2O]_{0.50}$@SiO_2 and $[Mn_2O]_{0.21}$-Py@SiO_2, using 5 mL of CH_3CN and $[H_2O_2]_0$ = 1.05 M.

			At 1 min		At 2 min		At 10 min	
Sample	**$m_{material}$ / mg**	**$[Mn^{III}_2]$ / mM**	**TON[a]**	**% H_2O_2[b]**	**TON[a]**	**% H_2O_2[b]**	**TON[a]**	**% H_2O_2[b]**
$[Mn_2O]_{0.21}$-Py@SiO_2 (e_1)	20.0	0.82	251	35	496	68	617	87
$[Mn_2O]_{0.21}$-Py@SiO_2 (e_2)	30.5	1.25	130	29	253	53	368	78
$[Mn_2O]_{0.50}$@SiO_2	11	0.8	312	42	440	60	587	80

[a] TON = mmols O_2 / mmols Mn^{III}_2; [b] % H_2O_2 decomposed.

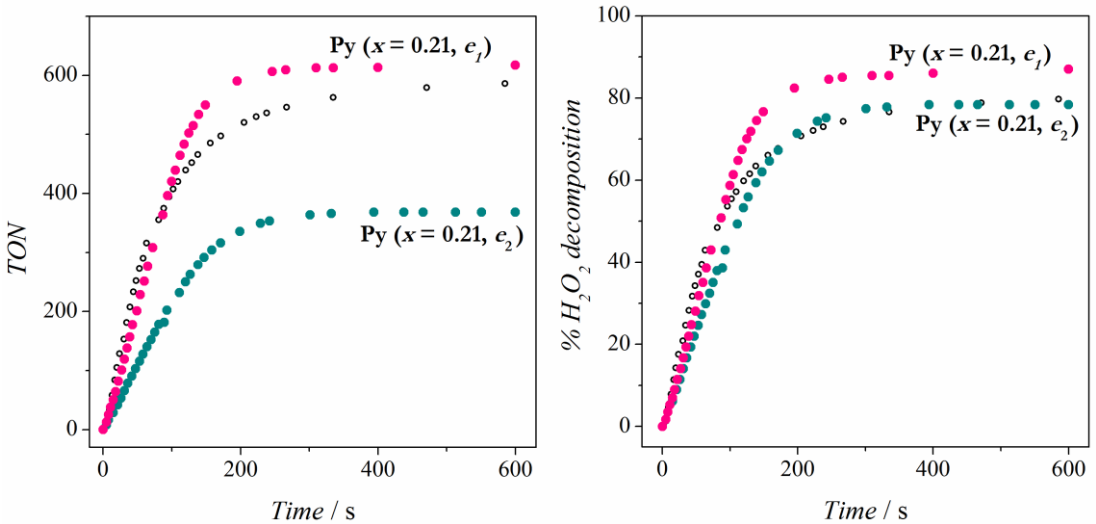

Figure 141. Catalase activity in CH_3CN-H_2O 9-1 (v/v) for materials $[Mn_2O]_{0.50}$@SiO_2 (open circles) and $[Mn_2O]_{0.21}$-Py@SiO_2 (colored lines), with $[H_2O_2]_0$ = 1.05 M. For material $[Mn_2O]_{0.21}$-Py@SiO_2 two different concentrations of Mn complex were used: 0.82 (e_1, pink) and 1.25 mM (e_2, dark cyan), based on $[Mn^{III}_2]$. For $[Mn_2O]_{0.5}$@SiO_2, $[Mn^{III}_2]$ = 0.8 mM.

Regarding the activity for different concentrations of Mn complex (e_1 and e_2), it is surprising that material $[Mn_2O]_{0.21}$-Py@SiO_2 is more active for the lowest concentration (0.82 mM, e_1). In terms of H_2O_2 decomposition, while the catalyst is able to reach a decomposition of 87% in 10 minutes (TON = 617) at the lowest concentration, it gets stuck at a decomposition of 78% (TON = 368) for $[Mn^{III}_2]$ = 1.25 mM (e_2).

The activity of this material for $[Mn^{III}_2]$ = 0.82 mM (e_1) is of the same magnitude as for $[Mn_2O]_{0.50}$@SiO_2 (with $[Mn^{III}_2]$ = 0.8 mM). However, the profile of the curves is different: for the pyridyl-modified material, the TONs are completely linear with time up to ~120 seconds. It also reaches saturation sooner, at ~180 seconds, and in a very abrupt way, approaching TON ≈ 620 and a H_2O_2 decomposition of 90%.

Material $[Mn_2O]_{0.21}$-Py@SiO_2 in experiment e_1 displays a very basic pH (~10.2) in acetonitrile-water media, significantly higher than that shown for material $[Mn_2O]_{0.50}$@SiO_2 (pH = 8.9). The higher value for the pyridyl functionalized material may be due to either its higher silanolate content or the presence of the Py functions in the solid. Figure 142 shows the activity of material $[Mn_2O]_{0.21}$-Py@SiO_2 (e_1) compared to those of compound **2** at basic pH. As observed, the activity of this material reaches a TON that is in the middle of the curves for **2** at pH = 9.8 (582) and 10.8 (~615). However, the profile of the curve is rather different, suggesting that the presence of the Py functions is not innocent. Even so, these results prove that the Py function has no negative effect on the catalase activity of these compounds.

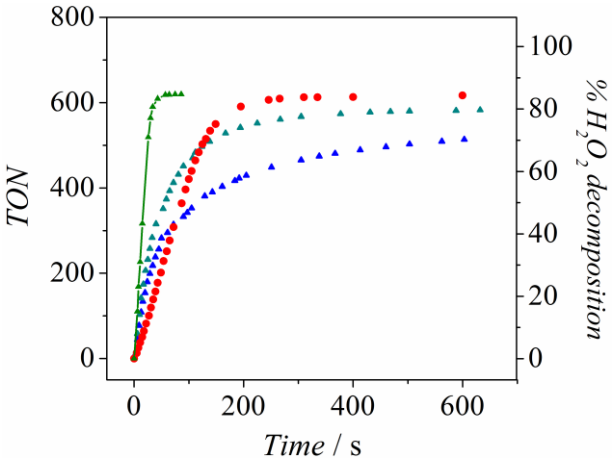

Figure 142. Catalase activity of material $[Mn_2O]_{0.21}$-Py@SiO_2 (0.82 mM based on $[Mn^{III}_2]$) (red) and for compound **2** at pH = 7.3 (blue), 9.8 (dark cyan), 10.8 (green) in acetonitrile-water 9-1 (v/v), with $[H_2O_2]_0$ = 1.05 M.

Material $[Mn_2O]_{0.12}$-Py@SiO_2. Analogously to the precedent case, two experiments were carried out for this material and the results were compared with those obtained for $[Mn_2O]_{0.21}$-Py@SiO_2 in experiment e_1, which loads more Mn complex. Two Mn complex

concentrations were used for these tests: (e_1) using the same weight of solid but lower concentration of active site than for material $[Mn_2O]_{0.21}$-Py@SiO_2; and (e_2) with almost the same concentration of active site as for $[Mn_2O]_{0.21}$-Py@SiO_2. These results are shown in Table 50 and Figure 143.

Table 50. List of conditions to perform the catalytic experiments in CH_3CN-H_2O 9-1 (v/v) for $[Mn_2O]_{0.21}$-Py@SiO_2 and $[Mn_2O]_{0.12}$-Py@SiO_2, using 5 mL of CH_3CN and $[H_2O_2]_0$ = 1.05 M.

			At 1 min		At 2 min		At 5 min	
Sample	**$m_{material}$ / mg**	**$[Mn^{III}_2]$ / mM**	**TON[a]**	**% H_2O_2[b]**	**TON[a]**	**% H_2O_2[b]**	**TON[a]**	**% H_2O_2[b]**
$[Mn_2O]_{0.12}$-Py@SiO_2 (e_1)	20.0	0.48	405	34	721	59	994	81
$[Mn_2O]_{0.12}$-Py@SiO_2 (e_2)	31.4	0.75	414	53	599	77	-	-
$[Mn_2O]_{0.21}$-Py@SiO_2 (e_1)	20	0.82	251	35	496	68	612	85

[a] TON = mmols O_2 / mmols Mn^{III}_2; [b] % H_2O_2 decomposed.

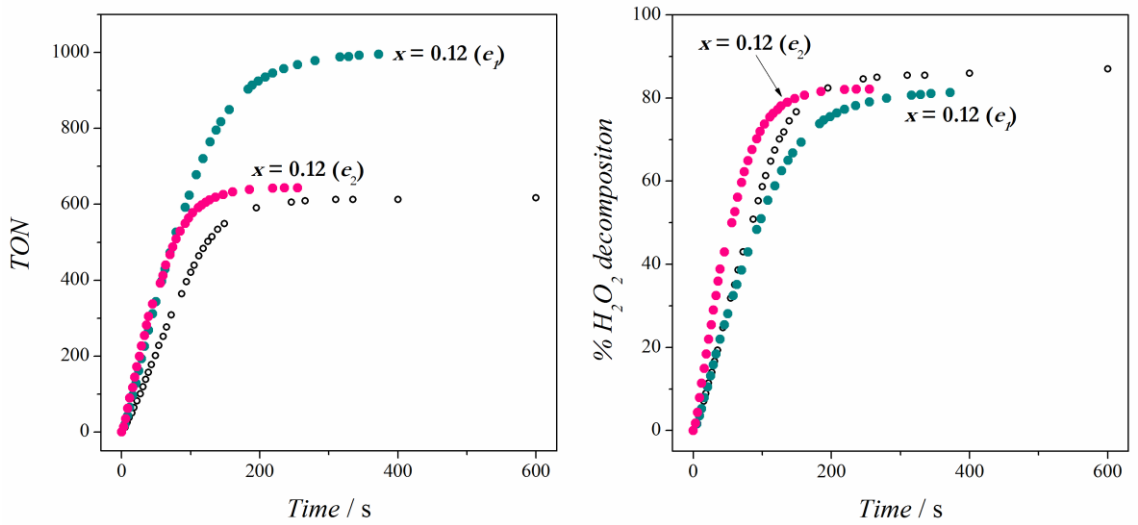

Figure 143. Catalase activity in CH_3CN-H_2O 9-1 (v/v) for materials $[Mn_2O]_{0.21}$-Py@SiO_2 (open circles) and $[Mn_2O]_{0.12}$-Py@SiO_2 (colored lines), with $[H_2O_2]_0$ = 1.05 M. For material $[Mn_2O]_{0.12}$-Py@SiO_2 two different concentrations were used: 0.48 (e_1, pink) and 0.75 mM (e_2, dark cyan), based on $[Mn^{III}_2]$. For $Mn_2O]_{0.21}$-Py@SiO_2, $[Mn^{III}_2]$ = 0.8 mM.

The slope in the first part of the TON versus time plot is related to the turnover frequency (TOF). For material $[Mn_2O]_{0.12}$-Py@SiO_2, the TOF is ~410 min^{-1} regardless of the concentration of active site in the reaction media (e_1 and e_2). This fact indicates that this material follows a first order kinetics in respect to the concentration of Mn complex. With the lower concentration of active site (Mn^{III}_2) (experiment e_1), the material nearly reaches a

TON of 1000. However, this material reaches saturation at ~80% of H_2O_2 decomposition for both concentrations of Mn complex (0.48 and 0.75 mM).

As may be observed, for a similar concentration of active site, the material with x = 0.12 (experiment e_2) is better catalyst than that with x = 0.21. The cause of this improvement could lie in the higher TMA-silanolate content of the current material that, consequently, yields a slightly higher pH of 10.8 than that observed for the material with x = 0.21 (pH = 10.2).

Material $[Mn_2O]_{0.04}$-Py@SiO_2. Two experiments were carried out with this material $[Mn_2O]_{0.04}$-Py@SiO_2, using Mn^{III}_2 concentrations of 0.16 (e_1) and 0.68 mM (e_2). The results of these tests are shown in Table 51 and Figure 144 and compared with those for $[Mn_2O]_{0.21}$-Py@SiO_2. In both concentrations material $[Mn_2O]_{0.04}$-Py@SiO_2 displays a very low activity.

Table 51 List of conditions to perform the catalytic experiments in CH_3CN-H_2O 9-1 (v/v) for $[Mn_2O]_{0.21}$-Py@SiO_2 and $[Mn_2O]_{0.04}$-Py@SiO_2, using 5 mL of CH_3CN and $[H_2O_2]_0$ = 1.05 M.

			At 1 min		At 2 min		At 10 min	
Sample	$m_{material}$ / mg	$[Mn^{III}_2]$ / mM	TON[a]	% H_2O_2[b]	TON[a]	% H_2O_2[b]	TON[a]	% H_2O_2[b]
$[Mn_2O]_{0.04}$-Py@SiO_2 (e_1)	20.4	0.16	16	<1	37	1	183	5
$[Mn_2O]_{0.04}$-Py@SiO_2 (e_2)	88	0.68	23	3	49	6	196	23
$[Mn_2O]_{0.21}$-Py@SiO_2 (e_1)	20	0.82	251	35	496	68	617	87

[a] TON = mmols O_2 / mmols Mn^{III}_2; [b] % H_2O_2 decomposed.

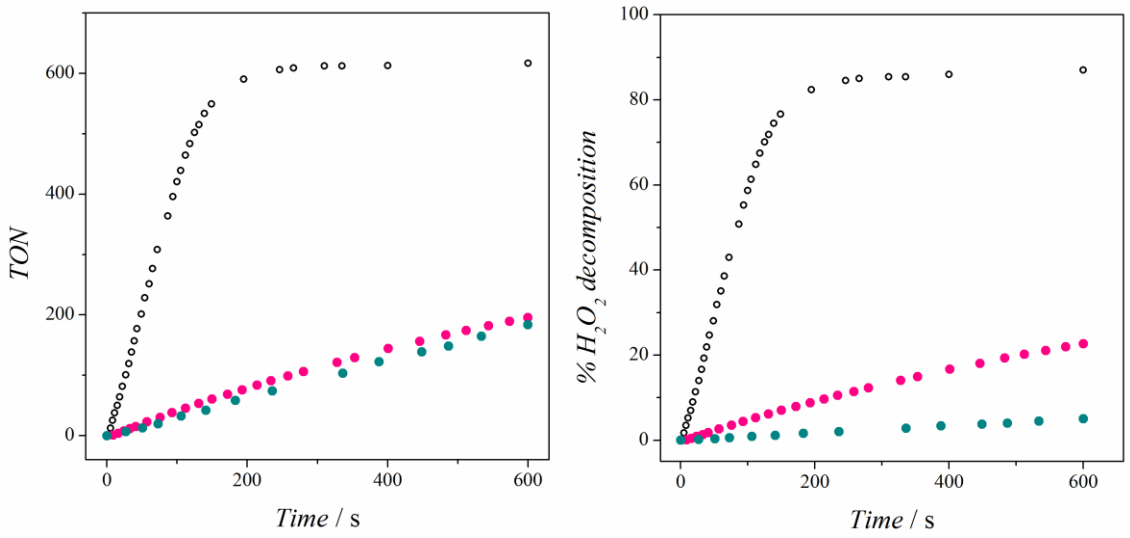

Figure 144. Catalase activity in CH_3CN-H_2O 9-1 (v/v) for materials $[Mn_2O]_{0.21}$-Py@SiO_2 (open circles) and $[Mn_2O]_{0.04}$-Py@SiO_2 (colored lines), with $[H_2O_2]_0$ = 1.05 M. For material $[Mn_2O]_{0.04}$-Py@SiO_2 two different concentrations were used: 0.16 (e_1, pink) and 0.68 mM (e_2, dark cyan), based on $[Mn^{III}_2]$. For $Mn_2O]_{0.21}$-Py@SiO_2, $[Mn^{III}_2]$ = 0.8 mM.

Experiment e_2 for this material was compared with the results obtained for material $[Mn_2O]_{0.21}$-Py@SiO_2 (e_1) at a similar concentration of Mn^{III}_2. Contrary to the previous one, $[Mn_2O]_{0.04}$-Py@SiO_2 displays a much lower activity than that with $x = 0.21$, being the hybrid material with the worst activity in this work. As may be observed, both the TON and H_2O_2 decomposition are low (<200 and < 25% after 10 min) in comparison to the other materials. These results are in accord with those shown for the non-functionalized material $[Mn_2O]_{0.1}$@SiO_2, which showed lower activity than expected, and reaffirm that the catalase activity of these materials is not only dependent on the concentration of active site but also on its local distribution in the pores.

Activity of material $[Mn_2O]_{0.21}$-Py@SiO_2 in pure water

The catalase activity of the pyridyl-modified material $[Mn_2O]_{0.21}$-Py@SiO_2 was tested in water under the same conditions as for its analogue without pyridyl function, $[Mn_2O]_{0.5}$@SiO_2. The results of this test are collected in Table 52 and Figure 145.

Table 52. Summary of catalytic results for compound **1** and **2** and material $[Mn_2O]_{0.5}$@SiO_2 with $[H_2O_2]_0 = 1.05$ M and $[Mn^{III}_2] = 0.8$ mM in water.

	At 1 min		At 2 min		At 10 min	
Sample	**TON[a]**	**% H_2O_2[b]**	**TON[a]**	**% H_2O_2[b]**	**TON[a]**	**% H_2O_2[b]**
$[Mn_2O]_{0.21}$-Py@SiO_2	79	11	187	25	534	73
$[Mn_2O]_{0.5}$@SiO_2	98	13	180	25	514	70

[a] TON = mmols O_2 / mmols Mn^{III}_2; [b] % H_2O_2 decomposed.

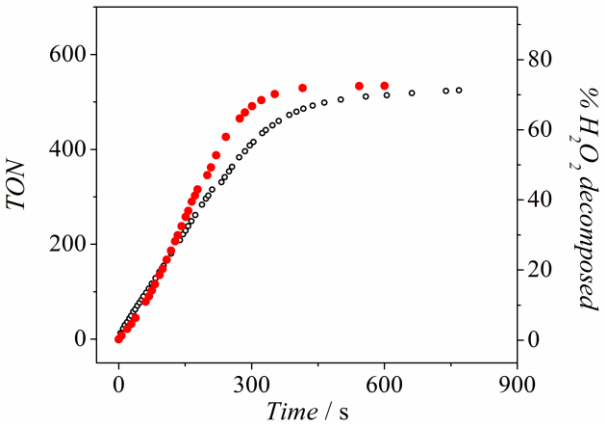

Figure 145. Catalase activity in water for the Py-modified material $[Mn_2O]_{0.21}$-Py@SiO_2 (red circles) and non-functionalized material $[Mn_2O]_{0.50}$@SiO_2 (open circles) (0.8 mM based on $[Mn^{III}_2]$), with $[H_2O_2]_0 = 1.05$ M.

Even though some slight but obvious differences may be observed in the shape of the curve, material $[Mn_2O]_{0.21}$-Py@SiO_2 displays a very similar activity to $[Mn_2O]_{0.5}$@SiO_2, showing similar H_2O_2 decomposition (around 70% at 10 min). Unfortunately, the catalase activity of material $[Mn_2O]_{0.21}$-Py@SiO_2 in water is still lower than in acetonitrile-water media.

To sum up, the hydrophobization of the pore surface with Py functions is not sufficient in order to limit the internal water diffusion and increase the stability of the Mn complex during the catalysis. Further experiments to overcome this limitation should be performed, such as a different surface functionalization or an external modification of the silica particles.

Stability of material $[Mn_2O]_{0.21}$-Py@SiO_2

The morphology and characteristics of material $[Mn_2O]_{0.21}$-Py@SiO_2 after 2 hours of reaction in pure water were analyzed. Two solids were isolated after one addition ($[Mn_2O]_{0.21}$-Py@$SiO_2^{\#W1}$) and two successive additions of H_2O_2 ($[Mn_2O]_{0.21}$-Py@$SiO_2^{\#W2}$), leading to H_2O_2/Mn^{III}_2 = 1629 and 3258, respectively (see details in the Experimental Section). The results are summarized in Table 53.

Table 53. Summary of properties for materials Py@SiO_2-TMA and $[Mn_2O]_{0.21}$-Py@SiO_2 and post-catalysis products.

Sample	Mesostructure	Porous volume / $cm^3\ g^{-1}$	% Weight loss[a]
Py@SiO_2-TMA	Yes	0.59	22.6
$[Mn_2O]_{0.21}$-Py@SiO_2	Yes	0.41	25.1
$[Mn_2O]_{0.21}$-Py@$SiO_2^{\#W1}$	Yes	0.52	14.8
$[Mn_2O]_{0.21}$-Py@$SiO_2^{\#W2}$	Yes	0.49	15.1

[a] Loss of the Mn complex ligands in the range 150–600 ºC, according to TGA.

Both materials $[Mn_2O]_{0.21}$-Py@$SiO_2^{\#W1}$ and $[Mn_2O]_{0.21}$-Py@$SiO_2^{\#W2}$ preserve the mesostructure of the former material $[Mn_2O]_{0.21}$-Py@SiO_2, as observed with the N_2 sorption isotherms (Figure 146). These are good results, taking into account that post-catalysis product obtained from the precedent material without pyridyl function, $[Mn_2O]$@$SiO_2^{\#W}$, showed no hexagonal array. This fact proves that the covering of the pore surface with pyridyl function stabilizes the material, as suggested above. Nevertheless, in the Py-modified material the pore volume increases and the weight loss corresponding to the Mn complex ligands decreased after the reaction (Table 53), suggesting that the pores are less loaded.

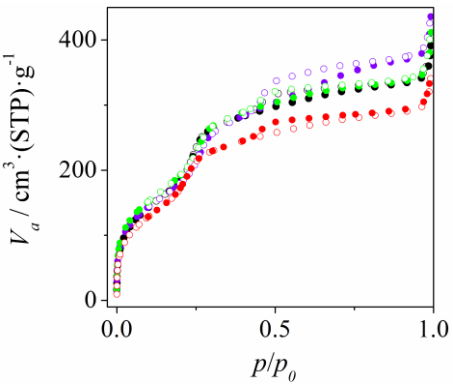

Figure 146. N_2 adsorption (full circles) and desorption (empty circles) isotherms at 77 K of materials $[Mn_2O]_{0.21}$-Py@$SiO_2^{\#W1}$ (purple), $[Mn_2O]_{0.21}$-Py@$SiO_2^{\#W2}$ (green), $[Mn_2O]_{0.21}$-Py@SiO_2 (cyan), and Py@SiO_2-TMA (black).

The TGA and N_2 sorption isotherms for the solids after one or two addition of H_2O_2, $[Mn_2O]_{0.21}$-Py@$SiO_2^{\#W1}$ and $[Mn_2O]_{0.21}$-Py@$SiO_2^{\#W2}$, present very similar profiles, but they differ from those of the starting material $[Mn_2O]_{0.21}$-Py@SiO_2 (Figure 146 and Figure 147). After the addition of H_2O_2, the pore volume increases (from 0.41 to ~0.50 cm g^{-1}) and the weight loss at ~250 °C in this starting material decreases from 10.5 to ~3%. This fact could indicate that some changes may be induced after the addition of H_2O_2; however, the same TG profile remains unchangeable regardless of the amount of H_2O_2 added to the solution.

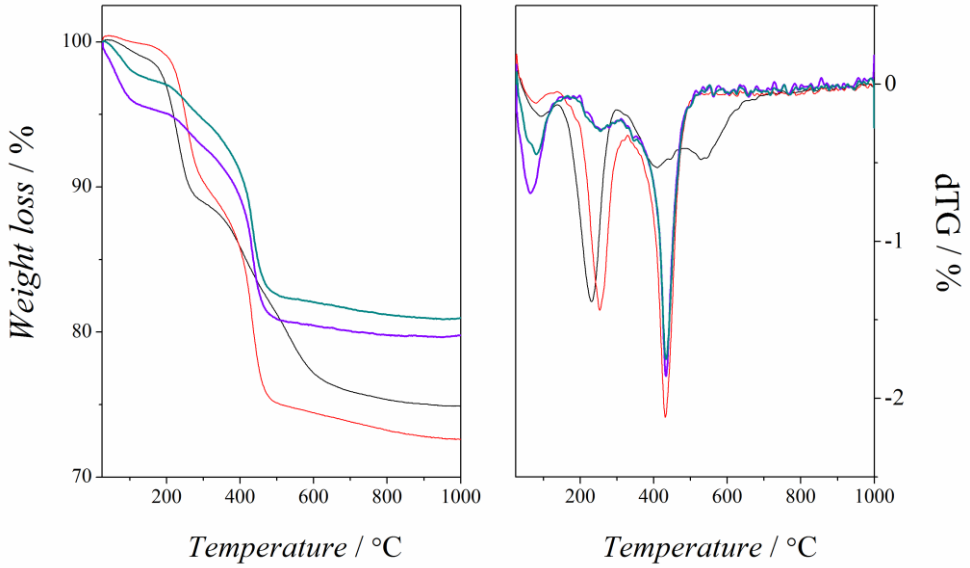

Figure 147. Weight loss (left) and derivative of weight loss (right) versus temperature for materials Py@SiO_2-TMA (black), $[Mn_2O]_{0.21}$-Py@SiO_2 (red), $[Mn_2O]_{0.21}$-Py@$SiO_2^{\#W1}$ (purple), and $[Mn_2O]_{0.21}$-Py@$SiO_2^{\#W2}$ (dark cyan).

The weight loss in the 150–600 °C range of the post-catalysis products (~15%), $[Mn_2O]_{0.21}$-Py@$SiO_2^{\#W1}$ and $[Mn_2O]_{0.21}$-Py@$SiO_2^{\#W2}$, is smaller than that for the support (22.6%),

Py@SiO_2-TMA, indicating that the organic/inorganic ratio is much higher for the support than for the materials after the catalysis. To obtain more information, elemental analyses and inductively coupled plasma optical emission spectrometry (ICP-OES) were performed for $[Mn_2O]_{0.21}$-Py@$SiO_2^{\#W2}$. Table 54 summarizes the results obtained from these analyses.

Table 54. Molar ratios calculated from elemental analyses and ICP-OES for materials $[Mn_2O]_{0.21}$-Py@SiO_2 and $[Mn_2O]_{0.21}$-Py@$SiO_2^{\#W2}$.

Sample	Mn_2/Si	C/Si	N/Si	N/C
$[Mn_2O]_{0.21}$-Py@SiO_2	0.017	1.32	0.17	0.13
$[Mn_2O]_{0.21}$-Py@$SiO_2^{\#W2}$	0.016	0.82	0.12	0.15

Si = total amount of silicon, inorganic and organic.

It is worth noting that Mn_2/Si ratio is very similar before and after the reaction. However, the C/Si and N/Si ratios are much smaller for the material obtained after the reaction, $[Mn_2O]_{0.21}$-Py@$SiO_2^{\#W2}$. This could be indicative of a partial unfastening of the Mn complex ligands, pyridyl function, and TMA^+ ions from the solid.

The IR spectrum of material $[Mn_2O]_{0.21}$-Py@$SiO_2^{\#W2}$ was recorded and compared with those of $[Mn_2O]_{0.21}$-Py@SiO_2 and Py@SiO_2-TMA (Figure 148). The results clearly show that TMA^+ ions have been released from the solid during the reaction. However, TMA^+ ions represent less than 2% of the weight in material $[Mn_2O]_{0.21}$-Py@SiO_2, so their loss does not explain the decrease (~10%) of the weight loss. Accordingly, either the ligands of the complex or the pyridyl function must have also been released. However, knowing which one will have left the pores in rather challenging. On the one hand, the narrow band at 1560 cm^{-1} of material Py@SiO_2-TMA, which is assigned to the pyridyl function, is much weaker in the post-catalysis product, $[Mn_2O]_{0.21}$-Py@$SiO_2^{\#W2}$. On the other hand, the presence of the band corresponding to the symmetric vibration of the COO group (1396 cm^{-1}) for $[Mn_2O]_{0.21}$-Py@$SiO_2^{\#W2}$ is not as clear as for $[Mn_2O]_{0.21}$-Py@SiO_2, since it is covered by the intense band assigned to the stretching of Si–O bonds.

Aiming to obtain additional clues, the support with pyridyl function, Py@SiO_2-TMA, was treated with H_2O_2 using an equivalent amount to that used for $[Mn_2O]_{0.21}$-Py@$SiO_2^{\#W1}$. TG analyses indicated that no significant loss of pyridyl occurred up to 24 hours of reaction. On the contrary, the amount of TMA^+ was reduced from ~9.1 to ~4.1% after 2 hours of reaction. However, the presence of the Mn ions in material $[Mn_2O]_{0.21}$-Py@SiO_2 may stimulate additional reactions that lead to the release of the PySi groups.

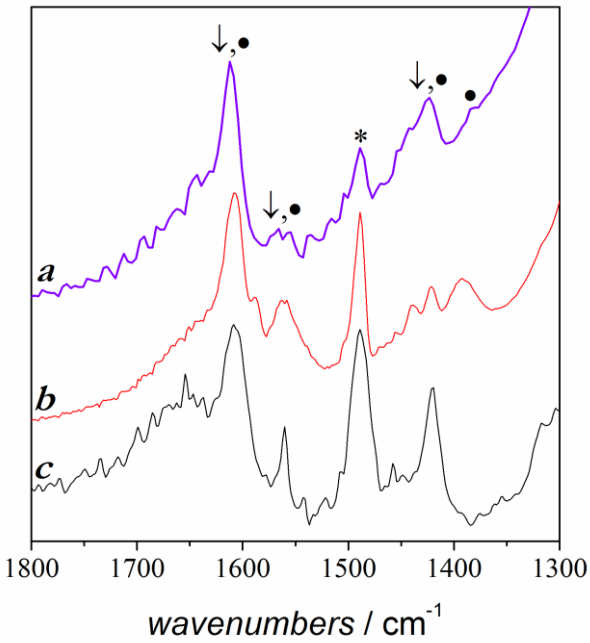

Figure 148. Infrared spectra (1800–1300 cm^{-1} window) for materials $[Mn_2O]_{0.21}$-Py@$SiO_2^{\#W1}$ (***a***), $[Mn_2O]_{0.21}$-Py@SiO_2 (***b***), and Py@SiO_2-TMA (***c***). The star (*), the arrows (↓) and circles (●) point out IR vibrations of TMA^+ ions, 4-pyridylethyl function, and Mn complex, respectively.

To sum up, the mesostructure of the pyridyl-modified hybrid material, $[Mn_2O]_{0.21}$-Py@SiO_2, is not altered during the reaction with H_2O_2 in water, contrary to what we observed with the non-functionalized material, $[Mn_2O]_{0.50}$@SiO_2. However, some changes take place during the catalysis that likely lead to the release of pyridyl function or the Mn complex ligands. However, this release could also be due to the treatment of the sample (washing and drying) before the measurements.

Summary

The non-functionalized hybrid material shows catalase activity and it is more efficient than the coordination compounds **1** and **2**. This fact is due to the presence of silanolate groups that likely buffers a basic pH and favors the catalyzed H_2O_2 decomposition. According to EPR spectroscopy and XPS analyses, the reaction seems to take place inside the support and that the Mn oxidation state swings between II and III.

This material is active in pure water, whereas the molecular compounds are not. However, the mesostructure of this material is disrupted during the reaction. Hence, functionalization of the pores was tested in order to increase the stability of both the silica walls and the Mn complex.

The catalase activity of the pyridyl-modified Mn-SiO_2 material, synthesized using different amounts of compound **1**, was tested. The results revealed that the catalase activity of these materials is dependent not only on the concentration of active center (Mn complex) but also on its local distribution in the pores.

The pyridyl-modified materials showed a better stability than those without functions, since the mesostructure is persevered after the reaction in water. However, the catalytic results are still below our expectations. Further experiments to overcome this limitation should be performed, such as a different surface functionalization or an external modification of the silica particles.

CONCLUSIONS

CONCLUSIONS

1. With benzoate derivative ligands one may obtain Mn compounds of different nuclearities and oxidation states.
2. To obtain dinuclear Mn^{III} compounds displaying ferromagnetic behavior, ethanol and perchlorate salts should be avoided. Benzoate derivatives with the substituent in *meta* position favor the ferromagnetic behavior.
3. The resulting Mn···Mn interaction in the Mn^{III}_2 compounds depends on the balance between structural and electronic parameters.
4. The contour plots considering the magnetic interaction and two structural parameters at the same time allowed us to analyze the correlation between parameters.
5. From the fit of the magnetization and magnetic susceptibility plots it is possible to determine the single-ion zero-field splitting (ZFS) parameters (D_{Mn} and E_{Mn}). Moreover, the relative orientation of the octahedra and the sign of the ZFS parameters is relevant for the overall magnetic properties at low temperature.
6. The dinuclear Mn^{III} compounds display catalytic activity towards the H_2O_2 disproportionation in acetonitrile. Their efficiency depends on the benzoate derivative used in the synthesis and on the position of the substituent in the aromatic ring.
7. The nitrate ions have a predominant effect over perchlorate ions on the catalase activity. The presence of nitrate ions in the reaction media could be favorable or unfavorable, depending on the compound.
8. The incorporation of the Mn^{III}_2 compounds inside mesoporous silica (MCM-41 type) by ionic exchange was successful, using both non-functionalized and pyridyl-modified support.
9. The mesostructure typical for MCM-41 mesoporous silica remains unaltered after the insertion of the Mn complex and the dinuclear Mn^{III} unit is preserved inside the solid.
10. These Mn-SiO_2 hybrid materials are more active towards the H_2O_2 disproportionation than the molecular analogues in acetonitrile, highly likely due to the increase of pH caused by the silanolate groups present in the hybrid materials.

11. The pyridyl function has no negative effect on the catalase activity and provides the mesostructure with more stability under the conditions of the reaction.

12. The catalase activity of these hybrid materials is not only sensitive to the Mn^{III}_2 concentration but also to its local distribution inside the pores.

13. These hybrid materials are active in water solution, whereas the molecular analogues display no activity.

14. Different kind of Mn^{II} compound, mono-, di-, or trinuclear, may be obtained depending on the presence or absence of perchlorate ions, the solvent, and ligands used in the synthesis.

15. Electron paramagnetic resonance (EPR) and the magnetic properties allow for the identification and differentiation of the Mn^{II} compound that may be obtained.

16. With EPR spectroscopy the magnitude of the Mn^{II} ZFS parameters may be determined. In some particular cases, the determination of the sign of D_{Mn} becomes plausible with this technique.

17. For the benzoic acid derivatives used in this work, the formation of dinuclear or tetranuclear Mn^{III} compounds seems to be dictated by the nitrogen-based ligand: while using 2,2'-bipyridine leads to the formation of dinuclear compounds, the use of 1,10-phenantroline gives tetranuclear compounds.

18. The tetranuclear compounds obtained in this work display a ground state with $S_T = 0$, contrary to those reported in the literature. This fact is caused by the differentiation of two Mn···Mn interactions between the central and terminal ions. Moreover, the assignment of each spin state to a particular spin configuration becomes impossible as these magnetic interactions become more different.

19. The heterometallic Mn^{IV}_6 wheels could not be obtained with the benzoic acid derivatives with R = MeO.

20. The size of the central cation in the heterometallic wheels is an important factor for the stability and/or insolubility of the wheels.

21. The alkaline earth ions are not innocent for the Mn···Mn interactions of the wheels, both structural and electronic modifications promoted by these ions affect the magnetic properties.

22. The dodecanuclear compound shows the behavior expected for a single-molecule magnet. In addition, it displays two peaks in the AC magnetic susceptibility plot, suggesting the coexistence of two different isomers.

23. The insertion of the Mn^{IV}-Ca^{2+} wheel inside *n*-propyl- or phenyl-modified mesoporous silica led to materials where the Mn_6Ca_2 cluster suffered important structural modifications.

24. The dodecanuclear compound was successfully inserted inside phenyl-modified mesoporous silica, preserving the behavior of a SMM. The support was not selective for a particular isomer.

FUTURE PERSPECTIVES

FUTURE PERSPECTIVES

In spite of the results presented in this work, there are still many unknown points to answer or new upcoming projects that may be started in a close future. In this part, some suggestions and ideas may be found.

1. Study the factors that dictate the sign and magnitude of the axial and rhombic anisotropies in both Mn^{III} and Mn^{II} ions. To do so, the determination and profound understanding of the ZFS of molecular compounds need to be performed. The magnetic measurements and, in some instances, EPR spectroscopy of these upcoming compounds should be performed. A much better determination of the Mn^{III} ion ZFS parameters could be performed using high-frequency high-field EPR spectroscopy. Theoretical calculations could also be a key tool to understand the nature of these parameters.

2. Understand what dictates the ferromagnetic coupling in the dinuclear Mn^{II} compounds with $\mu_{1,1}$-$RC_6H_4COO^-$ bridges.

3. For the tetranuclear compounds, the assignment of the magnetic coupling constants between terminal and central ions, J_2 and J_3 (Figure 68), to each bridging block, the double-carboxylate or single-carboxylate bridges. DFT calculations could be a very useful tool to achieve it.

4. Extend the syntheses of the Mn^{IV}_6 wheels to non-alkaline earth ions, to experimentally prove the structural limit of the wheels and to investigate the potential of the electronic modifications promoted by the central ions on the magnetic properties of the wheels.

5. The syntheses of heterometallic of Mn^{IV}-Ca^{2+} and Mn^{IV}-Sr^{2+} compounds that could be structural and functional models of the WOC, proving new synthetic routes.

6. Try to obtain the two isomers of the dodecanuclear compounds separately. The use of different solvents could favor the unique formation or crystallization of one of them.

7. Further in the characterization of the pyridyl-modified Mn-SiO_2 materials. It would be interesting to investigate the structure of the Mn complex inside the mesopores at a molecular level and its interaction with the silica walls. For instance, whether the Mn complex interacts with the pyridyl groups covalently or it is just hold through hydrogen

bonds. XANES, EXAFS, and paramagnetic solid NMR could be very useful techniques to acquire this information.

8. Perform energy-dispersive X-ray spectroscopy coupled to transmission electron microscopy (TEM-EDX), if possible, for all Mn-SiO_2 materials, to confirm the distribution of Mn complex inside the pores.

9. Do a second attempt to synthesize mesoporous silica with hydrophobic channels. A method that allows for the full coverage of the surface should be used, leaving no place to covalent interactions with the silanol groups of the support.

10. Transfer chemistry of the bulky Mn-SiO_2 materials to mesoporous silica nanoparticles. This step is crucial in order to guarantee the applicability of these materials for medical applications.

11. Perform the external functionalization of the hybrid material particles. However, with a bulky material, the external functionalization is very difficult to characterize because the external surface has an insufficient contribution. Thus, the external functionalization should be better studied using nanoparticles (~50–150 nm of size).

12. The external functionalization could be performed with poly(ethylene glycol) (PEG) silane. PEG is one of the most common polymers to externally functionalize nanoparticles that increase their stability and biocompatibility. As a first attempt, one may synthesized particles described by Bouchoucha *et al.*[325] That procedure provides PEGylated mesoporous silica particles of 150 nm large that should be compatible with further functionalization using the co-condensation method, as we used for the pyridyl modification.

13. The coating of hybrid material particles with an external layer to limit the diffusion of the solvent used in the catalytic tests. New methods that differ from the ones attempted here should be tested. An elegant approach is that described by Kim *et al.*,[326] where mesoporous silica nanoparticles were coated with a biopolymer by electrospraying.

14. Study the catalase activity versus the Mn^{III}_2 concentration for the molecular compounds to complete the kinetics study of this reaction.

APPENDIX

APPENDIX

Appendix I: Crystal data and structure refinement details

Dinuclear Mn^{III} Compounds

Table S1. Crystal data and structure refinement details for compounds **1** and **2**.

	1·H_2O·0.5 CH_3CN	**2**·CH_3CN
Formula	$C_{148}H_{142}Mn_8N_{26}O_{60}$[a]	$C_{38}H_{35}Cl_2Mn_2N_5O_{16}$
Fw (g/mol)	3670.28	998.49
Crystal color, habit	green, needle	Green, needle
***T* (K)**	100(2)	100(2)
λ (Mo Kα) / Å	0.71073	0.71073
Crystal size (mm)	0.65 x 0.26 x 0.21	0.57 x 0.07 x 0.02
Crystal system	Monoclinic	Monoclinic
Space group	*C*2/c	*P*21/c
***a* / Å**	16.3701(6)	17.826(7)
***b* / Å**	24.5812(9)	21.265(7)
***c* / Å**	9.9600(4)	10.759(4)
α / º	90º	90º
β / º	99.328(1)	95.72(1)
γ / º	90º	90º
***V* / Å^3**	3954.9(3)	4058(2)
Z	1	4
ρ_{calcd} / g·cm^{-3}	1.541	1.631
μ / mm^{-1}	0.718	0.835
***F*(000)**	1878	2032
θ range / º	2.39 to 25.08	1.15 to 20.81
Completeness to θ = 25.10 º	99.8%	99.5%
Index ranges	h = -19 → 19	h = -17 → 17
	k = -29 → 29	k = 0 → 21
	l = -11 → 11	l = 0 → 10
Data/restraints/parameters	3515 / 106 / 306	4226 / 1 / 562
GooF on F^2	1.110	0.824
R_1[b], ωR_2[c] [$I > 2\sigma(I)$]	0.0507, 0.1515	0.0352, 0.0768
R_1[b], ωR_2[c] (all data)	0.0520, 0.1525	0.0914, 0.0966

[a] 4 eq. of **1**·H_2O·0.5CH_3CN. [b] $R_1 = \sum ||F_o| - |F_c|| / \sum |F_o|$. [c] $\omega R_1 = \{\sum[\omega(F_o^2 - F_c^2)^2] / \sum[\omega(F_o^2)^2]\}^{1/2}$, $\omega = 1 / [\sigma^2(F_o^2) + (aP)^2 + bP]$, where $P = [\max(F_o^2, 0) + 2F_c^2] / 3$.

Table S2. Crystal data and structure refinement details for compounds **3**, **4**, and **5**.

	3·2CH_3CN	**4**·1/2 H_2O·1/2 CH_3CN	**5**
Formula	$C_{40}H_{36}Mn_2N_8O_{13}$[a]	$C_{74}H_{69}Mn_4N_{13}O_{29}$[b]	$C_{36}H_{32}Cl_2Mn_2N_4O_{16}$
Fw (g/mol)	946.65	1824.18	957.44
Crystal color, habit	Dark green, prism	Green, needle	Green, prism
***T* (K)**	100(2)	100(2)	100(2)
λ (Mo Kα) / Å	0.71073	0.71073	0.71073
Crystal size (mm)	0.25 x 0.22 x 0.21	0.42 x 0.20 x 0.05	0.54 x 0.46 x 0.33
Crystal system	Monoclinic	Triclinic	Triclinic
Space group	*C*2/*c*	$P\bar{1}$	$P\bar{1}$
***a* / Å**	24.3681(19)	9.8493(9)	10.0416(16)
***b* / Å**	13.7810(11)	14.2702(14)	14.598(3)
***c* / Å**	16.1592(13)	15.7977(16)	15.706(3)
α / °	90	114.076(4)	114.091(6)
β / °	130.004(3)	97.913(4)	100.507(6)
γ / °	90	94.134(4)	91.521(6)
***V* / Å^3**	4156.7(6)	1987.6(3)	2053.4(7)
Z	4	1	2
ρ_{calcd} / g·cm^{-3}	1.513	1.524	1.549
μ / mm^{-1}	0.683	0.713	0.821
***F*(000)**	1944	936	976
θ range / °	2.18 to 24.70	2.32 to 26.52	2.08 to 35.98
Completeness (to θ / °)	91.4% (24.70)	98.7% (26.52)	100.0% (25.00)
Index ranges	h = -28 → 28	h = -12 → 12	h = -16 → 15
	k = -16 → 16	k = -17 → 17	k = -23 → 22
	l = -18 → 18	l = -19 → 19	l = -24 → 23
Data/restraints/parameters	3234 / 0 / 286	8150 / 63 / 556	16188 / 286 / 592
GooF on F^2	1.091	1.158	1.023
R_1[c], ωR_2[d] [$I > 2\sigma(I)$]	0.0344, 0.0876	0.0842, 0.2440	0.0620, 0.1595
R_1[c], ωR_2[d] (all data)	0.0400, 0.0934	0.1058, 0.2564	0.0792, 0.1674

[a] **3**·2 CH_3CN. [b] 2eq. of **4**·1/2 H_2O·1/2 CH_3CN. [c] $R_1 = \sum ||F_o| - |F_c|| / \sum |F_o|$. [d] $\omega R_1 = \{\sum[\omega(F_o^2 - F_c^2)^2] / \sum[\omega(F_o^2)^2]\}^{1/2}$, $\omega = 1 / [\sigma^2(F_o^2) + (aP)^2 + bP]$, where $P = [\max(F_o^2, 0) + 2F_c^2] / 3$.

Table S3. Crystal data and structure refinement details for compounds **6** and **7**.

	6·1/3 CH_3CN·1/3H_2O	**7**
Formula	$C_{116}H_{113}Cl_6Mn_6N_{13}O_{49}$[c]	$C_{44}H_{47}Cl_2Mn_2N_4O_{14}$
Fw (g/mol)	3015.53	1036.64
Crystal color, habit	Brown, thin plate	Green, needle
***T* (K)**	293(2)	100(2)
λ (Mo Kα) / Å	0.71073	0.71073
Crystal size (mm)	0.2 x 0.03 x 0.03	0.35 x 0.08 x 0.03
Crystal system	Trigonal	Orthorhombic
Space group	$R\bar{3}$	*Pca*2(1)
***a* / Å**	25.409(7)	24.6687(18)
***b* / Å**	25.409(7)	13.5393(9)
***c* / Å**	35.1430(10)	28.996(2)
α / °	90	90
β / °	90	90
γ / °	120	90
***V* / Å^3**	19649(8)	9684.6(12)
Z	6	8
ρ_{calcd} / g·cm^{-3}	1.529	1.422
μ / mm^{-1}	0.777	0.699
***F*(000)**	9264	4280
θ range / °	1.48 to 32.38	2.17 to 22.98
Completeness (to θ / °)	99.8% (25.00)	99.7% (22.98)
Index ranges	h = -38 → 19	h = -27 → 27
	k = 0 → 38	k = -14 → 14
	l = 0 → 52	l = -31 → 28
Data/restraints/parameters	14081 / 38 / 591	12723 / 480 / 1244
GooF on F^2	0.881	1.030
R_1[b], ωR_2[c] [$I>2\sigma(I)$]	0.0470, 0.1094	0.0374, 0.0832
R_1[b], ωR_2[c] (all data)	0.1303, 0.1287	0.0486, 0.0881

. [a] 3 eq. of **6**·1/3 CH_3CN·1/3 H_2O. [b] $R_1 = \sum ||F_o| - |F_c|| / \sum |F_o|$. [c] $\omega R_1 = \{\sum[\omega(F_o^2 - F_c^2)^2] / \sum[\omega(F_o^2)^2]\}^{1/2}$, $\omega = 1 / [\sigma^2(F_o^2) + (aP)^2 + bP]$, where $P = [\max(F_o^2, 0) + 2F_c^2] / 3$.

Mn^{II} Compounds

Table S4. Crystal data and structure refinement details for Mn^{II} 3-methoxybenzoate ($[Mn_3(3\text{-}MeOC_6H_4COO)_6(EtOH)_2]_n$) and compounds **8**, **9**, and **10**.

Manganese(II) 3-methoxybenzoate ($[Mn_3(3\text{-}MeOC_6H_4COO)_6(EtOH)_2]_n$)			
Formula	$C_{52}H_{54}Mn_3O_{20}$	***Z***	2
Fw (g/mol)	1163.77	ρ_{calcd} / g·cm^{-3}	1.440
Crystal color, habit	Pale pink, prism	μ / mm^{-1}	0.771
T **(K)**	293(2)	***F*****(000)**	1202
λ **(Mo-K**α**)** / Å	0.71073	θ **range** / º	1.73 to 32.33
Crystal size (mm)	0.2 x 0.1x 0.1	**Completeness (to** θ **/** º**)**	93.7% (25.00)
Crystal system	Monoclinic	**Index ranges**	h = -13 → 12
Space group	*P*21/*c*		k = -27 → 27
a / Å	9.194(4)		l = -21 → 21
b / Å	20.052(7)	**Data/restraints/param.**	6798 / 2 / 364
c / Å	15.945(5)	**GooF on** F^2	1.184
α **,** β**,** γ / º	90, 114.05(2), 90	R_1[a], ωR_2[b] **[**$I > 2\sigma(I)$**]**	0.0630, 0.1741
V / Å^3	2684.4(17)	R_1[a], ωR_2[b] **(all data)**	0.0722, 0.1837

	8	**9**	**10**
Formula	$C_{56}H_{46}Cl_2Mn_2N_8O_{14}$	$C_{56}H_{46}Cl_2Mn_2N_8O_{14}$	$C_{56}H_{46}Cl_2Mn_2N_8O_{14}$
Fw (g/mol)	1235.79	1235.79	1235.79
Crystal color, habit	Yellow, prism	Yellow, prism	Yellow, prism
T **(K)**	293(2)	90(2)	293(2)
λ **(Mo-K**α**)** / Å	0.71073	0.71073	0.71073
Crystal size (mm)	0.2 x 0.1x 0.1	0.19x 0.12 x 0.10	0.2 x 0.1 x 0.1
Crystal system	Triclinic	Monoclinic	Triclinic
Space group	*P*-1	*P*21/*c*	*P*-1
a / Å	8.494(4)	9.1362(4)	9.1240(6)
b / Å	13.051(5)	23.6792(10)	12.579(6)
c / Å	14.288(5)	12.2498(5) A	13.411(6)
α / º	113.12(2)	90	63.45(2)
β / º	105.19(3)	92.8570(10)	88.31(4)
γ / º	92.03(3)	90	84.21(4)
V / Å^3	1388.6(10)	2646.80(19)	1369.6(9)
Z	1	2	1
ρ_{calcd} / g·cm^{-3}	1.478	1.551	1.498
μ / mm^{-1}	0.625	0.656	0.634
F**(000)**	634	1268	634
θ **range** / º	1.62 to 29.97	2.23 to 41.34	1.70 to 32.44
Completeness (to θ **/** º**)**	92.9% (25.00)	99.9% (41.34)	93.6%(25.00)
Index ranges	h = -10 → 10	h = -16 → 16	h = -12 → 12
	k = -17 → 16	k = -43 → 43	k = -16 → 18
	l = 0 → 19	l = -22 → 22	l = -0 → 20
Data/restraints/param.	6090 / 15 / 407	17755 / 0 / 370	7910 / 3 / 364
GooF on F^2	1.062	1.085	1.100
R_1[a], ωR_2[b] **[**$I > 2\sigma(I)$**]**	0.0347, 0.0977	0.0356, 0.0898	0.0676, 0.1717
R_1[a], ωR_2[b] **(all data)**	0.0385, 0.1006	0.0471, 0.0952	0.1049, 0.1951

[a] $R_1 = \sum ||F_o| - |F_c|| / \sum |F_o|$. [b] $\omega R_1 = \{\sum[\omega(F_o^2 - F_c^2)^2] / \sum[\omega(F_o^2)^2]\}^{1/2}$, $\omega = 1 / [\sigma^2(F_o^2) + (aP)^2 + bP]$, where $P = [\max(F_o^2, 0) + 2F_c^2] / 3$.

Table S5. Crystal data and structure refinement details for compounds **12**, **13**, and **14**.

	12	**13**	**14**
Formula	$C_{64}H_{46}Cl_2Mn_2N_8O_{14}$	$C_{32}H_{25}ClMnN_4O_8$	$C_{64}H_{46}Cl_2Mn_2N_8O_{14}$
Fw (g/mol)	1331.87	683.95	1331.87
Crystal color, habit	Yellow, prism	Yellow, prism	Yellow, prism
***T* (K)**	100(2)	100(2)	100(2)
λ (Mo-Kα) / Å	0.71073	0.71073	0.71073
Crystal size (mm)	0.32 x 0.30x 0.26	0.12 x 0.11 x 0.09	0.28 x 0.13 x 0.05
Crystal system	Triclinic	Triclinic	Monoclinic
Space group	*P*-1	*P*-1	*C*2/*m*
***a* / Å**	9.5795(16)	8.2965(7)	9.1362(4)
***b* / Å**	12.309(2)	13.4504(10)	23.6792(10)
***c* / Å**	13.644(3)	14.3581(12)	12.2498(5)
α / º	64.358(7)	102.403(3)	90
β / º	84.369(7)	91.449(4)	92.8570(10)
γ / º	84.183(7)	106.589(3)	90
***V* / Å^3**	1440.3(5)	1493.3(2)	2646.80(19)
Z	1	2	2
ρ_{calcd} / g·cm^{-3}	1.536	1.521	1.592
μ / mm^{-1}	0.609	0.592	0.632
***F*(000)**	682	702	1364
θ range / º	2.14 to 32.21	2.42 to 27.98	2.65 to 30.58
Completeness (to θ / º)	99.6% (32.21)	95.3% (25.00)	99.7% (30.58)
Index ranges	h = -14 → 14	h = -10 → 10	h = -20 → 21
	k = -18 → 18	k = -17 → 17	k = -28 → 28
	l = -20 → 20	l = -18 → 18	l = -13 → 11
Data/restraints/param.	10146 / 0 / 424	6591 / 112 / 451	4379 / 36 / 239
GooF on F^2	1.061	1.141	1.162
R_1[a], ωR_2[b] [$I > 2\sigma(I)$]	0.0476, 0.1143	0.0606, 0.1141	0.0746, 0.1727
R_1[a], ωR_2[b] (all data)	0.0644, 0.1221	0.0819, 0.1235	0.0811, 0.1762

[a] $R_1 = \sum ||F_o| - |F_c|| / \sum |F_o|$. [b] $\omega R_1 = \{\sum[\omega(F_o^2 - F_c^2)^2] / \sum[\omega(F_o^2)^2]\}^{1/2}$, $\omega = 1 / [\sigma^2(F_o^2) + (aP)^2 + bP]$, where $P = [\max(F_o^2, 0) + 2F_c^2] / 3$.

Table S6. Crystal data and structure refinement details for compounds **15**, **17**, and **19**.

	15	**17**	**19**
Formula	$C_{70}H_{58}Cl_2Mn_2N_8O_{12}$	$C_{72}H_{64}Mn_3N_6O_{18}$	$C_{28}H_{26}MnN_2O_8$
Fw (g/mol)	1384.02	1466.11	573.45
Crystal color, habit	Yellow, prism	Yellow, prism	Yellow, prism
***T* (K)**	302(2)	293 (2)	293(2)
λ (Mo-Kα) / Å	0.71073	0.71073	0.71073
Crystal size (mm)	0.21 x 0.18 x 0.17	0.1 x 0.09 x 0.07	0.58 x 0.22 x 0.15
Crystal system	Triclinic	Triclinic	Monoclinic
Space group	*P*-1	*P*-1	*Cc*
***a* / Å**	10.516(4)	11.201(10)	25.088(3)
***b* / Å**	12.247(4)	11.519(7)	20.956(3)
***c* / Å**	13.821(5)	14.455(10)	20.011(3)
α / º	67.567(13)	71.58(4)	90
β / º	84.331(17)	71.09(4)	102.342(5)
γ / º	78.406(16)	74.74(5)	90
***V* / Å^3**	1611.3(10)	1647(2)	10278(2)
Z	1	1	16
ρ_{calcd} / g·cm^{-3}	1.426	1.478	1.482
μ / mm^{-1}	0.545	0.645	0.569
***F*(000)**	714	757	4752
θ range / º	2.49 to 28.78	1.54 to 32.41	2.29 to 28.34
Completeness (to θ / º)	93.9% (25.00)	93.3% (25.00)	99.6% (28.34)
Index ranges	$h = -13 \rightarrow 13$	$h = -15 \rightarrow 16$	$h = -32 \rightarrow 33$
	$k = -13 \rightarrow 15$	$k = -17 \rightarrow 17$	$k = -27 \rightarrow 27$
	$l = 0 \rightarrow 17$	$l = -21 \rightarrow 21$	$l = -26 \rightarrow 26$
Data/restraints/param.	6619 / 4 / 427	9765 / 0 / 448	24219 / 4 / 1406
GooF on F^2	1.020	1.051	1.070
R_1[a], ωR_2[b] [$I > 2\sigma(I)$]	0.0659, 0.1290	0.0861, 0.1876	0.0407, 0.0871
R_1[a], ωR_2[b] (all data)	0.2201, 0.2160	0.1629, 0.218	0.0879, 0.1038

[a] $R_1 = \sum ||F_o| - |F_c|| / \sum |F_o|$. [b] $\omega R_1 = \{\sum[\omega(F_o^2 - F_c^2)^2] / \sum[\omega(F_o^2)^2]\}^{1/2}$, $\omega = 1 / [\sigma^2(F_o^2) + (aP)^2 + bP]$, where $P = [\max(F_o^2, 0) + 2F_c^2] / 3$.

Heterometallic Compounds with $[Mn^{IV}_6M_2O_9]^{10+}$ Core

Table S7. Crystal data and structure refinement details for compounds **22** and **23**.

	22·10 CH_3CN	**23**·10 CH_3CN
Formula	$C_{185}H_{230}Ca_2Mn_6N_{10}O_{39}$	$C_{185}H_{230}Mn_6N_{10}O_{39}Sr_2$
Fw (g mol^{-1})	3627.59	3722.67
Crystal color, habit	Dark red, solid plates	Dark red, prism
***T* (K)**	100(2)	100(2)
λ (Mo Kα) / Å	0.71073	0.71073
Crystal size (mm)	0.64 x 0.63 x 0.2	0.185 x 0.079 x 0.078
Crystal system	Hexagonal	Hexagonal
Space group	*P*63/m	*P*63/m
***a* / Å**	19.5284(13)	19.6062(6)
***b* / Å**	19.5284(13)	19.6062(6)
***c* / Å**	28.677(2)	28.9147(10)
α / °	90	90
β / °	90	90
γ / °	120	120
***V* / Å^3**	9471(1)	9625.8(5)
Z	2	2
ρ_{calcd} / g cm^{-3}	1.272	1.284
μ / mm^{-1}	0.516	1.003
***F*(000)**	3824	3896
θ range / °	2.09 to 25.10	2.08 to 26.39
Completeness to θ = 25.10°	99.8%	99.9%
Index ranges	$h = -23 \rightarrow 23$	$h = -24 \rightarrow 24$
	$k = -23 \rightarrow 23$	$k = -24 \rightarrow 18$
	$l = -34 \rightarrow 34$	$l = -35 \rightarrow 36$
Data/restraints/parameters	5757 / 5 / 376	6722 / 5 / 376
GooF on F^2	1.089	1.041
R_1[a], ωR_2[b] [$I > 2\sigma(I)$]	0.0545, 0.1330	0.0724, 0.1948
R_1[a], ωR_2[b] (all data)	0.0752, 0.1556	0.1037, 0.2184

[a] $R_1 = \sum ||F_o| - |F_c|| / \sum |F_o|$. [b] $\omega R_1 = \{\sum[\omega(F_o^2 - F_c^2)^2] / \sum[\omega(F_o^2)^2]\}^{1/2}$, $\omega = 1 / [\sigma^2(F_o^2) + (aP)^2 + bP]$, where $P = [\max(F_o^2, 0) + 2F_c^2] / 3$.

Tetranuclear Compounds with $[Mn^{III}_4O_2]^{8+}$ Core

Table S8. Crystal data and structure refinement details for compounds **24** and **25**.

	24·1/2EtOH·5/4CH_3CN·1/4H_2O	**25**·4CH_3CN
Formula	$C_{167}H_{144.50}Cl_2Mn_8N_{10.50}O_{55.50}$[a]	$C_{192}H_{210}Cl_4Mn_8N_{14}O_{46}$[b]
Fw (g/mol)	3696.85	4031.06
Crystal color, habit	red, prism	red, thin square
***T* (K)**	100(2)	100(2)
λ (Mo Kα) / Å	0.71073	0.71073
Crystal size (mm)	0.62 x 0.25 x 0.23	0.23 x 0.20 x 0.03
Crystal system	Triclinic	Monoclinic
Space group	*P1*	*P21/c*
***a* / Å**	16.254(3)	27.685(3)
***b* / Å**	16.408(3)	19.1531(18)
***c* / Å**	17.493(3)	18.3634(16)
α / °	111.443(6)	90
β / °	93.798(6)	91.828(3)
γ / °	103.048(6)	90
***V* / Å^3**	4172.9(13)	9732.3(16)
Z	1	2
ρ_{calcd} / g·cm^{-3}	1.471	1.376
μ / mm^{-1}	0.708	0.637
***F*(000)**	1898	4192
θ range / °	2.21 to 26.88	2.10 to 30.72
Completeness to θ_{max}	99.7%	98.0%
Index ranges	$h = -20 \rightarrow 20$	$h = -39 \rightarrow 39$
	$k = -20 \rightarrow 20$	$k = 0 \rightarrow 27$
	$l = -22 \rightarrow 22$	$l = 0 \rightarrow 26$
Data/restraints/parameters	34398/75/2240	29671/542/1243
GooF on F^2	1.104	0.995
R_1[b], ωR_2[c] [$I > 2\sigma(I)$]	0.0398, 0.1071	0.0680, 0.1694
R_1[b], ωR_2[c] (all data)	0.0430, 0.1115	0.1960, 0.2030

[a] 2 eq. of **1**·1/2EtOH·5/4CH_3CN·1/4H_2O; [b] 2 eq. of **2**·4CH_3CN; [c] $R_1 = \sum ||F_o| - |F_c|| / \sum |F_o|$; [d] $\omega R_1 = \{\sum[\omega(F_o^2 - F_c^2)^2] / \sum[\omega(F_o^2)^2]\}^{1/2}$, $\omega = 1 / [\sigma^2(F_o^2) + (aP)^2 + bP]$, where $P = [\max(F_o^2, 0) + 2F_c^2] / 3$.

Dodecanuclear Compound with $[Mn^{IV}_4Mn^{III}_8O_{16}]^{12+}$ Core

Table S9. Crystal data and structure refinement details for compound **26**.

	26·5 CH_3CN
Formula	$C_{138}H_{135}Mn_{12}N_5O_{64}$ [a]
Fw (g mol^{-1})	3546.79
Crystal color, habit	black, needle
***T* (K)**	100(2)
λ (Mo Kα) / Å	0.71073
Crystal size (mm)	0.54 x 0.33 x 0.05
Crystal system	Monoclinic
Space group	*P*2/*n*
***a* / Å**	17.3130(8)
***b* / Å**	17.2562(7)
***c* / Å**	25.7022(11)
α / °	90
β / °	97.641(2)
γ / °	90
***V* / Å^3**	7610.5(6)
Z	2
ρ_{calcd} / g cm^{-3}	1.548
μ / mm^{-1}	1.054
***F*(000)**	3620
θ range / °	2.20 to 25.15
Completeness to θ = 25.10°	99.3%
Index ranges	h = -20 → 20 k = -20 → 20 l = -30 → 30
Data/restraints/parameters	13562 / 31 / 986
GooF on F^2	1.042
R_1[a], ωR_2[b] [$I > 2\sigma(I)$]	0.0381, 0.1042
R_1[a], ωR_2[b] (all data)	0.0496, 0.1148

[a] $R_1 = \sum ||F_o| - |F_c|| / \sum |F_o|$. [b] $\omega R_1 = \{\sum[\omega(F_o^2 - F_c^2)^2] / \sum[\omega(F_o^2)^2]\}^{1/2}$, $\omega = 1 / [\sigma^2(F_o^2) + (aP)^2 + bP]$, where $P = [\max(F_o^2, 0) + 2F_c^2] / 3$.

Appendix II: Supplementary Material for Dinuclear Mn^{III} Compounds

Synthesis

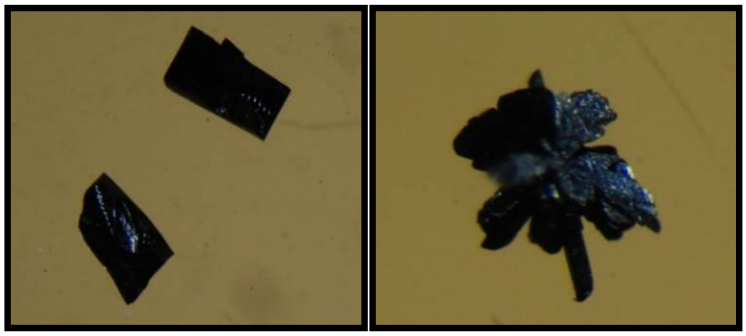

Figure S1. Photographs of crystals for compounds **3** (right) and **4** (left).

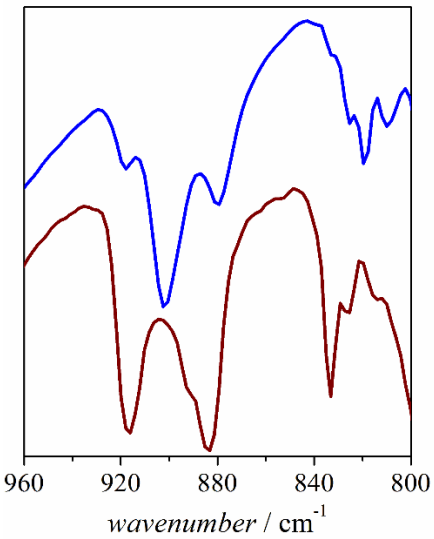

Figure S2. Transmittance infrared spectra (range 960–800 cm^{-1}) of compounds **3** (blue) and **4** (red).

Crystallography

[{Mn(bpy)(H_2O)}(μ-2-$MeOC_6H_4COO$)$_2$(μ-O){Mn(bpy)(NO_3)}]NO_3·H_2O·0.5 CH_3CN (1·H_2O·0.5CH_3CN). The crystal structure of compound **1** consists of a cationic complex, a nitrate ion and disordered solvent. The most relevant distances and angles are listed in Table S10.

The monodentate ligands of Mn(III) ions are disordered, being H_2O or NO_3^-, both found with 50% occupancy. Therefore, the two Mn(III) ions that form the complex are crystallographically equivalent. Each binuclear entity is connected to the neighbor through hydrogen bonds between a H_2O molecule and a NO_3^- ion (Figure S3). This interaction is

extended along a longitudinal axis, resulting in a one-dimensional supramolecular structure, where the position of the H_2O molecule and the NO_3^- ion within each already said couple is statistically dictated (Figure S3). Different longitudinal organizations are aligned in a zigzag layer where every chain is antiparallel to the previous one (Figure S4). A parallel-displaced π-π interaction may be found between bipyridine ligands of adjacent chains (Figure S3). Finally, the resulting layers are antiparallel stacked, giving place to channels that are filled with anion and solvent molecules, both of them highly disordered (Figure S4).

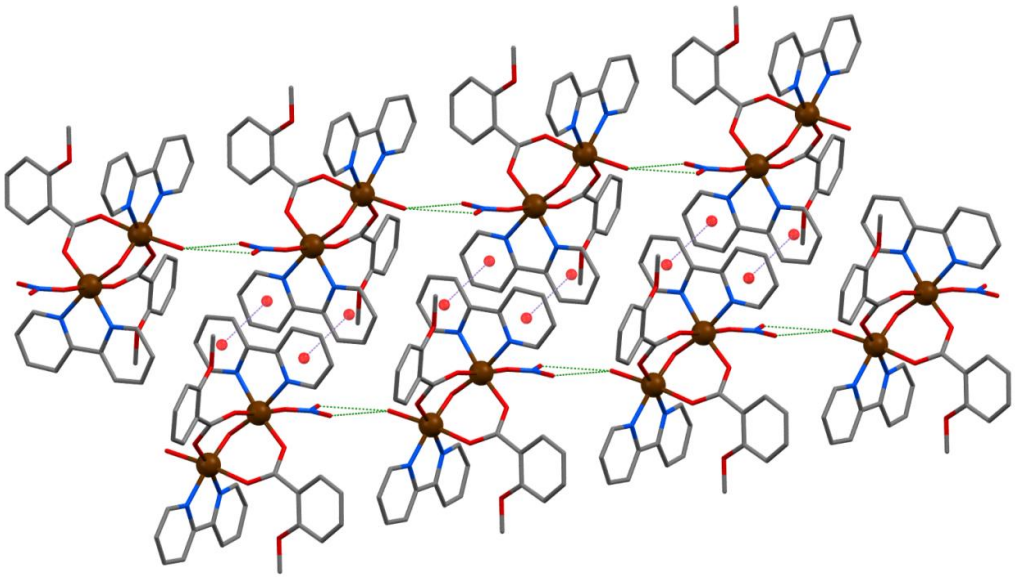

Figure S3. Two adjacent chains of the crystal structure of compound **1**. Hydrogen bonds are represented as green lines and π-π interactions as purple lines. Hydrogen atoms have been omitted for clarity. Color code: Mn^{III}, brown; O, red; C, dark gray; N, blue.

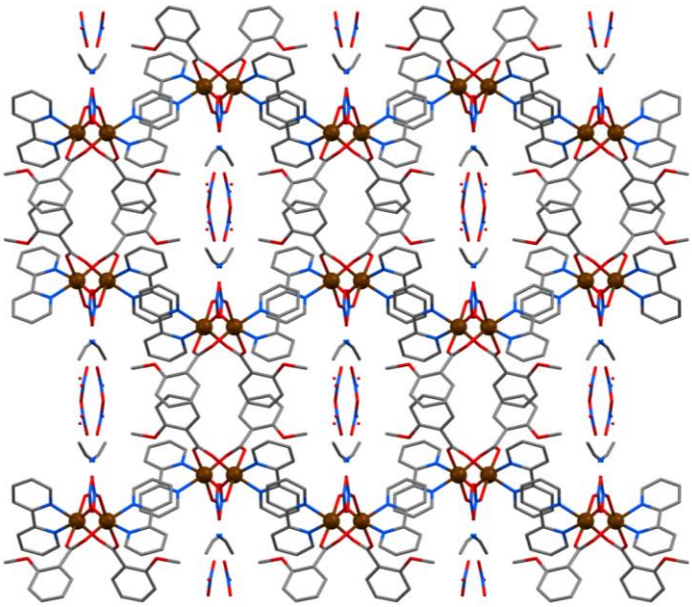

Figure S4. View from the c-axis of the packing of compound **1**. Hydrogen atoms have been omitted for clarity. Color code: Mn^{III}, brown; O, red; C, dark gray; N, blue.

{Mn(bpy)(H_2O)}(μ–2–$MeOC_6H_4COO$)$_2$(μ–O){Mn(bpy)(ClO_4)}]ClO_4·CH_3CN (2·CH_3CN). The crystal structure of compound **2** consists of a cationic complex, a perchlorate ion and an acetonitrile molecule. The most relevant distances and angles are listed in Table S11.

The binuclear complexes are connected through the non-coordinated perchlorate anions, which are bound to the water ligand *via* hydrogen bonds, being extended as a zigzag chain (Figure S5). No interaction is found between different chains. This chain-like structure is also found in an analogous compound reported by V. Gómez *et al.*[181]

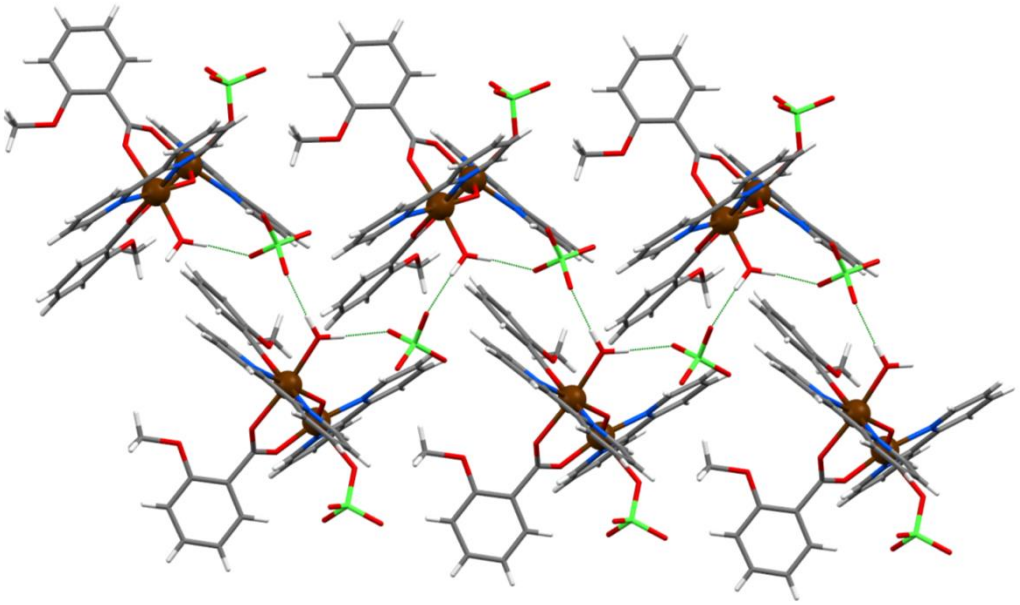

Figure S5. Hydrogen bonds (green line) in the crystal structure of compound **2**. Color code: Mn^{III}, brown; O, red; C, dark gray; N, blue; Cl, green; H, white

[{Mn(bpy)(NO_3)}$_2$(μ-3-$MeOC_6H_4COO$)$_2$(μ-O)]·2 CH_3CN (3·2 CH_3CN). The crystal structure of compound **3** consists of a neutral complex and two molecules of acetonitrile. The most relevant distances and angles are listed in Table S12.

A parallel-displaced π-π interaction may be found between bipyridine ligands of adjacent complexes, whose planes are at 3.2 Å, generating a helicoidally organized chain (Figure S6).

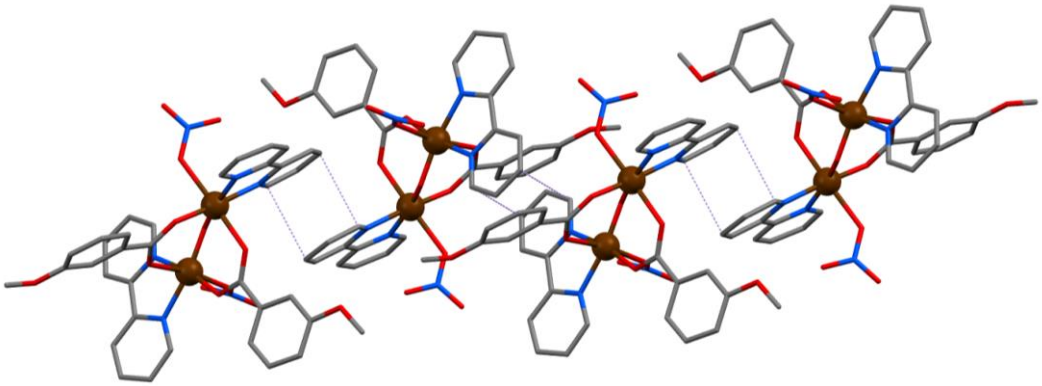

Figure S6. π-π interactions (purple lines) in the crystal structure of compound **3**. Hydrogen atoms have been omitted for clarity. Color code: Mn^{III}, brown; O, red; C, dark gray; N, blue.

[{Mn(bpy)(H_2O)}(μ-3-$MeOC_6H_4COO$)$_2$(μ-O){Mn(bpy)(NO_3)}]NO_3·1/2 H_2O·1/2 CH_3CN (4·1/2 H_2O·1/2 CH_3CN). The crystal structure of compound **4** consists of a cationic complex, a molecule of nitrate and two 50% occupancy molecules of water and acetonitrile. The most relevant distances and angles are listed in Table S13.

There are hydrogen bonds between the coordinated water molecule and the coordinated nitrate anion of the neighbour. Such interactions are extended along a longitudinal axis (Figure S7).

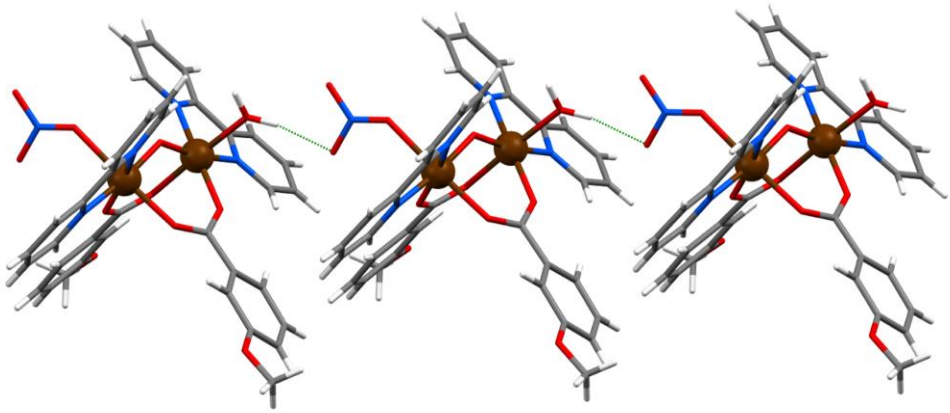

Figure S7. Hydrogen bonds (green lines) in the crystal structure of compound **4**. Color code: Mn^{III}, brown; O, red; C, dark gray; N, blue; H, white.

[{Mn(bpy)(H_2O)}(μ-3-$MeOC_6H_4COO$)$_2$(μ-O){Mn(bpy)(ClO_4)}]ClO_4 (5). Figure 21 shows the crystal structure of the cationic complex of compound **5**. The most relevant distances and angles are listed in Table S13.

As seen for compound **4**, hydrogen bonds are found between the coordinated water molecule and the coordinated perchlorate anion of the neighbor, generating a chain (Figure S8).

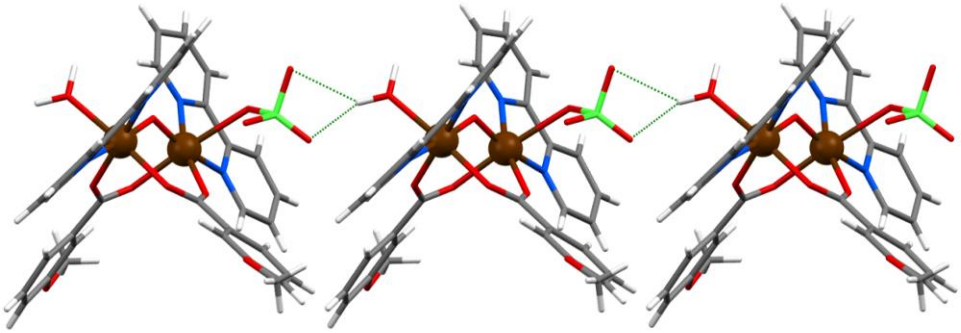

Figure S8. Hydrogen bonds (green lines) in the crystal structure of compound **5**. Color code: Mn^{III}, brown; O, red; C, dark gray; N, blue; Cl, green; H, white.

[{Mn(bpy)(EtOH)}(μ-4-MeOC$_6$H$_4$COO)$_2$(μ-O){Mn(bpy)(ClO$_4$)}]ClO$_4$·1/3 CH$_3$CN ·1/3 H$_2$O (6·1/3 CH$_3$CN ·1/3 H$_2$O). Figure 21 shows the crystal structure of the cationic complex of compound **6**. The most relevant distances and angles are listed in Table S13.

The complexes of compound **6** are situated around the 3-fold symmetry axis, leading to a three dimensional structure with channels that are filled with disordered solvent (Figure S9).

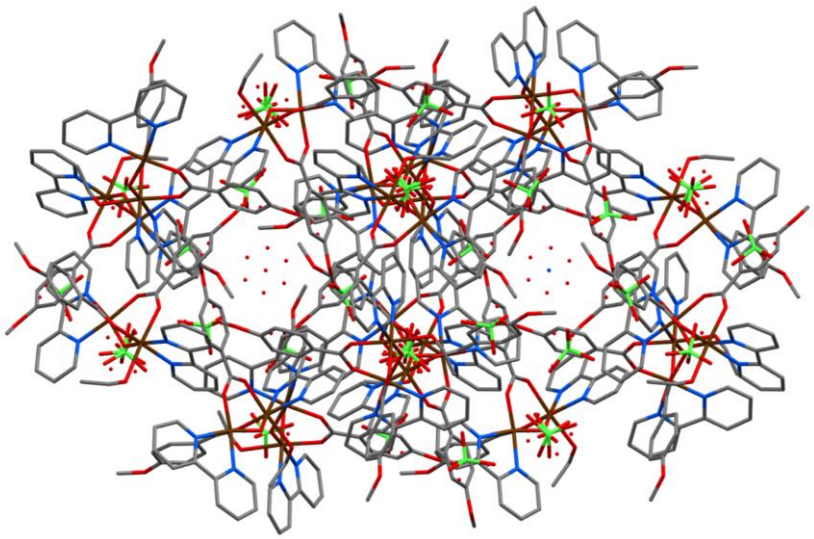

Figure S9. View from the c-axis of the packing of compound **6**. Hydrogen atoms have been omitted for clarity. Color code: Mn^{III}, brown; O, red; C, dark gray; N, blue; Cl, green.

[{Mn(bpy)(EtOH)}(μ-4-^{t}BuC$_6$H$_4$COO)$_2$(μ-O){Mn(bpy)(ClO$_4$)}]ClO$_4$ (7). The crystal structure of compound **7** consists of two different dinuclear complexes (shown in Figure 21)

and two perchlorate anions. The most relevant distances and angles are listed in Table S14. The two complexes are conformational isomers, whose most remarkable difference is the relative orientation of the octahedra, being 79.9 and 67.5º for each complex.

Tables with interatomic distances and angles for compounds 1–7

Table S10. Selected interatomic distances (Å) and angles (deg) for compound **1** with standard deviations in parentheses.

Mn1–O1	1.782(1)	Mn1···Mn1'	3.1412(9)
Mn1–O2	1.970(2)	Mn1–O1–Mn1'	123.5(2)
Mn1–O3	2.167(2)	O1–Mn1–N2	168.48(9)
Mn1–O5 / Mn1'–O6'	2.200(3)	O2–Mn1–N1	170.3(1)
Mn1–N1	2.067(3)	O3–Mn1–O5	174.7(1)
Mn1–N2	2.064(3)	O5–Mn1···Mn1'–O6'	78.1(1)
		O3–C11–C12–C13	36.2(5)

Symmetry codes: (') 1-x,y,1.5-z; (") 1-x,y,2.5-z.

Table S11. Selected interatomic distances (Å) and angles (deg) for compound **2** with standard deviations in parentheses.

Mn1–O1	1.784(4)	Mn2–O1	1.791(4)
Mn1–O3	1.965(4)	Mn2–O6	1.956(4)
Mn1–N2	2.056(5)	Mn2–N3	2.050(5)
Mn1–N1	2.060(5)	Mn2–N4	2.054(5)
Mn1–O5	2.177(4)	Mn2–O2	2.120(4)
Mn1–O8	2.219(4)	Mn2–O9	2.300(4)
O3–Mn1–N2	170.6(2)	O6–Mn2–N3	166.5(2)
O1–Mn1–N1	166.7(2)	O1–Mn2–N4	169.2(2)
O5–Mn1–O8	170.8(2)	O2–Mn2–O9	171.1(2)
Mn1···Mn2	3.139(2)	O5–C29–C30–C35	50.3(9)
Mn1–O1–Mn2	122.8(2)	O2–C21–C22–C27	8(1)
O8–Mn1···Mn2–O9	95.2(2)		

Symmetry codes: (') x,0.5-y,0.5+z.

Table S12. Selected interatomic distances (Å) and angles (deg) for compound **3** with standard deviations in parentheses.

Mn1–O1	1.7866(10)	O2–Mn1–N1	169.65(7)
Mn1–N2	2.0692(18)	O1–Mn1–N2	168.94(7)
Mn1–O2	1.9716(16)	O3–Mn1–O4	170.14(6)
Mn1–N1	2.0478(19)	O4–Mn1···Mn1'–O4'	117.24(8)
Mn1–O3	2.1799(17)	O3–C1'–C2'–C3'	16.9(4)
Mn1–O4	2.2456(19)		
Mn1···Mn1'	3.1628(7)		
Mn1–O1–Mn1'	124.54(12)		

Symmetry codes: (') -x,y,0.5-z

Table S13. Selected interatomic distances (Å) and angles (deg) for compounds **4**, **5** and **6** with standard deviations in parentheses.

	Compound 4	Compound 5	Compound 6
Mn1–O1	1.783(4)	1.7796(16)	1.7659(16)
Mn1–N2	2.058(5)	2.075(2)	2.055(2)
Mn1–O2	1.982(4)	1.9741(17)	1.9571(17)
Mn1–N1	2.081(6)	2.059(2)	2.063(2)
Mn1–O4	2.182(4)	2.1513(17)	2.1441(19)
Mn1–O6	2.171(5)	2.186(2)	2.2995(19)
Mn2–O1	1.779(4)	1.7856(16)	1.7873(16)
Mn2–N4	2.054(6)	2.055(2)	2.086(2)
Mn2–O5	1.964(4)	1.9587(17)	1.9227(18)
Mn2–N3	2.045(5)	2.0452(19)	2.0171(19)
Mn2–O3	2.189(4)	2.1234(17)	2.1218(17)
Mn2–O7	2.262(6)	2.4128(18)	2.483(2)
Mn1···Mn2	3.1555(12)	3.1457(6)	3.1301(6)
Mn1–O1–Mn2	124.7(2)	123.85(9)	123.50(9)
O1–Mn1–N2	169.2(2)	168.70(8)	169.79(8)
O2–Mn1–N1	169.0(2)	171.09(8)	168.09(8)
O6–Mn1–O4	173.36(18)	170.07(8)	172.42(7)
O1–Mn2–N4	168.4(2)	167.79(8)	169.77(8)
O5–Mn2–N3	168.4(2)	163.52(7)	165.92(8)
O3–Mn2–O7	175.09(18)	174.36(7)	166.11(7)
O6–Mn1···Mn2–O7	92.8(2)	102.25(9)	95.50(8)
O3–C1–C2–C3	16.8(9)	16.1(1)	16.8(4)
O4–C8–C9–C10	6.7(9)	5.3(3)	6.6(4)

Symmetry codes: (') x-1,y,z

Table S14. Selected interatomic distances (Å) and angles (deg) for compound **7** with standard deviations in parentheses.

Mn1–O1	1.779(3)	Mn3–O15	1.785(3)
Mn1–N2	2.057(4)	Mn3–N6	2.055(4)
Mn1–O2	1.940(3)	Mn3–O16	1.935(3)
Mn1–N1	2.063(4)	Mn3–N5	2.064(4)
Mn1–O4	2.143(3)	Mn3–O18	2.150(3)
Mn1–O6	2.232(3)	Mn3–O20	2.223(3)
Mn2–O1	1.792(3)	Mn4–O15	1.788(3)
Mn2–N4	2.048(4)	Mn4–N8	2.050(4)
Mn2–O5	1.930(3)	Mn4–O19	1.944(3)
Mn2–N3	2.040(4)	Mn4–N7	2.062(4)
Mn2–O3	2.205(3)	Mn4–O17	2.186(3)
Mn2–O7	2.302(3)	Mn4–O21	2.286(3)
Mn1···Mn2	3.0990(9)	Mn3···Mn4	3.1130(9)
Mn1–O1–Mn2	120.39(14)	Mn3–O15–Mn4	121.24(15)
O1–Mn1–N2	172.44(14)	O16–Mn3–N5	168.80(15)
O2–Mn1–N1	166.70(13)	O15–Mn3–N6	171.38(14)
O4–Mn1–O6	173.00(13)	O18–Mn3–O20	169.39(13)
O1–Mn2–N4	170.79(15)	O15–Mn4–N8	170.78(15)
O5–Mn2–N3	171.24(14)	O19–Mn4–N7	170.04(14)
O3–Mn2–O7	162.62(12)	O17–Mn4–O21	174.97(13)
O6–Mn1···Mn2–O7	79.9(1)	O20–Mn3···Mn4–O21	67.5(1)
O3–C1–C2–C3	0.3(6)	O17–C45–C46–C47	5.7(6)
O4–C8–C9–C10	0.3(6)	O18–C52–C53–C54	8.8(6)

Magnetic properties

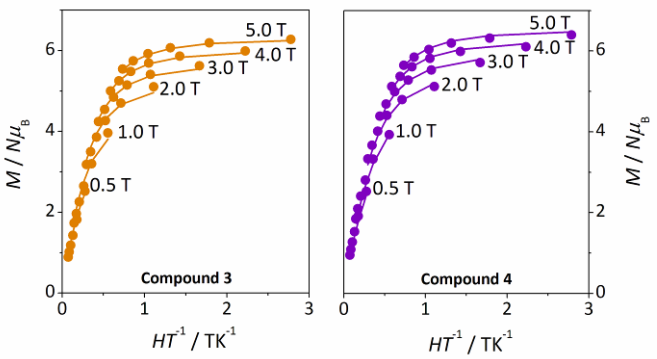

Figure S10. $M/N\mu\beta$ versus HT^{-1} plots for compounds **3** and **4**. The solid lines are the best fits of the experimental data.

Appendix III: Supplementary Material for Mn^{II} Compounds

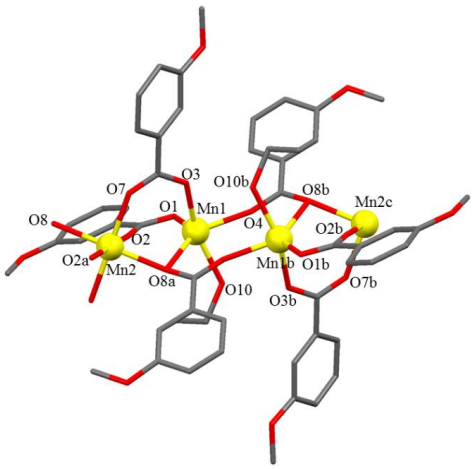

Figure S11. Crystal structures for manganese(II) 3-methoxybenzoate.

Table S15. Selected interatomic distances (Å) and angles (º) with standard deviations in parentheses for manganese(II) 3-methoxybenzoate.

Mn1–O4	2.123(2)	O4–Mn1–O8	132.63(8)	O2–Mn2–O2a	180.000(1)
Mn1–O3	2.129(2)	O1–Mn1–O8	124.55(9)	O7–Mn2–O7a	180.0
Mn1–O1	2.151(2)	O4–Mn1–O1	101.62(9)	O8–Mn2–O8a	180.0
Mn1–O10	2.222(2)				
Mn1–O8	2.283(2)	O3–Mn1–O1	104.1(1)	Mn2–O8–Mn1	98.24
Mn2–O2	2.129(2)	O3–Mn1–O8	92.90(8)		
Mn2–O7	2.145(2)	O3–Mn1–O4	84.84(9)		
Mn2–O8	2.184(2)	O10–Mn1–O1	93.2(1)		
Mn2···Mn1	3.378	O10–Mn1–O4	81.78(9)		
Mn1···Mn1b	3.592(1)	O10–Mn1–O8	85.32(8)		

Symmetry codes: (a) 1-x,-y,1-z; (b) -x,-y,1-z; (c) x-1,y,z.

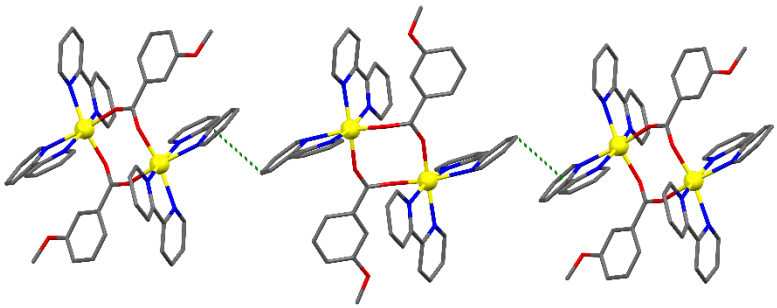

Figure S12. π-Stacking (green lines) between bpy ligands in the crystal structure of compound **9**. Color code: Mn, yellow; C, gray; O, red; N, blue.

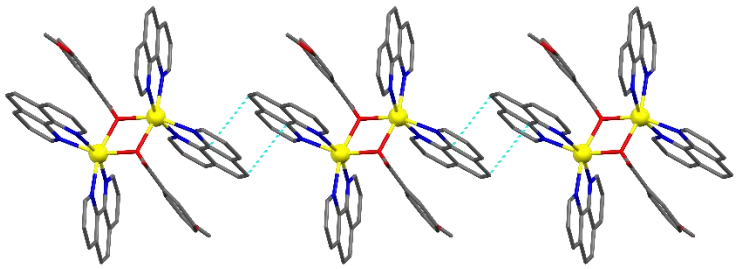

Figure S13. π-Stacking (cyan lines) between bpy ligands in the crystal structure of compound **12**. Color code: Mn, yellow; C, gray; O, red; N, blue.

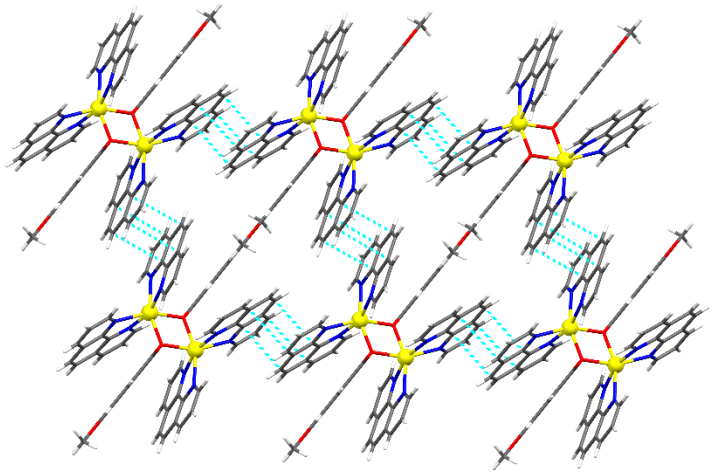

Figure S14. π-Stacking (cyan lines) between bpy ligands in the crystal structure of compound **14**. Color code: Mn, yellow; C, gray; O, red; N, blue; H, white.

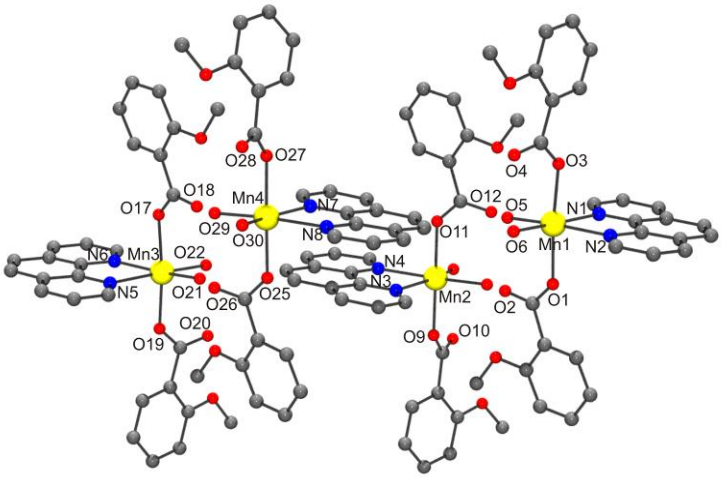

Figure S15. Crystal structure for compound **19**.

Table S16. Selected interatomic distances (Å) and angles (º) with standard deviations in parentheses for the mononuclear compound **19**.

Mn1–O1	2.154(3)	Mn3–O19	2.149(3)
Mn1–O3	2.156(3)	Mn3–O21	2.161(2)
Mn1–O5	2.164(2)	Mn3–O17	2.163(3)
Mn1–O6	2.179(2)	Mn3–O22	2.182(2)
Mn1–N2	2.266(3)	Mn3–N6	2.268(3)
Mn1–N1	2.285(3)	Mn3–N5	2.291(3)
O1–Mn1–O3	174.78(9)	O19–Mn3–O17	173.71(8)
O5–Mn1–N2	166.01(9)	O21–Mn3–N6	166.46(9)
O6–Mn1–N1	172.82(10)	O22–Mn3–N5	172.23(10)
Mn2–O9	2.150(3)	Mn4–O27	2.152(3)
Mn2–O11	2.159(3)	Mn4–O25	2.165(2)
Mn2–O13	2.1827(19)	Mn4–O30	2.1747(19)
Mn2–O14	2.183(2)	Mn4–O29	2.184(2)
Mn2–N3	2.294(3)	Mn4–N7	2.284(3)
Mn2–N4	2.303(2)	Mn4–N8	2.311(2)
O9–Mn2–O11	176.49(10)	O27–Mn4–O25	175.41(9)
O13–Mn2–N3	158.77(9)	O30–Mn4–N7	158.68(9)
O14–Mn2–N4	169.95(9)	O29–Mn4–N8	170.22(9)

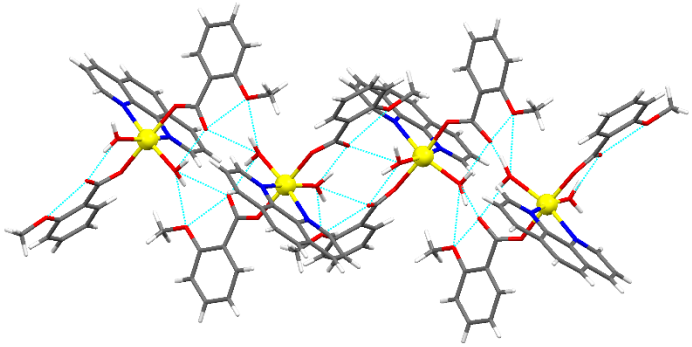

Figure S16. H bonds in the crystal structure of **19**.

Appendix IV: Supplementary Material for Heterometallic Compounds

Crystal Structures

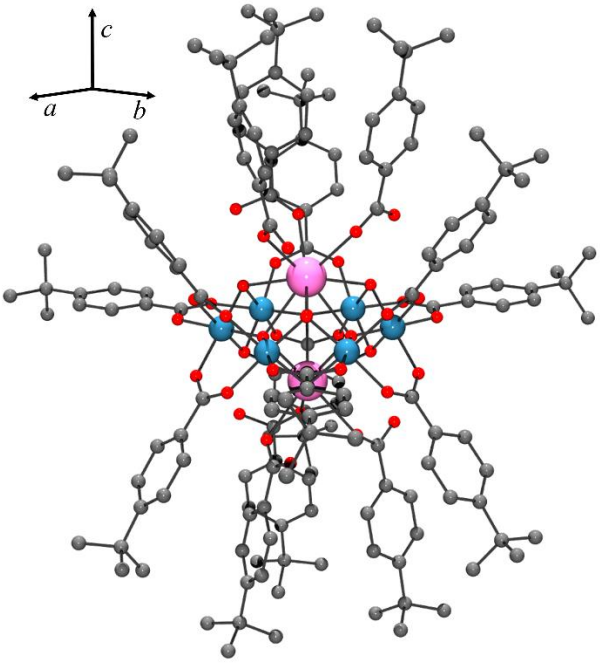

Figure S17. Crystal structure of compound **23**, with H atoms omitted for clarity. Color code: Mn^{IV}, blue; Sr, pale pink; O, red; C, gray.

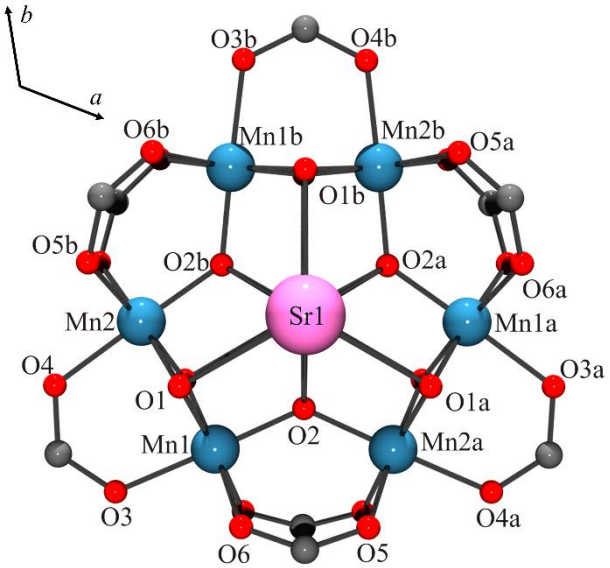

Figure S18. *c*-axis view of the crystal structure of compound **23**. The substituent 4-^{t}BuC$_6$H$_4$- has been omitted for better clarity.

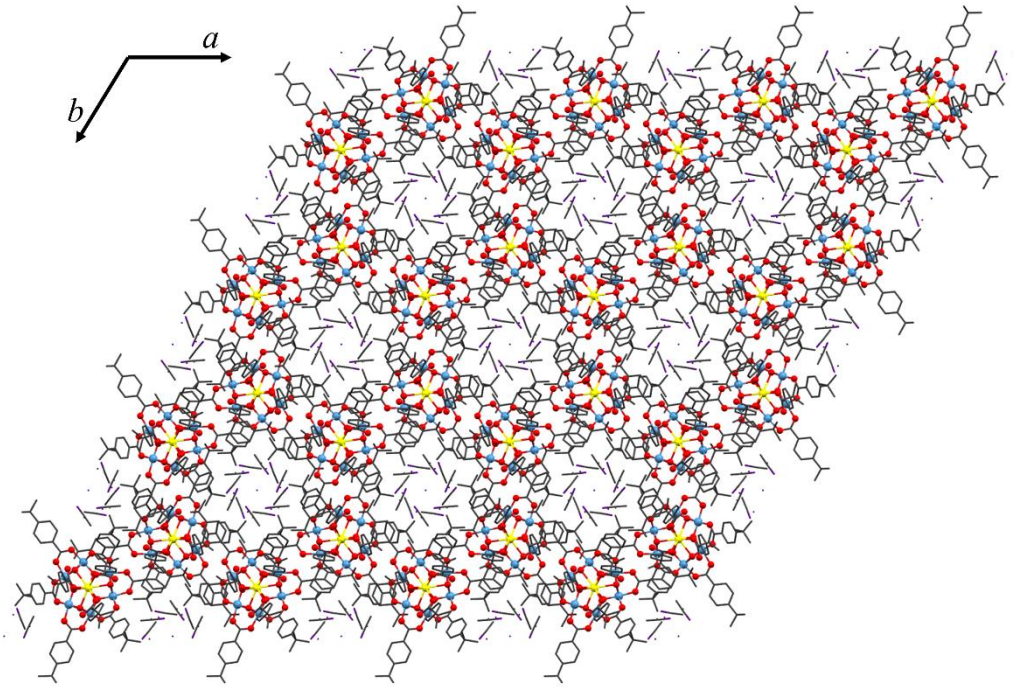

Figure S19. View from the *c*-axis of the packing of compound **22**. H atoms have been omitted for clarity. Color code: Mn^{IV}, blue; Ca, yellow; O, red; C, dark gray; N, purple.

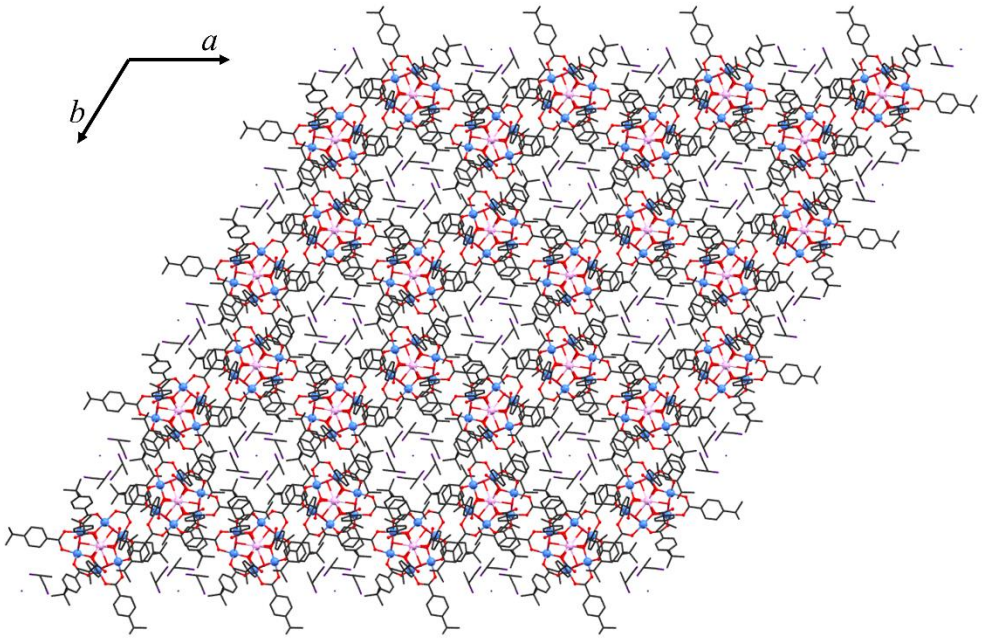

Figure S20. View from the *c*-axis of the packing of compound **23**. H atoms have been omitted for clarity. Color code: Mn^{IV}, blue; Sr, pink; O, red; C, dark gray; N, purple.

Magnetic Properties

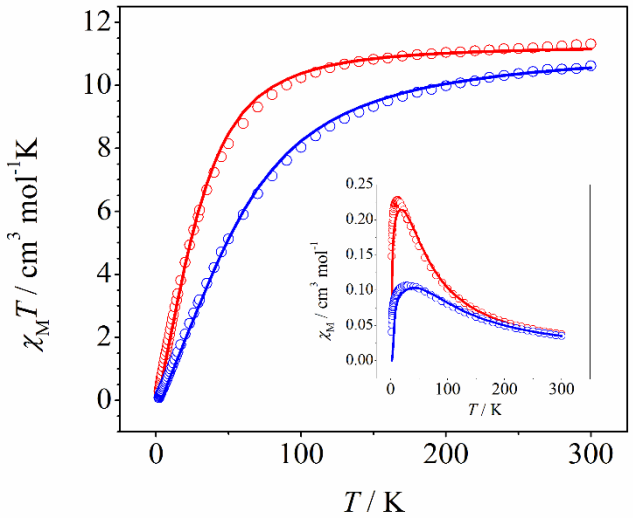

Figure S21. $\chi_M T$ versus T plots and χ_M versus T (inset) for compounds **22** (red) and **23** (blue); the solid line corresponds to the fit to the experimental data considering J_3 and $J_4 = 0$ (Fit 1).

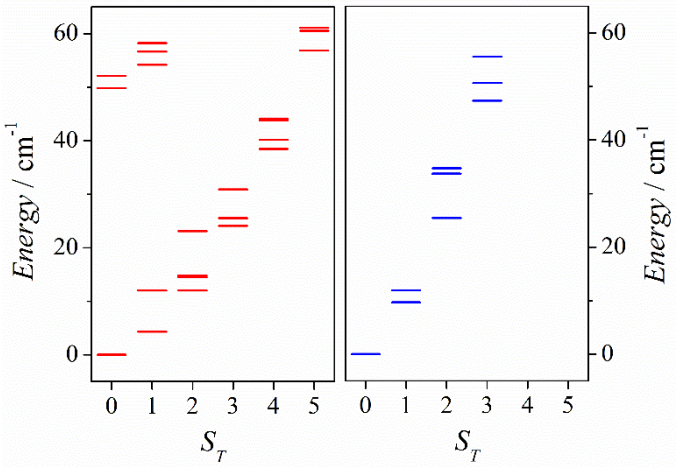

Figure S22. Diagram of first energy levels (up to 60 cm^{-1}) for S_T spin values at zero field calculated with the parameters listed in Table 1.3.3 (fit 2) for compounds **22** (red) and **23** (blue).

Theoretical Calculations

Table S17. (*top*) Relative energies (in cm^{-1}) for the calculated spin distributions in the Mn_6M_2 wheels. (*bottom*) Schematic representation of spin distributions into Mn ions (red and blue lines show short and large Mn···Mn distances, respectively).

E / cm^{-1}	Mg^{2+} *model**	22 (Ca^{2+}) *crystal*	Sr^{2+} *model**	23 (Sr^{2+}) *crystal*	M^{2+} absent *model**
ls1	250.9	55.8	-50.7	-132.9	-224.6
ls2	555.8	142.9	-66.8	-231.0	-276.9
ls3	506.9	280.3	122.1	114.7	203.9
ls4	**-159.4**	**-209.8**	**-268.8**	-455.7	**-856.8**
ls5	162.1	29.0	-78.7	-174.3	-336.0
ls6	992.3	247.0	-51.2	-249.9	-85.8
ls7	220.8	-97.0	-258.9	**-510.5**	-752.0
ls8	597.2	151.3	-51.7	-196.5	-162.0

* Hypothetical isoelectronic compounds using the geometry of **22**, but replacing Ca^{2+} ions with Mg^{2+} or Sr^{2+} ones or just removing the Ca^{2+} ions.

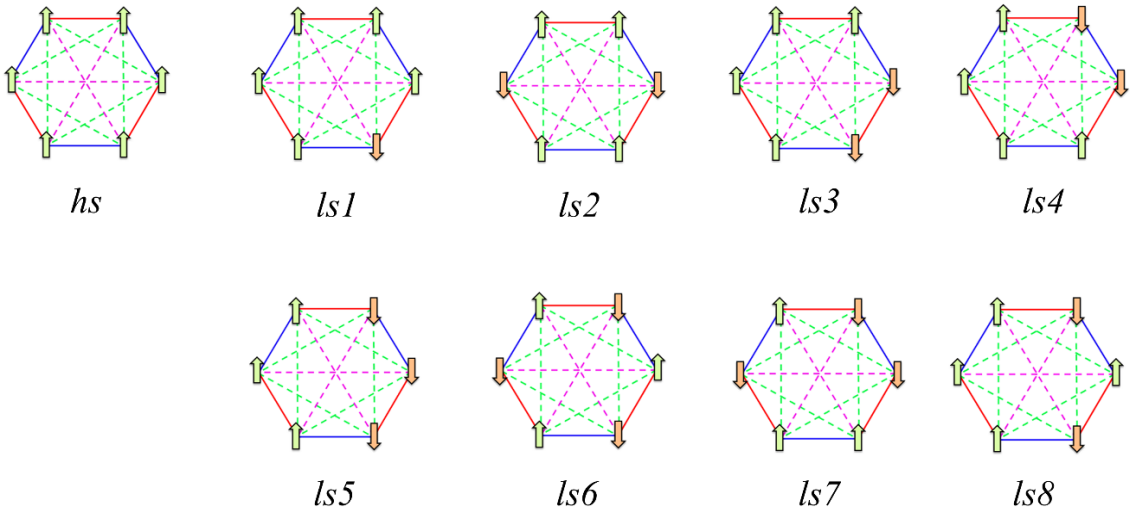

Appendix V: Supplementary Material for Tetranuclear Compounds

Crystal Structures

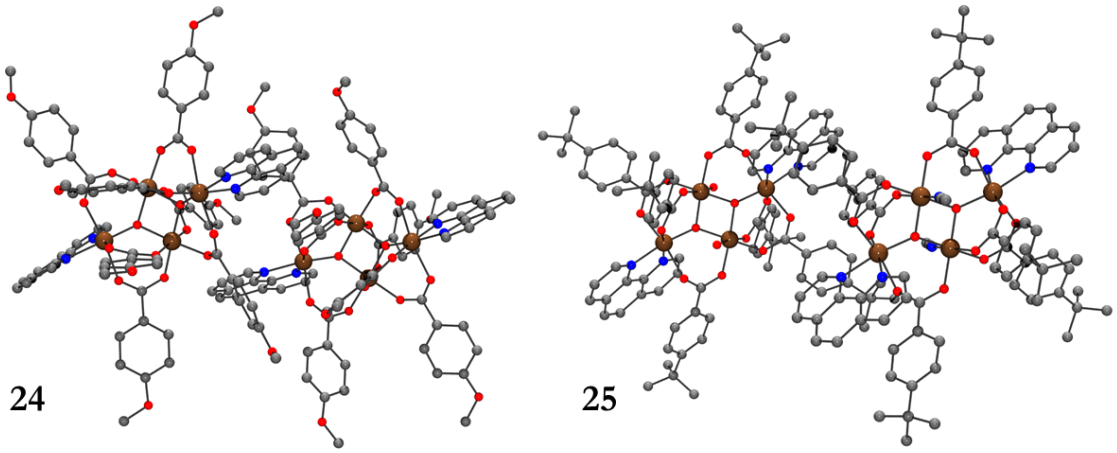

Figure S23. Crystal structure of the cationic complex of **24** and **25**. H atoms have been omitted for better clarity. Color code: Mn^{III}, brown; C, gray; N, blue; O, red.

Table S18. x, y, and z axes length and the elongated ($\perp$) and rhombic distortion (ρ) of each Mn ion for compounds **24** and **25**.

Compound	Mn centre	x / Å	y / Å	z / Å	Δ / %	ρ / %
24	Mn1	3.895	4.019	4.267	7.8	3.2
	Mn2	3.87	3.87	4.319	11.6	0.0
	Mn3	3.862	3.843	4.414	14.6	–0.5
	Mn4	3.883	4.035	4.297	8.5	3.9
	Mn5	3.827	3.846	4.283	11.6	0.5
	Mn6	3.83	3.868	4.449	15.6	1.0
	Mn7	3.898	4.021	4.334	9.5	3.2
	Mn8	3.923	3.98	4.36	10.3	1.5
25	Mn1	3.909	3.947	4.342	10.5	1.0
	Mn2	3.776	3.854	4.504	18.1	2.1
	Mn3	3.898	3.959	4.305	9.6	1.6
	Mn4	3.828	3.848	4.36	13.6	0.5

$\perp = (z - \overline{xy}) \,/\, \overline{xy}, \overline{xy} = (x + y)/2$; $\rho = (y - x) \,/\, x$

Magnetic Properties

Compound	Parameters	Constraints and restraints: Fit 1 $J_2 = J_3$ $D_{Mn} = 0$	Fit 2 $J_2 = J_3$ $D_{Mn} > -4.9$ cm^{-1}	Fit 3 $J_2 \neq J_3$ $D_{Mn} = 0$
24	$2J_1$ / cm^{-1}	–18.6	–18.2	–46.6
	$2J_2$ / cm^{-1}	–13.3	–13.4	–13.9
	$2J_3$ / cm^{-1}	–13.3	–13.4	–3.1
	D_{Mn} / cm^{-1}	0	–3.2	0
25	$2J_1$ / cm^{-1}	–17.9	–72.2	–50.1
	$2J_2$ / cm^{-1}	–11.5	–5.8	–13.3
	$2J_3$ / cm^{-1}	–11.5	–5.8	–6.3
	D_{Mn} / cm^{-1}	0	–4.9	0

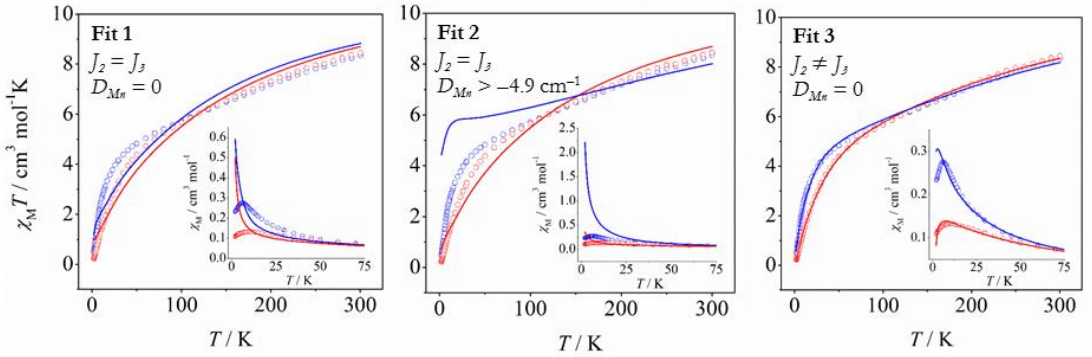

Figure S24. Results from different fits of the $\chi_M T$ versus T plots of compounds **24** (red) and **25** (blue). The solid lines correspond to the fit to the experimental data considering $J_2 = J_3$, omitting or including D_{Mn} (Fit 1 and 2, respectively), and considering $J_2 \neq J_3$ (Fit 3). The molecular weight of **25** was referred to one Mn_4 unit, considering an average formula between the two entities.

Table S19. Comparison of the average core parameters, distances (Å) and angles (º), for the $[Mn^{III}_2O_2]^{8+}$ subunits of the several $[Mn^{III}_4O_2]^{8+}$ compounds.

Compound	$Mn_c \cdots Mn_c$	Mn_c–O_b–Mn_c	Mn_c–O_b–O_b–Mn_c	$2J_1$ / cm^{-1}	*Ref.*
24	2.849	97.1	168	–45.5	This work
25	2.881	99.0	180	–43.0	This work
$[Mn_4O_2(NO_3)(O_2CEt)_6(bpy)_2]^+$	2.847	97.2	169	–33.0	256
$[Mn_4O_2(O_2CEt)_7(bpya)_2]^+$	2.871	97.2	170	–51.4	260
$[Mn_4O_2(O_2CMe)_7(bpy)_2]^+$	2.848	96.3	167	–47.0	246
$[Mn_4O_2(O_2CMe)_7(pic)_2]^-$	2.842	96.6	165	–49.2	259
$[Mn_4O_2(py)_2(O_2CMe)_6(dbm)_2]$	2.875	99.1	180	–29.8	327
$[Mn_4O_2(O_2CPh)_6(dpm)_2]$	2.841	98.5	179	–55.0	247

Abbreviations: bpya = bis(2-pyridyl)amine, bpy = 2,2'-bipyridine, pic = picolinate, py = pyridine, dbmH = dibenzoylmethane, dpmH = dipivaloylmethane; see Eq. 12 and Figure 68 for the J assignment.

Table S20. Comparison of the average core parameters, distances (Å) and angles (º), for the $[Mn_2O(RCOO)_2]^{2+}$ subunits of the several $[Mn^{III}_4O_2]$ compounds.

Compound	$Mn_c\cdots Mn_t$	$Mn_c–O_b–Mn_t$	$L–Mn_c\cdots Mn_t–L$	$2J_2$ / cm^{-1}	*Ref.*
24	3.307	124.4	87.4	– 15.1/–4.4	This work
25	3.256	121.0	97.8	– 14.7/–8.2	This work
$[Mn_4O_2(NO_3)(O_2CEt)_6(bpy)_2]^+$	3.258	121.8	74.1	–3.4	256
$[Mn_4O_2(O_2CEt)_7(bpya)_2]^+$	3.307	126.1	92.6	–6.6	260
$[Mn_4O_2(O_2CMe)_7(bpy)_2]^+$	3.301	123.7	82.5	–15.6	246
$[Mn_4O_2(O_2CMe)_7(pic)_2]^-$	3.311	125.0	82.3	–10.6	259
$[Mn_4O_2(py)_2(O_2CMe)_6(dbm)_2]$	3.308	123.2	105.1	–10.0	327
$[Mn_4O_2(O_2CPh)_6(dpm)_2]$	3.255	120.1	70	–0.8	247

$L–Mn_c\cdots Mn_c–L$ = torsion angle between the two Jahn-Teller axes. Abbreviations: bpya = bis(2-pyridyl)amine, bpy = 2,2'-bipyridine, pic = picolinate, py = pyridine, dbmH = dibenzoylmethane, dpmH = dipivaloylmethane. See Eq. 12 and Figure 68 for the *J* assignment.

Table S21. Comparison of the average core parameters, distances (Å) and angles (º), for the $[Mn_2O(RCOO)]$ unit of the several $[Mn^{III}_4O_2]$ complexes.

Compound	$Mn_c\cdots Mn_t$	$Mn_c–O_b–Mn_t$	$2J_3$ / cm^{-1}	*Ref.*
24	3.377	129.2	–15.1/–4.4	This work
25	3.366	126.1	–14.7/–8.2	This work
$[Mn_4O_2(NO_3)(O_2CEt)_6(bpy)_2]^+$	3.34	126.4	–3.4	256
$[Mn_4O_2(O_2CEt)_7(bpya)_2]^+$	3.444	130.7	–6.6	260
$[Mn_4O_2(O_2CMe)_7(bpy)_2]^+$	3.378	130.2	–15.6	246
$[Mn_4O_2(O_2CMe)_7(pic)_2]^-$	3.396	129.7	–10.6	259
$[Mn_4O_2(py)_2(O_2CMe)_6(dbm)_2]$	3.398	128.6	–10.0	327
$[Mn_4O_2(O_2CPh)_6(dpm)_2]$	3.362	126.0	–0.8	247

Abbreviations: bpya = bis(2-pyridyl)amine, bpy = 2,2'-bipyridine, pic = picolinate, py = pyridine, dbmH = dibenzoylmethane, dpmH = dipivaloylmethane; see Eq. 12 and Figure 68 for the *J* assignment.

Appendix VI: Supplementary Material for the Dodecanuclear Compound

Table S22. Selected interatomic distances in Å for **26**.

Mn···Mn distances		**Mn–O distances**			
Mn^{IV}···Mn^{IV}		Mn1–O1	1.8872(19)	Mn5–O4	1.918(2)
Mn6···Mn6a	2.8110(8)	Mn1–O7	1.986(2)	Mn5–O18	2.003(2)
Mn6···Mn7	2.8330(6)	Mn1–O9	2.145(2)	Mn5–O20	2.078(3)
Mn7···Mn7a	2.8187(8)	Mn2–O1	1.8881(18)	Mn6–O2	1.8683(18)
Mn7···Mn6a	2.9268(6)	Mn2–O2	1.8819(19)	Mn6–O1	1.8733(19)
Mn6···Mn7a	2.9268(6)	Mn2–O8	1.927(2)	Mn6–O5	1.8998(18)
		Mn2–O13	1.939(2)	Mn6–O12	1.911(2)
Mn^{III}···Mn^{IV} (double-oxo bridge)		Mn2–O10	2.165(2)	Mn6–O6	1.9143(19)
Mn2···Mn6	2.7612(6)	Mn2–O11	2.216(2)	Mn7–O4	1.865(2)
Mn4···Mn7	2.7624(6)	Mn3–O3	1.886(2)	Mn7–O3	1.8813(19)
		Mn3–O2	1.8869(19)	Mn7–O6	1.9041(19)
Mn^{III}···Mn^{IV} (single-oxo bridge)		Mn3–O15	1.963(2)	Mn7–O22	1.907(2)
Mn1···Mn6	3.4728	Mn3–O14	1.977(2)	Mn7–O5	1.9190(19)
Mn3···Mn6	3.4428(6)	Mn3–O24	2.165(2)		
Mn3···Mn7	3.4483(6)	Mn3–O23	2.178(2)		
Mn5···Mn7	3.4876	Mn4–O4	1.875(2)		
		Mn4–O3	1.904(2)		
Mn^{III}···Mn^{III}		Mn4–O17	1.935(2)		
Mn1···Mn2	3.3405	Mn4–O16	1.944(2)		
Mn2···Mn3	3.4060(5)	Mn4–O19	2.171(2)		
Mn3···Mn4	3.4147(7)	Mn4–O21	2.215(2)		
Mn4···Mn5	3.3491				

Symmetry codes: (a) -x+1/2,y,-z+1/2

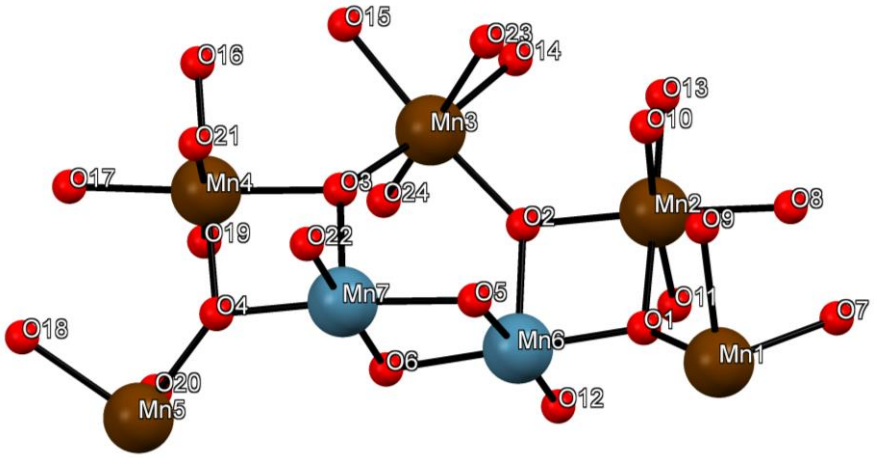

Figure S25. Asymmetric unit of the crystal structure for compound **26**. Carbon and hydrogen atoms have been omitted for clarity. Color code: Mn^{III}, brown; Mn^{IV}, blue; O, red.

Table S23. Selected interatomic distances in Å for **26**.

Label	x / Å	y / Å	z / Å	Δ / %	ρ / %
Mn1	3.873	3.873	4.290	10.8	0.0
Mn2	3.809	3.827	4.381	14.7	0.5
Mn3	3.850	3.863	4.343	12.6	0.3
Mn4	3.810	3.848	4.386	14.5	1.0
Mn5	3.921	3.921	4.156	6.0	0.0
Mn6*	3.778	3.788	3.811	0.7	0.3
Mn7*	3.784	3.797	3.811	0.5	0.3

* Mn^{IV} ions; $\Delta = (z - \overline{xy})/\overline{xy}$, $\overline{xy} = (x + y)/2$; $\rho = (y - x)/x$.

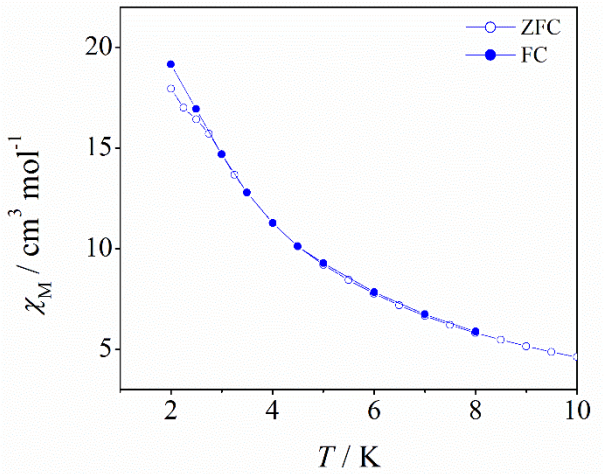

Figure S26. Zero-field-cooled (ZFC) and field-cooled (FC) magnetic susceptibilities versus temperature for compound **26**.

Appendix VII: Supplementary Material for Catalase-Biomimetic Mn-SiO_2 Materials

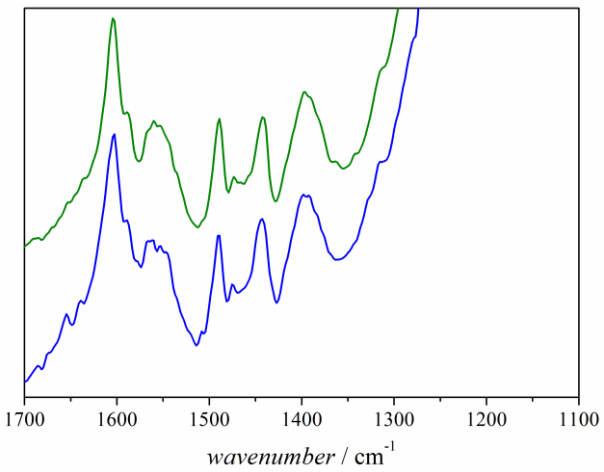

Figure S27. Infrared spectra (range 1700–1100 cm^{-1}) of material $[Mn_2O]_{0.5}$@SiO_2 synthesized from compounds **1** (blue line) and **2** (green line).

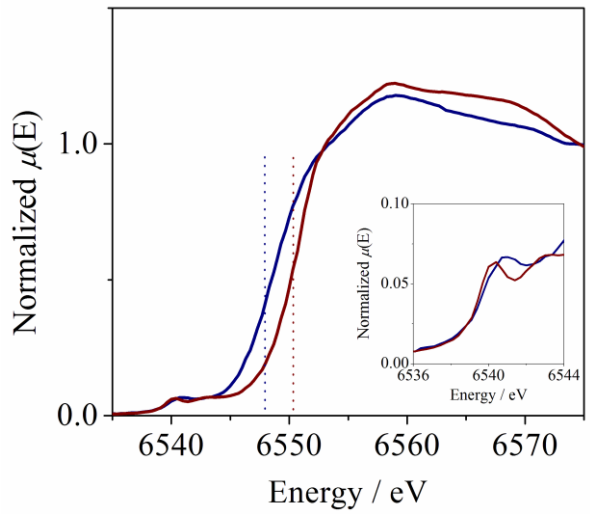

Figure S28. Mn XANES of compound **1** (blue) and material $[Mn_2O]_{0.5}$@SiO_2 (red); dash lines pointing edge positions approximately at the inflexion point; insert: zoom on the pre-edge part of the absorption.

Table S24. Mn 3s doublet splitting results for different Mn complexes.

Formula	Mn center	Mn ^5S / eV	Mn ^7S / eV	ΔMn 3s / eV
$[Mn_2O]_{0.5}$@SiO_2	Mn^{III}_2	88.6	83.0	5.6
$[Mn_3(MeOC_6H_4COO)(bpy)_2]$ (**17**)	Mn^{II}_3	89.9	83.7	6.2
$[Mn_2O(bpy)(H_2O)(2\text{-}MeOC_6H_4COO)_2(NO_3)](NO_3)$ (**1**)	Mn^{III}_2	89.2	83.6	5.6
$[Mn_2O_2(bpy)_4](ClO_4)_3$ [a]	$Mn^{III/IV}$	90.6	85.2	5.4
$[Mn^{IV}_6Ca_2O_9(4\text{-}^tBuC_6H_4COO)10(4\text{-}^tBuC_6H_4COOH)_5]$ (**22**)	Mn^{IV}_6	89.7	84.8	4.9

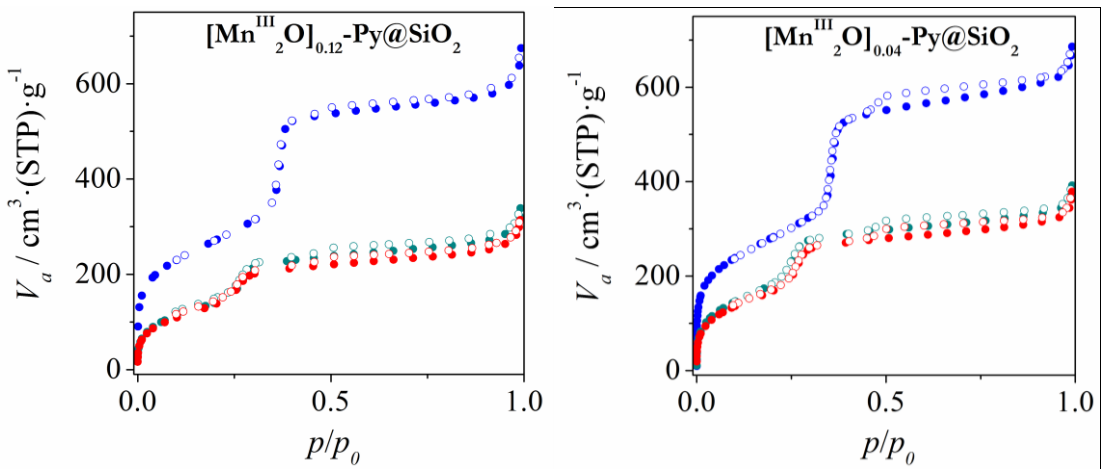

Figure S29. N_2 adsorption (full circles) and desorption (empty circles) isotherms at 77 K of materials SiO_2-Ex (blue), SiO_2-TMA (dark cyan) and $[Mn_2O]_x$-Py@SiO_2 (red) with x = 0.12 and 0.04.

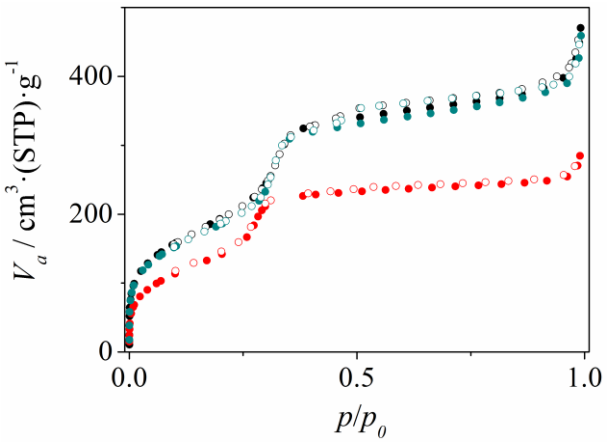

Figure S30. N_2 adsorption (full circles) and desorption (empty circles) isotherms at 77 K for $[Mn_2O]_{0.5}$@SiO_2 (red), the control experiment (no TEOS) (black), and the "coated" material (1320 mM of TEOS) (dark cyan).

TGA analysis

The thermogravimetric analysis (TGA) of material **$[Mn_2O]_{0.5}$@SiO_2** shows two main weight losses between 200 and 450 °C (Figure S31). The weight loss in this range of temperature is 21.9% and can be assigned to the decomposition of the ligands of the Mn complex and of the TMA^+ ions, and to the condensation of silanol groups; which are expected to account for 20.5%, 0.41% and ~1% from the empiric formula, respectively. The loss of TMA^+ ions is expected around 220 °C (observed in the TGA of SiO_2-TMA), but the contribution is so small that it cannot be noticed. In contrast, the condensation of silanol groups is extended from 200 to 1100 °C, showing no specific peak in the TG derivative though it is observed in the TGA of the extracted support (SiO_2-Ex). The experimental residual mass at 1100°C is 72.0% and it is also consistent with the calculated value (72.2%) considering that all Mn(III) ions are converted to MnO_2 in aerobic conditions. Moreover, the addition of the weight loss coming from the evaporation of water molecules (25–200 °C) and the condensation of silanol groups is in accord with the amount of water found from the elemental analyses (6.9%). Therefore, the highest contribution to the weight loss corresponds to Mn complex ligands.

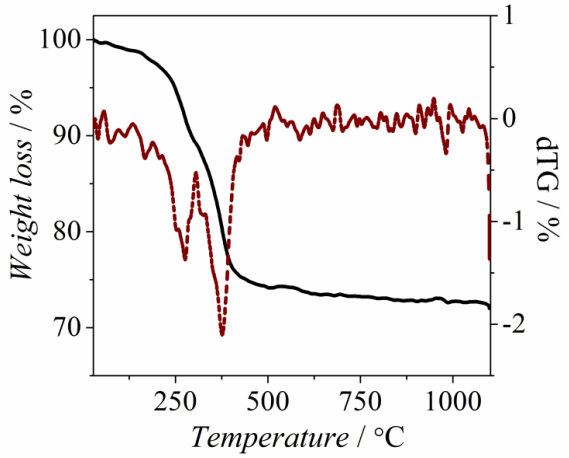

Figure S31. Weight loss (black line) and derivative of weight loss (red line) versus temperature for material $[Mn_2O]_{0.5}@SiO_2$.

For material **$[Mn_2O]_{0.1}@SiO_2$**, the weight loss versus temperature plot (shown in Figure S32) is rather different. There is a much more pronounced change centered at ~230 °C, mainly attributed to the decomposition of TMA^+ ions. The Mn-complex content is much smaller than in the previous case; hence, the weight loss corresponding to the decomposition of the ligands of the Mn complex is consistently much smaller. The experimental residual mass at 1100°C is 79.5% and it is also consistent with that calculated (78.7%) considering that all Mn(III) ions are converted to MnO_2 in aerobic conditions.

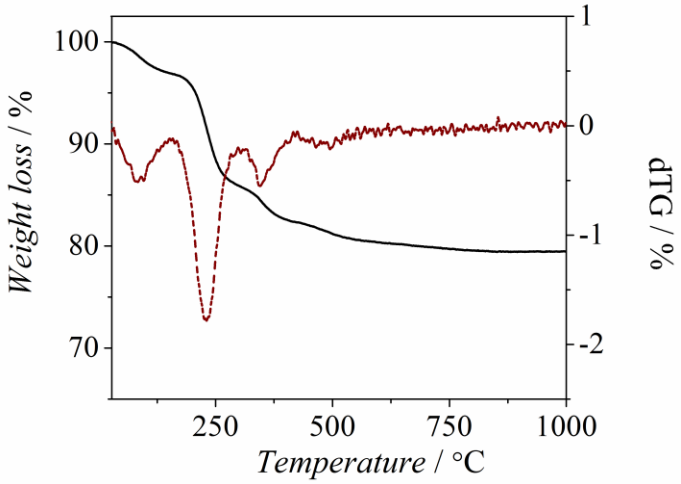

Figure S32. Weight loss (black line) and derivative of weight loss (red line) versus temperature for material $[Mn_2O]_{0.1}@SiO_2$.

The TG for material **Py@SiO_2-TMA** (Figure S33) shows to main weight losses: that in the range 180–300 °C (of ~10%), assigned to the TMA^+ ions; and that extended from 300 to 600 °C (of ~12%), assigned to the pyridyl function. Note that, additionally, the condensation of silanol groups takes place from 200 to 1000 °C and will correspond to a ~5% of the total

weight loss. The theoretical residual mass, which is 77.4%, has been calculated assuming that the Si atoms of the pyridyl function are converted to SiO_2 under aerobic conditions and at 1000 °C, and it is close to the that experimentally found (74.8%).

The TG for materials **$[Mn_2O]_x$-Py@SiO_2** show two main weight losses between 150 and 650 °C. The first one, which is centered around 250 °C, could be assigned to the decomposition of TMA^+ ions. However, this peak shifts from 229 to 252 °C upon increasing the amount of compound inserted, suggesting the addition of some other contribution in the weight loss. The weight loss between 300–650 °C corresponds to the decomposition of the Mn complex ligands and the 4-pyridylethyl groups. Contrary to that for Py@SiO_2, which exhibits two broad peaks, the TG derivatives in this range of temperatures show just one peak that shifts from 467 (for $x = 0.04$) to 431 °C (for $x = 0.21$) upon increasing the amount of Mn complex. Moreover, the decomposition of the 4-pyridyl groups is affected by the presence of the Mn compound, since the peak centered at 537 °C in the TG derivative of material Py@SiO_2-TMA decreases when the concentration of Mn compound increases until disappearing when $x = 0.21$. The residual mass calculated from the empirical formula ($x = 0.04$, 76.7%; $x = 0.12$, 73.9%; $x = 0.21$, 74.7%) are in accord with those found experimentally ($x = 0.04$, 76.0%; $x = 0.12$, 75.0%; $x = 0.21$, 72.4%), assuming that all Mn^{III} ions are oxidized to MnO_2 and all Si atoms are converted to SiO_2 at 1000 °C under aerobic conditions.

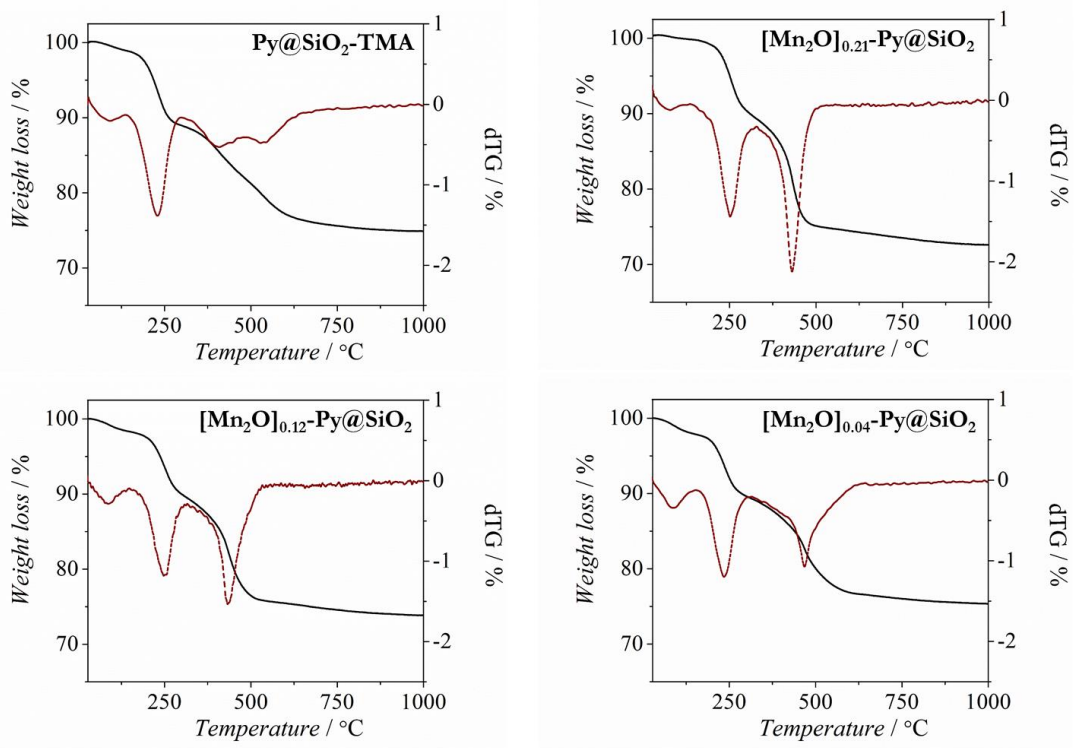

Figure S33. Weight loss (black line) and derivative of weight loss (red line) versus temperature for materials Py@SiO_2-TMA and $[Mn_2O]_x$-Py@SiO_2 with $x = 0.21$, 0.12, and 0.04.

Appendix VIII: Supplementary Material for Mn-SiO_2 Materials with Hydrophobic Functions

Synthesis and Characterization of Supports

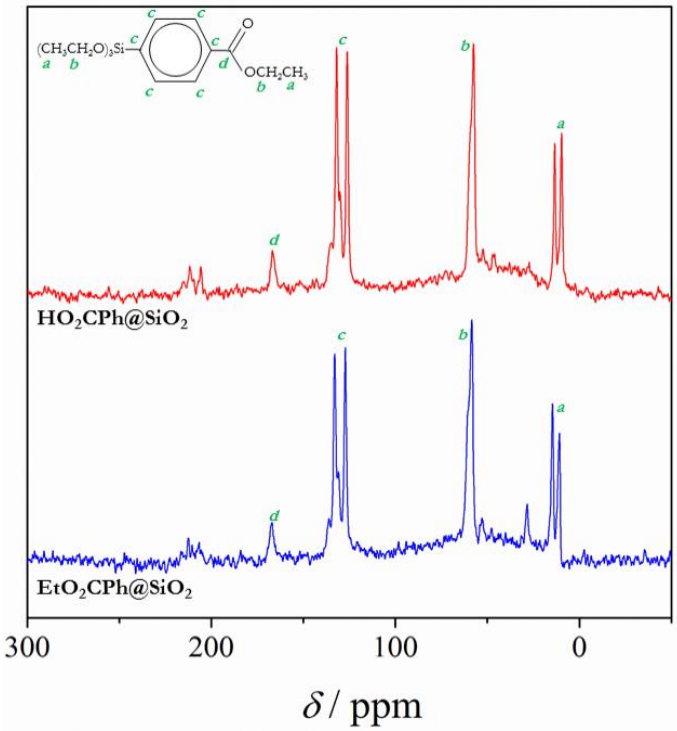

Figure S34. Solid ^{13}C CPMAS spectra for material $Et_2O_2CPh@SiO_2$, and for the failed attempt to obtain material $HO_2CPh@SiO_2$ under moderate conditions (acid hydrolysis in acetone-water media at 60 ºC).

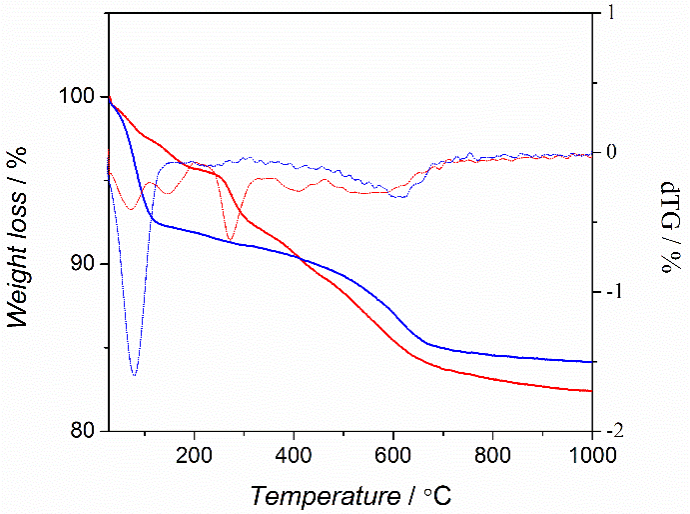

Figure S35. Weight loss (solid line) and derivative of weight loss (dash line) versus temperature for materials $EtO_2CPh@SiO_2$ (red) and $HO_2CPh@SiO_2$ (blue).

Insertion of the Mn^{IV}-Ca Compound (22) in $C_3@SiO_2$ and $Ph@SiO_2$

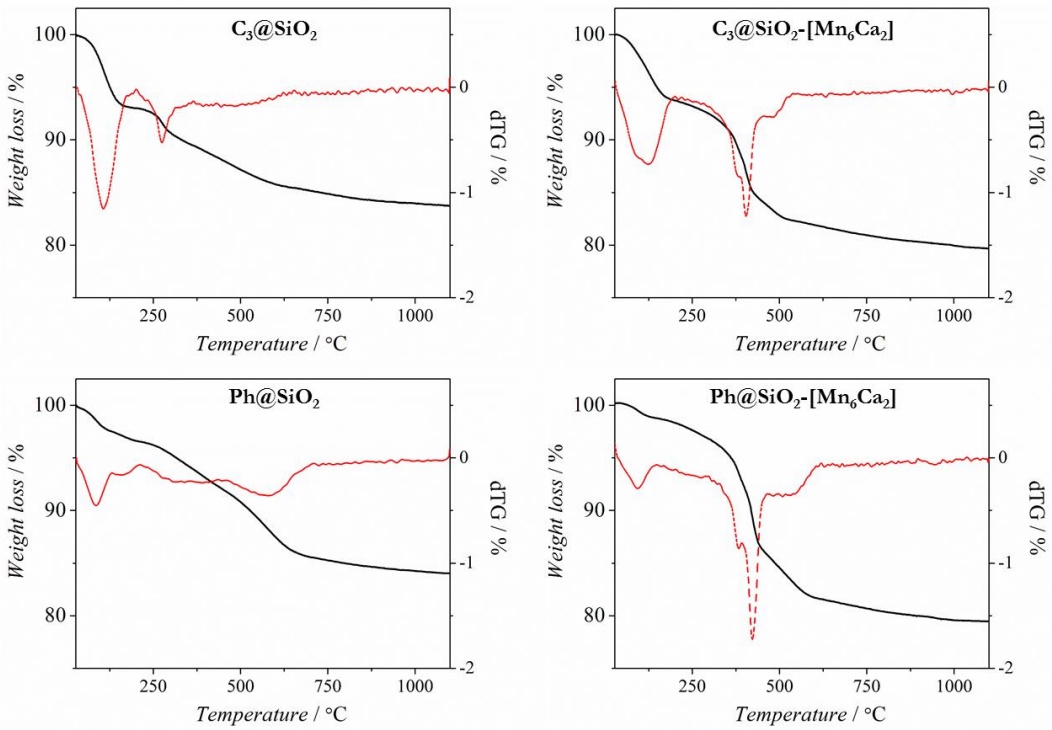

Figure S36. Weight loss (black) and derivative of weight loss (red) versus temperature for materials $C_3@SiO_2$, $Ph@SiO_2$, $C_3@SiO_2$-$[Mn_6Ca_2]$ and $Ph@SiO_2$-$[Mn_6Ca_2]$.

Insertion of the Mn_{12} Compound (26) in $Ph@SiO_2$

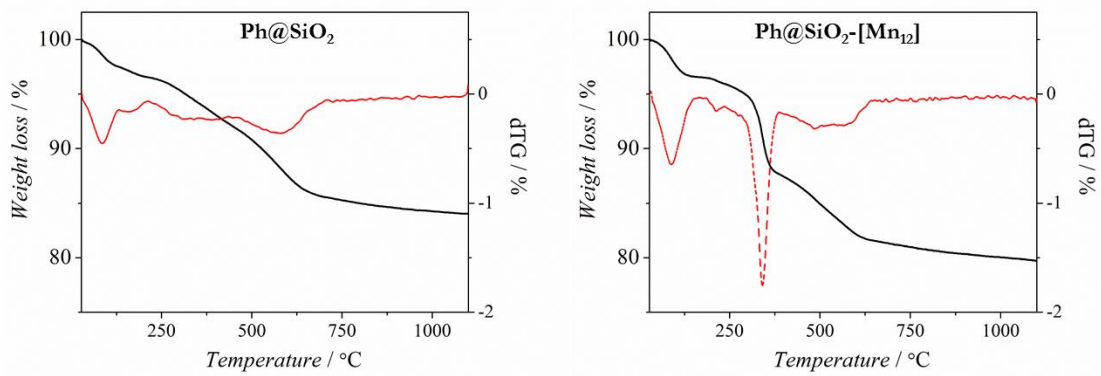

Figure S37. Weight loss (black) and derivative of weight loss (red) versus temperature for materials $Ph@SiO_2$ and $Ph@SiO_2$-$[Mn_{12}]$.

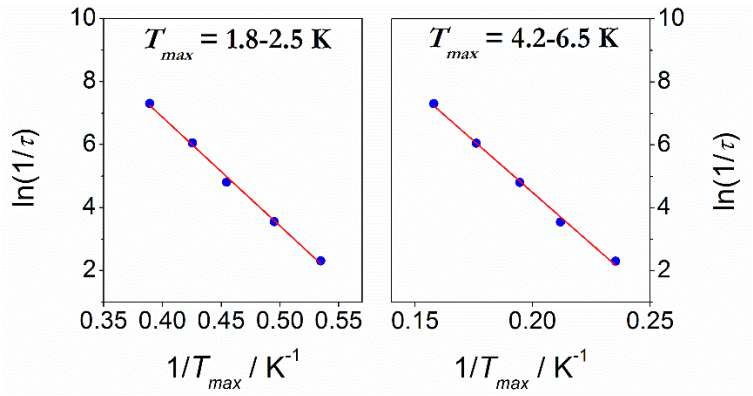

Figure S38. Arrhenius plot of the natural logarithm of the inverse relaxation time ($1/\tau$) versus the inverse absolute temperature of the maxima in the χ_M'' versus T plot ($1/T_{max}$).

Appendix IX: Supplementary Material for Catalytic Studies on Dinuclear Mn^{III} Compounds

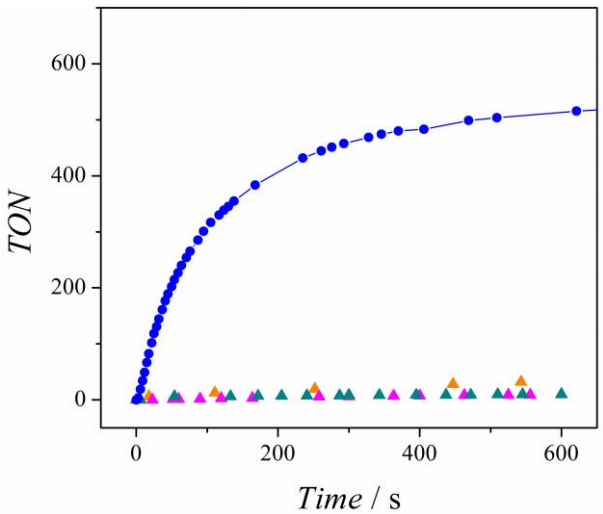

Figure S39. Catalase activity of 1.6 mM solutions of $Mn(NO_3)_2$ (pink triangles), $Mn(ClO_4)_2$ (dark cyan triangles), and MnO_2 (orange triangles) in acetonitrile-water 9-1 (v/v) for $[H_2O_2]_0$ = 1.05 M, compared with that displayed by a 0.8 mM solution of compound **1** (blue circles).

Table S25. Turnover number (TON) after 1 min from the addition of H_2O_2 over 0.8 mM acetonitrile solutions of compounds **1** and **2**, **7** and that one with *n*-R = 4-*t*Bu and X = NO_3.[192]

Comparison between compounds with *n*-R = 2-MeO			
		TON	
$[H_2O_2]$ (M)	$[NO_3^-]$ (mM)	**1** (2-MeO/NO_3)	**2** (2-MeO/ClO_4)
0.73	0	115	75
	1.8	-	117
1.05	0	226	175
	2.8	-	218
	94	-	206
Comparison between compounds with *n*-R = 4-*t*Bu			
		TON	
$[H_2O_2]$ (M)	$[NO_3^-]$ (mM)	**V**[192] (4-*t*Bu/NO_3)*	**7** (4-*t*Bu/ClO_4)
1.05	0	113	150
	~ 8	-	115

* **V**: $[\{Mn(bpy)(H_2O)\}_2(\mu\text{-}4\text{-}^t BuC_6H_4COO)_2(\mu\text{-}O)](NO_3)_2$

Table S26. Summary of catalytic results for compound **2** with $[H_2O_2]_0$ = 1.05 M and $[Mn^{III}_2]$ = 0.8 mM at different pH values in CH_3CN-H_2O 9-1 (v/v).

		At 1 min		At 10 min	
$[Et_3N]$ / mM	pH	TON[a]	% H_2O_2[b]	TON[a]	% H_2O_2[b]
0	6.0	182	25	437	60
1.3	7.3	295	40	514	70
2.5	9.8	374	51	582	79
3.8	10.8	618	84	-	-
12.9	11.8	635	87	-	-
19.0	12.0	731	100	-	-

[a] TON = mmols O_2 / mmols Mn^{III}_2; [b] % H_2O_2 decomposed.

REFERENCES

REFERENCES

(1) Murphy, A.; Dubois, G.; Stack, T. D. P. *J. Am. Chem. Soc.* **2003**, *125* (18), 5250–5251.
(2) Murphy, A.; Pace, A.; Stack, T. D. P. *Org. Lett.* **2004**, *6* (18), 3119–3122.
(3) Murphy, A.; Stack, T. D. P. *J. Mol. Catal. Chem.* **2006**, *251* (1–2), 78–88.
(4) Garcia-Bosch, I.; Company, A.; Fontrodona, X.; Ribas, X.; Costas, M. *Org. Lett.* **2008**, *10* (11), 2095–2098.
(5) Pijper, D.; Saisaha, P.; de Boer, J. W.; Hoen, R.; Smit, C.; Meetsma, A.; Hage, R.; van Summeren, R. P.; Alsters, P. L.; Feringa, B. L.; Browne, W. R. *Dalton Trans.* **2010**, *39* (43), 10375.
(6) Snider, B. B. *Chem. Rev.* **1996**, *96* (1), 339–364.
(7) Yagi, M.; Kaneko, M. *Chem. Rev.* **2001**, *101* (1), 21–36.
(8) Kahn, O. *Molecular magnetism*; VCH, 1993.
(9) Murrie, M.; Price, D. J. *Annu. Rep. Sect. Inorg. Chem.* **2007**, *103* (0), 20–38.
(10) Lippard, S. J.; Berg, J. M. *Principles of Bioinorganic Chemistry*; University Science Books, 1994.
(11) Gispert, J. R. *Química de coordinación*; Ediciones Omega, S.A., 2000.
(12) Winpenny, R. E. P. In *Comprehensive Coordination Chemistry II*; Meyer, T. J., Ed.; Pergamon: Oxford, 2003; pp 125–175.
(13) Tasiopoulos, A. J.; Vinslava, A.; Wernsdorfer, W.; Abboud, K. A.; Christou, G. *Angew. Chem. Int. Ed.* **2004**, *43* (16), 2117–2121.
(14) Deacon, G. B.; Phillips, R. J. *Coord. Chem. Rev.* **1980**, *33* (3), 227–250.
(15) Gómez, V.; Corbella, M. *Eur. J. Inorg. Chem.* **2009**, *2009*, 4471–4482.
(16) Gómez, V.; Corbella, M.; Font-Bardia, M.; Calvet, T. *Dalton Trans.* **2010**, *39* (48), 11664.
(17) Holm, R. H.; Solomon, E. I. *Chem. Rev.* **2004**, *104* (2), 347–348.
(18) Sessoli, R.; Tsai, H. L.; Schake, A. R.; Wang, S.; Vincent, J. B.; Folting, K.; Gatteschi, D.; Christou, G.; Hendrickson, D. N. *J. Am. Chem. Soc.* **1993**, *115* (5), 1804–1816.
(19) Sessoli, R.; Gatteschi, D.; Caneschi, A.; Novak, M. A. *Nature* **1993**, *365* (6442), 141–143.
(20) Christou, G.; Gatteschi, D.; Hendrickson, D. N.; Sessoli, R. *MRS Bull.* **2000**, *25* (11), 66–71.
(21) Boča, R. *Coord. Chem. Rev.* **2004**, *248* (9–10), 757–815.
(22) Gomez-Coca, S.; Cremades, E.; Aliaga-Alcalde, N.; Ruiz, E. *J. Am. Chem. Soc.* **2013**, *135* (18), 7010–7018.
(23) Cirera, J.; Ruiz, E.; Alvarez, S.; Neese, F.; Kortus, J. *Chem. – Eur. J.* **2009**, *15* (16), 4078–4087.
(24) Birdy, R. B.; Goodgame, M. *Inorg. Chim. Acta* **1981**, *50*, 183–187.
(25) Jacobsen, C. J. H.; Pedersen, E.; Villadsen, J.; Weihe, H. *Inorg. Chem.* **1993**, *32* (7), 1216–1221.
(26) Lynch, W. B.; Boorse, R. S.; Freed, J. H. *J. Am. Chem. Soc.* **1993**, *115* (23), 10909–10915.
(27) Wood, R. M.; Stucker, D. M.; Jones, L. M.; Lynch, W. B.; Misra, S. K.; Freed, J. H. *Inorg. Chem.* **1999**, *38* (23), 5384–5388.
(28) Goodgame, D. M. L.; Mkami, H. E.; Smith, G. M.; Zhao, J. P.; McInnes, E. J. L. *Dalton Trans.* **2003**, 34–35.
(29) Mantel, C.; Baffert, C.; Romero, I.; Deronzier, A.; Pécaut, J.; Collomb, M.-N.; Duboc, C. *Inorg. Chem.* **2004**, *43* (20), 6455–6463.
(30) Duboc, C.; Phoeung, T.; Jouvenot, D.; Blackman, A. G.; McClintock, L. F.; Pécaut, J.; Collomb, M.-N.; Deronzier, A. *Polyhedron* **2007**, *26* (18), 5243–5249.
(31) Duboc, C.; Phoeung, T.; Zein, S.; Pécaut, J.; Collomb, M.-N.; Neese, F. *Inorg. Chem.* **2007**, *46* (12), 4905–4916.
(32) Mantel, C.; Philouze, C.; Collomb, M.-N.; Duboc, C. *Eur. J. Inorg. Chem.* **2004**, *2004* (19), 3880–3886.
(33) Duboc, C.; Collomb, M.-N.; Pécaut, J.; Deronzier, A.; Neese, F. *Chem. – Eur. J.* **2008**, *14* (21), 6498–6509.
(34) Rich, J.; Castillo, C. E.; Romero, I.; Rodríguez, M.; Duboc, C.; Collomb, M.-N. *Eur. J. Inorg. Chem.* **2010**, *2010* (23), 3658–3665.

(35) Retegan, M.; Collomb, M.-N.; Neese, F.; Duboc, C. *Phys. Chem. Chem. Phys.* **2012**, *15* (1), 223–234.
(36) Berggren, G.; Huang, P.; Eriksson, L.; Anderlund, M. F. *Appl. Magn. Reson.* **2009**, *36* (1), 9–24.
(37) Gómez-Coca, S.; Aravena, D.; Morales, R.; Ruiz, E. *Coord. Chem. Rev.* **2015**, *289–290*, 379–392.
(38) Barán, E. J. *Química bioinorgánica*; McGraw-Hill/Interamericana de España, 1995.
(39) Pecoraro, V. L. *Manganese redox enzymes*; VCH, 1992.
(40) Dismukes, G. C. *Chem. Rev.* **1996**, *96* (7), 2909–2926.
(41) Gerey, B.; Gouré, E.; Fortage, J.; Pécaut, J.; Collomb, M.-N. *Coord. Chem. Rev.* **2016**, *319*, 1–24.
(42) Imlay, J. A. *Nat. Rev. Microbiol.* **2013**, *11* (7), 443–454.
(43) Nathan, C.; Cunningham-Bussel, A. *Nat. Rev. Immunol.* **2013**, *13* (5), 349–361.
(44) Imlay, J. A. *Annu. Rev. Biochem.* **2008**, *77* (1), 755–776.
(45) Walling, C. *Acc. Chem. Res.* **1975**, *8* (4), 125–131.
(46) Costa, V.; Moradas-Ferreira, P. *Mol. Aspects Med.* **2001**, *22* (4–5), 217–246.
(47) Sayre, L. M.; Perry, G.; Smith, M. A. *Chem. Res. Toxicol.* **2008**, *21* (1), 172–188.
(48) Warner, D. S.; Sheng, H.; Batinić-Haberle, I. *J. Exp. Biol.* **2004**, *207* (18), 3221–3231.
(49) Valko, M.; Leibfritz, D.; Moncol, J.; Cronin, M. T. D.; Mazur, M.; Telser, J. *Int. J. Biochem. Cell Biol.* **2007**, *39* (1), 44–84.
(50) Watson, J. *Open Biol.* **2013**, *3* (1), 120144.
(51) Day, B. J. *Biochem. Pharmacol.* **2009**, *77* (3), 285–296.
(52) Day, B. J. *Drug Discov. Today* **2004**, *9* (13), 557–566.
(53) Batinić-Haberle, I.; Rebouças, J. S.; Spasojević, I. *Antioxid. Redox Signal.* **2010**, *13* (6), 877–918.
(54) Day, B. J. *Antioxid. Redox Signal.* **2007**, *10* (2), 355–370.
(55) Escribano, A.; Amor, M.; Pastor, S.; Castillo, S.; Sanz, F.; Codoñer-Franch, P.; Dasí, F.; Navarro-García, M. M. *Thorax* **2014**, DOI: 10.1136/thoraxjnl-2014-205898.
(56) Gilgun-Sherki, Y.; Melamed, E.; Offen, D. *J. Neurol.* **2004**, *251* (3), 261–268.
(57) Karlík, M.; Valkovič, P.; Hančinová, V.; Krížová, L.; Tóthová, Ľ.; Celec, P. *Clin. Biochem.* **2015**, *48* (1–2), 24–28.
(58) Geldenhuys, W. J.; Darvesh, A. S. *Expert Rev. Neurother.* **2014**, *15* (1), 3–5.
(59) Colamartino, M.; Santoro, M.; Duranti, G.; Sabatini, S.; Ceci, R.; Testa, A.; Padua, L.; Cozzi, R. *Neurotox. Res.* **2014**, *27* (2), 106–117.
(60) Jaffer, O. A.; Carter, A. B.; Sanders, P. N.; Dibbern, M. E.; Winters, C. J.; Murthy, S.; Ryan, A. J.; Rokita, A. G.; Prasad, A. M.; Zabner, J.; Kline, J. N.; Grumbach, I. M.; Anderson, M. E. *Am. J. Respir. Cell Mol. Biol.* **2014**, *52* (1), 106–115.
(61) Tataranno, M. L.; Perrone, S.; Longini, M.; Buonocore, G. *Oxid. Med. Cell. Longev.* **2015**, *2015*, e108251.
(62) Nelson, D. P.; Kiesow, L. A. *Anal. Biochem.* **1972**, *49* (2), 474–478.
(63) Barynin, V. V.; Whittaker, M. M.; Antonyuk, S. V.; Lamzin, V. S.; Harrison, P. M.; Artymiuk, P. J.; Whittaker, J. W. *Structure* **2001**, *9* (8), 725–738.
(64) Antonyuk, S.; Antonyuk. *Kristallografiâ* **2000**, *45* (1), 111.
(65) Whittaker, J. W. *Arch. Biochem. Biophys.* **2012**, *525* (2), 111–120.
(66) Sheats, J. E.; Czernuszewicz, R. S.; Dismukes, G. C.; Rheingold, A. L.; Petrouleas, V.; Stubbe, J.; Armstrong, W. H.; Beer, R. H.; Lippard, S. J. *J. Am. Chem. Soc.* **1987**, *109* (5), 1435–1444.
(67) Signorella, S.; Hureau, C. *Coord. Chem. Rev.* **2012**, *256* (11–12), 1229–1245.
(68) Whittaker, M. M.; Barynin, V. V.; Igarashi, T.; Whittaker, J. W. *Eur. J. Biochem.* **2003**, *270* (6), 1102–1116.
(69) Kubota, R.; Asayama, S.; Kawakami, H. *Chem Commun* **2014**, *50* (100), 15909–15912.
(70) Ledesma, G. N.; Eury, H.; Anxolabéhère-Mallart, E.; Hureau, C.; Signorella, S. R. *J. Inorg. Biochem.* **2015**, *146*, 69–76.
(71) Kar, P.; Drew, M. G. B.; Ghosh, A. *Inorg. Chim. Acta* **2013**, *405*, 349–355.
(72) Kubota, R.; Imamura, S.; Shimizu, T.; Asayama, S.; Kawakami, H. *ACS Med. Chem. Lett.* **2014**, *5* (6), 639–643.

(73) Noritake, Y.; Umezawa, N.; Kato, N.; Higuchi, T. *Inorg. Chem.* **2013**, *52* (7), 3653–3662.
(74) Palopoli, C.; Duhayon, C.; Tuchagues, J.-P.; Signorella, S. *Dalton Trans.* **2014**, *43* (45), 17145–17155.
(75) Bihani, S. C.; Chakravarty, D.; Ballal, A. *Free Radic. Biol. Med.* **2016**, *93*, 118–129.
(76) Umena, Y.; Kawakami, K.; Shen, J.-R.; Kamiya, N. *Nature* **2011**, *473* (7345), 55–60.
(77) McEvoy, J. P.; Brudvig, G. W. *Chem. Rev.* **2006**, *106* (11), 4455–4483.
(78) Dau, H.; Haumann, M. *Coord. Chem. Rev.* **2008**, *252* (3–4), 273–295.
(79) Krewald, V.; Retegan, M.; Cox, N.; Messinger, J.; Lubitz, W.; DeBeer, S.; Neese, F.; Pantazis, D. A. *Chem. Sci.* **2015**, *6* (3), 1676–1695.
(80) Askerka, M.; Wang, J.; Brudvig, G. W.; Batista, V. S. *Biochemistry* **2014**, *53* (44), 6860–6862.
(81) Mukhopadhyay, S.; Mandal, S. K.; Bhaduri, S.; Armstrong, W. H. *Chem. Rev.* **2004**, *104* (9), 3981–4026.
(82) Hewitt, I. J.; Tang, J.-K.; Madhu, N. T.; Clérac, R.; Buth, G.; Anson, C. E.; Powell, A. K. *Chem. Commun.* **2006**, 2650–2652.
(83) Jerzykiewicz, L. B.; Utko, J.; Duczmal, M.; Sobota, P. *Dalton Trans.* **2007**, 825–826.
(84) Park, Y. J.; Ziller, J. W.; Borovik, A. S. *J. Am. Chem. Soc.* **2011**, *133* (24), 9258–9261.
(85) Kotzabasaki, V.; Siczek, M.; Lis, T.; Milios, C. J. *Inorg. Chem. Commun.* **2011**, *14* (1), 213–216.
(86) Mishra, A.; Wernsdorfer, W.; Abboud, K. A.; Christou, G. *Chem. Commun.* **2005**, 54–56.
(87) Koumousi, E. S.; Mukherjee, S.; Beavers, C. M.; Teat, S. J.; Christou, G.; Stamatatos, T. C. *Chem. Commun.* **2011**, *47* (39), 11128–11130.
(88) Nayak, S.; Nayek, H. P.; Dehnen, S.; Powell, A. K.; Reedijk, J. *Dalton Trans.* **2011**, *40* (12), 2699–2702.
(89) Kanady, J. S.; Tsui, E. Y.; Day, M. W.; Agapie, T. *Science* **2011**, *333* (6043), 733–736.
(90) Mukherjee, S.; Stull, J. A.; Yano, J.; Stamatatos, T. C.; Pringouri, K.; Stich, T. A.; Abboud, K. A.; Britt, R. D.; Yachandra, V. K.; Christou, G. *P. Natl. Acad. Sci. USA* **2012**, *109* (7), 2257–2262.
(91) Tsui, E. Y.; Tran, R.; Yano, J.; Agapie, T. *Nat. Chem.* **2013**, *5* (4), 293–299.
(92) Zhang, C.; Chen, C.; Dong, H.; Shen, J.-R.; Dau, H.; Zhao, J. *Science* **2015**, *348* (6235), 690–693.
(93) Yocum, C. F. *Coord. Chem. Rev.* **2008**, *252* (3–4), 296–305.
(94) Yang, J.; Hatakeyama, M.; Ogata, K.; Nakamura, S.; Li, C. *J. Phys. Chem. B* **2014**, *118* (49) 14215–14222.
(95) Polander, B. C.; Barry, B. A. *J. Phys. Chem. Lett.* **2013**, *4* (5), 786–791.
(96) Glatzel, P.; Schroeder, H.; Pushkar, Y.; Boron, T.; Mukherjee, S.; Christou, G.; Pecoraro, V. L.; Messinger, J.; Yachandra, V. K.; Bergmann, U.; Yano, J. *Inorg. Chem.* **2013**, *52* (10), 5642–5644.
(97) Park, Y. J.; Cook, S. A.; Sickerman, N. S.; Sano, Y.; Ziller, J. W.; Borovik, A. S. *Chem. Sci.* **2013**, *4* (2), 717–726.
(98) Tsui, E. Y.; Agapie, T. *Proc. Natl. Acad. Sci.* **2013**, *110* (25), 10084–10088.
(99) Lee, C.-I.; Lakshmi, K. V.; Brudvig, G. W. *Biochemistry* **2007**, *46* (11), 3211–3223.
(100) Pitari, F.; Bovi, D.; Narzi, D.; Guidoni, L. *Biochemistry* **2015**, *54* (38), 5959–5968.
(101) Koua, F. H. M.; Umena, Y.; Kawakami, K.; Shen, J.-R. *Proc. Natl. Acad. Sci.* **2013**, *110* (10), 3889–3894.
(102) Lohmiller, T.; Krewald, V.; Navarro, M. P.; Retegan, M.; Rapatskiy, L.; Nowaczyk, M. M.; Boussac, A.; Neese, F.; Lubitz, W.; Pantazis, D. A.; Cox, N. *Phys. Chem. Chem. Phys. PCCP* **2014**, *16* (24), 11877–11892.
(103) Boussac, A.; Rappaport, F.; Carrier, P.; Verbavatz, J.-M.; Gobin, R.; Kirilovsky, D.; Rutherford, A. W.; Sugiura, M. *J. Biol. Chem.* **2004**, *279* (22), 22809–22819.
(104) Colella, C.; Gualtieri, A. F. *Micropor. Mesopor. Mat.* **2007**, *105* (3), 213–221.
(105) Cejka, J.; Corma, A.; Zones, S. *Zeolites and Catalysis: Synthesis, Reactions and Applications*; John Wiley & Sons, 2010.
(106) Möller, K.; Bein, T. *Chem. Soc. Rev.* **2013**, *42* (9), 3689.
(107) Egeblad, K.; Christensen, C. H.; Kustova, M.; Christensen, C. H. *Chem. Mater.* **2008**, *20* (3), 946–960.
(108) Zhao, D.; Wan, Y.; Zhou, W. *Ordered Mesoporous Materials*; John Wiley & Sons, 2012.

(109) Fan, J.; Boettcher, S. W.; Tsung, C.-K.; Shi, Q.; Schierhorn, M.; Stucky, G. D. *Chem. Mater.* **2008**, *20* (3), 909–921.
(110) Huo, Q.; Margolese, D. I.; Ciesla, U.; Feng, P.; Gier, T. E.; Sieger, P.; Leon, R.; Petroff, P. M.; Schüth, F.; Stucky, G. D. *Nature* **1994**, *368* (6469), 317–321.
(111) Broekhoff, J. C. P.; De Boer, J. H. *J. Catal.* **1967**, *9* (1), 15–27.
(112) Huo, Q.; Margolese, D. I.; Ciesla, U.; Demuth, D. G.; Feng, P.; Gier, T. E.; Sieger, P.; Firouzi, A.; Chmelka, B. F. *Chem. Mater.* **1994**, *6* (8), 1176–1191.
(113) Beck, J. S.; Vartuli, J. C.; Roth, W. J.; Leonowicz, M. E.; Kresge, C. T.; Schmitt, K. D.; Chu, C. T. W.; Olson, D. H.; Sheppard, E. W. *J. Am. Chem. Soc.* **1992**, *114* (27), 10834–10843.
(114) Kresge, C. T.; Leonowicz, M. E.; Roth, W. J.; Vartuli, J. C.; Beck, J. S. *Nature* **1992**, *359* (6397), 710–712.
(115) Albela, B.; Bonneviot, L. *New J. Chem.* **2016**, *40* (5), 4115–4131.
(116) Bonneviot, L.; Morin, M.; Badiel, A. A. Patent WO 01/55031 A1, 2001.
(117) Reinert, P.; Garcia, B.; Morin, C.; Badiei, A.; Perriat, P.; Tillement, O.; Bonneviot, L. *Stud. Surf. Sci. Catal.* **2003**, *146*, 133–136.
(118) Chaignon, J.; Bouizi, Y.; Davin, L.; Calin, N.; Albela, B.; Bonneviot, L. *Green Chem.* **2015**, *17* (5), 3130–3140.
(119) Wan, Y.; Zhao. *Chem. Rev.* **2007**, *107* (7), 2821–2860.
(120) Kruk, M.; Cao, L. *Langmuir.* **2007**, *23* (13), 7247–7254.
(121) Barrett, E. P.; Joyner, L. G.; Halenda, P. P. *J. Am. Chem. Soc.* **1951**, *73* (1), 373–380.
(122) Anwander, R. *Chem. Mater.* **2001**, *13* (12), 4419–4438.
(123) Tahmassebi, D. C.; Sasaki, T. *J. Org. Chem.* **1994**, *59* (3), 679–681.
(124) Hwang, K.-O.; Yakura, Y.; Ohuchi, F. S.; Sasaki, T. *Mater. Sci. Eng. C* **1995**, *3* (2), 137–141.
(125) Shin, Y.; Liu, J.; Wang, L.-Q.; Nie, Z.; Samuels, W. D.; Fryxell, G. E.; Exarhos, G. J. *Angew. Chem. Int. Ed.* **2000**, *39* (15), 2702–2707.
(126) Hicks, J. C.; Dabestani, R.; Buchanan III, A. C.; Jones, C. W. *Inorg. Chim. Acta* **2008**, *361* (11), 3024–3032.
(127) Abry, S.; Albela, B.; Bonneviot, L. *Comptes Rendus Chim.* **2005**, *8* (3–4), 741–752.
(128) Abry, S.; Lux, F.; Albela, B.; Artigas-Miquel, A.; Nicolas, S.; Jarry, B.; Perriat, P.; Lemercier, G.; Bonneviot, L. *Chem Mater* **2009**, *21* (12), 2349–2359.
(129) Calmettes, S.; Albela, B.; Hamelin, O.; Ménage, S.; Miomandre, F.; Bonneviot, L. *New J. Chem.* **2008**, *32* (4), 727.
(130) Zhang, K.; Albela, B.; He, M.-Y.; Wang, Y.; Bonneviot, L. *Phys. Chem. Chem. Phys.* **2009**, *11* (16), 2912.
(131) Zhang, K.; Chen, H.-L.; Albela, B.; Jiang, J.-G.; Wang, Y.-M.; He, M.-Y.; Bonneviot, L. *Eur. J. Inorg. Chem.* **2011**, *2011* (1), 59–67.
(132) Chaignon, J.; Stiriba, S.-E.; Lloret, F.; Yuste, C.; Pilet, G.; Bonneviot, L.; Albela, B.; Castro, I. *Dalton Trans.* **2014**, *43* (25), 9704–9713.
(133) Du, L.; Li, J.; Chen, C.; Liu, Y. *Free Radic. Res.* **2014**, *48* (9), 1061–1069.
(134) Vivero-Escoto, J. L.; Slowing, I. I.; Trewyn, B. G.; Lin, V. S.-Y. *Small* **2010**, *6* (18), 1952–1967.
(135) Vallet-Regí, M.; Balas, F.; Arcos, D. *Angew. Chem. Int. Ed.* **2007**, *46* (40), 7548–7558.
(136) Slowing, I. I.; Vivero-Escoto, J. L.; Trewyn, B. G.; Lin, V. S.-Y. *J. Mater. Chem.* **2010**, *20* (37), 7924–7937.
(137) Yu, J.; Ge, L.; Liu, S.; Dai, P.; Ge, S.; Zheng, W. *Biosens. Bioelectron.* **2011**, *26* (5), 1936–1941.
(138) Csendes, Z.; Varga, G.; Nagy, N. V.; Bajnóczi, É. G.; Sipiczki, M.; Carlson, S.; Canton, S. E.; Metzinger, A.; Galbács, G.; Sipos, P.; Pálinkó, I. *Catal. Today* **2015**, *241, Part B*, 264–269.
(139) Yang, M.; Jiang, W.; Pan, Z.; Zhou, H. *J. Inorg. Organomet. Polym. Mater.* **2015**, *25* (5), 1289–1297.
(140) Xia, Y.; Qiu-Yun, C.; Jing-Bao, S. *Chin. J. Inorg. Chem.* **2012**, *28* (1), 164–170.
(141) Lascu, A.; Palade, A.; Fagadar-Cosma, G.; Creanga, I.; Ianasi, C.; Sebarchievici, I.; Birdeanu, M.; Fagadar-Cosma, E. *Mater. Res. Bull.* **2016**, *74*, 325–332.
(142) Rumberger, E. M. W.; Ahn, H. S.; Bell, A. T.; Tilley, T. D. *Dalton Trans.* **2013**, *42* (34), 12238–12247.
(143) Vallet-Regí, M.; Balas, F. *Open Biomed. Eng. J.* **2008**, *2* (1), 1–9.

(144) Aznar, E.; Oroval, M.; Pascual, L.; Murguía, J. R.; Martínez-Máñez, R.; Sancenón, F. *Chem. Rev.* **2016**, *116* (2), 561–718.
(145) Lewis, J. C. *Curr. Opin. Chem. Biol.* **2015**, *25*, 27–35.
(146) Lewis, J. C. *ACS Catal.* **2013**, *3* (12), 2954–2975.
(147) Pàmies, O.; Diéguez, M.; Bäckvall, J.-E. *Adv. Synth. Catal.* **2015**, *357* (8), 1567–1586.
(148) Rosati, F.; Roelfes, G. *ChemCatChem* **2010**, *2* (8), 916–927.
(149) Clemente-León, M.; Coronado, E.; Forment-Aliaga, A.; Martínez-Agudo, J. M.; Amorós, P. *Polyhedron* **2003**, *22* (14–17), 2395–2400.
(150) Clemente-León, M.; Coronado, E.; Forment-Aliaga, A.; Amorós, P.; Ramírez-Castellanos, J.; González-Calbet, J. M. *J. Mater. Chem.* **2003**, *13* (12), 3089–3095.
(151) Willemin, S.; Arrachart, G.; Lecren, L.; Larionova, J.; Coradin, T.; Clérac, R.; Mallah, T.; Guérin, C.; Sanchez, C. *New J. Chem.* **2003**, *27* (10), 1533.
(152) Coradin, T.; Larionova, J.; Smith, A. a.; Rogez, G.; Clérac, R.; Guérin, C.; Blondin, G.; Winpenny, R. e. p.; Sanchez, C.; Mallah, T. *Adv. Mater.* **2002**, *14* (12), 896–898.
(153) Balanda, M.; Pełka, R.; Fitta, M.; Laskowski, Ł.; Laskowska, M. *RSC Adv.* **2016**, *6* (54), 49179–49186.
(154) Farrugia, L. J. *J. Appl. Crystallogr.* **1999**, *32* (4), 837–838.
(155) Hübschle, C. B.; Sheldrick, G. M.; Dittrich, B. *J. Appl. Crystallogr.* **2011**, *44* (6), 1281–1284.
(156) Sheldrick, G. M. *Acta Crystallogr. A* **2007**, *64* (1), 112–122.
(157) Spek, A. L. *J. Appl. Crystallogr.* **2003**, *36* (1), 7–13.
(158) (IUCr) checkCIF http://checkcif.iucr.org/
(159) Müller, P. *Crystallogr. Rev.* **2009**, *15* (1), 57–83.
(160) Nakamoto, K. *Infrared and Raman Spectra of Inorganic and Coordination Compounds, Theory and Applications in Inorganic Chemistry*; John Wiley & Sons, 2008.
(161) Gispert, J. R. *Coordination Chemistry*; Wiley, 2008.
(162) Hay, P. J.; Thibeault, J. C.; Hoffmann, R. *J. Am. Chem. Soc.* **1975**, *97* (17), 4884–4899.
(163) Aromí, G.; Telser, J.; Ozarowski, A.; Brunel, L.-C.; Stoeckli-Evans, H.-M.; Krzystek, J. *Inorg. Chem.* **2005**, *44* (2), 187–196.
(164) Duboc, C.; Ganyushin, D.; Sivalingam, K.; Collomb, M.-N.; Neese, F. *J. Phys. Chem. A* **2010**, *114* (39), 10750–10758.
(165) Chilton, N. F.; Anderson, R. P.; Turner, L. D.; Soncini, A.; Murray, K. S. *J. Comput. Chem.* **2013**, *34* (13), 1164–1175.
(166) Sala, T.; Sargent, M. V. *J. Chem. Soc. Chem. Commun.* **1978**, 253–254.
(167) William J Geary. *Coord. Chem. Rev.* **1971**, *7*, 81–122.
(168) SADABS Version 2008/1 (Sheldrick, Bruker AXS Inc.).
(169) van der Sluis, P.; Spek, A. L. *Acta Crystallogr. A* **1990**, *46* (3), 194–201.
(170) Soler, J. M.; Artacho, E.; Gale, J. D.; García, A.; Junquera, J.; Ordejón, P.; Sánchez-Portal, D. *J. Phys. Condens. Matter* **2002**, *14* (11), 2745.
(171) Perdew, J. P.; Burke, K.; Ernzerhof, M. *Phys. Rev. Lett.* **1996**, *77* (18), 3865–3868.
(172) Kleinman, L.; Bylander, D. M. *Phys. Rev. Lett.* **1982**, *48* (20), 1425–1428.
(173) Troullier, N.; Martins, J. L. *Phys. Rev. B* **1991**, *43* (3), 1993–2006.
(174) Ruiz, E.; Alvarez, S.; Cano, J.; Polo, V. *J. Chem. Phys.* **2005**, *123* (16), 164110.
(175) Ruiz, E.; Rodríguez-Fortea, A.; Tercero, J.; Cauchy, T.; Massobrio, C. *J. Chem. Phys.* **2005**, *123* (7), 074102.
(176) Ruiz, E.; Alemany, P.; Alvarez, S.; Cano, J. *J. Am. Chem. Soc.* **1997**, *119* (6), 1297–1303.
(177) Ruiz, E.; Alemany, P.; Alvarez, S.; Cano, J. *Inorg. Chem.* **1997**, *36* (17), 3683–3688.
(178) Rodríguez-Fortea, A.; Alemany, P.; Alvarez, S.; Ruiz, E. *Inorg. Chem.* **2002**, *41* (14), 3769–3778.
(179) Ako, A. M.; Burger, B.; Lan, Y.; Mereacre, V.; Clérac, R.; Buth, G.; Gómez-Coca, S.; Ruiz, E.; Anson, C. E.; Powell, A. K. *Inorg. Chem.* **2013**, *52* (10), 5764–5774.
(180) Hotzelmann, R.; Wieghardt, K.; Floerke, U.; Haupt, H. J.; Weatherburn, D. C.; Bonvoisin, J.; Blondin, G.; Girerd, J. J. *J. Am. Chem. Soc.* **1992**, *114* (5), 1681–1696.
(181) Gómez, V.; Corbella, M.; Roubeau, O.; Teat, S. J. *Dalton Trans.* **2011**, *40* (44), 11968–11975.
(182) Corbella, M.; Costa, R.; Ribas, J.; Fries, P. H.; Latour, J.-M.; Öhrström, L.; Solans, X.; Rodríguez, V. *Inorg. Chem.* **1996**, *35* (7), 1857–1865.

(183) Fernández, G.; Corbella, M.; Aullón, G.; Maestro, M. A.; Mahía, J. *Eur. J. Inorg. Chem.* **2007**, *2007* (9), 1285–1296.
(184) Corbella, M.; Gómez, V.; Garcia, B.; Rodriguez, E.; Albela, B.; Maestro, M. A. *Inorg. Chim. Acta.* **2011**, *376* (1), 456–462.
(185) Bolm, C.; Meyer, N.; Raabe, G.; Weyhermüller, T.; Bothe, E. *Chem. Commun.* **2000**, 2435–2436.
(186) Wieghardt, K.; Bossek, U.; Nuber, B.; Weiss, J.; Bonvoisin, J.; Corbella, M.; Vitols, S. E.; Girerd, J. J. *J. Am. Chem. Soc.* **1988**, *110* (22), 7398–7411.
(187) Lal, T. K.; Mukherjee, R. *Inorg. Chem.* **1998**, *37* (10), 2373–2382.
(188) Mahapatra, S.; Lal, T. K.; Mukherjee, R. *Inorg. Chem.* **1994**, *33* (8), 1579–1580.
(189) Wu, F. J.; Kurtz, D. M.; Hagen, K. S.; Nyman, P. D.; Debrunner, P. G.; Vankai, V. A. *Inorg. Chem.* **1990**, *29* (26), 5174–5183.
(190) Vincent, J. B.; Folting, K.; Huffman, J. C.; Christou, G. *Biochem. Soc. Trans.* **1988**, *16* (5), 822–823.
(191) Vincent, J. B.; Tsai, H. L.; Blackman, A. G.; Wang, S.; Boyd, P. D. W.; Folting, K.; Huffman, J. C.; Lobkovsky, E. B.; Hendrickson, D. N.; Christou, G. *J. Am. Chem. Soc.* **1993**, *115* (26), 12353–12361.
(192) Corbella, M.; Fernández, G.; González, P.; Maestro, M.; Font-Bardia, M.; Stoeckli-Evans, H. *Eur. J. Inorg. Chem.* **2012**, *2012* (13), 2203–2212.
(193) Gómez, V.; Corbella, M.; Aullón, G. *Inorg Chem* **2010**, *49* (4), 1471–1480.
(194) Gómez, V.; Corbella, M. *Eur. J. Inorg. Chem.* **2012**, *2012* (19), 3147–3155.
(195) Escriche-Tur, L.; Corbella, M.; Font-Bardia, M.; Castro, I.; Bonneviot, L.; Albela, B. *Inorg. Chem.* **2015**, *54* (21), 10111–10125.
(196) Chen, C.; Zhu, H.; Huang, D.; Wen, T.; Liu, Q.; Liao, D.; Cui, J. *Inorg. Chim. Acta* **2001**, *320* (1–2), 159–166.
(197) Hammett, L. P. *Trans. Faraday Soc.* **1938**, *34* (0), 156–165.
(198) Hammett, L. P. *J. Am. Chem. Soc.* **1937**, *59* (1), 96–103.
(199) Schramm, V. L. *Manganese in Metabolism and Enzyme Function*; Elsevier, 2012.
(200) Sigel, H. *Metal Ions in Biological Systems: Volume 37: Manganese and Its Role in Biological Processes*; CRC Press, 2000.
(201) Miller, A.-F. *Curr. Opin. Chem. Biol.* **2004**, *8* (2), 162–168.
(202) Jackson, T. A.; Brunold, T. C. *Acc. Chem. Res.* **2004**, *37* (7), 461–470.
(203) Buy, C.; Girault, G.; Zimmermann, J.-L. *Biochemistry* **1996**, *35* (30), 9880–9891.
(204) Kappl, R.; Ranguelova, K.; Koch, B.; Duboc, C.; Hüttermann, J. *Magn. Reson. Chem.* **2005**, *43* (S1), S65–S73.
(205) Fernández, G.; Corbella, M.; Mahía, J.; Maestro, M. A. *Eur. J. Inorg. Chem.* **2002**, *2002* (9), 2502–2510.
(206) Albela, B.; Corbella, M.; Ribas, J.; Castro, I.; Sletten, J.; Stoeckli-Evans, H. *Inorg Chem* **1998**, *37* (4), 788–798.
(207) Gómez, V.; Corbella, M. *J. Chem. Crystallogr.* **2011**, *41* (6), 843–846.
(208) Gómez, V.; Corbella, M.; Mautner, F. A.; Roubeau, O.; Teat, S. J.; Font-Bardia, M.; Calvet, T. *Polyhedron* **2012**, *45* (1), 185–199.
(209) Oshio, H.; Ino, E.; Mogi, I.; Ito, T. *Inorg. Chem.* **1993**, *32* (25), 5697–5703.
(210) Ma, C.; Wang, W.; Zhang, X.; Chen, C.; Liu, Q.; Zhu, H.; Liao, D.; Li, L. *Eur. J. Inorg. Chem.* **2004**, *2004* (17), 3522–3532.
(211) Ma, Y.-S.; Tang, X.-Y.; Xue, F.-F.; Chen, B.; Dai, Y.-L.; Yuan, R.-X.; Roy, S. *Eur. J. Inorg. Chem.* **2012**, *2012* (8), 1243–1249.
(212) Durot, S.; Policar, C.; Pelosi, G.; Bisceglie, F.; Mallah, T.; Mahy, J.-P. *Inorg. Chem.* **2003**, *42* (24), 8072–8080.
(213) Nepveu, F.; Gaultier, N.; Korber, N.; Jaud, J.; Castan, P. *J. Chem. Soc. Dalton Trans.* **1995**, 4005–4013.
(214) Moon, D.; Kim, J.; Oh, M.; Suh, B. J.; Lah, M. S. *Polyhedron* **2008**, *27* (1), 447–452.
(215) Baca, S. G.; Malaestean, I. L.; Keene, T. D.; Adams, H.; Ward, M. D.; Hauser, J.; Neels, A.; Decurtins, S. *Inorg. Chem.* **2008**, *47* (23), 11108–11119.
(216) Menage, S.; Vitols, S. E.; Bergerat, P.; Codjovi, E.; Kahn, O.; Girerd, J. J.; Guillot, M.; Solans, X.; Calvet, T. *Inorg. Chem.* **1991**, *30* (12), 2666–2671.

(217) Tangoulis, V.; Malamatari, D. A.; Soulti, K.; Stergiou, V.; Raptopoulou, C. P.; Terzis, A.; Kabanos, T. A.; Kessissoglou, D. P. *Inorg. Chem.* **1996**, *35* (17), 4974–4983.
(218) Baca, S. G.; Sevryugina, Y.; Clérac, R.; Malaestean, I.; Gerbeleu, N.; Petrukhina, M. A. *Inorg. Chem. Commun.* **2005**, *8* (5), 474–478.
(219) Escuer, A.; Cordero, B.; Solans, X.; Font-Bardia, M.; Calvet, T. *Eur. J. Inorg. Chem.* **2008**, *2008* (32), 5082–5087.
(220) Milios, C. J.; Stamatatos, T. C.; Kyritsis, P.; Terzis, A.; Raptopoulou, C. P.; Vicente, R.; Escuer, A.; Perlepes, S. P. *Eur. J. Inorg. Chem.* **2004**, *2004* (14), 2885–2901.
(221) Tzima, T. D.; Sioros, G.; Duboc, C.; Kovala-Demertzi, D.; Melissas, V. S.; Sanakis, Y. *Polyhedron* **2009**, *28* (15), 3257–3264.
(222) Abragam, A.; Bleaney, B. *Electron Paramagnetic Resonance of Transition Ions*; OUP Oxford, 2012.
(223) Zein, S.; Duboc, C.; Lubitz, W.; Neese, F. *Inorg. Chem.* **2008**, *47* (1), 134–142.
(224) Carmieli, R.; Larsen, T. M.; Reed, G. H.; Zein, S.; Neese, F.; Goldfarb, D. *J. Am. Chem. Soc.* **2007**, *129* (14), 4240–4252.
(225) Hunter, S. C.; Podlesnyak, A. A.; Xue, Z.-L. *Inorg. Chem.* **2014**, *53* (4), 1955–1961.
(226) Pantazis, D. A.; Krewald, V.; Orio, M.; Neese, F. *Dalton Trans.* **2010**, *39* (20), 4959–4967.
(227) Krewald, V.; Neese, F.; Pantazis, D. A. *J. Am. Chem. Soc.* **2013**, *135* (15), 5726–5739.
(228) Langley, S. K.; Chilton, N. F.; Massi, M.; Moubaraki, B.; Berry, K. J.; Murray, K. S. *Dalton Trans.* **2010**, *39* (31), 7236–7249.
(229) Harden, N. C.; Bolcar, M. A.; Wernsdorfer, W.; Abboud, K. A.; Streib, W. E.; Christou, G. *Inorg. Chem.* **2003**, *42* (22), 7067–7076.
(230) Stamatatos, T. C.; Poole, K. M.; Foguet-Albiol, D.; Abboud, K. A.; O'Brien, T. A.; Christou, G. *Inorg. Chem.* **2008**, *47* (15), 6593–6595.
(231) Saalfrank, R. W.; Nakajima, T.; Mooren, N.; Scheurer, A.; Maid, H.; Hampel, F.; Trieflinger, C.; Daub, J. *Eur. J. Inorg. Chem.* **2005**, *2005* (6), 1149–1153.
(232) Koizumi, S.; Nihei, M.; Shiga, T.; Nakano, M.; Nojiri, H.; Bircher, R.; Waldmann, O.; Ochsenbein, S. T.; Güdel, H. U.; Fernandez-Alonso, F.; Oshio, H. *Chem. – Eur. J.* **2007**, *13* (30), 8445–8453.
(233) Koizumi, S.; Nihei, M.; Nakano, M.; Oshio, H. *Inorg. Chem.* **2005**, *44* (5), 1208–1210.
(234) Liu, T.; Wang, B.-W.; Chen, Y.-H.; Wang, Z.-M.; Gao, S. *Z. Für Anorg. Allg. Chem.* **2008**, *634* (4), 778–783.
(235) Saalfrank, R. W.; Scheurer, A.; Prakash, R.; Heinemann, F. W.; Nakajima, T.; Hampel, F.; Leppin, R.; Pilawa, B.; Rupp, H.; Müller, P. *Inorg. Chem.* **2007**, *46* (5), 1586–1592.
(236) Yang, P.-P. *Z. Für Anorg. Allg. Chem.* **2011**, *637* (5), 567–571.
(237) Abbati, G. L.; Cornia, A.; Fabretti, A. C.; Caneschi, A.; Gatteschi, D. *Inorg. Chem.* **1998**, *37* (7), 1430–1431.
(238) Yang, P.-P.; Song, H.-B.; Gao, X.-F.; Li, L.-C.; Liao, D.-Z. *Cryst. Growth Des.* **2009**, *9* (9), 4064–4069.
(239) Langley, S. K.; Berry, K. J.; Moubaraki, B.; Murray, K. S. *Dalton Trans.* **2009**, 973–982.
(240) Tasiopoulos, A. J.; Milligan; Abboud, K. A.; O'Brien, T. A.; Christou, G. *Inorg. Chem.* **2007**, *46* (23), 9678–9691.
(241) Wang, M.; Yuan, D.-Q.; Ma, C.-B.; Yuan, M.-J.; Hu, M.-Q.; Li, N.; Chen, H.; Chen, C.-N.; Liu, Q.-T. *Dalton Trans.* **2010**, *39* (31), 7276–7285.
(242) Stamatatos, T. C.; Oliver, K.; Abboud, K. A.; Christou, G. *Inorg. Chem.* **2011**, *50* (11), 5272–5282.
(243) Bhaduri, S.; Tasiopoulos, A. J.; Bolcar, M. A.; Abboud, K. A.; Streib, W. E.; Christou, G. *Inorg. Chem.* **2003**, *42* (5), 1483–1492.
(244) Delfs, C. D.; Stranger, R. *Inorg. Chem.* **2001**, *40* (13), 3061–3076.
(245) Albela, B.; El Fallah, M. S.; Ribas, J.; Folting, K.; Christou, G.; Hendrickson, D. N. *Inorg. Chem.* **2001**, *40* (5), 1037–1044.
(246) Vincent, J. B.; Christmas, C.; Chang, H. R.; Li, Q.; Boyd, P. D. W.; Huffman, J. C.; Hendrickson, D. N.; Christou, G. *J. Am. Chem. Soc.* **1989**, *111* (6), 2086–2097.
(247) Cañada-Vilalta, C.; Huffman, J. C.; Christou, G. *Polyhedron* **2001**, *20* (15–16), 1785–1793.
(248) Knapp, M. J.; Hendrickson, D. N.; Grillo, V. A.; Bollinger, J. C.; Christou, G. *Angew. Chem. Int. Ed. Engl.* **1996**, *35* (16), 1818–1820.
(249) Chen, Z.; Ma, Y.; Liang, F.; Zhou, Z. *J. Organomet. Chem.* **2008**, *693* (4), 646–654.

(250) Ma, Y.-S.; Yao, H.-C.; Hua, W.-J.; Li, S.-H.; Li, Y.-Z.; Zheng, L.-M. *Inorg. Chim. Acta* **2007**, *360* (5), 1645–1650.
(251) Taguchi, T.; Daniels, M. R.; Abboud, K. A.; Christou, G. *Inorg. Chem.* **2009**, *48* (19), 9325–9335.
(252) Ruiz, R.; Sangregorio, C.; Caneschi, A.; Rossi, P.; Gaspar, A. B.; Real, J. A.; Muñoz, M. C. *Inorg. Chem. Commun.* **2000**, *3* (7), 361–367.
(253) Pistilli, J.; Beer, R. H. *Inorg. Chem. Commun.* **2002**, *5* (3), 206–210.
(254) Tamane, T.; Tsubomura, T.; Sakai, K. *Acta Crystallogr. C* **1996**, *52* (4), 777–779.
(255) Wang, S.; Wemple, M. S.; Yoo, J.; Folting, K.; Huffman, J. C.; Hagen, K. S.; Hendrickson, D. N.; Christou, G. *Inorg. Chem.* **2000**, *39* (7), 1501–1513.
(256) Aromí, G.; Bhaduri, S.; Artús, P.; Folting, K.; Christou, G. *Inorg. Chem.* **2002**, *41* (4), 805–817.
(257) Chakov, N. E.; Zakharov, L. N.; Rheingold, A. L.; Abboud, K. A.; Christou, G. *Inorg. Chem.* **2005**, *44* (13), 4555–4567.
(258) Hołyńska, M.; Dehnen, S. *Z. Für Krist. Cryst. Mater.* **2011**, *226* (10), 769–772.
(259) Libby, E.; McCusker, J. K.; Schmitt, E. A.; Folting, K.; Hendrickson, D. N.; Christou, G. *Inorg. Chem.* **1991**, *30* (18), 3486–3495.
(260) Aromí, G.; Bhaduri, S.; Artús, P.; Huffman, J. C.; Hendrickson, D. N.; Christou, G. *Polyhedron* **2002**, *21* (18), 1779–1786.
(261) Bossek, U.; Hummel, H.; Weyhermüller, T.; Wieghardt, K.; Russell, S.; van der Wolf, L.; Kolb, U. *Angew. Chem. Int. Ed. Engl.* **1996**, *35* (13-14), 1552–1554.
(262) Oberhausen, K. J.; O'Brien, R. J.; Richardson, J. F.; Buchanan, R. M.; Costa, R.; Latour, J. M.; Tsai, H. L.; Hendrickson, D. N. *Inorg. Chem.* **1993**, *32* (21), 4561–4565.
(263) Arulsamy, N.; Glerup, J.; Hazell, A.; Hodgson, D. J.; McKenzie, C. J.; Toftlund, H. *Inorg. Chem.* **1994**, *33* (14), 3023–3025.
(264) Lis, T. *Acta Crystallogr. B* **1980**, *36* (9), 2042–2046.
(265) Boyd, P. D. W.; Li, Q.; Vincent, J. B.; Folting, K.; Chang, H. R.; Streib, W. E.; Huffman, J. C.; Christou, G.; Hendrickson, D. N. *J. Am. Chem. Soc.* **1988**, *110* (25), 8537–8539.
(266) Aubin, S. M. J.; Sun, Z.; Eppley, H. J.; Rumberger, E. M.; Guzei, I. A.; Folting, K.; Gantzel, P. K.; Rheingold, A. L.; Christou, G.; Hendrickson, D. N. *Inorg. Chem.* **2001**, *40* (9), 2127–2146.
(267) Sun, Z.; Ruiz, D.; Hendrickson, D. N.; Dilley, N. R.; Maple, M. B.; Soler, M.; Folting, K.; Christou, G.; Ribas, J. *Chem. Commun.* **1999**, 1973–1974.
(268) Lampropoulos, C.; Murugesu, M.; Harter, A. G.; Wernsdofer, W.; Hill, S.; Dalal, N. S.; Reyes, A. P.; Kuhns, P. L.; Abboud, K. A.; Christou, G. *Inorg. Chem.* **2013**, *52* (1), 258–272.
(269) Soler, M.; Wernsdorfer, W.; Abboud, K. A.; Huffman, J. C.; Davidson, E. R.; Hendrickson, D. N.; Christou, G. *J. Am. Chem. Soc.* **2003**, *125* (12), 3576–3588.
(270) Soler, M.; Artus, P.; Folting, K.; Huffman, J. C.; Hendrickson, D. N.; Christou, G. *Inorg. Chem.* **2001**, *40* (19), 4902–4912.
(271) Eppley, H. J.; Tsai, H.-L.; de Vries, N.; Folting, K.; Christou, G.; Hendrickson, D. N. *J. Am. Chem. Soc.* **1995**, *117* (1), 301–317.
(272) Thomas, L.; Lionti, F.; Ballou, R.; Gatteschi, D.; Sessoli, R.; Barbara, B. *Nature* **1996**, *383* (6596), 145–147.
(273) Fang, L. *Surface Engineering in Mesoporous Silica for Ti-Based Epoxidation Catalysis*; École Normale Supérieure de Lyon; Université Bernard-Lyon I; France, 2012.
(274) Sing, K. S. W. *Pure Appl. Chem.* **1985**, *57* (4), 603–619.
(275) Kruk, M.; Jaroniec, M.; Kim, J. M.; Ryoo, R. *Langmuir* **1999**, *15* (16), 5279–5284.
(276) Kruk, M.; Jaroniec, M.; Sayari, A. *Langmuir* **1997**, *13* (23), 6267–6273.
(277) Brunauer, S.; Emmett, P. H.; Teller, E. *J. Am. Chem. Soc.* **1938**, *60* (2), 309–319.
(278) Shull, C. G.; Elkin, P. B.; Roess, L. C. *J. Am. Chem. Soc.* **1948**, *70* (4), 1410–1414.
(279) Lippens, B. C.; de Boer, J. H. *J. Catal.* **1965**, *4* (3), 319–323.
(280) Franke, O.; Schulz-Ekloff, G.; Rathouský, J.; Stárek, J.; Zukal, A. *J. Chem. Soc. Chem. Commun.* **1993**, 724–726.
(281) Branton, P. J.; Hall, P. G.; Sing, K. S. W. *J. Chem. Soc. Chem. Commun.* **1993**, 1257–1258.
(282) Kruk, M.; Jaroniec, M.; Sayari, A. *J. Phys. Chem. B* **1997**, *101* (4), 583–589.

(283) Branton, P. J.; Hall, P. G.; Sing, K. S. W.; Reichert, H.; Schüth, F.; Unger, K. K. *J. Chem. Soc. Faraday Trans.* **1994**, *90* (19), 2965–2967.
(284) Gregg, S. J.; Sing, K. S. W. *Adsorption, surface area, and porosity*; Academic Press, 1991.
(285) Horváth, G.; Kawazoe, K. *J. Chem. Eng. Jpn.* **1983**, *16* (6), 470–475.
(286) Ph.D. thesis: Nicole, L. *Adsorption d'une molécule hydrophobe modèle, le C_{60}, sur des matériaux aux tensioactifs structurants : les MCM-41.* Université des Sciences et Techniques du Languedoc, Montpellier, France, 2002.
(287) Juan L. Vivero-Escoto; Brian G. Trewyn; Victor S.-Y. Lin. *Annu. Rev. Nano Res.* **2009**, *3*, 191–231.
(288) Trewyn, B. G.; Giri, S.; Slowing, I. I.; Lin, V. S.-Y. *Chem. Commun.* **2007**, 3236–3245.
(289) Slowing, I. I.; Vivero-Escoto, J. L.; Wu, C.-W.; Lin, V. S.-Y. *Adv. Drug Deliv. Rev.* **2008**, *60* (11), 1278–1288.
(290) Abry, S.; Thibon, A.; Albela, B.; Delichère, P.; Banse, F.; Bonneviot, L. *New J. Chem.* **2009**, *33* (3), 484.
(291) Zhang, K.; Lam, K.-F.; Albela, B.; Xue, T.; Khrouz, L.; Hou, Q.-W.; Yuan, E.-H.; He, M.-Y.; Bonneviot, L. *Chem. – Eur. J.* **2011**, *17* (50), 14258–14266.
(292) Manceau, A.; Marcus, M. A.; Grangeon, S. *Am. Mineral.* **2012**, *97*, 816–827.
(293) Chalmin, E.; Farges, F.; Jr, G. E. B. *Contrib. Mineral. Petrol.* **2008**, *157* (1), 111–126.
(294) Moulder, J. F. *Handbook of X-ray Photoelectron Spectroscopy: A Reference Book of Standard Spectra for Identification and Interpretation of XPS Data*; Physical Electronics Division, Perkin-Elmer Corporation, 1992.
(295) Bratt, A.; Barron, A. R. XPS of Carbon Nanomaterials. *Openstax CNX*, 2011.
(296) Cerrato, J. M.; Hochella, M. F.; Knocke, W. R.; Dietrich, A. M.; Cromer, T. F. *Environ. Sci. Technol.* **2010**, *44* (15), 5881–5886.
(297) Nelson, A. J.; Reynolds, J. G.; Christou, G. *J. Appl. Phys.* **2003**, *93* (5), 2536–2539.
(298) García-Martín, J.; López-Garzón, R.; Godino-Salido, M. L.; Cuesta-Martos, R.; Gutiérrez-Valero, M. D.; Arranz-Mascarós, P.; Stoeckli-Evans, H. *Eur. J. Inorg. Chem.* **2005**, *2005* (15), 3093–3103.
(299) Iler, R. K. *The Chemistry of Silica: Solubility, Polymerization, Colloid and Surface Properties and Biochemistry of Silica*; Wiley-Interscience: New York, 1979.
(300) Ph.D. thesis: Calmettes, S. *Conception d'un catalyseur par greffage d'un complexe de ruthénium en milieu confiné ; Application à l'oxydation sélective.* Ecole normale supérieure de lyon - ENS LYON, Université Claude Bernard - Lyon I, 2008.
(301) Lu, Y.; Yin, Y.; Mayers, B. T.; Xia, Y. *Nano Lett.* **2002**, *2* (3), 183–186.
(302) Pinho, S. L. C.; Pereira, G. A.; Voisin, P.; Kassem, J.; Bouchaud, V.; Etienne, L.; Peters, J. A.; Carlos, L.; Mornet, S.; Geraldes, C. F. G. C.; Rocha, J.; Delville, M.-H. *ACS Nano* **2010**, *4* (9), 5339–5349.
(303) Xingcui Guo, Z. Q. *Catal. Lett.* **2009**, *128* (3), 405–412.
(304) Liu, N.; Assink, R. A.; Brinker, C. J. *Chem. Commun.* **2003**, 370–371.
(305) Yang, C.; Zibrowius, B.; Schüth, F. *Chem. Commun.* **2003**, 1772–1773.
(306) Azmat, M. U.; Guo, Y.; Guo, Y.; Wang, Y.; Lu, G. *J. Mol. Catal. Chem.* **2011**, *336* (1–2), 42–50.
(307) Tsai, C.-T.; Pan, Y.-C.; Ting, C.-C.; Vetrivel, S.; Chiang, A. S. T.; Fey, G. T. K.; Kao, H.-M. *Chem. Commun.* **2009**, 5018–5020.
(308) Pan, Y.-C.; Wu, H.-Y.; Lee, L.-P.; Jheng, G.-L.; Fey, G. T. K.; Kao, H.-M. *Micropor. Mesopor. Mat.* **2009**, *123* (1–3), 78–90.
(309) Lin, C.-H.; Cheng, S.-H.; Liao, W.-N.; Wei, P.-R.; Sung, P.-J.; Weng, C.-F.; Lee, C.-H. *Int. J. Pharm.* **2012**, *429* (1–2), 138–147.
(310) Bek, D.; Gawin, R.; Grela, K.; Balcar, H. *Catal. Commun.* **2012**, *21*, 42–45.
(311) Sumiya, S.; Kubota, Y.; Oumi, Y.; Sadakane, M.; Sano, T. *Appl. Catal. Gen.* **2010**, *372* (1), 82–89.
(312) Schoenfeldt, N. J.; Notestein, J. M. *ACS Catal.* **2011**, *1* (12), 1691–1701.
(313) Bérubé, F.; Kaliaguine, S. *Micropor. Mesopor. Mat.* **2008**, *115* (3), 469–479.
(314) Ph.D. thesis: Fang, L. *Surface Engineering of Mesoporous Silica for Ti-Based Epoxidation Catalysts*; Lyon, École normale supérieure, 2012.
(315) Shimojima, A.; Umeda, N.; Kuroda, K. *Chem. Mater.* **2001**, *13* (10), 3610–3616.

(316) Musić, S.; Filipović-Vinceković, N.; Sekovanić, L. *Braz. J. Chem. Eng.* **2011**, *28* (1), 89–94.
(317) Fernández, G.; Corbella, M.; Alfonso, M.; Stoeckli-Evans, H.; Castro, I. *Inorg. Chem.* **2004**, *43* (21), 6684–6698.
(318) Angelici, R. J. *Synthesis and technique in inorganic chemistry*; University Science Books, 1986.
(319) Ph.D. thesis: V. Gómez. *Compuestos modelo de enzimas de manganeso. Estudio magnético y actividad catalítica.* Universitat de Barcelona, Spain, 2011.
(320) Gagliardi, L. G.; Castells, C. B.; Ràfols, C.; Rosés, M.; Bosch, E. *Anal. Chem.* **2007**, *79* (8), 3180–3187.
(321) Khangulov, S. V.; Pessiki, P. J.; Barynin, V. V.; Ash, D. E.; Dismukes, G. C. *Biochemistry* **1995**, *34* (6), 2015–2025.
(322) Stemmler, T. L.; Sossong, Thomas M.; Goldstein, J. I.; Ash, D. E.; Elgren, T. E.; Kurtz, Donald M.; Penner-Hahn, J. E. *Biochemistry* **1997**, *36* (32), 9847–9858.
(323) Barynin, V. V.; Hempstead, P. D.; Vagin, A. A.; Antonyuk, S. V.; Melik-Adamyan, W. R.; Lamzin, V. S.; Harrison, P. M.; Artymiuk, P. J. *J. Inorg. Biochem.* **1997**, *67* (1), 196.
(324) Palopoli, C.; Bruzzo, N.; Hureau, C.; Ladeira, S.; Murgida, D.; Signorella, S. *Inorg. Chem.* **2011**, *50* (18), 8973–8983.
(325) Bouchoucha, M.; C.-Gaudreault, R.; Fortin, M.-A.; Kleitz, F. *Adv. Funct. Mater.* **2014**, *24* (37), 5911–5923.
(326) Kim, T.-H.; Eltohamy, M.; Kim, M.; Perez, R. A.; Kim, J.-H.; Yun, Y.-R.; Jang, J.-H.; Lee, E.-J.; Knowles, J. C.; Kim, H.-W. *Acta Biomater.* **2014**, *10* (6), 2612–2621.
(327) Wang, S.; Folting, K.; Streib, W. E.; Schmitt, E. A.; McCusker, J. K.; Hendrickson, D. N.; Christou, G. *Angew. Chem. Int. Ed. Engl.* **1991**, *30* (3), 305–306.

SCIENTIFIC PUBLICATIONS

SCIENTIFIC PUBLICATIONS

Luis Escriche-Tur, Montserrat Corbella, Mercè Font-Bardia, Isabel Castro, Laurent Bonneviot, and Belén Albela. "*Biomimetic Mn-Catalases Based on Dimeric Manganese Complexes in Mesoporous Silica for Potential Antioxidant Agent*." Published in October the 20th of 2015 in ***Inorganic Chemistry***. **2015**, 54, 10111–10125. DOI: 10.1021/acs.inorgchem.5b01425

Abstract:

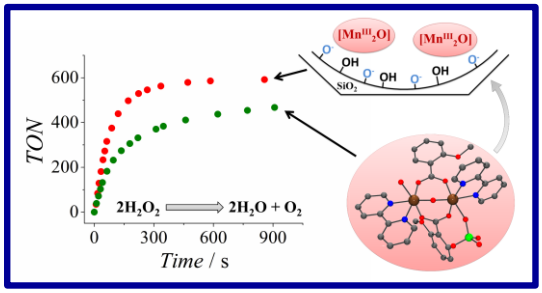

Two new structural and functional models of the Mn-catalase with formula [{Mn^{III}(bpy)(H_2O)}(μ-2-$MeOC_6H_4CO_2$)$_2$(μ-O){Mn^{III}(bpy)(X)}]X, where X = NO_3 (**1**) and ClO_4 (**2**) and bpy = 2,2'-bipyridine, were synthesized and characterized by X-ray diffraction. In both cases, a water molecule and an X ion occupy the monodentate positions. The magnetic properties of these compounds reveal a weak antiferromagnetic behavior ($2J = -2.2$ cm^{-1} for **1** and -0.7 cm^{-1} for **2**, using the spin Hamiltonian $H = -2JS_1S_2$) and negative zero-field splitting parameter D_{Mn} (-4.6 cm^{-1} and -3.0 cm^{-1} for **1**and **2**, respectively). This fact, together with the nearly orthogonal orientation of the Jahn–Teller axes of the Mn^{III} ions explain the unusual shape of $\chi_M T$ versus T plot at low temperature. Compound **1** presents a better catalase activity than **2** in CH_3CN-H_2O media, probably due to a beneficial interaction of the NO_3^- ion with the Mn complex in solution. These compounds were successfully inserted inside two-dimensional hexagonal mesoporous silica (MCM-41 type) leading to the same hybrid material ([Mn_2O]@SiO_2), without the X group. The manganese complex occupies approximately half of the available pore volume, keeping the silica's hexagonal array intact. Magnetic measurements of [Mn_2O]@SiO_2 suggest that most of the dinuclear unit is preserved, as a non-negligible interaction between Mn ions is still observed. The X-ray photoelectron spectroscopy analysis of the Mn 3s peak confirms that Mn remains as Mn^{III} inside the silica. The catalase activity study of material [Mn_2O]@SiO_2 reveals that the complex is more active inside the porous silica, probably due to the surface silanolate groups of the pore wall. Moreover, the new material shows catalase activity in water media, while the coordination compounds are not active.

Luis Escriche-Tur, Jesús Jover, Mercè Font-Bardia, Gabriel Aullón, and Montserrat Corbella. "*Magnetic Behavior of Heterometallic Wheels Having a* $[Mn^{IV}_6M_2O_9]^{10+}$ *Core with M =* Ca^{2+} *and* Sr^{2+}*.*" Published in December the 8th of 2015 in ***Inorganic Chemistry***. **2015**, *54* (24), pp 11596–11605. DOI: 10.1021/acs.inorgchem.5b02131

Abstract:

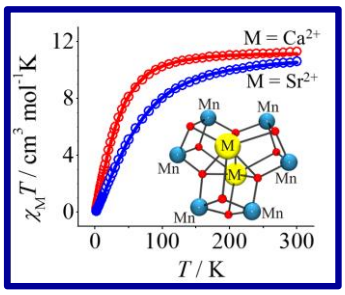

Two new heterometallic Mn^{IV}-M^{2+} compounds with formula [$Mn_6M_2O_9$(4-^{t}BuC_6H_4COO)$_{10}$(4-^{t}BuC_6H_4COOH)$_5$] (M = Ca^{2+} (**1**), Sr^{2+} (**2**)) have been crystallized. The core of both compounds consists of a planar Mn_6 ring, where the Mn^{IV} ions are alternatively bridged by (μ_3-O)$_2$(μ-RCOO) and (μ_4-O)(μ-RCOO)$_2$ ligands, and the two alkaline earth ions are located to both sides of the wheel, linked to the oxo bridges, generating three fused [$Mn_2M_2O_4$]$^{4+}$ cuboids. These compounds show a net antiferromagnetic behavior, more important for **2** (Sr^{2+}) than for **1** (Ca^{2+}). The fitting of the experimental data was

performed with the support of DFT calculations, considering four different exchange pathways: two between adjacent Mn^{IV} ions (J_1 and J_2) and two between nonadjacent Mn^{IV} ions (J_3 and J_4). The results of the analysis show that J_1 and J_2 are of the opposite sign, the ferromagnetic contribution corresponding to the $[Mn_2(\mu_4\text{-}O)(\mu\text{-}RCOO)_2]^{4+}$ unit (J_2). The influence of the M^{2+} ions in the magnetic behavior is analyzed for **1** and **2** and for three hypothetical models with the structural parameters of **1** containing Mg^{2+}, Sr^{2+}, or without the M^{2+}ions. In spite of the diamagnetic character of the alkaline earth ions, their influence on the magnetic behavior has been evidenced and correlated with their polarizing effect. Moreover, the magnetic interactions between nonadjacent ions are non-negligible.

Luis Escriche-Tur, Merce Font-Bardia, Belen Albela and Montserrat Corbella. *New insights into the comprehension of the magnetic properties of dinuclear Mn(III) compounds with general formula [{MnL(NN)}$_2$(μ-O)(μ-n-RC$_6$H$_4$COO)$_2$]X$_2$."* Published in May the 30th of 2016 in ***Dalton Transactions***. **2016**, 45, 11753–11764. DOI: 10.1039/C6DT01097K

Abstract:

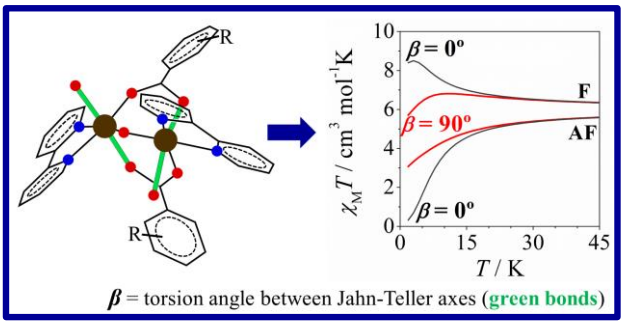

Five new dinuclear Mn(III) compounds with benzoato derivative bridges [{Mn(bpy)L}$_2$(μ-O)(μ-*n*-RC$_6$H$_4$COO)$_2$]X$_2$ (*n*-R = 3-MeO, 4-MeO and 4-*t*Bu, X = NO_3 and ClO_4) were synthesised and characterised. According to X-ray diffraction, the X anions tend to be coordinated to the Mn ions and may occupy the place of the monodentate ligand L. Two structural isomers that only differ in one of their monodentate ligands have been obtained with the 3-MeOC$_6$H$_4$COO$^-$ bridges. For all compounds, the Mn(III) ions display elongated octahedra with a pronounced rhombic distortion. To quantify these distortions separately, the elongation and rhombicity paràmetres ⊿ and ρ have been defined. The magnetic study shows a good relationship between the distortion of the coordination polyhedra and the zero field splitting parameters (D_{Mn} and E_{Mn}). From the magnetic data of a powder sample, it is possible to determine the sign and magnitude of D_{Mn} for ferromagnetic systems or weak antiferromagnetic systems with $D_{Mn} < 0$. For this kind of dinuclear compound, the R group at the *meta* position, the rhombic distortion of the octahedra, and large torsion angles between the Jahn–Teller axes lead to ferromagnetic interactions.

ACKNOWLEDGEMENTS

ACKNOWLEDGEMENTS

English version:

The last pages arrive and I could not finish this without mentioning how much I appreciated your company. People normally overflow the Acknowledgments with a huge list of names. I thought: "That would be too common". Besides, I could forget someone and that would be unforgivable. Instead, I decided to dedicate all of you some words, which I sincerely believe and come from my heart. To my family, to all my friends, whether we've shared moments in the lab or my spare time, to my colleagues, to all the people who collaborated with me, and to my Ph.D. advisors, the following words are for you.

Every single person that appears in your life is unique and have a relevance, an importance. Our personality is indeed molded after each interaction with others. What is a Ph.D.? For me, a Ph.D. is an opportunity for interacting with the world. Science have been a significant part of it. Nevertheless, what makes something important is not always the content, but the surroundings. In the peripheries of my duties, I've been constantly stumbling upon new or already known individuals, most of you with great personalities. Some of you have become a part of me, others already were.

I can't imagine having done the same without you. No matter if successes or fails, you were always there, in good and bad moments. Bitter or sweet, all that I remember now I do it because I care, and because I recognize the importance of your presence in my life. Just note this: it is not important what we do, but who we do it with.

Of course they are always ones with privileges, and those are reserved for my mom and dad, who, with all their efforts and knowledges, have granted me the opportunity to be here, and have advised me on my decisions to become who I am nowadays. For everything you've done for me, I sincerely thank you.

Catalan version:

El final s'acosta i no podria acabar això sense comunicar-vos quant he apreciat sa vostra companyia. Sa gent normalment inunda es Agraïments amb llistes llarguíssimes plenes de noms. Jo, vaig pensar: "Això seria massa comú". A més, podria oblidar-me algú i això seria imperdonable. En es seu lloc, he decidit dedicar-vos unes paraules que sincerament crec i que surten directament des meu cor. A sa meua família, a tots els meus amics, tant si han compartit moments en es laboratori com si hem compartit temps lliure, a nes companys de feina, a tota sa gent que ha col·laborat amb jo, i a nes meus mentors, ses següents paraules són per vosaltres.

Cada persona que apareix en sa teva vida és única i té una rellevància, una importància. De fet, sa nostra personalitat es modela després de cada interacció amb altres. Què és un doctorat? Per mi, un doctorat és una oportunitat per interaccionar amb el món. Sa ciència n'ha set una part significant. No obstant això, lo que fa que una cosa sigui important no sempre és es contingut, sinó s'entorn. Pes voltants de sa meua labor, he estat constantment interaccionant amb gent nova o ja coneguda, la majoria amb excel·lents personalitats. Alguns us heu convertit en part de jo, altres ja ho éreu.

No puc imaginar-me haver fet lo mateix sense vosaltres. No importa si es tractava d'èxits o fracassos, heu estat sempre allí, en bons i mals moments. Amarg o dolç, tot lo que record ara ho faig perquè m'importa, i perquè reconec sa importància de sa vostra presència en sa meua vida. Només tingueu en compte una cosa: el que fem no és tan important, sinó amb qui ho fem.

Com no, sempre hi ha alguns que tenen privilegis, i aquests privilegis estan reservats per sa Mami i es Papito, qui, amb tots es seus esforços i coneixements, m'han donat sa oportunitat d'estar aquí i m'han aconsellat en sa presa de dedicions per convertir-me en qui sóc avui en dia. Per tot lo que heu fet per jo, us dono ses gràcies.